METAL RESISTANCE IN MICROORGANISMS

EDITED BY: Rob Van Houdt, Jon L. Hobman, Raymond J. Turner and Jean-Yves Matroule

PUBLISHED IN: Frontiers in Microbiology

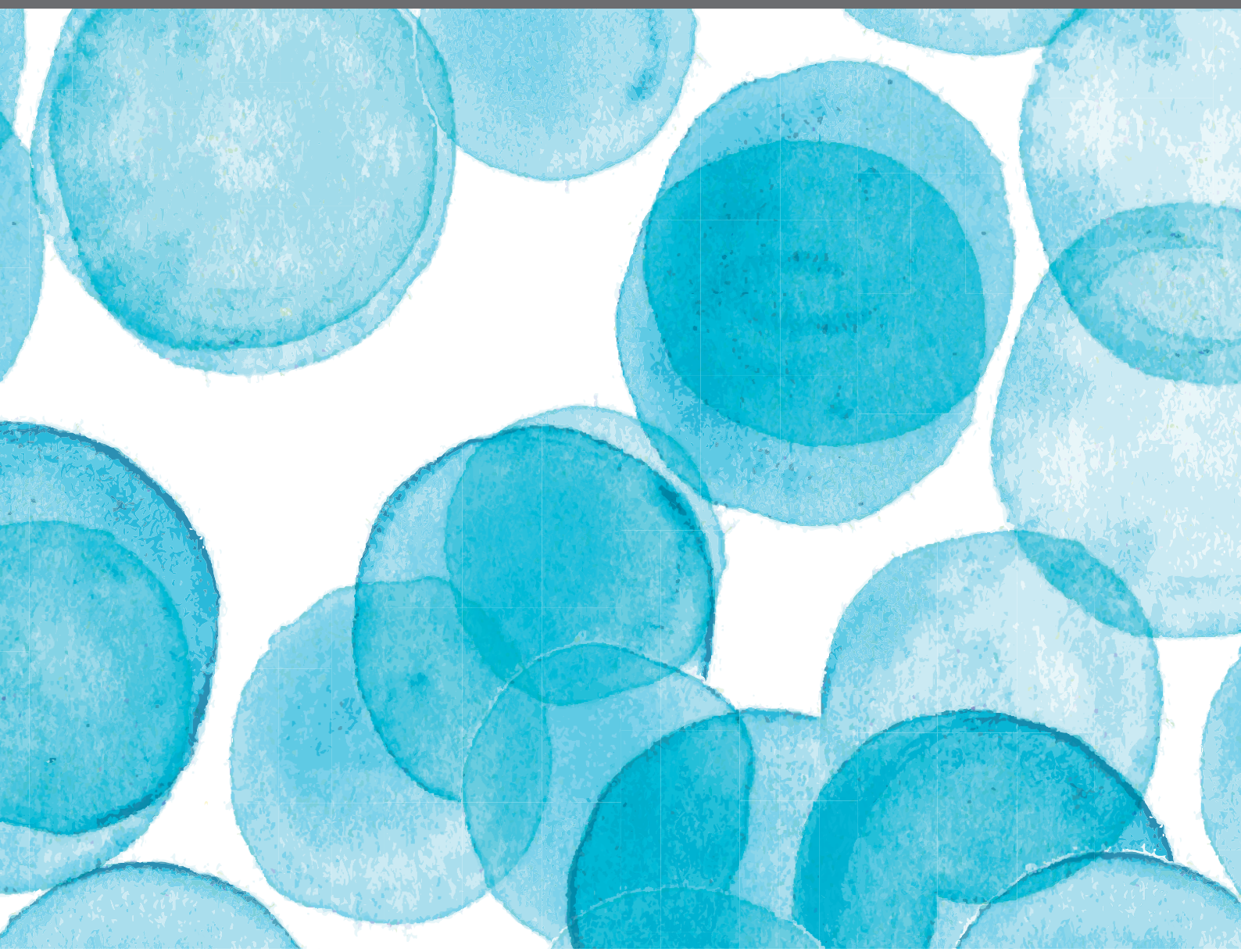

frontiers Research Topics

frontiers

ISSN 1664-8714
ISBN 978-2-88976-059-6
DOI 10.3389/978-2-88976-059-6

About Frontiers

Frontiers is more than just an open-access publisher of scholarly articles: it is a pioneering approach to the world of academia, radically improving the way scholarly research is managed. The grand vision of Frontiers is a world where all people have an equal opportunity to seek, share and generate knowledge. Frontiers provides immediate and permanent online open access to all its publications, but this alone is not enough to realize our grand goals.

Frontiers Journal Series

The Frontiers Journal Series is a multi-tier and interdisciplinary set of open-access, online journals, promising a paradigm shift from the current review, selection and dissemination processes in academic publishing. All Frontiers journals are driven by researchers for researchers; therefore, they constitute a service to the scholarly community. At the same time, the Frontiers Journal Series operates on a revolutionary invention, the tiered publishing system, initially addressing specific communities of scholars, and gradually climbing up to broader public understanding, thus serving the interests of the lay society, too.

Dedication to Quality

Each Frontiers article is a landmark of the highest quality, thanks to genuinely collaborative interactions between authors and review editors, who include some of the world's best academicians. Research must be certified by peers before entering a stream of knowledge that may eventually reach the public - and shape society; therefore, Frontiers only applies the most rigorous and unbiased reviews.
Frontiers revolutionizes research publishing by freely delivering the most outstanding research, evaluated with no bias from both the academic and social point of view. By applying the most advanced information technologies, Frontiers is catapulting scholarly publishing into a new generation.

What are Frontiers Research Topics?

Frontiers Research Topics are very popular trademarks of the Frontiers Journals Series: they are collections of at least ten articles, all centered on a particular subject. With their unique mix of varied contributions from Original Research to Review Articles, Frontiers Research Topics unify the most influential researchers, the latest key findings and historical advances in a hot research area! Find out more on how to host your own Frontiers Research Topic or contribute to one as an author by contacting the Frontiers Editorial Office: frontiersin.org/about/contact

METAL RESISTANCE IN MICROORGANISMS

Topic Editors:
Rob Van Houdt, Belgian Nuclear Research Centre, Belgium
Jon L. Hobman, University of Nottingham, United Kingdom
Raymond J. Turner, University of Calgary, Canada
Jean-Yves Matroule, University of Namur, Belgium

Citation: Van Houdt, R., Hobman, J. L., Turner, R. J., Matroule, J.-Y., eds. (2022). Metal Resistance in Microorganisms. Lausanne: Frontiers Media SA.
doi: 10.3389/978-2-88976-059-6

Table of Contents

frontiers | Frontiers in Microbiology

EDITORIAL
published: 11 April 2022
doi: 10.3389/fmicb.2022.899448

Editorial: Metal Resistance in Microorganisms

Rob Van Houdt[1]*, *Jon L. Hobman*[2], *Jean-Yves Matroule*[3] and *Raymond J. Turner*[4]

[1] Microbiology Unit, Belgian Nuclear Research Centre (SCK CEN), Mol, Belgium, [2] School of Biosciences, University of Nottingham, Sutton Bonington Campus, Sutton Bonington, United Kingdom, [3] Research Unit in Microorganisms Biology (URBM), Narilis Institute, University of Namur, Namur, Belgium, [4] Department of Biological Sciences, Faculty of Science, University of Calgary, Calgary, Alberta, Canada

Keywords: metals, resistance, adaptation, microorganisms, bioremediation

Editorial on the Research Topic

Metal Resistance in Microorganisms

The duality of metals puts them at the forefront of interest in microbial physiology. Whether metals have an essential biological role or not, at high concentrations they are extremely toxic as well as stable and recalcitrant. Nevertheless, modern technology is increasingly dependent on them. Excessive anthropogenic use generates continuous and increasing exposure to metals and metalloids. As a result, many environments are severely contaminated with metals. Although this creates serious environmental problems worldwide, the increasing demand for metals also drives efforts to meet this demand in a sustainable way as well as to increase the end-of-life recycling rate of them.

The interaction between microorganisms and metals is an area of active research. Microbes have co-evolved with the geological changes of the planet and have thus adapted to use metals in their biochemistry, but also have evolved to protect themselves against potential adverse interactions with metals. On the one hand, this teaches us how these interactions lead to adaptation and development of metal resistance, and on the other hand, how these processes can be exploited to remove or convert metals from contaminated environments, to recover them from waste streams, or to synthesize metal-based compounds using ecofriendly biological approaches. The interactions between microorganisms and metals have been studied at different levels. Often the first exploratory step is studying microbial communities in metal-contaminated environments, such as soil. These efforts broaden our knowledge of the diversity of bacterial species coping with metals, which could be exploited for bioremediation purposes (Yu et al.), and help to unravel the interactions between different community members in relation to metal tolerance and remediation (Lupini et al.).

Next, genomic insights, based on cultivable isolates or metagenomics approaches, mature the gene pool that is involved in metal resistance (Chen et al.; Huang et al.) as well as their genomic location and mobility, which will impact microbial adaptation (Huang et al.). In a subsequent step, the functional products of these genes and how these provide the ability to cope with metals can be scrutinized (Chen et al.; Rogiers et al.). Such data not only show how this is beneficial for bacteria in their specific niche, e.g., the survival of *Salmonella enterica* sv. Typhimurium in macrophages (Méndez et al.), but also how it can be employed for bio-based strategies for metal biomineralization, reduction and nanoparticle formation, as seen for tellurite and *Paenibacillus pabuli* (Farias et al.). The latter complements studies using cells and their metabolites, as evidenced by uranium phosphate biomineralization with *Penicillium simplicissimum* KS1 isolated from the

OPEN ACCESS

Edited and reviewed by:
Rustam Aminov,
University of Aberdeen,
United Kingdom

***Correspondence:**
Rob Van Houdt
rvhoudto@sckcen.be

Specialty section:
This article was submitted to Antimicrobials, Resistance and Chemotherapy, a section of the journal Frontiers in Microbiology

Received: *18 March 2022*
Accepted: *21 March 2022*
Published: *11 April 2022*

Citation:
Van Houdt R, Hobman JL, Matroule J-Y and Turner RJ (2022) Editorial: Metal Resistance in Microorganisms. Front. Microbiol. 13:899448. doi: 10.3389/fmicb.2022.899448

flood water of a former uranium mine (Schaefer et al.), and silver nanoparticle formation by a *Viridibacillus* sp. soil isolate (Singh and Mijakovic), respectively.

Finally, the regulatory cascade involved in the regulation of these genes needs to be unraveled in order to fully characterize resistance and adaptation. Not only does this provide insights into how bacteria are primed to respond to metal stress (Carvalho et al.), it also provides mechanistic insights into regulation, for instance the negative regulation of the NmtA metallothionein from *Anabaena* sp. strain PCC 7120 by the α5 SmtB/ArsR metalloregulator AzuR (Divya and Acharya). Insights that are essential if such systems are further applied or exploited in applications.

The diversity of studies within this Research Topic illustrates the variety of questions and challenges that remain in the field of metal-microbe interactions. Here, we have achieved the goal of sampling the latest research on molecular mechanisms deployed by bacteria and communities to adapt and resist metals.

AUTHOR CONTRIBUTIONS

RV, JH, J-YM, and RT wrote sections of the manuscript. All authors contributed to manuscript revision, read, and approved the submitted version.

Conflict of Interest: The authors declare that the research was conducted in the absence of any commercial or financial relationships that could be construed as a potential conflict of interest.

frontiers in Microbiology

ORIGINAL RESEARCH
published: 22 July 2021
doi: 10.3389/fmicb.2021.698834

Cadmium Pollution Impact on the Bacterial Community Structure of Arable Soil and the Isolation of the Cadmium Resistant Bacteria

Xiaoxia Yu[1†], JinTong Zhao[2†], Xiaoqing Liu[2], LiXin Sun[1], Jian Tian[2] and Ningfeng Wu[2*]*

[1] School of Water Resources and Environmental Engineering, East China University of Technology, Nanchang, China,
[2] Biotechnology Research Institute, Chinese Academy of Agricultural Sciences, Beijing, China

Microorganisms play an important role in the remediation of cadmium pollution in the soil and their diversity can be affected by cadmium. In this study, the bacterial community in arable soil samples collected from two near geographical sites, with different degrees of cadmium pollution at three different seasons, were characterized using Illumina MiSeq sequencing. The result showed that cadmium is an important factor to affect the bacterial diversity and the microbial communities in the high cadmium polluted area (the site H) had significant differences compared with low cadmium polluted area (the site L). Especially, higher concentrations of Cd significantly increased the abundance of Proteobacteria and Gemmatimonas whereas decreased the abundance of Nitrospirae. Moreover, 42 Cd-resistant bacteria were isolated from six soil samples and evaluated for potential application in Cd bioremediation. Based on their Cd-MIC [minimum inhibitory concentration (MIC) of Cd^{2+}], Cd^{2+} removal rate and 16S rDNA gene sequence analyses, three *Burkholderia* sp. strains (ha-1, hj-2, and ho-3) showed very high tolerance to Cd (5, 5, and 6 mM) and exhibited high Cd^{2+} removal rate (81.78, 79.37, and 63.05%), six *Bacillus* sp. strains (151-5,151-6,151-13, 151-20, and 151-21) showed moderate tolerance to Cd (0.8, 0.4, 0.8, 0.4, 0.6, and 0.4 mM) but high Cd^{2+} removal rate (84.78, 90.14, 82.82, 82.39, 81.79, and 84.17%). Those results indicated that *Burkholderia* sp. belonging to the phylum Proteobacteria and *Bacillus* sp. belonging to the phylum Firmicutes have developed a resistance for cadmium and may play an important role in Cd-contaminated soils. Our study provided baseline data for bacterial communities in cadmium polluted soils and concluded that Cd-resistant bacteria have potential for bioremediation of Cd-contaminated soils.

Keywords: cadmium pollution, bacterial diversity, seasonal change, Cd-resistant bacteria, bioremediation

OPEN ACCESS

Edited by:
Raymond J. Turner,
University of Calgary, Canada

Reviewed by:
Katy Juarez,
Universidad Nacional Autónoma de México, Mexico
Nikolaos Remmas,
Democritus University of Thrace, Greece

****Correspondence:***
Jian Tian
tianjian@caas.cn
Ningfeng Wu
wuningfeng@caas.cn

† These authors have contributed equally to this work

Specialty section:
This article was submitted to Antimicrobials, Resistance and Chemotherapy, a section of the journal Frontiers in Microbiology

Received: *22 April 2021*
Accepted: *02 July 2021*
Published: *22 July 2021*

Citation:
Yu X, Zhao J, Liu X, Sun L, Tian J and Wu N (2021) Cadmium Pollution Impact on the Bacterial Community Structure of Arable Soil and the Isolation of the Cadmium Resistant Bacteria. Front. Microbiol. 12:698834. doi: 10.3389/fmicb.2021.698834

INTRODUCTION

Heavy metal soil pollution has become a severe environmental problem due to the rapid development of industries such as mining, smelting and agriculture. Moreover, one of the most serious and widespread heavy metal contaminants is cadmium (Cd) (MEP, 2014; Huang et al., 2019). Cd is toxic even at low concentrations of 0.001–0.1 mg L^{-1} and can be accumulated in the human body through the food chain. Once Cd levels become critical, humans can develop emphysema and osteoporosis; and eventually the damage to the lungs, kidneys and liver becomes

irreversible. People suffering from severe chronic Cd poisoning develop the itai-itai disease (Satarug et al., 2017; Genchi et al., 2020; Đukić-Ćosić et al., 2020). Consequently, engineering to remedy heavy metal contaminated soil, especially Cd contaminated soil, is urgently needed.

Soil is an important habitat for a diverse group of microorganisms that play an important role in the soil environment. Microorganisms are regarded as sensors of disturbances in the soil ecosystem since they are far more sensitive to environmental stress than macroorganisms (Khan et al., 2010; Yang et al., 2016; Zhang et al., 2016). Moreover, microorganisms in soil are mainly involved in material decomposition, an important process in maintaining soil biological activity as well as regulating soil nutrient circulation. Stable microbial communities mediate soil environment by stabilizing soil structure and maintaining soil physical and chemical conditions (Bissett et al., 2013). Characteristics of microbial community composition and activity were often used as indicators of soil quality (Hamman et al., 2007; Rubin et al., 2013). Many studies have concentered on changes in soil properties owing to the presence of cadmium as it negatively impacts the indigenous microorganism community, impairing the ecological function they provide (Harichová et al., 2012). Therefore, it is indispensable to analyze the response of microbial communities structure in cadmium contaminated soils.

Owing to the difficulty in comprehensively assessing the structure of the microbial communities associated with using traditional techniques, previous research have explored the effects of cadmium contamination on microbial communities using approaches such as denaturing gradient gel electrophoresis (DGGE) (Wang et al., 2006; Zhang et al., 2009), random amplified polymorphic DNA (RAPD) (Wang et al., 2007a), and phospholipid fatty acids (PLFA) (Liao et al., 2010). These approaches, however, only provide limited insights into the bacterial profiles. Recently, the application of high-throughput sequencing based rRNA for evaluating microbial communities is widely used (Luo et al., 2019; Duan et al., 2020).

In addition, microorganisms have large specific surface areas and high metabolic activity, which making them particularly susceptible to the presence of heavy metals in the soil and impeding their ecological function via adsorption, fixation, complexation, dissolution, oxidation reduction, etc. (Vodyanitskii and Plekhanova, 2014). Moreover, a number of soil microbes have been reported effective in the remediation of heavy metals. For example, Suksabye et al. (2016) reported that the addition of *Pseudomonas aeruginosa* or *Bacillus subtilis* to the soil could reduce the amount of Cd in rice grains obtained from Cd contaminated soil as a result of their Cd remediating characteristic. Currently, microbial remediation of heavy metal contaminated soil is regarded a cost-effective, biotechnology approach (Jin et al., 2018). Therefore, it is necessary to isolate Cd-resistant and Cd-adsorbing microorganisms from Cd contaminated soil, which can be used the remediation of Cd polluted soil.

In this study, firstly we explored the microbial community structure of two sites with significantly different Cd levels but of similar geographical location. We also collected samples from both sites during different seasons. High-throughput sequence analysis of 16S rRNA V3-V4 region was used to characterize the microbial taxa and operational taxonomic units (OTUs) distribution in the different samples. This comprehensive analysis enabled us to correlate microbial taxa and OTUs to Cd contamination, thereby illustrating (1) the effects of Cd exposure on microbial community structure in the soil, and (2) the seasonality of microbial activity at the different sites. Secondly, in order to excavate the available microbial resources, 42 Cd-resistant bacteria were isolated and evaluated for potential application in Cd bioremediation.

MATERIALS AND METHODS

Soil Sites and Samples

Soil samples (0–20 cm) were collected from two different arable soil fields located around a mining area in Xiangtan, Hunan Province, China: L site (27°33′N, 113°15′E) and H site (27°46′N, 112°52′E). The distance between the two regions was about 1.3 km. Moreover, three different seasonal samples of both areas were collected: LA and HA in April 2016; LJ and HJ in July 2016; LO and HO in October 2016. Each time three replicates were sampled and stored at −70°C. Samples were divided in three; one part was used for Miseq, the other to determine the Cd concentration and the last one to isolate Cd-resistant bacteria.

Cd Concentration Analysis

To determine total Cd concentration in the soil samples, 0.5 g air dried sample was digested with 7 mL nitric acid and 3 mL hydrofluoric acid in a polytetrafluoroethylene digestion vessel using a microwave accelerated reaction instrument (CEM-MARS6 Xpress, United States). After complete digestion, the total, water-soluble and filter solution of all samples were measured with a 7,700× Inductively Coupled Plasma Mass Spectrometer (Agilent Technologies, Japan). A heavy metal uncontaminated soil sample (GSS-7, shown in **Table 1**) was used as a standard negative control.

DNA Extraction and 16S rRNA V3–V4 Region Amplicon Sequencing

Total microbial community DNA of all samples were extracted following the Mobio Power Soil DNA isolation Kit protocols. V3-V4 regions of 16S rRNA were amplified using the primers 338F (5′-ACTCCTACGGGAGGCAGCAG-3′) and 806R (5′-GGACTACHVGGGTWTCTAAT-3′). Sequencing of the amplicons was outsourced to Allwegene (Beijing, China);

TABLE 1 | Total cadmium content of samples.

Samples	Total Cd (mg/kg)	Samples	Total Cd (mg/kg)
LA	0.46 ± 0.023	HA	27.11 ± 3.23
LJ	0.36 ± 0.061	HJ	53.70 ± 0.68
LO	0.39 ± 0.12	HO	8.52 ± 1.01
GSS-7	0.11		

amplicons were sequenced on an Illumina Miseq platform. All the sequences data have been submitted to NCBI (National Center for Biotechnology Information), accession numbers were: SAMN07643022 (HA1), SAMN07644976 (HA2), SAMN07644984 (HA3); SAMN07644992 (HJ1), SAMN07644993 (HJ2), SAMN07644994 (HJ3); SAMN07644995 (HO1), SAMN07644997 (HO2), SAMN07645000 (HO3); SAMN07645001 (LA1), SAMN07645003 (LA2), SAMN07645004 (LA3); SAMN07645005 (LJ1), SAMN07645006 (LJ2), SAMN07645007 (LJ3); SAMN07645009 (LO1), SAMN07645010 (LO2), and SAMN07645011 (LO3).

Sequence Analysis

Sequence analysis of the 16S rRNA V3-V4 region amplicon sequences was performed using QIIME Pipeline, Version 1.8.0 (Caporaso et al., 2010). Firstly, low quality reads (average quality score <20) were trimmed and paired-ends sequences were merged to be single sequence according to their overlap sequence (>10 bp). Then, sequences from the samples were distinguished on the basis of the barcodes and primers. Finally, chimeras were deleted using USEARCH (Edgar et al., 2011) and the smaller sequences were removed by MOTHER (Schloss et al., 2009). These high quality sequences were subsequently used for downstream analysis. OTUs were clustered using a 97% identity threshold using UCLUST v1.2.22 (Edgar, 2010) and representative OUT sequence was obtained. Moreover, singleton OUT was removed. A total of 338,077 final sequences were gained for all the samples after filtering for low quality sequences. OTUs were annotated using the Ribosomal Database Project classifier (Wang et al., 2007b). Alpha-diversity (Chao 1, observed species, goods coverage and Shannon) and beta-diversity [principal component analysis (PCA) and Metastats] were analyzed based on Miseq sequence data.

Isolation and Identification of Cd-Resistant Bacteria

To isolate Cd-resistant bacteria, soil samples (2 g) were placed in sterile 0.9% NaCl (18 mL) at 30°C and shaken at 200 rpm for 0.5 h to completely separate bacteria from soil. After settling for several minutes, an aliquot of the suspension was serially diluted (from 10^{-1} and 10^{-4}). Each diluted solution was spread onto an Burk agar plates (0.8 g/L KH_2PO_4, 0.262 g/L $K_2HPO_4{\cdot}3H_2O$, 1 g/L $(NH_4)_2SO_4$, 0.2 g/L $MgSO_4{\cdot}3H_2O$, 1 g/L yeast extract, and 1.5% agar) containing progressively higher concentrations of $CdCl_2$ (1, 3, and 5 mM). To isolate Cd-resistant and bio-safe *Bacillus* bacteria, the bacterial enrichment cultures were heat-shocked at 80°C for 20 min and aerobic *Bacillus* sp. were isolated from the soil by plating on LB agar plates containing different concentrations of $CdCl_2$ (0, 0.5, 1, and 2 mM). Bacterial growth was observed after incubation at 30°C for 24 h. Single colony was picked with sterilized wire loop and re-streaked on $CdCl_2$ supplemented LB agar plates and again incubated at 30°C for 24 h. The process was repeated until the pure culture was obtained. Genomic DNA was isolated using the TIANamp Bacteria DNA kit (TIANGEN Biotech). The 16S rRNA gene was amplified from the extracted DNA using the universal primers the universal forward primer 27f (5′-AGAGTTTGATCCTGGCTCAG-3′) and reverse primer 1492r (5′-TACGGTTACCTTGTTACGACTT-3′). The amplification products were cloned in the pGM-T (TIANGEN Biotech) vector using competent *Escherichia coli* TOP10 cells (TIANGEN Biotech). Sequencing was carried out using T7 and SP6 primers and compared to the GenBank database using the NCBI BLAST program.

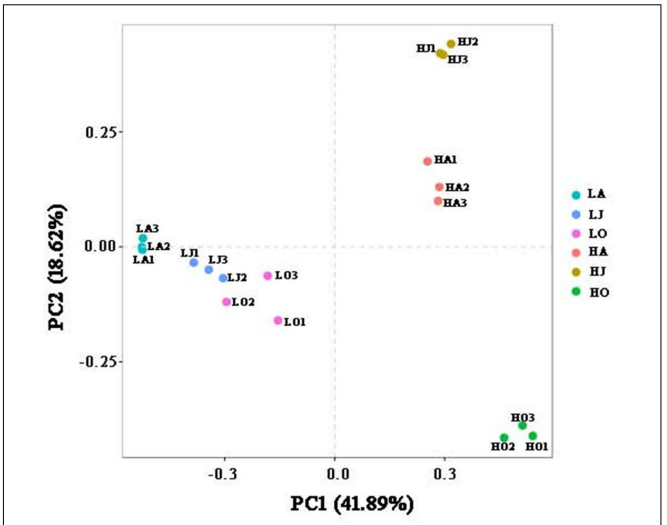

FIGURE 1 | Principal component analysis (PCA) displaying beta-diversity of microbial diversity between samples. PCA was calculated using weighted Unifrac distance. A total of 41.89 and 18.62% of the variations in the bacterial communities could be explained by the first and second principal components, respectively.

Evaluation of Cadmium Resistance and Determination of Cadmium Removal Rate

To evaluate growth in a liquid medium of isolated bacteria, the MIC of Cd^{2+} (MIC-Cd) was determined. LB medium (800 μL) with different concentrations of Cd^{2+} was dispensed into 96-well (12 × 8) microtiter plates (96 × 2-mL wells) with a multi-channel micropipette (rows A to H: 0, 1, 2, 3, 4, 5, 6, and 7 mM). Single colonies of the test strains were inoculated into 3 mL of LB medium and cultured overnight. The test culture (15 μL) was then inoculated into each well of the prepared 96-well plate. After 24 h at 30°C and 750 rpm in an incubator (Heidolph, Viertrieb, Germany), 200 μL of the cell suspension was transferred to a 96-well plate and the turbidity at OD_{600} was measured.

To determine the Cd^{2+} adsorption of isolated bacteria, growth of cells was grown in LB liquid medium supplementation with 0.1 mM $CdCl_2$ and shaken at 200 rpm at 30°C for 24 h. Cells were harvested by centrifugation at 12,000 rpm for 10 min and the supernatant then diluted to an appropriate concentration for analysis. Cd^{2+} concentrations in culture supernatants were measured via atomic absorption spectrophotometry (Z-2000, Hitachi, Japan), with Cd^{2+} removal rate being calculated using the following equation:

Removal rate (%) = $(C_i - C_e)/C_i \times 100$
where C_i and C_e are the initial and equilibrium Cd^{2+} concentrations (mM), respectively.

RESULTS

Cd Concentration of Different Samples

Cd concentrations in all the samples were shown in **Table 1**. Cd concentrations were significantly higher in samples collected from site H (8.52–53.70 mg kg^{-1}) as compared to site L (0.36–0.46 mg kg^{-1}). Among six samples, the Cd concentrations of HJ (53.70 mg kg^{-1}) was highest while the Cd concentrations of LJ was lowest (0.36 mg kg^{-1}). Moreover, Cd concentrations of soil samples from site L were similar across the different seasons, whereas there was an obvious seasonal effect on the Cd concentrations for the H site samples. Specifically, the Cd content of HJ was about 2.0-fold and 6.3-fold higher than that of HA and HO, respectively.

Effects of Cd Concentration and Seasons on Soil Microbial Community Structure

Rarefaction curve analysis showed that the quantity of OTUs was enough to reach saturation, indicated that the sequencing depth was sufficient to characterize the microbial community composition (**Supplementary Figure 1**). The OTU densities of soil samples from site H increased with increasing Cd concentration (HJ > HA > HO), while the OTU density of sample LJ with the lower Cd contamination level was higher than those of sample LA and LO (**Supplementary Table 1**). Comparison of the different sites in the same season showed that HA and HJ have more defined OTUs than LA and LJ, respectively. Bacterial alpha diversity, including the chao1, observed species, PD whole tree and Shannon, varied among the six soil samples. We observed the highest diversity at location with HJ, whereas the lowest diversity at location with HO (**Supplementary Figure 2**). However, results of the PCA supported the previous results, showing that soil microbial communities clustered strongly based on Cd concentration grade (**Figure 1**). A total of 41.89 and 18.62% of the variations in the bacterial communities could be explained by the first and second principal components, which also indicated that the cadmium concentration is the key factor to affect the bacterial diversity of the soil (**Figure 1**). Further, all samples from site L (LA, LJ, and LO) clustered tightly whereas samples from site H were more dispersed (**Figure 1**). These results indicated that the seasonal change in microbial community structure in high Cd contaminated soil was more distinct than in low Cd contaminated soil.

Effects of Cd Concentration and Seasons on Soil Microbial Community Composition and Diversity

A total of 338,077 high-quality bacterial 16S rRNA gene sequences were obtained from 18 samples, ranging from 10,812 to 23,059 sequences per sample (**Supplementary Table 1**).

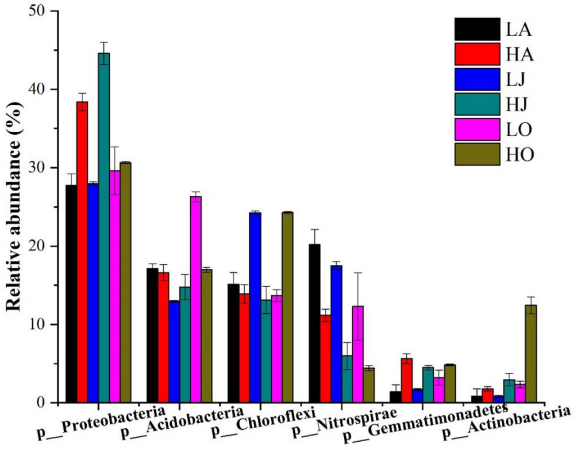

FIGURE 2 | Community composition of dominant bacterial phyla for six samples of different Cd concentrations (LA: 0.46 mg/kg; LJ: 0.36 mg/kg; LO: 0.39 mg/kg; HA: 27.11 mg/kg; HJ: 53.70 mg/kg; HO: 8.52 mg/kg). The relative abundances of Proteobacteria (HA:38.4%, LA:27.77%; HJ:44.59%, LJ:27.98%; HO:30.65%, and LO:29.60%) and Gemmatimonadetes (HA:5.62%, LA: 1.41%; HJ:4.48%, LJ:1.69%; HO:4.82%, and LO:3.21%) at the site H were higher than that of site L, whereas the abundance of Nitrospirae (HA: 11.16%, LA: 20.17%; HJ: 5.98%, LJ: 17.49%; HO: 4.43%, and LO: 12.28%) at the site H was lower than that of site L.

Among the total 16S rRNA gene sequences, 71 sequences were classified as archaea, accounting for 0.02% of total sequences. The remaining sequences belonged to bacteria (338006 of 338077), accounting for 99.98% of the 16S rRNA gene sequences, and presented 47 phyla. Specifically, the dominant phyla, consisting of 1% (relative abundance) or more to total community composition, are shown in **Figure 2**. Proteobacteria (27.77–44.59%), Acidobacteria (12.95–26.29%), Chloroflexi (13.11–24.28%), Nitrospirae (4.43–20.17%), Gemmatimonadetes (1.40–5.62%), and Actinobacteria (0.80–12.43%) were the six largest phyla in all samples. Among these more abundant phyla, it was observed that the relative abundances of Proteobacteria, Gemmatimonadetes, and Actinobacteria at the site H were higher than that of site L, whereas the abundance of Nitrospirae at the site H was lower than that of site L (**Figure 2**). Additionally, we found that the relative abundances of five levels (phylum, class, order, family, and genus) of *Gemmatimonas* at the site H were all higher than that of site L. However, the relative abundances of four levels (phylum, class, order, and family) of *Nitrospira* at the site H were all lower than that of site L while the abundances of *Nitrospira* at the site H was higher than that of site L (**Supplementary Figure 3**).

Figure 3 shows a heatmap of soil bacterial community for six samples of different Cd content at the genus level. From the corresponding cluster analysis of the 20 abundant bacterial genera, the *Bryobacter*, *Geobacter*, *Gemmatimonas*, *Haliangium*, *Anaeromyxobacter*, *Nitrospira*, *Candidatus of Koribacter*, and *Candidatus of Solibacter* had higher contents in most soil samples. Among these more abundant bacterial genera, it was observed that the relative abundances of *Gemmatimonas, Haliangium*, and

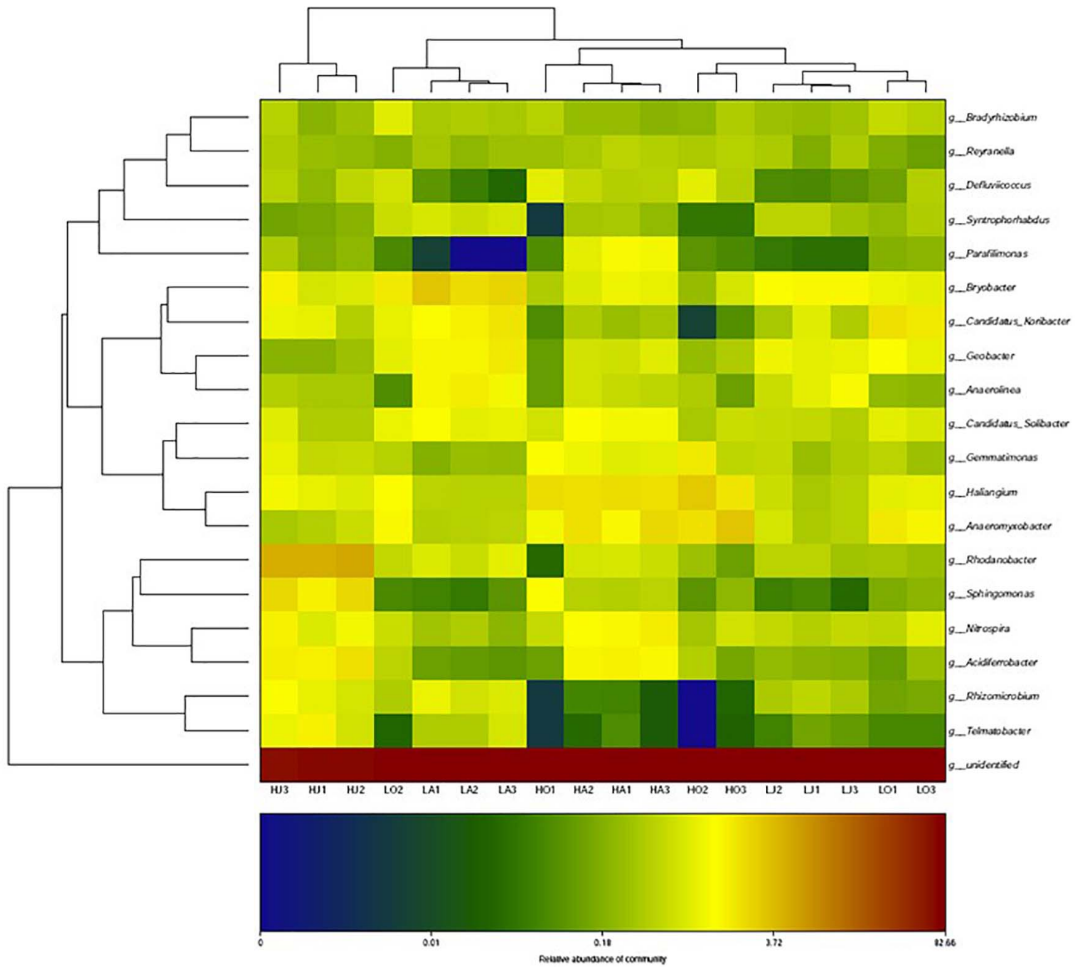

FIGURE 3 | Heatmap of the cluster analysis for top-20 most abundant bacteria at genus-level for the six samples of different Cd concentrations (LA: 0.46 mg/kg; LJ: 0.36 mg/kg; LO: 0.39 mg/kg; HA: 27.11 mg/kg; HJ: 53.70 mg/kg; HO: 8.52 mg/kg).

Anaeromyxobacter at the site H were all higher than that of site L, whereas the abundance of *Bryobacter*, *Geobacter*, and *Candidatus of Koribacter* at site H were all lower than that of site L. Specifically, the abundance of *Rhodanobacter*, *Sphingomonas*, *Nitrospira*, *Acidiferrobacter*, *Rhizomicrobium*, and *Telmatobacter* at the site HJ were significantly higher than that of LJ (**Figure 3**).

Further, relative abundances of dominant phyla and genera were influenced by the season. For Proteobacteria, relative abundance (LA: 27.77%, LJ: 27.98%, and LO: 29.60%) were similar in the different seasons at site L, but very different at site H (HA: 38.4%, HJ: 44.59%, and HO: 30.65%). Contrastingly, Acidobacteria abundance at site L (LA: 17.12%, LJ: 12.95%, and LO: 26.29%) were strongly dependent on the season in which the soil sample was taken, whereas seasonality did not greatly affect its abundance at site H (HA: 16.60%, HJ: 14.77%, and HO: 16.95%). In the case of *Nitrospira* abundance, seasonal changes were observed at both sites (LA: 20.17%, LJ: 17.49%, and LO: 12.28%; HA: 11.16%, HJ: 5.98%, and HO: 4.43%) (**Table 2**). Additionally, the relative abundances of the 20 abundant bacterial genera at site H and L were different in varying seasons (**Figure 3**). Taken together, these data clearly suggest that seasonal conditions impact the soil microbiome and the abundance of susceptible populations during seasons responded to the soil Cd content.

To further assess the relative influence of total Cd concentration on microbial taxa, the Pearson correlations between the relative abundant phyla and Cd were calculated (**Table 2**). The results showed that the relative abundances of Proteobacteria (r = 0.989), Gemmatimonas (r = 0.623), Saccharibacteria (r = 0.910), Cyanobacteria (r = 0.712), Chlamydiae (r = 0.691), and Bacteroidetes (r = 0.681) all positively correlated with Cd concentration, while the abundance of Nitrospirae (r = −0.596) and Spirochaetae (r = −0.659) correlated negatively with Cd concentration (**Table 2**). Of the Proteobacteria, the relative abundances of Alphaproteobacteria, Betaproteobacteria, and Gammaproteobacteria were all found to be positively correlated with Cd concentration with the exception of Deltaproteobacteria (**Table 2**). In agreement, the phylum Proteobacteria has previously been reported to be associated with Cd.

Isolation of Cd-Resistant Bacteria and Their Potential for Reducing Cd Concentration

Once having a basic understanding of the bacterial community response to Cd pollution, the potential of microbial bioremediation to reduce Cd levels was investigated. Firstly, the Cd-resistant bacteria were isolated. A total of 17 strains of different morphological bacteria (Colony morphology of partial Cd-resistant strains were showed in **Figure 4A**) were isolated from six Cd-contaminated samples using Bulk agar plates containing 1, 2, and 3 mM Cd^{2+}. Then the MIC-Cd values and the Cd^{2+} removal efficiency of those isolates and 1 negative control strains (*E. coil* BL21) were determined (**Supplementary Table 2**). Among them, the strains ho-3, ha-1, and hj-2 exhibited the higher level of Cd^{2+} resistance than other strains. In detail, the Cd-MIC value of ho-3, ha-1, and hj-2 was 6, 5, and 5 mM, respectively, markedly higher than that of the control strain *E. coli* BL21 (Cd-MIC: 2 mM Cd^{2+}) (**Figure 4B**). However, as shown in **Figure 4C**, ha-1 exhibited the highest Cd^{2+} removal efficiency (81.78%), which was higher than that observed for ho-3 (63.05%) and hj-2 (79.37%), whilst the cadmium removal efficiency of *E. coli* BL21 was 9.57%. These results indicate that Cd-resistant bacteria have potential for bioremediation of Cd-contaminated soils. In addition, all of the 17 bacteria were identified through 16S rDNA analysis (**Supplementary Table 2**). Interestingly, ha-1, hj-2, and ho-3 were identified as *Burkholderia sp.*, which belong to the class of Betaproteobacteria, phylum Proteobacteria. Those results further emphasized the importance of Proteobacteria in Cd pollution remediation. However, the genus *Burkholderia* contains large number of diverse species which include many phytopathogens, such that a group of 17 closely related *Burkholderia* species, the *Burkholderiacepacia* complex (BCC), are responsible for prevalent and potentially lethal pulmonary infections in immunocompromised individuals, such as individuals with cystic (Elshafie and Camele, 2021). Consequently, both Cd resistant and biosafety strains were further screened.

Isolation of *Bacillus* sp. Bacteria With Cd-Resistance From Samples HJ and LJ and Evaluation of Their Cd^{2+} Removal Rate

Bacillus sp. are well-known biocontrol agents against various fungal plant pathogens (Jangir et al., 2018). To isolate Cd-resistant and bio-safe bacteria, *Bacillus* sp. were isolated from the soil samples. According to the above results, there were significant differences in Cd content (HJ: 53.70 mg kg^{-1}, LJ: 0.36 mg kg^{-1}) and microbial community structure between soil samples HJ and LJ (OTUs no. of HJ: 2093, OTUs no. of LJ:1843) although these two soil samples were collected at the same season (**Table 1** and **Supplementary Table 1**). Thus, we focused on screening *Bacillus* sp. with Cd-resistance from HJ and LJ samples. **Supplementary Figure 4** showed that the observation of the screening Cd-resistant *Bacillus* sp. strains on

TABLE 2 | Pearson correlation and t-test analysis of the relative abundance of microbial phyla, classes, and cadmium content.

	LA	LJ	LO	HA	HJ	HO	r^e	p^f
Cd (mg/kg)	0.460	0.360	0.390	27.110	53.700	8.520		
p^a__Proteobacteria (%)	27.770	27.975	29.605	38.396	44.592	30.652	0.989	0.087
c^b__Alphaproteobacteria (%)	5.561	4.368	6.017	7.145	12.458	7.806	0.921	0.108
c__Betaproteobacteria (%)	5.776	4.882	6.027	7.823	9.649	4.173	0.892	0.240
c__Gammaproteobacteria (%)	3.476	2.733	2.748	4.868	11.253	2.109	0.941	0.191
c__Deltaproteobacteria (%)	12.855	15.873	14.740	18.485	11.190	16.542	−0.329	0.395
p__Acidobacteria (%)	17.121	12.947	26.287	16.597	14.766	16.951	−0.340	0.256
p__Chloroflexi (%)	15.130	24.264	13.691	13.902	13.114	24.276	−0.460	0.466
p__Nitrospirae (%)	20.174	17.488	12.281	11.166	5.980	4.433	−0.596	0.006
c__Nitrospira (%)	20.174	17.488	12.281	11.166	5.980	4.433	−0.596	0.006
o__Nitrospirales (%)	20.174	17.488	12.281	11.166	5.980	4.433	−0.596	0.006
f__Nitrospiraceae (%)	15.048	11.798	6.538	6.868	4.521	1.801	−0.468	0.011
p__Gemmatimonadetes (%)	1.408	1.687	3.209	5.624	4.476	4.819	0.623	0.031
c__Gemmatimonadetes (%)	1.408	1.687	3.209	5.624	4.476	4.819	0.623	0.031
o^c__Gemmatimonadales (%)	1.084	1.387	2.920	5.165	4.342	4.711	0.635	0.023
f^d__Gemmatimonadaceae (%)	1.084	1.387	2.920	5.165	4.342	4.711	0.635	0.023
p__Actinobacteria (%)	0.854	0.800	2.342	1.777	2.942	12.433	−0.011	0.133
p__Saccharibacteria (%)	0.022	0.006	0.016	0.131	0.675	0.247	0.910	0.093
p__Cyanobacteria (%)	0.474	0.394	0.428	0.173	1.306	0.150	0.712	0.404
p__Chlamydiae (%)	0.404	0.356	0.117	0.207	0.760	0.111	0.691	0.371
p__Bacteroidetes (%)	2.485	1.478	1.321	2.933	3.255	0.368	0.681	0.322
p__Spirochaetae	0.630	0.469	0.438	0.178	0.100	0.038	−0.659	0.002

P^a represents phylum, C^b represents class, o^c represents order, f^d represents family, r^e represents the Pearson correlation coefficient between the bacterial relative abundance and Cd concentration in soil, p^f represent the p-value of the bacterial relative abundance difference between the H and L samples in t-test analysis.

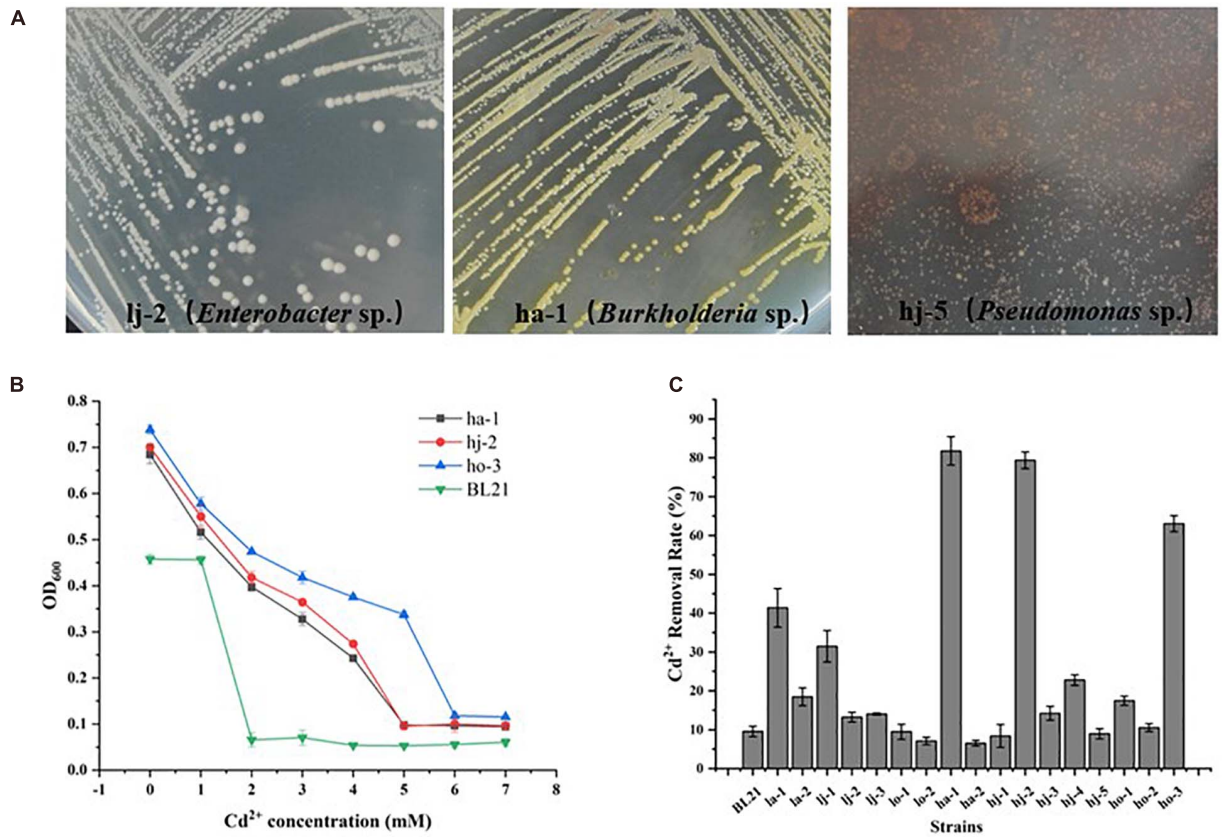

FIGURE 4 | Colony morphology of Cd-resistant bacteria and evaluation of their minimum inhibitory concentration of Cd^{2+} (Cd-MIC) and Cd^{2+} removal rate. **(A)** Colony morphology of partial Cd-resistant strains. **(B)** Determination of Cd-MIC for Cd-resistant bacteria in varied at different concentrations of Cd. **(C)** Evaluation of Cd^{2+} removal rate for Cd-resistant bacteria, which was measured in LB liquid medium supplementation with 0.1 mM $CdCl_2$ and shaken at 200 rpm at 37°C for 24 h.

the LB agar containing 1mM Cd^{2+} after incubation at 30°C for 24 h. For HJ, more than 100 colonies were grown on LB agar, whilst about 15 large colonies were screened for LJ in same conditions (**Supplementary Figure 4**). Additionally, the diversity of microbial morphology in HJ was significantly higher than that in LJ (**Supplementary Figure 4**). Those results were accordance with the microbial community diversity of samples HJ and LJ.

Finally, a total of 21 strains were isolated from HJ while only 4 strains were obtained from LJ. All strains were identified as *Bacillus* sp. (**Supplementary Table 3**). And the Cd-MIC and Cd^{2+} removal rate of those 25 strains were showed in **Supplementary Table 3** and **Figure 5**. The result showed that *Bacillus* sp. strains 151-6 isolated from HJ exhibited the highest Cd^{2+} removal efficiency (90.14%), which was higher than that observed for ha-1 (81.78%). Except for 151-6, the Cd^{2+} removal rate of other five *Bacillus* sp. strains isolated from HJ were more than 80% (151-5: 84.78%, 151-13: 82.39%, 151-21: 81.79%, and 151-23: 84.18%). However, the Cd^{2+} removal rate of 4 *Bacillus* sp. strains (named as 152-1, 152-2, 152-3, and 152-4) obtained from LJ was 15.84, 17.92, 7.74, and 37.94%, respectively. Additionally, the Cd-MIC of *Bacillus* sp. strains were lower than that of *Burkholderia* sp. strains while some of the *Bacillus* sp. strains exhibited higher Cd^{2+} removal rate. Those results indicated that *Bacillus* sp. strains may have a great potential in remediation of cadmium contamination.

DISCUSSION

The function of soil ecosystem depends heavily on soil microbes as they can promote material circulation, nutrient transformation, energy flow, organic matter decomposition and other ecosystem-related biochemical processes (Lozupone et al., 2007; Luo et al., 2019). Many studies use soil microbial communities to evaluate the ecological status of heavy metal contaminated soils (Stefanowicz et al., 2010; Gómez-Sagasti et al., 2012; Burges et al., 2015). Detecting changes in microbial populations and activities is generally more feasible than directly evaluating the physicochemical properties of soil, as the identification of soil microbes may contribute to the evaluation of remediation treatment. The application of high-throughput sequencing based rRNA is more accurate for evaluating soil microbial communities (Luo et al., 2019).

Previous studies have reported that the presence of heavy metals can influence the microbial diversity and also change

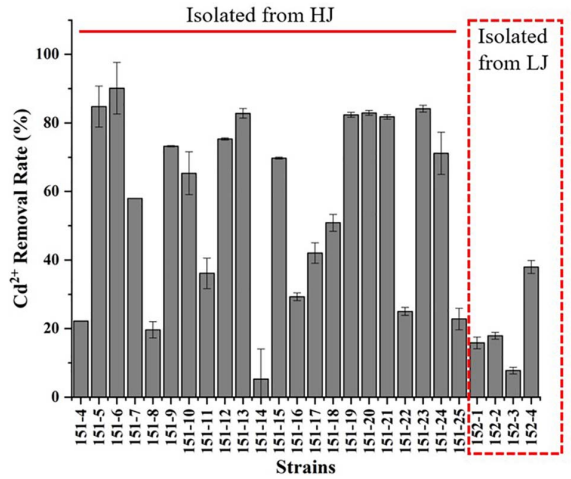

FIGURE 5 | Evaluation of Cd^{2+} removal rate for Cd-resistant *Bacillus* sp. bacteria, which was measured in LB liquid medium supplementation with 0.1 mM $CdCl_2$ and shaken at 200 rpm at 37°C for 24 h.

the community structure and function (Luo et al., 2019; Duan et al., 2020). Wang et al. (2006) found that low contend of heavy metals can stimulate the growth of microorganisms, while at greater concentrations, an inhibitory effect becomes more prominent, which often leads negatively correlated outcomes. Hence, the concentration of Cd in the soil is critical. In this study, we found that there was an obvious seasonal effect on the Cd concentrations for the H site samples. It may be caused by the change of soil basic parameters in different seasons, such as precipitations, temperature, oxygen, pH and so on (Zhang et al., 2007; Yang et al., 2016; Zoghlami et al., 2018). Previous study has reported that the soil Cd content around rice roots was also greatly varied with growing seasons in Hunan Province, China, and the most important factors were humidity and temperature (Liu et al., 2017). Soil Cd concentration in Apr. (HA) might be more likely to subside to deep soil due to high humidity. Whilst soil Cd content in Jul. (HJ) was significant increase might since soluble Cd^{2+} was moved from deep soil to surface layer because of evaporation. On the contrary, soil Cd content in Oct. (HO) was subsided again might be because of low temperature and soil moisture transform. However, the Cd content of soil samples from site L were similar across the different seasons, probably as the Cd concentration in the soil was relatively low and could not cause significant change.

There is considerable debate about the effects of Cd on microbial growth. Previous study reports that Cd addition (>1 mg kg^{-1}) of red paddy soil can inhibit soil microbial biomass (Guo et al., 2018). However, as to yellow cinnamon soils under *Xanthoceras sorbifolium* Bunge and forest soils of Haplic Cambisols in Northeast China, the opposite result was found (Jiang et al., 2018; Duan et al., 2020). Hence, the effects of Cd on microorganism are closely related to the concentrations of Cd and soil type. In our study we found that a significant increase in bacterial diversity with increasing Cd concentrations in site H (**Supplementary Table 1** and **Supplementary Figure 2**), where the soil type is yellow. The result is consistent with the study on yellow cinnamon soils, who found that for all Cd groups (10–100 mg kg^{-1}), 100 mg kg^{-1} of Cd treatment soil bacterial diversity of yellow cinnamon soils under *X. sorbifolium* Bunge was higher than that of 10 mg kg^{-1}.

One previous study also reported a variation in bacterial community response to Cd contamination of agricultural paddy soil (Luo et al., 2019). Our results also illustrate changes in the bacterial community composition caused by the Cd polluted (**Figures 2**, **3**, **Supplementary Figure 3**, and **Table 2**). This is probably as the community readjustment in response to the introduction of Cd, decreased the number of metal-sensitive microorganisms and increased the number of resistant microorganisms in the soil, which eventually led to changes in community composition. The adaption mechanism of these bacterial populations may be attributed to different microorganism life activities. In our study, the relative abundance of Proteobacteria (r = 0.989) and Gemmatimonas (r = 0.623) were all positively correlated with Cd concentration, while the abundance of Nitrospirae (r = −0.596) and Spirochaetae (r = −0.659) correlated negatively with Cd concentration (**Table 2**), suggesting that Proteobacteria and Gemmatimonas are Cd-tolerant, whereas Nitrospirae and Spirochaetae are Cd-sensitive. In agreement, the phylum Proteobacteria has previously been reported to be associated with Cd. A large number of isolated and identified strains that resisted Cd or absorbed Cd belong to Proteobacteria and include *Burkholderia* (Wang et al., 2020), *Sphingomonas* (Cheng et al., 2021), *Pseudomona* (Chellaiah, 2018), and *Rhizobium* (Li et al., 2019). Also many Gram-negative bacteria belonging to Proteobacteria such as *Acinetobacter*, *Ralstonia* (also named *Cupriavidus*) and *Comamonas* exclusively exist in a Cd-cultivation library of mine tailing (Zhang et al., 2007). Moreover, the result of isolating Cd-resistant bacteria showed that three *Burkholderia* sp. (ha-1, hj-2, and ho-3) exhibited strong Cd-tolerance and high Cd^{2+} removal rate. Our study confirms that Proteobacteria may have developed a resistance for Cd and play an important role in Cd-contaminated soils. As for Gemmatimonas, the relative abundances of five levels (phylum, class, order, family, and genus) of *Gemmatimonas* at the site H were all higher than that of site L, suggesting that *Gemmatimonas* are Cd-resistant. The resistance mechanism is related to the precipitation-dissolution balance, which limits the dynamic changes of free metal ions in the soil (Abbas et al., 2018). *Gemmatimonas aurantiaca*, which makes up about 2% of soil bacterial communities, has been reported to accumulate polyphosphate (Zhang et al., 2003). Moreover, the accumulation of polyphosphate has been linked with heavy metal tolerance in bacteria, yeasts and fungi (Trilisenko et al., 2017; Kulakovskaya, 2018; Sathendra et al., 2018; Kolhe et al., 2020). Therefore, it is possible that *Gemmatimonas* can accumulate polyphosphate and precipitate of Cd^{2+} in the soil and therefore explains the higher abundance of this phylum at site H. For microbial communities, heavy metal-resistance species can compensate for the loss of metal-sensitive species, ensuring a stable microecological environment (Awasthi et al., 2014). Nitrospirae, a major bacteria group in our soil samples, possesses a higher heavy metal sensitivity, as reported by previous study (Luo et al., 2019). We found that the relative abundances

of four levels (phylum, class, order, and family) of *Nitrospira* at the site H were all lower than that of site L while the abundances of *Nitrospira* at the site H was higher than that of site L (**Supplementary Figure 3**). Nitrospira are nitrite-oxidizing bacteria (Han et al., 2017) and generally Cd can inhibit nitrification efficiency (Li et al., 2015; Wang et al., 2016), the highly Cd contaminated soils at site H were believed to inhibit growth of Nitrospira. Whereas the result of the abundances of *Nitrospira* with response of Cd was opposite. We inferred that the genus annotation may not be completely.

Identifying key heavy metal-resistant bacterial under Cd stress is very important for remediation of Cd-contaminated soils. In this study, we found that two *Bacillus* sp. strains, 151-6 (Cd^{2+} removal rate: 91.22%, Cd-MIC: 0.4 mM) and 151-25 (Cd^{2+} removal rate: 22.80%, Cd-MIC: 1.0 mM), isolated from the same soil sample but exhibit significant differences in Cd^{2+} resistance and Cd^{2+}adsorption. Our previous work has elucidated the mechanism of Cd-resistance of 151-6 and 151-25, a cadmium efflux system accessory protein and a cadmium resistance protein, was found to play a major role on the Cd^{-} resistance (Yu et al., 2020). Future, the mechanism of Cd-adsorption of 151-6 and 151-25 will be explored. Of course, we also paid attention to the relative abundance of *Bacillus* sp. in soil samples HJ and LJ, which was 0.050 and 0.017%, respectively. This data is consistent with isolation result of *Bacillus* sp. bacteria from samples HJ and LJ. The result indicated that *Bacillus* sp. strains may have a great potential in remediation of cadmium contamination.

Finally, many studies have reported that microbial communities can influenced by specific soil physicochemical properties, such as pH, organic matter, available phosphorus, hydrolytic nitrogen and so on. Unfortunately, we overlooked the effect of these factors on microbial community and the concentration of Cd at the beginning of our experiment. Thus, the basic physiochemical parameters of the six samples were not obtained. However, we recollected the soil samples of the site H and L in June 2021, and the pH and organic matter were measured. The soil pH of the site H and L was 5.04 and 6.56, respectively. And the organic matter of the site H and L was 60.14 and 36.58 g/kg, respectively. The pH value is the key determinant affecting the solubility and liquidity of metal ions, and heavy metal mobility and bioavailability increase due to competition for ligand between H^{+} ions and dissolved metals. Organic matter can enhance the accumulation of organic carbon in the soil, thus increasing the adsorption of Cd^{2+} in the soil. It is likely that the dynamic changes of microbial community structure, cause by heavy metals, may be closely related to the type and chemical morphology of metals and soil physicochemical properties.

In conclusion, we characterized the diversity of the bacterial community in two different Cd contaminated soils collected in three different seasons by high throughput Illumina MiSeq sequencing. The result showed that long-term Cd pollution and season change could cause remarkable changes in bacterial population abundance and composition structure. Then, to excavate the available microbial resources, 42 Cd-resistant bacteria were isolated and evaluated for potential application in Cd bioremediation. Our results showed that both selected *Burkholderia* sp. and *Bacillus* sp. strains have potential for bioremediation of Cd-contaminated soils. Therefore, our study provided baseline data for bacterial communities in cadmium polluted soils and concluded that Cd-resistant bacteria have potential for bioremediation of Cd-contaminated soils.

DATA AVAILABILITY STATEMENT

The datasets presented in this study can be found in online repositories. The names of the repository/repositories and accession number(s) can be found in the article/**Supplementary Material**.

AUTHOR CONTRIBUTIONS

XY, JZ, JT, and NW conceived and coordinated the study and wrote the manuscript. XY, JZ, and JT designed, performed, and analyzed the experiments. XL and LS provided technical assistance and contributed to the preparation of the figures. All authors reviewed the results and approved the final version of the manuscript.

FUNDING

This research was supported by the National Natural Science Foundation of China (NSFC, Grant No. 31770124) and the Natural Science Foundation of Jiangxi Province (20202BABL213039).

ACKNOWLEDGMENTS

We would like to thank our teacher Yunliu Fan for her assistance and guidance. We also thank all colleagues in our lab for constructive discussion and technical support.

SUPPLEMENTARY MATERIAL

The Supplementary Material for this article can be found online at: https://www.frontiersin.org/articles/10.3389/fmicb.2021.698834/full#supplementary-material

REFERENCES

Abbas, S., Rafatullah, M., Hossain, K., Ismail, N., Tajarudin, H., and Khalil, H. A. (2018). A review on mechanism and future perspectives of cadmium-resistant bacteria. *Int. J. Environ. Sci. Technol.* 15, 243–262. doi: 10.1007/s13762-017-1400-5

Awasthi, A., Singh, M., Soni, S. K., Singh, R., and Kalra, A. (2014). Biodiversity acts as insurance of productivity of bacterial communities

under abiotic perturbations. *ISME J.* 8, 2445–2452. doi: 10.1038/ismej.2014.91

Bissett, A., Brown, M. V., Siciliano, S. D., and Thrall, P. H. (2013). Microbial community responses to anthropogenically induced environmental change: towards a systems approach. *Ecol. Lett.* 16, 128–139. doi: 10.1111/ele.12109

Burges, A., Epelde, L., and Garbisu, C. (2015). Impact of repeated single-metal and multi-metal pollution events on soil quality. *Chemosphere* 120, 8–15. doi: 10.1016/j.chemosphere.2014.05.037

Caporaso, J. G., Kuczynski, J., Stombaugh, J., Bittinger, K., Bushman, F. D., Costello, E. K., et al. (2010). QIIME allows analysis of high-throughput community sequencing data. *Nat. Methods* 7, 335–336.

Chellaiah, E. R. (2018). Cadmium (heavy metals) bioremediation by *Pseudomonas aeruginosa*: a minireview. *Appl. Water Sci.* 8:154.

Cheng, C., Wang, R., Sun, L., He, L., and Sheng, X. (2021). Cadmium-resistant and arginine decarboxylase-producing endophytic *Sphingomonas* sp. C40 decreases cadmium accumulation in host rice (Oryza sativa Cliangyou 513). *Chemosphere* 275:130109. doi: 10.1016/j.chemosphere.2021.130109

Duan, C., Liu, Y., Zhang, H., Chen, G., and Song, J. (2020). Cadmium pollution impact on the bacterial community of haplic cambisols in Northeast China and inference of resistant genera. *J. Soil Sci. Plant Nutr.* 20, 1156–1170. doi: 10.1007/s42729-020-00201-5

Đukić-Ćosić, D., Baralić, K., Javorac, D., Djordjevic, A. B., and Bulat, Z. (2020). An overview of molecular mechanisms in cadmium toxicity. *Curr. Opin. Toxicol.* 19, 56–62. doi: 10.1016/j.cotox.2019.12.002

Edgar, R. C. (2010). Search and clustering orders of magnitude faster than BLAST. *Bioinformatics* 26, 2460–2461. doi: 10.1093/bioinformatics/btq461

Edgar, R. C., Haas, B. J., Clemente, J. C., Quince, C., and Knight, R. (2011). UCHIME improves sensitivity and speed of chimera detection. *Bioinformatics* 27, 2194–2200. doi: 10.1093/bioinformatics/btr381

Elshafie, H. S., and Camele, I. (2021). An overview of metabolic activity, beneficial and pathogenic aspects of *Burkholderia* Spp. *Metabolites* 11:321. doi: 10.3390/metabo11050321

Genchi, G., Sinicropi, M. S., Lauria, G., Carocci, A., and Catalano, A. (2020). The effects of cadmium toxicity. *Int. J. Environ. Res. Public Health* 17:3782.

Gómez-Sagasti, M. T., Alkorta, I., Becerril, J. M., Epelde, L., Anza, M., and Garbisu, C. (2012). Microbial monitoring of the recovery of soil quality during heavy metal phytoremediation. *Water Air Soil Pollut.* 223, 3249–3262. doi: 10.1007/s11270-012-1106-8

Guo, B., Chen, X., Jing, F., Zhang, X., Yang, Z., Liu, W., et al. (2018). Effects of exogenous cadmium on microbial biomass and enzyme activity in red paddy soil. *J. Agro Environ. Sci.* 37, 1850–1855.

Hamman, S. T., Burke, I. C., and Stromberger, M. E. (2007). Relationships between microbial community structure and soil environmental conditions in a recently burned system. *Soil Biol. Biochem.* 39, 1703–1711. doi: 10.1016/j.soilbio.2007.01.018

Han, J., Shi, J., Zeng, L., Xu, J., and Wu, L. (2017). Impacts of continuous excessive fertilization on soil potential nitrification activity and nitrifying microbial community dynamics in greenhouse system. *J. Soils Sediments* 17, 471–480. doi: 10.1007/s11368-016-1525-z

Harichová, J., Karelová, E., Pangallo, D., and Ferianc, P. (2012). Structure analysis of bacterial community and their heavy-metal resistance determinants in the heavy-metal-contaminated soil sample. *Biologia* 67, 1038–1048. doi: 10.2478/s11756-012-0123-9

Huang, Y., Wang, L., Wang, W., Li, T., He, Z., and Yang, X. (2019). Current status of agricultural soil pollution by heavy metals in China: a meta-analysis. *Sci. Total Environ.* 651, 3034–3042. doi: 10.1016/j.scitotenv.2018.10.185

Jangir, M., Pathak, R., Sharma, S., and Sharma, S. (2018). Biocontrol mechanisms of *Bacillus* sp., isolated from tomato rhizosphere, against *Fusarium oxysporum f.* sp. lycopersici. *Biol. Control* 123, 60–70. doi: 10.1016/j.biocontrol.2018.04.018

Jiang, W., Yu, X., Tian, Y., Chai, Y., Xiong, Y., Zhong, X., et al. (2018). Effects of cd stress on soil microorganism of *Xanthoceras sorbifolium* Bunge. *Jiangsu Agri. Sci.* 46, 228–231.

Jin, Y., Luan, Y., Ning, Y., and Wang, L. (2018). Effects and mechanisms of microbial remediation of heavy metals in soil: a critical review. *Appl. Sci.* 8:1336. doi: 10.3390/app8081336

Khan, S., Hesham Ael, L., Qiao, M., Rehman, S., and He, J. Z. (2010). Effects of Cd and Pb on soil microbial community structure and activities. *Environ. Sci. Pollut. Res. Int.* 17, 288–296. doi: 10.1007/s11356-009-0134-4

Kolhe, N., Zinjarde, S., and Acharya, C. (2020). Impact of uranium exposure on marine yeast, Yarrowia lipolytica: insights into the yeast strategies to withstand uranium stress. *J. Hazard. Mater.* 381:121226. doi: 10.1016/j.jhazmat.2019.121226

Kulakovskaya, T. (2018). Inorganic polyphosphates and heavy metal resistance in microorganisms. *World J. Microbiol. Biotechnol.* 34:139.

Li, G., Puyol, D., Carvajal-Arroyo, J. M., Sierra-Alvarez, R., and Field, J. A. (2015). Inhibition of anaerobic ammonium oxidation by heavy metals. *J. Chem. Technol. Biotechnol.* 90, 830–837. doi: 10.1002/jctb.4377

Li, Y., Yu, X., Cui, Y., Tu, W., Shen, T., Yan, M., et al. (2019). The potential of cadmium ion-immobilized *Rhizobium pusense* KG 2 to prevent soybean root from absorbing cadmium in cadmium-contaminated soil. *J. Appl. Microbiol.* 126, 919–930. doi: 10.1111/jam.14165

Liao, M., Zhang, H., Yu, S., Chen, C., and Huang, C. (2010). "Effects of cadmium and mercury alone and in combination on the soil microbial community structural diversity," in *Molecular Environmental Soil Science at the Interfaces in the Earth's Critical Zone*, eds J. Xu and P. M. Huang (Berlin: Springer), 337–341. doi: 10.1007/978-3-642-05297-2_99

Liu, Y., Zhang, C., Zhao, Y., Sun, S., and Liu, Z. (2017). Effects of growing seasons and genotypes on the accumulation of cadmium and mineral nutrients in rice grown in cadmium contaminated soil. *Sci. Total Environ.* 579, 1282–1288. doi: 10.1016/j.scitotenv.2016.11.115

Lozupone, C. A., Hamady, M., Kelley, S. T., and Knight, R. (2007). Quantitative and qualitative β diversity measures lead to different insights into factors that structure microbial communities. *Appl. Environ. Microbiol.* 73, 1576–1585. doi: 10.1128/aem.01996-06

Luo, L., Xie, L., Jin, D., Mi, B., Wang, D., Li, X., et al. (2019). Bacterial community response to cadmium contamination of agricultural paddy soil. *Appl. Soil Ecol.* 139, 100–106. doi: 10.1016/j.apsoil.2019.03.022

MEP (2014). *The Ministry of Land and Resources Report on the National Soil Contamination Survey*. China: MEP.

Rubin, B. E., Gibbons, S. M., Kennedy, S., Hampton-Marcell, J., Owens, S., and Gilbert, J. A. (2013). Investigating the impact of storage conditions on microbial community composition in soil samples. *PloS One* 8:e70460. doi: 10.1371/journal.pone.0070460

Satarug, S., Vesey, D. A., and Gobe, G. C. (2017). Kidney cadmium toxicity, diabetes and high blood pressure: the perfect storm. *Tohoku J. Exp. Med.* 241, 65–87. doi: 10.1620/tjem.241.65

Sathendra, E. R., Kumar, R. P., and Baskar, G. (2018). "Microbial transformation of heavy metals," in *Waste Bioremediation*, eds S. Varjani, E. Gnansounou, B. Gurunathan, D. Pant, and Z. Zakaria (Singapore: Springer), 249–263. doi: 10.1007/978-981-10-7413-4_13

Schloss, P. D., Westcott, S. L., Ryabin, T., Hall, J. R., Hartmann, M., Hollister, E. B., et al. (2009). Introducing mothur: open-source, platform-independent, community-supported software for describing and comparing microbial communities. *Appl. Environ. Microbiol.* 75, 7537–7541. doi: 10.1128/aem.01541-09

Stefanowicz, A. M., Niklińska, M., Kapusta, P., and Szarek-Łukaszewska, G. (2010). Pine forest and grassland differently influence the response of soil microbial communities to metal contamination. *Sci. Total Environ.* 408, 6134–6141. doi: 10.1016/j.scitotenv.2010.08.056

Suksabye, P., Pimthong, A., Dhurakit, P., Mekvichitsaeng, P., and Thiravetyan, P. (2016). Effect of biochars and microorganisms on cadmium accumulation in rice grains grown in Cd-contaminated soil. *Environ. Sci. Pollut. Res.* 23, 962–973. doi: 10.1007/s11356-015-4590-8

Trilisenko, L., Kulakovskaya, E., and Kulakovskaya, T. (2017). The cadmium tolerance in Saccharomyces cerevisiae depends on inorganic polyphosphate. *J. Basic Microbiol.* 57, 982–986. doi: 10.1002/jobm.201700257

Vodyanitskii, Y. N., and Plekhanova, I. (2014). Biogeochemistry of heavy metals in contaminated excessively moistened soils (analytical review). *Eurasian Soil Sci.* 47, 153–161. doi: 10.1134/s1064229314030090

Wang, C., Huang, Y., Yang, X., Xue, W., Zhang, X., Zhang, Y., et al. (2020). Burkholderia sp. Y4 inhibits cadmium accumulation in rice by increasing essential nutrient uptake and preferentially absorbing cadmium. *Chemosphere* 252:126603. doi: 10.1016/j.chemosphere.2020.126603

Wang, H., Wang, Y.-P., Lin, Q., Shi, J.-Y., and Chen, Y.-X. (2006). Analysis of rhizosphere microbial community structures in heavy metal-contaminated

soils using PCR and denaturation gradient gel electrophoresis(DGGE). *J. Agro Environ. Sci.* 25, 903–907.

Wang, J., Lu, Y., and Shen, G. (2007a). Combined effects of cadmium and butachlor on soil enzyme activities and microbial community structure. *Environ. Geol.* 51, 1221–1228. doi: 10.1007/s00254-006-0414-y

Wang, Q., Garrity, G. M., Tiedje, J. M., and Cole, J. R. (2007b). Naive Bayesian classifier for rapid assignment of rRNA sequences into the new bacterial taxonomy. *Appl. Environ. Microbiol.* 73, 5261–5267. doi: 10.1128/aem.00062-07

Wang, Y., Ji, M., Zhao, Y., and Zhai, H. (2016). Recovery of nitrification in cadmium-inhibited activated sludge system by bio-accelerators. *Bioresour. Technol.* 200, 812–819. doi: 10.1016/j.biortech.2015.10.089

Yang, F., An, F., Ma, H., Wang, Z., Zhou, X., and Liu, Z. (2016). Variations on soil salinity and sodicity and its driving factors analysis under microtopography in different hydrological conditions. *Water* 8:227. doi: 10.3390/w8060227

Yu, X., Ding, Z., Ji, Y., Zhao, J., Liu, X., Tian, J., et al. (2020). An operon consisting of a P-type ATPase gene and a transcriptional regulator gene responsible for cadmium resistances in Bacillus vietamensis 151–6 and Bacillus marisflavi 151–25. *BMC Microbiol.* 20:18. doi: 10.1186/s12866-020-1705-2

Zhang, C., Nie, S., Liang, J., Zeng, G., Wu, H., Hua, S., et al. (2016). Effects of heavy metals and soil physicochemical properties on wetland soil microbial biomass and bacterial community structure. *Sci. Total Environ.* 557-558, 785–790. doi: 10.1016/j.scitotenv.2016.01.170

Zhang, H., Sekiguchi, Y., Hanada, S., Hugenholtz, P., Kim, H., Kamagata, Y., et al. (2003). Gemmatimonas aurantiaca gen. nov., sp. nov., a gram-negative, aerobic, polyphosphate-accumulating micro-organism, the first cultured representative of the new bacterial phylum Gemmatimonadetes phyl. nov. *Int. J. Syst. Evol. Microbiol.* 53(Pt 4), 1155–1163. doi: 10.1099/ijs.0.02520-0

Zhang, H. B., Yang, M. X., Shi, W., Zheng, Y., Sha, T., and Zhao, Z. W. (2007). Bacterial diversity in mine tailings compared by cultivation and cultivation-independent methods and their resistance to lead and cadmium. *Microb. Ecol.* 54, 705–712. doi: 10.1007/s00248-007-9229-y

Zhang, Y., Zhang, X., Zhang, H., He, Q., Zhou, Q., Su, Z., et al. (2009). Responses of soil bacteria to long-term and short-term cadmium stress as revealed by microbial community analysis. *Bull. Environ. Contam. Toxicol.* 82, 367–372. doi: 10.1007/s00128-008-9613-4

Zoghlami, R. I., Hamdi, H., Boudabbous, K., Hechmi, S., Khelil, M. N., and Jedidi, N. (2018). Seasonal toxicity variation in light-textured soil amended with urban sewage sludge: interaction effect on cadmium, nickel, and phytotoxicity. *Environ. Sci. Pollut. Res.* 25, 3608–3615. doi: 10.1007/s11356-017-0637-3

Conflict of Interest: The authors declare that the research was conducted in the absence of any commercial or financial relationships that could be construed as a potential conflict of interest.

frontiers in Microbiology

ORIGINAL RESEARCH
published: 07 September 2021
doi: 10.3389/fmicb.2021.731711

Comparative Genomic Analysis Uncovered Evolution of Pathogenicity Factors, Horizontal Gene Transfer Events, and Heavy Metal Resistance Traits in Citrus Canker Bacterium *Xanthomonas citri* subsp. *citri*

Chien-Jui Huang[1], Ting-Li Wu[2], Po-Xing Zheng[2], Jheng-Yang Ou[2], Hui-Fang Ni[3] and Yao-Cheng Lin[2]**

[1] Department of Plant Medicine, National Chiayi University, Chiayi, Taiwan, [2] Biotechnology Center in Southern Taiwan, Agricultural Biotechnology Research Center, Academia Sinica, Tainan, Taiwan, [3] Department of Plant Protection, Chiayi Agricultural Experiment Station, Taiwan Agricultural Research Institute, Chiayi, Taiwan

OPEN ACCESS

Edited by:
Jean-Yves Matroule, University of Namur, Belgium

Reviewed by:
Yong-Qiang He, Guangxi University, China
Dawei Xin, Northeast Agricultural University, China

***Correspondence:**
Chien-Jui Huang
chienjui.huang@mail.ncyu.edu.tw
Yao-Cheng Lin
yalin@sinica.edu.tw

Specialty section:
This article was submitted to Antimicrobials, Resistance and Chemotherapy, a section of the journal Frontiers in Microbiology

Received: *28 June 2021*
Accepted: *18 August 2021*
Published: *07 September 2021*

Citation:
Huang C-J, Wu T-L, Zheng P-X, Ou J-Y, Ni H-F and Lin Y-C (2021) Comparative Genomic Analysis Uncovered Evolution of Pathogenicity Factors, Horizontal Gene Transfer Events, and Heavy Metal Resistance Traits in Citrus Canker Bacterium Xanthomonas citri subsp. citri. Front. Microbiol. 12:731711. doi: 10.3389/fmicb.2021.731711

Background: Worldwide citrus production is severely threatened by Asiatic citrus canker which is caused by the proteobacterium *Xanthomonas citri* subsp. *citri*. Foliar sprays of copper-based bactericides are frequently used to control plant bacterial diseases. Despite the sequencing of many *X. citri* strains, the genome diversity and distribution of genes responsible for metal resistance in *X. citri* subsp. *citri* strains from orchards with different management practices in Taiwan are not well understood.

Results: The genomes of three *X. citri* subsp. *citri* strains including one copper-resistant strain collected from farms with different management regimes in Taiwan were sequenced by Illumina and Nanopore sequencing and assembled into complete circular chromosomes and plasmids. CRISPR spoligotyping and phylogenomic analysis indicated that the three strains were located in the same phylogenetic lineages and shared ∼3,000 core-genes with published *X. citri* subsp. *citri* strains. These strains differed mainly in the CRISPR repeats and pathogenicity-related plasmid-borne transcription activator-like effector (TALE)-encoding *pthA* genes. The copper-resistant strain has a unique, large copper resistance plasmid due to an unusual ∼40 kbp inverted repeat. Each repeat contains a complete set of the gene cluster responsible for copper and heavy metal resistance. Conversely, the copper sensitive strains carry no metal resistance genes in the plasmid. Through comparative analysis, the origin and evolution of the metal resistance clusters was resolved.

Conclusion: Chromosomes remained constant among three strains collected in Taiwan, but plasmids likely played an important role in maintaining pathogenicity and developing bacterial fitness in the field. The evolution of pathogenicity factors and

horizontal gene transfer events were observed in the three strains. These data suggest that agricultural management practices could be a potential trigger for the evolution of citrus canker pathogens. The decrease in the number of CRISPR repeats and *pthA* genes might be the result of adaptation to a less stressful environment. The metal resistance genes in the copper resistant *X. citri* strain likely originated from the Mauritian strain not the local copper-resistant *X. euvesicatoria* strain. This study highlights the importance of plasmids as 'vehicles' for exchanging genetic elements between plant pathogenic bacteria and contributing to bacterial adaptation to the environment.

Keywords: *Xanthomonas citri* subsp. *citri*, copper resistance, whole-genome sequence, TALE, plasmid, plasticity

INTRODUCTION

Xanthomonas spp. are a large group of Gram-negative bacteria that cause disease in more than 400 different plant hosts (Timilsina et al., 2020); however, the host range of the individual species is often restricted to a single or a handful of plants in the same botanical family. To aid explanation of this phenomenon, the term "pathovar" was coined and is defined as an intra-subspecific group of strains causing the same disease with host and tissue specificity (Timilsina et al., 2020). Most *Xanthomonas* species infect plants by first colonizing the surface of aerial organs then entering through stomata or wounds; the host may show symptoms. Asiatic citrus canker caused by *Xanthomonas citri* subsp. *citri* is a serious threat to citrus production in most citrus-growing regions in the world (Brunings and Gabriel, 2003; Ference et al., 2018). *X. citri* subsp. *citri* is a genetically monomorphic bacterium (Leduc et al., 2015; Richard et al., 2017b) and has spread geographically from its Asiatic origin to many citrus-growing regions including Taiwan (Pruvost et al., 2014; Leduc et al., 2015; Huang and Ni, 2017). Recent advances in high throughput sequencing have made it possible to sequence the whole genomes of groups within the microbial community rather than a handful of loci (multilocus sequence typing, MLST) and the reconstruction of the repetitive sequence regions such as the complete CRISPR unit (CRISPR spoligotyping) (Jeong et al., 2019). These advances have allowed the detailed study of the evolution, ecology and dissemination of bacterial pathogens (Vinatzer et al., 2014; Timilsina et al., 2019). Genetically monomorphic bacteria have been considered to have low adaptive potential because of low genetic variability (Achtman, 2008). Yet, how these bacteria adapted to diverse environmental conditions and evolved resistance to antibacterial compounds remains unclear.

Citrus canker pathogens are commonly classified into the three pathotypes: A, B and C. Pathotype A was first reported in Asia in the early nineteenth century (Fawcett and Jenkins, 1933) and later spread to all citrus producing regions worldwide. The first genome of *X. citri* subsp. *citri* strain 306 was completely sequenced in 2002 (da Silva et al., 2002). Two variant forms of pathotype A, namely A^* and A^W, have been found in Southeast Asia and Southern Florida in the past 30 years (Timilsina et al., 2020). These variants of the pathotype A showed apparent intraspecific diversity and host specialization. After the reference genome of the pathotype A strain 306 was sequenced, a combination of whole genome sequencing and comparative analysis has contributed to the discovery of polymorphisms associated with potential mechanisms of adaptation in genetically monomorphic bacterium *X. citri* subsp. *citri* (Zhang et al., 2015; Richard et al., 2017b; Gochez et al., 2018). To date, multiple factors including transcription activator-like effectors (TALEs), plasmid-mediated horizontal gene transfers and transposons have been found to play important roles in adaptation, evolution and spread of pathogenicity determinants of *X. citri* subsp. *citri* (Ferreira et al., 2015; Richard et al., 2017b, 2021; Gochez et al., 2018).

TALEs belonging to the PthA family of type III secretion system effector proteins (T3SEs) are the main pathogenicity factor of *X. citri* subsp. *citri* (Brunings and Gabriel, 2003; Abe and Benedetti, 2016; Roeschlin et al., 2019). When injected into host cells, PthA proteins activate expression of disease susceptibility or resistance genes (Brunings and Gabriel, 2003; Abe and Benedetti, 2016; Roeschlin et al., 2019). PthA proteins consist of an N-terminal region for secretion, a central DNA-binding domain and a C-terminal region containing nuclear localization signals and an acidic transcriptional activation domain (Boch and Bonas, 2010). The central DNA-binding domain of the PthA family is composed of almost identical tandem repeats of 33 to 34 amino acids (Boch and Bonas, 2010). Each repeat contains a repeat-variable diresidue (RVD) at the 12th and 13th positions (Boch and Bonas, 2010). In addition, the number of tandem repeats are variable among PthA proteins (Brunings and Gabriel, 2003; Abe and Benedetti, 2016; Roeschlin et al., 2019). The reference *X. citri* subsp. *citri* strain 306 carries four TALE-encoding *pthA* genes located on the plasmids pXAC33 (*pthA1* and *pthA2*) and pXAC64 (*pthA3* and *pthA4*) (da Silva et al., 2002). The *pthA1*, *pthA2*, *pthA3* and *pthA4* genes of strain 306 harbor 16.5, 15.5, 15.5, and 17.5 copies of repeats, respectively (da Silva et al., 2002). Recently, comparative analysis of completely sequenced plasmids from *X. citri* subsp. *citri* revealed clues to rearrangements of plasmids and reshuffling of TALEs among citrus canker strains (Gochez et al., 2018). Furthermore, an experimental evolution study showed that in less than 30 cycles of repeated infections, *X. citri* subsp. *citri* could accumulate sufficient mutations and rearrangements of repeats of TALEs to cause pathogenicity in incompatible hosts (Teper and Wang, 2021).

Copper-based bactericides have been widely used for control of plant bacterial diseases throughout the world. However, frequent applications of copper-based bactericides induce the

evolution and development of bacterial strains that are either resistant or tolerant to copper (Hseu and Hsu, 1991; Wu et al., 1995; Canteros et al., 2008; Behlau et al., 2012b, 2013). Copper resistant (Cu^R) strains of *X. citri* subsp. *citri* have been found across the world (Behlau et al., 2011, 2013). Large-sized plasmids carrying copper resistance genes (*cop* genes) are predominantly present in Cu^R xanthomonads (Behlau et al., 2011, 2012a). The *cop* genes in xanthomonads associated with citrus and solanaceous hosts have been identified and organized in a cluster (Behlau et al., 2011; Timilsina et al., 2019). In Cu^R *Xanthomonas* strains, *copL*, *copA*, and *copB* genes in the *cop* cluster play a major role in copper resistance (Behlau et al., 2011). In addition to the *copLAB* cluster, the plasmid-borne cluster of *copABCD* genes has been also identified in Cu^R strains of *X. arboricola* pv. *juglandis* (Lee et al., 1994) and *X. citri* subsp. *citri* (Richard et al., 2017b). Copper resistance plasmids of xanthomonads can be mobilized from a donor cell to a copper sensitive (Cu^S) recipient cell through conjugation (Behlau et al., 2011, 2012a). Recently, copper tolerant (Cu^T) *X. ctri* subsp. *citri* strains whose chromosomal genes *cohA* and *cohB* (homologous to *copA* and *copB)* were increasingly expressed in the presence of copper, were found in Brazil, but they are not precursors of Cu^R strains (Marin et al., 2019).

Asiatic citrus canker is an important epidemic disease of citrus production worldwide. Previously we used phylogenetic analysis of copper resistance genes *copLAB* in combination with polymorphism analysis of complete *copB* genes to track the possible origin of Cu^R *X. citri* subsp. *citri* strains from Taiwan (Lai et al., 2021). However, hitherto nothing has been known about the detailed genome composition of *X. citri* subsp. *citri* in orchards located in different regions managed under distinct agricultural practices. Thus, the aim of this study was to explore the genetic basis of *X. citri* subsp. *citri* by comparative analysis of complete genomes of three strains collected from two regions in Taiwan, including one Cu^R strain. The high quality genome assembly and annotation of the three strains were compared with published *X. citri* genomes by CRISPR spoligotyping and core genome analysis to reveal the phylogenetic positions of these three strains. By analyzing the structure and variation of the *pthA* genes, we provided evidence of plasmid fusion in the sequenced genomes. Furthermore, comparative analysis of the copper and arsenate gene cluster helped decipher the origin of citrus canker pathogens with resistance to either copper or heavy metals.

MATERIALS AND METHODS

Collection of Strains

Two *X. citri* subsp. *citri* strains B2 and T4 were isolated from the leaves of *Citrus reticulata* cvs. "Shiranui" and "Tainung Giant," respectively, from a commercial citrus orchard in Taichung, Taiwan (Geolocation: 24.27 N, 120.78 E), where copper-based bactericides and fungicides have been routinely applied during the citrus growing season, on October 7, 2016. The other strain, SN3-3, was collected from the leaf of *Citrus sinensis* cv. "Suenaga" in an orchard with minimal management that has not applied bactericides and fungicides in Chiayi, Taiwan, (Geolocation: 243.48 N, 120.46 E, Chiayi Agricultural Experiment Branch, Taiwan Agricultural Research Institute) on April 14, 2016.

Phenotypic Characterization

The pathogenicity of the three strains was tested based on the previously published method (Huang and Ni, 2017). Briefly, leaves of citrus cv. Murcott were infiltrated with bacterial suspensions (1×10^6 CFU/ml). Symptom development was observed 14 days after the inoculation.

Copper sensitivity test was performed according to the method in Lai et al. (2021). The three strains, cultured overnight on NA (Nutrient agar, Difco) plates, were streaked on NA plates supplemented with 0, 0.1, 0.2, 0.4, 0.6, 0.7, 0.8, 1.6, and 3.2 mM $CuSO_4$. Stains sensitive, tolerant, or resistant to copper were differentiated by their ability to grow on NA plates with maximum concentrations of $\leq$0.6, 0.6–0.8 and $\geq$0.8 mM $CuSO_4$, respectively, as rated by Behlau et al. (2013) and Marin et al. (2019).

Illumina Data Generation

Genomic DNA from the three strains was prepared using Bacteria Genomic DNA kit (Geneaid, Taiwan). Nuclei were isolated according to the manufacturer's instructions. Purity and quantity of DNA samples were estimated using the Qubit dsDNA HS Assay Kit (Thermo-Fisher Scientific) and Agilent BioAnalyzer 2100 High Sensitivity DNA Kit (Agilent). Sequencing libraries were prepared using Nextera DNA Flex Library Prep Kit (Illumina). Whole genome shotgun sequencing was performed on an Illumina MiSeq instrument using MiSeq Reagent Kit v.3 to generate 2×300 bp paired-end reads with an average of 2.8–3.1 million paired-end Illumina reads per genome. On average, the final coverage of the assembled genomes exceeded $200 \times$ of the Illumina reads (**Supplementary Table 1**).

Nanopore Data Generation

High molecular weight DNA was prepared using a modified phenol/chloroform protocol as previously described (Chiang-Ni et al., 2012). The gDNA was sheared using the Covaris g-TUBE (Covaris) to select fragment sizes ranging from 6 to 20 kb. The sheared gDNA was further selected using BluePippin with a 0.75% agarose gel cassette (Sage Science) to select gDNA fragment sizes ranging from 6 to 20 kb. Nanopore sequencing libraries were prepared using the PCR free, ligation-based sequencing kit (SQK-LSK109) with the native barcoding expansion (EXP-NBD104) for sample multiplexing. Nanopore sequencing was performed on an Oxford Nanopore MinION device (R9.4 flow cell FLO-MIN106D). In total, we obtained 161K–183K Nanopore reads for each strain and the average Nanopore read length was 8,875 bp and the L50 was 48,138 bp long.

Genome Assembly and Annotation

The quality of the reads was evaluated using FastQC (v.0.11.9) (Andrews, 2010) and the low quality reads were subsequently removed by Trimmomatic (v.0.36) (Bolger et al., 2014) for the Illumina reads, and Nanofilt (v.2.6.0) (De Coster et al., 2018) for the Nanopore reads. The base quality of the Nanopore reads of

greater than 1k bp was further improved by the corresponding high quality Illumina reads using FMLRC (v.1.0.0) (Wang et al., 2018). Taking advantage of the strengths of different algorithms in dealing with the repetitive regions, each strain was assembled by Canu (v.1.8) (Nurk et al., 2020), Flye (v.2.5) (Kolmogorov et al., 2019) and wtdbg2 (v.2.5) (Ruan and Li, 2020) individually to produce multiple versions of the draft genomes. These draft assemblies of each strain were then compared and merged by BLASTN (v.2.10.1) (Altschul et al., 1990) with manual inspection to produce a consensus assembly. The per-base accuracy was improved by Pilon (Walker et al., 2014) using the trimmed Illumina reads. On average, the final coverage of the assembled genomes exceeded 200 ×. The exact sequences of the duplicated TALE repeats and the large inverted repeats of plasmids were based on a second round of local *de novo* assembly using soft-clipped Illumina and Nanopore reads surrounding the draft *pthA* genes or the copper resistance gene cluster. The duplicated blocks were identified based on the proviso that the Illumina read coverage was more than two times higher than the background coverage of the corresponding plasmid sequence. The exact duplicated junction sites were then determined by high quality Nanopore long reads. Ambiguous regions where the sequencing depth was lower or higher than two times the standard deviation of the mean coverage were identified (Wang et al., 2021) and were locally reassembled and/or experimentally verified.

The genome sequences of the three strains were individually resolved into a single circular chromosome. All plasmid sequences were completely circularized as well (**Supplementary Table 1**). The genome annotation was performed by a local NCBI prokaryotic genome annotation pipeline (PGAP) (Lomsadze et al., 2018) with manual curation. In brief, the PGAP pipeline of the Docker image (v.2019-08-22.build3958) was used to perform the initial genome annotation. The assigned annotations were manually checked [Artemis (Carver et al., 2012)], e.g., correct start and stop codon), by comparative analysis with the published *X. citri* genomes (BLASTP (Altschul et al., 1990)).

Whole Genome Comparison

Two complementary approaches based on the diversity of nucleotide sequences and protein coding genes were used for the genome-wide analysis to understand the overall genome variations. Assembled chromosome and plasmid sequences were compared with published *X. citri* genomes (**Supplementary Table 2**) to identify conserved and novel sequence elements. Whole genome sequence comparison was conducted by a series of bioinformatics tools including BLAST (v.2.10.1) (Altschul et al., 1990), fastANI (v.1.20) (Jain et al., 2018), Harvest (Treangen et al., 2014) and MUMmer (v.4.0.0rc1) (Kurtz et al., 2004). The whole genome similarity metrics of the three strains were estimated using the alignment-free approximate sequence mapping algorithm of fast Average Nucleotide Identity (fastANI) (Jain et al., 2018) with default settings. To further understand the origin of these three strains, whole genome sequences of 33 completely assembled *X. citri* strains (**Supplementary Table 2**) were included in the phylogeny analysis. The Parsnp algorithm in the Harvest suite (Treangen et al., 2014) used the maximum unique matches (MUMs) from the suffix graph data structure of the whole genome sequences to identify regions of the core-genome. The algorithm then performed multiple sequence alignments of multiple MUMs for subsequent variant calling and produced a SNP tree.

Synteny Analysis, Pan-Genome, and Core Genes

The orthologous relationships between B2, T4 and SN3-3 was investigated. The protein coding genes of these three strains were searched using all-against-all BLASTP (Altschul et al., 1990). The BLASTP result was analyzed by a scalable unsupervised cluster algorithm TribeMCL (Enright et al., 2002) and the orthologous and paralogous relationships were presented as networks based on the *e*-values. The genome collinearity analysis was based on the genome synteny information calculated by i-ADHoRe 3.0 (Proost et al., 2012).

To further expand the analysis of gene repositories of *X. citri*, we compared protein coding genes of 79 *Xanthomonas* genomes (two *X. albilineans*, two *X. oryza* and 75 *X. citri*) (**Supplementary Table 2**) by BLASTP (Altschul et al., 1990) and TribeMCL (Enright et al., 2002) clustering. The homolog of the gene matrix in each genome was used as an input to calculate the average number of genes added with each additional genome using a method modified from Meric et al. (2014). Genes that were presented in more than one genome were considered as pan-genome and genes that were shared in at least two genomes were considered as core-genome. To obtain sufficient resolution of the phylogenetic positions, a total of 1,512 orthologous genes with a strict one-to-one relationship in 75 *X. citri* strains were used to construct the phylogenetic tree. In brief, protein sequences of single copy core genes were individually aligned by MUSCLE (Edgar, 2004) and gaps in the multiple sequence alignments were removed by Trimal (Capella-Gutierrez et al., 2009). Individual sequence alignments were concatenated to create a 478,302 amino acid-long sequence of each strain. Maximum likelihood phylogenetic trees were inferred by RAXML-NG (Kozlov et al., 2019) with 1000 bootstrap replicates (v.1.0.1, -model LG+G8+F –seed 2 –bs-trees 1000) and visualized by Figtree[1].

TALE Identification and CRISPR Analysis

The location and classification of TALEs were manually searched by BLASTN (Altschul et al., 1990) based on collected TALE sequences including short inverted repeats (IR), mobile insertion cassettes (MICs) and the Tn3 transposon *TnXax1* (Ferreira et al., 2015). Two short palindromic sequences and passenger genes were manually inspected as well. The structure of CRISPR and the Cas proteins were detected by CRISPRCasFinder (Couvin et al., 2018). CRISPRCasFinder integrated multiple tools to determine the hidden Markov model (HMM) profile of Cas proteins, the maximal repeat structure, the entropy of repeats, the sequence similarity and the size of spacers, and the sequence similarity with known CRISPR, and eventually assigned different levels of evidence code. The spacer sequences were further identified by BLASTN following the spoligotypes

[1]https://github.com/rambaut/figtree/releases

classification in Jeong et al. (2019). Phages and their integration sites were identified using PHASTER (Arndt et al., 2016) where published redundant phage/prophage sequences had been curated and the completeness scores were assigned to the identified phage regions.

Copper and Arsenate Gene Cluster Analysis

The copper resistance gene clusters in the assembled plasmids were identified by comparison with known copper resistance genes in the plasmid pCuR (Gochez et al., 2018) and pLH201.1 (Richard et al., 2017a). Initial BLASTN hits were manually inspected and only regions with >60% sequence identity and >70% coverage of the query sequence were considered as the candidate area. Protein coding genes were then predicted using the PGAP pipeline (Lomsadze et al., 2018) and manually curated using Artemis (Carver et al., 2012). Comparative analysis results of gene clusters in pT4p2, pCuR and pLH201.1 were visualized by Artemis and Circos (Krzywinski et al., 2009).

Horizontal Transfer of Copper Resistance Genes

Horizontal transfer of *cop* genes between different *X. citri* subsp. *citri* strains was tested according to the method in Behlau et al. (2012a). The strain T4 with copper resistance and rifampicin sensitivity was used as a donor. Spontaneous rifampicin resistant mutants of Cu^S strains B2Rif and SN3-3Rif were used as recipients. Bacterial strains were mated on NA plates at 28°C for 24 h. After mating, bacterial cells were scraped, suspended, and plated at dilutions on NA amended with rifampicin (50 mg/L) to estimate the population of the recipient. To select transconjugants, bacterial suspensions were plated at dilutions on NA supplemented with rifampicin (50 mg/L) and 0.8 mM $CuSO_4$. The conjugation frequency was calculated as the ratio between the number of transconjugants and the population of the recipient (Behlau et al., 2012a).

RESULTS

Complete Genome Sequence of Three *X. citri* Strains

The three strains of *X. citri* subsp. *citri* were able to cause similar levels of canker symptoms on Murcott leaves. No difference among the three strains was observed with regard to induction of symptoms. Furthermore, the strain T4 was characterized as a Cu^R strain which was able to grow on NA plates supplemented with 0.8 mM $CuSO_4$ (Lai et al., 2021). The other two strains B2 and SN3-3, which could not grow on NA plates supplemented with more than 0.4 mM $CuSO_4$, both showed sensitivity to copper.

To advance understanding of the genome structure and the molecular makeup of the Taiwan *X. citri* subsp. *citri*, we applied hybrid assembly by combining short read (Illumina) and long read (Nanopore MinION) sequencing technologies in an integrated bioinformatics workflow. Three type A strains, including two strains from one conventional commercial orchard (B2, copper sensitive and T4, copper resistant), and one strain from an orchard with minimal management (SN3-3, copper sensitive) were assembled into gap-free chromosome sequences (**Supplementary Table 1**).

The chromosome sequences of the three strains were resolved into a single circular chromosome with length 5,120,747 bp (B2, accession number CP059999), 5,194,482 bp (T4, CP059992) and 5,192,310 bp (SN3-3, CP060002), respectively. To facilitate the comparative analysis, *DnaA* was organized in the beginning of the completely assembled genomes. The three conserved DnaA boxes of the *oriC* region could be identified between *DnaA* and *DnaN* (da Silva et al., 2002; Yen et al., 2002; Qian et al., 2005). The terminator of replication of each strain was located at around 2.5 Mb of the chromosome sequence. The replichore of the three strains could be identified based on the GC skew plot (Grigoriev, 1998). The assembled chromosome sequence length and GC content (64.76∼64.84%) (**Figure 1**) were in the same range as the published *X. citri* subsp. *citri* genomes (Timilsina et al., 2020). Through the genome assemblies, we also identified two plasmids in B2 (pB2_V1, 137,420 bp, CP060000; pB2_V3, 94,653 bp, CP060001), two plasmids in T4 (pT4p1, 99,130 bp, CP059993; pT4p2, 312,426 bp, CP059994) and one plasmid in SN3-3 (pSN3-3, 63,921 bp, CP060003). All plasmid sequences were completely circularized as well (**Supplementary Table 1**).

Using the NCBI prokaryotic genome annotation pipeline (PGAP) (Lomsadze et al., 2018) with manual curation, we identified 4,489 (B2), 4,557 (T4) and 4,539 (SN3-3) protein coding genes in the chromosomes with average coding capacity of 87.2, 87.1, and 87.1%, respectively. The leading strand and the lagging strand harbored a similar number of coding genes. Despite the *X. citri* reference genome 306 being published in 2002 and many genome sequences having been completed afterwards, gene function of a large part of the genome remains unknown. By comparison with the UniProt protein database and the manually collected *Xanthomonas* protein sequences from NCBI, ∼20% of the protein coding genes were predicted to be hypothetical genes. In addition to protein coding genes, all three strains contain 106 non-coding genes including 6 rRNA genes, 54 tRNA genes and 46 ncRNA genes (**Supplementary Table 1**).

Low Nucleotide Sequence Diversity of Chromosomes

To further understand the similarity and possible origin of these three strains, we applied multiple complementary approaches to analyze the genome sequences. We first compared the chromosome sequence of the three strains to investigate the possible large scale chromosomal changes. The three strains shared high sequence identity and collinearity (**Supplementary Figure 1**). We then examined the nucleotide sequence divergence at the whole genome level. Instead of using the conventional approach for calculating average nucleotide identity (ANI) of orthologous genes, we applied an alignment-free, whole-genome average nucleotide identity (FastANI) analysis (Jain et al., 2018) to determine the pairwise ANI values. The three strains sequenced in this study were found to share very high levels of sequence identity (>99.96%) and there were no significant differences

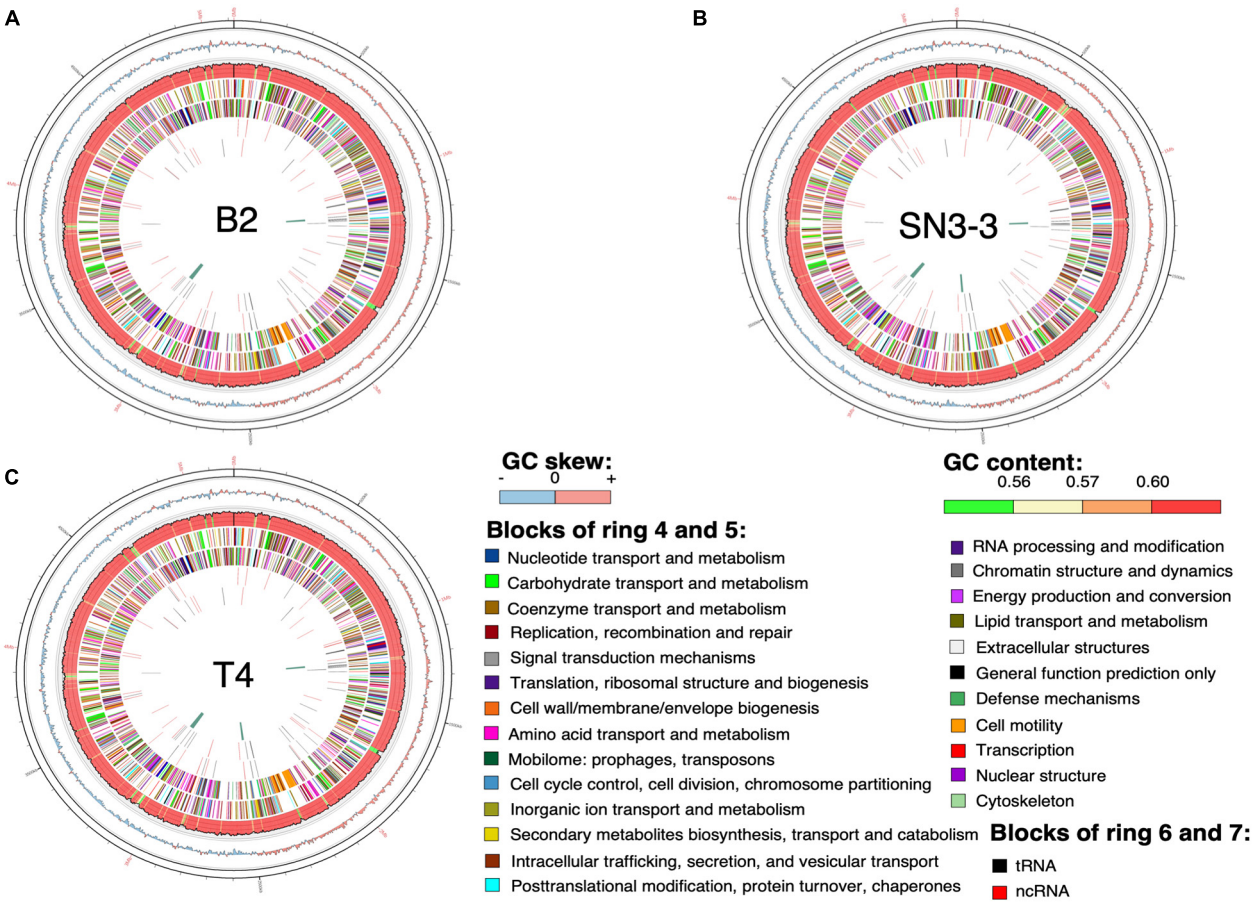

FIGURE 1 | Chromosome organization and genome annotation. **(A–C)** Overview of three assembled chromosomes and the distribution of genetic elements. Circles from outermost to innermost represent: (1) position, the grid is 100 kb; (2) GC skew with 2500-bp sliding widow and 2500-bp step; (3) GC content in the same sliding window and step size as GC skew; predicted protein-coding sequence (CDS) with known function (4) of the plus strand and (5) the minus strand; predicted RNA of (6) the plus strand and (7) the minus strand; (8) phage sequence.

among them (**Supplementary Table 3**). By focusing on the orthologous chromosome sequences conserved in these three strains and 33 assembled *X. citri* strains in the same pathovars (**Supplementary Table 2**), we used Parsnp in the Harvest package to perform the core-genome alignment (Treangen et al., 2014). *X. citri* strains of the same pathotype were grouped in the same phylogenetic clade (**Supplementary Figure 2**). Three strains sequenced in this study, B2, T4 and SN3-3, were all classified into the pathotype A. However, these strains were respectively grouped with strains from different geographic origins (**Supplementary Figure 2**). In particular, T4 shared higher sequence similarity with the reference strain A306 from Brazil and the other strains from Argentina whereas B2 was closer to the strains from Jiangxi, China. SN3-3 was closer to strains from Jiangxi and Guangdong, China.

Spoligotype Classification by CRISPR Spacer Array

We analyzed the compositions and orders of CRISPR and spacer array of our strains by CRISPRCasFinder (Couvin et al., 2018). Following the presence and absence of spacer patterns (spoligotypes, spacer oligonucleotide) (Jeong et al., 2019), B2 contained 19 spacer/repeat units, T4 contained 18 units and SN3-3 contained 17 units, corresponding to spacer Xcc_01 to Xcc_23; spacer Xcc_8, Xcc_10, Xcc_11 and Xcc_14 were absent in these strains (Jeong et al., 2019). In particular, B2 and SN3-3 shared a common Xcc_3 whereas Xcc_9 and Xcc_12 were only seen in B2 and T4 (**Figure 2**). According to the spoligotype classification by Jeong et al. (2019), B2 belongs to spoligotype 8 (China, Florida, Reunion islands), T4 belongs to spoligotype 14 (Brazil, Mali) and SN3-3 belongs to the spoligotype 21 (Japan). The CRISPR spacer arrays demonstrated that our strains of the same pathotype A belonged to the different spoligotypes originally from East Asia, the Indian Ocean, and South America.

Core Genome Phylogeny

Orthologous genes were first identified by an all-against-all BLASTP search and the BLASTP result was subsequently analyzed by the Markov chain based TribeMCL (Enright et al., 2002) to divide them into orthologous groups. The

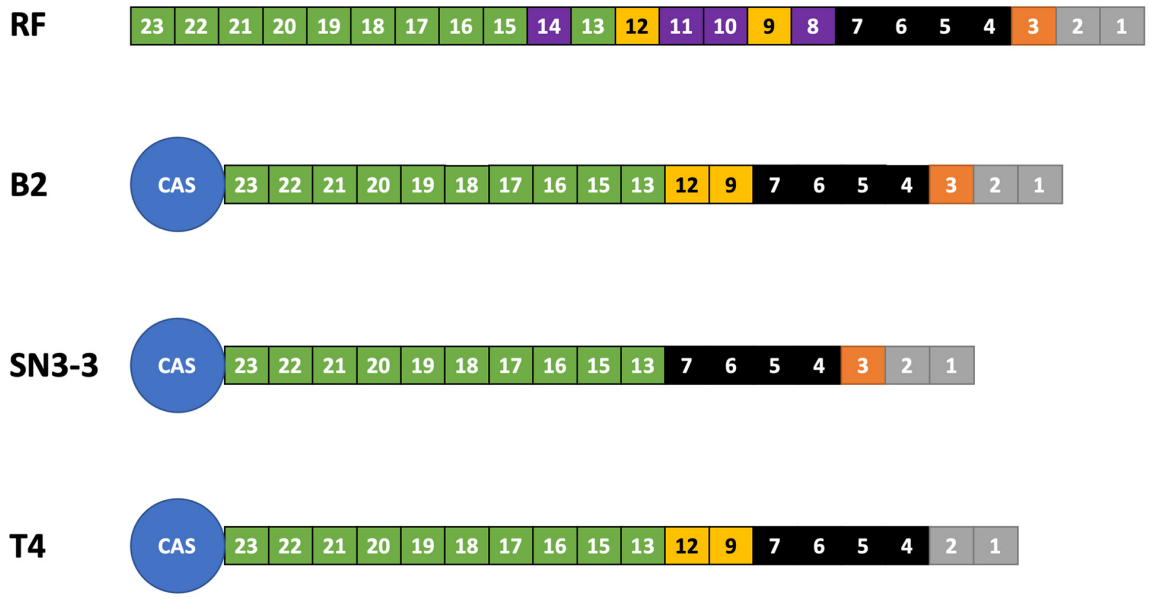

FIGURE 2 | CRISPR spoligotyping. Overview of the CRISPR/Cas locus. The reference (RF) array annotation is based on *X. citri* 306 (CP009016). The colors of the boxes indicate spacer sequences that correspond to the reference. Purple: absent in the sequenced genomes of this study.

orthologous information was then used by the synteny based gene family analysis (Proost et al., 2012) to determine genes in the collinearity region. In total, 4,090 orthologous genes were shared between the three strains and did not show chromosome rearrangements (**Supplementary Figure 1**). Around 144–237 genes are strain specific and were found in only one of the genomes (**Supplementary Figure 3**). Detailed functional analysis by GO enrichment of these strain specific genes indicated that most of them were enriched with transposon activity-related genes (**Supplementary Table 4**). This result indicated that the chromosome variations between the three strains, though minimal, were likely associated with the transposon activities.

To better understand the chromosome dynamics of *X. citri* strains, we conducted pan-genome analysis with protein coding genes of our three sequenced strains in this study and 76 published *Xanthomonas* genomes. Orthologous genes of 79 strains (including two *X. albilineans*, two *X. oryza* and 75 *X. citri*) (**Supplementary Table 2**) were determined by the combination of an all-against-all BLASTP search and TribeMCL clustering. We identified 6,342 ortholog clusters that were shared between more than two strains. That is, 99.7% of the genes in one strain were shared in at least one of the 78 sequenced strains. Within the 79 *Xanthomonas* genomes used for the comparison, the pan-genome size was around 5,000 genes and the core-genome size was less than 2,000 genes (Timilsina et al., 2019; **Supplementary Figure 4**). Nevertheless, when four outgroup species (2 *X. albilineans*, 2 *X. oryza*) were removed from the analysis, the pan-genome size remained around 5,000 genes but the core-genome size increased to ∼3,000 genes (**Figure 3A**). The number of core genes identified in our study is comparable with those obtained from 58 *X. perforans* strains (Timilsina et al., 2019).

We used the phylogenomics approach to further understand the phylogenetic positions of three strains in this study and other published genomes. Based on the core genome analysis, we selected 1,512 orthologous genes that had a strict one-to-one single copy relationship to construct the phylogenetic tree. A tree inference tool based on the maximum likelihood (ML) method (Kozlov et al., 2019) was used to construct the phylogenetic tree. As expected, the strains of different pathotypes were clustered on different clades of the phylogenetic tree with high bootstrap value support for each lineage (**Figure 3B**) and correspondence to the origin of the collection. The pathotype A strains including the reference strain 306 and our three strains were placed together in the same clade together with strains from China, Florida, Argentina and Brazil. On the other hand, four strains from Reunion were placed in an independent clade (Richard et al., 2021).

Type II and Type III Secretion Systems

In *Xanthomonas*, the type II secretion system (T2SS) is used to translocate folded proteins from the periplasm into the extracellular milieu (Korotkov et al., 2012) and the type III secretion system (T3SS) is essential to pathogenicity through modulating host plant physiology and enabling evasion of host immune responses (Timilsina et al., 2020). In the T2SS, we identified two operons, each containing eleven genes of the general secretory pathway (Gsp) (Korotkov et al., 2012) as was previously reported in the reference strain 306 genome (da Silva et al., 2002; **Supplementary Figure 5A** and **Supplementary Table 5**). *GspO* could be identified in the chromosome but is not located in the two Gsp operons. Gene clusters encoding for *hrp* (hypersensitive response and pathogenicity), *hrc* (*hrp* conserved) and *hpa* (*hrp* associated) of the T3SS (Alegria et al., 2004) were

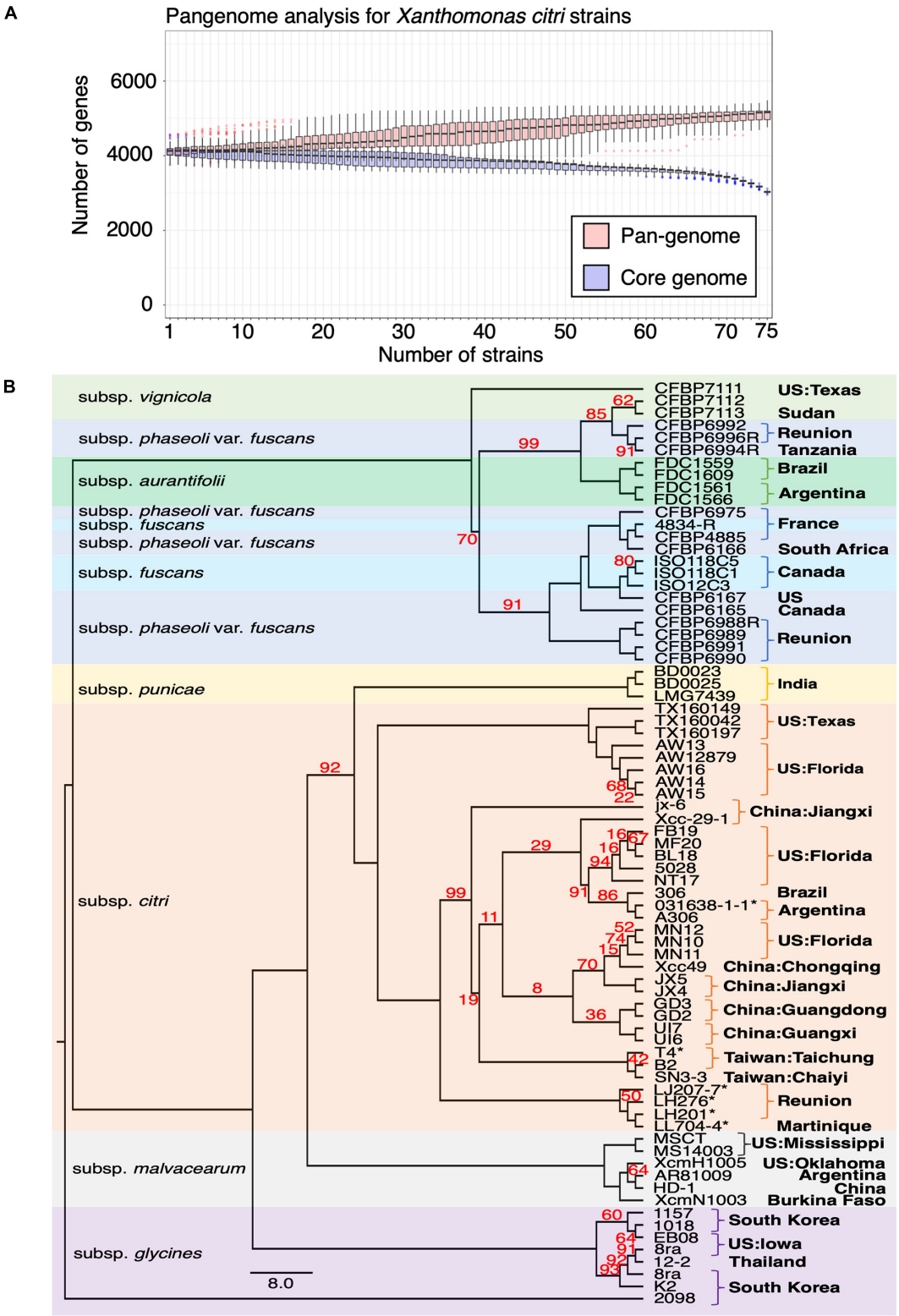

FIGURE 3 | Pangenome analysis of Xanthomonas genomes. **(A)** Pangenome analysis of 75 *X. citri* genomes. **(B)** The core genomes of 75 *X. citri* sp. strains showed a phylogenetic relationship and shared geographic origins. Maximum likelihood phylogeny based on concatenated sequences of 1,512 core genes. The asterisks (*) indicate copper-resistant strains, and branches with bootstrap value < 100 support are labeled with red numbers.

identified in the chromosome (**Supplementary Figure 5B** and **Supplementary Table 5**). Overall, the T2SS and T3SS were highly conserved in the three sequenced strains.

TALE Variation and Plasmid Fusion

Compared with the chromosome sequences, the plasmid sequences showed higher diversity in plasmid length and number of genes (**Supplementary Figure 6**; Timilsina et al., 2020). In total, we identified five plasmids in three strains. The plasmid size ranged from 64 to 312 kb and the GC content was around 60%, which was lower than the average of 64% of the chromosomes (**Supplementary Table 1**). We tried to determine the plasmid copy number in each genome based on the relative whole genome sequencing coverage with the chromosome (Pena-Gonzalez et al., 2018). On average, we estimated the genomes contained 2.6, 3.6, 4.4, 3.5, and 1.6 copies of pB2_V1, pB2_V3, pSN3-3, pT4p1, and pT4p2, respectively (**Supplementary Figure 7**).

A sequence similarity search of plasmid sequences by BLASTN indicated pT4p2 contained the copper resistance gene cluster as indicated in Gochez et al. (2018). The other four plasmids (pB2_V1, pB2_V3, pSN3-3, and pT4p1) sharing high similarity with known plasmid sequences showed a high level of sequence rearrangement (**Figure 4** and **Supplementary Figures 6**, **8**). For instance, mobile genetic elements including Tn3-like transposon and the subclass of insertion sequence (IS) elements were highly variable between the four pathogenicity-related plasmids. Analysis of repeat-variable diresidues (RVDs; Ferreira et al., 2015) indicated that TALE repeats were seen in these four plasmids which contained different copy numbers of *pthA* encoding genes with various sizes of TALEs (**Supplementary Table 6**). Three copies of *pthA* gene were found in strains SN3-3, four copies in T4 and eight copies in strain B2.

Based on the TALE classification, Class I contained *pthA2* and *pthA3* genes, Class II contained *pthA4* and Class III contained *pthA1* (Gochez et al., 2018). These three Classes were seen together in plasmids pSN3-3, pB2_V1, and pT4p1 (**Figure 4**) and represented the signature of plasmid fusion events (**Figures 5**, **Supplementary Figures 6, 8**, and **Supplementary Table 6**). The size of pSN3-3 is similar to that of pXAC64 of the reference strain 306 but the *pthA* genes of strain SN3-3 carry different copies of repeats (**Supplementary Table 6**), which are shorter and not comparable with those of the reference strain 306 (da Silva et al., 2002). On the other hand, *pthA2* and *pthA4* on pSN3-3 partially overlapped with each other (**Figure 5** and **Supplementary Table 6**).

Plasmid pT4p1 was highly similar to plasmid pP2 of the Cu^R strain Xc-03-1638-1-1 (**Supplementary Figure 6** and **Supplementary Table 6**; Gochez et al., 2018). The two plasmids were almost identical with only 23 bp difference and contained the exact copy number of all four classes of *pthA1* genes. Plasmid pT4p1 had 4 *pthA* genes of 3 classes including two genes with 15.5 (Class I: *pthA2* and *pthA3*), one with 17.5 (Class II: *pthA4*) and one with 21.5 (Class III: *pthA1*) repeats comparable with the second largest plasmids of Cu^R strains pLH276.2 and pLL074-4.2 (Gochez et al., 2018; **Supplementary Table 6**). The plasmids of strain B2 had 8 *pthA* genes of 3 classes including two genes with 13.5 (unclassified class: *pthA2/1*), three with 15.5 (Class III) and two with 17.5 (Class II) repeats partially comparable to the pathogenicity plasmids of Cu^R strains (Gochez et al., 2018; **Supplementary Table 6**). The effector genes *xopE2* (Ferreira et al., 2015) and *pthA4* (Roeschlin et al., 2019) that are involved in the suppression of the hypersensitive response of the host were also identified in these four pathogenicity-associated plasmids.

Structures and Origins of the Copper and Arsenate Resistance Gene Clusters

The Cu^R strain T4 had the largest plasmid pT4p2 among the three sequenced strains (**Supplementary Table 1**) for which the sequence is similar to the copper resistance plasmids pLH201.1 and pCuR (**Figure 6**). Interestingly, the sequence of pT4p2 is larger than those two plasmids due to an unusual ∼40 Kbp inverted repeat. We further confirmed the junction size of the inverted repeat by PCR (**Supplementary Figure 9**). On the other hand, pT4p2 shared the same inverted repeat pattern as observed in pLH3.1 of *X. perforans* LH3 (CP018472) (**Supplementary Figure 10**), where the strain LH3 was collected from a tomato orchard in Mauritius in 2010 (Richard et al., 2017b). Each inverted repeat contains a complete set of the copper resistance gene cluster, except *copCDG* are missing (**Figures 6**, **7**). Analysis of *cop* gene clusters revealed that three groups of copper resistance gene clusters could be identified across a diverse set of bacterial species. pLH201.1 and pCuR belonged to Group I. The pT4p2 and copper resistance plasmids from *X. perforans*, *Stenotrophomonas,* and *Pseudoxanthomonas* sharing the same arrangement of the *cop* gene cluster belonged to Group II (**Figure 7** and **Supplementary Table 7**). In particular, in the NCBI nucleotide database, a unique region between the copper-arsenate clusters was only identified in pT4p2, pLH3.1 and the plasmids of six other *Xanthomonas* strains that were tomato pathogens, with the exception of pXAC219 that was isolated from the citrus leaf. Plasmids of these strains shared 99% sequence coverage and >96% sequence identity (**Supplementary Table 8**). The third group, Group III, contained a more diverse set of *cop* gene clusters where the plasmid backbone was extremely similar to pCuR (Richard et al., 2017b) but only *copF* and *copA* shared 70% nucleotide sequence identity with those in pCuR.

To further support our idea about the origin of the copper resistance cluster, we then compared the structure of the arsenate gene cluster. The arsenate cluster was mostly composed of either three (*arsRBC*) or five (*arsRDABC*) genes and expressed in a single transcriptional unit in soil bacteria (Achour et al., 2007). Interestingly, the *X. citri* arsenate gene cluster which was grouped together with that of *Stenotrophomonas* was composed of four (*arsRCHB*) genes (**Figure 8**). Furthermore, the transposases between the arsenate and copper clusters showed higher sequence similarity to those of *X. perforans* whereas two endonucleases corresponding to pCuR and pLH3.1 were adjacent to each other (**Supplementary Figure 10**).

Moreover, the *ars* and *cop* gene clusters responsible for resistance to heavy metals including copper and arsenate are adjacent to each other with higher GC content (62.3%) compared

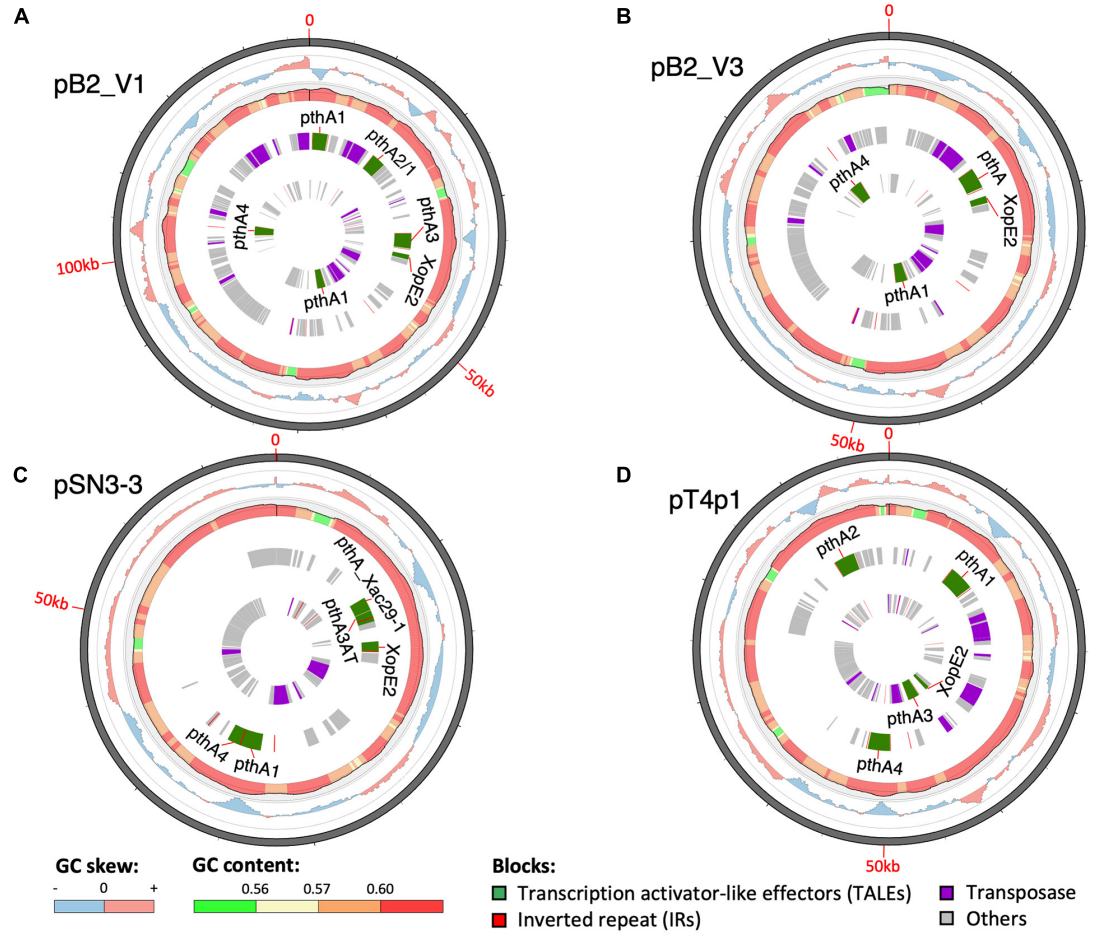

FIGURE 4 | Plasmid organization. **(A)** pB2_V1, **(B)** pB2_V3, **(C)** pSN3-3, and **(D)** pT4p1. Circles from outermost to innermost represent: (1) GC skew, (2) GC content, (3) reverse, and (4) forward direction of repetitive sequences. Green: TALEs. Red: inverted repeats. Purple: transposase. Gray: other CDS/genes: gray.

with other genomic regions (58.6%) and flanked by two Tn3-like transposons (**Figure 6** and **Supplementary Figure 11**). In addition to the abnormal GC content and transposon insertions, *merR* and *cusAB* associated with heavy metal resistance in bacteria were found in the pT4p2. The MerR transcriptional regulator family controlled the expression of *copA* in *Escherichia coli* and responded to environmental stimuli, such as heavy metals or antibiotics (Brown et al., 2003). In pT4p2, *MerR* is 7 Kbp away from the *ars* cluster but the heavy metal efflux pump *cusAB* is next to the *ars* cluster (300 bp). The close proximity of *MerR* and *cusAB* to the heavy metal cluster was also observed in pLH201.1 (Richard et al., 2017b). In addition, the heavy metal resistance gene clusters in pT4p2 were surrounded by two *Tra* gene clusters. The T4 strain showed the conjugation ability and the pT4p2 encoded 16 Tra proteins that are essential for conjugation. Similar to the pCuR and pLH201.1 arrangement, *Tra* genes of pT4p2 located in two different regions of the plasmid with *TraID* in one side and other 14 *Tra* genes grouped into another cluster. Overall, the complete set of *Tra* genes in the pT4p2 and the high sequence similarity of heavy metal resistance gene clusters with other published plasmids indicated that the heavy metal resistance gene was likely acquired from other microbes.

Conjugative Transfer of Copper Resistance Genes

The copper resistance genes can be transferred from the Cu^R strain T4 to the Cu^S strains B2Rif and SN3-3Rif through bacterial conjugation (**Supplementary Table 9**). The transconjugants showed the same level of copper resistance as the donor strain T4. The frequency of conjugative gene transfer ranged from 10^{-8} to 10^{-5} transconjugants per recipient (**Supplementary Table 9**). B2Rif received the Cu^R genes from T4 more frequently than SN3-3Rif (**Supplementary Table 9**).

DISCUSSION

In this study, the genome and plasmid sequences of three *X. citri* subsp. *citri* strains from Taiwan were completely sequenced and assembled using the combination of Illumina short-reads and Oxford Nanopore long-reads. Whole genome sequencing

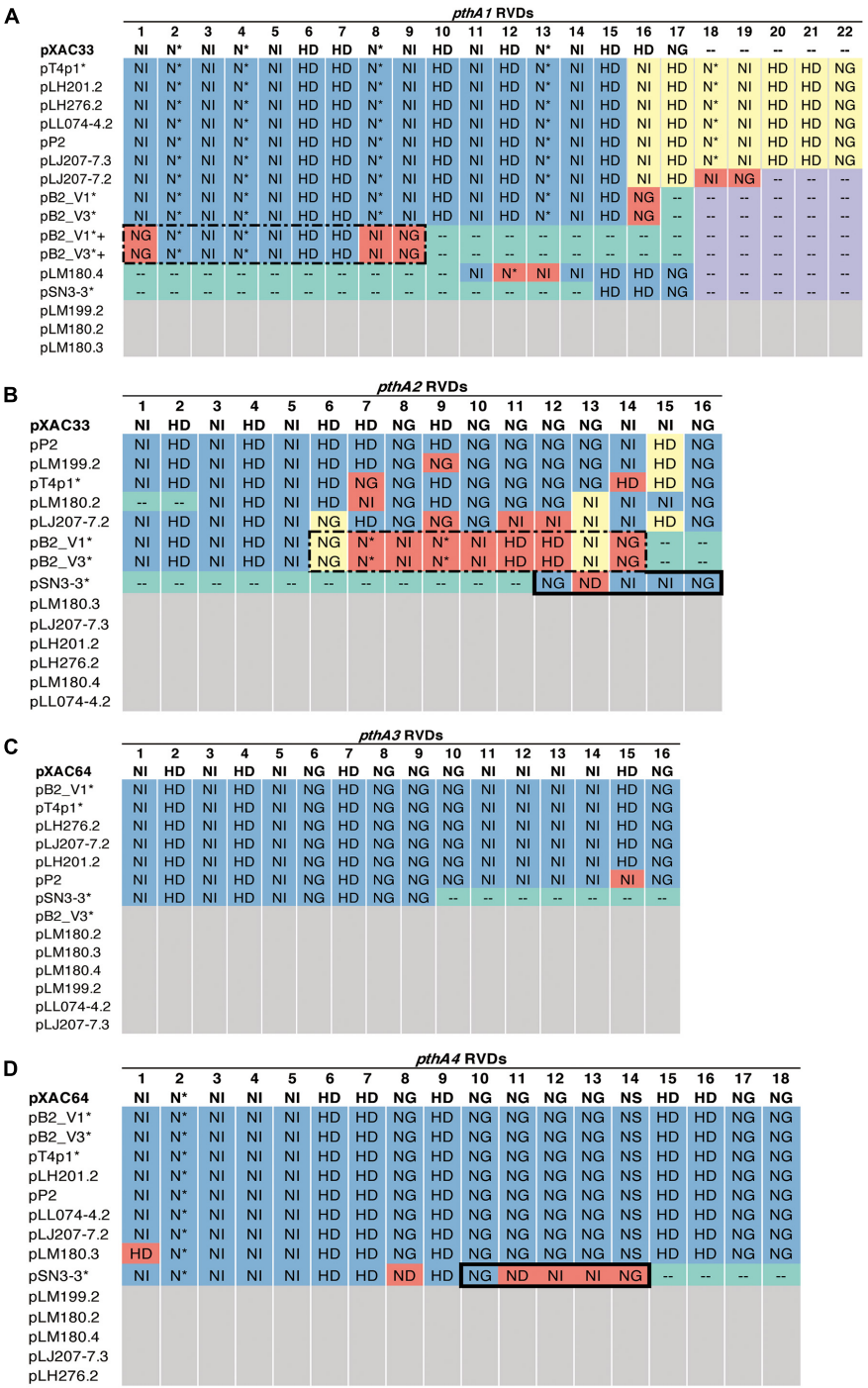

FIGURE 5 | RVD profile of *pthA* genes. The asterisks (*) indicate plasmids sequenced in this study. NI (Asn-Ile) recognizes A; HD (His-Asp) recognizes C (but not 5′-methyl-C); NG (Asn-Gly) recognizes T and 5′-methyl-C; NN (Asn-Asn) recognizes G or A; NS (Asn-Ser) recognizes A,T,C or G; N* (Asn-*) recognizes C or T [47]. Blue: identical to the reference. Purple: absent, the same as the reference. Green: absent, different from the reference. Yellow: > 50% sequence similarity with the reference. Red: unique. White: no such *pthA* genes. **(A)** Plus sign (+): merged *pthA* genes. **(A,B)** Dashed box: nine *pthA1* repeats were merged with *pthA2* repeats. **(B,D)** Solid box: five *pthA2* repeats were merged with *pthA4* repeats.

has been widely used to understand the pathogenic, taxonomic and phylogenetic status of the xanthomonads (Zhang et al., 2015; Bansal et al., 2017; Patane et al., 2019). Previous studies lacked the resolution of repetitive or duplicate regions as they could not be precisely resolved by the short-read sequencing method and the bioinformatic algorithm (Triplett et al., 2011;

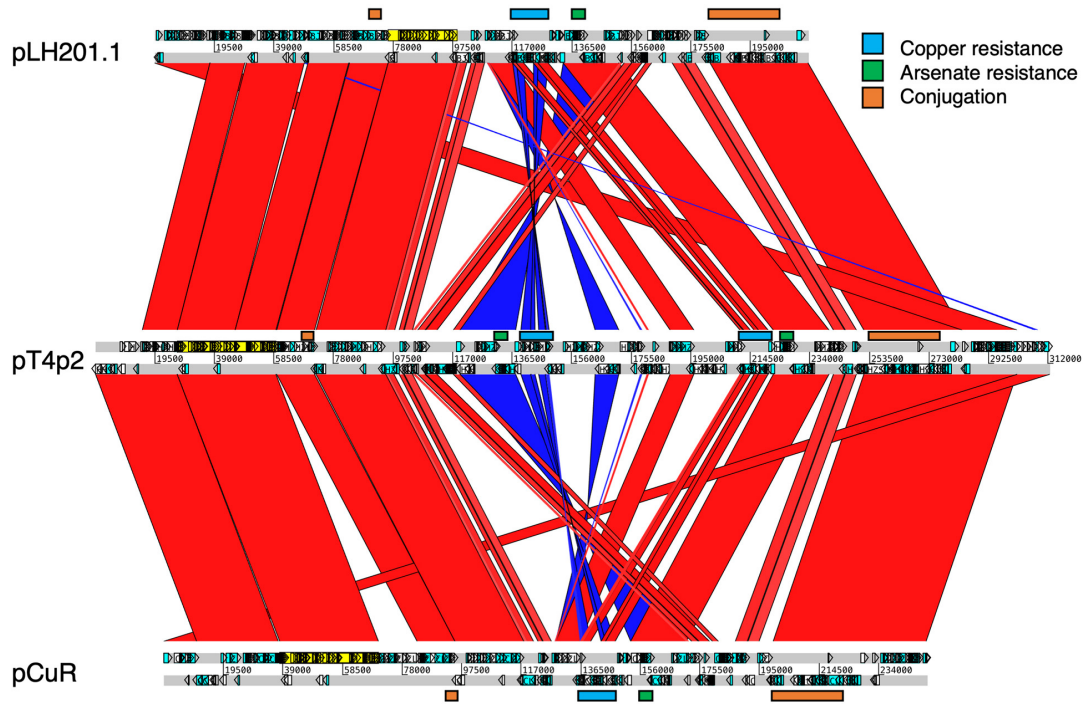

FIGURE 6 | Comparison of plasmids containing copper resistance genes in pT4p2, pCur and pLH201.1. Syntenic regions are presented in red color and inverted regions are in blue. Genes involved in copper/arsenate resistance and conjugation are highlighted along the plasmid sequences.

Fonseca et al., 2019). Recently, with the availability of the long-read sequencing method and the advances in genome assembly (Kolmogorov et al., 2019), complex genome structures can be fully resolved. Correspondingly, the genome and plasmid sequence dynamics of *X. citri*. from different geographic locations have gradually emerged (Gochez et al., 2018; Roach et al., 2020; Richard et al., 2021).

The assembled chromosome sequence length, GC content (64.76∼64.84%) and number of genes (**Figures 1A–C**) are in the same range as the published complete *X. citri* subsp. *citri* (Timilsina et al., 2020). The 75 *X. citri* genomes showed a high level of genome conservation where 2,529 ortholog genes had a strict one-to-one single copy relationship within *X. citri* strains. The large core-genome size (**Figure 3A**) and the pangenome analysis (Loiseau et al., 2018) indicated that the *X. citri* strains showed a 'close' genome signature where strains shared a large common gene repertoire. In contrast, the *Xanthomonas* genus was an 'open' genome where gene gain and loss events frequently occurred within different *Xanthomonas* lineages (Timilsina et al., 2020).

Comparing chromosome sequences and gene contents did not reveal many differences between *X. citri* subsp. *citri* strains. In fact, the pangenome analysis confirmed that strains in the *X. citri* subsp. *citri* were rather conserved and the core genome was composed of 2,529 one-to-one ortholog genes and ∼3,000 genes (i.e., detected in all 75 strains) (**Figure 3A**). Nevertheless, the core genome size of this study is smaller than the 4,347 genes of 221 strains in the previous study (Richard et al., 2021). The differences in the three pan-genome analysis strategies likely explain the inconsistency between the studies. First, only protein coding genes in the chromosomes were considered for the orthologous relationships in this study (Timilsina et al., 2019); however, the study by Richard et al. included the plasmid genes in the analysis (Richard et al., 2021). A high gene turnover rate (gain or loss of genes) was observed due to uneven frequencies of acquiring or losing a single large plasmid in different lineages (Richard et al., 2021). The ease of horizontal gene transfer of the entire plasmid between strains has made plasmids the main driver of host adaptation (Ruh et al., 2017). To focus on changes in the chromosome sequences, we decided to focus only on genes of the chromosomes.

Secondly, we used orthology-based analysis where predicted protein coding genes of each of the *de novo* assembled genomes were used to identify orthologous genes among sequenced strains. The advantage of this strategy is that it did not restrict the analysis in one particular reference strain. That is, unique genome fragments and gene contents that existed in one particular strain could be identified. The main drawback was that each sequencing project applied different gene prediction methods and this might introduce biases in gene models due to technical artifacts. An alternative approach would be based on the read coverage of the whole genome resequencing data (Richard et al., 2021). Using this approach, one strain was selected as the reference genome where resequencing reads were mapped to the reference genome sequence. The presence and absence of the gene was then evaluated based on the pre-defined cut-off of read depth

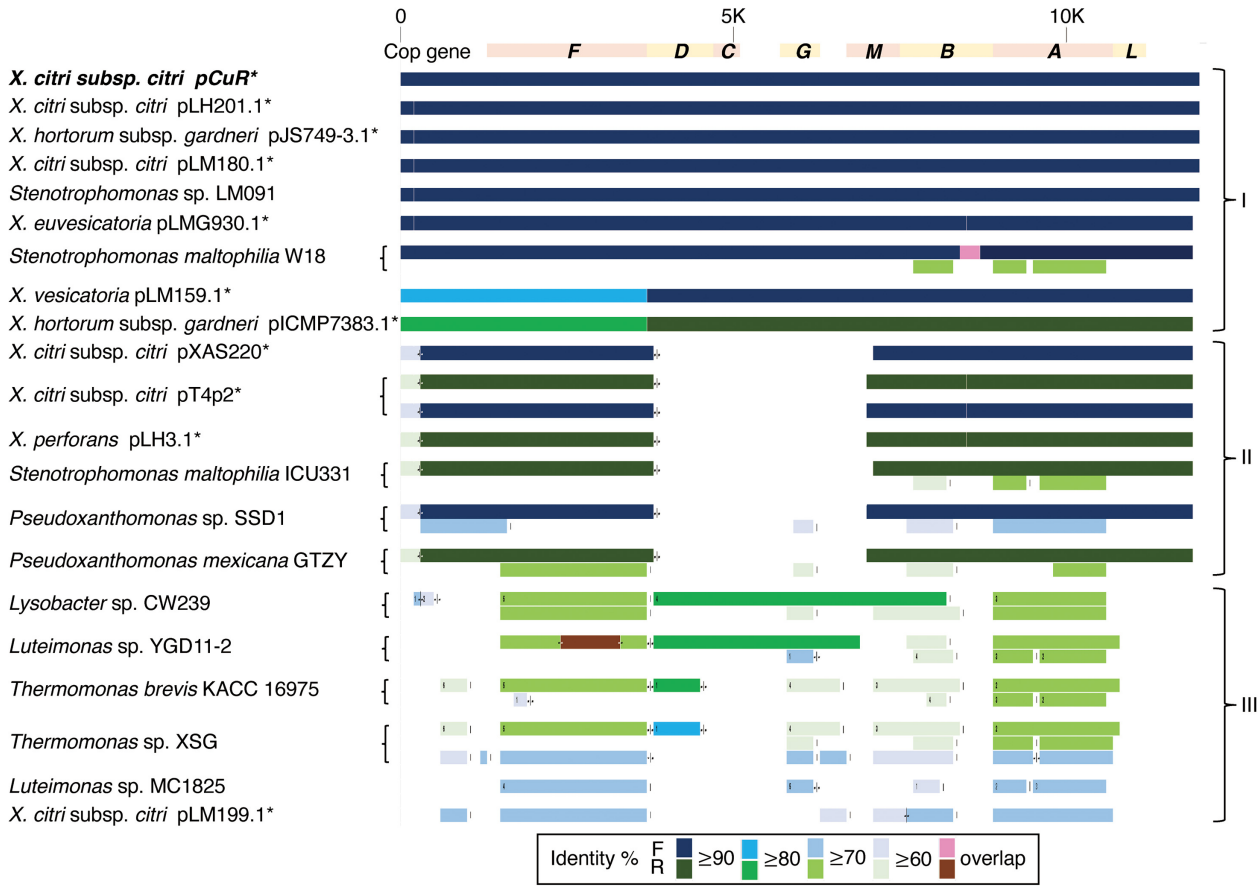

FIGURE 7 | Comparison of gene gain and loss in the copper resistance gene cluster.

and coverage of the gene length. This method could avoid the fragmented genomes and truncated gene models due to the short read assemblies. Nevertheless, variations due to paralogs, gene copy number or pseudogenization could not be identified. Despite the differences in the exact number of genes of the core genome, our result agrees with previous analysis (Timilsina et al., 2019) in concluding that *X. citri* subsp. *citri* is a monomorphic bacterium and the gene numbers are conservative in the lineage (Timilsina et al., 2019).

The pathotype classification is in agreement with the core-genome phylogenetic analysis in showing that these three strains clustered with the pathotype A strains from different geographic origins (Jeong et al., 2019). However, the exact phylogenetic relationship between the three strains sequenced in this study could not be clearly resolved and we did not date the time scale of the evolutionary history (**Figure 3B**). The three strains were placed in an independent clade with 100% bootstrap value support. The long branch length with strains from other geographic origins suggest that three strains diverged from a common ancestor.

The gap-free complete genome sequences offered a unique opportunity to study the structure of the repetitive sequences such as CRISPR repeats and spacers in detail since their order and the exact copy number have often been mis-assembled in the draft genome assemblies (Wang et al., 2021). In particular, spoligotyping provided an alternative method to infer the evolutionary history and the common ancestor of the microbial strains. Among sequenced *X. citri* subsp. *citri* strains, the CRISPR array contains a conserved array of 23 spacers and could be used to infer the evolutionary trajectory among the observed spoligotypes (Jeong et al., 2019). This method was based on the principle associated with the order of the CRISPR array, where the *cas* genes tend to be associated with more recently acquired CRISPR repeats. For instance, spacer Xcc_23 is likely to be a newly acquired spacer/repeat unit where spacer Xcc_1 might be the oldest spacer (Jeong et al., 2019). The results of the CRISPR array are consistent with the notion that *X. citri* originated from a common ancestor and formed a monophyletic clade (Bansal et al., 2018). Furthermore, strains B2 and T4 from the commercial orchard under conventional management have more CRISPR repeats than the strain SN3-3 which was from the orchard with minimal management. This result implied that the number of CRISPR repeats could be affected by types of agricultural management. Furthermore, B2 and T4 originated from the same orchard but differed in composition of CRISPR repeats. Xcc_3 was found in B2 but not in T4 (**Figure 2**). Thus,

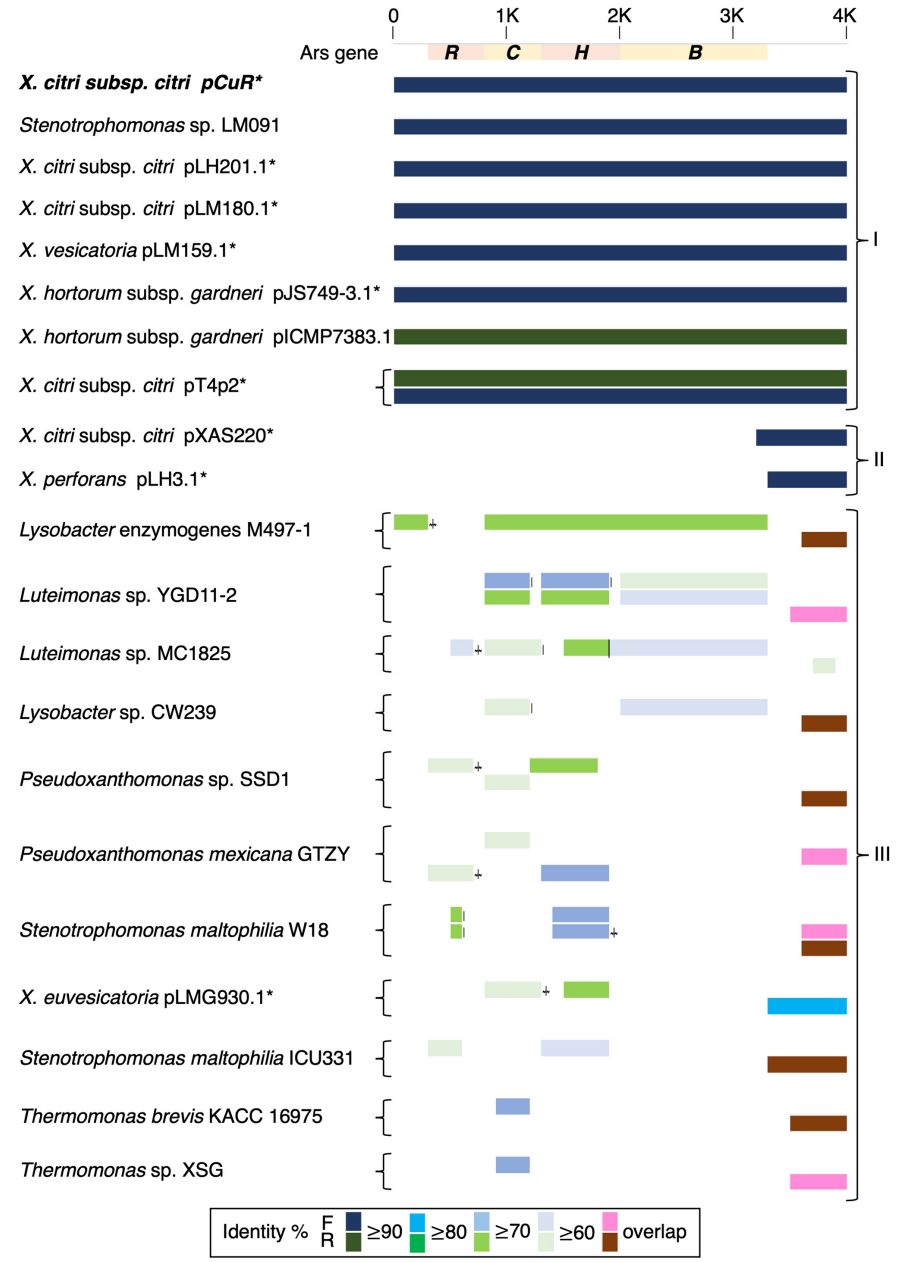

FIGURE 8 | Comparison of gene gain and loss in the arsenate resistance gene cluster.

X. citri subsp. *citri* in an orchard could evolve into various strains with diverse compositions of CRISPR repeats. The spoligotyping data indicated the rapid evolution and diversity of *X. citri* subsp. *citri* pathotype A in Asia.

The function of CRISPR/Cas systems has been proven to be an adaptive bacterial defense system against phage infections. New CRISPR spacers are introduced in the bacterial chromosome near the leader sequence (Datsenko et al., 2012). Yet, frame-shift mutation of *csd1*/*cas8c* genes caused by a short tandem repeat of two base pairs (AG) was found in the majority of *X. citri* strains, suggesting that the CRISPR defense system was mutationally inactivated to further acquire new spacers (Jeong et al., 2019). The results also suggest that most of the 25 spoligotype patterns found in *X. citri* could evolve by either random deletion of a single spacer/repeat unit or simultaneous deletion of adjacent spacer/repeat units (Jeong et al., 2019). Accordingly, deletion events could occur more often in SN3-3 than in the other 2 strains since SN3-3 had fewer CRISPR repeats than B2 and T4. An extra AG is also present in the *csd1*/*cas8c* genes of our *X. citri* subsp. *citri* strains (**Supplementary Figure 12**) reflecting inactivation of the CRISPR system due to frame-shift mutation. Moreover, the CRISPR repeat profile data implied that

B2 and T4 could acquire more resistance to phage infections than SN3-3. It will be intriguing to explore whether minimal agricultural management could induce more deletion of CRISPR repeats in citrus canker pathogens or reduce diversity of phages in an orchard.

Plasmids are highly dynamic and present another source of the *X. citri* genome diversity. The number and size of plasmids vary between *X. citri* strains and are important contributors to pathogenicity due to their ease of acquisition of foreign genomic elements through recombination and horizontal gene transfer (Timilsina et al., 2020; Rodriguez-Beltran et al., 2021). Mobile genetic elements are known to facilitate the exchange or transfer of genomic fragments between chromosomes and plasmids (Blair et al., 2015). Metagenomic analysis of wastewater identified that antibiotic selection pressure significantly increased the abundance of antibiotic resistance genes, reduced the diversity of the microbial community and in particular, increased the occurrence and abundance of mobile genetic elements (Zhao et al., 2021). Despite the high sequence variability, genes in several important functional categories such as conjugative transfer (*traY*, *traD* and *mobD/A/L*), the type IV secretion system (*vir2/3/4/6/8/9/11*), toxin/antitoxin system (family *vapC* or *pemK/mazF*) and core genes (*repA*, *parA*, XRE family transcriptional regulator) were found in all of our plasmids (Gruber et al., 2016).

Multiple types of insertion sequences and transposons including IS3, IS4, ISxac3, ISxac2, TnpA and Tn3 were identified in the plasmids (**Figure 4**). The xanthomonad Tn3 family transposons were located near different TALEs. The TnXax1 transposable element of Tn3 family in xanthomonadaceae were flanked by short inverted repeat (IR) sequences forming a generic structure of mobile insertion cassettes (MICs; Gochez et al., 2018). In particular, the genetic content of TnXax1 was organized in the following order from left IR (IRL) to right IR (IRR): *mlt* + *TnpA* (transposase) + *TnpR* (resolvase)/*TnpS*/*TnpT* (recombinase) + passenger gene as observed in other Xanthomonas strains (Lima-Mendez et al., 2020). The structure of the MICs in the plasmids of this study was similar to *TnXax1* containing the same passenger genes, Tn3 transposons and inverted repeats (IRs; Ferreira et al., 2015). The *pthA* genes in the four pathogenicity-related plasmids were surrounded by the same IRR and IRL as in the pXAC64 plasmid of *X. citri* 306.

TALEs are located on plasmids in *X. citri* strains with high variability in order to adapt to different hosts (Ferreira et al., 2015; Timilsina et al., 2020; **Figures 4**, **5** and **Supplementary Table 6**). The variability of the TALE repeats has been considered to be a strategy to diversify selection pressure to escape the detection of the host R genes (Doucoure et al., 2018). The changes in repeat arrays in *X. oryzea* TALEs were mainly associated with repeat deletion, and recombination with other TALEs (Teper and Wang, 2021). Furthermore, Teper and Wang (2021) demonstrated that two to five mismatched TALE repeats of *X. citri* subsp. *citri* was sufficient to escape the host NB-LRR recognition and promote disease symptoms in sweet orange. Our data revealed that most *pthA4* genes from different *X. citri* subsp. *citri* strains have the same number and RVD of tandem repeats (**Figure 5** and **Supplementary Table 6**). Surprisingly, the *pthA4* of strain SN3-3 was not only short (13.5 repeats) but also merged with *pthA2*.

It has been estimated that the optimal functional length of TALEs contained 15.5–19.5 RVD repeats whereas TALEs with fewer than 6.5 repeats did not perform gene activation and could be by-products of recombination events (Boch and Bonas, 2010; Gochez et al., 2018). Nevertheless, some 'non-classical' TALEs with unusually short lengths of RVD repeats but that maintain their biological function, have been reported recently (Roeschlin et al., 2019). We also identified a fusion of *pthA1* and *pthA4* in pSN3-3 and *pthA1* that was surrounded by a solo IR sequence containing only 2.5 RVD repeats (**Figure 5** and **Supplementary Table 6**). The *pthA4* was indispensable for canker elicitation but *pthA1* and *pthA3* could contribute to additive roles in developing disease symptoms (Abe and Benedetti, 2016). Since PthA4 is the TALE required for pathogenicity and SN3-3 was collected from a citrus farm with minimal management, we speculated that the PthA4 with 13.5 RVD repeats was sufficient to develop pathogenicity and maintain bacterial fitness under the agroecosystem with low selection pressure. Our data is in full agreement with the notion that the presence of the Tn3-like transposons around TALEs likely contributed to the generation of diverse TALEs of *X. citri* (Ferreira et al., 2015).

The genomic signatures of the three strains supported the occurrence of independent events of plasmid fusion. Compared with the reference genome of strain 306 (da Silva et al., 2002), we were able to identify the recombination event that caused the plasmid co-integration and the fusion of *pthA* genes (**Figure 5**). Unlike different *pthA* classes that were separated in two plasmids in pXAC33 and pXAC64 (da Silva et al., 2002), pB2_V1 and pT4p1 each contained three *pthA* classes in one plasmid (**Supplementary Table 6**). Furthermore, pB2_V1 contained two copies of *pthA1* class with high sequence identity and pB2_V1 and pB2_V3 both contained a unique class of *pthA2*/*pthA1* fusion with 13.5 RVD repeats (**Figures 5A,B** and **Supplementary Table 6**). The plasmid size of pSN3-3 was similar to pXAC64 of strain 306 (da Silva et al., 2002) but also had three classes of *pthA* and the fusion of *pthA1*/*pthA4* in one plasmid (**Figures 5B,D**).

The whole genome sequence of T4 clarified that the *cop* gene cluster is borne on the big plasmid pT4p2. Though the copper resistance in different *Xanthomonas* strains might be acquired through independent events, *cop* genes in the plasmids were genetically related (Richard et al., 2017b) and the backbones of the plasmids are highly similar. Based on the nucleotide sequence identity and presence and absence of *cop* genes, we could divide plasmids, based on the copper cluster, into three groups (**Figure 7**). Group I, including the reference plasmid pCuR and pLM091 from *Stenotrophomonas* (Richard et al., 2017b), contained the complete set of *copLABCDMGF* genes without gaps and shared high sequence identity (>90%) with plasmids in this group. On the other hand, the most dissimilar group (Group III), including pLM199 from Argentina, had sequence identity with pCuR that was ∼70% and failed to produce PCR amplicons using primers of the *copLAB* system (Richard et al., 2017b). A distinct copper transposon region (TnpLM199) containing an alternative copper resistance system *copABCD* was identified in the Argentinian strain LM199 genome (Richard et al., 2017b).

The pT4p2 was classified in Group II together with pLH3.1 of *X. perforans* and chromosome sequences from other microbials. In particular, a unique nucleotide region between the copper and arsenate cluster was only identified in pT4p2 and pLH3.1. A detailed analysis of the 1,857 bp spacer nucleotide sequence between the copper and arsenate cluster in the NCBI Nucleotide database revealed that only seven *Xanthomonas* strains contained this fragment. Among these seven strains, the spacer sequence was not located on the same plasmid as that containing copper resistance genes in the *X. euvesicatoria* strain LMG930. This result is in agreement with a previous analysis that revealed that the *copB* genes carried by pT4p2 and LMG930 were grouped in the 'Variant IV' group and shared a combination of 3, 300 and 36 bp gaps in the complete *copB* sequences (Lai et al., 2021). On the other hand, the other six *Xanthomonas* strains showed high levels of sequence coverage (99%) and nucleotide identity (>96%) (**Supplementary Table 8**). In particular, pLH3.1 of *X. euvesicatoria* did not only show high identity of the spacer sequence but also the *cop* genes (**Supplementary Figure 10**). Accordingly, the comparative genome analysis data provided evidence that pT4p2 could originate from pLH3.1 carried by Mauritian *X. perforans* LMG930. Although Cu^R *X. euvesicatoria* pv. *perforans* populations have prevalently occurred in domestic tomato orchards in Taiwan since 1989 (Burlakoti et al., 2018), only the variant V group of the *copB* gene was carried by *X. euvesicatoria* pv. *perforans* strains in our recent survey (Lai et al., 2021). Thus, pT4p2 might not originate from local Cu^R strains of *X. euvesicatoria* pv. *perforans*. However, we cannot exclude the possibility that other xanthomonads in other production areas in Taiwan, on other citrus or solanaceous cultivars which carry pLH3.1/pT4p2-like plasmids, could be found by increasing the number of Cu^R xanthomonad populations studied. A further survey of Cu^R xanthomonad populations on various hosts in combination with comparative genomic analysis will help to decipher the distribution and spread of Cu^R plasmids in xanthomonads.

Our whole genome sequencing data clarified that the *copLAB* cluster is located in the plasmid pT4p2 associated with heavy metal resistance. Horizontal transfer of copper resistance between bacteria occurs more frequently when the *cop* genes are located in the mobile plasmids (Behlau et al., 2012a). The *Tra* cluster responsible for the mobility of the plasmid was found in the Cu^R plasmid pT4p2. The data of conjugative transfer proved that pT4p2 is a mobile plasmid and able to horizontally transfer between different strains of *X. citri* subsp. *citri* (**Supplementary Table 9**). The Cu^S recipient cells became as resistant to copper as the donor cells while receiving *cop* genes *via* conjugation. Accordingly, the horizontal transfer of plasmid borne *cop* genes between citrus canker xanthomonads may potentially increase Cu^R xanthomonad populations to reduce the disease control efficacy of copper bactericides.

It is worth noting that the copper resistance gene clusters were located on the plasmid of *Xanthomonas* strains but were present in the chromosomes of *Stenotrophomonas, Pseudoxanthomonas, Lysobacter, Luteimonas* and *Thermomonas* (**Figure 7**). These Xanthomonadaceae microbes were either human pathogens (Crossman et al., 2008) or presented in the agricultural environment (Turrini et al., 2021) and some are known for carrying heavy metal resistance genes and mobile genetic elements. These environmental microbes could serve as a reservoir for the transfer of heavy metal resistance genes to microbes living in the surrounding environment.

We speculated that one copper resistance cluster in pT4p2 was inserted next to the arsenate cluster due to the Tn3-like transposon activity. Moreover, the additional copy of the arsenate and copper cluster might be the byproduct of conjugation where plasmids were transferred as a single-strand DNA during the conjugation and subsequently activated the bacterial SOS stress response. The recombination or mutagenesis frequencies of genomic fragments were then induced and increased the bacterial evolution rate (Rodriguez-Beltran et al., 2021). The high density of transposable elements around the heavy metal resistance clusters (**Supplementary Figure 10**) increased the probability that the duplicated fragment was inserted around the same location.

The whole genome sequences of the three strains in this study reflected the potential effect of agricultural practices or agroecosystems on diversification of citrus bacterial canker pathogens. A large sampling of microbes from the same environment over a long period of time would likely improve our understanding of how agricultural practices impact the microbial community.

CONCLUSION

Complete genome sequencing of three *X. citri* subsp. *citri* pathotype A strains from two distant orchards and a comparison with the published genomes in this study clearly illustrated plasticity in chromosomes and plasmids. Our results revealed the evolution of pathogenicity factors and horizontal gene transfer events in the three strains. Type of agricultural management could be a potential trigger for evolution of pathotype A of *X. citri* subsp. *citri*. Surprisingly, conventional management might induce less deletion of CRISPR repeats in *X. citri* subsp. *citri* or increase the diversity of phages in the orchard. Thus, the *X. citri* subsp. *citri* strains under conventional management might have more CRIPSR repeats for immunity to phage infections compared with the strain from the orchard with minimal management. Moreover, the *cop* gene cluster together with the arsenate resistance gene cluster were only carried by the huge plasmid in the Cu^R strain of *X. citri* subsp. *citri*. Collectively, plasmids represented a hotspot for exchanging foreign genomic elements and accelerated the adaptation of *X. citri* subsp. *citri* to the agroecosystem.

DATA AVAILABILITY STATEMENT

The dataset generated for this study including sequencing reads, genome assemblies and genome annotation have been deposited at NCBI under BioProject PRJNA644481. The *X. citri* strains that support the findings of this study are available on request from C-JH.

AUTHOR CONTRIBUTIONS

C-JH, H-FN, and Y-CL conceived and designed the experiments. T-LW, P-XZ, and J-YO performed next-generation sequencing and bioinformatics analysis. C-JH, T-LW, and Y-CL interpreted the data. C-JH, T-LW, and Y-CL wrote the manuscript with input from all co-authors. All authors read and approved the final manuscript.

FUNDING

This research was funded by the Ministry of Science and Technology (MOST, grant numbers 104-2313-B-415-013-MY2, 107-2311-B-415-004, and 108-2313-B-415-006-MY2) to C-JH, the Innovative Translational Agricultural Research Program (AS-KPQ-108-ITAR-10) and Academia Sinica Institutional funding to Y-CL. These funding bodies played no role in the design of the study, collection, analysis or interpretation of data, or in writing the manuscript.

ACKNOWLEDGMENTS

We thank the AS-BCST Bioinformatics Core for the computational support, and Miranda Loney for English editing.

SUPPLEMENTARY MATERIAL

The Supplementary Material for this article can be found online at: https://www.frontiersin.org/articles/10.3389/fmicb.2021.731711/full#supplementary-material

Supplementary Figure 1 | Highly conserved chromosome sequences of the three sequenced strains. Each collinearity block represents >5000 bp alignment and >99% sequence identity by BLASTN.

Supplementary Figure 2 | Phylogenetic analysis based on whole genome comparison. The asterisks indicate copper-resistant strains.

Supplementary Figure 3 | Shared and unique protein coding genes in three sequenced strains.

Supplementary Figure 4 | Pangenome analysis of 79 *X. citri* genomes.

Supplementary Figure 5 | Type II and III secretion systems. **(A)** Two operons of the type II secretion system. **(B)** Gene cluster of the type III secretion system.

Supplementary Figure 6 | Pairwise comparison of plasmids. Upper panel: copper resistance plasmids. Lower panel: pathogenicity related plasmids. Blue line: syntenic region in the same direction. Green: syntenic region in the reverse direction. Orange: secondary alignment. a. plasmids sequenced in this study.

Supplementary Figure 7 | Estimated plasmid copy number based on the Nanopore sequencing coverage.

Supplementary Figure 8 | Multiple plasmid alignment of pXAC33, pXAC64 and non-CuR plasmids sequenced in this study. **(A)** Mauve alignment including pXAC33, pxAC64 and plasmids in this study. **(B)** Mauve alignment of plasmids in this study. Syntenic regions share the same color.

Supplementary Figure 9 | Genome assembly confirmation of the copper-resistance plasmid pT4p2. **(A)** Genome structure of the 40 kbp inverted repeat. **(B)** PCR product of the PF1-CF1 primer pair and **(C)** PCR product of the PF1-CR3 primer pair.

Supplementary Figure 10 | Inverted duplication of metal-resistance clusters between pT4p2 and pLH3.1. Orange box (Cop): location of copper resistance gene clusters. Pink box (Ars): arsenate-resistant gene clusters. Tns: transposase.

Supplementary Figure 11 | Comparison of plasmids containing copper resistance genes in pT4p2, pCur and pLH201.1. Circles from outermost to innermost represent: (1) position and genes, the grid is 10 kbp [pink, pT4p2 of strain T4; yellow, pLH201.1 (NZ_CP018859.1) of strain LH201; white, pCuR (NZ_CP023286.1) of strain 03-1638-1-1]; (2) GC content with 2000-bp sliding window and 200-bp step; (3) regions with similar gene content and nucleotide sequence identity >90%, and alignment length >1 kb between plasmids.

Supplementary Figure 12 | Multiple sequence alignment of csd1 and cas8c genes. Black box, around 530 nt, indicates the AG frameshift.

Supplementary Table 1 | Summary of assembly and annotation statistics.

Supplementary Table 2 | Strains used for pan-genome analysis.

Supplementary Table 3 | Pairwise nucleotide sequences identified by fastANI.

Supplementary Table 4 | GO enrichment of strain specific genes.

Supplementary Table 5 | Gene clsters of the type II and type III secretion systems.

Supplementary Table 6 | TALEs and repeat number of RVDs in plasmids.

Supplementary Table 7 | Strains used for copper and arsenate resistance gene cluster alignment.

Supplementary Table 8 | Strains containing the unique spacer repeat between the copper and arsenate resistance gene clusters.

Supplementary Table 9 | Conjugation frequency of plasmid-borne copper resistance genes transferred between different *Xanthomonas citri* subsp. *citri* strains *in vitro*.

REFERENCES

Abe, V. K., and Benedetti, C. E. (2016). Additive roles of PthAs in bacterial growth and pathogenicity associated with nucleotide polymorphisms in effector-binding elements of citrus canker susceptibility genes. *Mol. Plant Pathol.* 17, 1223–1236. doi: 10.1111/mpp.12359

Achour, A. R., Bauda, P., and Billard, P. (2007). Diversity of arsenite transporter genes from arsenic-resistant soil bacteria. *Res. Microbiol.* 158, 128–137. doi: 10.1016/j.resmic.2006.11.006

Achtman, M. (2008). Evolution, population structure, and phylogeography of genetically monomorphic bacterial pathogens. *Annu. Rev. Microbiol.* 62, 53–70. doi: 10.1146/annurev.micro.62.081307.162832

Alegria, M. C., Docena, C., Khater, L., Ramos, C. H., Da Silva, A. C., and Farah, C. S. (2004). New protein-protein interactions identified for the regulatory and structural components and substrates of the type III Secretion system of the phytopathogen *Xanthomonas axonopodis Pathovar citri*. *J. Bacteriol.* 186, 6186–6197. doi: 10.1128/JB.186.18.6186-6197.2004

Altschul, S. F., Gish, W., Miller, W., Myers, E. W., and Lipman, D. J. (1990). Basic local alignment search tool. *J. Mol. Biol.* 215, 403–410. doi: 10.1016/S0022-2836(05)80360-2

Andrews, S. (2010). *FastQC: a Quality Control Tool for High Throughput Sequence Data. Babraham Bioinformatics*. Cambridge: Babraham Institute.

Arndt, D., Grant, J. R., Marcu, A., Sajed, T., Pon, A., Liang, Y., et al. (2016). PHASTER: a better, faster version of the PHAST phage search tool. *Nucleic Acids Res.* 44, W16–W21. doi: 10.1093/nar/gkw387

Bansal, K., Kumar, S., and Patil, P. B. (2018). Complete genome sequence reveals evolutionary dynamics of an emerging and variant pathovar of *Xanthomonas euvesicatoria*. *Genome Biol. Evol.* 10, 3104–3109. doi: 10.1093/gbe/evy238

Bansal, K., Midha, S., Kumar, S., and Patil, P. B. (2017). Ecological and evolutionary insights into *Xanthomonas citri* pathovar diversity. *Appl. Environ. Microbiol.* 83:e02993-16. doi: 10.1128/AEM.02993-16

Behlau, F., Canteros, B. I., Jones, J. B., and Graham, J. H. (2012a). Copper resistance genes from different xanthomonads and citrus epiphytic bacteria confer resistance to *Xanthomonas citri* subsp. *citri*. *Eur. J. Plant Pathol.* 133, 949–963. doi: 10.1007/s10658-012-9966-8

Behlau, F., Canteros, B. I., Minsavage, G. V., Jones, J. B., and Graham, J. H. (2011). Molecular characterization of copper resistance genes from *Xanthomonas citri* subsp. *citri* and *Xanthomonas alfalfae* subsp. *citrumelonis*. *Appl. Environ. Microbiol.* 77, 4089–4096. doi: 10.1128/AEM.03043-10

Behlau, F., Hong, J. C., Jones, J. B., and Graham, J. H. (2013). Evidence for acquisition of copper resistance genes from different sources in citrus-associated xanthomonads. *Phytopathology* 103, 409–418. doi: 10.1094/PHYTO-06-12-0134-R

Behlau, F., Jones, J. B., Myers, M. E., and Graham, J. H. (2012b). Monitoring for resistant populations of *Xanthomonas citri* subsp. *citri* and epiphytic bacteria on citrus trees treated with copper or streptomycin using a new semi-selective medium. *Eur. J. Plant Pathol.* 132, 259–270. doi: 10.1007/s10658-011-9870-7

Blair, J. M., Webber, M. A., Baylay, A. J., Ogbolu, D. O., and Piddock, L. J. (2015). Molecular mechanisms of antibiotic resistance. *Nat. Rev. Microbiol.* 13, 42–51. doi: 10.1038/nrmicro3380

Boch, J., and Bonas, U. (2010). *Xanthomonas* AvrBs3 family-type III effectors: discovery and function. *Annu. Rev. Phytopathol.* 48, 419–436. doi: 10.1146/annurev-phyto-080508-081936

Bolger, A. M., Lohse, M., and Usadel, B. (2014). Trimmomatic: a flexible trimmer for Illumina sequence data. *Bioinformatics* 30, 2114–2120. doi: 10.1093/bioinformatics/btu170

Brown, N. L., Stoyanov, J. V., Kidd, S. P., and Hobman, J. L. (2003). The MerR family of transcriptional regulators. *FEMS Microbiol. Rev.* 27, 145–163. doi: 10.1016/S0168-6445(03)00051-2

Brunings, A. M., and Gabriel, D. W. (2003). *Xanthomonas citri*: breaking the surface. *Mol. Plant Pathol.* 4, 141–157. doi: 10.1046/j.1364-3703.2003.00163.x

Burlakoti, R. R., Hsu, C. F., Chen, J. R., and Wang, J. F. (2018). Population dynamics of *Xanthomonads* associated with bacterial spot of tomato and pepper during 27 years across Taiwan. *Plant Dis.* 102, 1348–1356. doi: 10.1094/PDIS-04-17-0465-RE

Canteros, B. I., Rybak, M., Gochez, A., Velazquez, P., Rivadeneira, M., Mitidieri, M., et al. (2008). Occurrence of copper resistance in *Xanthomonas axonopodis* pv. *citri* in Argentina. *Phytopathology* 98:S30.

Capella-Gutierrez, S., Silla-Martinez, J. M., and Gabaldon, T. (2009). trimAl: a tool for automated alignment trimming in large-scale phylogenetic analyses. *Bioinformatics* 25, 1972–1973. doi: 10.1093/bioinformatics/btp348

Carver, T., Harris, S. R., Berriman, M., Parkhill, J., and Mcquillan, J. A. (2012). Artemis: an integrated platform for visualization and analysis of high-throughput sequence-based experimental data. *Bioinformatics* 28, 464–469. doi: 10.1093/bioinformatics/btr703

Chiang-Ni, C., Zheng, P. X., Tsai, P. J., Chuang, W. J., Lin, Y. S., Liu, C. C., et al. (2012). Environmental pH changes, but not the LuxS signalling pathway, regulate SpeB expression in M1 group A streptococci. *J. Med. Microbiol.* 61, 16–22. doi: 10.1099/jmm.0.036012-0

Couvin, D., Bernheim, A., Toffano-Nioche, C., Touchon, M., Michalik, J., Néron, B., et al. (2018). CRISPRCasFinder, an update of CRISRFinder, includes a portable version, enhanced performance and integrates search for Cas proteins. *Nucleic Acids Res.* 46, W246–W251. doi: 10.1093/nar/gky425

Crossman, L. C., Gould, V. C., Dow, J. M., Vernikos, G. S., Okazaki, A., Sebaihia, M., et al. (2008). The complete genome, comparative and functional analysis of *Stenotrophomonas maltophilia* reveals an organism heavily shielded by drug resistance determinants. *Genome Biol.* 9:R74. doi: 10.1186/gb-2008-9-4-r74

da Silva, A. C., Ferro, J. A., Reinach, F. C., Farah, C. S., Furlan, L. R., Quaggio, R. B., et al. (2002). Comparison of the genomes of two *Xanthomonas* pathogens with differing host specificities. *Nature* 417, 459–463. doi: 10.1038/417459a

Datsenko, K. A., Pougach, K., Tikhonov, A., Wanner, B. L., Severinov, K., and Semenova, E. (2012). Molecular memory of prior infections activates the CRISPR/Cas adaptive bacterial immunity system. *Nat. Commun.* 3:945. doi: 10.1038/ncomms1937

De Coster, W., D'hert, S., Schultz, D. T., Cruts, M., and Van Broeckhoven, C. (2018). NanoPack: visualizing and processing long-read sequencing data. *Bioinformatics* 34, 2666–2669. doi: 10.1093/bioinformatics/bty149

Doucoure, H., Perez-Quintero, A. L., Reshetnyak, G., Tekete, C., Auguy, F., Thomas, E., et al. (2018). Functional and genome sequence-driven characterization of tal effector gene repertoires reveals novel variants with altered specificities in closely related Malian *Xanthomonas oryzae* pv. *oryzae* strains. *Front. Microbiol.* 9:1657. doi: 10.3389/fmicb.2018.01657

Edgar, R. C. (2004). MUSCLE: a multiple sequence alignment method with reduced time and space complexity. *BMC Bioinformatics* 5:113. doi: 10.1186/1471-2105-5-113

Enright, A. J., Van Dongen, S., and Ouzounis, C. A. (2002). An efficient algorithm for large-scale detection of protein families. *Nucleic Acids Res.* 30, 1575–1584. doi: 10.1093/nar/30.7.1575

Fawcett, H., and Jenkins, A. (1933). Records of citrus canker from herbarium specimens of the genus *Citrus* in England and the United States. *Phytopathology* 23, 820–824.

Ference, C. M., Gochez, A. M., Behlau, F., Wang, N., Graham, J. H., and Jones, J. B. (2018). Recent advances in the understanding of *Xanthomonas citri* ssp. *citri* pathogenesis and citrus canker disease management. *Mol. Plant Pathol.* 19, 1302–1318. doi: /10.1111/mpp.12638

Ferreira, R. M., De Oliveira, A. C., Moreira, L. M., Belasque, J. Jr., Gourbeyre, E., Siguier, P., et al. (2015). A TALE of transposition: Tn3-like transposons play a major role in the spread of pathogenicity determinants of *Xanthomonas citri* and other xanthomonads. *mBio* 6, e02505–e02514. doi: 10.1128/mBio.02505-14

Fonseca, N. P., Patane, J. S. L., Varani, A. M., Felestrino, E. B., Caneschi, W. L., Sanchez, A. B., et al. (2019). Analyses of seven new genomes of *Xanthomonas citri* pv. *aurantifolii* Strains, causative agents of citrus canker B and C, Show a reduced repertoire of pathogenicity-related genes. *Front. Microbiol.* 10:2361. doi: 10.3389/fmicb.2019.02361

Gochez, A. M., Huguet-Tapia, J. C., Minsavage, G. V., Shantaraj, D., Jalan, N., Strauss, A., et al. (2018). Pacbio sequencing of copper-tolerant *Xanthomonas citri* reveals presence of a chimeric plasmid structure and provides insights into reassortment and shuffling of transcription activator-like effectors among *X. citri* strains. *BMC Genomics* 19:16. doi: 10.1186/s12864-017-4408-9

Grigoriev, A. (1998). Analyzing genomes with cumulative skew diagrams. *Nucleic Acids Res.* 26, 2286–2290. doi: 10.1093/nar/26.10.2286

Gruber, C. J., Lang, S., Rajendra, V. K., Nuk, M., Raffl, S., Schildbach, J. F., et al. (2016). Conjugative DNA transfer is enhanced by plasmid R1 partitioning proteins. *Front. Mol. Biosci.* 3:32. doi: 10.3389/fmolb.2016.00032

Hseu, S. H., and Hsu, S. T. (1991). Sensitivity of strains of *Xanthomonas campestris* pv. *vesicatoria* from Taiwan to copper and other agrochemicals. *Plant Prot. Bull.* 33, 410–419.

Huang, C. J., and Ni, H. F. (2017). First report of *Citrus depressa* as a new natural host of *Xanthomonas citri* subsp. *citri* pathotype A in Taiwan. *J. Plant Pathol.* 99:289.

Jain, C., Rodriguez, R. L., Phillippy, A. M., Konstantinidis, K. T., and Aluru, S. (2018). High throughput ANI analysis of 90K prokaryotic genomes reveals clear species boundaries. *Nat. Commun.* 9:5114. doi: 10.1038/s41467-018-07641-9

Jeong, K., Muñoz-Bodnar, A., Rojas, N. A., Poulin, L., Rodriguez-R, L. M., Gagnevin, L., et al. (2019). CRISPR elements provide a new framework for the genealogy of the citrus canker pathogen *Xanthomonas citri* pv. *citri*. *BMC genomics* 20:917. doi: 10.1186/s12864-019-6267-z

Kolmogorov, M., Yuan, J., Lin, Y., and Pevzner, P. A. (2019). Assembly of long, error-prone reads using repeat graphs. *Nat. Biotechnol.* 37, 540–546. doi: 10.1038/s41587-019-0072-8

Korotkov, K. V., Sandkvist, M., and Hol, W. G. (2012). The type II secretion system: biogenesis, molecular architecture and mechanism. *Nat. Rev. Microbiol.* 10, 336–351. doi: 10.1038/nrmicro2762

Kozlov, A. M., Darriba, D., Flouri, T., Morel, B., and Stamatakis, A. (2019). RAxML-NG: a fast, scalable and user-friendly tool for maximum likelihood phylogenetic inference. *Bioinformatics* 35, 4453–4455. doi: 10.1093/bioinformatics/btz305

Krzywinski, M., Schein, J., Birol, I., Connors, J., Gascoyne, R., Horsman, D., et al. (2009). Circos: an information aesthetic for comparative genomics. *Genome Res.* 19, 1639–1645. doi: 10.1101/gr.092759.109

Kurtz, S., Phillippy, A., Delcher, A. L., Smoot, M., Shumway, M., Antonescu, C., et al. (2004). Versatile and open software for comparing large genomes. *Genome Biol.* 5:R12. doi: 10.1186/gb-2004-5-2-r12

Lai, Y.-R., Lin, C.-H., Chang, C.-P., Ni, H.-F., Tsai, W.-S., and Huang, C.-J. (2021). Distribution of copper resistance gene variants of *Xanthomonas citri* subsp. *citri* and *Xanthomonas euvesicatoria* pv. *perforans*. *Plant Prot. Sci.* 57, 206–216. doi: 10.17221/160/2020-PPS

Leduc, A., Traore, Y. N., Boyer, K., Magne, M., Grygiel, P., Juhasz, C. C., et al. (2015). Bridgehead invasion of a monomorphic plant pathogenic bacterium: *Xanthomonas citri* pv. *citri*, an emerging citrus pathogen in Mali and Burkina Faso. *Environ. Microbiol.* 17, 4429–4442. doi: 10.1111/1462-2920.12876

Lee, Y. A., Hendson, M., Panopoulos, N. J., and Schroth, M. N. (1994). Molecular cloning, chromosomal mapping, and sequence analysis of copper resistance genes from *Xanthomonas campestris* pv. *juglandis*: homology with small blue copper proteins and multicopper oxidase. *J. Bacteriol.* 176, 173–188. doi: 10.1128/jb.176.1.173-188.1994

Lima-Mendez, G., Oliveira Alvarenga, D., Ross, K., Hallet, B., Van Melderen, L., Varani, A. M., et al. (2020). Toxin-antitoxin gene pairs found in Tn3 family transposons appear to be an integral part of the transposition module. *mBio* 11:e00452-20. doi: 10.1128/mBio.00452-20

Loiseau, C., Hatte, V., Andrieu, C., Barlet, L., Cologne, A., De Oliveira, R., et al. (2018). PanGeneHome : a web interface to analyze microbial pangenomes. *J. Bioinform. Comput. Syst. Biol.* 1:108.

Lomsadze, A., Gemayel, K., Tang, S., and Borodovsky, M. (2018). Modeling leaderless transcription and atypical genes results in more accurate gene prediction in prokaryotes. *Genome Res.* 28, 1079–1089. doi: 10.1101/gr.230615.117

Marin, T. G. S., Galvanin, A. L., Lanza, F. E., and Behlau, F. (2019). Description of copper tolerant *Xanthomonas citri* subsp. *citri* and genotypic comparison with sensitive and resistant strains. *Plant Pathol.* 68, 1088–1098. doi: 10.1111/ppa.13026

Meric, G., Yahara, K., Mageiros, L., Pascoe, B., Maiden, M. C., Jolley, K. A., et al. (2014). A reference pan-genome approach to comparative bacterial genomics: identification of novel epidemiological markers in pathogenic *Campylobacter*. *PLoS One* 9:e92798. doi: 10.1371/journal.pone.0092798

Nurk, S., Walenz, B. P., Rhie, A., Vollger, M. R., Logsdon, G. A., Grothe, R., et al. (2020). HiCanu: accurate assembly of segmental duplications, satellites, and allelic variants from high-fidelity long reads. *Genome Res.* 30, 1291–1305. doi: 10.1101/gr.263566.120

Patane, J. S. L., Martins, J. Jr., Rangel, L. T., Belasque, J., Digiampietri, L. A., Facincani, A. P., et al. (2019). Origin and diversification of *Xanthomonas citri* subsp. *citri* pathotypes revealed by inclusive phylogenomic, dating, and biogeographic analyses. *BMC Genomics* 20:700. doi: 10.1186/s12864-019-6007-4

Pena-Gonzalez, A., Rodriguez, R. L., Marston, C. K., Gee, J. E., Gulvik, C. A., Kolton, C. B., et al. (2018). Genomic characterization and copy number variation of *Bacillus anthracis* plasmids pXO1 and pXO2 in a historical collection of 412 strains. *mSystems* 3:e00065-18. doi: 10.1128/mSystems.00065-18

Proost, S., Fostier, J., De Witte, D., Dhoedt, B., Demeester, P., Van De Peer, Y., et al. (2012). i-ADHoRe 3.0—fast and sensitive detection of genomic homology in extremely large data sets. *Nucleic Acids Res.* 40:e11. doi: 10.1093/nar/gkr955

Pruvost, O., Magne, M., Boyer, K., Leduc, A., Tourterel, C., Drevet, C., et al. (2014). A MLVA genotyping scheme for global surveillance of the citrus pathogen *Xanthomonas citri* pv. *citri* suggests a worldwide geographical expansion of a single genetic lineage. *PLoS One* 9:e98129. doi: 10.1371/journal.pone.0098129

Qian, W., Jia, Y., Ren, S. X., He, Y. Q., Feng, J. X., Lu, L. F., et al. (2005). Comparative and functional genomic analyses of the pathogenicity of phytopathogen *Xanthomonas campestris* pv. campestris. *Genome Res.* 15, 757–767. doi: 10.1101/gr.3378705

Richard, D., Boyer, C., Verniere, C., Canteros, B. I., Lefeuvre, P., and Pruvost, O. (2017a). Complete genome sequences of six copper-resistant *Xanthomonas citri* pv. citri strains causing asiatic citrus canker, obtained using long-read technology. *Genome Announc.* 5:e00010-e17. doi: 10.1128/genomeA.00010-17

Richard, D., Pruvost, O., Balloux, F., Boyer, C., Rieux, A., and Lefeuvre, P. (2021). Time-calibrated genomic evolution of a monomorphic bacterium during its establishment as an endemic crop pathogen. *Mol. Ecol.* 30, 1823–1835. doi: 10.1111/mec.15770

Richard, D., Ravigne, V., Rieux, A., Facon, B., Boyer, C., Boyer, K., et al. (2017b). Adaptation of genetically monomorphic bacteria: evolution of copper resistance through multiple horizontal gene transfers of complex and versatile mobile genetic elements. *Mol. Ecol.* 26, 2131–2149. doi: 10.1111/mec.14007

Roach, R., Mann, R., Gambley, C., Shivas, R., Chapman, T., and Rodoni, B. (2020). Pathogenicity and copper tolerance in Australian *Xanthomonas* species associated with bacterial leaf spot. *Crop Prot.* 127:104923. doi: 10.1016/j.cropro.2019.104923

Rodriguez-Beltran, J., Delafuente, J., Leon-Sampedro, R., Maclean, R. C., and San Millan, A. (2021). Beyond horizontal gene transfer: the role of plasmids in bacterial evolution. *Nat. Rev. Microbiol.* 19, 347–359. doi: 10.1038/s41579-020-00497-1

Roeschlin, R. A., Uviedo, F., Garcia, L., Molina, M. C., Favaro, M. A., Chiesa, M. A., et al. (2019). PthA4(AT), a 7.5-repeats transcription activator-like (TAL) effector from *Xanthomonas citri* ssp. *citri*, triggers citrus canker resistance. *Mol. Plant Pathol.* 20, 1394–1407. doi: 10.1111/mpp.12844

Ruan, J., and Li, H. (2020). Fast and accurate long-read assembly with wtdbg2. *Nat. Methods* 17, 155–158. doi: 10.1038/s41592-019-0669-3

Ruh, M., Briand, M., Bonneau, S., Jacques, M. A., and Chen, N. W. G. (2017). *Xanthomonas* adaptation to common bean is associated with horizontal transfers of genes encoding TAL effectors. *BMC Genomics* 18:670. doi: 10.1186/s12864-017-4087-6

Teper, D., and Wang, N. (2021). Consequences of adaptation of TAL effectors on host susceptibility to *Xanthomonas*. *PLoS Genet.* 17:e1009310. doi: 10.1371/journal.pgen.1009310

Timilsina, S., Pereira-Martin, J. A., Minsavage, G. V., Iruegas-Bocardo, F., Abrahamian, P., Potnis, N., et al. (2019). Multiple recombination events drive the current genetic structure of *Xanthomonas perforans* in Florida. *Front. Microbiol.* 10:448. doi: 10.3389/fmicb.2019.00448

Timilsina, S., Potnis, N., Newberry, E. A., Liyanapathiranage, P., Iruegas-Bocardo, F., White, F. F., et al. (2020). *Xanthomonas* diversity, virulence and plant-pathogen interactions. *Nat. Rev. Microbiol.* 18, 415–427. doi: 10.1038/s41579-020-0361-8

Treangen, T. J., Ondov, B. D., Koren, S., and Phillippy, A. M. (2014). The Harvest suite for rapid core-genome alignment and visualization of thousands of intraspecific microbial genomes. *Genome Biol.* 15:524. doi: 10.1186/s13059-014-0524-x

Triplett, L. R., Hamilton, J. P., Buell, C. R., Tisserat, N. A., Verdier, V., Zink, F., et al. (2011). Genomic analysis of *Xanthomonas oryzae* isolates from rice grown in the United States reveals substantial divergence from known *X. oryzae* pathovars. *Appl. Environ. Microbiol.* 77, 3930–3937. doi: 10.1128/AEM.00028-11

Turrini, P., Artuso, I., Tescari, M., Lugli, G. A., Frangipani, E., Ventura, M., et al. (2021). Draft genome sequence and secondary metabolite biosynthetic potential of the *Lysobacter niastensis* type strain DSM 18481. *Microbiol. Resour. Announc.* 10:e01296-20. doi: 10.1128/MRA.01296-20

Vinatzer, B. A., Monteil, C. L., and Clarke, C. R. (2014). Harnessing population genomics to understand how bacterial pathogens emerge, adapt to crop hosts, and disseminate. *Annu. Rev. Phytopathol.* 52, 19–43. doi: /10.1146/annurev-phyto-102313-045907

Walker, B. J., Abeel, T., Shea, T., Priest, M., Abouelliel, A., Sakthikumar, S., et al. (2014). Pilon: an integrated tool for comprehensive microbial variant detection and genome assembly improvement. *PloS one* 9:e112963. doi: 10.1371/journal.pone.0112963

Wang, J. R., Holt, J., Mcmillan, L., and Jones, C. D. (2018). FMLRC: hybrid long read error correction using an FM-index. *BMC bioinformatics* 19:50. doi: 10.1186/s12859-018-2051-3

Wang, P., Meng, F., Moore, B. M., and Shiu, S. H. (2021). Impact of short-read sequencing on the misassembly of a plant genome. *BMC Genomics* 22:99. doi: 10.1186/s12864-021-07397-5

Wu, Y. F., Hsu, S. T., and Tzeng, K. C. (1995). Association of plasmid with copper resistance in strains of *Xanthomonas campestris* pv. *vesicatoria* from Taiwan. *Plant Prot. Bull.* 37, 209–218.

Yen, M. R., Lin, N. T., Hung, C. H., Choy, K. T., Weng, S. F., and Tseng, Y. H. (2002). oriC region and replication termination site, dif, of the *Xanthomonas campestris* pv. campestris 17 chromosome. *Appl. Environ. Microbiol.* 68, 2924–2933. doi: 10.1128/AEM.68.6.2924-2933.2002

Zhang, Y., Jalan, N., Zhou, X., Goss, E., Jones, J. B., Setubal, J. C., et al. (2015). Positive selection is the main driving force for evolution of citrus canker-causing *Xanthomonas*. *ISME J.* 9, 2128–2138. doi: 10.1038/ismej.2015.15

Zhao, R., Feng, J., Huang, J., Li, X., and Li, B. (2021). Reponses of microbial community and antibiotic resistance genes to the selection pressures of ampicillin, cephalexin and chloramphenicol in activated sludge reactors. *Sci. Total Environ.* 755:142632. doi: 10.1016/j.scitotenv.2020.142632

Conflict of Interest: The authors declare that the research was conducted in the absence of any commercial or financial relationships that could be construed as a potential conflict of interest.

Publisher's Note: All claims expressed in this article are solely those of the authors and do not necessarily represent those of their affiliated organizations, or those of the publisher, the editors and the reviewers. Any product that may be evaluated in this article, or claim that may be made by its manufacturer, is not guaranteed or endorsed by the publisher.

frontiers in Microbiology

ORIGINAL RESEARCH
published: 07 September 2021
doi: 10.3389/fmicb.2021.718963

Impact of Tellurite on the Metabolism of *Paenibacillus pabuli* AL109b With Flagellin Production Explaining High Reduction Capacity

*Pedro Farias[1], Romeu Francisco[1], Lorrie Maccario[2], Jakob Herschend[2], Ana Paula Piedade[3], Søren Sørensen[2] and Paula V. Morais[1]**

[1] Department of Life Sciences, CEMMPRE, University of Coimbra, Coimbra, Portugal, [2] Section of Microbiology, Department of Biology, University of Copenhagen, Copenhagen, Denmark, [3] CEMMPRE, Department Mechanical Engineering, University of Coimbra, Coimbra, Portugal

OPEN ACCESS

Edited by:
Rob Van Houdt, Belgian Nuclear Research Centre, Belgium

Reviewed by:
Felipe Arenas, University of Santiago, Chile
Vijay Kumar, Institute of Himalayan Bioresource Technology (CSIR), India

***Correspondence:**
Paula V. Morais
pvmorais@ci.uc.pt

Specialty section:
This article was submitted to Antimicrobials, Resistance and Chemotherapy, a section of the journal Frontiers in Microbiology

Received: *01 June 2021*
Accepted: *10 August 2021*
Published: *07 September 2021*

Citation:
Farias P, Francisco R, Maccario L, Herschend J, Piedade AP, Sørensen S and Morais PV (2021) Impact of Tellurite on the Metabolism of Paenibacillus pabuli AL109b With Flagellin Production Explaining High Reduction Capacity. Front. Microbiol. 12:718963. doi: 10.3389/fmicb.2021.718963

Tellurium (Te) is a metalloid with scarce and scattered abundance but with an increased interest in human activity for its uses in emerging technologies. As is seen for other metals and metalloids, the result of mining activity and improper disposal of high-tech devices will lead to niches with increased abundance of Te. This metalloid will be more available to bacteria and represent an increasing selective pressure. This environmental problem may constitute an opportunity to search for microorganisms with genetic and molecular mechanisms of microbial resistance to Te toxic anions. Organisms from Te-contaminated niches could provide tools for Te remediation and fabrication of Te-containing structures with added value. The objective of this study was to determine the ability of a high metal-resistant *Paenibacillus pabuli* strain ALJ109b, isolated from high metal content mining residues, to reduce tellurite ion, and to evaluate the formation of metallic tellurium by cellular reduction, isolate the protein responsible, and determine the metabolic response to tellurite during growth. *P. pabuli* ALJ109b demonstrated to be resistant to Te (IV) at concentrations higher than reported for its genus. It can efficiently remove soluble Te (IV) from solution, over 20% in 8 h of growth, and reduce it to elemental Te, forming monodisperse nanostructures, verified by scattering electron microscopy. Cultivation of *P. pabuli* ALJ109b in the presence of Te (IV) affected the general protein expression pattern, and hence the metabolism, as demonstrated by high-throughput proteomic analysis. The Te (IV)-induced metabolic shift is characterized by an activation of ROS response. Flagellin from *P. pabuli* ALJ109b demonstrates high Te (0) forming activity in neutral to basic conditions in a range of temperatures from 20°C to 37°C. In conclusion, the first metabolic characterization of a strain of *P. pabuli* response to Te (IV) reveals a highly resistant strain with a unique Te (IV) proteomic response. This strain, and its flagellin, display, all the features of potential tools for Te nanoparticle production.

Keywords: ***Paenibacillus*** **sp., genome, proteome, flagellin, tellurite**

INTRODUCTION

The study of the Te–bacteria interaction has been mainly focused on resistance to soluble Te ions, particularly the reduction of Te (IV) and Te (VI) to Te (0). This characteristic resulted in a growing interest in isolation and characterization of new organisms with potential in Te ion reduction from a large number of different environments, such as sea sediments (Csotonyi et al., 2006; Ollivier et al., 2008), mine tailings (Maltman et al., 2015), and fouled waters (Chien and Han, 2009). These environments can provide organisms with novel genes and processes to deal with toxic Te (IV), different from those identified in the majority of bacterial strains studied so far, mainly from clinical settings. Tellurite resistance by reduction (TeR) targets the Te oxyanions, and to this date, few mechanisms have been identified as TeR. Among the most well-described genetic clusters involved in tellurium ion resistance are the mechanisms encoded by the gene cluster *terZABCDEF* (Kormutakova et al., 2000), the *tehAB* gene cluster (Lohmeier-Vogel et al., 2004), or the *kilA* operon (Turner et al., 1994, 1995). The relation of these specific Te resistance mechanisms with Te (IV) reduction is in most cases still to be proven. Several works describe mechanisms of Te resistance by unspecific intracellular reduction of Te ions, implicating reducing agents such as nitrate reductases or elements of the respiratory chain (Sabaty et al., 2001; Chasteen et al., 2009; Theisen et al., 2013; Alavi et al., 2014). In most of these cases, TeR is viewed as the main mechanism for Te resistance. Bioreduction of Te occurs when cells interact with soluble and toxic forms of Te (IV) and Te (VI) and convert the oxyanions to an inert and insoluble form. Bioreduction is a relevant biotechnological characteristic to determine, as varies among different organisms; therefore, for new bacterial strains, the reduction efficiency should be determined. The bioreduction to Te can lead to the formation of nanostructures (Baesman et al., 2007; Zare et al., 2012; Presentato et al., 2016; Wang et al., 2018). As verified for other metals, the formation of Te-containing intra-/extra-cellular nanostructures can be monitored by following the bioreduction process. A diversity of microorganisms has shown the capacity to form these nanostructures, such as *Enterobacter cloacae* (Contreras et al., 2018), *Shewanella* sp. (Vaigankar et al., 2018), and *Ochrobactrum* sp. (Zonaro et al., 2017), and extensive work performed on *Rhodobacter capsulatus* (Borghese et al., 2014; Borghese et al., 2017). An increasing interest in understanding the formation of these structures is the result of the growing potential range of applications for bio-produced nanoparticles covering fields such as optical imaging (Plaza et al., 2016) or novel battery technology (Kim et al., 2015). Growing attention has been given to *Paenibacillus* spp. for its potential in biotechnological applications (Jimoh and Lin, 2019; Du et al., 2021). To this date, some studies on the interactions of *Paenibacillus* strains with metals have been produced (Knuutinen et al., 2019; Ogunyemi et al., 2020) but only a few concerning Te (Chien and Han, 2009). Strains of *Paenibacillus* have been characterized for their biochemistry and proteomics and considered of interest in rhizostabilization of cadmium (Kumari and Thakur, 2018) for their high metal resistance, siderophore production, biocontrol activities, and xenobiotic degradation. Additionally, *Paenibacillus* is also known to produce extracellular polysaccharides with high metal ion uptake ability (Prado Acosta et al., 2005). Nowadays, technologies such as differential proteomics give new perspectives in molecular mechanisms of stress response and metal resistance (Moreno and Rojo, 2013; Djoko et al., 2017). Therefore, it can be applied for determining the impact of Te (IV) on microorganism metabolism.

Residues from the Panasqueira mine in the center of Portugal showed to have *Paenibacillus* in their microbial community, which were isolated in the presence of Te. Considering their metabolic versatility, we hypothesized that the genomic and metabolic characterization of the strain would bring to knowledge new biological strategies to cope with Te, able to be explored biotechnologically.

In this work, we aimed to study the metabolism of a *Paenibacillus pabuli* strain ALJ109b able to resist and to reduce Te (IV) to elemental Te. The resulting Te structures were characterized and revealed an organized structure at the nanoscale size. The genome and proteome analysis performed to describe the *P. pabuli* ALJ109b response to Te (IV) revealed the diversity of strategies of this strain to cope with the metalloid. *P. pabuli* ALJ109b showed to shift its metabolism to deal with the Te (IV)-induced oxidative stress and is able to resist high Te (IV) concentrations by reducing the metalloid. Moreover, the *P. pabuli* ALJ109b flagellin was identified as part of the TeR process. The protein was cloned in a recombinant system and its ability to reduce Te (IV) demonstrated.

The current study offers new insights on the metabolism activated by *Paenibacillus* strain in the presence of Te (IV) and identifies the mechanisms by which this strain, using flagellin, effectively produces Te nanoparticles. Flagellin demonstrates potential application in Te (IV) decontamination and in the fabrication of Te nanoparticles.

RESULTS

Tellurite Resistance and Reduction by *Paenibacillus pabuli* ALJ109b

The growth of *P. pabuli* ALJ109b in the presence and in the absence of Te (IV) was followed. The strain was able to grow in up to 5×10^{-4} M Te (IV). Specific growth rates considered early and late (8 h) exponential growth time points, based on the growth curve for this strain for strain *P. pabuli* ALJ109b. The specific growth rates were similar to the control condition in concentrations up to 2.5×10^{-4} M Te (IV) but decreased at the concentration of 5×10^{-4} M Te (IV) (**Figure 1A**). *Escherichia coli* BL21 was not able to grow in the presence of Te (IV).

Considering that 5×10^{-4} M Te (IV) was the lowest concentration that affected *P. pabuli* ALJ109b growth, Te (IV) reduction was evaluated at this concentration. At a concentration of 5×10^{-4} M Te (IV), *P. pabuli* ALJ109b showed Te (IV) depletion efficiencies in the order of 1.25 $\Delta mg.DO^{-1}$ and a reduction rate at 8 h of 0.06 $\Delta mg.DO^{-1}.h^{-1}$ (**Table 1**). This reduction rate allowed for a removal of 20.66% of initial Te (IV) within 8 h, reaching 33.17% in the later stationary phase (20 h).

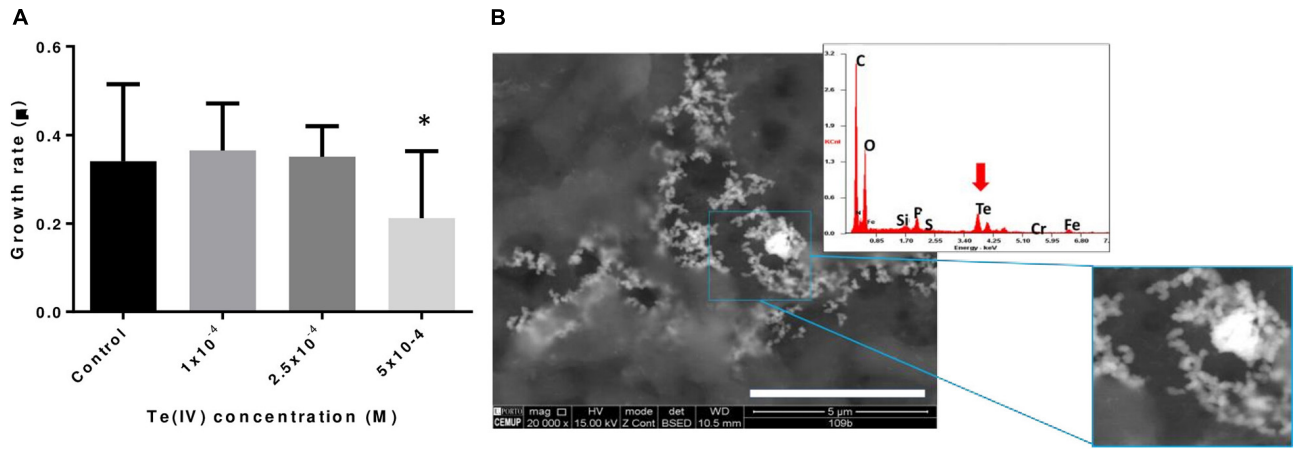

FIGURE 1 | Impact of tellurite in bacterial growth and tellurite reduction. **(A)** Specific growth rates of *Paenibacillus pabuli* ALJ109b at increasing concentrations of Te (IV): control without metal, 1×10^{-4} M Te (IV), 2.5×10^{-4} M, and 5×10^{-4} M. Experiments were conducted in triplicate, and statistical significance indicated $^{*}p \leq 0.05$. **(B)** SEM micrographs of Te nanostructures produced with *P. pabuli* ALJ109b cells grown in the presence of 5×10^{-4} M Te (IV). A magnification is present for clarification of the nanostructure shape. High-density metal deposits are represented in white. The EDS spectrum was obtained from reads in an electrodense area. The red arrow highlights Te detection in the spectrum.

TABLE 1 | Reduction efficiencies, reduction rates, and percentage of Te (IV) depletion all through the growth of *Paenibacillus pabuli* ALJ109b in the presence of 5×10^{-4} M of Te (IV).

Time (h)	2	4	6	8	20
Re (Δmg.DO^{-1})	28.89	21.71	16.53	4.14	3.19
SD (±)	0.17	0.28	0.18	0.12	0.07
Rr (Δmg.DO^{-1}.h^{-1})	14.45	5.43	2.75	0.52	0.16
SD (±)	0.08	0.07	0.03	0.02	0.00
Te (IV) depletion (%)	18.31	17.03	24.70	20.66	33.17
SD (±)	0.86	0.68	0.76	0.76	0.97

A visual demonstration of Te (IV) reduction was observed in SEM imaging of *P. pabuli* ALJ109b with 5×10^{-4} M Te (IV). Te-containing nanoparticles are visualized in electron-dense aggregates of structures with clear spheroid organization (**Figure 1B**). The observed spheroid structures are sized at the nanometer scale, < 100 nm, and therefore can be classified as nanoparticles.

Metabolic and Stress-Related Impact of Te (IV)

Variation in metabolic activity in response to Te (IV) was tracked by using MTT assay. MTT assay demonstrated that in the presence of 1×10^{-3} M of Te (IV), *P. pabuli* ALJ109b dropped its activity by 17% when compared to the control situation (**Figure 2A**). The response to oxidative stress induced by Te (IV) was demonstrated by evaluating the production of reactive oxygen species using a ROS assay in *P. pabuli* ALJ109b. ROS formation increased 2.3-fold at the concentration of 5×10^{-4} M of Te (IV), when compared to the control without Te (IV). Continuous tracking of ROS formation revealed that *P. pabuli* ALJ109b, when grown in the presence of Te (IV), was able to maintain or even decrease its intracellular ROS levels compared to the control situation after 5 h and 30 min (**Figure 2B**).

Genomic and Proteomic Potential for Te (IV) Resistance

Draft genomes of *P. pabuli* ALJ109b were obtained from Illumina sequencing. *P. pabuli* ALJ109b' had a 6.8-Mb genome, which was assembled into 46 contigs. A total of 6,105 identified CDS regions, 6,210 genes, 7 rRNAs, 1 tmRNA, and 97 tRNAs were identified. Potential occurrence of plasmid analysis, using PlasFlow software package, did not identify any plasmid-marked contig. A genome phylogenetic identification of *Paenibacillus* strain ALJ109b identified the strain as belonging to the species *Paenibacillus pabuli* (*P. pabuli* ALJ109b) with a FastANI score of 99.04% similarity.

A detailed analysis of genetic determinants with relation to Te (transport, resistance, reduction) was performed by PSI-Blast search of the annotated genome. No known Te (IV) transporters were identified in the *P. pabuli* ALJ109b genome. Few genetic determinants with experimentally confirmed Te (IV) resistance activity were detected. These included a near-complete *ars* operon (Pp_CDS_2955 to Pp_CDS_2957), as well as the isolated *ter* operon component, *terC* (Pp_CDS_900), and a *kilA* gene from the *kilAB*/*cysK* gene cluster Pp_CDS_1611. Gene-coding proteins with demonstrated Te (IV)-reducing ability were identified and are further characterized in the last section of the results, *vide infra*.

The comparative proteomic analysis of *P. pabuli* proteins obtained in both Te (IV)-treated and no-treatment conditions was determined using five independent biological replicates. Using the NCBI pipeline annotation from the genome sequence of *P. pabuli* ALJ109b, a reference proteome was created from the strains' complete CoDing Sequences (CDS). The number of CDS regions detected and identified corresponds to 44% (2828)

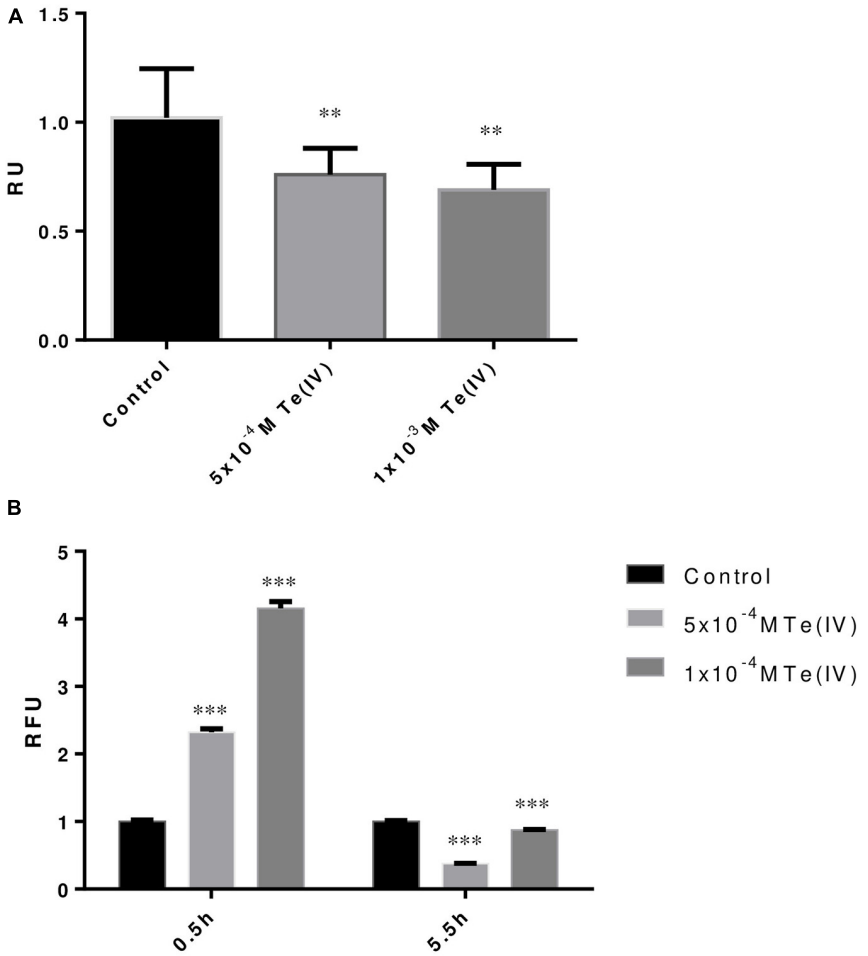

FIGURE 2 | Tellurite-induced stress response of *Paenibacillus pabuli* ALJ109b. **(A)** MTT assay of strain *P. pabuli* ALJ109b. Relative units (RU) represent the ratio between the absorbance (MTT) of each treatment compared to control (without metal). **(B)** ROS assays showing two incubation periods with H_2DCFDA. Relative fluorescence units (RFU) represent the ratio between the fluorescence intensity (ROS) of each treatment compared to control (without metal). Data shown are the mean values (±standard deviations) obtained from three independent experiments. Significant difference of values from treatment from the value of Control computed by one-way ANOVA $^{**}p \leq 0.01$, $^{***}p \leq 0.001$.

proteins of its reference proteome. Of the 2,828 proteins, 59% of these annotated sequences (1667) were assigned to, at least, one functional pathway.

Impact of Te (IV) in Metabolic Pathways

The analysis of the proteomes obtained by LC-MS revealed some shifts in the metabolic pathways of cells grown in the presence of Te (IV). The proteome resulting from the growth of *P. pabuli* ALJ109b, with and without Te (IV), reveals 1,832 identifiable proteins. From these, 204 proteins were exclusively found when the strain was grown in one of the conditions (**Figure 3A**). In more detail, 164 proteins were exclusively found in the presence of Te (IV), 68 had a positive significant change in abundance (SCA), and 75 additional proteins had a negative SCA (**Figures 3A,B**). In the absence of Te (IV), 40 proteins were exclusively found. A full list of exclusive and SCA proteins can be found in the supplementary material (**Supplementary Tables 1**, **2**).

The detected and identified SCA and exclusive proteins that were assigned to a functional pathway were used to determine the activation or inactivation of the pathways they were a part of. The significance of the activation/inactivation of each pathway was calculated based on the number of proteins detected in relation to the size of the pathway (number of proteins in the pathway present in the reference proteome). The growth of *P. pabuli* ALJ109b in the presence of Te (IV) was associated with a significant change in the representation of the metabolic pathway (level 3) of ABC transporters. When comparing the ABC transporter SCA proteins in both Te (IV) and control growth, we observed that three proteins contribute positively to the metabolic pathway (D-ribose pyranase [EC:5.4.99.62]; L-cystine transport system substrate-binding protein and the potD—spermidine/putrescine transport system substrate-binding protein) and three proteins contributed negatively (LplA, putative aldouronate transport system substrate-binding protein; LplB, putative

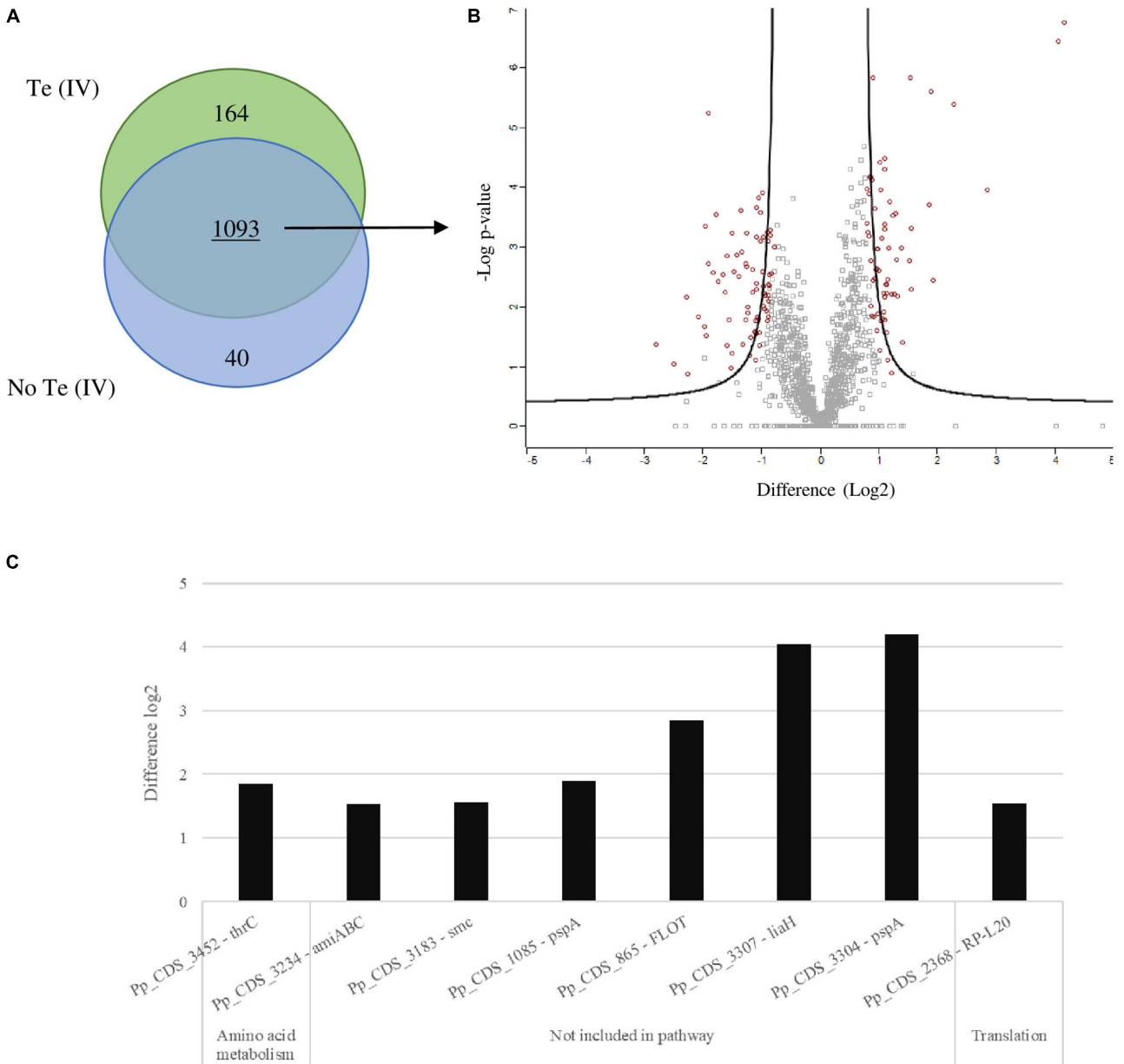

FIGURE 3 | Differential proteomics in *Paenibacillus*. Schematic representations of the determination of significant change in abundance (SCA) of proteins obtained for growth of *Paenibacillus pabuli* ALJ109b in Control [without Te (IV)] and 5×10^{-4} M of Te (IV). Each test condition was performed in triplicate. **(A)** Venn diagram representing the total proteins obtained, exclusive to each test and combined. **(B)** Volcano plot showing total shared proteins between tests (Welsh t test; FDR-0.05; S0 > 1), those with SCA indicated by large red circles. **(C)** Highest overexpressed proteins (log2 over 1.5) result from LC-MS analyses; proteins are grouped according to KEGG functional pathways.

aldouronate transport system permease protein; and TroB, manganese/zinc/iron transport system ATP- binding protein) (**Supplementary Figure 1**). The protein Pp_CDS_1334—potD is linked to stress response by the same mechanism described for stress response mediated by lysin described by Olin-Sandoval et al. (2019). Therefore, in *P. pabuli* ALJ109 the polyamine-harvesting mechanism, observed by potD overexpression, may be part of the response to the oxidative stress observed by ROS reduction over time. It is also shown that a detailed analysis of overexpressed proteins, co-located in the genome, highlights other pathways that are overexpressed in *P. pabuli* ALJ109b. Several clusters of amino acids biosynthesized are overexpressed or are exclusive in the presence of Te (IV) such as Pp_CDS_700/701—lysine biosynthesis; Pp_CDS_724/726/730—methionine salvage; Pp_CDS_2315/2316—methionine synthesis; and Pp_CDS_3451–3453—threonine and homoserine synthesis (**Supplementary Figure 2**). Two other pathways are highlighted,

the overexpressed *lia* operon and the Te (IV) exclusive *ars* operon. Other overexpressed pathways remain with unknown function (**Supplementary Figure 2**).

Proteins of Interest in Te (IV) Reduction

The presence of Te (IV) induced a significant change in the abundance of proteins that are not assigned to specific pathways, as is the case of thioredoxin reductase (EC 1.8.1.9) involved in defense against oxidative stress. Evaluation of proteins independently shows that the highest overregulation was observed for Pp_CDS_3304—PspA, phage shock protein A; Pp_CDS_3307—LiaH, similar to PspA; and the Pp_CDS_865—FLOT, flotillin, with increases of $\log_2$ 4.2, $\log_2$ 4.1, and $\log_2$ 2.8 times (**Figure 3C**; **Supplementary Table 1**), respectively. Apart from the aforementioned, some other proteins are also significantly overexpressed (**Figure 3C**). These are mostly not included in any functional metabolic pathway, except for Pp_CDS_3452—thrC involved in amino acid metabolism and Pp_CDS_2368—RP-L20, a constituent of the ribosomal machinery. Of those not included in any functional pathway, most are implicated in stress response, such as the abovementioned *lia* operon elements and FLOT; the remaining Pp_CDS_3183—smc is involved in chromosome condensation and partitioning, and Pp_CDS_3234—amiABC is involved in peptidoglycan recycling. A significant number of proteins identified remain hypothetical or with unrecognized function (**Supplementary Table 1**).

A detailed analysis of the *P. pabuli* ALJ109b genome allowed the identification of proteins with either demonstrated Te (IV)-reducing activity, i.e., nitrate reductase EC 1.7.99.4 (Sabaty et al., 2001), thioredoxin reductase EC 1.8.1.9, alkyl hydroperoxide reductase EC 1.11.1.26 (Arenas-Salinas et al., 2016), dihydrolipoamide dehydrogenase EC 1.8.1.4 (Arenas et al., 2014), Isocitrate dehydrogenase EC 1.1.1.42 (Reinoso et al., 2013) or FAD-dependent oxireductase EC 1.4.3.3 (Pugin et al., 2014) or the putative Te (IV)-reducing activity, i.e., catalase EC 1.11.1.6 (Calderón et al., 2006), 6-phosphogluconate dehydrogenase EC 1.1.1.44 (Sandoval et al., 2015) or Type II—NADH dehydrogenase EC 1.6.99.3 (Díaz-Vásquez et al., 2015). For the proteins with hypothetical Te (IV)-reducing activity, all those with a molybdopterin-containing motif found in the *P. pabuli* ALJ109b genome—oxidoreductase molybdopterin-binding (superfamily) (Pp_CDS_1271); uncharacterized molybdopterin-containing oxireductase YuiH (Pp_CDS_1962), and CTP:molybdopterin cytidylyltransferase EC 2.7.7.76 (Pp_CDS_4487)—were included. All the proteins identified were recovered in the high-throughput proteomic analysis except for mercury reductase (EC 1.16.1.1); flavorubredoxin reductase (EC 1.7.2.5), and the putative pyridine nucleotide-disulfide oxidoreductase YkgC. None of the proteins displayed an SCA in the presence of Te (IV) (**Table 2**); in the case of flavorubredoxin, this is due to the protein only being required in anaerobioses.

In contrast, the protein profile analysis, obtained by SDS–PAGE, revealed two proteins with clear overexpression in the presence of 5×10^{-4} M Te (IV), enolase, and flagellin (**Figure 4** and **Table 3**). Viewing the LC-MS results, no enolase or phosphopyruvate hydratase homologue is also found exclusively or overexpressed in the presence of 5×10^{-4} M Te (IV). This result is therefore not clear. A deeper understanding of the metal-reducing ability of flagellin was performed.

TABLE 2 | Identification of known proteins with Te (IV)-reducing ability and proteins with putative Te (IV)-reducing ability in the *Paenibacillus pabuli* ALJ109b reference proteome with abundance change (SCA) when strain ALJ109b grows in the presence of 5×10^{-4} M of Te (IV).

Protein	Reference proteome ID	log2 difference
Nitrate reductase EC 1.7.99.4	Pp_CDS_1648	No SCA
Thioredoxin reductase EC 1.8.1.9	Pp_CDS_151	No SCA
Alkyl hydroperoxide reductase EC 1.11.1.26	Pp_CDS_2353	No SCA
Flavorubredoxin reductase EC 1.7.2.5	Not found	–
Mercuric reductase EC 1.16.1.1	Not found	–
Putative pyridine nucleotide-disulfide oxidoreductase YkgC	Not found	–
Dihydrolipoamide dehydrogenase EC 1.8.1.4	Pp_CDS_558	No SCA
	Pp_CDS_2587	
	Pp_CDS_4841	
FAD-dependent oxireductase EC 1.4.3.3	Pp_CDS_234	No SCA
Tipe II—NADH dehydrogenase EC 1.6.99.3	Pp_CDS_1274	No SCA
	Pp_CDS_1275	
	Pp_CDS_3377	
	Pp_CDS_3392	
	Pp_CDS_4316	
	Pp_CDS_5529	
Catalase EC 1.11.1.6	Pp_CDS_117	No SCA
	Pp_CDS_197	
	Pp_CDS_1308	
	Pp_CDS_2224	
	Pp_CDS_5110	
	Pp_CDS_5236	
6-Phosphogluconate dehydrogenase EC 1.1.1.44	Pp_CDS_2448	No SCA
	Pp_CDS_3328	
	Pp_CDS_5214	
Isocitrate dehydrogenase EC 1.1.1.42	Pp_CDS_1977	
Molybdopterin-containing proteins		
Oxidoreductase molybdopterin-binding (superfamily)	Pp_CDS_1271	No SCA
Uncharacterized molybdopterin-containing oxireductase YuiH	Pp_CDS_1962	
CTP:molybdopterin cytidylyltransferase EC 2.7.7.76	Pp_CDS_4487	

Characterization of Te (IV)-Reducing Ability of Flagellin

The cloning of *P. pabuli* AL109b flagellin in *E. coli* BL21 produced a 37-kDa protein that was used for Te (IV) reduction (**Figure 5**). As described by most literature, heterologous flagellin often produced inclusion bodies during protein extraction

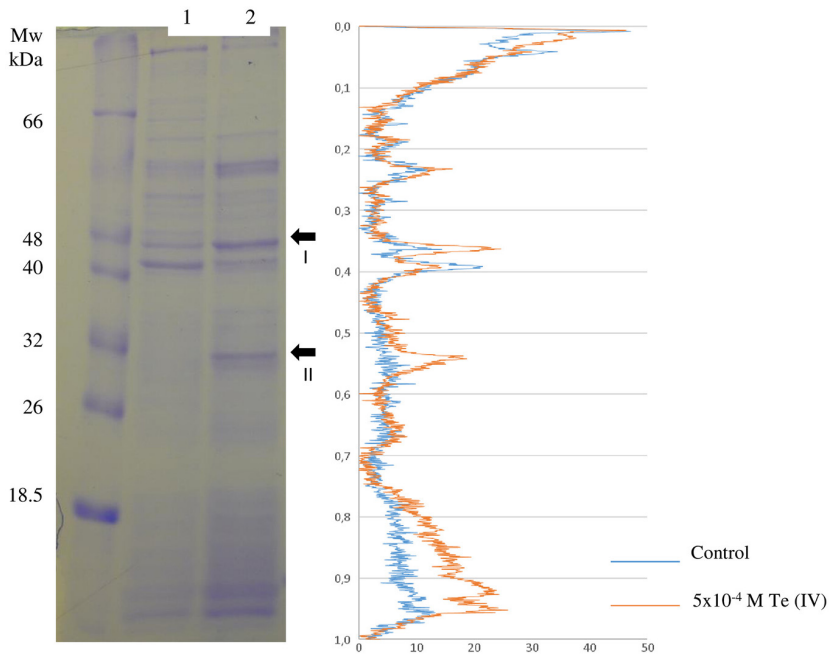

FIGURE 4 | Differential expression of total proteins from *Paenibacillus pabuli* ALJ109b. (Right) Denaturing gel comparing total protein from (1) Control (without metal) and (2) 5×10^{-4} M Te (IV). Fragments indicated in lane 2 (arrows) were excised, purified, and identified by MS/MS, with resulting identification in the table. (Left) Lane comparison of band intensities and densitogram, from control (blue) and metal treatment (orange).

TABLE 3 | Identification by MS of fragments purified from denaturing 2D gel electrophoresis (**Figure 4**).

ID	Description	Coverage (%)	Peptides	AAs	MW (kDa)
I	Enolase OS = Bacillus sp. FJAT-27264 OX = 1850362 GN = eno PE = 3 SV = 1	44	17	428	45.7
II	Flagellin OS = Bacillus filamentosus OX = 1402861 GN = B1B01_04555 PE = 3 SV = 1	5	2	286	31

protocols. This was resolved with an incubation in guanidine HCl that resolubilized the protein (**Figure 5**). Te (IV)-reducing assays demonstrated that flagellin is effective in reducing Te (IV) to its elemental form Te (0) (**Figure 6A**). Levels of Te (0) formation were variable depending on pH, temperature, and Te (IV) concentration. Higher pH increased Te (0) formation with a peak activity of 24,450 $U.mg^{-1}$ at pH 9, in 1×10^{-3} M Te (IV) (**Figure 6B**). An increase in temperature was mostly followed by an increase in Te (0) formation with peak reducing activity increasing from 567 to 23,100 $U.mg^{-1}$ from 20°C to 37°C, in 1×10^{-3} M Te (IV) (**Figure 6C**). Results obtained in higher pH and temperature conditions were more reproducible. The rate of Te (0) formation, in most test conditions, increased with the increase in initial Te (IV) concentration from 5×10^{-4} to 1×10^{-3} M of Te (IV) and reached a plateau at the highest concentration of 2×10^{-3} M of Te (IV) (**Figures 6A–C**).

Analysis of the *P. pabuli* ALJ109b FlaA sequence showed a 256-amino acid protein; it is included in the group of flagellins with the shortest length and therefore one with a short, exposed domain D2/D3 (≈136–169). A comparison with closely related FlaA sequences from *P. pabulis* strains reveals that N and C terminal D0 domains remain conserved with higher sequence variations observed in N terminal D1a/b domains and D2 D3 domains. Overall, FlaA (Pp_CDS_1131) contains a more positive net charge and contains a higher number of long R groups.

DISCUSSION

The evaluation Te (IV) resistance of *P. pabuli* AL109b and its ability to maintain similar growth kinetics in the presence of Te (IV), up to 2.5×10^{-4} M, indicates a highly resistant phenotype, over 1-fold from the best *Paenibacillus* sp. described in the literature (Chien and Han, 2009). Resistance to a concentration of 5×10^{-4} M Te (IV) is significantly higher than that reported for strains with known Te (IV) resistance mechanisms such as *Escherichia coli* with *ter*BCDE (Kormutakova et al., 2000), or similar to the resistance demonstrated for *R. capsulatus*, a model system for the study of the microbial interaction with Te (IV) for the last decades (Borghese et al., 2014).

P. pabuli ALJ109b reduced 20.7% of Te (IV) in 8 h from a solution at a concentration of 5×10^{-4} M. Reporting Te (IV) reduction efficiency and reduction rates this way limits comparison but allows for determination of the efficiency of

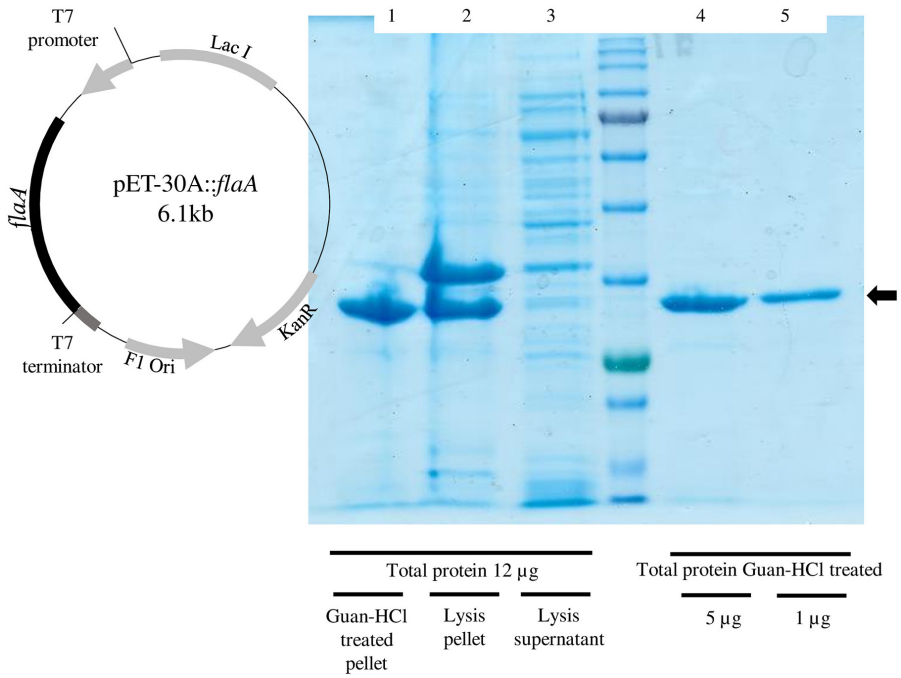

FIGURE 5 | Confirmation of FlaA expression and purification in *Escherichia coli* BL21. (Right) Graphical representation of recombinant plasmid pET-30A::*flaA*. (Left) Denaturing electrophoresis with demonstration of *flaA* expression (black arrow). Lane 1—post lysis guanidine–HCl-treated fraction; lane 2—the post lysis-insoluble fraction; lane 3—post lysis-soluble fraction; all samples loaded are normalized with 12 µg of total protein. In lanes 4 and 5 are, respectively, 5 and 2 µg of total protein, post guanidine–HCl treatment.

processes that rely on biomass limitations and have specific timeframes. Nevertheless, the rate of Te (IV) reduction is, to our understanding, high. Still, the analysis of the strain genome showed that the reduction ability was not related to known specific Te (IV) reduction mechanisms. The residue formed by the Te reduced was composed of spherical structures of less than 100 µm, classifying them as nanoparticles. All the structures observed present the same shape, indicating a monodisperse synthesis unlike what is seen for *Bacillus selenireducens* that form nanorods, shards, and rosettes (Baesman et al., 2007) or the membrane fractions of *Lysinibacillus sp.* ZYM-1 that form various shapes of Te plates (Zhang et al., 2010). Instead, the monodisperse synthesis of Te nanostructures by *P. pabuli* ALJ109b resembles that of *Rhodococcus aetherivorans* BCP1 (Presentato et al., 2018) or *Bacillus sp.* BZ (Zare et al., 2012). A monodisperse bioproduction of spheroid-shaped nanoparticles represents a promising new process in nanoparticle production.

The first evaluation of the impact of Te on the metabolism of *P. pabuli* ALJ109b was performed using MTT to follow the activity of the cells, and by quantifying ROS formation. The cells reduced their activity up to 17% in the presence of Te (IV). The presence of Te (IV) induced the formation of ROS, as previously described in other strains (Chasteen et al., 2009). By continuously tracking ROS formation, it was clear that *P. pabuli* ALJ109b activated mechanisms to counteract Te (IV)-induced ROS, justifying looking for the proteins involved in the control of the excess ROS formed. The analysis of the metabolic pathways that are selected in the presence of Te (IV) showed a significant change in the representation of the metabolic pathway (level 3) of ABC transporters supported in PotD overexpression, which was previously linked to the response to the oxidative stress (Olin-Sandoval et al., 2019). It is noteworthy that none of the proteins overexpressed in ABC transporter metabolic function are indicative of a Te (IV) transporter, which validates the previous hypothesis that metal efflux is not a Te (IV) resistance mechanism in this strain (Llyod-Jones et al., 1994).

A detailed analysis of overexpressed proteins, co-located in the genome, highlights that clusters of amino acid biosynthesis are overexpressed in *P. pabuli* ALJ109b. This effect is opposite to what is seen in proteomic studies where, under Ni or Cd stress, bacterial cells decrease amino acid synthesis (Cheng et al., 2009; Izrael-Živković et al., 2018). In the particular case of *P. pabuli* ALJ109b, the biosynthesis of specific amino acids may not be a result of increased protein synthesis, as this pathway is not overrepresented. Instead, the biosynthesis of amino acids may be related to the production of intermediaries in specific pathways. A particular example is lysine harvesting and biosynthesis which has been demonstrated to stimulate NADPH production to prevent imbalances in the redox state under oxidative conditions (Olin-Sandoval et al., 2019). Moreover, the *lia* operon and the Te (IV)-exclusive *ars* operon are also overexpressed. In previous works, the *lia* operon was identified as a genetic mechanism involved in cell envelope stress response (Suntharalingam et al., 2009). Regarding the *ars* operon, it has been proposed that the arsenical efflux pump ArsC is involved in modifying the substrate-binding site of the anion-translocating

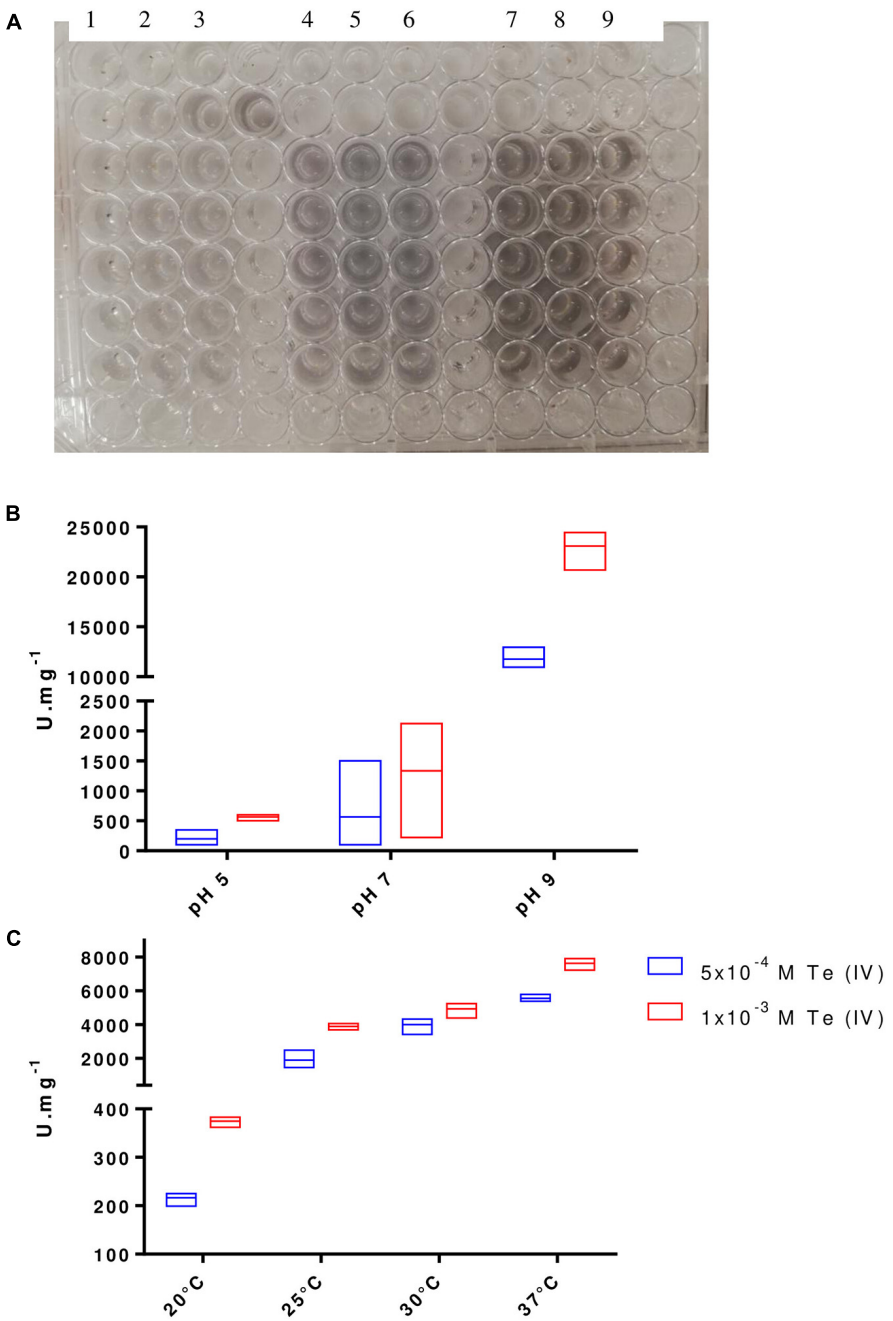

FIGURE 6 | Te (0) formation by FlaA. **(A)** Te (0) formation visible by the appearance of black precipitates in each reaction mixture (individual wells). Test conditions represented Control—columns 1, 2, 3; 5×10^{-4} M Te (IV)—columns 4, 5, 6; and 1×10^{-3} M Te (IV)—columns 7, 8, 9. Optimal pH **(B)** and temperature **(C)** of Te (0) forming activity for FlaA at 1 μg with 2 Te (IV) concentrations, 5×10^{-4} M Te (IV) and 1×10^{-3} M Te (IV). Boxes indicate mean and higher/lower value from three independent replicates.

ATPase, thus conferring moderate levels of resistance to Te (IV) (Turner et al., 1992a).

The presence of Te (IV) induced a significant change in the abundance of proteins that were not assigned to a metabolic pathway (KEGG pathway database), as is the case of some of the proteins with the highest fold change in the presence of Te (IV). The overexpression of PspA and LiaH, phage shock protein A, and flotillin are indicative of stress response activation in *P. pabuli* ALJ109 involving cell wall integrity maintenance under Te (IV) exposure. The protein PspA and its homologue LiaH, is often recognized, in differential proteomic profiling as a marker protein for stress response, acting by maintaining cytoplasmic membrane integrity and/or the proton-motive force (Wenzel et al., 2012; Tsai et al., 2015).

These may contribute to preservation of cell wall integrity, essential for the maintenance of cellular metabolic activity demonstrated by the MTT assay. Other proteins that could also be related to the maintenance of the homeostasis of the cell, identified as overexpressed, were related to ribosomal machinery, chromosome condensation and partitioning, and recycling of peptidoglycan (**Supplementary Figure 1** and **Supplementary Table 1**). These proteins neither are known Te (IV) reducers nor present the enzymatic activity commonly associated with Te (IV)-reducing ability, i.e., presence of molybdenum as a cofactor. The genomic and proteomic analysis of the genome revealed the existence of several proteins with demonstrated or putative Te (IV)-reducing activity (**Table 1**), but none were significantly increased in the presence of Te (IV). No possible comparison could be made with previous reports since there are no reported proteomic studies that allow an inter-genus comparison of Te (IV) reduction. Therefore, an undescribed mechanism must be responsible for Te (IV) reduction in *P. pabuli* ALJ109b.

The 2D denaturing electrophoresis was used also to obtain a differential protein expression, and the results differed from LC-MS analysis. Enolase and flagellin, detected by SDS-PAGE, were not detected overexpressed in LC-MS results. Detection of flagellin may be limited for being bonded to Te. As is the case for metallothioneins, a flagellin-Te molecule may be resistant to the proteolytic activity of trypsin (Wang et al., 2007). Metal binding to exposed amino acid residues impedes the binding of trypsin to lysine and/or arginine residues and its proteolytic activity. Enolase, like the abovementioned proteins, has not an expected enzymatic activity commonly associated with a Te (IV) reducer. On the other hand, the overexpression observed for flagellin may be a direct response to the presence of Te (IV). Other studies already demonstrated the ability of flagellin monomers of binding several metals such as Ag, Au, Cu, Co, Pd, and Cd (Kumara et al., 2007), Pb (Chen et al., 2019), and Ag (Gopinathan et al., 2013), to surface-exposed amino acid residues. Flagellin has been associated with TeNP production in *Rhodobacter capsulatus* (Borghese et al., 2020) without being determined its function, if any, in the TeNP assembly.

The heterologous produced flagellin was used to evaluate the Te (IV) binding to flagellin and reduction to its elemental form Te (0). *P. pabuli* ALJ109 flagellin showed a higher reducing activity at 4°C and for a temperature up to 37°C. When compared to previous results, FlaA demonstrates a Te (0) formation activity, at similar pH and temperature, higher than the flavoproteins from *E. coli* NorW and YkgC, ∼660 and 870 $U.mg^{-1}$ protein, respectively, and lower than *E. coli* flavoprotein GorA, ∼30,000 $U.mg^{-1}$ protein (Arenas-Salinas et al., 2016). When comparing Te (0) formation activity with crude cell extracts from multiple strains (Figueroa et al., 2018), FlaA outperforms all extracts in an average of 10-fold higher activity. To this date, Te (IV) reduction has been reported for several proteins (**Table 1**), but for most proteins their involvement in further nanoparticle formation has not been described. Further characterization of flagellin from *P. pabuli* ALJ109b could add knowledge in biobased strategies to Te (IV) reduction and/or TeNP formation.

CONCLUSION

In this study, we identified a highly Te (IV)-resistant *Paenibacillus* strain from an industrial resulting environment. The genome sequencing analysis and differential proteomics revealed a specific metabolic response to Te (IV) in *P. pabuli* ALJ109b for the first time. The response to Te (IV) involved the overexpression of marker proteins for stress response such as phage shock protein and the chaperon PotD. Proteins related to oxidative stress response, particularly associated with cell wall or cell envelope, are overrepresented. Te (IV) showed to induce ROS generation that the strain solved by activating specific metabolic pathways. The genomic and high-throughput proteomics analyses did not identify any known Te (IV) resistance mechanisms; nevertheless, *P. pabuli* ALJ109b uses Te (IV) reduction as a defense mechanism. We demonstrated that *P. pabuli* ALJ109b uses flagellin, FlaA, as a Te (IV)-reducing agent and that this protein has a high Te (0) formation activity at room temperature and pH of 9.

It is also demonstrated in this work for the first time the metabolic response to Te (IV) in a highly resistant *Paenibacillus* strain. The flagellin purified from *P. pabuli* ALJ109b is an effective Te (IV) reducer with potential in nanoparticle fabrication.

METHODS

Bacterial Strain Isolation and Growth

Paenibacillus pabuli ALJ 109b was isolated from a mine sediment originated in the Aljustrel copper mine (37°52′07.3″N 8°09′24.7″W), in southern Portugal. Sediment samples were suspended in 50% diluted LB. The samples were incubated at 25°C for 7 days in an orbital shaker. The culture medium was incremented with sodium tellurite (Sigma-Aldrich, St. Louis, MO, United States) at regular times, increasing from 5×10^{-4}, 1×10^{-3}, 3×10^{-3}, 5×10^{-3}, up to 1×10^{-2} M. Prior to each Te (IV) enrichment, an aliquot of the suspension was plated in 50% diluted LB agar for selection of isolates.

For Te (IV) resistance assay, two strains were tested, *Escherichia coli* BL21 (commercially obtained) and *P. pabuli* ALJ109b. *E. coli* BL21 was tested for growth in Te (IV) to demonstrate if the strain was resistant to Te (IV). Blackening of the growth media was indicative of Te (IV) reduction. Both were tested in LB with increasing concentrations of Te (IV), 1×10^{-4}, 2.5×10^{-4}, and 5×10^{-4} M, while comparing against growth in the absence of Te (IV). *E. coli* BL21 was incubated at 37°C wile *P. pabuli* LJ109b at 25°C. Statistically significant variations of the specific growth rates, for each Te (IV) concentration versus control, were determined by performing a t test, using GraphPad Prism version 8.0, $^{*}\ p \leq 0.05$.

Tellurite Reduction and Nanoparticle Formation in *P. pabuli* ALJ109b

The reduction of Te (IV) by *P. pabuli* ALJ109b was determined at 5×10^{-4} M. Aliquots for Te (IV) reduction testing were recovered at four times, lag/early exponential, mid exponential, late exponential, and late stationary growth phases. Cells were

centrifuged 20 min at 4000 *g*, the pellets were preserved for further tests, and the supernatant was stored for evaluation of Te (IV) reduction. Quantitative depletion of sodium Te (IV) was quantified using a chromophore diethyldithiocarbamate (DDTC) method adapted from Turner and colleagues (Turner et al., 1992b). The reagent mixture was prepared with final concentrations of 1 mM DDTC and 0.5 M Tris–HCl pH 7 buffer, and each sample was incubated for no more than 15 min prior to absorbance reading at 340 nm. Quantitative data were obtained from a minimum of three experimental replicates.

The efficiency of Te (IV) depletion (reduction efficiency—Re) was determined as the ratio of the absolute variation of Te (IV) in grams, from time 0 (T0) to late exponential growth (Tf), per growth, expressed as a variation on optical density, Tf – T0. The reduction rate was determined as reason of the Re per time at Tf, as demonstrated in the equation.

$$R_e = \frac{|\Delta Te|}{\Delta DO(\mathrm{Tf} - \mathrm{To})} \qquad R_r = R_e / t\,(Tf)$$

Demonstration of Te precipitation was performed by scanning electron microscopy with coupled energy-dispersive X-ray spectroscopy (SEM-EDS), in backscattered electrons mode (BSE). The evaluation was made on cell preparations recovered from the late exponential phase in the presence of 5×10^{-4} M Te (IV). Cell pellets from cultures were collected by centrifugation at 4000 *g*, washed twice in saline phosphate buffer (PBS 1×), and resuspended in 0.1 ml of the same buffer.

Droplets of cell concentrate ≈30 μl were dried in a 5 × 5-mm stainless steel plate, at room temperature, followed by two-step fixation with 2.5% glutaraldehyde and by dehydration with increasing ethanol concentration, 70%/80%/90%/95%.

SEM micrographs were obtained on a FEI Quanta 400 FEG ESEM, and EDS analysis was accomplished using an Oxford INCA Energy 350 equipped with the SAMX IDEFIX software, with an accelerating voltage of 15 kV and a beam current of 20 nÅ.

Tellurite-Induced Stress Response

Stress response was determined by tracking the regulation of metabolic activity using 3-(4,5-dimethylthiazol-2-yl)-2,5-diphenyltetrazolium bromide assay (MTT assay) (Caldeira et al., 2020) and by determining the formation of reactive oxidative species (ROS) by using 2,7-dichlorofluorescein-diacetate (H_2DCFDA) assay (Jakubowski, 2000). Cells were grown in LB broth supplemented with Te (IV), 5×10^{-4} M, 1×10^{-3} M, and a control without metal. For MTT assays, strain *P. pabuli* ALJ109b was incubated for 6 h, collected by centrifugation at 13.300 *g* for 10 min, and washed twice with growth media. Dilutions were prepared to obtain cell suspensions with OD 0.2 in growth media. For formazan crystal formation, 200 μl of cell suspension was mixed with 20 μl of MTT solution and incubated for 1 h at 25°C. Crystals were retrieved by centrifugation at 13.300 *g* for 2 min; these were then resuspended in 2.5 ml of DMSO and incubated 1 h at room temperature. Absorbance of the mixture solution was read at 550 nm. For ROS determination, the strain was incubated until reaching an OD of 0.3. Cells were washed twice with PBS, incubated in 25 μM H_2DCFDA for 30 min at 25°C, retrieved by centrifugation, and again washed twice with PBS. Intracellular ROS levels were determined by lysing cell pellets by pasteurization, for 20 min at 80°C. After centrifugation, supernatants were collected and fluorescence were read hourly during 15 h (λem = 527 nm and λex = 495 nm). For both MTT and ROS assays, the values were compared as the ratio between the values of the test condition (with metal) and the value of the control without metal. All assays were performed in triplicates. Statistical significance accessed by one-way ANOVA between test conditions replicates means, using GraphPad Prism version 8.0, $^{**}p \leq 0.01$, $^{***}p \leq 0.001$.

Genome Sequencing, Annotation, and Strain Identification

Strain AlJ109b was grown in liquid media LB broth, streaked from a single colony. Cells were collected, and DNA was extracted using a DNeasy PowerSoil Kit (Qiagen), according to manufacturer instructions. Libraries of total genomic DNA were prepared using Nextera XT Preparation Kit (Illumina, San Diego, CA, United States) following the manufacturer's instructions. Libraries were purified using HighPrep PCR Clean-up beads (MagBio Genomics, Inc.). Fragment analyzer 5200 (Agilent NGS Fragment 1-6000 pb methods) was used to check the fragment size distribution and molarity of each library. Nine-picomolar libraries were sequenced on an Illumina MiSeq System based at the Section of Microbiology in the Department of Biology of Copenhagen University with 2 × 300bp chemistry (MiSeq Reagent Kit v3). Pairing, trimming, and assembly based on Bruijn graphs were performed using CLC Genomics Workbench v9.5.4 (Qiagen) using default parameters. Resulting contigs were submitted to GhostKOALA (KEGG Orthology And Links Annotation) annotated genomes as reference proteome (Kanehisa et al., 2016). In GhostKOALA, Kegg identifiers (K numbers) were assigned to the sequence data by GHOSTX searches, against a nonredundant set of KEGG GENES. Genome annotation was performed upon submission to the GenBank databank using NCBI Prokaryotic Genome Annotation Pipeline for determination of coding sequences (CDS) as well as RNA sequences. Potential occurrence of plasmids was determined by searching for genomic signatures using PlasFlow 1.1 software package (Krawczyk et al., 2018).

Genome phylogeny was determined by using rMLST (Jolley et al., 2012) and PhyloPhlan (Segata et al., 2013) analyses, and similarity results were calculated by average nucleotide identity, using ANI calculator, Kostas software (Goris et al., 2007).

Comparative Methodologies for Differential Proteomics

For determining the impact of Te (IV) in total protein expression, *P. pabuli* ALJ109b was grown in LB broth containing Te (IV), 5×10^{-4} M, 1×10^{-3} M, or a control without metal. Upon reaching the late exponential growth phase, cells were collected by centrifugation and washed twice in PBS 1×.

For the comparison of differential proteomics using denaturing gel electrophoresis, the cell pellet was resuspended in 0.9 ml STB solution (0.075 $g.l^{-1}$ Tris, 0.345 $ml.l^{-1}$ HCl (1.72 N), 0.5 $ml.l^{-1}$ β-mercaptoethanol, and 0.5 $g.l^{-1}$ sacarose) and mixed after adding 0.1 ml of SDS 20%. Cell suspension was sonicated with continued on/off cycles of 10 s for 4 min, on an ice water mixture, heated at 95°C for 10 min, and cooled on ice. Lastly, the suspension was centrifuged at 14,000 rpm for 10 min, and the supernatant was harvested. Total protein obtained was quantified by using Bradford reagent (Bio-Rad®, Hercules, CA, United States), and 12 μg of total protein was aliquoted by mixing with 7 μl of loading buffer (Morris formulation) and boiled 10 min before loading on a denaturing gel. Protein separation was obtained in a 12% acrylamide/bisacrylamide denaturing gel (SDS 0.1%). Electrophoresis was performed at room temperature for 1 h at 120 V. The molecular marker used for size reference (kDa) was the Low Molecular Weight Protein Marker (NZYTech, Lisboa, Portugal). Visualization of proteins was performed by staining with Coomassie Blue followed by destaining with a methanol/acetic acid solution. From the visual analysis and densitogram comparison (Quantity One, Bio-Rad), selected fragments were excised and stored in ultrapure water for MS/MS identification.

For the comparison of differential proteomics using LC-MS, cell pellets from treated and untreated conditions were lysed by resuspension in lysis buffer (guanidinium hydrochloride 6 M, tris(2-carboxyethyl)phosphine (TCEP) 10 mM, 2-chloroacetamide (CAA) 40 mM, HEPES 50 mM, pH 8.5). Samples were heated and disrupted by sonication as mentioned above and normalized at 30 μg for trypsin digestion. The samples were four-fold diluted in digestion buffer (acetonitrile (ACN) 10%, HEPES 50 mM pH 8.5) and then incubated for 4 h with trypsin (1:100 trypsin-to-protein ratio) (Sigma T6567) at room temperature with horizontal shaking at 500 rpm. Trypsin was inactivated with trifluoroacetic acid, and debris was removed by centrifugation (10,000 *g*, 10 min). The tryptic peptides were fractionated using a stage tip protocol as described by Rappsilber (Rappsilber et al., 2007). A total of three C18 plugs were gently punched out from the filter disk with the help of the sampling tool syringe. Plugs were placed at the tip of a 200-μl pipette tip with a plunger and activated with 30 μl methanol by centrifugation at 1,000 *g* for 2 min, followed by 30 μl 100% ACN, and finally 2 × 30 μl of 3% ACN with 1% TFA. Peptides were loaded onto the filter unit by centrifugation at 1,000 *g*. Bound peptides were washed twice using 30 μl of 0.1% formic acid (FA). Peptides were eluted using two rounds of 30 μl 60% ACN in 0.1% FA, with centrifugation between each round. Liquid was evaporated, and peptides were redissolved in 2% ACN with 1% TFA. The peptide concentration in the samples was estimated with a NanoDrop, and 1.5 μg peptide was loaded for analysis on a Q Exactive (Thermo Scientific, Bremen, Germany).

Mass Spectrometry

The samples were analyzed by liquid chromatography tandem mass spectrometry (LC-MS/MS), and data were recorded in a data-dependent manner, automatically switching between MS and MS/MS acquisition, on a Q Exactive (Thermo Scientific, Bremen, Germany). An EASY nLC-1000 liquid chromatography system (Thermo Scientific, Odense, Denmark) was coupled to the mass spectrometer through an EASY-Spray source, and peptide separation was performed on 15-cm EASY-Spray columns (Thermo Scientific) with 2-μm-size C18 particles and the inner diameter of 75 μm. The mobile phase consisted of solvents A (0.1% FA) and B (80% ACN in 0.1% FA). The initial concentration of solvent B was 6%, and hereafter gradients were applied to reach the following concentrations: 14% B in 18.5 min, 25% B in 19 min, 38% B in 11.5 min, 60% B in 10 min, 95% B in 3 min, and 95% B for 7 min. The total length of the gradient was 70 min. The full scans were acquired in the Orbitrap with a resolution of 120,000, and a maximum injection time of 50 ms was applied. For the full scans, the range was adjusted to 350–1,500 m/z. The top 10 most abundant ions from the full scan were sequentially selected for fragmentation with an isolation window of 1.6 m/z (Kelstrup et al., 2012) and excluded from re-selection for a 60-s time period. For the MS/MS scans, the resolution was adjusted to 120,000 and maximum injection time of 80 ms. Ions were fragmented in a higher-energy collision dissociation cell with normalized collision energy of 32% and analyzed in the Orbitrap.

Construction and Purification of a Recombinant *P. pabuli* ALJ109b Flagellin

With information provided by the genome of *P. pabuli* ALJ109b, a set of cloning primers was designed for the insertion of the *flaA* gene in plasmid pET 30A, *Eco*RI_flaA (sense) 5′ CCG GAA TTC ATG ATT ATC AAT CAC AAC TTA CCA, and *Sal*I_flaA_R (antisense) 5′ ACG GCG TCG ACT TAA CGA AGC AAG GAC AA. Amplification of the target sequence was performed using the abovementioned primers in a PCR reaction, for a final volume of 50 μl, using 2 U Platinum™ Taq DNA Polymerase (Invitrogen), 0.2 mM of each dNTP, PCR Buffer (1×), 1.5 mM $MgCl_2$, 0.4 μM primers, and 2 ng DNA template. The PCR program involved initial denaturation at 94°C (5 min), followed by 30 cycles of 94°C (1 min), 61°C (1 min), and 72°C (45 s).

The PCR-amplified DNA fragments with approximately 700 bp, as well as the plasmid pET 30A, were digested with the restriction enzymes *Eco*RI and *Sal*I. The digested amplified fragments were purified and ligated into the pET 30A expression vector for 1 h at room temperature using 0.5 U of T4 DNA ligase (Thermo Scientific, Waltham, MA, United States). The resulting plasmid pET 30A::flaA was transformed into competent *E. coli* BL21 cells. The correct construction was confirmed by sequencing the complete DNA fragments cloned into the plasmid (Stabvida). *E. coli* BL21 bacterial cells, containing the plasmid pET 30A::flaA, were grown in LB broth containing kanamycin (50 $\mu g.ml^{-1}$), at 37°C 140 rpm. Inducing agent IPTG (Sigma-Aldrich) was added (5×10^{-4} M) at an optical density of 0.5 (Abs 600 nm), and cells resumed growth for 5 h. Cells were harvested by centrifugation at 4,000 *g* for 15 min, resuspended in protein lysis buffer STB, and lysed by mechanical sheering in an Emulsiflex®-C3 High-Pressure Homogenizer (Avestin, ONCE, Canada), 2 cycles at 1,500–2,000 psi. The lysis product was centrifuged 10,000 *g*, for 20 min, the supernatant harvested and stored, and the resulting pellet subjected to a guanidine–HCl

(6 M) treatment for 1 h at 30°C. Finally, a soluble fraction was obtained by centrifugation at 10,000 *g*, for 20 min, aliquoted, and stored at 4°C in the presence of a proteinase inhibitor complete, EDTA-Free (Roche, Basel, Switzerland). Confirmation of the recombinant protein FlaA was performed in a denaturing gel electrophoresis as described above using as a size (kDa) reference the NZYColour Protein Marker II (NZYTech).

Demonstration of *in vitro* Te (IV) Reduction Ability by FlaA

Demonstration of the Te (IV)-reducing ability by FlaA was determined by incubating the protein extract with increasing concentrations of soluble Te (IV) and tracking the formation of elemental Te spectrophotometrically, by measuring the absorbance at 500 nm. Protocol was adapted from Figueroa and colleagues (Figueroa et al., 2018). All tests were performed in a final volume of 200 μl with 1 μg of FlaA, in a buffer mixture containing Tris–HCl pH 8, 50 mM, $K_2H_2PO_4$/$KHPO_4$ (1:1) 50 mM, and β-mercaptoethanol 1 mM. Determination of optimal Te (IV)-reducing activity by FlaA was tested with variations in initial Te (IV) concentration from 0 M (control) to 5×10^{-5} M to 1×10^{-3} M (5×10^{-4} M increments), variation in pH from 5, 7, to 9, and variation in temperature from 20°C, 25°C, 30°C, to 37°C. Results are expressed in units of Te (0) formation activity (U) with U = 1 equivalent to an increase of 0.001 in absorbance (500 nm) per minute per volume of reaction. Specific activity was calculated as U per mg of protein. All tests were conducted in triplicates.

DATA AVAILABILITY STATEMENT

The datasets presented in this study can be found in online repositories. The names of the repository/repositories and accession number(s) can be found below: http://www.proteomexchange.org/, PXD017546; https://www.ncbi.nlm.nih.gov/genbank/, PRJNA606039.

AUTHOR CONTRIBUTIONS

PF did the data curation, performed all benchwork, analyzed all data using bioinformatic and statistical analyses and wrote the original draft. RF did the heading of field sampling and processing of some analyses in the laboratory, assisting in strain isolations and growth and reduction assays, reviewed the statistical analyses, and reviewed and edited the manuscript. LM headed in genome sequencing and analyses of sequencing data and reviewed and edited the manuscript. JH headed the proteomic assays and analyses of data resulting from proteomic analyses and reviewed and edited the manuscript. AP performed all imaging assays included in the form of scattering electronic microscopy micrographs. SS conceptualized part of the experiment, supervised the laboratory and bioinformatic analyses on the genome sequencing and proteomics, and reviewed and edited the manuscript. PVM conceptualized the whole experiment and secured the funding, supervised the laboratory, bioinformatics, and statistical analyses, and contributed to the original draft and revised the manuscript. All authors contributed to the article and approved the submitted version.

FUNDING

This work was supported by the projects by Biorecover under grant agreement n° 821096, funded by the European Union Horizon 2020. This research is also sponsored by FEDER funds through the program COMPETE and by national funds through FCT, under the project UIDB/0285/2020. PF was supported by a grant from FCT (SFRH/BD/124091/2016). Mass spectrometry analysis was performed at DTU Proteomics Core, Technical University of Denmark.

SUPPLEMENTARY MATERIAL

The Supplementary Material for this article can be found online at: https://www.frontiersin.org/articles/10.3389/fmicb.2021.718963/full#supplementary-material

Supplementary Figure 1 | Pathways from *Paenibacillus pabuli* ALJ109b showing metabolic change in the presence of Te (IV). SCA proteins were mapped with subsystems classifications from KEGG, top extended bar plot with positive SCA and bottom extended bar plot with negative SCA. Level 3 KEGG pathways were analyzed for regulation using a Fisher's exact test. FDR adjusted *p*-values are presented for each pathway, *p*-values equal or under 0.05 were considered for determining significant pathways. Black bars display pathway size compared to the size of reference proteome, which can be grouped in pathways. Blue bars display the ratio of SCA proteins in the pathway compared to the total amount of SCA proteins in pathways.

Supplementary Figure 2 | Integration of proteomic information in genome *Paenibacillus pabuli* ALJ109b. Schematic representation of over/down expressed and exclusive identified protein positioned in the theoretical arrangement of the genome (merged contigs). Highlighted features of, contiguous, over expressed pathways are detailed table.

REFERENCES

Alavi, S., Amoozegar, M. A., and Khajeh, K. (2014). Enzyme(s) responsible for tellurite reducing activity in a moderately halophilic bacterium, *Salinicoccus iranensis* strain QW6. *Extremophiles* 18, 953–961. doi: 10.1007/s00792-014-0665-6

Arenas, F. A., Leal, C. A., Pinto, C. A., Arenas-Salinas, M. A., Morales, W. A., Cornejo, F. A., et al. (2014). On the mechanism underlying tellurite reduction by *Aeromonas caviae* ST dihydrolipoamide dehydrogenase. *Biochimie* 102, 174–182. doi: 10.1016/j.biochi.2014.03.008

Arenas-Salinas, M., Vargas-Pérez, J. I., Morales, W., Pinto, C., Muñoz-Díaz, P., Cornejo, F. A., et al. (2016). Flavoprotein-mediated tellurite reduction: structural basis and applications to the synthesis of tellurium-containing nanostructures. *Front. Microbiol.* 7:1160. doi: 10.3389/fmicb.2016.01160

Baesman, S. M., Bullen, T. D., Dewald, J., Zhang, D., Curran, S., Islam, F. S., et al. (2007). Formation of tellurium nanocrystals during anaerobic growth of bacteria that use Te oxyanions as respiratory electron acceptors. *Appl. Environ. Microbiol.* 73, 2135–2143. doi: 10.1128/AEM.02558-06

Borghese, R., Baccolini, C., Francia, F., Sabatino, P., Turner, R. J., and Zannoni, D. (2014). Reduction of chalcogen oxyanions and generation of nanoprecipitates

by the photosynthetic bacterium *Rhodobacter capsulatus*. *J. Hazard. Mater.* 269, 24–30. doi: 10.1016/j.jhazmat.2013.12.028

Borghese, R., Brucale, M., Fortunato, G., Lanzi, M., Mezzi, A., Valle, F., et al. (2017). Reprint of "Extracellular production of tellurium nanoparticles by the photosynthetic bacterium *Rhodobacter capsulatus*". *J. Hazard. Mater.* 324, 31–38. doi: 10.1016/j.jhazmat.2016.11.002

Borghese, R., Malferrari, M., Brucale, M., Ortolani, L., Franchini, M., Rapino, S., et al. (2020). Structural and electrochemical characterization of lawsone-dependent production of tellurium-metal nanoprecipitates by photosynthetic cells of *Rhodobacter capsulatus*. *Bioelectrochemistry* 133:107456. doi: 10.1016/j.bioelechem.2020.107456

Caldeira, J. B., Morais, P. V., and Branco, R. (2020). Exploiting the biological response of two *Serratia fonticola* strains to the critical metals, gallium and indium. *Sci. Rep.* 10:20348. doi: 10.1038/s41598-020-77447-7

Calderón, I. L., Arenas, F. A., Pérez, J. M., Fuentes, D. E., Araya, M. A., Saavedra, C. P., et al. (2006). Catalases are NAD(P)H-dependent tellurite reductases. *PLoS One* 1:e70. doi: 10.1371/journal.pone.0000070

Chasteen, T. G., Fuentes, D. E., Tantaleán, J. C., and Vásquez, C. C. (2009). Tellurite: history, oxidative stress, and molecular mechanisms of resistance: review article. *FEMS Microbiol. Rev.* 33, 820–832. doi: 10.1111/j.1574-6976.2009.00177.x

Chen, B., Fang, L., Yan, X., Zhang, A., Chen, P., Luan, T., et al. (2019). A unique Pb-binding flagellin as an effective remediation tool for Pb contamination in aquatic environment. *J. Hazard. Mater.* 363, 34–40. doi: 10.1016/j.jhazmat.2018.10.004

Cheng, Z., Wei, Y. Y. C., Sung, W. W. L., Glick, B. R., and McConkey, B. J. (2009). Proteomic analysis of the response of the plant growth-promoting bacterium *Pseudomonas putida* UW4 to nickel stress. *Proteome Sci.* 7:18. doi: 10.1186/1477-5956-7-18

Chien, C.-C., and Han, C.-T. (2009). Tellurite resistance and reduction by a *Paenibacillus* sp. isolated from heavy metal-contaminated sediment. *Environ. Toxicol. Chem. SETAC* 28, 1627–1632. doi: 10.1897/08-521.1

Contreras, F., Vargas, E., Jiménez, K., Muñoz-Villagrán, C., Figueroa, M., Vásquez, C., et al. (2018). Reduction of gold (III) and tellurium (IV) by *Enterobacter cloacae* MF01 results in nanostructure formation both in aerobic and anaerobic conditions. *Front. Microbiol.* 9:3118. doi: 10.3389/fmicb.2018.03118

Csotonyi, J. T., Stackebrandt, E., and Yurkov, V. (2006). Anaerobic respiration on tellurate and other metalloids in bacteria from hydrothermal vent fields in the Eastern Pacific Ocean. *Appl. Environ. Microbiol.* 72, 4950–4956. doi: 10.1128/AEM.00223-06

Díaz-Vásquez, W. A., Abarca-Lagunas, M. J., Cornejo, F. A., Pinto, C. A., Arenas, F. A., and Vásquez, C. C. (2015). Tellurite-mediated damage to the *Escherichia coli* NDH-dehydrogenases and terminal oxidases in aerobic conditions. *Arch. Biochem. Biophys.* 566, 67–75. doi: 10.1016/j.abb.2014.10.011

Djoko, K. Y., Phan, M. D., Peters, K. M., Walker, M. J., Schembri, M. A., and McEwan, A. G. (2017). Interplay between tolerance mechanisms to copper and acid stress in *Escherichia coli*. *Proc. Natl. Acad. Sci. U.S.A.* 114, 6818–6823. doi: 10.1073/pnas.1620232114

Du, J., Duan, S., Miao, J., Zhai, M., and Cao, Y. (2021). Purification and characterization of chitinase from *Paenibacillus* sp. *Biotechnol. Appl. Biochem.* 68, 30–40. doi: 10.1002/bab.1889

Figueroa, M., Fernandez, V., Arenas-Salinas, M., Ahumada, D., Muñoz-Villagrán, C., Cornejo, F., et al. (2018). Synthesis and antibacterial activity of metal(loid) nanostructures by environmental multi-metal(loid) resistant bacteria and metal(loid)-reducing flavoproteins. *Front. Microbiol.* 9:959. doi: 10.3389/fmicb.2018.00959

Gopinathan, P., Ashok, A. M., and Selvakumar, R. (2013). Bacterial flagella as biotemplate for the synthesis of silver nanoparticle impregnated bionanomaterial. *Appl. Surf. Sci.* 276, 717–722. doi: 10.1016/j.apsusc.2013.03.159

Goris, J., Konstantinidis, K. T., Klappenbach, J. A., Coenye, T., Vandamme, P., and Tiedje, J. M. (2007). DNA–DNA hybridization values and their relationship to whole-genome sequence similarities. *Int. J. Syst. Evol. Microbiol.* 57, 81–91. doi: 10.1099/ijs.0.64483-0

Izrael-Živković, L., Rikalović, M., Gojgić-Cvijović, G., Kazazić, S., Vrvić, M., Brčeski, I., et al. (2018). Cadmium specific proteomic responses of a highly resistant: *Pseudomonas aeruginosa* san ai. *RSC Adv.* 8, 10549–10560. doi: 10.1039/c8ra00371h

Jakubowski, W. (2000). 2,7-dichlorofluorescein oxidation and reactive oxigen species: what does it measure? *Cell Biol. Int.* 24, 757–760. doi: 10.1006/cbir.2000.0556

Jimoh, A. A., and Lin, J. (2019). Enhancement of *Paenibacillus* sp. D9 lipopeptide biosurfactant production through the optimization of medium composition and its application for biodegradation of hydrophobic pollutants. *Appl. Biochem. Biotechnol.* 187, 724–743. doi: 10.1007/s12010-018-2847-7

Jolley, K. A., Bliss, C. M., Bennett, J. S., Bratcher, H. B., Brehony, C., Colles, F. M., et al. (2012). Ribosomal multilocus sequence typing: universal characterization of bacteria from domain to strain. *Microbiology* 158, 1005–1015. doi: 10.1099/mic.0.055459-0

Kanehisa, M., Sato, Y., and Morishima, K. (2016). BlastKOALA and GhostKOALA: KEGG tools for functional characterization of genome and metagenome sequences. *J. Mol. Biol.* 428, 726–731. doi: 10.1016/j.jmb.2015.11.006

Kelstrup, C. D., Young, C., Lavallee, R., Nielsen, M. L., and Olsen, J. V. (2012). Optimized fast and sensitive acquisition methods for shotgun proteomics on a quadrupole orbitrap mass spectrometer. *J. Proteome Res.* 11, 3487–3497. doi: 10.1021/pr3000249

Kim, M. G., Kim, D., Kim, T., Park, S., Kwon, G., Kim, M. S., et al. (2015). Unusual Li-ion storage through anionic redox processes of bacteria-driven tellurium nanorods. *J. Mater. Chem. A* 3, 16978–16987. doi: 10.1039/C5TA04038H

Knuutinen, J., Bomberg, M., Kemell, M., and Lusa, M. (2019). Ni(II) interactions in boreal *Paenibacillus* sp., *Methylobacterium* sp., *Paraburkholderia* sp., and *Pseudomonas* sp. strains isolated from an acidic, ombrotrophic bog. *Front. Microbiol.* 10:2677. doi: 10.3389/fmicb.2019.02677

Kormutakova, R., Klucar, L., and Turna, J. (2000). DNA sequence analysis of the tellurite-resistance determinant from clinical strain of *Escherichia coli* and identification of essential genes. *Biometals* 13, 135–139. doi: 10.1023/A:1009272122989

Krawczyk, P. S., Lipinski, L., and Dziembowski, A. (2018). PlasFlow: predicting plasmid sequences in metagenomic data using genome signatures. *Nucleic Acids Res.* 46:e35. doi: 10.1093/nar/gkx1321

Kumara, M. T., Tripp, B. C., and Muralidharan, S. (2007). Self-assembly of metal nanoparticles and nanotubes on bioengineered flagella scaffolds. *Chem. Mater.* 19, 2056–2064. doi: 10.1021/cm062178b

Kumari, M., and Thakur, I. S. (2018). Biochemical and proteomic characterization of *Paenibacillus* sp. ISTP10 for its role in plant growth promotion and in rhizostabilization of cadmium. *Bioresour. Technol. Rep.* 3, 59–66. doi: 10.1016/j.biteb.2018.06.001

Llyod-Jones, G., Osborn, A. M., Ritchie, D. A., Strike, P., Hobman, J. L., Brown, N. L., et al. (1994). Accumulation and intracellular fate of tellurite in tellurite-resistant *Escherichia coli*: a model for the mechanism of resistance. *FEMS Microbiol. Lett.* 118, 113–119. doi: 10.1111/j.1574-6968.1994.tb06812.x

Lohmeier-Vogel, E. M., Ung, S., and Turner, R. J. (2004). In vivo 31P nuclear magnetic resonance investigation of tellurite toxicity in *Escherichia coli*. *Appl. Environ. Microbiol.* 70, 7342–7347. doi: 10.1128/AEM.70.12.7342-7347.2004

Maltman, C., Piercey-Normore, M. D., and Yurkov, V. (2015). Tellurite-, tellurate-, and selenite-based anaerobic respiration by strain CM-3 isolated from gold mine tailings. *Extremophiles* 19, 1013–1019. doi: 10.1007/s00792-015-0776-8

Moreno, R., and Rojo, F. (2013). The contribution of proteomics to the unveiling of the survival strategies used by *Pseudomonas putida* in changing and hostile environments. *Proteomics* 13, 2822–2830. doi: 10.1002/pmic.201200503

Ogunyemi, S. O., Zhang, M., Abdallah, Y., Ahmed, T., Qiu, W., Ali, M. A., et al. (2020).). The bio-synthesis of three metal oxide nanoparticles (ZnO, MnO_2, and MgO) and their antibacterial activity against the bacterial leaf blight pathogen. *Front. Microbiol.* 11:588326. doi: 10.3389/fmicb.2020.588326

Olin-Sandoval, V., Yu, J. S. L., Miller-Fleming, L., Alam, M. T., Kamrad, S., Correia-Melo, C., et al. (2019). Lysine harvesting is an antioxidant strategy and triggers underground polyamine metabolism. *Nature* 572, 249–253. doi: 10.1038/s41586-019-1442-6

Ollivier, P. R. L., Bahrou, A. S., Marcus, S., Cox, T., Church, T. M., and Hanson, T. E. (2008). Volatilization and precipitation of tellurium by aerobic, tellurite-resistant marine microbes. *Appl. Environ. Microbiol.* 74, 7163–7173. doi: 10.1128/AEM.00733-08

Plaza, D. O., Gallardo, C., Straub, Y. D., Bravo, D., and Pérez-Donoso, J. M. (2016). Biological synthesis of fluorescent nanoparticles by cadmium and tellurite resistant Antarctic bacteria: exploring novel natural nanofactories. *Microb. Cell Fact.* 15:76. doi: 10.1186/s12934-016-0477-8

Prado Acosta, M., Valdman, E., Leite, S. G. F., Battaglini, F., and Ruzal, S. M. (2005). Biosorption of copper by *Paenibacillus polymyxa* cells and their exopolysaccharide. *World J. Microbiol. Biotechnol.* 21, 1157–1163. doi: 10.1007/s11274-005-0381-6

Presentato, A., Piacenza, E., Anikovskiy, M., Cappelletti, M., Zannoni, D., and Turner, R. J. (2016). *Rhodococcus aetherivorans* BCP1 as cell factory for the production of intracellular tellurium nanorods under aerobic conditions. *Microb. Cell Fact.* 15:204. doi: 10.1186/s12934-016-0602-8

Presentato, A., Piacenza, E., Darbandi, A., Anikovskiy, M., Cappelletti, M., Zannoni, D., et al. (2018). Assembly, growth and conductive properties of tellurium nanorods produced by *Rhodococcus aetherivorans* BCP1. *Sci. Rep.* 8:3923. doi: 10.1038/s41598-018-22320-x

Pugin, B., Cornejo, F. A., Muñoz-Díaz, P., Muñoz-Villagrán, C. M., Vargas-Pérez, J. I., Arenas, F. A., et al. (2014). Glutathione reductase-mediated synthesis of tellurium-containing nanostructures exhibiting antibacterial properties. *Appl. Environ. Microbiol.* 80, 7061–7070. doi: 10.1128/AEM.02207-14

Rappsilber, J., Mann, M., and Ishihama, Y. (2007). Protocol for micro-purification, enrichment, pre-fractionation and storage of peptides for proteomics using StageTips. *Nat. Protoc.* 2, 1896–1906. doi: 10.1038/nprot.2007.261

Reinoso, C. A., Appanna, V. D., and Vásquez, C. C. (2013). α-ketoglutarate accumulation is not dependent on isocitrate dehydrogenase activity during tellurite detoxification in *Escherichia coli*. *Biomed Res. Int.* 2013:784190. doi: 10.1155/2013/784190

Sabaty, M., Avazeri, C., Pignol, D., and Vermeglio, A. (2001). Characterization of the reduction of selenate and tellurite by nitrate reductases. *Appl. Environ. Microbiol.* 67, 5122–5126. doi: 10.1128/AEM.67.11.5122-5126.2001

Sandoval, J. M., Arenas, F. A., García, J. A., Díaz-Vásquez, W. A., Valdivia-González, M., Sabotier, M., et al. (2015). *Escherichia coli* 6-phosphogluconate dehydrogenase aids in tellurite resistance by reducing the toxicant in a NADPH-dependent manner. *Microbiol. Res.* 177, 22–27. doi: 10.1016/j.micres.2015.05.002

Segata, N., Börnigen, D., Morgan, X. C., and Huttenhower, C. (2013). PhyloPhlAn is a new method for improved phylogenetic and taxonomic placement of microbes. *Nat. Commun.* 4:2304. doi: 10.1038/ncomms3304

Suntharalingam, P., Senadheera, M. D., Mair, R. W., Leìvesque, C. M., and Cvitkovitch, D. G. (2009). The LiaFSR system regulates the cell envelope stress response in *Streptococcus* mutans. *J. Bacteriol.* 191, 2973–2984. doi: 10.1128/JB.01563-08

Theisen, J., Zylstra, G. J., and Yee, N. (2013). Genetic evidence for a molybdopterin-containing tellurate reductase. *Appl. Environ. Microbiol.* 79, 3171–3175. doi: 10.1128/AEM.03996-12

Tsai, W. C., Kuo, T. Y., Lin, C. Y., Lin, J. C., and Chen, W. J. (2015). *Photobacterium damselae* subsp. *piscicida* responds to antimicrobial peptides through phage-shock-protein A (PspA)-related extracytoplasmic stress response system. *J. Appl. Microbiol.* 118, 27–38. doi: 10.1111/jam.12672

Turner, R. J., Hou, Y., Weiner, J. H., and Taylor, D. E. (1992a). The arsenical ATPase efflux pump mediates tellurite resistance. *J. Bacteriol.* 174, 3092–3094. doi: 10.1128/jb.174.9.3092-3094.1992

Turner, R. J., Weiner, J. H., and Taylor, D. E. (1992b). Use of diethyldithiocarbamate for quantitative determination of tellurite uptake by bacteria. *Anal. Biochem.* 204, 292–295. doi: 10.1016/0003-2697(92)90240-8

Turner, R. J., Weiner, J. H., and Taylor, D. E. (1994). In vivo complementation and site-specific mutagenesis of the tellurite resistance determinant *kilAtelAB* from IncPα plasmid RK2Te(r). *Microbiology* 140, 1319–1326. doi: 10.1099/00221287-140-6-1319

Turner, R. J., Weiner, J. H., and Taylor, D. E. (1995). The tellurite-resistance determinants *tehAtehI3* and *k/aAk/aBte/B* have different biochemical requirements. *Microbiology* 3, 3133–3140. doi: 10.1099/13500872-141-12-3133

Vaigankar, D. C., Dubey, S. K., Mujawar, S. Y., D'Costa, A., and Shyama, S. K. (2018). Tellurite biotransformation and detoxification by *Shewanella baltica* with simultaneous synthesis of tellurium nanorods exhibiting photo-catalytic and anti-biofilm activity. *Ecotoxicol. Environ. Saf.* 165, 516–526. doi: 10.1016/j.ecoenv.2018.08.111

Wang, R., Sens, D. A., Garrett, S., Somjii, S., Sens, M. A., and Lu, X. (2007). The resistance of metallothionein to proteolytic digestion: an LC-MS/MS analysis. *Electrophoresis* 28, 2942–2952. doi: 10.1002/elps.200600835

Wang, Z., Bu, Y., Zhao, Y., Zhang, Z., Liu, L., and Zhou, H. (2018). Morphology-tunable tellurium nanomaterials produced by the tellurite-reducing bacterium *Lysinibacillus* sp. ZYM-1. *Environ. Sci. Pollut. Res.* 25, 20756–20768. doi: 10.1007/s11356-018-2257-y

Wenzel, M., Kohl, B., Münch, D., Raatschen, N., Albada, H. B., Hamoen, L., et al. (2012). Proteomic response of *Bacillus subtilis* to lantibiotics reflects differences in interaction with the cytoplasmic membrane. *Antimicrob. Agents Chemother.* 56, 5749–5757. doi: 10.1128/AAC.01380-12

Zare, B., Faramarzi, M. A., Sepehrizadeh, Z., Shakibaie, M., Rezaie, S., and Shahverdi, A. R. (2012). Biosynthesis and recovery of rod-shaped tellurium nanoparticles and their bactericidal activities. *Mater. Res. Bull.* 47, 3719–3725. doi: 10.1016/j.materresbull.2012.06.034

Zhang, J., Zhang, Y., Richmond, W., and Wang, H. (2010). Processing technologies for gold-telluride ores. *Int. J. Miner. Metall. Mater.* 17, 1–10. doi: 10.1007/s12613-010-0101-6

Zonaro, E., Piacenza, E., Presentato, A., Monti, F., Anna, R. D., Lampis, S., et al. (2017). *Ochrobactrum* sp. MPV1 from a dump of roasted pyrites can be exploited as bacterial catalyst for the biogenesis of selenium and tellurium nanoparticles. *Microb. Cell Fact.* 16:215. doi: 10.1186/s12934-017-0826-2

Conflict of Interest: The authors declare that the research was conducted in the absence of any commercial or financial relationships that could be construed as a potential conflict of interest.

Publisher's Note: All claims expressed in this article are solely those of the authors and do not necessarily represent those of their affiliated organizations, or those of the publisher, the editors and the reviewers. Any product that may be evaluated in this article, or claim that may be made by its manufacturer, is not guaranteed or endorsed by the publisher.

frontiers in Microbiology

ORIGINAL RESEARCH
published: 20 September 2021
doi: 10.3389/fmicb.2021.712564

Overexpression of *mqsR* in *Xylella fastidiosa* Leads to a Priming Effect of Cells to Copper Stress Tolerance

*Isis Gabriela Barbosa Carvalho[1], Marcus Vinicius Merfa[2], Natália Sousa Teixeira-Silva[1], Paula Maria Moreira Martins[1], Marco Aurélio Takita[1] and Alessandra Alves de Souza[1]**

[1] Centro de Citricultura Sylvio Moreira, Instituto Agronômico, Cordeirópolis, Brazil, [2] Department of Entomology and Plant Pathology, Auburn University, Auburn, AL, United States

Copper-based compounds are widely used in agriculture as a chemical strategy to limit the spread of multiple plant diseases; however, the continuous use of this heavy metal has caused environmental damage as well as the development of copper-resistant strains. Thus, it is important to understand how the bacterial phytopathogens evolve to manage with this metal in the field. The MqsRA Toxin–Antitoxin system has been recently described for its function in biofilm formation and copper tolerance in *Xylella fastidiosa*, a plant-pathogen bacterium responsible for economic damage in several crops worldwide. Here we identified differentially regulated genes by *X. fastidiosa* MqsRA by assessing changes in global gene expression with and without copper. Results show that *mqsR* overexpression led to changes in the pattern of cell aggregation, culminating in a global phenotypic heterogeneity, indicative of persister cell formation. This phenotype was also observed in wild-type cells but only in the presence of copper. This suggests that MqsR regulates genes that alter cell behavior in order to prime them to respond to copper stress, which is supported by RNA-Seq analysis. To increase cellular tolerance, proteolysis and efflux pumps and regulator related to multidrug resistance are induced in the presence of copper, in an MqsR-independent response. In this study we show a network of genes modulated by MqsR that is associated with induction of persistence in *X. fastidiosa*. Persistence in plant-pathogenic bacteria is an important genetic tolerance mechanism still neglected for management of phytopathogens in agriculture, for which this work expands the current knowledge and opens new perspectives for studies aiming for a more efficient control in the field.

Keywords: persister cells, toxin-antitoxin (TA), phytopathogenic bacteria, copper tolerance system, stress adaptation

OPEN ACCESS

Edited by:
Raymond J. Turner, University of Calgary, Canada

Reviewed by:
Bork Ansgar Berghoff, Justus-Liebig-Universität Gießen, Germany
Xiuli Hao, Huazhong Agricultural University, China

***Correspondence:**
Alessandra Alves de Souza
desouza@ccsm.br; alessandra.coletta@sp.gov.br

Specialty section:
This article was submitted to Antimicrobials, Resistance and Chemotherapy, a section of the journal Frontiers in Microbiology

Received: *20 May 2021*
Accepted: *09 August 2021*
Published: *20 September 2021*

Citation:
Carvalho IGB, Merfa MV, Teixeira-Silva NS, Martins PMM, Takita MA and de Souza AA (2021) Overexpression of mqsR in Xylella fastidiosa Leads to a Priming Effect of Cells to Copper Stress Tolerance. Front. Microbiol. 12:712564. doi: 10.3389/fmicb.2021.712564

INTRODUCTION

Xylella fastidiosa is a phytopathogen with a broad host range that affects plants worldwide (Almeida et al., 2019). Plant diseases caused by this bacterium include citrus variegated chlorosis (CVC), Pierce's disease (PD) in grapevines, and the olive quick decline syndrome (OQDS), which constitute important threats for these crops (Almeida et al., 2019; Saponari et al., 2019; Coletta-Filho et al., 2020). Copper-based compounds are widely used in agriculture as a chemical strategy to limit

the spread of multiple plant diseases (Lamichhane et al., 2018). Although *X. fastidiosa* is not itself controlled by copper spraying, biocomplexes containing copper, zinc, and citric acid have been used to control *X. fastidiosa* in olive groves (Girelli et al., 2019). Copper has an important contribution in crop protection; however, there are many issues related to the use of this heavy metal such as phytotoxicity, soil accumulation, negative effects on soil biota, and development of copper-resistant strains (Lamichhane et al., 2018). Thus, regarding plant-pathogen interaction, it is important to understand how the bacterial phytopathogens evolve to deal with this metal in the field.

In *X. fastidiosa*, the *mqsRA* toxin–antitoxin (TA) system type II is a genetic mechanism that has been associated with tolerance to copper stress (Muranaka et al., 2012). There are six types of TA system, which are distinct according to the action, nature, and mechanisms used by the antitoxins to neutralize the activities of the toxins (Page and Peti, 2016). Typically, in these systems, the toxin gene product is a protein and the antitoxin gene is a non-coding RNA (in types I and III) or a protein (in types II, IV, V, and VI) (Page and Peti, 2016; Harms et al., 2018). Bacterial toxin-antitoxin (TA) systems encode a stable toxin that disrupts cellular function and its labile cognate antitoxin in the same operon. The antitoxin neutralizes toxin activity under normal conditions, while proteases degrade the antitoxin under stress, allowing the toxin activity (Wang and Wood, 2011; Fisher et al., 2017). Moreover, the antitoxin usually regulates the expression of its own TA operon by binding to a palindromic sequence in the promoter region and repressing its transcription (Wang et al., 2011). TA systems have been shown to play a role in persistence, biofilm formation, cell movement, pathogenicity, DNA maintenance, and phage-defense (Wang et al., 2011; Wen et al., 2014; Shidore and Triplett, 2017). In addition, they are highly expressed in persister cells and, thus, are generally responsible for the persistence phenotype (Wang and Wood, 2011; Fisher et al., 2017). A persister cell constitutes a tolerant cell (Lewis, 2010) originating from a population that displays antibiotic persistence, being a subpopulation phenomenon (sometimes referred to as heterotolerance) (Balaban et al., 2019), while, a tolerant cell is the capacity of an entire population of bacteria to survive a bactericidal antibiotic exposure (Balaban et al., 2019). Multidrug resistance in bacteria can occur by distinct ways like the accumulation of the resistance factors like plasmids or genes, each one encoding for resistance to a particular agent, and can or cannot occur along with the activity of multidrug efflux pumps (Nikaido, 2009).

The *mqsRA* TA system was originally described in *Escherichia coli* and shown to be involved in biofilm and persister cell formation (Wang and Wood, 2011). The toxin *mqsR* was the most induced gene in *E. coli* persisters and the first TA system to reduce persister formation upon deletion, while increasing this phenotype after overexpression (Kim and Wood, 2010). It has been demonstrated that *X. fastidiosa* may form persister cells under copper stress (Muranaka et al., 2012; Merfa et al., 2016), representing an important survival strategy still unexplored in plant pathogenic bacteria (Martins et al., 2018).

The MqsRA TA system is composed of the MqsR toxin, which is an endoribonuclease that degrades messenger RNA (mRNA) with GCU motifs and the MqsA antitoxin that binds and inactivates the toxin via its N-terminal domain (Brown et al., 2009; Yamaguchi et al., 2009; Lee et al., 2014). Due to its ability to selectively degrade mRNA, MqsR also acts as a global regulator (Wood et al., 2013). Thus, aiming to identify genes modulated by MqsR in *X. fastidiosa*, we overexpressed this toxin under the control of its native promoter and performed RNA-Seq when growing cells under normal and upon copper stress conditions.

Our results show that MqsR is a key gene regulator in the pathway tolerance of *X. fastidiosa* to copper stress, mediating several genes that prompt the cells to enter in a state that suggests the formation of persisters. In addition, copper induces MqsR-independent responses related to proteolysis and multidrug resistance through transcriptional regulator, transporters, and efflux pumps in order to increase the bacterial tolerance to this metal. This study presents unexplored mechanisms in phytopathogens that could have important impacts on how they can deal with agrochemicals and highlight the persistence phenomenon that could be occurring in the field.

MATERIALS AND METHODS

Bacterial Strains and Transformation

The bacterial strains used in this study were the *X. fastidiosa* wild-type strain 11399 (Coletta-Filho et al., 2001; Niza et al., 2016) and 11399 overexpressing *mqsR* under the control of its native promoter (*Xf-mqsR*) (Merfa et al., 2016) (**Supplementary Table 1**). The increased amount of MqsR was previously confirmed by Western blot (Merfa et al., 2016). We transformed *X. fastidiosa* 11399 strain with the pXF20 empty vector (Lee et al., 2010), by electroporation (1.8 kV, 200 Ω, 25 μF) to serve as negative control (*Xf*-EV). The transformants were grown on selective medium PWG (phytone peptone; BD Biosciences, San Jose, CA, United States) 4.0 (g/L), trypticase peptone (BD) 1.0 (g/L), K_2HPO_4 (Sigma, St. Luis, MO, United States) 1.2 (g/L), hemin chloride stock (Sigma) 10 (mL/L), KH_2PO_4 1.0 (g/L), Gelzan (Sigma) 8.0 (g/L), $MgSO_4{:}7H_2O$, 0.4 (g/L), phenol red stock (Sigma; 0.2% (w/v) phenol red in distilled water) 10 (mL/L), glutamine (Sigma) 4 (g/L), and bovine serum albumin fraction-five (BSA) (Sigma) 3 (g/L); this medium was prepared according Davis et al. (1981) plates supplemented with 50 μg/mL kanamycin. The transformation was confirmed by PCR using a specific pair of primers to detect the pXF20 plasmid (**Supplementary Figure 1**). The primers used to confirm this transformation are oriV-pXF20-F 5'-GGTTTGTGAAAGCGCAGTG and trfA-pXF20-R 5'-ATTGCCAATTTGGACAGATG. The *Xf*-EV and *Xf-mqsR* strains were routinely grown on selective PWG plates supplemented with 50 μg/mL kanamycin at 28°C for 7 days.

Copper Sensitivity Assay

To evaluate the effects of copper on *X. fastidiosa* growth and formation of persisters, *Xf*-EV and *Xf-mqsR* cells were grown in PW broth (PWG without Gelzan) (Davis et al., 1981) and treated with 3 mM $CuSO_4.5H_2O$ (Sigma). Control samples of both strains were grown in non-copper PW broth. Cells

grown on solid PW were harvested from plates, resuspended in PBS buffer, and the optical density ($OD_{600\ nm}$) was adjusted to 0.3 and inoculated into PW broth to grow for another 7 days. The cells were then collected and the $OD_{600\ nm}$ was adjusted to 0.1. From each of these bacterial suspensions, 10-mL aliquots were inoculated into 90 mL fresh PW broth and incubated at 28°C for 14 days at 150 rpm. Subsequently, *Xf*-EV and *Xf-mqsR* cells were exposed to 0 ("C-0" for *Xf*-EV, and "M-0" for *Xf-mqsR*) and 3 mM copper ("C-3" for *Xf*-EV and "M-3" for *Xf-mqsR*) for 24 h (Merfa et al., 2016). Each treatment was performed in duplicates for each strain. The cells of each culture were collected, rinsed with DEPC water, and resuspended in 11 mL of PBS buffer. An aliquot of 1 mL from each suspension was used to determine colony formation units (CFU/mL), and to perform electron microscopy analysis, as described below. The cells of the remaining 10 mL were collected under the same conditions and stored at −80°C for RNA extraction. Three independent biological replicates were performed.

Bacterial Growth Under Copper Stress

Aliquots of the entire experimental condition described above (**Supplementary Figure 2**) were collected to determine the CFU/mL of each biological experiment at the following time course: inoculation time (t0), 14 days after growth (stationary phase, Campanharo et al., 2003) in fresh PW broth when copper was added (t1) and 24 h after copper treatment (t2), completing 15 days of growth. From each sample, a 10-fold serial dilution was performed and plated in PWG to estimate CFU. Four replicates were used for each sample, which were grown at 28°C for 30 days. The measurements were performed in triplicates, and results were scored as the means ± standard deviation and compared using the Student's *t*-test ($p \leq 0.05$).

Scanning Electron Microscopy

Scanning electron microscopy was performed under the experimental conditions described above (**Supplementary Figure 2**). Briefly, an aliquot of the planktonic and biofilm cells was sampled 24 h after copper addition for each *X. fastidiosa* strain. Controls without copper were also collected for both *Xf*-EV and *Xf-mqsR*. Samples were centrifuged and resuspended in RNA Later solution (Thermo Fisher Scientific, Waltham, MA, United States), frozen in liquid nitrogen and stored at −80°C. For microscopy analysis, cells were thawed, centrifuged, fixed in 2.5% glutaraldehyde in 0.2 M sodium cacodylate buffer (v/v) and kept at 4°C until use. Preparation of samples for visualization was done according to Kozlowska et al. (2014). Electron micrographs were captured with a magnification of 4000 × using a Hitachi TM 3000 scanning electron microscope (Hitachi, Tokyo, Japan). The *Xf*-EV and *Xf-mqsR* cells were measured using the ImageJ software (ImageJ, 2018) to determine the length and proportion of elongated and small cells at 100 cells per treatment. Only cells longer than 4.0 μm were considered elongated (Liu et al., 2014; Merfa et al., 2016), while only cells with a length smaller than 2.0 μm were considered small. The length of each cell in each treatment was analyzed through comparison of means by one-way analysis of variance (ANOVA) followed by Holm–Sidak multiple comparison test or Tukey's HSD test ($p \leq 0.05$).

RNA Isolation and RNA-Seq

RNA-Seq reads were produced from 12 RNA samples: three from non-treated *Xf*-EV cells, three from non-treated *Xf-mqsR*, three from copper-treated cells of *Xf*-EV, and three from copper-treated *Xf-mqsR* cells. Total RNA was extracted using the hot phenol method (Khodursky et al., 2003), treated with DNase I RNase free (Qiagen, Hilden, Germany), purified using the RNeasy Plus Kit (Qiagen, Hilden, Germany) and eluted in 30 μL of RNase-free water. Concentrations were determined by spectrophotometry (NanoDrop 8000, Thermo Fisher Scientific). Ribo-Zero rRNA^{TM} Removal Kit (Illumina, San Diego, CA, United States) was used for rRNA removal. The depleted RNA was precipitated using ethanol according to the manufacturer's instructions and resuspended in 10 μL of RNase-free water. Samples were quantified for the presence of rRNA using the 2100 Bioanalyzer system (Agilent Technologies, Santa Clara, CA, United States) at the Life Sciences Core Facility (LaCTAD). cDNA libraries were prepared using the Illumina TruSeq Stranded mRNA Library Prep Kit (Illumina). Sequencing was performed using the HiSeq High Output kit (Illumina) on a HiSeq 2500 system (Illumina), run with 2 × 100 bp paired-end reads.

RNA-Seq Data Analysis

The sequencing reads were analyzed in the FastQC program (Wingett and Andrews, 2018) and processed using Trimmomatic (Bolger et al., 2014) to remove adapters and extremities with poor quality. The reads were mapped to the genome of *X. fastidiosa* 9a5c (NCBI BioProject accession PRJNA271) using the STAR program (Dobin et al., 2013). From the mapped data, the gene-mapped reads were counted using the Subread package (Liao et al., 2019). Standardization and analysis of differential gene expression ($p < 0.05$) was performed using the EdgeR package (Robinson et al., 2010), computed using data from all three biological replicates. Differentially expressed genes obtained from EdgeR analyses were used for functional categorization by Blast2GO (Götz et al., 2008). Venny 2.1.0 (Oliveros, 2007) was used to show exclusive genes regulated in *Xf-mqsR* under copper stress.

Data Validation by Quantitative Real Time-PCR (RT-qPCR)

RNA samples were obtained from three other experiments using the same experimental condition as the RNA-Seq. A total of 250 ng of purified RNA from each condition was used as input for cDNA synthesis with the Reverse Transcription System kit (Promega, Madison, WI, United States). RT-qPCR was performed using the GoTaq qPCR Master Mix (Promega) in an ABI PRISM 7500 Sequence Detection System (Applied Biosystems, Foster City, CA, United States). Relative expression values were normalized to the *X. fastidiosa* 16S ribosomal RNA endogenous control (Merfa et al.,

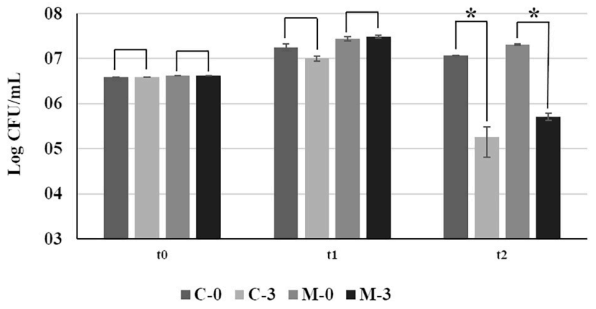

FIGURE 1 | Bacterial growth of *Xf*-EV and *Xf-mqsR* under normal conditions and after copper stress at different time points. C-0: *Xf*-EV; C-3: *Xf*-EV + 3 mM $CuSO_4$; M-0: *Xf-mqsR*; M-3: *Xf-mqsR* + 3 mM $CuSO_4$. t0: initial inoculum; t1: 14 days of growth; t2: 24 h after copper treatment, at the end of 15 days. Three independent experiments were performed with similar results. * indicates statistical significance by Student's *t*-test ($p \leq 0.05$, $n = 4$).

2016). Cycling parameters were performed according to the manufacturer's protocol. The relative expression quantification (RQ) was calculated as previously described (Livak and Schmittgen, 2001). The selected genes are based on the RNA-Seq analysis of M-0 and M-3 (**Supplementary Table 2**). Three independent biological replicates were used for data validation.

Palindrome Search

The motif 5'-ACC (N)7 GTT-3' (Merfa et al., 2016), used as target sequence for DNA binding by the antitoxin MqsA, was searched in the genome of *X. fastidiosa* strain 9a5c using PATLOC (Mrazek and Xie, 2006), and also at the differentially expressed genes (DEG) data set herein generated.

RESULTS

MqsR Overexpression Changes *X. fastidiosa* Phenotype

To evaluate the effects of copper on wild-type *X. fastidiosa* and the *mqsR*-overexpressing strain, bacterial growth with and without copper was evaluated. In a previous work we verified that overexpression of MqsR increased the formation of persister cells under 3 mM of copper stress (Merfa et al., 2016). Here, to access the phenotypic and genetic regulation mediated by MqsR, we used the same condition, where copper was added after 15 days of bacterial growth.

At the time of the inoculation (t0), and after 15 days of growth in fresh PW broth (t1), no significant difference in bacterial growth was observed between C-0 and M-0 (**Figure 1**). However, 24 h after addition of copper (t2), there was a significant reduction in population size of approximately 100-fold between copper-treated samples (C-3 and M-3) and their respective untreated controls (C-0 and M-0) (**Figure 1**). We observed an approximately 10% increase in cell survival after copper treatment in populations overexpressing *mqsR* (M-3) in comparison to the control (C-3). However, the difference in CFU counts between M-3 and C-3 was not significant ($F = 0.06$, $p = 0.11$) (**Figure 1**).

To verify possible phenotypic changes in *X. fastidiosa* cells potentially caused by the overexpression of *mqsR* and copper treatment, samples from each experimental condition were used for scanning electron microscopy. Under normal growth condition, biofilm and planktonic cells in C-0 did not show any significant morphological change (**Figures 2A,B**). However, when copper was added (C-3) a reduction was observed in biofilm size (**Figure 2C**), and curiously, copper induced aggregation and elongated cells in the planktonic condition (**Figure 2D**, red arrows).

On the other hand, *X. fastidiosa* overexpressing *mqsR* (M-0) presented more elongated cells even without copper stress (**Figures 2E,F**, red arrows), and at an even greater extent than C-3 (**Figure 2D**, red arrows). In addition, *X. fastidiosa* overexpressing *mqsR* (M-0) displayed a phenotypic heterogeneity that can be demonstrated by the presence of a higher population of shorter cells when compared to the other treatments (**Figure 2F**, blue arrows). Elongated cells were also observed in *X. fastidiosa* overexpressing *mqsR* in presence of copper (M-3) in both biofilm and planktonic conditions (**Figures 2G,H**, red arrows).

Microscopy images for each condition ($n = 100$) were used for counting elongated and short cells in the planktonic fraction (**Figures 2I,J**). The results showed a good agreement with the visual observation, with a higher population of elongated cells in *X. fastidiosa* overexpressing *mqsR* (M-0) compared to C-0. Copper induced an increase of elongated cells in both populations (C-3 and M-3). Interestingly the number of elongated cells in M-0 is naturally even higher than C-3 (**Figure 2I**). Similarly, higher percentages of short cells were observed in presence of copper (C-3 and M-3) or *X. fastidiosa* overexpressing *mqsR* (M-0) (**Figure 2J**).

Overall, these results show that besides copper treatment, *mqsR* overexpression also led to changes in *X. fastidiosa* morphology and pattern of aggregation, culminating in a global phenotypic heterogeneity. Interestingly, heterogeneous phenotypes in single bacterial populations have been described as indicative of persister cells (Michiels et al., 2016; Fisher et al., 2017).

RNA-Seq Data

RNA-Seq reads were produced for C-0, C-3, M-0, and M-3 (**Supplementary Figure 3**). Raw sequencing reads were deposited under the NCBI Bio-Project ID PRJNA718853. Average post-trim read length ranged from 36 to 105 bp, the reads aligned to the genome of *X. fastidiosa* 9a5c. Variable rRNA and small RNA depletion efficiencies between samples resulted in 0–7.3% in library preparation. Mapped reads were used to determine transcript boundaries and normalized expression for all protein-coding genes by EdgeR (**Supplementary Material 1**, **Data Sets 1–5**). Pearson's correlation coefficient for protein-coding gene expression between experimental replicates ranged from 0.89 to 0.93. Highlighted DEGs of libraries were characterized according

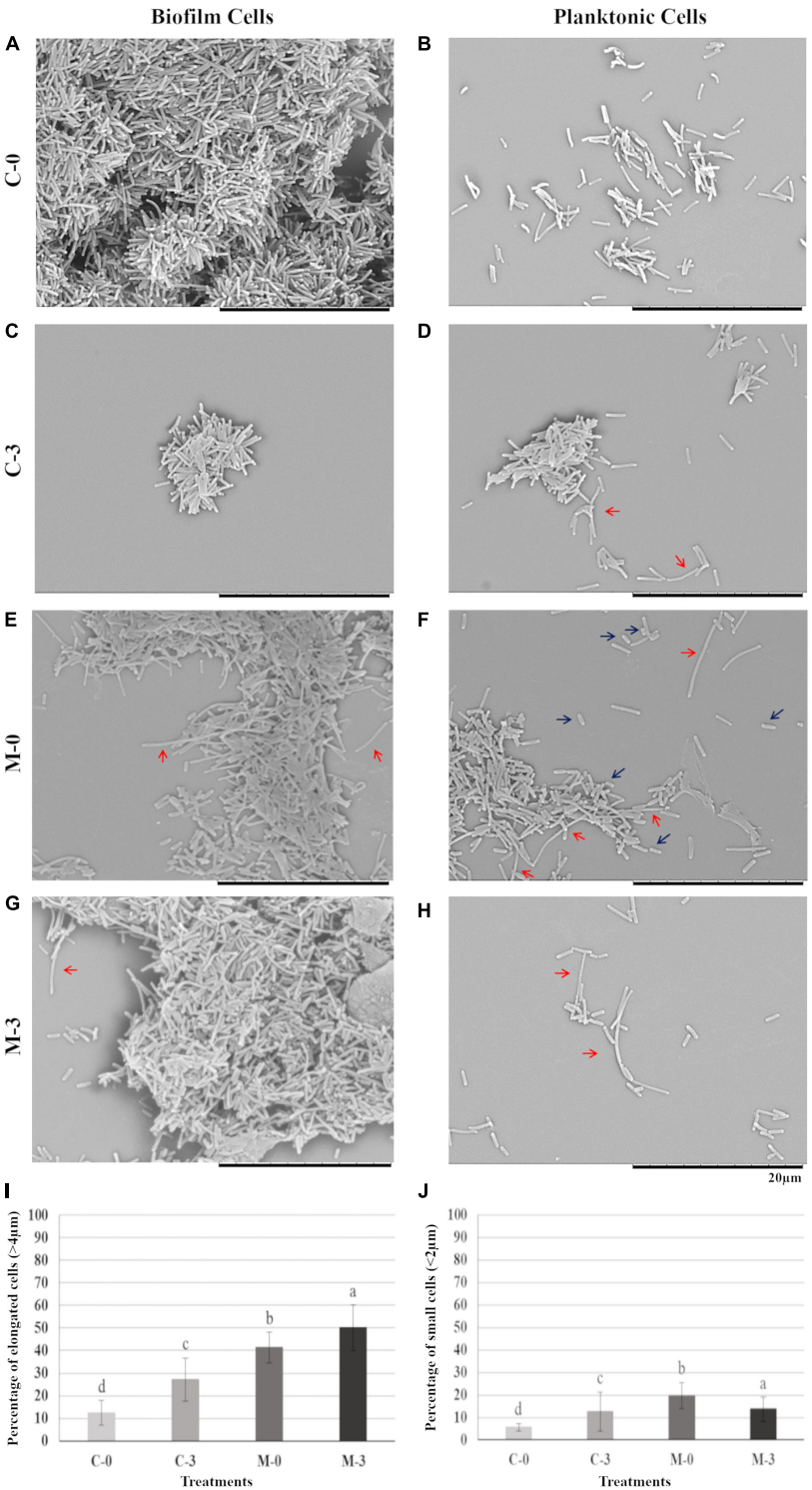

FIGURE 2 | Biofilm and planktonic behavior of *Xf*-EV and *Xf-mqsR* cells under copper stress. Left column: cells in biofilm. Right column: planktonic cells. **(A,B)** Representative pictures of C-0: *Xf*-EV cells without copper treatment. **(C,D)** Representative pictures of C-3: *Xf*-EV cells treated with 3 mM $CuSO_4$. **(E,F)** Representative pictures of M-0: *Xf-mqsR* cells without copper treatment. **(G,H)** Representative pictures of M-3: *Xf-mqsR* cells treated with 3 mM $CuSO_4$. Red arrows show elongated cells and blue arrows show short cells. Scale bar: 20 µm. **(I)** Percentage of planktonic cells longer than 4.0 µm. **(J)** Percentage of planktonic cells shorter than 2.0 µm in the different treatments. Different letters on top of column bars indicate significant difference as analyzed by one-way ANOVA in SigmaPlot followed by Tukey's HSD test ($p \leq 0.05$; $n = 3$ biological replicates, with 100 internal replicates each). C-0: *Xf*-EV cells without copper treatment; C-3: *Xf*-EV cells treated with 3 mM of $CuSO_4$; M-0: *Xf-mqsR* cells without copper treatment; M-3: *Xf-mqsR* cells treated with 3 mM of $CuSO_4$.

to the biological process by Blast2GO (**Supplementary Material 1**, **Data Sets 6–11**).

mqsR Differentially Modulates Global Gene Expression of *X. fastidiosa*

To investigate global expression changes likely to be associated with the phenotypes described above, we performed RNA sequencing analysis. To identify which genes were modulated by MqsR under normal growth conditions, we assessed the pairwise comparison between M-0/C-0 libraries (without copper treatment). Amongst the DEGs, 189 genes showed upregulation by the overexpression of *mqsR* alone, while 164 genes were downregulated (**Supplementary Material 1**, **Data Set 1**; $p < 0.05$). RNA-Seq expression values ($\log_2$ fold-change) were confirmed by RT-qPCR for 10 selected genes based on **Table 1**, with a Pearson correlation coefficient of 0.89 (**Supplementary Figure 4**). According to the data obtained through RNA-Seq (**Supplementary Material 1**, **Data Set 1**), the selected genes that are possibly modulated by MqsR are listed in **Table 1**.

Functional categorization of these 353 DEGs comprised genes associated with peptide metabolic process, transport, proteolysis, transcriptional regulation, and RNA metabolic processes (**Figure 3**, **Supplementary Material 1**, and **Data Sets 6, 7**). Genes associated with proteolysis were exclusively downregulated, including the proteases *clpA* and *clpP*. On the other hand, genes related to peptide metabolism were exclusively upregulated, including those related to ribosomal subunit scaffolding of RNA polymerase (RNAP), such as *rpoA* and *rpoZ*. These genes are also listed in the regulatory function category, together with *mqsR*, *lysR,* and the post-transcriptional regulator *hfq*, which were induced. The regulators genes *mqsR*, *rpoZ*, and *lysR* are related to bacterial survival, stress responses, and pathogenicity (Maddocks and Oyston, 2008; Santiago et al., 2015; Merfa et al., 2016; Weiss et al., 2017). *rpoZ* mutants of *Mycobacterium smegmatis* were deficient in motility and biofilm formation, consequently affecting the formation of extracellular matrix (Mathew and Chatterji, 2006). Besides, the overexpression of transcriptional regulator type LysR from *X. fastidiosa* in *E. coli* was described to a play role in maturation of biofilm during its development (Santiago et al., 2015). In *X. fastidiosa*, it is important to emphasize that the formation of biofilm is characterized as the main pathogenicity mechanism (Coletta-Filho et al., 2020). The transport category included the upregulation of *tolC* and *acrB*, both related to efflux pumps (Weston et al., 2018) and bacterial persistence (Pu et al., 2016). Efflux pumps are important for broad cellular homeostasis during stress responses. They export a wide variety of compounds, such as signaling molecules and antimicrobial compounds (Langevin and Dunlop, 2018). *rlpA*, a gene involved in cell division (Jorgenson et al., 2014; Berezuk et al., 2018), was downregulated, and *fimD*, which is involved with type I fimbrial adhesin (Meng et al., 2005), was upregulated. These genes are involved in bacterial physiology and biofilm formation, respectively. Furthermore, our results showed TA-related genes. The *relE* (XF_RS12805) toxin was downregulated by MqsR; this gene is associated with inhibition translation by cleavage of mRNA in the ribosome (Fiebig et al., 2010). Another toxin, *parE* gene, was upregulated and it is responsible for inhibiting gyrase and thereby blocks chromosome replication (Jiang et al., 2002). Modulation of *relE* and *parE* suggests that these bacterial cells maintain basal activities with reduced metabolism as shown in persister cells (Lewis, 2007). In addition, the repression of *rlpA*, inhibiting cell division and induction of the toxin encoding *parE* (Yuan et al., 2011), which inhibits bacterial division, could contribute with the observed elongated phenotype. Taken together, these observations suggest that overexpression of *mqsR* contributes to bacterial survival during stress response by activating pathogenicity regulators and inhibiting proteolysis and cell division.

Overexpression of *mqsR* Modulates Translation in *X. fastidiosa* Under Copper Stress

To identify the influence of copper on the gene expression, the following pairwise comparisons of the sequencing libraries were performed: i. M-3/M-0, and ii. C-3/C-0. Each pairwise comparison generated 417 and 662 DEGs, respectively. The M-3/M-0 comparison resulted in 238 upregulated and 179 downregulated genes (**Supplementary Material 1**, **Data Set 2**), while the C-3/C-0 analysis resulted in 335 upregulated and 327 downregulated genes (**Supplementary Material 1**, **Data Set 3**).

To verify *X. fastidiosa* genes modulated by MqsR in response to copper stress, a Venn diagram was used to compare the up- and downregulated genes in the M-3/M-0 and C-3/C-0 libraries (**Figure 4**). This comparison provided genes modulated only by *mqsR*-overexpressing cells under copper stress (M-3/M-0), resulting exclusively in 111 upregulated and 84 downregulated genes (**Figure 4** and **Supplementary Material 1**, **Data Set 4**).

In the search for genes oppositely modulated between *Xf*-EV (C-3/C-0) and *Xf-mqsR* (M-3/M-0), a set of nine genes were found to be downregulated in C-3/C-0 and upregulated in M-3/M-0. Of those, there is the *yeiP* elongation factor (XF_RS09585), three ribosomal subunits (XF_RS00715, XF_RS00285, XF_RS09575), the *msrB* (XF_RS03590) and *yuxK* (XF_RS04035), the aminotransferase *astC* (XF_RS06015, also known as *argM* or *cstC*), and two hypothetical proteins (XF_RS03860, XF_RS05645). Interestingly though, the ribosomal protein (XF_RS12125) was the only one showing an opposite behavior, being induced in C-3/C-0 but suppressed in M-3/M-0. This protein is involved in translation, and accordingly, this category was downregulated in M-3/M-0. In *E. coli,* it is known that persister cells have very low metabolism, with non-growing cells as a result of a depletion in translation and, thus, in protein production capacity, cessation of transcription and reduction in ATP production (Kwan et al., 2013; Kim et al., 2018). Moreover, the ability to wake up from this persister state was related to ribosome content (Kim et al., 2018). Our results show categories such as peptide metabolic processes and translation downregulated, suggesting low-metabolism and depletion of protein production in *X. fastidiosa* in such condition.

TABLE 1 | Genes modulated by MqsR in *X. fastidiosa*.

Functional group	Gene name*	Locus Tag**	Protein	Product	LogFC
Peptide metabolic process	Chaperone protein *clpB*	XF_RS01600	WP_010892912.1	Chaperone protein ClpB	−1.47
	Molecular chaperone	XF_RS00340	WP_010892630.1	Molecular chaperone	1.66
Proteolysis	ATP-dependent Clp protease proteolytic subunit	XF_RS05040	WP_010893698.1	ATP-dependent Clp protease proteolytic subunit	−1.08
	ATP-dependent Clp protease ATP-binding subunit *clpA*	XF_RS06080	WP_010893944.1	ATP-dependent Clp protease ATP-binding subunit ClpA	−0.878
	Peptidase S14	XF_RS02140	WP_042462775.1	Clp protease ClpP	−0.70
	Protease HtpX	XF_RS11410	WP_010895042.1	Protease HtpX	−1.30
Cell division	Hypothetical protein *(rlpA)*	XF_RS09450	WP_010894633.1	Septal ring lytic Transglycosylase RlpA family protein	−1.11
Toxins	Hypothetical protein (Colicin V)	XF_RS01135	WP_010892803.1	Hypothetical protein	4.33
	Bacteriocin	XF_RS10410	WP_010894853.1	Bacteriocin	0.680
Regulatory functions	Transcriptional regulator	XF_RS07310	WP_010894181.1	Transcriptional regulator	2.25
	LysR family transcriptional regulator	XF_RS07605	WP_031336630.1	LysR family transcriptional regulator	2.74
	DNA-binding response regulator	XF_RS01630	WP_004083627.1	DNA-binding response regulator ompR	−0.843
	AraC family transcriptional regulator	XF_RS05305	WP_010893760.1	AraC family transcriptional regulator	−0.864
	Hypothetical protein	XF_RS07050	WP_042463203.1	Hypothetical protein (Helix-turn-helix XRE-family like proteins)	2.25
	RNA polymerase-binding protein *dksA*	XF_RS04240	WP_010893509.1	RNA polymerase-binding protein DksA	−0.85
	DNA-directed RNA polymerase subunit alpha (*rpoA*)	XF_RS04985	WP_004090142.1	DNA-directed RNA polymerase subunit alpha	1.32
	DNA-directed RNA polymerase subunit omega (*rpoZ*)	XF_RS06345	WP_010894003.1	DNA-directed RNA polymerase subunit omega	1.10
	RNA-binding protein Hfq	XF_RS00365	WP_010892636.1	RNA-binding protein Hfq	1.11
Attachment/motility					
Fimbrial adhesins	Fimbrial protein (*fimD*)	XF_RS00335	WP_010892629.1	Fimbrial biogenesis outer membrane usher protein	1.21
Transporters	Membrane protein *(tolC*)	XF_RS11265	WP_010895004.1	Membrane protein	0.755
	multidrug transporter	XF_RS09045	WP_010894536.1	AcrB/AcrD/AcrF family protein	0.809
TA system	Addiction module antidote protein	XF_RS12375	WP_010895238.1	DNA-binding protein	−1.94
	Plasmid stabilization protein *(parE*)	XF_RS09000	WP_010894527.1	Type II toxin-antitoxin system RelE/ParE family toxin	1.13
	Antitoxin (*mqsA*)	XF_RS10795	WP_010894926.1	Antitoxin	1.06
	HP (*mqsR*)	XF_RS10790	WP_010894925.1	Type II toxin-antitoxin system MqsR family toxin	4.47
	Addiction module protein	XF_RS12370	WP_004091397.1	Type II toxin-antitoxin system RelE/ParE family toxin	−2.41
	Cytotoxic translational repressor of toxin-antitoxin stability system (*relE*)	XF_RS12805	WP_080507186.1	RelE_type II toxin-antitoxin system RelE/ParE family toxin	−0.823
Quorum sensing	Long-chain fatty acid–CoA ligase (*rpfB*)	XF_RS01220	WP_010892826	Chemical binding	0.789

**Nomenclature according to GenBank.*
***Locus Tag corresponds to GenBank accession numbers.*

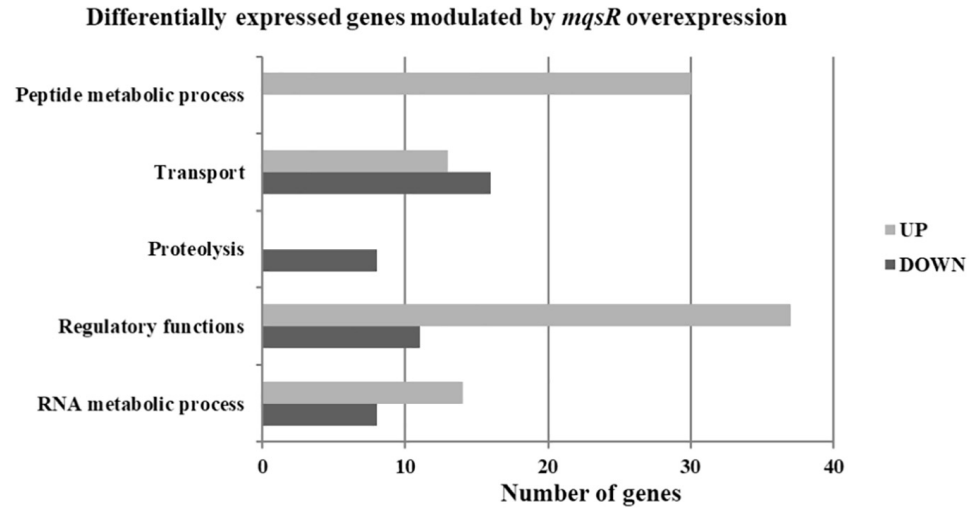

FIGURE 3 | Gene ontology categorization of differentially expressed genes in *X. fastidiosa* in response to overexpression of *mqsR*. Genes were classified by functional category of biological processes using Blast2GO. UP: upregulated genes; DOWN: downregulated genes.

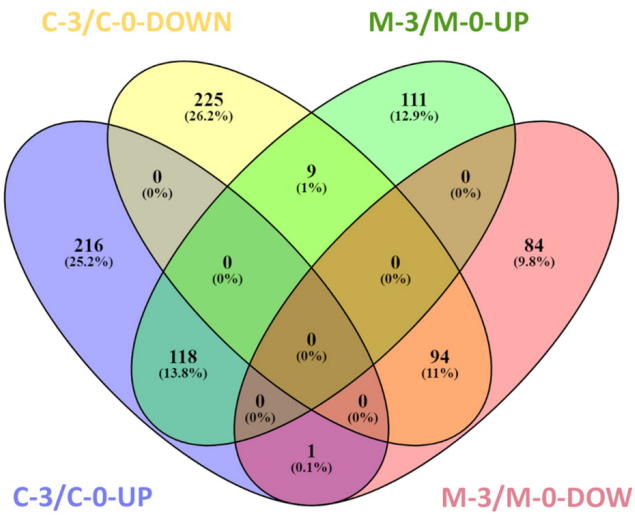

FIGURE 4 | Venn diagram representing the number of up and downregulated genes in *X. fastidiosa* under copper stress. M-3/M-0: pairwise comparison between the M-3 (*Xf-mqsR* + CuSO4) and M-0 (*Xf-mqsR*) libraries. C-3/C-0: pairwise comparison between the C-3 (*Xf*-EV + CuSO4) and C-0 (*Xf*-EV) libraries. UP: upregulated genes; DOWN: downregulated genes.

Finally, 94 genes remained downregulated, and 118 genes were upregulated in both conditions. We believe that these sets of genes are modulated due to treatment with copper itself and are likely to be independent of MqsR functions (**Supplementary Material 1**, **Data Set 5**).

Next, the functional characterization of the M-3/M-0 data set was performed to identify which genes are differentially modulated by the overexpression of MqsR under copper stress. RNA-Seq $\log_2$ fold-change values were confirmed by RT-qPCR for 10 selected genes selected from **Table 2** with a Pearson correlation coefficient of 0.93 (**Supplementary Figure 4**). Genes related to translation and peptide metabolic processes were exclusively repressed in the M-3/M-0 libraries, whereas proteolysis and drug metabolic processes were induced (**Figure 5A** and **Supplementary Material 1**, **Data Sets 8, 9**). Other categories identified in this analysis included transport, regulatory functions, and RNA metabolic processes. Therefore, besides lowering the metabolism, the cells activate these specific salvage mechanisms allowing copper tolerance.

The proteolysis category included another peptidase S4 *clpP* (XF_RS02140) and *tldD* (XF_RS04775) metalloprotease, important regulators of bacterial metabolism. These genes are related to protein degradation. Although yet unclear, *tldD* was described as a putative regulator of chromosome-encoded TA system activities (Hu et al., 2012). Among the upregulated genes involved in transport, there were genes that encode

TABLE 2 | Genes modulated by MqsR in *X. fastidiosa* under copper stress.

Functional group	Gene name*	Locus Tag**	Protein	Product	LogFC
Peptide metabolic process	Chaperone protein ClpB	XF_RS01600	WP_010892912.1	Chaperone protein ClpB	0.8
	Molecular chaperone GroES	XF_RS02575	WP_004088683.1	Molecular chaperone GroES	1.12
	Molecular chaperone DnaK	XF_RS10150	WP_010894786.1	Molecular chaperone DnaK	1.19
Proteolysis	Protease modulator HflC	XF_RS01875	WP_010892981.1	Protease modulator HflC	−0.946
	ATP-dependent protease	XF_RS05000	WP_010893691.1	ATP-dependent protease	−0.926
	ATP-dependent Clp protease proteolytic subunit	XF_RS05040	WP_010893698.1	ATP-dependent Clp protease proteolytic subunit	−0.197
	Peptidase S14	XF_RS02140	WP_042462775.1	Clp protease ClpP	1.70
Toxins	Hypothetical protein (Colicin V)	XF_RS01135	WP_010892803.1	Hypothetical protein	−1.40
Regulatory functions	Fis family transcriptional regulator	XF_RS13495	WP_010894455.1	Fis family transcriptional regulator	−1.55
	RNA polymerase-binding protein DksA	XF_RS04240	WP_010893509.1	RNA polymerase-binding protein DksA	0.93
	DNA-directed RNA polymerase subunit omega (*rpoZ*)	XF_RS06345	WP_010894003.1	DNA-directed RNA polymerase subunit omega	0.914
	HP	XF_RS07050	WP_042463203.1	HP (Helix-turn-helix XRE-family like proteins)	1.11
Attachment/motility					
Afimbrial adhesins	Surface protein (*hsf*)	XF_RS06465	WP_010894030.1	Surface protein	2.00
	Hemagglutinin (*pspA*)	XF_RS13660	WP_010894644.1	Filamentous hemagglutinin	2.21
Fimbrial adhesin	Fimbrial protein (*pilO*)	XF_RS01560	WP_010892902.1	Fimbrial protein	−1.87
TA systems	Addiction module antitoxin RelB	XF_RS07275	WP_042463224.1	Type II toxin-antitoxin system RelE/ParE family toxin	1.40
	Antitoxin (*mqsA*)	XF_RS10795	WP_010894926.1	Antitoxin	2.39
	HP (*mqsR*)	XF_RS10790	WP_010894925.1	Type II toxin-antitoxin system MqsR family toxin	0.83
Transporters	MFS transporter	XF_RS07585	WP_010894236.1	MFS transporter	1.49
	ion transporter	XF_RS06010	WP_010893927.1	Ion transporter	1.32
Copper homeostasis	Copper homeostasis protein CutC	XF_RS05650	WP_042463096.1	Copper homeostasis protein CutC	2.22

**Nomenclature according to GenBank.*
***Locus Tag corresponds to GenBank accession numbers.*

ion transporters and sulfate transporters belonging to the ABC transporter family. ABC transporters are known to be involved in the influx or efflux of a wide diversity of molecules, and also with antimicrobial peptide resistance (Orelle et al., 2019). The categories associated with translation and peptide metabolic process showed downregulated genes encoding ribosomal subunits and the elongation factors EF-Tu and EF-G. Interestingly EF-Tu is described as the most enriched protein in *X. fastidiosa* outer membrane vesicles (OMVs) important for pathogen systemic dissemination throughout the host xylem vessels (Feitosa-Junior et al., 2019). The category linked to regulatory functions showed various downregulated genes, such as the global regulator *fis*, which is involved in virulence and pathogenicity. The rice pathogen *Dickeya zeae* showed remarkably decreased virulence capacity after *fis* deletion (Lv et al., 2018). This global virulence regulator is involved in exopolysaccharide production, motility, biofilm formation, and cellular aggregation in *Dickeya zeae*. All these processes are of utmost importance for *X. fastidiosa* pathogenicity, being associated with host colonization. The *rpoA* and a DNA-binding regulator hypothetical protein (XF_RS07050) were also repressed in the overexpressing strain under copper treatment.

To identify genes exclusively modulated by MqsR under copper stress, we analyzed the gene ontology of the 111 upregulated genes and 84 downregulated genes presented in **Figures 4**, **5B** (**Supplementary Material 1**, **Data Sets 4, 10, 11**). The exclusively downregulated categories included translation and the peptide metabolic process (**Figure 5B** and **Supplementary Material 1**, **Data Sets 10, 11**). Other categories identified were transport, regulatory functions, and RNA metabolic process. The genes *dksA* and *rpoZ* from the regulatory functions group are transcriptional regulators associated with stress responses (Mathew and Chatterji, 2006; Wang et al., 2018) and were induced under copper stress. The highlighted genes that are modulated by MqsR under copper stress are listed in **Table 2**.

Considering all the above-mentioned results, we built a hypothetical model for the *mqsR* overexpression and its influence on the *X. fastidiosa* regulatory mechanisms under normal and copper-induced stress conditions (**Figure 6**).

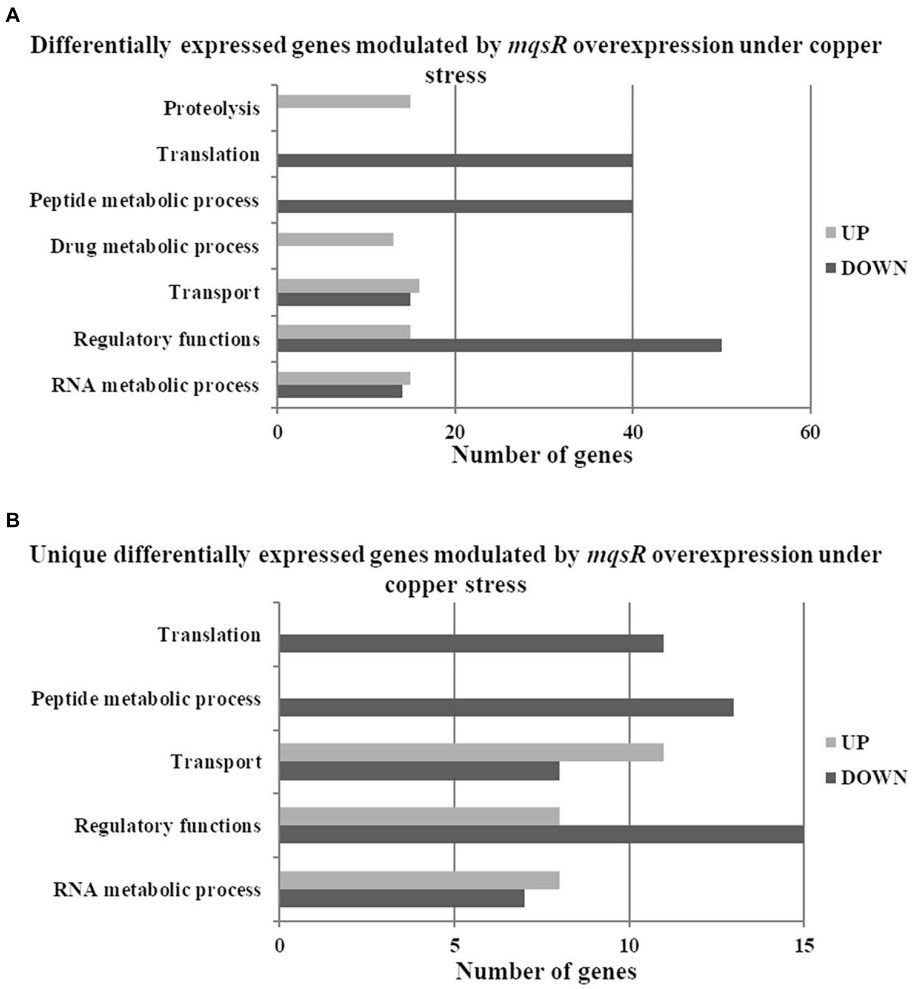

FIGURE 5 | Gene Ontology categorization of differentially expressed genes in *X. fastidiosa* overexpressing *mqsR* in response to copper. **(A)** Genes were classified by functional category of biological processes using Blast2GO. **(B)** Categorization of differentially expressed genes unique to *Xf-mqsR* in response to copper. UP: upregulated genes; DOWN: downregulated genes.

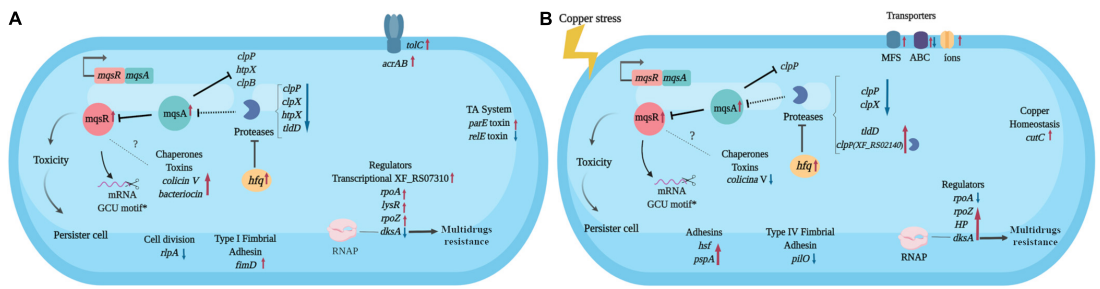

FIGURE 6 | Hypothetical model of the *X. fastidiosa* MqsR-dependent regulon. Response to overexpression of *mqsR* in *X. fastidiosa* **(A)** and under copper stress **(B)**. Arrows pointing to the side (→) indicate direct regulation and up (↑) red arrows indicate upregulation, while ⊥ indicates inhibition and down (↓) blue arrows indicate downregulation. Dashes indicate direct binding and dotted lines indicate hypothetical regulations. *Demonstrated by Lee et al. (2014). The figure was created in BioRender.com.

DISCUSSION

Copper-containing compounds are among the most used chemicals in agriculture (Lamichhane et al., 2018). The antimicrobial effects of copper were previously attributed to stress-induced responses in many bacterial plant pathogens (Wright et al., 2019; Martins et al., 2021), including *X. fastidiosa* (Rodrigues et al., 2008; Muranaka et al., 2012; Merfa et al., 2016; Ge et al., 2021). In this bacterium, the MqsRA TA system was reported to play a key role when the pathogen is under

copper stress. MqsRA is likely to function as an indicator for exogenous stressors through the induction of cell elongation, formation of structured biofilm aggregations, and reduction in cell movement (Merfa et al., 2016). To better understand the roles the toxin MqsR may be playing over stress-induced responses in *X. fastidiosa*, we assessed the major phenotypic outcomes and the global transcriptional profile of the *mqsR*-overexpressing strain under copper-stress conditions through microscopy and RNA-Seq analysis.

The *mqsR* overexpression triggers genetic response where cells activate genes associated to stress adaptation (**Figure 6A**), from which many are conserved in the presence of copper (**Figure 6B**). These characteristics suggest that increasing the amount of MqsR leads to a priming effect of cells to stresses that normally induce expression of *mqsR*, like copper. We observed an approximately 10% increase in cell survival after copper treatment in the population overexpressing *mqsR* and considering that, in stationary phase, only up to ∼1% of cells are persisters (Keren et al., 2004; Lewis, 2007), we can infer that a higher number of persisters were present under this condition. Therefore, our results demonstrate that the presence of the stressor is not needed to induce the genes and consequent cell morphology changes when *mqsR* is overexpressed. These morphologies include the elongated cell formation and population heterogeneity, indicative of persister cell activation (Michiels et al., 2016; Fisher et al., 2017), which is supported by *tolC* induction (**Figure 6A**), that was associated with *E. coli* persistence (Pu et al., 2016). Indeed, the presented results fit perfectly in the mathematical model in which systems that do not present bistability produce the hysteretic switch to the persistent state (Fasani and Savageau, 2013), represented in our condition by the overexpression of *mqsR*.

Besides, the overexpression of *mqsR* in *E. coli* exhibited cellular toxicity, resulting in increased persister cell formation (Kim et al., 2010). Taken together and with previous results (Muranaka et al., 2012; Merfa et al., 2016), the role of mqsR in *X. fastidiosa* seems to be similar to *E. coli* which involves the induction of persister cells.

It has been demonstrated that the MqsRA TA system in *X. fastidiosa* likely autoregulates its own expression to balance the toxin and antitoxin in the most beneficial ratio for the cells to oppose the stress (Merfa et al., 2016). The *mqsR* overexpression itself presents a stress condition to the cell, thus to inactivate the toxin, the antitoxin MqsA should be produced to reach a T:A balance (Brown et al., 2013). Indeed, we observed an induction of *mqsA* under both conditions (**Figures 6A,B**). An upregulation of *hfq* in *Xf-mqsR* was observed in both conditions with and without copper stress. The *hfq* gene encodes an RNA chaperone that, among other regulatory functions, is related to the downregulation of proteases (Kim and Wood, 2010). It suggests that *hfq* is a key gene in the autoregulation of the MqsRA TA system, and we propose it could be one of the factors responsible for keeping the ideal T:A ratio in the cell by controlling the expression of proteases and consequently the cell morphologies observed in this work.

The genes modulated *clpP*, *hfq*, and *clpB* by MqsR in *X. fastidiosa* resemble those modulated by the same regulon in *E. coli* (Kim et al., 2010). These genes are involved in stress responses and contribute to toxicity and, consequently, to persister cell formation in *E. coli* (Kim and Wood, 2010; Kim et al., 2010). Differences in the global transcriptional profile were also observed, suggesting a potential *X. fastidiosa*-exclusive mechanism. Among the exclusive genes modulated by MqsR only in *X. fastidiosa* are two gene regulators (XF_RS07050 and XF_RS07310). The regulator XF_RS07310 has the same type of HTH domain as the MqsA antitoxin, suggesting that it could also bind to promoter regions of target genes and modulate their expression. Some regulators related to bacterial survival and stress responses previously described in several bacteria were also modulated (Maddocks and Oyston, 2008; Santiago et al., 2015; Merfa et al., 2016; Weiss et al., 2017).

The MqsA antitoxin regulates the expression of *mqsRA* and other genes in *E. coli* by binding to palindromic sequences in their promoter regions and repressing their expression (Brown et al., 2009; Wang and Wood, 2011; Soo and Wood, 2013). The MqsA antitoxin encoded by *X. fastidiosa* has the same amino acid residues in its HTH domain responsible for DNA binding (Merfa et al., 2016). Therefore, we searched for the MqsA-like palindromic sequence 5'-AAC (N)7 GTT in the genome of *X. fastidiosa* (**Supplementary Table 3**), seeking to identify those genes that were specifically differentially expressed in our RNA-Seq analyses. We investigated gene regulations in conditions where *mqsRA* expression is increased, such as under copper stress and *mqsR* overexpression. We verified 526 palindromic regions throughout the *X. fastidiosa* genome, with 77 corresponding to intergenic regions (**Supplementary Table 3**). Among the DEGs, a few showed the searched palindromic sequence in their intergenic regions (**Supplementary Table 4**). These genes included *clpP*, *htpX*, *clpB*, and *rpfB*, besides *mqsR* itself. According to data RNA-Seq, *clpP* and *clpB* genes remained downregulated, while *mqsA* expression remained upregulated, suggesting that MqsA may be regulating proteolysis under stress conditions in *mqsR* overexpression.

In our model, copper stress induces responses independent of MqsR involving protein degradation and multidrug resistance. When *mqsR* is overexpressed under copper stress, other *clpP* (XF_RS02140) and *tldD* encoding proteases were induced (**Figure 6B**). Thus, the observed upregulation of proteases could contribute to the consequent upregulation of *mqsRA*. The regulator *dksA*, which plays an important role in the multidrug resistance in *E. coli* (Wang et al., 2018), shifted from downregulation in normal growth conditions to upregulation under copper stress, supporting its role of multidrug resistance. Copper also induces the expression of transporter genes associated with multidrug efflux pumps including *cutC*, which is specific for copper efflux (Rodrigues et al., 2008; Li et al., 2009). It has been shown that multidrug efflux pumps induce persistence, and persister cells combine active efflux with passive numbness to survive antibiotic attacks (Pu et al., 2016). This demonstrates the interplay between resistance and tolerance mechanisms, which are complementary and redundant bacterial strategies to survive under stress conditions (Lewis, 2007).

Overall, with the results herein presented, we were able to expand the knowledge on the genes and mechanisms associated with MqsR, as well as the function of the MqsRA TA system in *X. fastidiosa*. MqsR regulates genes that alter cell behavior in order to prime them to respond to environmental stress, which is related to induction of persistence. The persistence in

plant-pathogenic bacteria is an important tolerance mechanism to this agrochemical which is still neglected in the management of agricultural diseases.

DATA AVAILABILITY STATEMENT

The datasets generated and analyzed for this study can be found under the NCBI Bio-Project ID PRJNA718853. Other data used in this study are available on request from the corresponding author.

AUTHOR CONTRIBUTIONS

AS and MT conceived and designed this research, provided reagents, analytical tools, and revised the manuscript. IC and PM conducted the experiments and analyzed the data. IC, MM, NT-S, MT, and AS wrote the manuscript. IC, MM, PM, MT, and AS contributed to the interpretation of the data and provided intellectual input. All authors read and approved the final manuscript.

FUNDING

This work was supported by a research grant from the Fundação de Amparo à Pesquisa do Estado de São Paulo (FAPESP-2013/10957-0) and also from INCT Citrus (Proc. CNPQ465440/2014-2 and FAPESP 2014/50880-0). IC was an MSc. student from the Graduate Program in Tropical and Subtropical Agriculture (IAC), supported by a fellowship from FAPESP (2016/15741-4) and Coordenação de Aperfeiçoamento de Pessoal de Nível Superior (CAPES, grant 001). NT-S and PM are post-doctoral fellows supported by FAPESP (2019/01447-5 and 2018/18550, respectively). AS and MT are recipients of research fellowships from Conselho Nacional de Desenvolvimento Científico e Tecnológico (CNPq).

ACKNOWLEDGMENTS

We thank the staff of the Life Sciences Core Facility (LaCTAD) from the State University of Campinas (UNICAMP) for the RNA-Seq (Genomics) analysis.

SUPPLEMENTARY MATERIAL

The Supplementary Material for this article can be found online at: https://www.frontiersin.org/articles/10.3389/fmicb.2021.712564/full#supplementary-material

Supplementary Figure 1 | *X. fastidiosa* transformed with the pXF20 empty vector.

Supplementary Figure 2 | Experimental design.

Supplementary Figure 3 | Reads of RNA-Seq.

Supplementary Figure 4 | Validation RNA-Seq data.

Supplementary Table 1 | Bacterial strains and plasmids.

Supplementary Table 2 | Primers used for real-time quantitative PCR.

Supplementary Table 3 | MqsA-like palindromic sequences (5'-AAC (N)7 GTT-3') found in the genome of *X. fastidiosa* 9a5c.

Supplementary Table 4 | Genes with the MqsA-like palindromic sequence identified in the RNA-Seq.

Supplementary Data Set 1 | Differential gene expression analysis between the M-0/C-0.

Supplementary Data Set 2 | Differential gene expression analysis between the M-3/M-0.

Supplementary Data Set 3 | Differential gene expression analysis between the C-3/C-0.

Supplementary Data Set 4 | Differential gene expression analysis between the downregulated and upregulated genes from the C-3/C-0 and M-3/M-0.

Supplementary Data Set 5 | Venn diagram of differentially expressed genes in M-3/M-0 and C-3/C-0.

Supplementary Data Set 6 | Functional characterization of proteins encoded by genes downregulated by MqsR in *X. fastidiosa* from **Figure 3**.

Supplementary Data Set 7 | Functional characterization of proteins encoded by genes upregulated by MqsR in *X. fastidiosa* from **Figure 3**.

Supplementary Data Set 8 | Functional characterization of proteins encoded by genes upregulated by MqsR in *X. fastidiosa* under copper stress from **Figure 5A**.

Supplementary Data Set 9 | Functional characterization of proteins encoded by genes downregulated by MqsR in *X. fastidiosa* under copper stress from **Figure 5A**.

Supplementary Data Set 10 | Functional characterization of proteins encoded by unique genes downregulated by MqsR in *X. fastidiosa* under copper stress from **Figure 5B**.

Supplementary Data Set 11 | Functional characterization of proteins encoded by unique genes upregulated by MqsR in *X. fastidiosa* under copper stress from **Figure 5B**.

REFERENCES

Almeida, R. P. P., De La Fuente, L., Koebnik, R., Lopes, J. R. S., Parnell, S., and Scherm, H. (2019). Addressing the new global threat of *Xylella fastidiosa*. *Phytopathology* 109, 172–174. doi: 10.1094/PHYTO-12-18-0488-FI

Balaban, N. Q., Helaine, S., Lewis, K., Ackermann, M., Aldridge, B., Andersson, D. I., et al. (2019). Definitions and guidelines for research on antibiotic persistence. *Nat. Rev. Microbiol.* 17, 441–448. doi: 10.1038/s41579-019-0196-3

Berezuk, A. M., Glavota, S., Roach, E. J., Goodyear, M. C., Krieger, J. R., and Khursigara, C. M. (2018). Outer membrane lipoprotein RLPA is a novel periplasmic interaction partner of the cell division protein FTSK in *Escherichia coli*. *Sci. Rep.* 81:12933. doi: 10.1038/s41598-018-30979-5

Bolger, A. M., Lohse, M., and Usadel, B. (2014). Trimmomatic: a flexible trimmer for Illumina sequence data. *Bioinformatics* 30, 2114–2120. doi: 10.1093/bioinformatics/btu170

Brown, B. L., Grigoriu, S., Kim, Y., Arruda, J. M., Davenport, A., Wood, T. K., et al. (2009). Three dimensional structure of the MQSR:MqsA complex: a novel TA pair comprised of a toxin homologous to RELE and an antitoxin with unique properties. *PLoS Pathog.* 5:e1000706. doi: 10.1371/journal.ppat.1000706

Brown, B. L., Lord, D. M., Grigorius, S., Peti, W., and Pages, R. (2013). The *Escherichia coli* toxin MqsR destabilizes the transcriptional repression complex formed between the antitoxin MqsA and the mqsRA operon promoter. *J. Biol. Chem.* 288, 1286–1294. doi: 10.1074/jbc.M112.421008

Campanharo, J. C., Lemos, M. V. F., Lemos, E. G., and de, M. (2003). Growth optimization procedures for the phytopathogen *Xylella fastidiosa*. *Curr. Microbiol.* 462, 0099–0102. doi: 10.1007/S00284-002-3829-Z

Coletta-Filho, H., Della, Takita, M. A., De Souza, A. A., Aguilar-Vildoso, C. I., and Machado, M. A. (2001). Differentiation of strains of *Xylella fastidiosa* by a variable number of tandem repeat analysis. *Appl. Environ. Microbiol.* 67, 4091–4095. doi: 10.1128/AEM.67.9.4091-4095.2001

Coletta-Filho, H. D., Castillo, A. I., Laranjeira, F. F., de Andrade, E. C., Silva, N. T., de Souza, A. A., et al. (2020). Citrus variegated chlorosis: an overview of 30 years of research and disease management. *Trop. Plant Pathol.* 45, 175–191. doi: 10.1007/s40858-020-00358-5

Davis, M. J., French, W. J., and Schaad, N. W. (1981). Axenic culture of the bacteria associated with phony disease of peach and plum leaf scald. *Curr. Microbiol.* 6, 309–314. doi: 10.1007/BF01566883

Dobin, A., Davis, C. A., Schlesinger, F., Drenkow, J., Zaleski, C., Jha, S., et al. (2013). STAR: ultrafast universal RNA-seq aligner. *Bioinformatics* 29, 15–21. doi: 10.1093/bioinformatics/bts635

Fasani, R. A., and Savageau, M. A. (2013). Molecular mechanisms of multiple toxin-antitoxin systems are coordinated to govern the persister phenotype. *Proc. Natl. Acad. Sci. U.S.A.* 110, E2528–E2537. doi: 10.1073/PNAS.1301023110

Feitosa-Junior, O. R., Stefanello, E., Zaini, P. A., Nascimento, R., Pierry, P. M., Dandekar, A. M., et al. (2019). Proteomic and metabolomic analyses of *Xylella fastidiosa* OMV-enriched fractions reveal association with virulence factors and signaling molecules of the DSF family. *Phytopathology* 109, 1344–1353. doi: 10.1094/PHYTO-03-19-0083-R

Fiebig, A., Castro Rojas, C. M., Siegal-Gaskins, D., and Crosson, S. (2010). Interaction specificity, toxicity and regulation of a paralogous set of ParE/RelE-family toxin-antitoxin systems. *Mol. Microbiol.* 77, 236–251. doi: 10.1111/j.1365-2958.2010.07207.x

Fisher, R. A., Gollan, B., and Helaine, S. (2017). Persistent bacterial infections and persister cells. *Nat. Rev. Microbiol.* 15, 453–464. doi: 10.1038/nrmicro.2017.42

Ge, Q., Liu, R., Cobine, P. A., Potnis, N., and De La Fuente, L. (2021). Phenotypic and phylogenetic characterization of cu homeostasis among *Xylella fastidiosa* Strains. *Pathogens* 10:495. doi: 10.3390/pathogens10040495

Girelli, C. R., Angilè, F., Coco, L. D., Migoni, D., Zampella, L., Marcelletti, S., et al. (2019). 1H-NMR metabolite fingerprinting analysis reveals a disease biomarker and a field treatment response in xylella fastidiosa subsp. Pauca-infected olive trees. *Plants* 8:115. doi: 10.3390/plants8050115

Götz, S., García-Gómez, J. M., Terol, J., Williams, T. D., Nagaraj, S. H., Nueda, M. J., et al. (2008). High-throughput functional annotation and data mining with the Blast2GO suite. *Nucleic Acids Res.* 36, 3420–3435. doi: 10.1093/nar/gkn176

Harms, A., Brodersen, D. E., Mitarai, N., and Gerdes, K. (2018). Toxins, targets, and triggers: an overview of toxin-antitoxin biology. *Mol. Cell* 70, 768–784. doi: 10.1016/j.molcel.2018.01.003

Hu, Y., Peng, N., Han, W., Mei, Y., Chen, Z., Feng, X., et al. (2012). An archaeal protein evolutionarily conserved in prokaryotes is a zinc-dependent metalloprotease. *Biosci. Rep.* 32, 609–618. doi: 10.1042/BSR20120074

ImageJ. (2018). Available online at: https://imagej.nih.gov/ij/all-notes.html (accessed March 25, 2021).

Jiang, Y., Pogliano, J., Helinski, D. R., and Konieczny, I. (2002). PARE toxin encoded by the broad-host-range plasmid RK2 is an inhibitor of *Escherichia coli* gyrase. *Mol. Microbiol.* 44, 971–979. doi: 10.1046/j.1365-2958.2002.02921.x

Jorgenson, M. A., Chen, Y., Yahashiri, A., Popham, D. L., and Weiss, D. S. (2014). The bacterial septal ring protein RlpA is a lytic transglycosylase that contributes to rod shape and daughter cell separation in *Pseudomonas aeruginosa*. *Mol. Microbiol.* 93, 113–128. doi: 10.1111/mmi.12643

Keren, I., Kaldalu, N., Spoering, A., Wang, Y., and Lewis, K. (2004). Persister cells and tolerance to antimicrobials. *FEMS Microbiol. Lett.* 230, 13–18. doi: 10.1016/S0378-1097(03)00856-5

Khodursky, A. B., Bernstein, J. A., Peter, B. J., Rhodius, V., Wendisch, V. F., and Zimmer, D. P. (2003). "*Escherichia coli* spotted double-strand dna microarrays: rna extraction, labeling, hybridization, quality control, and data management," in *Functional Genomics*, eds M. J. Brownstein and A. Khodursky (New Jersey, NJ: Humana Press), 61–78. doi: 10.1385/1-59259-364-x:61

Kim, J. S., Yamasaki, R., Song, S., Zhang, W., and Wood, T. K. (2018). Single cell observations show persister cells wake based on ribosome content. *Environ. Microbiol.* 20, 2085–2098. doi: 10.1111/1462-2920.14093

Kim, Y., Wang, X., Zhang, X. S., Grigoriu, S., Page, R., Peti, W., et al. (2010). *Escherichia coli* toxin/antitoxin pair MqsR/MqsA regulate toxin CSPD. *Environ. Microbiol.* 12, 1105–1121. doi: 10.1111/j.1462-2920.2009.02147.x

Kim, Y., and Wood, T. K. (2010). Toxins HHA and CSPD and small RNA regulator HFQ are involved in persister cell formation through MQSR in *Escherichia coli*. *Biochem. Biophys. Res. Commun.* 391, 209–213. doi: 10.1016/j.bbrc.2009.11.033

Kozlowska, J., Vermeer, L. S., Rogers, G. B., Rehnnuma, N., Amos, S.-B. T. A., Koller, G., et al. (2014). Combined systems approaches reveal highly plastic responses to antimicrobial peptide challenge in *Escherichia coli*. *PLoS Pathog.* 10:e1004104. doi: 10.1371/journal.ppat.1004104

Kwan, B. W., Valenta, J. A., Benedik, M. J., and Wood, T. K. (2013). Arrested protein synthesis increases persister-like cell formation. *Antimicrob. Agents Chemother.* 57, 1468–1473. doi: 10.1128/AAC.02135-12

Lamichhane, J. R., Osdaghi, E., Behlau, F., Köhl, J., Jones, J. B., and Aubertot, J. N. (2018). Thirteen decades of antimicrobial copper compounds applied in agriculture. *Review. Agron. Sustain. Dev.* 38:28. doi: 10.1007/s13593-018-0503-9

Langevin, A. M., and Dunlop, M. J. (2018). Stress introduction rate alters the benefit of AcrABTolC efflux pumps. *J. Bacteriol.* 200:e00525. doi: 10.1128/JB.00525-17

Lee, M. W., Rogers, E. E., and Stenger, D. C. (2010). Functional characterization of replication and stability factors of an incompatibility group P-1 plasmid from *Xylella fastidiosa*. *Appl. Environ. Microbiol.* 76, 7734–7740. doi: 10.1128/AEM.01921-10

Lee, M. W., Tan, C. C., Rogers, E. E., and Stenger, D. C. (2014). Toxin-antitoxin systems Mqsr/YGIT and DINJ/RELE of *Xylella fastidiosa*. *Physiol. Mol. Plant Pathol.* 87, 59–68. doi: 10.1016/j.pmpp.2014.07.001

Lewis, K. (2007). Persister cells, dormancy and infectious disease. *Nat. Rev. Microbiol.* 5, 48–56. doi: 10.1038/nrmicro1557

Lewis, K. (2010). Persister cells. *Annu. Rev. Microbiol.* 64, 357–372. doi: 10.1146/annurev.micro.112408.134306

Li, Y., Du, J., Zhang, P., and Ding, J. (2009). Crystal structure of human copper homeostasis protein CutC reveals a potential copper-binding site. *J. Struct. Biol.* 169, 399–405. doi: 10.1016/j.jsb.2009.10.012

Liao, Y., Smyth, G. K., and Shi, W. (2019). The R package Rsubread is easier, faster, cheaper and better for alignment and quantification of RNA sequencing reads. *Nucleic Acids Res.* 47:e47. doi: 10.1093/nar/gkz114

Liu, D., Almeida, R., Coletta-Filho, H., and Lopes, J. (2014). "*Xylella fastidiosa*," in *Manual of Security Sensitive Microbes and Toxins*, ed. D. Liu (Boca Raton, FL: CRC Press), 841–850.

Livak, K. J., and Schmittgen, T. D. (2001). Analysis of relative gene expression data using real-time quantitative PCR and the 2-ΔΔCT method. *Methods* 25, 402–408. doi: 10.1006/meth.2001.1262

Lv, M., Chen, Y., Liao, L., Liang, Z., Shi, Z., Tang, Y., et al. (2018). Fis is a global regulator critical for modulation of virulence factor production and pathogenicity of Dickeya zeae. *Sci. Rep.* 8:341. doi: 10.1038/s41598-017-18578-2

Maddocks, S. E., and Oyston, P. C. F. (2008). Structure and function of the LYSR-type transcriptional regulator (LTTR) family proteins. *Microbiology* 154, 3609–3623. doi: 10.1099/mic.0.2008/022772-0

Martins, P. M. M., Merfa, M. V., Takita, M. A., and De Souza, A. A. (2018). Persistence in phytopathogenic bacteria: Do we know enough? *Front. Microbiol.* 9:1099. doi: 10.3389/fmicb.2018.01099

Martins, P. M. M., Wood, T. K., and de Souza, A. A. (2021). Persister cells form in the plant pathogen xanthomonas citri subsp. citri under different stress conditions. *Microorganisms* 9:384. doi: 10.3390/microorganisms9020384

Mathew, R., and Chatterji, D. (2006). The evolving story of the omega subunit of bacterial RNA polymerase. *Trends Microbiol.* 14, 450–455. doi: 10.1016/j.tim.2006.08.002

Meng, Y., Li, Y., Galvani, C. D., Hao, G., Turner, J. N., Burr, T. J., et al. (2005). Upstream migration of *Xylella fastidiosa* via pilus-driven twitching motility. *J. Bacteriol.* 187, 5560–5567. doi: 10.1128/JB.187.16.5560-5567.2005

Merfa, M. V., Niza, B., Takita, M. A., and De Souza, A. A. (2016). The MqsRA toxin-antitoxin system from *Xylella fastidiosa* plays a key role in bacterial fitness, pathogenicity, and persister cell formation. *Front. Microbiol.* 7:904. doi: 10.3389/fmicb.2016.00904

Michiels, J. E., Van den Bergh, B., Verstraeten, N., and Michiels, J. (2016). Molecular mechanisms and clinical implications of bacterial persistence. *Drug Resist. Updat.* 29, 76–89. doi: 10.1016/j.drup.2016.10.002

Mŕazek, J., and Xie, S. (2006). Pattern locator: a new tool for finding local sequence patterns in genomic DNA sequences. *Bioinformatics* 22, 3099–3100. doi: 10.1093/bioinformatics/btl551

Muranaka, L. S., Takita, M. A., Olivato, J. C., Kishi, L. T., and de Souza, A. A. (2012). Global expression profile of biofilm resistance to antimicrobial compounds in the plant-pathogenic bacterium *Xylella fastidiosa* reveals evidence of persister cells. *J. Bacteriol.* 194, 4561–4569. doi: 10.1128/JB.00436-12

Nikaido, H. (2009). Multidrug resistance in bacteria. *Annu. Rev. Biochem.* 78, 119–146. doi: 10.1146/annurev.biochem.78.082907.145923

Niza, B., Merfa, M. V., Alencar, V. C., Menegidio, F. B., Nunes, L. R., Machado, M. A., et al. (2016). Draft genome sequence of 11399, a transformable citrus-pathogenic strain of *Xylella fastidiosa*. *Genome Announc.* 4:e01124. doi: 10.1128/genomeA.01124-16

Oliveros, J. C. (2007). *Venny. An Interactive Tool for Comparing Lists with Venn's Diagrams*. Available online at: https://bioinfogp.cnb.csic.es/tools/venny/ (accessed February 2, 2021).

Orelle, C., Mathieu, K., and Jault, J. M. (2019). Multidrug ABC transporters in bacteria. *Res. Microbiol.* 170, 381–391. doi: 10.1016/j.resmic.2019.06.001

Page, R., and Peti, W. (2016). Toxin-antitoxin systems in bacterial growth arrest and persistence. *Nat. Chem. Biol.* 12, 208–214. doi: 10.1038/nchembio.2044

Pu, Y., Zhao, Z., Li, Y., Zou, J., Ma, Q., Zhao, Y., et al. (2016). Enhanced efflux activity facilitates drug tolerance in dormant bacterial cells. *Mol. Cell* 62, 284–294. doi: 10.1016/j.molcel.2016.03.035

Robinson, M. D., McCarthy, D. J., and Smyth, G. K. (2010). edgeR: a Bioconductor package for differential expression analysis of digital gene expression data. *Bioinformatics* 26, 139–140. doi: 10.1093/bioinformatics/btp616

Rodrigues, C. M., Takita, M. A., Coletta-Filho, H. D., Olivato, J. C., Caserta, R., Machado, M. A., et al. (2008). Copper resistance of biofilm cells of the plant pathogen *Xylella fastidiosa*. *Appl. Microbiol. Biotechnol.* 77, 1145–1157. doi: 10.1007/s00253-007-1232-1

Santiago, A. S., Santos, C. A., Mendes, J. S., Toledo, M. A. S., Beloti, L. L., Souza, A. A., et al. (2015). Characterization of the LysR-type transcriptional regulator YcjZ-like from Xylella fastidiosa overexpressed in *Escherichia coli*. *Protein Expr. Purif.* 113, 72–78. doi: 10.1016/j.pep.2015.05.003

Saponari, M., Giampetruzzi, A., Loconsole, G., Boscia, D., and Saldarelli, P. (2019). *Xylella fastidiosa* in olive in apulia: where we stand. *Phytopathology* 109, 175–186. doi: 10.1094/PHYTO-08-18-0319-FI

Shidore, T., and Triplett, L. R. (2017). Toxin-antitoxin systems: implications for plant disease. *Annu. Rev. Phytopathol.* 55, 161–179. doi: 10.1146/annurev-phyto-080516-035559

Soo, V. W. C., and Wood, T. K. (2013). Antitoxin MqsA represses curli formation through the master biofilm regulator CsgD. *Sci. Rep.* 3:3186. doi: 10.1038/srep03186

Wang, J., Cao, L., Yang, X., Wu, Q., Lu, L., and Wang, Z. (2018). Transcriptional analysis reveals the critical role of RNA polymerase-binding transcription factor, DksA, in regulating multi-drug resistance of *Escherichia coli*. *Int. J. Antimicrob. Agents* 52, 63–69. doi: 10.1016/j.ijantimicag.2018.05.002

Wang, X., Kim, Y., Hong, S. H., Ma, Q., Brown, B. L., Pu, M., et al. (2011). Antitoxin MQSA helps mediate the bacterial general stress response. *Nat. Chem. Biol.* 7, 359–366. doi: 10.1038/nchembio.560

Wang, X., and Wood, T. K. (2011). Toxin-antitoxin systems influence biofilm and persister cell formation and the general stress response. *Appl. Environ. Microbiol.* 77, 5577–5583. doi: 10.1128/AEM.05068-11

Weiss, A., Moore, B. D., Tremblay, M. H. J., Chaput, D., Kremer, A., and Shaw, L. N. (2017). The ω subunit governs RNA polymerase stability and transcriptional specificity in Staphylococcus aureus. *J. Bacteriol.* 199:e00459. doi: 10.1128/JB.00459-16

Wen, Y., Behiels, E., and Devreese, B. (2014). Toxin-antitoxin systems: their role in persistence, biofilm formation, and pathogenicity. *Pathog. Dis.* 70, 240–249. doi: 10.1111/2049-632X.12145

Weston, N., Sharma, P., Ricci, V., and Piddock, L. J. V. (2018). Regulation of the AcrAB-TolC efflux pump in *Enterobacteriaceae*. *Res. Microbiol.* 169, 425–431. doi: 10.1016/j.resmic.2017.10.005

Wingett, S. W., and Andrews, S. (2018). FastQ screen: a tool for multi-genome mapping and quality control. *F1000Res.* 7:1338. doi: 10.12688/f1000research.15931.2

Wood, T. K., Knabel, S. J., and Kwan, B. W. (2013). Bacterial persister cell formation and dormancy. *Appl. Environ. Microbiol.* 79, 7116–7121. doi: 10.1128/AEM.02636-13

Wright, B. W., Kamath, K. S., Krisp, C., and Molloy, M. P. (2019). Proteome profiling of *Pseudomonas aeruginosa* PAO1 identifies novel responders to copper stress. *BMC Microbiol.* 19:69. doi: 10.1186/s12866-019-1441-7

Yamaguchi, Y., Park, J. H., and Inouye, M. (2009). MqsR, a crucial regulator for quorum sensing and biofilm formation, is a GCU-specific mRNA interferase in *Escherichia coli*. *J. Biol. Chem.* 284, 28746–28753. doi: 10.1074/jbc.M109.032904

Yuan, J., Yamaichi, Y., and Waldor, M. K. (2011). The three *Vibrio cholerae* chromosome II-encoded ParE toxins degrade chromosome I following loss of chromosome II. *J. Bacteriol.* 193, 611–619. doi: 10.1128/JB.01185-10

Conflict of Interest: The authors declare that the research was conducted in the absence of any commercial or financial relationships that could be construed as a potential conflict of interest.

Publisher's Note: All claims expressed in this article are solely those of the authors and do not necessarily represent those of their affiliated organizations, or those of the publisher, the editors and the reviewers. Any product that may be evaluated in this article, or claim that may be made by its manufacturer, is not guaranteed or endorsed by the publisher.

frontiers in Microbiology

ORIGINAL RESEARCH
published: 22 December 2021
doi: 10.3389/fmicb.2021.802926

Effect of Temperature and Cell Viability on Uranium Biomineralization by the Uranium Mine Isolate *Penicillium simplicissimum*

Sebastian Schaefer[1]†, Robin Steudtner[1], René Hübner[2], Evelyn Krawczyk-Bärsch[1]* and Mohamed L. Merroun[3]*

[1]Institute of Resource Ecology, Helmholtz-Zentrum Dresden-Rossendorf, Dresden, Germany, [2]Institute of Ion Beam Physics and Materials Research, Helmholtz-Zentrum Dresden-Rossendorf, Dresden, Germany, [3]Department of Microbiology, University of Granada, Granada, Spain

OPEN ACCESS

Edited by:
Raymond J. Turner,
University of Calgary, Canada

Reviewed by:
Erika Kothe,
Friedrich Schiller University Jena, Germany
Errol Duncan Cason,
University of the Free State, South Africa

***Correspondence:**
Evelyn Krawczyk-Bärsch
e.krawczyk-baersch@hzdr.de
Sebastian Schaefer
s.schaefer@unsw.edu.au

†Present address:
Sebastian Schaefer
School of Chemical Engineering, University of New South Wales, Sydney, NSW, Australia

Specialty section:
This article was submitted to Antimicrobials, Resistance and Chemotherapy, a section of the journal Frontiers in Microbiology

Received: 27 October 2021
Accepted: 22 November 2021
Published: 22 December 2021

Citation:
Schaefer S, Steudtner R, Hübner R, Krawczyk-Bärsch E and Merroun ML (2021) Effect of Temperature and Cell Viability on Uranium Biomineralization by the Uranium Mine Isolate Penicillium simplicissimum. Front. Microbiol. 12:802926. doi: 10.3389/fmicb.2021.802926

The remediation of heavy-metal-contaminated sites represents a serious environmental problem worldwide. Currently, cost- and time-intensive chemical treatments are usually performed. Bioremediation by heavy-metal-tolerant microorganisms is considered a more eco-friendly and comparatively cheap alternative. The fungus *Penicillium simplicissimum* KS1, isolated from the flooding water of a former uranium (U) mine in Germany, shows promising U bioremediation potential mainly through biomineralization. The adaption of *P. simplicissimum* KS1 to heavy-metal-contaminated sites is indicated by an increased U removal capacity of up to 550 mg U per g dry biomass, compared to the non-heavy-metal-exposed *P. simplicissimum* reference strain DSM 62867 (200 mg U per g dry biomass). In addition, the effect of temperature and cell viability of *P. simplicissimum* KS1 on U biomineralization was investigated. While viable cells at 30°C removed U mainly extracellularly *via* metabolism-dependent biomineralization, a decrease in temperature to 4°C or use of dead-autoclaved cells at 30°C revealed increased occurrence of passive biosorption and bioaccumulation, as confirmed by scanning transmission electron microscopy. The precipitated U species were assigned to uranyl phosphates with a structure similar to that of autunite, *via* cryo-time-resolved laser fluorescence spectroscopy. The major involvement of phosphates in U precipitation by *P. simplicissimum* KS1 was additionally supported by the observation of increased phosphatase activity for viable cells at 30°C. Furthermore, viable cells actively secreted small molecules, most likely phosphorylated amino acids, which interacted with U in the supernatant and were not detected in experiments with dead-autoclaved cells. Our study provides new insights into the influence of temperature and cell viability on U phosphate biomineralization by fungi, and furthermore highlight the potential use of *P. simplicissimum* KS1 particularly for U bioremediation purposes.

Keywords: biomineralization, bioremediation, fungal biomass, uranium, waste water, *Penicillium simplicissimum*

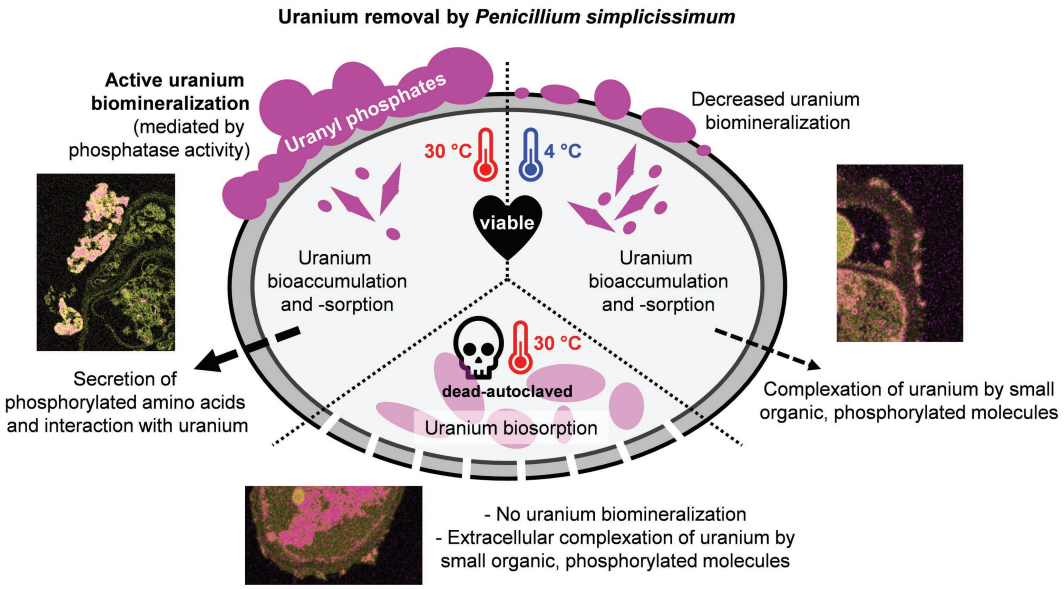

GRAPHICAL ABSTRACT |

INTRODUCTION

As a result of former uranium (U) mining and milling activities, large amounts of wastewater containing high concentrations of U and other heavy metals have been generated, with the potential risk of contaminating the surrounding environment. Once disposed into the environment, U could eventually reach the top of the food chain and be ingested by humans, causing health risks like severe kidney and liver damage (Keith et al., 2013). Therefore, it is necessary not only to clean up contaminated sites, but also to treat U-contaminated wastewater in order to prevent heavy metal release to the environment. The former U mine in Königstein (Germany) represents such a contaminated site. Between 1984 and 1990, the radionuclide U was extracted from the rock material, mainly composed of sandstone, by *in-situ* leaching – i.e., injection of sulfuric acid into the underground rock. The resulting U-bearing, acidic liquid was collected and further processed to finally recover the heavy metal (Zeißler et al., 2006). Since the closure of U mining activities in Germany, the sub-surface of the mine has been remediated by controlled flooding to prevent the contamination of aquifers. At present, the flooding water is still characterized by relatively high concentrations of U (~8–9 mg/L) and a low pH of 2.9 owing to the acidic leaching process (Kassahun et al., 2015). Furthermore, the concentration of heavy metals like cadmium, nickel, and zinc are elevated (Zirnstein, 2015). The water consequently has to be pumped to the surface and is currently treated by a conventional, chemical wastewater treatment plant.

Such chemical treatments are time- and cost-intensive, however (Azubuike et al., 2016; Verma and Kuila, 2019). Depending on the on-site situation, chemistry-based techniques often generate hazardous waste and become less efficient at decreasing pollutant concentrations (Azubuike et al., 2016; Verma and Kuila, 2019). For several years, science has been concerned with alternative bioremediation approaches. Bioremediation aims to use suitable microorganisms to prospectively support or outperform chemical treatment. Microorganisms used in bioremediation should fulfill several criteria including: (i) high tolerance to heavy metals and radionuclides; (ii) metabolic versatility; and (iii) ability to reduce solubility and mobility of the inorganic contaminants. Microbial interaction mechanisms with heavy metals are mainly clustered into passive and active processes, based on their dependence on active cell metabolism. In the passive biosorption process, the cationic heavy metal, for example U(VI), binds to components of the fungal cell wall, e.g., phosphorylated polysaccharides and intracellularly to negatively charged functional groups like phosphate or carbonate groups (Tsezos and Volesky, 1982; González-Muñoz et al., 1997; Lloyd and Macaskie, 2002; Limcharoensuk et al., 2015; Kulkarni et al., 2016; Bano et al., 2018; Lopez-Fernandez et al., 2018; Segretin et al., 2018). Active microbial interaction mechanisms are further subdivided into anaerobic enzymatic reduction, biomineralization, and bioaccumulation. Bioaccumulation describes the active, controlled uptake of heavy metals (e.g., *via* siderophores) and their subsequent intracellular precipitation, which is still under investigation (Limcharoensuk et al., 2015; Gerber et al., 2018; Segretin et al., 2018). Microorganisms can also secrete negatively charged metabolites, such as hydrogen phosphates, hydrogen carbonates, oxalates, or hydroxides. This process is called biomineralization and leads to extracellular precipitation and detoxification (Merroun et al., 2011; Kaewdoung et al., 2016; Chandwadkar et al., 2018).

Besides bacteria, various fungal species have been detected at uranium mining sites and are known for their elevated heavy-metal adaption and tolerance (De Silóniz et al., 2002; Anahid et al., 2011; Zirnstein et al., 2012; Gerber et al., 2018;

Glukhova et al., 2018; Stępniewska et al., 2020; Coelho et al., 2020a). Therefore, they are considered as putative candidates for bioremediation approaches to remove heavy metals from contaminated soil or wastewater (Song et al., 2019; Coelho et al., 2020b). In terms of fungal biomineralization and biosorption of U, phosphates and extracellular phosphatase activity have been reported to be the key players (Liu et al., 2010; Günther et al., 2014; Liang et al., 2015, 2016; Vázquez-Campos et al., 2015; Zheng et al., 2017; Wollenberg et al., 2021). While different physico-chemical parameters like pH or background medium composition have been assessed for their influence on the biomineralization of U, the impact of metabolic activity is not yet fully investigated. In the present study, the fungal strain *Penicillium simplicissimum*, isolated from the flooding water of the former U mine in Königstein (Germany), was investigated toward its potential use for bioremediation purposes, particularly for U-contaminated sites. We focused on changes in the uranium bioremoval by *P. simplicissimum* KS1 depending on temperature and cell viability to unravel metabolic reliance. Additionally, the ability of *P. simplicissimum* KS1 to effectively remove U was compared to the *P. simplicissimum* reference strain DSM 62867 to investigate an adaption to U-contaminated environments.

MATERIALS AND METHODS

Microorganisms and Culture Conditions

The fungus *P. simplicissimum* KS1 was isolated from the flooding water of the former U mine in Königstein (Germany) by culture-dependent methods using Sabouraud-Dextrose (SD, bacto-peptone 5.0 g/L, casein peptone 5.0 g/L, glucose 40.0 g/L, and Carl Roth) medium (Gerber et al., 2015), adapted from Odds (1991). As a comparative fungal species, *P. simplicissimum* DSM 62867 was purchased from DSMZ (Leibniz Institute DSMZ-German Collection of Microorganisms and Cell Cultures). Both strains were grown in SD medium at 30°C and 130 rpm (Thermoshake EA2, C. Gerhardt) for 72 h and stored at 4°C on SD agar plates after growth at 30°C for 72 h.

DNA Isolation and Sanger Sequencing of the Fungal Isolate KS1

The DNA of KS1 was isolated by following the protocol for alkaline DNA extraction (Birnboim and Doly, 1979). A purification and concentration step were performed according to the instructions of the DNA Clean & Concentrator™-5 Kit (Zymo Research). A fungal-characteristic DNA fragment of the internal transcribed spacer (ITS) region of the 18S rRNA gene was amplified by PCR using the primers ITS5 and ITS4 (both Thermo Fisher Scientific), according to Martin and Rygiewicz (2005). The obtained PCR products were purified (DNA Clean & Concentrator™-5 Kit) and sequenced by Sanger sequencing performed by GATC Biotech. The obtained sequences were aligned and compared to those in the nucleotide-nucleotide Basic Local Alignment Search Tool (blastn) database of the National Center for Biotechnology Information (NCBI).[1] The Sanger sequencing results are available on NCBI GenBank® under accession number SAMN22830865.

Fungal U Removal Capacity Studies

To investigate the removal capacity of U, the fungal cells were grown in SD medium for 72 h. Afterwards the cells were separated from the medium and washed twice by sterile filtration and resuspension in sterile-filtered tap water (pH = 5.0). Five milliliters culture were subsequently diluted in 45 ml sterile-filtered tap water (pH = 5.0) to reach a final dry biomass (DBM) of 0.10 ± 0.02 g/L. A uranyl stock solution [$UO_2(NO_3)_2$] was added to a final concentration of 0.1 mM. The samples were incubated for 52 h with agitation at 130 rpm at 4 and 30°C, using pre-tempered chemicals. Sterile-filtered samples, each with a volume of 500 µl, were regularly taken. To each sample, 5 µl of concentrated nitric acid was added immediately. The samples were stored at 4°C and used for determination of the U concentration by means of inductively coupled plasma mass spectrometry (ICP-MS) using a NexION 350X (PerkinElmer). To determine the effect of cell viability on U removal, grown fungal cells in SD medium were autoclaved for 30 min at 121°C. The autoclaved cell culture was centrifuged and washed twice with sterile-filtered tap water (pH = 5.0), then further treated as described above. The DBM was determined after performing the respective experiment. Thereby, cells were separated from the medium by sterile filtration on a pre-dried, weighed filter. The biomass on the filter was subsequently dried overnight at 80°C before final weighing.

Determination of Orthophosphate Concentration and Acid-Phosphatase Activity

In order to determine the orthophosphate concentration and the acid-phosphatase activity involved in fungal U removal, washed fungal cells (DBM 0.10 ± 0.02 g/L) were either suspended in 100 ml SD medium or in 100 ml sterile-filtered tap water (pH = 5.0). The cells in SD medium were incubated for 52 h at 30°C and 130 rpm. The cells in sterile-filtered tap water (pH = 5.0) were further prepared and incubated as described in section "Fungal U Removal Capacity Studies." Samples of each experiment were sterile-filtered after 52 h, and 1 ml of each sample was analyzed for its orthophosphate concentration. To this end, an ion chromatograph system Dionex™ Integrion™ HPIC™ (Thermo Fisher Scientific) was utilized with the following equipment: analytical column (Dionex IonPac, AS23 – 4 µm, RFIC, 2x 250mm), guard column (Dionex IonPac, AG23 – 4 µm, RFIC, 2x 50 mm), and eluent 4.5 mM Na_2CO_3/0.8 mM $NaHCO_3$. Additionally, 1 ml of the samples was analyzed for its acid-phosphatase activity following the instructions of the Acid Phosphatase Activity Fluorometric Assay Kit (Sigma-Aldrich): 200 µl of each sample and control solution were pipetted in a 96-well plate and analyzed for fluorescence using the microplate luminescence reader Mithras 2 (Berthold Technologies), equipped

[1]https://blast.ncbi.nlm.nih.gov/Blast.cgi (Accessed May 18, 2017).

with 355 × 40 excitation and 460 × 25 emission filter, for 30 s with a counting time of 0.1 s and a lamp energy of 40%. All experiments were performed in triplicate.

Scanning Electron Microscopy

For SEM measurements, fungal cells of the two *P. simplicissimum* strains KS1 and DSM 62867 were treated with U for 52 h, as described in section "Fungal U Removal Capacity Studies." The cells were recovered by centrifugation (10 min, 13,793 *g*, 4°C). The supernatant was removed, and the pellet was further processed for SEM at the *Centro de Instrumentación Científica* (University of Granada, Spain), according to Anderson (1951). The specimens were imaged using a S-4800 microscope (Hitachi) operated at an accelerating voltage of 10 kV. For qualitative chemical analysis, energy-dispersive X-ray spectroscopy (EDXS) was carried out at 30 keV using a conventional Si(Li) detector with a S-UTW window. Additional studies were performed using a GEMINI FESEM microscope (Carl Zeiss) operated at an accelerating voltage of 20 kV.

High-Angle Annular Dark-Field Scanning Transmission Electron Microscopy (HAADF-STEM)

For HAADF-STEM measurements, U interaction experiments with *P. simplicissimum* KS1 or DSM 62867 were performed at 30°C and, in the case of *P. simplicissimum* KS1, additionally at 4 and 30°C with autoclaved, non-viable cells (as described in section "Fungal U Removal Capacity Studies"). After 52 h, the cells were immediately centrifuged (10 min, 13,793 *g*, 4°C). The supernatant was removed, the pellet was washed three times with sterile-filtered tap water (pH = 5.0) and subsequently fixed with glutardialdehyde at 1% (v/v) from 50% stock solution (v/v) and stored at 4°C. The *P. simplicissimum* DSM 62867 sample was further processed for STEM analysis at the *Centro de Instrumentación Científica* (University of Granada, Spain), according to Renau Piqueras and Megias Megias (1998). *Penicillium simplicissimum* KS1 samples were further prepared at the Advanced Imaging/Electron Microscopy facility of the Center for Molecular and Cellular Bioengineering (Technische Universität Dresden, Germany). HAADF-STEM imaging and spectrum imaging analysis based on EDXS were performed at 200 kV with a Talos F200X microscope equipped with an X-FEG electron source and a Super-X EDX detector system (FEI). Prior to STEM analysis, the specimen – mounted on a high-visibility low-background holder – was placed for 2 s inside Model 1,020 Plasma Cleaner (E. A. Fischione Instruments Inc.).

Cryo-TRLFS Measurements

For the determination of potential U(VI) species formed by the *P. simplicissimum* strain KS1, time-resolved laser-induced fluorescence spectroscopy (TRLFS) was used. The detection limit for aqueous U is currently 0.2 µg/L (Bernhard and Geipel, 2007). The cryo-TRLFS samples were prepared as described in section "Fungal U Removal Capacity Studies" using a fungal DBM of around 0.25 g/L. Thereby, *P. simplicissimum* KS1 was studied in the presence of 0.1 mM U(VI) at 4 and 30°C. Additionally, autoclaved cells were investigated at 30°C at an initial U(VI) concentration of 0.1 mM. As control samples, *P. simplicissimum* KS1 was prepared without U(VI), and 0.1 mM U(VI) solutions without fungal biomass were measured after an incubation at 30°C. All samples were incubated for 48 h. After the interaction experiments, the cell pellets were separated from the supernatant by centrifugation at 5445 *g* for 20 min. The pellets were washed twice with sterilized tap water (pH 5.0), and both supernatant and fungal biomass were separately shock-frozen in plastic cuvettes by liquid nitrogen and stored at −80°C. The U(VI) luminescence at 153 K was measured after excitation with laser pulses at 266 nm (Minilite high-energy solid-state laser; Continuum) and an average pulse energy of 300 mJ. The emission of the samples was recorded using an iHR550 spectrograph (HORIBA Jobin Yvon) and an ICCD camera (HORIBA Jobin Yvon) in the 425.0–625.0 nm wavelength range by averaging 100 laser pulses and using a gate time of 10 ms. TRLFS spectra were analyzed and deconvoluted by means of parallel factor analysis (PARAFAC) using the N-way toolbox with Matlab R2015a (Andersson and Bro, 2000). PARAFAC is known to be a valuable tool for luminescence data deconvolution, since PARAFAC data processing delivers information about speciation, individual emission spectra, and luminescence decays in both chemical and biological systems (Bader et al., 2016, 2019; Drobot et al., 2016).

RESULTS AND DISCUSSION

Isolation and Physiological Characterization of the Fungal Isolate *Penicillium simplicissimum* KS1

Using culture-dependent methods, *P. simplicissimum* KS1 was previously isolated on SD medium from the flooding water of the former U mine in Königstein (Germany; Gerber et al., 2015). Compared to the other isolated eukaryotic and prokaryotic strains, *P. simplicissimum* KS1 displayed a high U removal capacity (Gerber et al., 2015) and was therefore chosen for further studies. By sequencing the ITS 18S rRNA gene and comparison with blastn (NCBI), *P. simplicissimum* KS1 (accession: SAMN22830865) displayed a maximum phylogenetic identity with *P. simplicissimum* (accession: MH856014.1; 100% query cover; 98.49% identity) and the taxonomical synonymous *Penicillium pulvilorum* (accession: KF624805.1; 100% query cover; 98.35% identity). The microbial diversity in the flooding water is known to be dominated by iron- and sulfur-oxidizing bacteria, as well as iron-reducing bacteria (Zirnstein, 2015; Gerber, 2019). However, archaea and eukaryotes, including fungal species, were detected as well (Zirnstein et al., 2012; Zirnstein, 2015; Gerber, 2019). Previously, our group isolated another heavy metal-tolerant fungal species from the flooding water of Königstein that belongs to the division of Basidiomycota (Gerber et al., 2018) – in contrast to *P. simplicissimum* KS1, which is an ascomycetous fungus.

To further characterize the fungal isolate, suitable carbon sources for the enrichment of the fungus were investigated

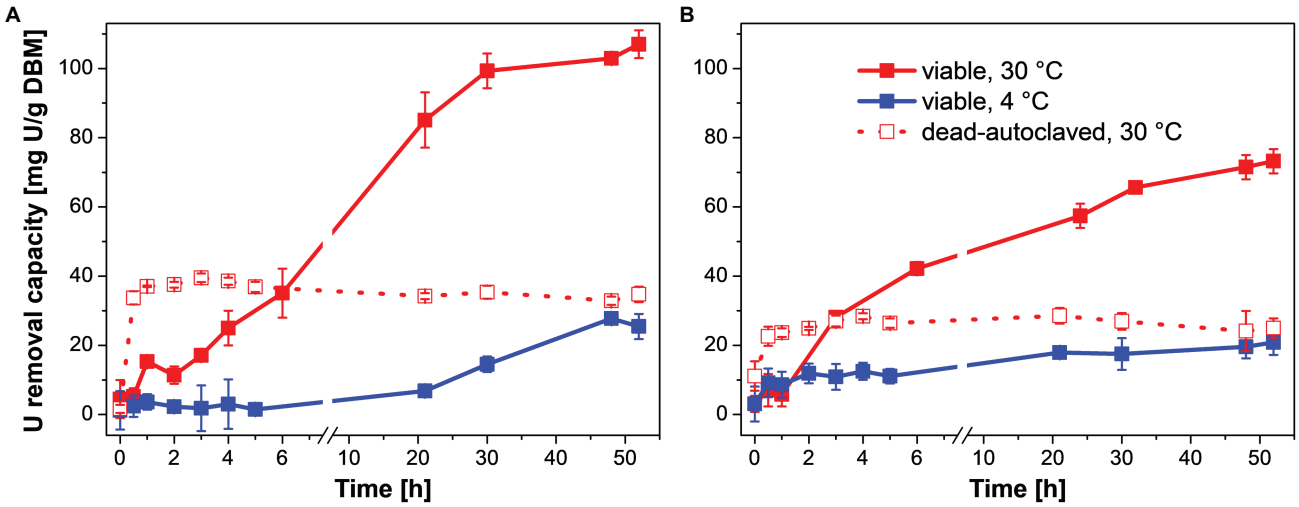

FIGURE 1 | U removal capacity of *Penicillium simplicissimum* KS1 **(A)** and DSM 62867 **(B)** at ~0.1 g DBM/L over 52 h at 4°C (blue) and 30°C (red) and 0.1 mM initial U concentration. At 30°C, viable (straight line) and dead-autoclaved cells (dotted line) were studied. SDs are depicted as error bars.

(**Supplementary Table 1**). *Penicillium simplicissimum* KS1 showed good growth in the presence of glucose and fructose, and medium growth with galactose, mannose, saccharose, and xylose, whereas no growth was observed in ethanol, lactate, oxalic acid, and sodium acetate. The total organic content of the flooding water at the mining site in Königstein is below 1 mg/L (Zirnstein, 2015). It would therefore have to be enriched with carbon sources and the biomass itself for *in-situ* bioremediation. Alternatively, the presence and growth of microorganisms in the flooding water may be obtained through the biodegradation of underground wood constructions, which leads to a decomposition into mono- and polysaccharides (e.g., arabinose, glucose, xylose, and galactose; Baraniak et al., 2002).

In addition, the tolerance of *P. simplicissimum* KS1 toward selected heavy metals in solution was studied to evaluate its suitability for bioremediation applications (**Supplementary Table 2**). The highest tolerance was observed toward chromium (>22 mM) and zinc (>15 mM), whereas nickel and U inhibited the growth of *P. simplicissimum* KS1 at concentrations of 0.2 and 0.7 mM, respectively. The highest toxicity of nickel but lower for zinc is in good agreement with the observations of Anahid et al. (2011). The reported distinctly higher tolerance concentrations by Anahid et al. (2011) might be caused by the utilization of a *P. simplicissimum* strain that could be more tolerant to heavy metals due to (i) a potentially artificially increased heavy-metal adaption of the fungal strain *via* sub-culturing prior to the metal tolerance test or (ii) a naturally stronger adaption to heavy metal – e.g., due to a heavy-metal-exposed place of origin. Also, the heavy-metal tolerance was investigated on solid media in contrast to liquid media which was used in the present work. The fungal yeast *Rhodosporidium toruloides* was also isolated from the flooding water of the former U mine in Königstein and likewise showed elevated heavy-metal tolerance (Gerber et al., 2018). While this fungal strain was more tolerant toward U (up to 6 mM), its tolerance toward chromium, copper, cadmium, and zinc is low compared to *P. simplicissimum* KS1 (Gerber et al., 2018). This finding highlights the suitability of *P. simplicissimum* KS1 for bioremediation purposes involving various heavy metals.

U Bio-Association Studies: Effect of Temperature and Cell Viability

The influence of temperature and cell viability on the U removal capacity of *P. simplicissimum* KS1 and the *P. simplicissimum* reference strain DSM 62867 was investigated (**Figure 1**). *Penicillium simplicissimum* DSM 62867 was selected as a most likely reference strain that is not heavy-metal-adapted; since contrary to *P. simplicissimum* KS1, the strain was isolated from pristine soil samples in Germany. Kinetic U removal studies at different temperatures (4 and 30°C) and cell viability over 52 h suggested a three-phase U removal for both fungal strains (**Figure 1**). The U concentration was set to 0.1 mM, representing the U concentration that could emerge in the mining site resulting from a prospectively envisaged rise of flooding levels. Currently, the U concentration in Königstein (Germany) ranges between ~0.03 and 0.04 mM. Two temperatures were chosen: the optimal growth temperature for fungal species (30°C), plus a lower temperature (4°C), so as to study a possible metabolic influence on U interaction.

First, U may have been removed passively by biosorption of *P. simplicissimum* as indicated by a linear increase in U removal during the first 5 h at 30°C (**Figure 1**, straight red line). This linear increase was followed by a less-steep increase in U removal at 30°C up to 24–30 h of incubation. This second phase was significantly reduced with a temperature decrease to 4°C (**Figure 1**, blue line) demonstrating active metabolic processes additionally involved in passive biosorption during the U removal at 30°C (viable *P. simplicissimum* KS1 30°C: 107 mg U/g DBM, 4°C: 27 mg U/g DBM; viable *P. simplicissimum*

DSM 62867 30°C: 72 mg U/g DBM, 4°C: 20 mg U/g DBM). Furthermore, a decline in apparent cell viability after 24 h at 30°C was observed for *P. simplicissimum* KS1 (**Supplementary Figure 1**), which overlaps with the decrease in slope of U removal capacity, as well as a plateau after around 30 h. This suggests a third process entailing passive U biosorption of dead fungal biomass (Pang et al., 2011). Similar U removal processes were reported for other U-tolerant fungal species, driven by active bioaccumulation and passive biosorption (Gerber et al., 2018; Wollenberg et al., 2021).

To support our hypothesis that active metabolic processes are involved in U removal by *P. simplicissimum* KS1 and DSM 62867, the U removal capacity of dead-autoclaved fungal biomass at 30°C was also studied (**Figure 1**, dotted red lines). Thus, viable cells revealed higher U accumulation values compared to those of dead-autoclaved cells after 2 days (*P. simplicissimum* KS1 viable: 107 mg U/g DBM, dead: 34 mg U/g DBM; *P. simplicissimum* DSM 62867 viable: 72 mg U/g DBM, dead: 24 mg U/g DBM). U removal by dead cells is driven by immediate passive biosorption, as reported for various fungal species (Pang et al., 2011; Gerber et al., 2018; Wollenberg et al., 2021); and it can even surpass the U removal of viable cells *via* sorption to released or exposed compounds upon cell death, like lipopolysaccharides or phosphates, as seen for *Coniochaeta fodinicola* (Vázquez-Campos et al., 2015). Our observation implies a more prominent involvement of active metabolic processes in the U removal of *P. simplicissimum* KS1 – for instance biomineralization and intracellular accumulation – than passive biosorption. For both strains, dead-autoclaved fungal biomass removed more U from the solution when compared to viable cells at 4°C, which may be explained by additional available binding sites, both intra- and extracellularly, due to damaged cell walls.

Moreover, *P. simplicissimum* KS1 removed more U from the solution than *P. simplicissimum* DSM 62867 under similar environmental conditions (**Figure 1**) and *P. simplicissimum* KS1 showed a slower response to the U stress at 4°C. Both these observations support an adaption of the fungal isolate to heavy-metal stress, as compared to the reference strain, which was not exposed to heavy metals before isolation.

Remarkably, *P. simplicissimum* KS1 was able to remove up to 80% of the initially introduced U from solution after 48 h, depending on the fungal biomass concentration (**Supplementary Figure 2**). With an increase in fungal biomass from 0.05 to 0.58 g/L, an exponential decrease in U removal capacity (normalized by the actual biomass) was observed for both *P. simplicissimum* KS1 and DSM 62867. Overall, *P. simplicissimum* DSM 62867 removed less U than *P. simplicissimum* KS1, especially for a biomass of around 0.1 g/L and lower, as can be seen in **Figure 1** for a fixed DBM around 0.1 g/L. The maximum U removal capacity of *P. simplicissimum* KS1 of ~550 mg U/g DBM outperformed not only the reference strain *P. simplicissimum* DSM 62867 (~200 mg U/g DBM), but also other fungal species including *Saccharomyces cerevisiae*, *Rhizopus* sp., and *R. toruloides* (**Supplementary Table 3**), which again proves its great potential for bioremediation purposes. However, a direct comparison of those values is difficult; the experimental conditions vary between different studies and, especially, the physicochemical conditions of the respective experimental setup (pH, temperature, or biomass concentration) are known to tremendously affect the U removal capacity of microorganisms (Bustard et al., 1997; Gerber et al., 2018; Zheng et al., 2018). For this reason, only the maximum U removal capacities, observed respectively, are compared in **Supplementary Table 3**.

HAADF-STEM Characterization of U Biomineralization by *P. simplicissimum* KS1 Cells

HAADF-STEM imaging combined with EDXS-based element distribution analysis was performed to investigate the effect of temperature and cell viability on the cellular localization of U complexes and the underlying interaction mechanisms of U with the fungus *P. simplicissimum* KS1 (**Figure 2**). Metabolically active fungal cells were incubated with 0.1 mM U for 48 h at 4 and 30°C, in addition to dead-autoclaved cells, which were only incubated at 30°C for the same time and at the same U concentration.

Spectrum imaging analysis of the samples showed significant differences in the amount of accumulated U and its cellular localization. For metabolically active and viable cells at 30°C (**Figure 2**, top row), large extracellular U precipitations were detected, in addition to low intracellular amounts of U accumulations. The extracellular U precipitations showed an amorphous nature, and thus differed structurally from the needle-like objects observed intracellularly. Additional SEM studies combined with EDXS analysis (**Supplementary Figures 3**, **4**) confirmed that the removed U is localized extracellularly by *P. simplicissimum* KS1 (and DSM 62867). The structure of the U accumulations evoked a biomineralization-mediated precipitation (Liang et al., 2015).

With a decrease in temperature to 4°C (**Figure 2**, center row), *P. simplicissimum* KS1 appeared to accumulate U at the cell surface and intracellularly. Large extracellular accumulations, as detected at 30°C, were not observed at 4°C. These results indicate that the large extracellular U accumulations were driven by a metabolically active process, i.e., biomineralization. Biomineralization relies on the activity of enzymes, such as phosphatases, to degrade organic phosphates, giving rise to the generation of orthophosphate. Biomineralization is therefore barely observable at lower temperatures and metabolically inactive cells (Liang et al., 2015). Due to cell death after 24 h at 30°C and putative damage to the fungal cell wall, U perhaps entered the cells; this would have been followed by passive biosorption by negatively charged functional groups and might have been bound to the release of cellular compounds, plus cell wall, and membrane fragments (Vázquez-Campos et al., 2015).

Inactivation of *P. simplicissimum* KS1 by autoclavation, with incubation at 30°C (**Figure 2**, bottom row), led to U precipitations that were mainly visible intracellularly, along with minor U biosorption at the cell surface. Considering the control samples of untreated viable and untreated dead-autoclaved cells (**Supplementary Figure 5**), the dead-autoclaved cells showed

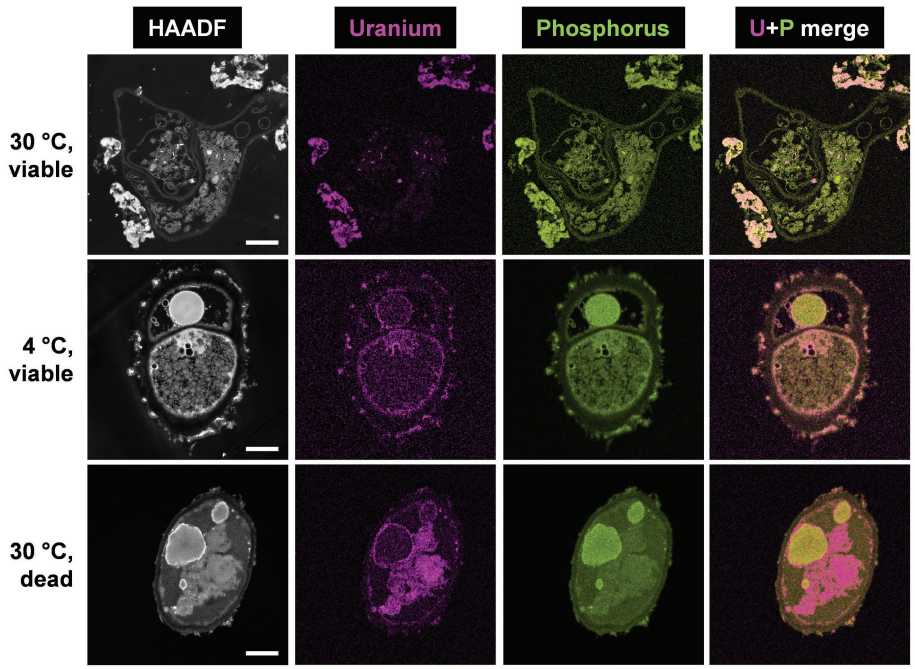

FIGURE 2 | HAADF-STEM micrographs of viable *P. simplicissimum* KS1 at 30 and 4°C (top and center rows) and dead-autoclaved cells at 30°C (bottom row) together with EDXS-based element distributions for uranium (magenta) and phosphorus (green). The fungal isolate was incubated in 0.1 mM U (background electrolyte: sterile-filtered tap water pH 5.0) for 48 h. The scale bars indicate 1 µm.

partial detachments of the cell wall, possibly offering additional binding sites for U and facilitating the influx of the heavy metal and subsequent passive intracellular U biosorption. The use of dead fungal biomass for bioremediation of U-contaminated wastewater is an alternative approach (Vázquez-Campos et al., 2015; Coelho et al., 2020b). Under the experimental conditions chosen by Vázquez-Campos et al. (2015), dead fungal biomass removed more U compared to the viable cells. Yet, other fungal species – *P. simplicissimum* KS1 (**Figure 1**) in the present work, or *R. toruloides* (Gerber et al., 2018) – removed elevated amounts of U by viable cells. Hence, the fungal isolate *P. simplicissimum* KS1 could represent a source for both bioremediation approaches to remove U from wastewater – exploiting viable or dead cells.

EDXS-based element mapping in **Figure 2** revealed U association with phosphorus, which indicates biomineralization and biosorption of U phosphates extra- and intracellularly. The contribution of phosphorus in U bioprecipitation has been previously reported (Liu et al., 2010; Günther et al., 2014; Liang et al., 2015, 2016; Vázquez-Campos et al., 2015; Zheng et al., 2017; Wollenberg et al., 2021). However, phosphorus was not solely detected superimposed upon the U signal (**Supplementary Figure 6**). Other elements, such as nitrogen, could be explained by putative biosorption of U by biopolymers (for example, chitin, cellulose and its derivatives) after damaging the fungal cell wall and passive biosorption of amino functionalities (Galun et al., 1984; Zhao et al., 2016).

For comparison, *P. simplicissimum* DSM 62867 and its interaction with U at 30°C were studied by means of HAADF-STEM and SEM as well (**Supplementary Figures 4**, **7**). Similar to *P. simplicissimum* KS1, SEM revealed extracellular U biomineralization, although spectrum imaging analysis displayed some minor differences. Most notably, the amount of intracellular U accumulation increased significantly. The differences between *P. simplicissimum* KS1 and DSM 62867 indicated an adaptation of *P. simplicissimum* KS1 to U. Uranium is not as prominently present intracellularly in the fungal isolate, which may have adapted its metabolic response to heavy metal environmental stress, as observed previously in increased heavy metal resistance and U removal from solution.

Determination of Extracellular Orthophosphate and Phosphatase Activity of *P. simplicissimum* KS1 in the Presence of U

Based on the microscopic data, phosphates appear to be crucially relevant for the U removal *via* active biomineralization by *P. simplicissimum* KS1. Since this might have been mediated by phosphatase activity, the quantification of orthophosphate concentration and phosphatase activity of *P. simplicissimum* KS1 and DSM 62867 were studied in sterile-filtered tap water with an initial U concentration of 0.1 mM and without U in SD medium (**Figure 3**).

Overall, *P. simplicissimum* KS1 showed a substantially higher phosphatase activity and extracellular orthophosphate concentration than *P. simplicissimum* DSM 62867, independent of the studied media. This pivotal observation is in good agreement with the HAADF-STEM results (**Figure 2**; **Supplementary Figures 6**, **7**). There, *P. simplicissimum* KS1

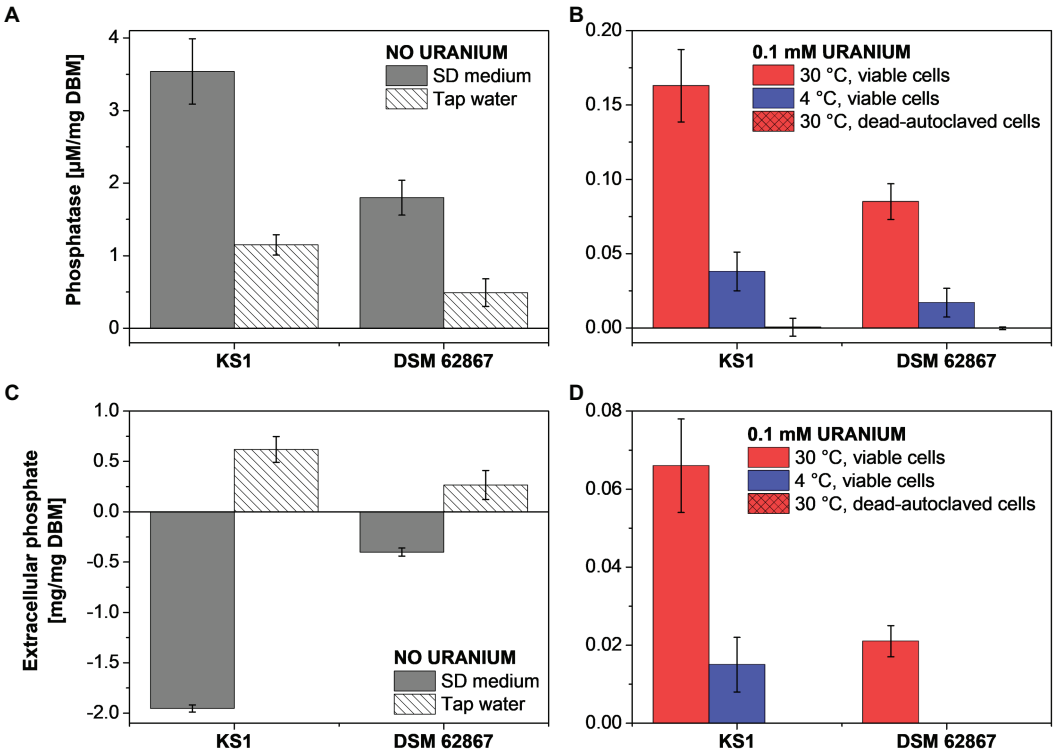

FIGURE 3 | Phosphatase activity **(A,B)** and extracellular phosphate **(C,D)** determination of *P. simplicissimum* KS1 and DSM 62867 after 48 h incubation without U in SD medium or tap water **(A,C)** and with 0.1 mM U in tap water **(B,D)**.

demonstrated a higher extracellular amount of phosphorus, overlapping with the U signal. Furthermore, the phosphatase activity decreased with a decreasing amount of nutrients (i.e., in presence of tap water), decreasing temperature, and dead-autoclaved cells. As shown before, such results point to the major role of active metabolic processes for U removal.

In addition, a temperature decline of samples with dead cells led to a decreasing amount of extracellular phosphate. These results are in line with those obtained by HAADF-STEM (**Figure 2**), where viable *P. simplicissimum* KS1 cells at 30°C showed prominent biomineralization, probably driven by phosphatases, decreasing with temperature declining to 4°C, and not detected with dead-autoclaved cells. The importance of phosphates and phosphatases in the removal of U by bacteria (Beazley et al., 2007; Kulkarni et al., 2016) and the contribution of phosphate transporter genes in U tolerance of *S. cerevisiae* (Sakamoto et al., 2012) have been described in the literature and come to support their observed involvement in U precipitation by *P. simplicissimum* KS1 and DSM 62867.

Identification of Bio-Associated and Extracellular U Species: Cryo-TRLFS Studies

Cryo-TRLFS was used to investigate the effect of temperature and cell viability on the luminescence properties (i.e., emission bands) of the U species associated with or produced by the cells of the fungal isolate *P. simplicissimum* KS1. To this end, the supernatant and fungal biomass were measured separately after the incubation with 0.1 mM U(VI). Together with the kinetic, microscopic, and spectrophotometric experiments, the obtained data would help to identify processes by which the fungal isolate interacts with the radionuclide.

PARAFAC studies based on cryo-TRLFS spectra of the U-treated fungal biomass (0.1 mM U for 48 h and a fungal DBM of ~0.25 g/L) showed two dominant U(VI) species (**Figures 4A,B**). At varying temperature (4 and 30°C) and depending on fungal cell viability (viable or dead-autoclaved), the two species were detected in different proportions (**Figure 4B**). The first species (U species 1, green) dominated all three samples and was characterized by three main emission bands at 497.1, 519.0, and 540.2 nm, as shown in the luminescence spectrum (**Figure 4A**). With 92% (~64 mg U/g DBM) at 30°C and viable cells, this U species was proportionally and quantitatively more prominent as compared to viable cells at 4°C (60%, ~14 mg U/g DBM) and dead-autoclaved cells at 30°C (87%, ~11 mg U/g DBM). Given this observation and the lower fine structure when compared to the second species, proportionally less-present (U species 2, black), it was assumed that the dominating species represented a bio-associated organic U phosphate species that was produced actively and passively by the fungal cells. The second species, having a greater fine structure and shifted emission bands (505.4, 527.6, and 551.6),

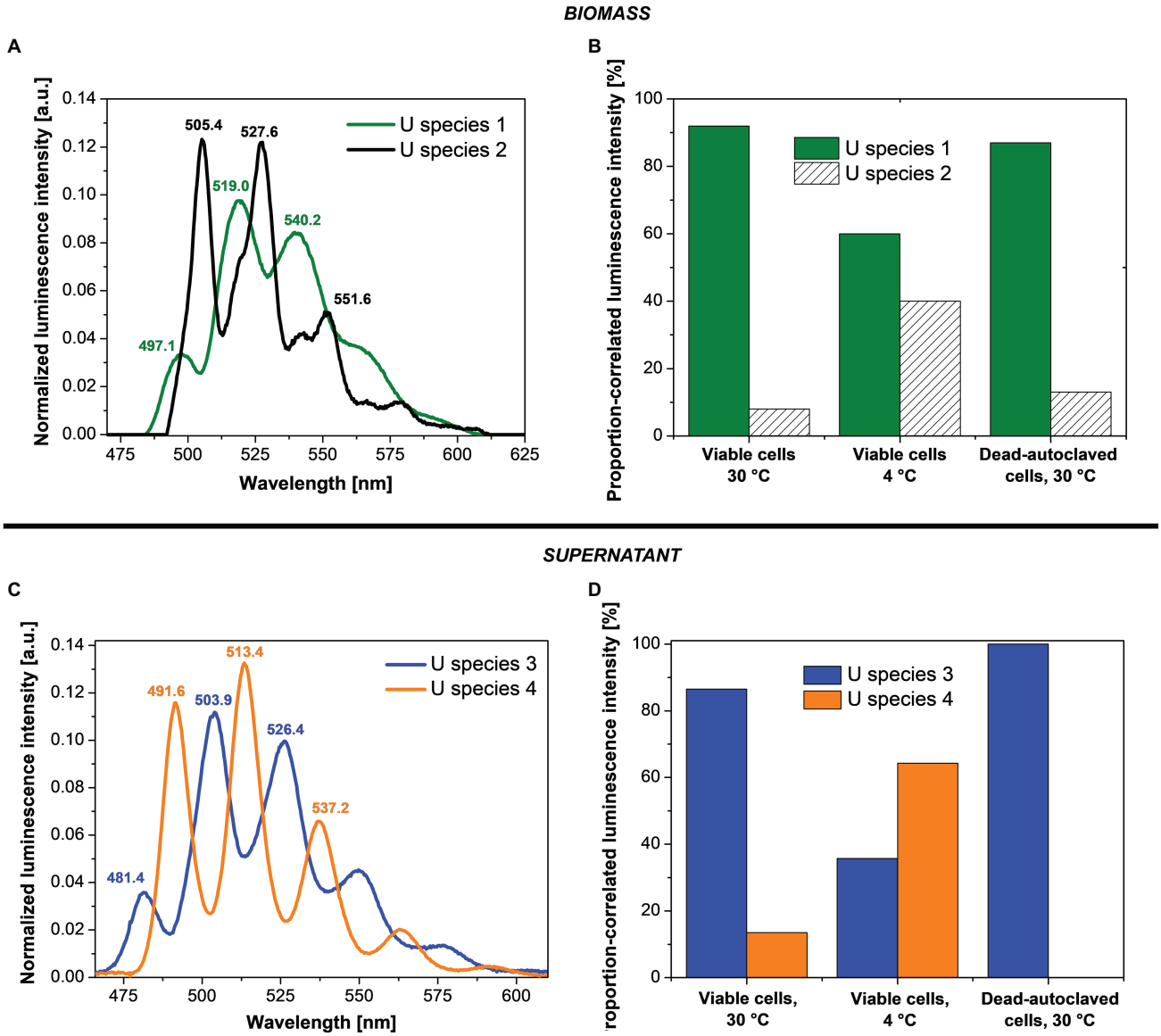

FIGURE 4 | Deconvoluted luminescence spectra **(A,C)** and species distribution **(B,D)** based on the PARAFAC analyses of *P. simplicissimum* KS1 biomass (top) and supernatant (bottom) after 48 h incubation with 0.1 mM U(VI) at pH 5.0.

was assumed to correspond to a more homogenous, inorganic U(VI) phosphate species (Wang et al., 2008), which could be produced actively by fungal phosphatase activity.

In addition to the two bio-associated U(VI) species detected, two further species (named U species 3 and 4) were calculated *via* PARAFAC in the resulting supernatant after the incubation of *P. simplicissimum* KS1 in 0.1 mM U(VI; **Figures 4C,D**). U species 3 (**Figure 4C**, blue) showed emission bands at 481.4, 503.9, and 526.4 nm; U species 4 (**Figure 4C**, orange) at 491.6, 513.4, and 537.2 nm. Both species were more homogenous than the bio-associated species 1. As for the bio-associated species, U species 3 and 4 were detected in different proportions depending on cell viability and temperature (**Figure 4D**). U species 3 was dominant in the supernatant of dead-autoclaved cells (100%) and viable cells at 30°C (87%), but at 4°C, U species 4 (64%) surpassed species 3 (36%). U species 4 was only present to 10% in viable cells at 30°C and not detectable in the supernatant of dead-autoclaved cells at 30°C. Thus, U species 4 was most likely only secreted actively by viable cells, displaying increased proportions at low temperature (4°C). Remarkably, uranyl nitrate, the initially added uranium species, was not observed. This indicates that all the uranium in solution interacted with biological matter.

Identification of the exact uranyl species based on the emission bands of reference compounds is difficult due to varying experimental conditions and thus different complexing agents and resulting spectral shifts. All four species can

TABLE 1 | Luminescence emission bands of the two determined U(VI) species of *Penicillium simplicissimum* KS1 cells exposed to 0.1 mM U(VI) compared to band positions of reference spectra of organic uranyl phosphate species.

	Luminescence emission bands (nm)			References
Bio-associated U(VI) species 1, pH 5.0	497.1	519.0	540.2	This work
UO_2-adenosine monophosphate	497	519	542	Merroun et al., 2003
UO_2-fructose(6)-phosphate	497.1	519.0	543.3	Barkleit et al., 2004
UO_2-PO_3-O-R (Lipopolysaccharides)	498.1	519.6	542.9	Barkleit et al., 2008
Bio-associated U(VI) species 2, pH 5.0	505.4	527.6	540.2	This work
Autunite	504.0	524.2	548.0	Geipel et al., 2000
Supernatant U(VI) species 3, pH 5.0	481.4	503.9	526.4	This work
UO_2-phosphocholine	481.1	497.2	517.6	Koban and Bernhard, 2007
UO_2-phosphoserine	482.0	496.2	516.5	Koban and Bernhard, 2007
UO_2-HP-threonine	483.7	501.8	523.4	Günther et al., 2006
Supernatant U(VI) species 4, pH 5.0	491.6	513.4	537.2	This work
U(VI)-tryptophan	490	510	530	Wollenberg et al., 2021
U(VI)-phosphotyrosine	492	515	539	Wollenberg et al., 2021
U(VI)-phosphothreonine	494	515	537	Wollenberg et al., 2021

Error of emission bands: ±0.5 nm.

be assigned to U(VI) phosphate species of organic or inorganic origin in view of their characteristic spectral shapes. Accordingly, these species in particular could also be actively produced by fungal phosphatase activity. A comparison of the emission bands obtained in the present work with those described in the literature (**Table 1**) shows U species 1 to share characteristic emission bands with organic phosphate ligands, e.g., adenosine-monophosphate, fructose(6)-phosphate, or lipopolysaccharides at the cell wall through biosorption (Merroun et al., 2003; Barkleit et al., 2004, 2008). The bio-associated inorganic uranyl phosphate species (U species 2) showed emission bands similar to those of autunite (Geipel et al., 2000), as previously reported for various fungal species, and could resemble the needle-shaped uranyl phosphate structures in **Figure 2** (Günther et al., 2014; Gerber et al., 2018; Lopez-Fernandez et al., 2018). Furthermore, the supernatant U species 3 and 4 revealed emission bands approximately matching those of other organic ligands – i.e., phospholipids (phosphocholine and phosphoserine) and phosphorylated amino acids (threonine, tyrosine, and tryptophan; Günther et al., 2006; Koban and Bernhard, 2007; Wollenberg et al., 2021). An involvement of organic uranyl species in fungal U removal was described for the acid-tolerant fungus *Coniochaeta fodinicola* (Vázquez-Campos et al., 2015). Contrary to *P. simplicissimum* KS1, the dead-autoclaved *Coniochaeta* biomass removed more U (~45 mg U/g DBM) when compared to viable cells (16 mg U/g DBM; Vázquez-Campos et al., 2015). The authors concluded that phosphates, polysaccharides, and organic acids were released after cell death, hence were not available for U sorption in the case of viable cells (Vázquez-Campos et al., 2015). Recently, Wollenberg et al. (2021) observed *via* TRLFS that phosphorylated amino acids, released by fungal species, interacted with uranium. In the fungus *Schizophyllum commune*, tryptophan and related indole derivatives, related to the emission bands of the only actively secreted U(VI) species 4, could act as messenger molecules in the stress response of *S. commune* (Wollenberg et al., 2021). The suggested scenarios, in combination with active release of organic ligands before cellular death, could explain the higher U removal by viable *P. simplicissimum* KS1 cells than by dead-autoclaved cells (**Figure 1**) and is supported by the superimposed EDXS signals of phosphorus and U (**Figure 2**) and increased extracellular orthophosphate concentration after U exposure (**Figure 3**).

Hypothetical Interaction Mechanism of *P. simplicissimum* KS1 With U(VI)

To sum up, cell viability and temperature critically influence the interaction of the fungus *P. simplicissimum* KS1 with U(VI). Through kinetic experiments (**Figure 1**), EDXS-based spectrum imaging analysis (**Figure 2**), fluorometric and chromatographic analyses of phosphatase and orthophosphate (**Figure 3**), and TRLFS studies (**Figure 4**), these parameters were investigated, their results being summarized in **Supplementary Table 4** and pictured in the **Graphical Abstract**.

By studying the parameters cell viability and temperature, it was concluded that *P. simplicissimum* KS1 removes U(VI) actively from solution at 30°C, mainly *via* extracellular biomineralization, aside from minor biosorption and bioaccumulation. At 4°C with viable cells and after incubation with dead-autoclaved cells at 30°C, less U(VI) was removed (and slower at 4°C), thus indicating a key role of metabolic processes in heavy-metal interaction. The uranium precipitations were mainly identified extracellularly, again decreasing in amount when experimental conditions changed to lower temperatures or dead-autoclaved cells. Therefore, the extracellular U(VI) precipitations were mainly produced actively *via* biomineralization. Phosphatase activity and extracellular orthophosphate concentration were moreover decreased, further supporting the hypothesis of active biomineralization driving U(VI) removal from solution. Ultimately, the U speciation studies revealed organic and inorganic U(VI) phosphates and additional organic ligands (i.e., phosphorylated amino acids), which could act as actively secreted messenger molecules.

CONCLUSION

The results presented here highlight the potential of the heavy metal-adapted fungal isolate *P. simplicissimum* KS1 for bioremediation of U- and other heavy-metal-contaminated sites. The elevated U removal capacity of the fungal isolate

is compared to that of the non-U-adapted reference strain *P. simplicissimum* DSM 62867. Although, intra- and extracellular U accumulations are observable for both strains, the extracellular U precipitations are greater for *P. simplicissimum* KS1. Electron microscopy, TRLFS and ICP-MS studies revealed a temperature- and cell viability-dependent U biomineralization, thus indicating its dependency on active cell metabolism. Compared to viable *P. simplicissimum* KS1 cells at 30°C, a decrease in temperature to 4°C or the incubation with dead-autoclaved cells at 30°C decreased extracellular biomineralization, which was replaced by passive biosorption and bioaccumulation. Bio-associated U species were mainly assigned to uranyl phosphates by EDXS and TRLFS. Additionally, the fungus secreted small phosphorylated amino acids, driven by temperature and cell viability, that interacted with U and could act as messenger molecules. Our outcomes demonstrate not only the efficient removal of U from solutions by *P. simplicissimum* KS1, hence its potential for the bioremediation of U-contaminated sites, but also the key role of temperature and cell viability in terms of metabolic influence on the interaction of the fungus with U.

For the bioremediation of U-contaminated waters, as in the former U mine in Königstein (Germany), *P. simplicissimum* KS1 might be a candidate to support cost- and time-intensive chemical treatment. Since this fungal strain is present in the flooding water already, sub-surface systems enriching the fungus by the addition of an environmental-friendly carbon source (e.g., glucose or fructose) are imaginable, as well as aboveground systems exploiting the available pumps and engines.

Prospectively, further experiments are needed to evaluate the U removal capacity of the fungal isolate for *in-situ* bioremediation on the industrial scale. In addition, U recovery experiments should be performed.

DATA AVAILABILITY STATEMENT

The original contributions presented in the study are included in the article/**Supplementary Material**; further inquiries can be directed to the corresponding authors.

AUTHOR CONTRIBUTIONS

SS carried out the experiments, wrote the original draft of the manuscript with support from RS, RH, EK-B, MM, and edited it after the internal revisions. RS introduced SS into cryo-TRLFS measurements and performed the computational analysis *via* PARAFAC. RH conducted the electron microscopy experiments and provided critical feedback to the project. EK-B and MM supervised the project, helped in interpreting the results, and reviewed the manuscript. All authors contributed to the article and approved the submitted version.

FUNDING

This work was supported by the Bundesministerium für Bildung und Forschung (BMBF) grant no. 02NUK030 F (TransAqua). Funding of TEM TALOS at the HZDR Ion Beam Center TEM facilities by the German Federal Ministry of Education and Research (BMBF grant no. 03SF0451) in the framework of HEMCP is acknowledged. The open-access publication fees were kindly covered by the library of the Helmholtz-Zentrum Dresden-Rossendorf (Germany). SS was partially supported during his research stay in Granada (Spain) by the Talent Acquisition Program ("Programa de Captación de Talento en Grados Universitarios"), funded by the University of Granada (Spain).

ACKNOWLEDGMENTS

SS acknowledges the *Centro de Instrumentacion Cientifica* within the University of Granada (Spain) for SEM and TEM measurements and sample preparation. The authors are grateful to A. Chlupka, C. Eckardt, S. Gurlit, S. Gürtler, and S. Schubert (Helmholtz-Zentrum Dresden-Rossendorf, Germany) for ICP-MS measurements and acknowledge the use of the HZDR Ion Beam Center TEM facilities (Germany). The authors thank the Wismut GmbH (Germany) for allowing access to the sampling site and supporting water sampling. The authors would like to acknowledge Jean Louise Sanders for language editing of the original and revised versions of the article. We are also grateful to the guest editor and the two reviewers for their insightful comments on the manuscript which improved our work significantly.

SUPPLEMENTARY MATERIAL

The Supplementary Material for this article can be found online at: https://www.frontiersin.org/articles/10.3389/fmicb.2021.802926/full#supplementary-material

REFERENCES

Anahid, S., Yaghmaei, S., and Ghobadinejad, Z. (2011). Heavy metal tolerance of fungi. *Sci. Iran.* 18, 502–508. doi: 10.1016/j.scient.2011.05.015

Anderson, T. F. (1951). Techniques for the preservation of three-dimensional structure in preparing specimens for the electron microscope. *Trans. N. Y. Acad. Sci.* 13, 130–134. doi: 10.1111/j.2164-0947.1951.tb01007.x

Andersson, C., and Bro, R. (2000). The N-way toolbox for Matlab. *Chemom. Intell. Lab. Syst.* 52, 1–4. doi: 10.1016/S0169-7439(00)00071-X

Azubuike, C. C., Chikere, C. B., and Okpokwasili, G. C. (2016). Bioremediation techniques–classification based on site of application: principles, advantages, limitations and prospects. *World J. Microbiol. Biotechnol.* 32, 180. doi: 10.1007/s11274-016-2137-x

Bader, M., Moll, H., Steudtner, R., Lösch, H., Drobot, B., Stumpf, T., et al. (2019). Association of Eu(III) and cm(III) onto an extremely halophilic archaeon. *Environ. Sci. Pollut. Res.* 26, 9352–9364. doi: 10.1007/s11356-019-04165-7

Bader, M., Müller, K., Foerstendorf, H., Drobot, B., Schmidt, M., Musat, N., et al. (2016). Multistage bioassociation of uranium onto an extremely

halophilic archaeon revealed by a unique combination of spectroscopic and microscopic techniques. *J. Hazard. Mater.* 327, 225–232. doi: 10.1016/j.jhazmat.2016.12.053

Bano, A., Hussain, J., Akbar, A., Mahmood, K., Anwar, M., Hasni, M., et al. (2018). Biosorption of heavy metals by obligate halophilic fungi. *Chemosphere* 199, 218–222. doi: 10.1016/j.chemosphere.2018.02.043

Baraniak, L., Bernhard, G., and Nitsche, H. (2002). Influence of hydrothermal wood degradation products on the uranium adsorption onto metamorphic rocks and sediments. *J. Radioanal. Nucl. Chem.* 253, 185–190. doi: 10.1023/A:1019657503952

Barkleit, A., Geipel, G., Roßberg, A., and Bernhard, G. (2004). Uranium(VI) complexes with sugar phosphates in aqueous solution. *Radiochim. Acta* 92, 903–908. doi: 10.1524/ract.92.12.903.55114

Barkleit, A., Moll, H., and Bernhard, G. (2008). Interaction of uranium(VI) with lipopolysaccharide. *Dalton Trans.* 21, 2879–2886. doi: 10.1039/b715669c

Beazley, M. J., Martinez, R. J., Sobecky, P. A., Webb, S. M., and Taillefert, M. (2007). Uranium biomineralization as a result of bacterial phosphatase activity: insights from bacterial isolates from a contaminated subsurface. *Environ. Sci. Technol.* 41, 5701–5707. doi: 10.1021/es070567g

Bernhard, G., and Geipel, G. (2007). Bestimmung der Bindungsform des Urans in Mineralwässern. *Vom Wasser* 105, 7–10.

Birnboim, H. C., and Doly, J. (1979). A rapid alkaline extraction procedure for screening recombinant plasmid DNA. *Nucleic Acids Res.* 7, 1513–1523. doi: 10.1093/nar/7.6.1513

Bustard, M., Higgins, D., McHardy, F., McKerr, G., and MChale, A. P. (1997). "Characterization of uranium binding to residual biomass in distillery spent wash," in *Studies in Environmental Science*. ed. D. L. Wise (Boston MA, USA: Elsevier), 531–545.

Chandwadkar, P., Misra, H. S., and Acharya, C. (2018). Uranium biomineralization induced by a metal tolerant *Serratia* strain under acid, alkaline and irradiated conditions. *Metallomics* 10, 1078–1088. doi: 10.1039/C8MT00061A

Coelho, E., Reis, T. A., Cotrim, M., Mullan, T. K., and Corrêa, B. (2020a). Resistant fungi isolated from contaminated uranium mine in Brazil shows a high capacity to uptake uranium from water. *Chemosphere* 248:126068. doi: 10.1016/j.chemosphere.2020.126068

Coelho, E., Reis, T. A., Cotrim, M., Rizzutto, M., and Corrêa, B. (2020b). Bioremediation of water contaminated with uranium using *Penicillium piscarium*. *Biotechnol. Prog.* 36:e30322. doi: 10.1002/btpr.3032

De Silóniz, M.-I., Payo, E.-M., Callejo, M.-A., Marquina, D., and Peinado, J. M. (2002). Environmental adaptation factors of two yeasts isolated from the leachate of a uranium mineral heap. *FEMS Microbiol. Lett.* 210, 233–237. doi: 10.1016/S0378-1097(02)00607-9

Drobot, B., Bauer, A., Steudtner, R., Tsushima, S., Bok, F., Patzschke, M., et al. (2016). Speciation studies of metals in trace concentrations: the mononuclear uranyl(VI) hydroxo complexes. *Anal. Chem.* 88, 3548–3555. doi: 10.1021/acs.analchem.5b03958

Galun, M., Keller, P., Malki, D., Feldstein, H., Galun, E., Siegel, S., et al. (1984). Removal of uranium (VI) from solution by fungal biomass: inhibition by iron. *Water Air Soil Pollut.* 21, 411–414. doi: 10.1007/BF00163640

Geipel, G., Bernhard, G., Rutsch, M., Brendler, V., and Nitsche, H. (2000). Spectroscopic properties of uranium(VI) minerals studied by time-resolved laser-induced fluorescence spectroscopy (TRLFS). *Radiochim. Acta* 88, 757–762. doi: 10.1524/ract.2000.88.9-11.757

Gerber, U. (2019). Investigations on indigenous microorganisms isolated from a former uranium mine and their interaction mechanisms with uranium: a possible bioremediation study. [dissertation]. Germany: Helmholz-Zentrum Dresden-Rossendorf, Germany: Friedrich-Schiller-Universität Jena.

Gerber, U., Hübner, R., Rossberg, A., Krawczyk-Bärsch, E., and Merroun, M. L. (2018). Metabolism-dependent bioaccumulation of uranium by *Rhodosporidium toruloides* isolated from the flooding water of a former uranium mine. *PLoS One* 13:e0201903. doi: 10.1371/journal.pone.0201903

Gerber, U., Krawczyk-Bärsch, E., and Arnold, T. (2015). "Isolated microorganisms from the flooding water of a former uranium mine in Königstein (Saxony, Germany) and their interactions with uranium." *Annual Reports 2014 - Institute of Resource Ecology*.

Glukhova, L. B., Frank, Y. A., Danilova, E. V., Avakyan, M. R., Banks, D., Tuovinen, O. H., et al. (2018). Isolation, characterization, and metal response of novel, acid-tolerant *Penicillium* spp. from extremely metal-rich waters at a mining site in Transbaikal (Siberia, Russia). *Microb. Ecol.* 76, 911–924. doi: 10.1007/s00248-018-1186-0

González-Muñoz, M. T., Merroun, M. L., Ben Omar, N., and Arias, J. M. (1997). Biosorption of uranium by *Myxococcus xanthus*. *Int. Biodeterior. Biodegradation* 40, 107–114. doi: 10.1016/S0964-8305(97)00041-3

Günther, A., Geipel, G., and Bernhard, G. (2006). Complex formation of U(VI) with the amino acid L-threonine and the corresponding phosphate ester O-phospho-L-threonine. *Radiochim. Acta* 94, 845–851. doi: 10.1524/ract.2006.94.12.845

Günther, A., Raff, J., Merroun, M. L., Rossberg, A., Kothe, E., and Bernhard, G. (2014). Interaction of U(VI) with *Schizophyllum commune* studied by microscopic and spectroscopic methods. *Biometals* 27, 775–785. doi: 10.1007/s10534-014-9772-1

Kaewdoung, B., Sutjaritvorakul, T., Gadd, G. M., Whalley, A. J. S., and Sihanonth, P. (2016). Heavy metal tolerance and biotransformation of toxic metal compounds by new isolates of wood-rotting fungi from Thailand. *Geomicrobiol J.* 33, 283–288. doi: 10.1080/01490451.2015.1048394

Kassahun, A., Jenk, U., and Paul, M. (2015). "Investigation of microbial *in-situ* remediation of uranium mine site pollutants in the flooded mine Königstein." in *Agreeing on Solutions for more Sustainable Mine Water Management – Proceedings of the 10th ICARD & IMWA Annual Conference*; April 21-24, 2015.

Keith, S., Faroon, O., Roney, N., Scinicariello, F., Wilbur, S., Ingerman, L., et al. (2013). "*Toxicological Profile for Uranium*." Atlanta (GA): Agency for Toxic Substances and Disease Registry (US), 20, 1005–1006.

Koban, A., and Bernhard, G. (2007). Uranium(VI) complexes with phospholipid model compounds: a laser spectroscopic study. *J. Inorg. Biochem.* 101, 750–757. doi: 10.1016/j.jinorgbio.2007.01.001

Kulkarni, S., Misra, C. S., Gupta, A., Ballal, A., and Apte, S. K. (2016). Interaction of uranium with bacterial cell surfaces: inferences from phosphatase-mediated uranium precipitation. *Appl. Environ. Microbiol.* 82, 4965–4974. doi: 10.1128/AEM.00728-16

Liang, X., Csetenyi, L., and Gadd, G. M. (2016). Uranium bioprecipitation mediated by yeasts utilizing organic phosphorus substrates. *Appl. Microbiol. Biotechnol.* 100, 5141–5151. doi: 10.1007/s00253-016-7327-9

Liang, X., Hillier, S., Pendlowski, H., Gray, N., Ceci, A., and Gadd, G. M. (2015). Uranium phosphate biomineralization by fungi. *Environ. Microbiol.* 17, 2064–2075. doi: 10.1111/1462-2920.12771

Limcharoensuk, T., Sooksawat, N., Sumarnrote, A., Awutpet, T., Kruatrachue, M., Pokethitiyook, P., et al. (2015). Bioaccumulation and biosorption of Cd(2+) and Zn(2+) by bacteria isolated from a zinc mine in Thailand. *Ecotoxicol. Environ. Saf.* 122, 322–330. doi: 10.1016/j.ecoenv.2015.08.013

Liu, M., Dong, F., Yan, X., Zeng, W., Hou, L., and Pang, X. (2010). Biosorption of uranium by *Saccharomyces cerevisiae* and surface interactions under culture conditions. *Bioresour. Technol.* 101, 8573–8580. doi: 10.1016/j.biortech.2010.06.063

Lloyd, J., and Macaskie, L. (2002). "Chapter 11 Biochemical basis of microbe-radionuclide interactions," in *Radioactivity in the Environment. Vol. 2.* eds. M. J. Keith-Roach and F. R. Livens (Amsterdam, Netherlands: Elsevier), 313–342.

Lopez-Fernandez, M., Romero-González, M., Günther, A., Solari, P. L., and Merroun, M. L. (2018). Effect of U(VI) aqueous speciation on the binding of uranium by the cell surface of *Rhodotorula mucilaginosa*, a natural yeast isolate from bentonites. *Chemosphere* 199, 351–360. doi: 10.1016/j.chemosphere.2018.02.055

Martin, K. J., and Rygiewicz, P. T. (2005). Fungal-specific PCR primers developed for analysis of the ITS region of environmental DNA extracts. *BMC Microbiol.* 5:28. doi: 10.1186/1471-2180-5-28

Merroun, M. L., Geipel, G., Nicolai, R., Heise, K.-H., and Selenska-Pobell, S. (2003). Complexation of uranium (VI) by three eco-types of *Acidithiobacillus ferrooxidans* studied using time-resolved laser-induced fluorescence spectroscopy and infrared spectroscopy. *Biometals* 16, 331–339. doi: 10.1023/A:1020612600726

Merroun, M. L., Nedelkova, M., Ojeda, J., Reitz, T., Lopez-Fernandez, M., Arias, J., et al. (2011). Bio-precipitation of uranium by two bacterial isolates recovered from extreme environments as estimated by potentiometric titration, TEM and X-ray absorption spectroscopic analyses. *J. Hazard. Mater.* 197, 1–10. doi: 10.1016/j.jhazmat.2011.09.049

Odds, F. C. (1991). Sabouraud('s) agar. *J. Med. Vet. Mycol.* 29, 355–359. doi: 10.1080/02681219180000581

Pang, C., Liu, Y.-H., Cao, X.-H., Li, M., Huang, G.-L., Hua, R., et al. (2011). Biosorption of uranium(VI) from aqueous solution by dead fungal biomass of *Penicillium citrinum*. *Chem. Eng. J.* 170, 1–6. doi: 10.1016/j.cej.2010.10.068

Renau Piqueras, J., and Megias Megias, L. (1998). *Manual de técnicas de microscopia electrónica (M.E.T.): Aplicaciones biológicas (Fuera de Colección)*. Granada, Spain: Editorial Universidad de Granada.

Sakamoto, F., Nankawa, T., Ohnuki, T., Fujii, T., and Iefuji, H. (2012). Yeast genes involved in uranium tolerance and uranium accumulation: a functional screening using the nonessential gene deletion collection. *Geomicrobiol. J.* 29, 470–476. doi: 10.1080/01490451.2011.581330

Segretin, A., Cazón, J., and Donati, E. (2018). "Bioaccumulation and biosorption of heavy metals: microorganisms and bioremediation," in *Heavy Metals in the Environment*. ed. E. R. Donati (Boca Raton FL, USA: CRC Press), 93–113.

Song, W., Wang, X., Sun, Y., Hayat, T., and Wang, X. (2019). Bioaccumulation and transformation of U(VI) by sporangiospores of *Mucor circinelloides*. *Chem. Eng. J.* 362, 81–88. doi: 10.1016/j.cej.2019.01.020

Stępniewska, H., Uzarowicz, Ł., Błońska, E., Kwasowski, W., Słodczyk, Z., Gałka, D., et al. (2020). Fungal abundance and diversity as influenced by properties of technosols developed from mine wastes containing iron sulphides: a case study from abandoned iron sulphide and uranium mine in Rudki, south-Central Poland. *Appl. Soil Ecol.* 145:103349. doi: 10.1016/j.apsoil.2019.08.011

Tsezos, M., and Volesky, B. (1982). The mechanism of uranium biosorption by *Rhizopus arrhizus*. *Biotechnol. Bioeng.* 24, 385–401. doi: 10.1002/bit.260240211

Vázquez-Campos, X., Kinsela, A. S., Collins, R. N., Neilan, B. A., Aoyagi, N., and Waite, T. D. (2015). Uranium binding mechanisms of the acid-tolerant fungus *Coniochaeta fodinicola*. *Environ. Sci. Technol.* 49, 8487–8496. doi: 10.1021/acs.est.5b01342

Verma, S., and Kuila, A. (2019). Bioremediation of heavy metals by microbial process. *Environ. Sci. Technol.* 14:100369. doi: 10.1016/j.eti.2019.100369

Wang, Z., Zachara, J., Liu, C., Gassman, P., Felmy, A., and Clark, S. (2008). A cryogenic fluorescence spectroscopic study of uranyl carbonate, phosphate and oxyhydroxide minerals. *Radiochim. Acta* 96, 591–598. doi: 10.1524/ract.2008.1541

Wollenberg, A., Kretzschmar, J., Drobot, B., Hübner, R., Freitag, L., Lehmann, F., et al. (2021). Uranium(VI) bioassociation by different fungi: a comparative study into molecular processes. *J. Hazard. Mater.* 411:125068. doi: 10.1016/j.jhazmat.2021.125068

Zeißler, K.-O., Nindel, K., and Hertwig, T. (2006). "Hydrochemical aspects of the flooding of the mine Königstein: a water mixing model for recognizing the influence of groundwater by contaminated water," in *Uranium in the Environment*. eds. B. J. Merkel and A. Hasche-Berger (Berlin Heidelberg, Germany: Springer), 713–719.

Zhao, C., Liu, J., Tu, H., Li, F., Li, X., Yang, J., et al. (2016). Characteristics of uranium biosorption from aqueous solutions on fungus *Pleurotus ostreatus*. *Environ. Sci. Pollut. Res.* 23, 24846–24856. doi: 10.1007/s11356-016-7722-x

Zheng, X. Y., Shen, Y. H., Wang, X. Y., and Wang, T. S. (2018). Effect of pH on uranium(VI) biosorption and biomineralization by *Saccharomyces cerevisiae*. *Chemosphere* 203, 109–116. doi: 10.1016/j.chemosphere.2018.03.165

Zheng, X.-Y., Wang, X.-Y., Shen, Y.-H., Lu, X., and Wang, T.-S. (2017). Biosorption and biomineralization of uranium(VI) by *Saccharomyces cerevisiae*: crystal formation of chernikovite. *Chemosphere* 175, 161–169. doi: 10.1016/j.chemosphere.2017.02.035

Zirnstein, I. (2015). Charakterisierung der Mikroorganismen im sauren Grubenwasser des ehemaligen Uranbergwerks Königstein. [dissertation]. Germany: Helmholz-Zentrum Dresden-Rossendorf, Germany: Technische Universität Dresden.

Zirnstein, I., Arnold, T., Krawczyk-Bärsch, E., Jenk, U., Bernhard, G., and Röske, I. (2012). Eukaryotic life in biofilms formed in a uranium mine. *MicrobiologyOpen* 1, 83–94. doi: 10.1002/mbo3.17

Conflict of Interest: The authors declare that the research was conducted in the absence of any commercial or financial relationships that could be construed as a potential conflict of interest.

Publisher's Note: All claims expressed in this article are solely those of the authors and do not necessarily represent those of their affiliated organizations, or those of the publisher, the editors and the reviewers. Any product that may be evaluated in this article, or claim that may be made by its manufacturer, is not guaranteed or endorsed by the publisher.

frontiers in Microbiology

ORIGINAL RESEARCH
published: 12 January 2022
doi: 10.3389/fmicb.2021.782363

AzuR From the SmtB/ArsR Family of Transcriptional Repressors Regulates Metallothionein in *Anabaena* sp. Strain PCC 7120

T. V. Divya[1,2] *and Celin Acharya*[1,2]*

[1] *Molecular Biology Division, Bhabha Atomic Research Centre, Mumbai, India,* [2] *Homi Bhabha National Institute, Mumbai, India*

OPEN ACCESS

Edited by:
Rob Van Houdt, Belgian Nuclear Research Centre, Belgium

Reviewed by:
Vicente Mariscal, Institute of Plant Biochemistry and Photosynthesis, Spanish National Research Council (CSIC), Spain
Andrés González, Aragón Institute for Health Research (IIS Aragón), Spain

***Correspondence:**
Celin Acharya
celin@barc.gov.in

Specialty section:
This article was submitted to Antimicrobials, Resistance and Chemotherapy, a section of the journal Frontiers in Microbiology

Received: *24 September 2021*
Accepted: *30 November 2021*
Published: *12 January 2022*

Citation:
Divya TV and Acharya C (2022) AzuR From the SmtB/ArsR Family of Transcriptional Repressors Regulates Metallothionein in Anabaena sp. Strain PCC 7120. Front. Microbiol. 12:782363. doi: 10.3389/fmicb.2021.782363

Metallothioneins (MTs) are cysteine-rich, metal-sequestering cytosolic proteins that play a key role in maintaining metal homeostasis and detoxification. We had previously characterized NmtA, a MT from the heterocystous, nitrogen-fixing cyanobacterium *Anabaena* sp. strain PCC 7120 and demonstrated its role in providing protection against cadmium toxicity. In this study, we illustrate the regulation of *Anabaena* NmtA by AzuR (Alr0831) belonging to the SmtB/ArsR family of transcriptional repressors. There is currently no experimental evidence for any functional role of AzuR. It is observed that *azuR* is located within the *znuABC* operon but in the opposite orientation and remotely away from the *nmtA* locus. Sequence analysis of AzuR revealed a high degree of sequence identity with *Synechococcus* SmtB and a distinct α5 metal binding site similar to that of SmtB. In order to characterize AzuR, we overexpressed it in *Escherichia coli* and purified it by chitin affinity chromatography. Far-UV circular dichroism spectroscopy indicated that the recombinant AzuR protein possessed a properly folded structure. Glutaraldehyde cross-linking and size-exclusion chromatography revealed that AzuR exists as a dimer of ∼28 kDa in solution. Analysis of its putative promoter region [100 bp upstream of *nmtA* open reading frame (ORF)] identified the presence of a 12–2–12 imperfect inverted repeat as the *cis*-acting element important for repressor binding. Electrophoretic mobility shift assays (EMSAs) showed concentration-dependent binding of recombinant dimeric AzuR with the promoter indicating that NmtA is indeed a regulatory target of AzuR. Binding of AzuR to DNA was disrupted in the presence of metal ions like Zn^{2+}, Cd^{2+}, Cu^{2+}, Co^{2+}, Ni^{2+}, Pb^{2+}, and Mn^{2+}. The metal-dependent dissociation of protein–DNA complexes suggested the negative regulation of metal-inducible *nmtA* expression by AzuR. Overexpression of *azuR* in its native strain *Anabaena* 7120 enhanced the susceptibility to cadmium stress significantly. Overall, we propose a negative regulation of *Anabaena* MT by an α5 SmtB/ArsR metalloregulator AzuR.

Keywords: *Anabaena* 7120, AzuR, regulation, metallothionein, cadmium stress

INTRODUCTION

Trace metal ions are crucial for nearly all aspects of metabolism in the prokaryotic cells. These are involved in various biological processes like enzymatic reactions that require metal ions as cofactors, for folding and structural stabilization of the proteins or for the maintenance of the metal-sensing regulatory factors (Rees, 2002; Bertini et al., 2007; Chandrangsu et al., 2017). Although the essential metal ions are indispensable, these are toxic in excess amounts (Chandrangsu et al., 2017). As a result, the microorganisms have developed mechanisms to regulate the homeostasis of the essential metal ions. Metal homeostasis is mediated by balancing the uptake, storage, transfer, and efflux of the metals so that the cellular requirements are fulfilled and the right metal is introduced into the right macromolecule in the cells for various biological processes (Tottey et al., 2005; Waldron and Robinson, 2009).

Metallothioneins (MTs) are cysteine-rich, low-molecular-weight, metal-sequestering proteins that are known to bind metal ions via metal–thiolate clusters and are involved in maintaining homeostasis of physiologically important metals like zinc (Zn^{2+}) and copper (Cu^{2+}) (Klaassen et al., 1999; Blindauer, 2011). Apart from binding to the essential metals, MTs are implicated in the detoxification of toxic metals including cadmium (Cd^{2+}) and mercury (Hg^{2+}) from the cells (Klaassen et al., 1999). MTs are induced in the presence of ionic species of various metals like Cd, Zn, Cu, Hg, Au, Ag, Co, Bi, Pb, Ni, and Cr (Palmiter, 1987; Huckle et al., 1993) as well as oxidative stress (Andrews, 2000). MT expression is strictly regulated owing to its role in maintaining metal homeostasis. While eukaryotic MT gene expression has been shown to be under positive regulation (Klaassen et al., 1999), prokaryotic MT expression is proposed to be negatively regulated (Turner and Robinson, 1995). The first characterized prokaryotic MT is *Synechococcus* sp. SmtA (Blindauer and Leszczyszyn, 2010). The *smtA* gene expression is negatively regulated by a zinc responsive transcriptional repressor SmtB (Erbe et al., 1995; Turner et al., 1996) of the SmtB/ArsR family of transcriptional regulatory proteins. The SmtB/ArsR family of proteins bind to specific regulatory sequences present upstream of the gene. Derepression of transcription by such regulators results from direct binding of the metal to the repressor, which inhibits its binding to the operator/promoter (O/P) region of the gene under regulation (Busenlehner et al., 2003; Osman and Cavet, 2010).

Analysis of the genome sequence of *Anabaena* PCC 7120 (hereby referred as *Anabaena* 7120) revealed two SmtB-like repressors of the SmtB/ArsR family, namely, (a) AztR (All7621) and (b) AzuR (Alr0831) (Liu et al., 2005). AztR has been identified as a Zn^{2+}/Pb^{2+}/Cd^{2+}-responsive metalloregulator constituting a Zn^{2+}/Pb^{2+}/Cd^{2+} efflux operon (*aztAR* operon) regulating AztA, a Zn^{2+}-translocating CPx-ATPase (Liu et al., 2005, 2008). However, presently, there is no experimental evidence toward the functionality and regulation of the other repressor, AzuR in *Anabaena* 7120, that shares 60% identity with SmtB (**Figure 1A**). Previously, we had identified and characterized a MT from the heterocystous, filamentous cyanobacterium *Anabaena* 7120 (also belonging to the BmtA family) referred to as NmtA. Overexpression of NmtA in its native strain conferred tolerance to cadmium stress (Divya et al., 2018). We had observed increased abundance of the *nmtA* transcripts in the presence of elevated concentrations of metal ions like Zn^{2+}, Cu^{2+}, and Cd^{2+} (Divya et al., 2018), indicating transcriptional regulation of *nmtA* expression. It is proposed that the expression of the proteins associated with metal homeostasis is largely regulated at the transcriptional level in bacteria (Finney and O'Halloran, 2003). It is, therefore, worthwhile to explore whether AzuR, which is an SmtB-like repressor, has any role in the regulation of NmtA expression in *Anabaena* 7120.

The present study provides a comprehensive characterization of *Anabaena* AzuR (Alr0831). We show here that AzuR indeed binds to the upstream region of the *nmtA* open reading frame (ORF). DNA binding was repressed in the presence of various divalent metal ions, indicating a negative regulation of *nmtA* expression by AzuR. Our results showed that overexpression of *azuR* in *Anabaena* enhanced the susceptibility of the recombinant strain to cadmium stress significantly. The present investigation advances our understanding of the mechanisms of metal-regulated gene expression in the nitrogen-fixing cyanobacterium *Anabaena* 7120.

MATERIALS AND METHODS

Organism and Growth Conditions

Anabaena 7120 cultures were grown in BG-11 liquid medium, pH 7.2, with combined nitrogen (17 mM $NaNO_3$) under continuous illumination (30 $\mu Em^{-2}\ s^{-1}$) without or with shaking (100 rpm) at 27°C ± 2°C (Allen, 1968). *Escherichia coli* cultures were grown in Luria–Bertani (LB) medium at 37°C (DH5α, HB101) or 30°C (SHuffle) with shaking at 120 rpm. The neomycin antibiotic was used for recombinant *Anabaena* cultures in BG-11 liquid medium (15 $\mu g\ ml^{-1}$) or BG-11 agar plates (25 $\mu g\ ml^{-1}$), whereas chloramphenicol (34 $\mu g\ ml^{-1}$) or carbenicillin (100 $\mu g\ ml^{-1}$) was used for *E. coli* cultures. Primers, plasmids, *E. coli*, and *Anabaena* strains used in this study are listed in **Table 1**.

Bioinformatic Analysis

Alignment of DNA and protein sequences was determined using ClustalW (Thompson et al., 1994) and Clustal Omega (Madeira et al., 2019), respectively. Jalview was used to visualize and edit aligned protein sequences (Waterhouse et al., 2009). A phylogenetic tree was constructed using MEGA version X (Kumar et al., 2018) by the maximum likelihood method. The I-TASSER software was used to predict the tertiary structure of AzuR and metal-binding residues (Zhang, 2008; Roy et al., 2010; Yang et al., 2015). Pattern search analysis of conserved sequences was carried out using the online tool Pattern Locator (Mrázek and Xie, 2006). The −10 and −35 boxes of the upstream region of *nmtA* were predicted from BPROM (Salamov and Solovyevand, 2011).

Cloning, Expression, and Purification of AzuR

The *azuR* ORF (363 bp) was PCR amplified from *Anabaena* 7120 genomic DNA and cloned into pTwin1 vector at *Nde*I–*Sap*I sites.

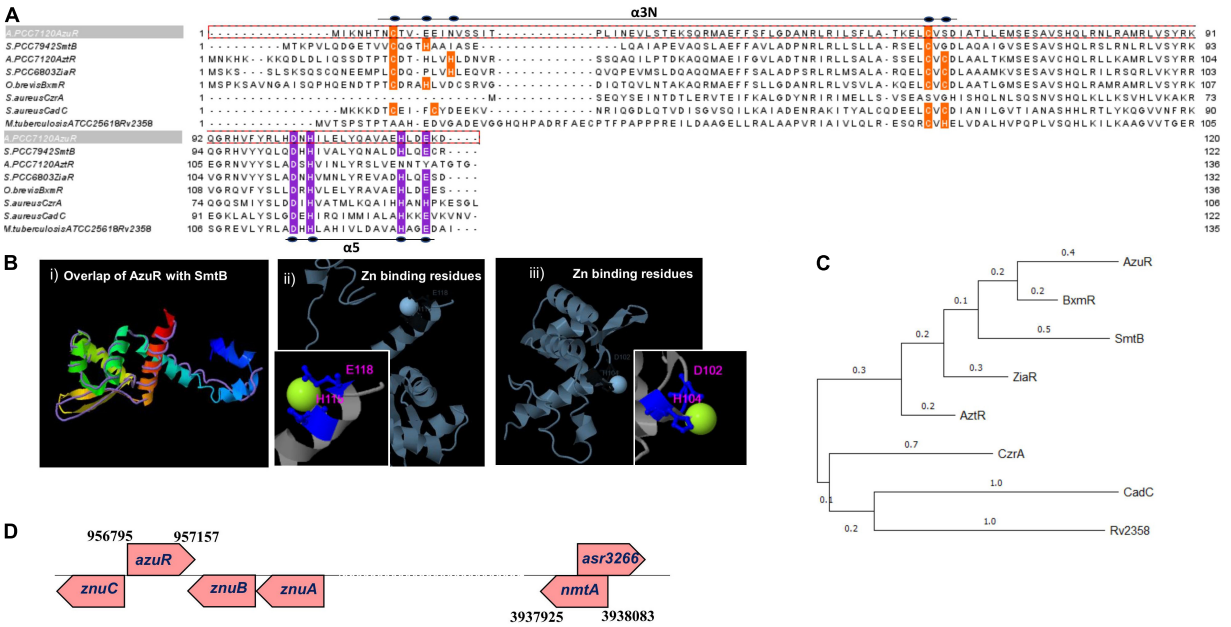

FIGURE 1 | Sequence analysis, structural modeling, phylogeny, and genomic organization of AzuR. **(A)** Multiple sequence alignment of AzuR with representative SmtB/ArsR family transcriptional repressors, SmtB (P30340), AztR (Q8ZS91), ZiaR (P9WMI4), BxmR (Q55940), CzrA (O85142), and CadC (P20047). The metal-sensing amino acids present in the α5 site are highlighted in purple, and the residues present in the α3N site are indicated in orange. **(B)** Structure of AzuR. (i) The tertiary structure model of AzuR was generated by using SmtB as the template by I-TASSER with the overlap of SmtB (PDB ID: 1R23) shown as traces in purple. Ligand (Zn^{2+}) binding residues predicted by I-TASSER with (ii) *Staphylococcus aureus* CadC (PDB ID: 1U2W) and (iii) *Synechococcus* PCC 7942 SmtB (PDB ID: 1R22). Zn^{2+} is shown in neon green and the metal-binding residues are indicated in blue. **(C)** Phylogenetic tree generated with representative sequences aligned by Clustal Omega using MEGA X software with 500 bootstrap replicates. The tree is drawn to scale, with branch lengths measured in the number of substitutions per site. **(D)** Schematic representation of the genetic locus of *azuR* ORF with respect to *nmtA* ORF in the *Anabaena* genome.

The resulting construct pTwin*azuR* was confirmed by sequencing and transformed into an *E. coli* SHuffle strain. Overexpression of chitin-binding domain (CBD)-tagged AzuR was induced by the addition of 0.5 mM IPTG. The protein purification was carried out by chitin affinity chromatography as per the manufacturer's protocol (New England Biolabs). The protein was cleaved from its tag and eluted following incubation with 40 mM DTT at 4°C for 3 days. CBD was also eluted as the contaminating protein. This eluate was loaded onto the fresh chitin resin after DTT removal. The flow-through was collected, which contained purified *Anabaena* AzuR without CBD. The purified protein band following electrophoresis on 15% SDS-PAGE was excised and processed for LC-MS/MS analysis (Q Exactive Plus BioPharma High-Resolution Orbitrap MS system, Thermo Fischer Scientific) at the Sophisticated Analytical Instrument Facility (SAIF), IIT Bombay, India. Spectrum was acquired in positive ion mode in a mass range from 350 to 2,000 m/z. The resultant spectrum was used for peptide identification using the *Anabaena* 7120 protein database available at UniProt.

Structural Characterization of AzuR

Determination of the oligomeric status of AzuR was done by glutaraldehyde cross-linking of protein in the native state. Purified AzuR was incubated with 10 mM glutaraldehyde at room temperature (RT) for 10–15 min in 10 mM Tris, pH 7.5. To this, a cracking buffer without or with DTT (50 mM) was added. The resulting cross-linked protein was analyzed by 15% SDS-PAGE. The native molecular mass of AzuR was determined by size-exclusion chromatography (AKTA FPLC system, GE Healthcare) using the GE Superdex 75 column equilibrated with 20 mM Tris, 100 mM NaCl, pH 7.5 at 25°C at a flow rate of 0.5 ml min^{-1}. The column was previously calibrated using a set of gel filtration markers [bovine serum albumin (66 kDa), ovalbumin (44 kDa), carbonic anhydrase (44.3 kDa), and cytochrome c (29 kDa)] (GE Healthcare).

Analysis of the secondary structure of AzuR was performed by circular dichroism (CD) spectroscopy (MOS-500 Biologic CD spectrometer equipped with a Peltier-type thermostatic cell holder) at 25°C. The CD spectrum was recorded in the wavelength range of 200–260 nm using a cuvette with a path length cell of 0.1 mm. The samples were prepared in 10 mM Tris buffer, pH 7.5. The alpha helical content was calculated using the online tool K2D2 (Perez-Iratxeta and Andrade-Navarro, 2008). CD spectra were also recorded for titrations of AzuR with increasing concentrations of zinc (molar equivalents ranging from 1 to 10).

Rapid Amplification of cDNA Ends

Total RNA was isolated from *Anabaena* 7120 treated with 10 μM cadmium for 1 h as described earlier (Divya et al., 2018). cDNA was synthesized with 0.5 μg of total RNA using ReadyScript cDNA Synthesis Mix (Sigma-Aldrich). Following dA tailing of

TABLE 1 | Primers, plasmids, and strains used in the study.

Primer	Description	References
nmtA Rev	CGCGGATCCTTAACAGCCACAGCCATTATG	Divya et al., 2018
*azuR*_pTwinC Fwd	GGTGGTCATATGATTAAAAATCACACAAATTGTAC	This study
*azuR*_pTwinC Rev	GGTTGCTCTTCCGCAATCTTTTTCGTCCAAATG	This study
*azuR_Nde*I Fwd	GGAATTCCATATGATTAAAAATCACACAAATTG	This study
*azuR_Bam*HI Rev	CGGGATCCCTAATCTTTTTCGTCCAAATG	This study
Prom_Fwd	ATTATTTCCTCCGTTTTCACTTGTG	This study
Prom_Rev	AAACGTATTATATAACCTAATTGTTAC	This study
Oligo(dT) anchor primer	GACCACGCGTATCGATGTCGACTTTTTTTTTTTTTTT	5′3′ RACE kit, Roche
16S Fwd	CACACTGGGACTGAGACAC	Pinto et al. (2012)
16S Rev	CTGCTGGCACGGAGTTAG	
Plasmid		
pTwin1	Expression vector resulting in protein fusion with CBD and cleavable intein tag, Cb^R	NEB
pTwin*azuR*	360 bp *azuR* fragment cloned in pTwin1 vector	This study
pFPN	Cb^R, Kan^R, integrative expression vector	Chaurasia et al., 2008
pAM1956	Kan^R, promoterless gfpmutII reporter gene	Yoon and Golden, 1998
pFPN*azuR*	363 bp *azuR* fragment cloned in pFPN	This study
pAM*psbA*	*Xma*I-*Sal*I fragment from pFPN cloned in pAM1956 vector	
pAM*azuR*	*Xma*I-*Sal*I fragment from pFPN*azuR* cloned in pAM1956	This study
pAM*nmtA*	*Xma*I-*Sal*I fragment from pFPN*nmtA* cloned in pAM1956 vector	Divya et al., 2018
***E. coli* strain**		
DH5α	F^- *recA41 endA1 gyrA96 thi-1 hsdR17* (r^{k-} m^{k-}) *supE44 relA*λ *lacU169*	Lab collection
BL21(DE3)pLysS	F^- *ompT gal dcm lon hsdS*$_B$ (r_B^- m_B^-) λ(DE3) pLysS (Cm^R)	Lab collection
HB101	F^- *mcrB mrr hsdS20* (r_B^- m_B^-) *recA13leuB6 ara-14 proA2 lacY1 galK2 xyl-5 mtl-1 rpsL20* (Sm^R) *lnV44* λ$^-$	Lab collection
HB101R2	Donor strain carrying pRL623 (encoding methylase) and pRL443 (conjugal plasmid)	Elhai et al., 1997
SHuffle T7 Express lysY	MiniF lysY (CamR)/fhuA2 lacZ:T7 gene1 [lon] ompT ahpC gal λatt:pNEB3-r1-cDsbC (SpecR, laclq) ΔtrxB sulA11 R(mcr-73:miniTn10–TetS)2 [dcm] R(zgb-210:Tn10 –TetS) endA1 Δgor Δn114:IS10	NEB
***Anabaena* strain**		
Anabaena PCC 7120	Wild-type strain	Lab collection
An*psbA*$^+$	*Anabaena* 7120 harboring light inducible promoter *psbA* from PFPN, Nm^R	This study
An*azuR*$^+$	*Anabaena* 7120 harboring pAM*azuR,* Nm^R	This study
An*nmtA*$^+$	*Anabaena* 7120 harboring pAM*nmtA,* Nm^R	This study

cDNA by terminal transferase (Roche), PCR was performed with the oligo(dT)-anchor primer and *nmtA* primer as listed in **Table 1**. The PCR product was then sequenced.

Electrophoretic Mobility Shift Assay

The putative promoter region (100 bp DNA sequence upstream of *nmtA* ORF) was PCR amplified (primers listed in **Table 1**) and end-labeled with DIG-ddUTP as per manufacturer's instructions (Roche). Two nanograms of a DIG-labeled probe (P_{nmtA}) was incubated with various concentrations of AzuR protein in a total reaction volume of 20 μl containing 20 mM Tris–Cl (pH 7.5) and 1 mM EDTA at RT for 30 min. The DNA–protein complexes were resolved on 10% native PAGE in 0.5× TBE. Separated complexes were electroblotted onto a nylon membrane, cross-linked with UV, and stored at 4°C. It was probed with an anti-DIG antibody and developed using a colorimetric substrate, NBT-BCIP, according to the manufacturer's protocol (DIG High Prime DNA Labeling and Detection Starter Kit I, Roche). The bands were quantified by the ImageJ software, and the data were fitted to Hill's equation. Each experiment was repeated three times. In order to evaluate the specificity of interaction of the DNA-AzuR protein binding, electrophoretic mobility shift assay (EMSA) was performed with 100 ng of AzuR (360 nM) with either 20 ng of P_{nmtA} or 20 ng of non-specific DNA (*nmtA* gene). For protein specificity, 20 ng of P_{nmtA} with non-specific proteins like AnLexA, BSA, or NmtA, each at 360 nM concentration, was taken for EMSA. The DNA–protein complexes were resolved on 10% native PAGE and visualized by ethidium bromide staining. To evaluate whether different divalent metal ions affect the binding of AzuR to the target 100 bp DNA, EMSAs were carried out in the presence of 100 μM of various metals. The metal salts used in the study were $ZnSO_4.7H_2O$, $CdCl_2.1/2H_2O$, $CuSO_4.5H_2O$, $Co(NO_3)_2.6H_2O$, $NiSO_4.7H_2O$, $MnCl_2.4H_2O$, and $Pb(NO_3)_2$. EMSAs were also carried out in the presence of 1 mM DTT (Erbe et al., 1995) for reactions containing all the aforesaid metals.

Overexpression of AzuR in *Anabaena* 7120

Overexpression of *azuR* gene in its native strain was achieved by triparental conjugation (Divya et al., 2018). The *azuR* gene was cloned downstream to the light-inducible *psbA*1 promoter in the pFPN vector at *Nde*I and *Bam*HI sites. A *Sal*I–*Xma*I fragment from pFPN*azuR* was excised and cloned into the

E. coli/*Anabaena* shuttle vector pAM1956 upstream of the promoterless *gfpmut2* gene. pAM*azuR* was then transferred into *Anabaena* 7120. The recombinant *Anabaena* strain was designated as An*azuR*$^+$. In a similar way, An*nmtA*$^+$ (*Anabaena* strain overexpressing NmtA) was also generated. An*psbA*$^+$ (*Anabaena* harboring pAM1956 with constitutive expression of GFP) was generated by excising the P_{psbA1} fragment from the pFPN vector and cloning it into the vector pAM1956 upstream of the promoterless *gfpmut2* gene and transferred conjugally into *Anabaena* 7120. The recombinant *Anabaena* strains were repeatedly subcultured and maintained under the selective pressure of neomycin (Nm^{15}). Visualization of GFP fluorescence in the recombinant cells confirmed the expression of the *azuR* gene placed upstream of the *gfpmut2* gene.

Transcript Analysis by RT-PCR

For RT-PCR, 1 μg RNA was used for cDNA synthesis (ReadyScript cDNA Synthesis Mix, Sigma-Aldrich). RT-PCR was carried out with *azuR*-specific primers (**Table 1**) with 16S rRNA serving as the internal control. RT-PCR products were resolved by electrophoresis on 1% agarose gel and detected by staining with ethidium bromide. For quantification of *nmtA* transcripts, real-time PCR was performed with *nmtA*-specific primers in Qiagen rotor-Gene Q real-time PCR cycler. 16S rRNA was used as the internal control.

Cadmium Exposure Studies

Exponential phase cultures (3-day-old cultures) of An*psbA*$^+$, An*nmtA*$^+$, and An*azuR*$^+$ were inoculated in BG-11 N^+ (Nm^{15}) liquid medium at a chlorophyll *a* (Chl*a*) density of ∼4 μg ml^{-1} and incubated for 10 days under illumination without or with cadmium at 10 and 20 μM concentrations. Growth was assessed by measuring Chl*a* content at regular intervals. For spot assays, exponentially growing cultures of An*psbA*$^+$, An*nmtA*$^+$, and An*azuR*$^+$ were spotted onto BG-11 N^+ (Nm^{25}) agar plates without or with cadmium (10, 20, and 40 μM) at the chlorophyll density mentioned in the figure and incubated under continuous illumination for 7 days.

Microscopy of *Anabaena* Strains

Bright-light and fluorescence microscopy (FM) images were taken at ×600/×1,500 magnification on a Carl Zeiss Axioscope 40 microscope with a charge coupled device (CCD) AxioCam MRc camera (Zeiss). Green fluorescence of GFP was visualized using a Hg-arc lamp (excitation BP: 450–490 nm, emission LP: 515 nm). Chl*a* fluorescence of *Anabaena* was visualized with green light excitation (excitation BP: 546/12, emission LP: 590 nm). It should be noted here that the microscopic settings for GFP fluorescence used the emission filter ($\lambda_{emission}$: 515 nm) that could detect both GFP and Chl*a* fluorescence. For scanning electron microscopy (SEM), exponential-phase cells of WT, An*psbA*$^+$, An*nmtA*$^+$, and An*azuR*$^+$ were harvested by centrifugation, and the resulting cell pellets were washed with 0.9% NaCl and fixed with 2.5% glutaraldehyde at 4°C for 1–2 h. Post fixation, the cells were serially dehydrated in 20, 30, 50, 70, 90, and 100% ethanol. The dehydrated sample was then gold coated with a sputtering device (Q 150R ES, Quorum) and visualized using SEM (EVO 18 Research, Carl Zeiss, United Kingdom).

Statistical Analysis

Growth experiments were repeated three times. Average values with standard deviations are shown for a representative experiment. For determination of cell size, data are represented as average values ± standard deviation. One-way ANOVA was employed for calculating the significance of the difference in cell size between WT, An*psbA*$^+$, An*nmtA*$^+$, and An*azuR*$^+$ cultures.

RESULTS AND DISCUSSION

Sequence Analysis and Genomic Context of AzuR (Alr0831)

The genome of *Anabaena* PCC 7120 harbors two proteins belonging to the ArsR-SmtB family of proteins, All7621 and Alr0831. The ArsR-SmtB family of transcriptional metalloregulators represses the expression of genes/operons involved in maintaining metal homeostasis or toxic metal detoxification (Osman and Cavet, 2010). Among the 15 characterized metal binding motifs (Saha et al., 2017), the metal-sensing members of the regulators include two structurally diverse metal-binding sites, namely, α3N, and α5 (Busenlehner et al., 2003). All7621 in *Anabaena* 7120 encodes for AztR, a regulator of AztA [Zn(II)/Pb(II) CPx-ATPase efflux pump] (Liu et al., 2005), and belongs to the α3N group of proteins. The α3N site consists of cysteine thiolate ligands—two from the α3 helix with signature motifs $Cx_{1-2}C$ or Cx_2CD and one or two cysteine ligands derived from the amino-terminus (Saha et al., 2017). The sequence analysis of the yet-uncharacterized Alr0831 (AzuR) revealed the absence of a functional α3N site in AzuR as it contained only one cysteine residue each in the α3 helix and at the amino-terminus (**Figure 1A**). Protein sequence alignment of AzuR with the *Synechococcus* transcriptional repressor SmtB showed 60% sequence identity, and the key amino acids in the α5 site important for metal sensing, i.e., His, Glu, and Asp in SmtB (VanZile et al., 2000, 2002), were found to be conserved in AzuR (**Figure 1A**). It is likely that the function of AzuR is similar to that of SmtB owing to the high degree of sequence identity. Tertiary structure prediction of AzuR using the software I-TASSER showed the presence of all the secondary structural folds (α1–α5, β1, and β2) similar to that of SmtB (**Figure 1B**, i). Structural modeling predicted zinc-binding residues Asp102 and His104 (**Figure 1B**, ii) of AzuR comparable to that of *Staphylococcus aureus* CadC as well as His115 and Glu118 (**Figure 1B**, iii) similar to that of *Synechococcus* SmtB. Hence, AzuR could possibly be grouped into α5 SmtB/ArsR metalloregulators with the signature motif $DxHx_{10}Hx_2E$ present in the α5 helix (**Figure 1A**). Phylogenetic analysis of representative sequences from SmtB/ArsR family members showed that AzuR shared maximum identity to BxmR (67%), which contain both α3N and α5 sites (**Figure 1C**). It also showed that SmtB (α5) and proteins belonging to different groups—ZiaR (α3N, α5), AztR (α3N), BxmR (α3N, α5), and AzuR (α5)—evolved independently but were linked to a common ancestor (**Figure 1C**).

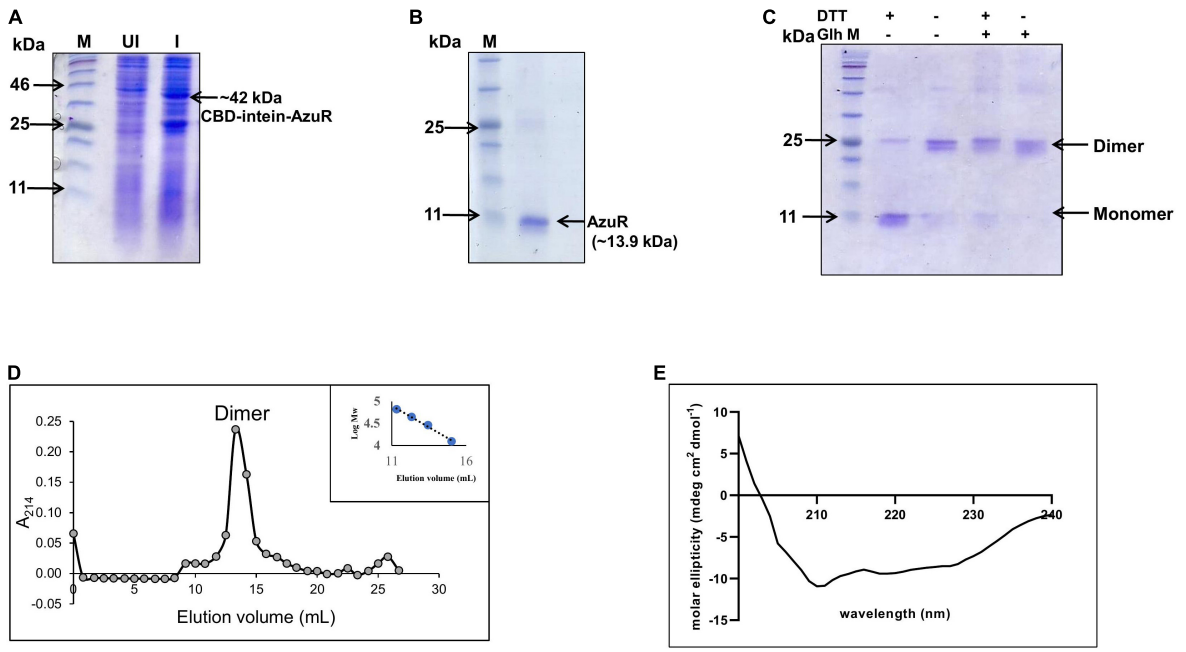

FIGURE 2 | Overexpression and purification of AzuR. **(A)** Overexpression of AzuR. Whole-cell protein extracts (30 μg) of uninduced (UI) and induced (I) with 0.5 mM IPTG from *E. coli* SHuffle (pTwin*azuR*) cells were resolved on 15% SDS-PAGE, followed by visualization with Coomassie Brilliant Blue (CBB) staining. The lane marked as M is the protein molecular weight marker (NEB P7712). **(B)** Purification of AzuR (Alr0831). AzuR was purified by chitin affinity chromatography followed by thiol-mediated removal of the CBD tag. The purified AzuR protein corresponding to the monomer under reducing conditions on 15% SDS-PAGE is indicated by the arrow. The molecular mass in kDa is indicated on the left-hand side. The lane marked as M is the protein molecular weight marker (NEB P7712). **(C)** Cross-linking of AzuR with glutaraldehyde. The purified AzuR (5 μg) was cross-linked with glutaraldehyde (Glh) without or with the addition of DTT (50 mM) in the Laemmli buffer. The proteins were separated on 15% SDS-PAGE followed by staining with Coomassie Brilliant Blue. **(D)** Size-exclusion chromatography profile of the purified AzuR protein using Superdex 75. The calibration curve of standard proteins is shown in the inset. The calibration equation, $y = -0.195x + 7.0463$ ($R^2 = 0.992$), was used for the molecular weight calculation of AzuR. **(E)** CD spectrum of purified AzuR showing 67.5% α helical content. Gray circles represent elution volume corresponding to different fractions and blue circles represent the standard molecular weight markers used.

Several metal-responsive proteins and their repressors of SmtB/ArsR family members have been shown to exist as operons. For example, BmtA (MT of *Oscillatoria brevis*) and its repressor BxmR (Liu et al., 2004), ZiaA (Zn efflux protein of *Synechocystis* PCC 6803) and its repressor ZiaR (Thelwell et al., 1998), and AztA (Zn^{2+}-translocating CPx-ATPase) and its repressor AztR (Liu et al., 2005) are organized in operons. In *Synechococcus* PCC 7942, the *smtB* gene and *smtA* gene are separated by 100 bp, forming a divergon (Huckle et al., 1993). However, there is a deviation in the genetic organization of *Anabaena* MT, which is not organized in an operon. The *nmtA* ORF (located between positions 3938083 and 3937925) is present within a larger ORF of an unknown protein, asr3266, but in the opposite orientation (Bose et al., 2006). Similarly, the putative regulator *azuR* is not placed adjacent to the *nmtA* locus but is present within the ZnuABC operon (**Figure 1D**). Alr0831 is positioned at 956795→957157 between alr0830 (ZnuC, ABC transporter permease protein) and alr0832 (ZnuA, ABC transporter ATP binding protein) in the opposite orientation. Similar to AzuR, the SmtB ortholog has been identified within an operon with an ABC-type transporter system in other cyanobacteria like *Nodularia* and *Anabaena variabilis* (Blindauer, 2008). Analysis of the genomic organization of other prokaryotic MTs like *Pseudomonas* MT also revealed an absence of regulatory protein adjacent to the *Pseudomonas fluorescens* Q2-87 MT locus. Also, the genes adjacent to the *Pseudomonas* MT gene code for proteins of unknown function (Habjanič et al., 2020). Genomic arrangement of MT and its regulator as operons apparently is not mandatory as such regulators function as *trans*-acting factors on *cis*-regulatory elements.

Overexpression, Purification, and Structural Characterization of AzuR

To characterize the regulatory role of AzuR, the corresponding gene (*alr0831*) was cloned in the pTwin1 vector. The resulting construct pTwin*azuR* was expressed in the *E. coli* SHuffle strain. Induction with IPTG expressed a ∼42 kDa protein corresponding to CBD-tagged AzuR (**Figure 2A**). The cloning at *Nde*I–*Sap*I sites ensured that no extra amino acids were incorporated in the purified protein following removal of the tag. AzuR was purified by chitin affinity chromatography, and the removal of the CBD tag was achieved by thiol-induced cleavage with 40 mM DTT at 4°C. The purified AzuR was visualized on SDS-PAGE as a monomer under reducing conditions with a molecular weight of ∼13.9 kDa (**Figure 2B**), which was further confirmed with LC-MS/MS analysis. The MS analysis identified

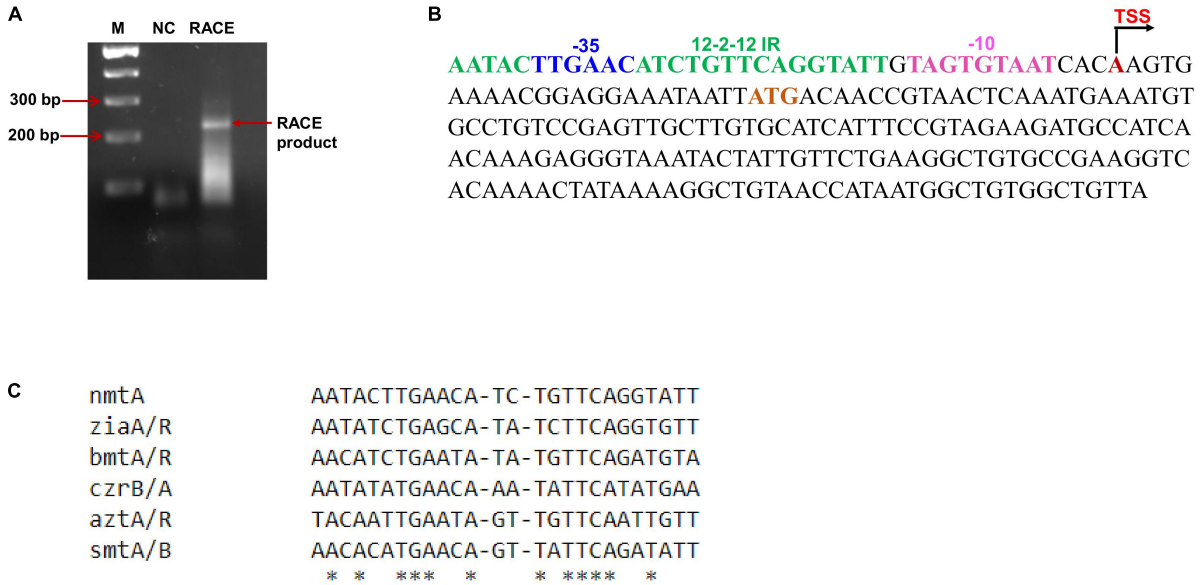

FIGURE 3 | Mapping of transcriptional start site and inverted repeats. **(A)** Mapping of transcriptional start site by RACE was performed with RNA isolated from *Anabaena* cells treated with cadmium. The RACE product is indicated by an arrow. M, 100 bp DNA ladder (NEB). **(B)** Sequence analysis of the *nmtA* ORF and upstream region. The inverted repeat sequence is highlighted in green; the red A is the transcriptional start site (TSS); the sequences highlighted in pink and blue represent the –10-like box and –35 box, respectively; and the start codon ATG is highlighted in brown. **(C)** Sequence alignment of inverted repeat present upstream of the *nmtA* ORF with other characterized repeats essential for repressor binding by ClustalW. An asterisk (*) indicates the conserved bases across all sequences.

six unique peptides, showing 77% coverage of the *Anabaena* AzuR protein sequence.

The SmtB/ArsR family of proteins binds to the regulatory DNA sequences as homodimers (Osman and Cavet, 2010). To ascertain the native form of AzuR, the oligomeric status of AzuR was evaluated by glutaraldehyde cross-linking. The protein was predominantly found to be present in the dimeric state as observed by glutaraldehyde cross-linking (**Figure 2C**). The dimeric state was also confirmed with size-exclusion chromatography (**Figure 2D**). This is in agreement with the previously characterized SmtB/ArsR family of prokaryotic metalloregulatory transcriptional repressors that existed as stable dimers in solution (Busenlehner et al., 2001; Liu et al., 2005, 2008). It was observed that AzuR existed as a monomer under reducing conditions and dimer under non-reducing conditions (**Figure 2C**). These observations suggested the involvement of cysteine residues in AzuR dimerization. Secondary structure analysis by CD showed that AzuR is composed of 67.5% α helical content (**Figure 2E**), suggesting that the purified recombinant AzuR protein was properly folded. This is in agreement with the theoretical secondary structure prediction of AzuR using the SOPMA software, which projected 67% α helical content followed by 17% random coil and 11% extended strand.

Mapping and Characterization of AzuR-DNA Binding Sequence

The SmtB/ArsR family of transcriptional regulators binds to 12–2–12 inverted repeats present upstream or within the genes that they regulate (Erbe et al., 1995; Turner et al., 1996). RACE analysis with total RNA isolated from the cadmium-treated (IC_{50} 10 μM) *Anabaena* 7120 showed an ∼200 bp cDNA product (**Figure 3A**). Sequence analysis of the product identified the transcriptional start site (TSS) to be at 23 nt upstream of the translational start of the *nmtA* ORF (**Figure 3B**). The palindromic sequence (12–2–12 imperfect inverted repeat), corresponding to the consensus of the α3N and α5 groups of SmtB/ArsR-binding sites (Saha et al., 2017), was found to be located 36 nt upstream of the *nmtA* translation start site (**Figure 3B**). Its position overlaps with the theoretical prediction of the −35 element of the promoter. It is shown that the *cis*-regulatory element of metal-inducible operons is composed of one or two inverted 12–2–12 repeats present in the vicinity or overlapping the transcriptional start site of the gene under regulation. For example, one of the two such inverted 12–2–12 repeats found in *Synechococcus* 7942 was essential for the regulation of *smtA* expression by its repressor, SmtB (Turner et al., 1996). Similarly, the *Synechocystis zia* O/P region has a single 12–2–12 inverted repeat between the −10 box and the translational start site of *ziaA*, which is regulated by a divergently transcribed repressor, *ziaR* (Thelwell et al., 1998). Pattern search analysis was performed with the conserved bases in the 12–2–12 imperfect repeat along the entire *Anabaena* 7120 genome. Similar repeats were found at sites upstream and within other genes that include *all1178*, which codes for a two-component hybrid sensor and regulator, *alr7622* (also designated as *aztA*), encoding for cation-transporting ATPase and other hypothetical proteins (**Table 2**). The conserved 12–2–12 inverted repeat of SmtB/ArsR-regulated O/Ps are shown in **Figure 3C**. Although *nmtA* and its putative regulator *azuR* do not constitute an operon in *Anabaena* 7120,

the inverted 12–2–12 imperfect repeat could be located at the appropriate upstream distance from the *nmtA* translation start site. Although the *azuR* ORF is present within the *znuABC* operon, a detailed search for conserved bases in the 12–2–12 imperfect repeat following global search analysis by PATLOC in the close vicinity of the *znuABC* operon (corresponding to the 500 bp upstream region to 500 bp downstream of the operon) and within the operon did not show any such repeat

TABLE 2 | *Anabaena* genes possessing conserved sequences in the 12–2–12 inverted repeat identified by PATLOC.

S. No.	Inverted repeat	Position	Gene and distance
Chromosome			
1. *	AATACTTGAGTA-AT-TTATCAAGTTCT	1386159–1386184	*all1178* (two-component hybrid sensor and regulator) (<-); 314–2429
2.	AATACCTGAACA-GA-TGTTCAAGTATT	3938119–3938144	*asr3266* (hypothetical protein) (->); 10 *all3267* (hypothetical protein) (<-); 56
3. *	CACAATTGATGA-TA-TCTTCACCTGGG	4556777–4556802	*alr3769* (hypothetical protein) (->); 314–383
4.	TAAATGTGATGA-TA-TCATCACATTTA	5585215–5585240	*alr4684* (hypothetical protein) (->); 291 *alr4685* (hypothetical protein) (->); 849
Alpha plasmid			
5.	GAAAACTGAGTA-AT-TTATCAATTGCT	40552–40577	*asr7047* (hypothetical protein) (->); −12 *alr7048* (hypothetical protein) (->); 66
Beta plasmid			
6.*	TACAATTGAATA-GT-TGTTCAATTGTT	114477–114502	*alr7622* (cation-transporting ATPase) (->); 13–2601
7.*	GAAATTTGAAAA-CT-TCCTCACCTCAA	153412–153437	*alr7649* (hypothetical protein) (->); 5492–2228

**Denotes repeat sequence present within the gene.*
Arrows represent transcription direction.

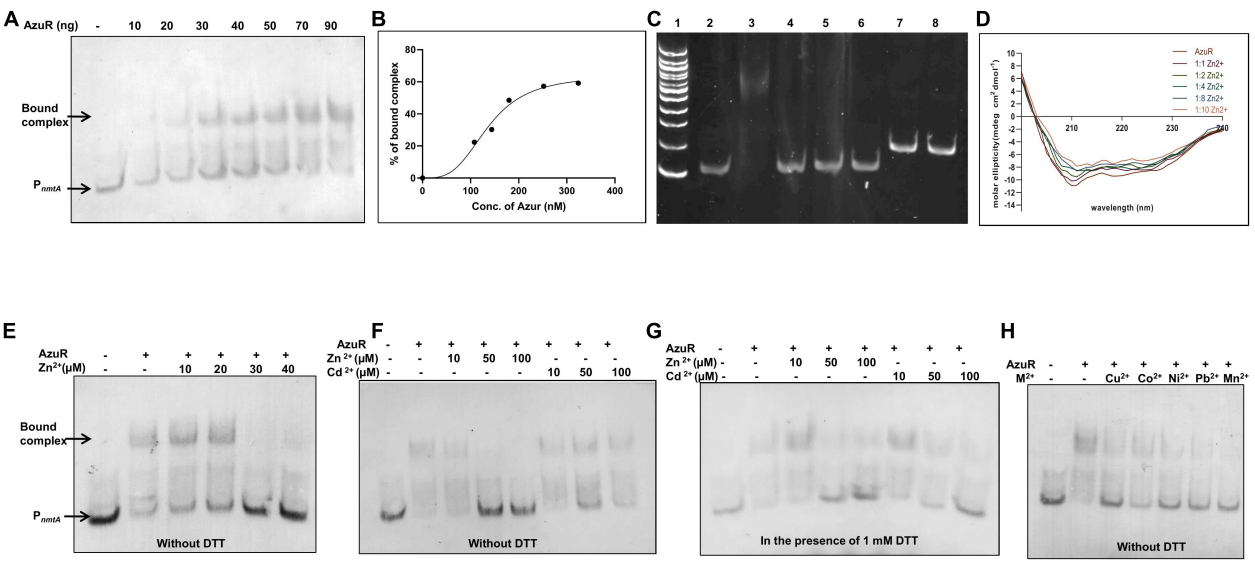

FIGURE 4 | Binding of AzuR to the upstream region of *nmtA*. **(A)** Electrophoretic mobility shift assay (EMSA) of DIG-labeled 100 bp DNA sequence upstream of *nmtA* (2 ng) with purified AzuR. Different concentrations of AzuR protein were incubated with DIG-labeled DNA, and the assay mixtures were resolved on 10% native PAGE in 0.5× TBE. Detection with the DIG-labeled probe was carried out as per manufacturer's protocol (Roche) using NBT-BCIP. Lane 1 contains 2 ng of P_{nmtA}. Lanes 2–8 contain increasing concentrations of AzuR as indicated. Representative data from three independent experiments are shown. **(B)** Representative plot showing the percentage of bound complex against the concentration of AzuR protein fitted to the Hill equation. **(C)** EMSA for evaluation of non-specific interaction of DNA–protein binding. Lane 1: 100 bp DNA ladder. Lane 2: 20 ng of 100 bp P_{nmtA} only or with 360 nM (100 ng) AzuR (lane 3) or 360 nM (478 ng) BSA (lane 4) or 360 nM (41 ng) NmtA (lane 5) or 360 nM (158 ng) AnLexA (lane 6). Lane 7 contains 20 ng of the *nmtA* gene only or with 360 nM (100 ng) AzuR (lane 8). The DNA–protein complexes were resolved on 10% native PAGE and visualized by ethidium bromide staining. **(D)** The CD spectrum of AzuR was recorded with increasing molar equivalents of zinc, which was an average of three scans. **(E)** EMSA of P_{nmtA} with AzuR in the presence of Zn^{2+}. Lane 1 contains 2 ng of P_{nmtA}. Lanes 2–7 contain DNA with 100 ng of AzuR in the presence of increasing concentrations of Zn^{2+} as indicated. EMSA of P_{nmtA} with AzuR protein with Zn^{2+} and Cd^{2+} in the absence of DTT **(F)** or in the presence of 1 mM DTT **(G)**. Lane 1 contains 2 ng of probe only. Lanes 2–8 contain P_{nmtA} with 100 ng of AzuR, lanes 3–5 with increasing concentrations of Zn^{2+}, and lanes 6–8 with increasing concentrations of Cd^{2+} as indicated in **(F,G)**. **(H)** EMSA of DNA probe with 70 ng of AzuR with 100 μM of divalent cations as indicated in the figure. All the reactions were performed in the absence of DTT.

sequence in the entire analyzed region. The regulation of the *znuABC* operon by the *zur* (*all2473*)/*furB* regulator has been demonstrated previously in *Anabaena* 7120 (Napolitano et al., 2012). Zur (zinc uptake regulator), known to be the master regulator for zinc homeostasis in *Anabaena* 7120, regulated the expression of genes involved in zinc homeostasis like *alr0830* (ZnuC), *alr0833* (ZnuA), and *all7621* (AztR). On analysis, we did not find *zur*-binding sequences upstream of the *azuR* ORF, indicating that the global regulator of zinc homeostasis, Zur, did not regulate *azuR* expression.

Anabaena 7120 AztA is transcriptionally regulated by AztR (belonging to the SmtB/ArsR family) by recognizing and binding to the inverted 12–2–12 imperfect repeat region. EMSA studies done with AztR and the *nmtA/bmtA* upstream region showed its binding *in vitro* (Tottey et al., 2007). Similar inverted repeat sequences identified by AztR and AzuR indicate that AztR and AzuR might be sharing the function of regulating AztA and NmtA. As described above, AztR belongs to the α3N group and AzuR to the α5 group of the SmtB/ArsR family. The α5 group members sense physiologically important metals like Zn^{2+}, Cu^{2+}, Co^{2+}, and Ni^{2+}, while the α3N group prefers larger, more thiophilic metal ions like Cd^{2+} or Pb^{2+} (Busenlehner et al., 2003). It is possible that AzuR and AztR preferred different groups of metal ions but could regulate both MT and efflux proteins, thus enabling the cell to respond to a wide range of metal ions.

AzuR Binds to the Upstream Sequence of *nmtA* Open Reading Frame

Electrophoretic mobility shift assays (EMSAs) were done in order to identify the AzuR-DNA binding site using a 100 bp fragment (P_{nmtA}) upstream of the *nmtA* gene (probe) containing the 12–2–12 inverted repeat sequence. The results showed that AzuR could bind and form complexes with P_{nmtA} in a concentration-dependent manner (**Figure 4A**). The Hill coefficient of AzuR binding to DNA was calculated to be 2.48 ± 1.14 (>1) (**Figure 4B**), which indicated positive cooperative binding (Hill, 1910). SmtB has been shown to bind to the *smt* O/P in a multimeric state (Erbe et al., 1995). The positive cooperative binding suggested that AzuR bound to the target DNA as an oligomer similar to that of SmtB. The specificity of DNA–protein binding was confirmed by using the *nmtA* gene or DNA-binding protein LexA from *Anabaena* 7120 (AnLexA) or other proteins like BSA and NmtA. No retardation in the mobility of P_{nmtA} was observed in the presence of AnLexA. Also, AzuR could not bind to the *nmtA* gene sequence, confirming that AzuR regulated *nmtA* expression by binding to the upstream sequence and not to its internal region (**Figure 4C**). Our results established the specific binding of P_{nmtA} with the AzuR protein.

SmtB senses metal ions through the α5 site. Zinc binding to residues present in this site allosterically regulates the DNA

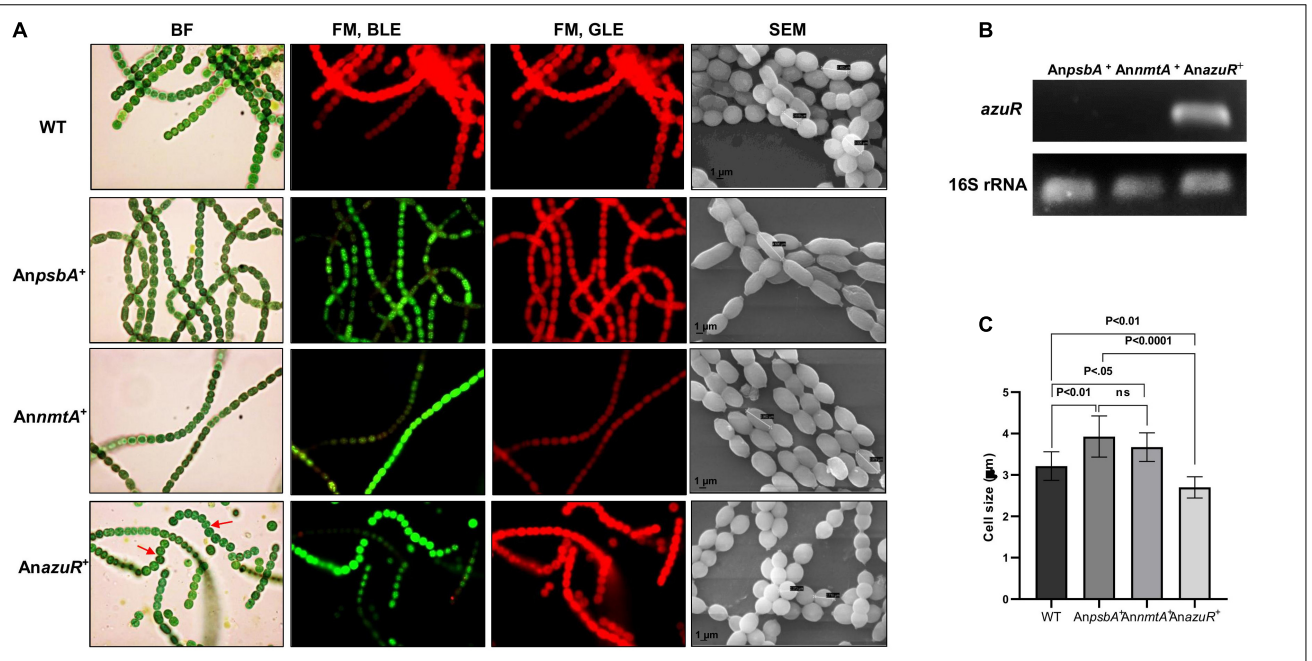

FIGURE 5 | Overexpression of AzuR in *Anabaena* 7120. **(A)** Effect of AzuR overexpression on the morphology of *Anabaena* 7120. Bright-field (BF) and FM photomicrographs under blue light excitation (BLE) (excitation 470 nm, emission 508 nm) and green light excitation (GLE) (excitation 520 nm, emission 680 nm) at ×1,500 magnification and scanning electron micrographs (SEMs) at ×100,000 magnification of WT, An*psbA*$^+$, An*nmtA*$^+$, and An*azuR*$^+$. Non-uniformity of cell stacking in An*azuR*$^+$ filament is indicated by red arrows in BF micrographs. **(B)** Confirmation of overexpression of *azuR* transcripts by RT-PCR. Total RNA of 1 µg was used for cDNA synthesis, which served as a template for PCR performed with *azuR*-specific primers. The amplified products were resolved on 1% agarose gel and visualized by ethidium bromide staining. The lower panel represents the products of 16S rRNA used as control. **(C)** Plot of average cell size of WT, An*psbA*$^+$, An*nmtA*$^+$, and An*azuR*$^+$ as analyzed by SEM is presented. One-way ANOVA was employed for calculating significance of the difference. Data shown here represent mean ± standard deviation (n = 13), ns, non-significant.

binding activity of SmtB to the *smtA* O/P region (VanZile et al., 2002) similar to other reported SmtB/ArsR repressors (Busenlehner et al., 2003). The bound Zn^{2+} changes the conformation of the protein, which inhibits the DNA binding. Since AzuR contains a similar α5 site, the conformational changes in AzuR as a result of metal binding was assessed by CD spectra of the protein in the presence of various concentrations of zinc (**Figure 4D**). The degree of the alpha helical region progressively decreased with increasing concentrations of zinc, indicating the changes in the secondary structure of AzuR in the presence of zinc. To further confirm whether zinc or other metal ions interfered with the AzuR DNA binding ability, EMSA was carried out in the presence of various metal ions. Dissociation of the DNA–AzuR complex was clearly evident with increasing concentrations of Zn^{2+} (**Figures 4E,F**). The interaction of Cd^{2+} with AzuR also disrupted the binding with P_{nmtA} (**Figure 4F**); however, the disruption was more prominent in the presence of DTT (**Figure 4G**), emphasizing the requirement of free sulfhydryls for Cd^{2+} binding to AzuR *in vitro*. It was interesting to see the reversal of AzuR binding to P_{nmtA} in the presence of other divalent metal ions like Cu^{2+}, Co^{2+}, Ni^{2+}, Pb^{2+}, and Mn^{2+} (**Figure 4H**), suggesting that AzuR not only senses toxic metal ions like Cd^{2+} and Pb^{2+} but also is capable of sensing essential metal ions like Zn^{2+}, Cu^{2+}, Co^{2+}, Ni^{2+}, and Mn^{2+}. EMSAs attempted with metals other than Zn^{2+} and Cd^{2+} in the presence of DTT showed visible precipitates in the binding reaction and hence were not included here.

We have previously observed the induction of *nmtA* in the presence of Cd^{2+}, Zn^{2+}, and Cu^{2+} (Divya et al., 2018). AzuR, therefore, can be proposed as a negative regulator of *nmtA* as it binds to regulatory DNA sequence in the absence of the metals and the repression is relieved in the presence of metal ions. In view of our results, it can be suggested that AzuR might have a larger role in the metal resistance system of *Anabaena* 7120.

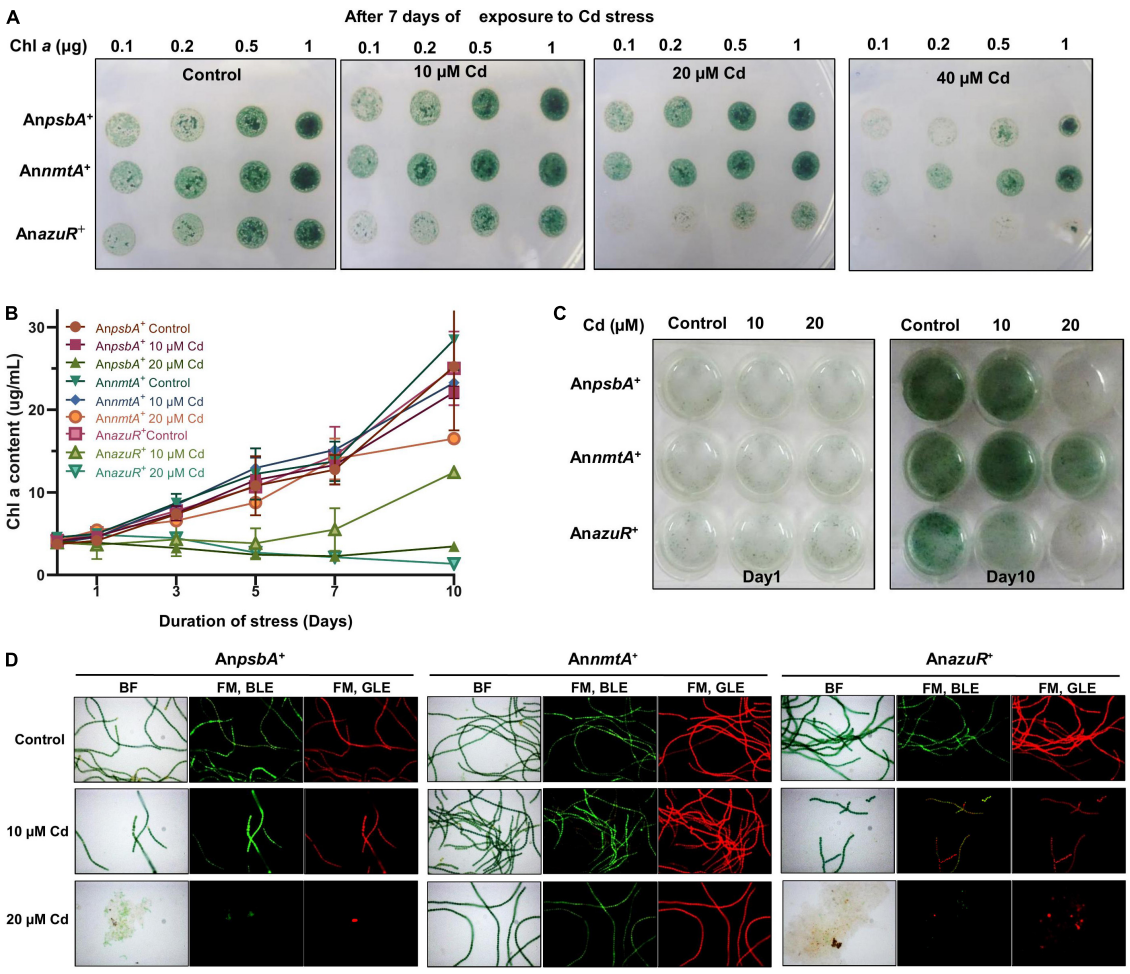

FIGURE 6 | Effect of AzuR overexpression on cadmium exposure. **(A)** Spot assays of An*psbA*$^+$, An*nmtA*$^+$, and An*azuR*$^+$ following exposure to cadmium stress for 7 days. The cell densities are indicated in terms of Chl*a* content (µg). **(B)** Growth kinetics of An*psbA*$^+$, An*nmtA*$^+$, and An*azuR*$^+$ as assessed by contents of Chl*a*. **(C)** The recombinant cultures were exposed to 10 or 20 µM cadmium for 10 days, and subsequently, the cultures were transferred to 12-well microtiter plate and photographed. **(D)** BF and FM microphotographs under BLE (excitation 470 nm, emission 508 nm) and GLE (excitation 520 nm, emission 680 nm) at ×600 magnification of An*psbA*$^+$, An*nmtA*$^+$, and An*azuR*$^+$ cells after 10 days of cadmium exposure.

Overexpression of *Anabaena* AzuR (Alr0831) and the Alterations in the Cell Morphology

Overexpression of transcriptional regulators has been previously studied in *Anabaena* sp. (Wu et al., 2007). To gain insights into the effect of AzuR on various characteristics or phenotype of *Anabaena* 7120, we constructed a recombinant strain of *Anabaena* 7120 that overexpressed AzuR. The *azuR* gene was cloned and overexpressed constitutively in *Anabaena* 7120 from a strong light-inducible promoter, P_{psbA}. GFP fluorescence of the downstream reporter gene was the first indication of successful *azuR* gene expression (**Figure 5A**). GFP fluorescence was visualized in *Anabaena* harboring an empty vector with P_{psbA} upstream of the *gfpmut2* gene, An*psbA*$^+$ and *Anabaena* overexpressing *nmtA*, and An*nmtA*$^+$ (**Figure 5A**). WT cells did not show any such GFP fluorescence (**Figure 5A**). The observation of few cells appearing red in the filaments of recombinant cells under FM and blue-light excitation (BLE) conditions could be due to partial or reduced GFP expression (**Figure 5A**). The filament length in An*azuR*$^+$, An*psbA*$^+$, and An*nmtA*$^+$ was comparable to that of WT *Anabaena* cells. The uniformity of the cell stacking in An*azuR*$^+$ filaments appeared to be compromised as compared to those in the filaments of WT, An*psbA*$^+$, and An*nmtA*$^+$. However, the Chl*a* fluorescence in An*azuR*$^+$ cells was intact and equivalent to that observed for WT, An*psbA*$^+$, or An*nmtA*$^+$ cells (**Figure 5A**). A substantial increase in *azuR* transcript level was seen in RT-PCR performed with RNA isolated from An*azuR*$^+$ as compared to An*psbA*$^+$ and An*nmtA*$^+$, thus confirming the overexpression of the regulator *in vivo* (**Figure 5B**).

Scanning electron microscopy (SEM) analysis of exponential-phase cells of An*azuR*$^+$ revealed a significant decrease in cell size with the cells showing spherical and globular morphology in contrast to An*psbA*$^+$, An*nmtA*$^+$, and WT cells (**Figure 5A**). The average cell size of An*azuR*$^+$ cells was found to be 2.70 ± 0.26 μm as compared to 3.92 ± 0.50 μm for An*psbA*$^+$ and 3.67 ± 0.34 μm for An*nmtA*$^+$. The cell size of An*azuR*$^+$ was lesser than the WT cells (3.214 ± 0.34 μm) (**Figure 5C**). Similar morphological changes regarding cell stacking and cell size were observed following overexpression of the global transcriptional regulator FurA in *Anabaena* 7120 (González et al., 2010). The elongated cell phenotype seen in An*psbA*$^+$ and An*nmtA*$^+$ cells could be because of stress owing to neomycin and heterologous GFP overexpression. The gross morphological changes in An*azuR*$^+$ as compared to the empty vector An*psbA*$^+$ indicate the possible involvement of AzuR in the regulation of genes involved in functions other than metal homeostasis. Chromatin immunoprecipitation (ChIP) studies need to be done in the future to identify direct binding of targets of AzuR in the *Anabaena* genome.

AzuR Overexpression Renders *Anabaena* 7120 Sensitive to Cadmium Stress

DNA binding studies by EMSA showed that AzuR bound to the upstream region of the *nmtA* ORF *in vitro*. Evaluation of *nmtA* expression levels in An*azuR*$^+$ by qRT-PCR with 16S rRNA as internal control showed the downregulation of *nmtA* expression in An*azuR*$^+$ by ∼32-fold as compared to its empty vector An*psbA*$^+$. These results are in agreement with the negative regulation of *nmtA* transcription by AzuR *in vivo*.

Previously, overexpression of NmtA in *Anabaena* 7120 had conferred tolerance to cadmium stress (Divya et al., 2018). Since the negative regulation of *nmtA* transcription by AzuR was observed here, we were interested to see the effect of the overexpression of AzuR on the cadmium tolerance ability of *Anabaena* 7120. We compared the response of cadmium stress in An*azuR*$^+$, An*psbA*$^+$, and An*nmtA*$^+$ cultures. Spot assays showed increased sensitivity of An*azuR*$^+$ cells to cadmium stress following 7 days of exposure (**Figure 6A**). Growth of An*azuR*$^+$ assessed in terms of Chl*a* content showed a substantial decrease even at concentrations of 10 μM cadmium as compared to An*psbA*$^+$ (**Figure 6B**). Growth kinetics studies in the presence of 20 μM cadmium resulted in almost complete bleaching of cultures of both An*psbA*$^+$ and An*azuR*$^+$ after 10 days of exposure to the stress (**Figure 6C**) including extensive cell lysis in An*azuR*$^+$ culture (**Figure 6D**). In contrast, filaments of An*nmtA*$^+$ appeared intact, long, and healthy on exposure to cadmium (**Figure 6D**). The spot assays and growth studies assessed in terms of Chl*a* contents (**Figures 6A–C**) of An*nmtA*$^+$ also supported the microscopy observations, which are in agreement with our previous results showing superior tolerance of An*nmtA*$^+$ against cadmium stress (Divya et al., 2018). The GFP and Chl*a* fluorescence were found to be unaffected in An*nmtA*$^+$ similar to An*azuR*$^+$ and An*psbA*$^+$ in the presence

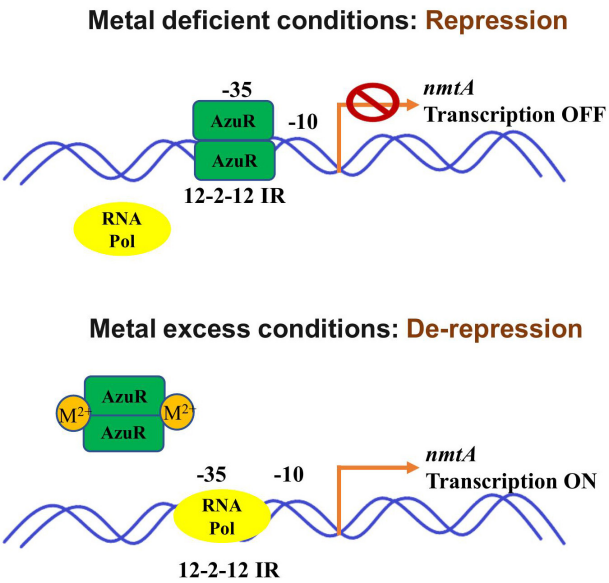

FIGURE 7 | Schematic representation of *Anabaena* NmtA regulation by AzuR. In the absence of metals, binding of AzuR to the upstream region of the *nmtA* ORF blocks the binding site for the RNA polymerase transcription initiation complex, resulting in repression of *nmtA*. At elevated concentrations of the metals, the binding of AzuR to DNA is disrupted as a result of structural changes in the protein due to metal binding. This leads to the induction of *nmtA* transcription in the presence of metals.

of cadmium (**Figure 6D**). The toxic effects of cadmium on the photosynthetic machinery have been studied extensively in *Synechocystis* PCC 6803 (Tóth et al., 2012). The major proteins involved in photosynthetic machinery include zinc-containing enzymes like carbonic anhydrase and sulfhydryl groups in ribulose-5-phosphate kinase among others that lose their activity by replacement with cadmium (Tóth et al., 2012). MTs play a key role in metal detoxification by directly binding to the toxic metal, which results in lesser bioavailability (Klaassen et al., 1999). This protects the essential metalloproteins from the toxic metal. Since AzuR overexpression leads to a decrease in basal *nmtA* expression, the protective role of NmtA in imparting cadmium tolerance could be obliterated, resulting in the susceptibility of An*azuR*$^+$ to cadmium stress, which was evident from its decreased growth and increased cell lysis. The susceptibility of Ana*zuR*$^+$ to cadmium stress confirms the negative regulation of *nmtA* expression at the physiological level in *Anabaena*.

CONCLUSION

We have characterized the role of AzuR belonging to the SmtB/ArsR family of metalloregulators in the regulation of *Anabaena* MT NmtA. The sequence analysis of AzuR (Alr0831) identified a distinct α5 metal binding site similar to that of SmtB. Although the *azuR* gene locus was found to be situated remotely away from the *nmtA* locus, analysis of the region upstream of the *nmtA* ORF identified the presence of 12–2–12 imperfect inverted repeats, which are reportedly important for binding of metalloregulators belonging to the SmtB/ArsR family of proteins. EMSAs showed AzuR binding with putative P_{nmtA}, indicating that NmtA is a regulatory target of AzuR. Dissociation of the protein–DNA complex was observed not only in the presence of toxic metal ions like Cd^{2+} and Pb^{2+} but also in the presence of essential metal ions like Zn^{2+}, Cu^{2+}, Co^{2+}, Ni^{2+}, and Mn^{2+}, which suggested negative regulation of metal-inducible *nmtA* expression by AzuR. On the basis of our findings, we propose a model for *Anabaena* NmtA regulation by AzuR (**Figure 7**). In the absence of metals or basal conditions, the binding of AzuR to the upstream region of the *nmtA* ORF blocks the binding site for the RNA polymerase transcription initiation complex, resulting in the repression of *nmtA*. At elevated concentrations of the metals, the binding of AzuR to DNA is disrupted as a result of conformational changes in the protein resulting from metal binding. This leads to the induction of *nmtA* transcription in the presence of metals as seen earlier in our studies (Divya et al., 2018). The sensing of a large number of metal ions implies a greater role of AzuR in the modulation of metal ions in the intracellular environment in *Anabaena* 7120.

Although we have largely focused on the role of AzuR in MT regulation, the presence of *cis*-regulatory elements important for repressor binding at several locations in the *Anabaena* 7120 genome indicates that AzuR might act as a global transcriptional regulator. It will be interesting to study the role of AzuR beyond metal homeostasis. The similar inverted repeats recognized by AztR (repressor of CPx-ATPase) and AzuR (repressor of MT) suggest that these two repressors could share regulation of their respective effector genes *in vivo*. The direct interaction between the two regulators and possibly the cross-talk between the two processes of metal sequestration and efflux would help us to understand the regulation of the metal homeostasis system in *Anabaena*.

DATA AVAILABILITY STATEMENT

The original contributions presented in the study are included in the article/supplementary material, further inquiries can be directed to the corresponding author.

AUTHOR CONTRIBUTIONS

CA conceived, designed, and supervised the research. TVD performed the experiments. CA and TVD analyzed the data, wrote the draft of the manuscript, and revised the manuscript. Both authors approved the submitted version.

ACKNOWLEDGMENTS

We wish to acknowledge SAIF, IIT Bombay, for protein identification by O-HRLC-MS. We are grateful to Arvind Kumar, MBD, BARC, for *Anabaena* LexA protein. We thank Manisha Banerjee, MBD, BARC, for extending help in CD spectroscopy and Gagan Deep Gupta and Hiral Mistry, RB & HSD, BARC, for help in size-exclusion chromatography. We gratefully acknowledge H. S. Misra, MBD, BARC, for the support and encouragement during the course of this study.

REFERENCES

Allen, M. M. (1968). Simple conditions for growth of unicellular blue-green algae on plates. *J. Phycol.* 4, 1–4. doi: 10.1111/j.1529-8817.1968.tb04667.x

Andrews, G. K. (2000). Regulation of metallothionein gene expression by oxidative stress and metal ions. *Biochem. Pharmacol.* 59, 95–104. doi: 10.1016/S0006-2952(99)00301-9

Bertini, G., Gray, H. B., Gray, H., Valentine, J. S., Stiefel, E. I., and Stiefel, E. (2007). *Biological Inorganic Chemistry: Structure and Reactivity*. Melville, NY: University Science Books.

Blindauer, C. A. (2008). Zinc-handling in cyanobacteria: an update. *Chem. Biodivers.* 5, 1990–2013. doi: 10.1002/cbdv.200890183

Blindauer, C. A. (2011). Bacterial metallothioneins: past, present, and questions for the future. *J. Biol. Inorg. Chem.* 16, 1011–1024. doi: 10.1007/s00775-011-0790-y

Blindauer, C. A., and Leszczyszyn, O. I. (2010). Metallothioneins: unparalleled diversity in structures and functions for metal ion homeostasis and more. *Nat. Prod. Rep.* 27, 720–741. doi: 10.1039/B906685N

Bose, M., Slick, D., Sarto, M. J., Murphy, P., Roberts, D., Roberts, J., et al. (2006). Identification of SmtB/ArsR cis elements and proteins in archaea using the prokaryotic intergenic exploration database (PIGED). *Archaea* 2, 39–49. doi: 10.1155/2006/837139

Busenlehner, L. S., Cosper, N. J., Scott, R. A., Rosen, B. P., Wong, M. D., and Giedroc, D. P. (2001). Spectroscopic properties of the metalloregulatory Cd (II) and Pb (II) sites of S. aureus pI258 CadC. *Biochemistry* 40, 4426–4436. doi: 10.1021/bi010006g

Busenlehner, L. S., Pennella, M. A., and Giedroc, D. P. (2003). The SmtB/ArsR family of metalloregulatory transcriptional repressors: structural insights into prokaryotic metal resistance. *FEMS Microbiol. Rev.* 27, 131–143. doi: 10.1016/S0168-6445(03)00054-8

Chandrangsu, P., Rensing, C., and Helmann, J. D. (2017). Metal homeostasis and resistance in bacteria. *Nat. Rev. Microbiol.* 15, 338–350. doi: 10.1038/nrmicro.2017.15

Chaurasia, A. K., Parasnis, A., and Apte, S. K. (2008). An integrative expression vector for strain improvement and environmental applications of the nitrogen fixing cyanobacterium, *Anabaena* sp. strain PCC7120. *J. Microbiol. Methods* 73, 133–141. doi: 10.1016/j.mimet.2008.01.013

Divya, T. V., Chandwadkar, P., and Acharya, C. (2018). NmtA, a novel metallothionein of *Anabaena* sp. strain PCC 7120 imparts protection against cadmium stress but not oxidative stress. *Aquat. Toxicol.* 199, 152–161. doi: 10.1016/j.aquatox.2018.03.035

Elhai, J., Vepritskiy, A., Muro-Pastor, A. M., Flores, E., and Wolk, C. P. (1997). Reduction of conjugal transfer efficiency by three restriction activities of *Anabaena* sp. strain PCC 7120. *J. Bacteriol.* 179, 1998–2005. doi: 10.1128/jb.179.6.1998-2005.1997

Erbe, J. L., Taylor, K. B., and Hall, L. M. (1995). Metalloregulation of the cyanobacterial smt locus: indentification of SmtB binding sites and direct interaction with metals. *Nucleic Acids Res.* 23, 2472–2478. doi: 10.1093/nar/23.13.2472

Finney, L. A., and O'Halloran, T. V. (2003). Transition metal speciation in the cell: insights from the chemistry of metal ion receptors. *Science* 300, 931–936. doi: 10.1126/science.1085049

González, A., Bes, M. T., Barja, F., Peleato, M. L., and Fillat, M. F. (2010). Overexpression of FurA in *Anabaena* sp. PCC 7120 reveals new targets for this regulator involved in photosynthesis, iron uptake and cellular morphology. *Plant Cell Physiol.* 51, 1900–1914. doi: 10.1093/pcp/pcq148

Habjanič, J., Mathew, A., Eberl, L., and Freisinger, E. (2020). Deciphering the enigmatic function of *Pseudomonas* metallothioneins. *Front. Microbiol.* 11:1709. doi: 10.3389/fmicb.2020.01709

Hill, A. V. (1910). The possible effects of the aggregation of the molecules of haemoglobin on its dissociation curves. *J. Physiol.* 40, 4–7.

Huckle, J. W., Morby, A. P., Turner, J. S., and Robinson, N. J. (1993). Isolation of a prokaryotic metallothionein locus and analysis of transcriptional control by trace metal ions. *Mol. Microbiol.* 7, 177–187. doi: 10.1111/j.1365-2958.1993.tb01109.x

Klaassen, C. D., Liu, J., and Choudhuri, S. (1999). Metallothionein: an intracellular protein to protect against cadmium toxicity. *Annu. Rev. Pharmacool. Toxicol.* 39, 267–294. doi: 10.1146/annurev.pharmtox.39.1.267

Kumar, S., Stecher, G., Li, M., Knyaz, C., and Tamura, K. (2018). MEGA X: molecular evolutionary genetics analysis across computing platforms. *Mol. Biol. Evol.* 35:1547. doi: 10.1093/molbev/msy096

Liu, T., Chen, X., Ma, Z., Shokes, J., Hemmingsen, L., Scott, R. A., et al. (2008). A Cu(I)-sensing ArsR family metal sensor protein with a relaxed metal selectivity profile. *Biochemistry* 47, 10564–10575. doi: 10.1021/bi801313y

Liu, T., Golden, J. W., and Giedroc, D. P. (2005). A zinc (II)/lead (II)/cadmium (II)-inducible operon from the cyanobacterium *Anabaena* is regulated by AztR, an α3N SmtB/ArsR metalloregulator. *Biochemistry* 44, 8673–8683. doi: 10.1021/bi050450+

Liu, T., Nakashima, S., Hirose, K., Shibasaka, M., Katsuhara, M., Ezaki, B., et al. (2004). A novel cyanobacterial SmtB/ArsR family repressor regulates the expression of a CPx-ATPase and a metallothionein in response to both Cu (I)/Ag (I) and Zn (II)/Cd (II). *J. Biol. Chem.* 279, 17810–17818. doi: 10.1074/jbc.M310560200

Madeira, F., Park, Y. M., Lee, J., Buso, N., Gur, T., Madhusoodanan, N., et al. (2019). The EMBL-EBI search and sequence analysis tools APIs in 2019. *Nucleic Acids Res.* 47, W636–W641. doi: 10.1093/nar/gkz268

Mrázek, J., and Xie, S. (2006). Pattern locator: a new tool for finding local sequence patterns in genomic DNA sequences. *Bioinformatics* 22, 3099–3100. doi: 10.1093/bioinformatics/btl551

Napolitano, M., Rubio, M. Á, Santamaria-Gomez, J., Olmedo-Verd, E., Robinson, N. J., and Luque, I. (2012). Characterization of the response to zinc deficiency in the cyanobacterium *Anabaena* sp. strain PCC 7120. *J. Bacteriol.* 194, 2426–2436. doi: 10.1128/JB.00090-12

Osman, D., and Cavet, J. S. (2010). Bacterial metal-sensing proteins exemplified by ArsR-SmtB family repressors. *Nat. Prod. Rep.* 27, 668–680. doi: 10.1039/B906682A

Palmiter, R. D. (1987). "Molecular biology of metallothionein gene expression," in *Metallothionein II. Experientia Supplementum*, Vol. 52, eds J. H. R. Kägi and Y. Kojima (Basel: Birkhäuser), doi: 10.1007/978-3-0348-6784-9_4

Perez-Iratxeta, C., and Andrade-Navarro, M. A. (2008). K2D2: estimation of protein secondary structure from circular dichroism spectra. *BMC Struct. Biol.* 8:25. doi: 10.1186/1472-6807-8-25

Pinto, F., Pacheco, C. C., Ferreira, D., Moradas-Ferreira, P., and Tamagnini, P. (2012). Selection of suitable reference genes for RT-qPCR analyses in cyanobacteria. *PLoS One* 7:e34983. doi: 10.1371/journal.pone.0034983

Rees, D. C. (2002). Great metalloclusters in enzymology. *Annu. Rev. Biochem.* 71, 221–246. doi: 10.1146/annurev.biochem.71.110601.135406

Roy, A., Kucukural, A., and Zhang, Y. (2010). I-TASSER: a unified platform for automated protein structure and function prediction. *Nat. Protoc.* 5, 725–738. doi: 10.1038/nprot.2010.5

Saha, R. P., Samanta, S., Patra, S., Sarkar, D., Saha, A., and Singh, M. K. (2017). Metal homeostasis in bacteria: the role of ArsR–SmtB family of transcriptional repressors in combating varying metal concentrations in the environment. *Biometals* 30, 459–503. doi: 10.1007/s10534-017-0020-3

Salamov, V. S. A., and Solovyevand, A. (2011). "Automatic annotation of microbial genomes and metagenomic sequences," in *Metagenomics and Its Applications in Agriculture, Biomedicine and Environmental Studies*, ed. R. W. Li (Hauppauge, NY: Nova Science Publishers), 61–78.

Thelwell, C., Robinson, N. J., and Turner-Cavet, J. S. (1998). An SmtB-like repressor from *Synechocystis* PCC 6803 regulates a zinc exporter. *Proc. Natl. Acad. Sci. U.S.A.* 95, 10728–10733.

Thompson, J. D., Higgins, D. G., and Gibson, T. J. (1994). CLUSTAL W: improving the sensitivity of progressive multiple sequence alignment through sequence weighting, position-specific gap penalties and weight matrix choice. *Nucleic Acids Res.* 22, 4673–4680. doi: 10.1093/nar/22.22.4673

Tóth, T., Zsiros, O., Kis, M., Garab, G., and Kovacs, L. (2012). Cadmium exerts its toxic effects on photosynthesis via a cascade mechanism in the cyanobacterium, *Synechocystis* PCC 6803. *Plant Cell Environ.* 35, 2075–2086. doi: 10.1111/j.1365-3040.2012.02537.x

Tottey, S., Harvie, D. R., and Robinson, N. J. (2005). Understanding how cells allocate metals using metal sensors and metallochaperones. *Acc. Chem. Res.* 38, 775–783. doi: 10.1021/ar0300118

Tottey, S., Harvie, D. R., and Robinson, N. J. (2007). "Understanding how cells allocate metals," in *Molecular Microbiology of Heavy Metals. Microbiology Monographs*, Vol. 6, eds D. H. Nies and S. Silver (Berlin: Springer), doi: 10.1007/7171_2006_072

Turner, J. S., Glands, P. D., Samson, A. C., and Robinson, N. J. (1996). Zn 2+-sensing by the cyanobacterial metallothionein repressor SmtB: different motifs mediate metal-induced protein-DNA dissociation. *Nucleic Acids Res.* 24, 3714–3721. doi: 10.1093/nar/24.19.3714

Turner, J. S., and Robinson, N. J. (1995). Cyanobacterial metallothioneins: biochemistry and molecular genetics. *J. Ind. Microbiol.* 14, 119–125. doi: 10.1007/BF01569893

VanZile, M. L., Chen, X., and Giedroc, D. P. (2002). Allosteric negative regulation of smt O/P binding of the zinc sensor, SmtB, by metal ions: a coupled equilibrium analysis. *Biochemistry* 41, 9776–9786. doi: 10.1021/bi020178t

VanZile, M. L., Cosper, N. J., Scott, R. A., and Giedroc, D. P. (2000). The zinc metalloregulatory protein *Synechococcus* PCC7942 SmtB binds a single zinc ion per monomer with high affinity in a tetrahedral coordination geometry. *Biochemistry* 39, 11818–11829. doi: 10.1021/bi001140o

Waldron, K. J., and Robinson, N. J. (2009). How do bacterial cells ensure that metalloproteins get the correct metal? *Nat. Rev. Microbiol.* 7, 25–35. doi: 10.1038/nrmicro2057

Waterhouse, A. M., Procter, J. B., Martin, D. M., Clamp, M., and Barton, G. J. (2009). Jalview Version 2—a multiple sequence alignment editor and analysis workbench. *Bioinformatics* 25, 1189–1191. doi: 10.1093/bioinformatics/btp033

Wu, X., Lee, D. W., Mella, R. A., and Golden, J. W. (2007). The *Anabaena* sp. strain PCC 7120 asr1734 gene encodes a negative regulator of heterocyst development. *Mol. Microbiol.* 64, 782–794. doi: 10.1111/j.1365-2958.2007.05698.x

Yang, J., Yan, R., Roy, A., Xu, D., Poisson, J., and Zhang, Y. (2015). The I-TASSER Suite: protein structure and function prediction. *Nat. Methods* 12, 7–8. doi: 10.1038/nmeth.3213

Yoon, H. S., and Golden, J. W. (1998). Heterocyst pattern formation controlled by a diffusible peptide. *Science* 282, 935–938. doi: 10.1126/science.282.5390.935

Zhang, Y. (2008). I-TASSER server for protein 3D structure prediction. *BMC Bioinformatics* 9:40. doi: 10.1186/1471-2105-9-40

Conflict of Interest: The authors declare that the research was conducted in the absence of any commercial or financial relationships that could be construed as a potential conflict of interest.

Publisher's Note: All claims expressed in this article are solely those of the authors and do not necessarily represent those of their affiliated organizations, or those of the publisher, the editors and the reviewers. Any product that may be evaluated in this article, or claim that may be made by its manufacturer, is not guaranteed or endorsed by the publisher.

frontiers in Microbiology

ORIGINAL RESEARCH
published: 28 January 2022
doi: 10.3389/fmicb.2021.784575

Genomic Insights Into Cadmium Resistance of a Newly Isolated, Plasmid-Free *Cellulomonas* sp. Strain Y8

Jinghao Chen[1,2†], Likun Wang[1†], Wenjun Li[1,2], Xin Zheng[1] and Xiaofang Li[1]*

[1] *Hebei Key Laboratory of Soil Ecology, Center for Agricultural Resources Research, Institute of Genetics and Developmental Biology, Chinese Academy of Sciences, Shijiazhuang, China,* [2] *University of Chinese Academy of Sciences, Beijing, China*

Our current knowledge on bacterial cadmium (Cd) resistance is mainly based on the functional exploration of specific Cd-resistance genes. In this study, we carried out a genomic study on Cd resistance of a newly isolated *Cellulomonas* strain with a MIC of 5 mM Cd. Full genome of the strain, with a genome size of 4.47 M bp and GC-content of 75.35%, was obtained through high-quality sequencing. Genome-wide annotations identified 54 heavy metal-related genes. Four potential Cd-resistance genes, namely *zntAY8*, *copAY8*, *HMTY8,* and *czcDY8*, were subjected to functional exploration. Quantitative PCR determination of *in vivo* expression showed that *zntAY8, copAY8,* and *HMTY8* were strongly Cd-inducible. Expression of the three inducible genes against time and Cd concentrations were further quantified. It is found that *zntAY8* responded more strongly to higher Cd concentrations, while expression of *copAY8* and *HMTY8* increased over time at lower Cd concentrations. Heterologous expression of the four genes in Cd-sensitive *Escherichia coli* led to different impacts on hosts' Cd sorption, with an 87% reduction by *zntAY8* and a 3.7-fold increase by *HMTY8*. In conclusion, a Cd-resistant *Cellulomonas* sp. strain was isolated, whose genome harbors a diverse panel of metal-resistance genes. Cd resistance in the strain is not controlled by a dedicated gene alone, but by several gene systems collectively whose roles are probably time- and dose-dependent. The plasmid-free, high-GC strain Y8 may provide a platform for exploring heavy metal genomics of the *Cellulomonas* genus.

Keywords: cadmium resistance, *Cellulomonas* sp., *zntA*, *copA*, gene expression, full genome

OPEN ACCESS

Edited by:
Rob Van Houdt,
Belgian Nuclear Research Centre, Belgium

Reviewed by:
Sylvia McDevitt,
Skidmore College, United States
Norma Cecilia Martinez-Gomez,
University of California, Berkeley, United States

***Correspondence:**
Xiaofang Li
xfli@sjziam.ac.cn

† These authors have contributed equally to this work

Specialty section:
This article was submitted to Antimicrobials, Resistance and Chemotherapy, a section of the journal Frontiers in Microbiology

Received: *28 September 2021*
Accepted: *17 December 2021*
Published: *28 January 2022*

Citation:
Chen J, Wang L, Li W, Zheng X and Li X (2022) Genomic Insights Into Cadmium Resistance of a Newly Isolated, Plasmid-Free Cellulomonas sp. Strain Y8. Front. Microbiol. 12:784575. doi: 10.3389/fmicb.2021.784575

INTRODUCTION

Microbial Cd resistance has been extensively studied in the past decades. A *Staphylococcus aureus* strain with plasmid-borne Cd resistance was first reported in 1968 (Sweeney and Cohen, 1968). Since then, a number of studies were conducted on bacterial species like *S. aureus*, *Cupriavidus metallidurans*, *Escherichia coli,* and *Bacillus subtilis* for Cd-resistance (Nies et al., 1989; Nucifora et al., 1989; Rensing et al., 1997; Solovieva and Entian, 2002). More recently, strains with superior Cd tolerance were isolated for various purpose (Baati et al., 2020; Kotoky and Pandey, 2020; Minari et al., 2020; Shi et al., 2020). For example, the *Cupriavidus* sp. strain WS2 has a minimal inhibitory

concentration of 8 mM Cd (Shi et al., 2020), while that of the wild-type *E. coli* strain BL21 is below 1.2 mM (Qin et al., 2019).

Our current knowledge on genetic mechanisms of bacterial Cd tolerance is based on the exploration of specific resistance genes or operons like *cad*, *czc,* and *znt* (Diels et al., 1995; Binet and Poole, 2000; Munkelt et al., 2004; Okkeri and Haltia, 2006; Monchy et al., 2007). All of them are found to play a vital role in the translocation/extrusion of intracellular Cd. They mainly fall into three categories including P-type ATPases, RND-driven efflux systems and cation diffusion facilitators (CDF; Nies, 2003). P-type ATPases and CDF transporters may function in transporting Cd from cytoplasm to periplasm (Paulsen and Saier, 1997; Busch and Saier, 2002; Saier et al., 2006; Scherer and Nies, 2009; Shamim et al., 2014), while RND-driven efflux systems such as CzcCBA probably export metals from periplasm to outside the cells (Legatzki et al., 2003; Stroebel et al., 2007). This two-step exporting mechanism by transporters of overlapping substrate specificity was commonly applied in the exporting of toxic substances in G^- bacteria (Tal and Schuldiner, 2009). In G^+ bacteria where lack an outer membrane for the RND-driven efflux system to work, P-type ATPases are more common. Members of the P_{IB}-family ATPases contain six to eight transmembrane (TM) helices, an ATP-binding domain and some strictly conserved motifs like the CPC motif (Arguello, 2003; Argüello et al., 2007; Smith et al., 2014). P_{IB}-type ATPases can both transport monovalent cations such as Cu^+ and Ag^+ (e.g., CopA) (Sitsel et al., 2015; Purohit et al., 2018) and divalent cations such as Zn^{2+}, Cd^{2+}, and Pb^{2+} (e.g., CadA and ZntA) (Sharma et al., 2000; Wang et al., 2014; Sitsel et al., 2015). Some ATPases (e.g., CzcP) containing a conserved SPC motif are also known to transport Cd^{2+}, Co^+, Zn^{2+}, Cu^+, and Fe^{2+} (Scherer and Nies, 2009; Zielazinski et al., 2012; Smith et al., 2015; Patel et al., 2016). With the advent of the omics era (Methé and Lasa, 2013), there is a need to explore genetic systems for bacterial Cd resistance at the genomic level.

In this study, we aim to examine the genetic determinants for Cd resistance of a newly isolated *Cellulomonas* sp. strain Y8 at a genome-scale. A highly Cd-tolerant bacterial strain Y8 was isolated from a farmland soil and identified as a member of the *Cellulomonas* genus. Two Cd-resistant *Cellulomonas* sp. strains have been reported currently (Dell'Amico et al., 2005; Fouché, 2018) while little is known about their genetic mechanism. Metabolic potentials, Cd resistance and cell morphology were tested to characterize the strain. A high-quality full genome of strain Y8 was obtained through next-generation sequencing, based on which a genome-wide screening of metal-resistance genes were conducted. Four genes with Cd-resistance potential were subjected to quantitative PCR determination of *in vivo* expression in response to Cd stress, and heterologous expression in *E. coli* for functional verification. Of them, two potential P_{IB}–type ATPases *zntA* and *copA* and an ACR3 family gene *HMT* were strongly Cd-inducible, but differentially expressed over time course and against Cd concentrations. Besides, *zntAY8* reduced *E. coli*'s intracellular Cd by 87%, while *copA* and *HMT* increased that by 3.2- and 3.7-folds, respectively. The strain Y8 characterized here can be a platform for exploring heavy metal genomics of the *Cellulomonas* genus.

MATERIALS AND METHODS

Strain Isolation and Identification

Soil samples used in this study were collected from an agro-ecosystem experimental station (37°53′ N, 114°41′ E). Soil suspensions were vortexed for 60 s, followed by serial dilution and spreading onto Luria-Bertani agar medium (tryptone 10.00 g/L, yeast extract 5 g/L, $NaCl_2$ 10.00 g/L, Agar 15.00 g/L) with 16 mM $CdCl_2$. Plates were incubated at 30°C for 90 days, and single colonies from the plates were transferred to new LB medium plates for purification.

Genomic DNA of isolates was extracted using the PureLink Pro 96 Genomic DNA Purification Kit (Thermo Fisher Scientific, United States) following the manufacture's instruction. The universal primers 27f and 1492r were used for 16S rRNA gene amplification (Weisburg et al., 1991). PCR products were purified after agarose gel electrophoresis and then sequenced for phylogenetic identification. Sequence alignment was performed using ClustalX (Larkin et al., 2007). DNA-DNA hybridization (DDH) and average nucleotide identity (ANI) calculation were performed using GGDC 2.1 and ANI calculator, respectively (Meier-Kolthoff et al., 2013; Jain et al., 2018).

A representative strain, namely Y8, was subjected to phenotypic characterization by BeNa Culture Collection (BNCC), Beijing, China using a VITEK 2 GP kit (Terhune, 2017). Antibiotic resistance test was performed on LB medium supplemented with antibiotics at the common working concentrations.

Full-Genome Sequencing

High-throughput sequencing was performed for strain Y8 to obtain its complete genome. The sequencing and genome assembly methods have been reported elsewhere (Chen et al., 2019b). Briefly, the genome sequencing is completed by Genewiz (Nanjing, CN) using the Illumina HiSeq (San Diego, United States) and PacBio RS II platforms (Menlo Park, United States) according to standard protocols (Chen et al., 2019a).

Genome Annotation

Prodigal v2.6.3 (Tennessee, United States) was used to explore coding genes following the developer's instruction. Transfer RNAs (tRNAs) were detected in the genome using tRNAscan-SE v2.0 (Santa Cruz, United States) with default parameters (Lowe and Eddy, 1997). rRNA genes were identified by RNAmmer (Oslo, Norway) (Lagesen et al., 2007). Protein-coding genes were assigned using BLASTp against five mainstream databases including the Non-redundant Protein Database (Pruitt et al., 2005), Kyoto encyclopedia of genes and genomes (KEGG) (Kanehisa and Goto, 2000), Cluster of Orthologous Groups of proteins (KOG) (Tatusov et al., 1997), Gene Ontology (GO) (Harris et al., 2004), and Carbohydrate-Active enZYmes Database (Lombard et al., 2014). Clusters of orthologous genes (COGs) were retrieved from Y8, *C. hominis* and *C. denverensis* genomes using the OrthoFinder 1.1.8 stand-alone tool (Oxford, United Kingdom) (Emms and Kelly, 2015). Whole-genome based

phylogenetic tree was constructed using Composition Vector Tree Version 3 (CVTree3)[1] according to the online manual (Zuo et al., 2018). Circular representation of Y8's genome was performed using Circos (Krzywinski et al., 2009), where the calculation of average G+C content and GC skew was completed using an in-house Perl v5.28 scripts.

Cadmium Resistance Characterization

Minimum inhibitory concentration (MIC) test was conducted using the plate diluting method (Aleem et al., 2003). The MIC was defined as the lowest concentration that completely inhibited visible bacterial growth after overnight incubation (Andrews, 2001). Growth curves were determined using the method described in our previous study with minor modifications (Zheng et al., 2019; Xing et al., 2020). A Cd gradient of 0, 1, 2, 3, 4, 5, 6, and 7 mM in LB medium plates was used to test growth of strain Y8. Cell density was measured by a biophotometer (Eppendorf, Germany) at a 2-h interval until the control reached the stationary phase.

Cell morphology was observed by scanning electron microscopy (SEM). Briefly, cells were incubated overnight in LB liquid medium with or without Cd (0, 1, and 4 mM) for 4 h. Harvested cells were fixed with glutaraldehyde (2%, final conc.) overnight at 4°C. Fixative and salts were washed from the samples by centrifuging and re-suspending the pellet in Millipore® water. A total of 50 μl re-suspensions were incubated in a 1.5 ml tube at room temperature for 1 h. Samples were dehydrated by soaking sequentially in ethanol solutions with five gradient concentrations of 30, 46, 63, 82, and 96% for 5 min each. After critical point drying (CPD, Quorum K850), images (FEI scanning electron microscope, HITACHI Regulus 8100) were taken following the standard instructions.

Cd bioaccumulation capacity of Y8 was determined following the method described elsewhere (Zheng et al., 2019). Briefly, the strain Y8 were cultured overnight, then transferred into 100 ml LB liquid medium with 10 μM of Cd. After 48 h incubation, cells were harvested by centrifugation and dried. The sample was digested using 8 ml of 65% HNO_3, and dissolved in 2 ml Millipore® water for Cd determination using a Zeenit 700 P atomic absorption spectrometer (Analytik Jena, Germany) equipped with a flame atomizer.

Screening of Cadmium Resistance Genes

Candidate metal transport/resistance genes were examined genome-wide based on the genome annotation. These genes were further analyzed following the criteria of gene length, functional domains/motifs and operon organization. Known Cd resistance genes are normally with a length > 900 bp, contain common metal binding motifs like CxC, and mostly are arranged in operons and not constitutively expressed (Das et al., 2016). Domain analysis was performed using Pfam 33.1 (El-Gebali et al., 2019). Transmembrane helices in proteins were predicted using TMHMM Server v. 2.0 (Krogh et al., 2001). Phylogenetic analysis was performed using MEGA 7.0 (Kumar et al., 2016). Operons were predicted via FGENESB (Solovyev and Asaf, 2011). All the candidate genes were manually re-checked by searching them against the NCBI Nr database (Pruitt et al., 2005) and UniProt database (UniProt Consortium, 2019).

RNA Extraction and cDNA Library Construction

Expression levels of four candidate Cd-resistance genes in strain Y8 in response to Cd stress were determined. A Cd gradient of 1, 4, and 16 mM were added directly upon inoculation (OD_{600} = 0.1), and cell samples were collected at different time points (0, 0.5, 3, 6, and 9 h) for RNA extraction. Controls were without Cd added. RNA was isolated using the MoBio microbial RNA isolation kit according to manufacturer's instructions. Purified RNA was eluted in nuclease free water and 1 mg of RNA from each Cd treatment group was subjected to DNase treatment (30 min, 37°C). cDNA synthesis reaction was conducted with a cDNA synthesis kit (Qiagen).

Real-Time PCR

Real-time PCR was performed in 20 μl reaction volumes containing 10 μl of the 2 × SYBR Green mastermix (ABI). The thermal conditions for PCR reactions include initial denaturation for 10 min at 95°C, followed by 40 cycles of denaturation for 15 s at 95°C and annealing for 60 s at 60°C for gene amplifications. Real-time PCR was carried out in an ABI 7000 PCR system and melting curve analysis was performed within the temperature range of 67–95°C. The Ct values were determined, and *thyA* gene was used as an internal reference (Yan et al., 2019).

Chemical Synthesis of Candidate Genes

Chemical synthesis of all candidate gene was completed by Sangon Shanghai, China. The vector pTR modified based on pUC19 (Li et al., 2020) was employed to carry the four potential resistance genes. The pTR vector contains a tobacco plastid 16S ribosomal RNA gene (P16S) promoter, multiple cloning sites and a *rrnB* T1 terminator (BBa_B0010) located between the restriction endonuclease (RE) site *Hin*dIII and *Eco*RI. All selected genes were reverse transcript to 5′–3′ direction. For sequences with locally excessive G+C content (>90%), the codons were optimized to better translate them in *E. coli*. Meanwhile, suitable RE sites were added to both ends of all the sequences. All of recombinants were enzymatically digested according to their designed RE sites, and sequenced to double-check the quality.

Functional Verification of Candidate Cadmium Resistance Genes

Four recombinants containing the synthesized gene, pTR-*zntAY8,* pTR-*copAY8*, pTR-*HMTY8,* and pTR-*czcDY8*, were subjected to functional tests via heterologous expression in *E. coli* DH5α (F-, Φ80, lacZ, ΔM15, Δ *lacU*169, recA1, *endA1*, *hsdR17*, *supE44*, *thi-1*, *gyrA*, *relA1*, λ*pir*). Cd-sensitive *E. coli* RW 3110 (F-, λ^-, *IN(rrnD-rrnE)1*, *zntA1(CdS,ZnS)::kan*, *rph-1*) was employed as host cells for further functional verification (Li et al., 2020). The plasmid pTR without any candidate genes was transformed into RW 3110 to generate a negative control. The threshold Cd

[1]http://cvtree.online/v3/cvtree/

concentration used to test transformants for Cd resistance is 0.3 mM, which was determined in our previous study (Li et al., 2020). The grow curve of all transformants was tested as follows. Briefly, transformant cells were incubated overnight. Aliquots of cells were then inoculated into 100 ml LB liquid medium supplied with Cd with a starting OD_{600} of 0.1, and incubated at 37°C. The optical density at 600 nm was measured by spectrophotometer every hour for 12 h.

Metal bioaccumulation assay was conducted according to our previous study with minor modifications (Xing et al., 2020). Four transformants and the control were cultured overnight. Five ml of each was then inoculated into 100 ml LB liquid medium (10 μM, Cd) and incubated for 6 h. The cells were collected by centrifugation at 4,000 × g, rinsed triple times using water rigorously and subsequently dried, weighed, and digested in 7 ml of 65% HNO_3. The digested mixture was dissolved in 2 ml Millipores water and the metal content was measured using ICP-MS. Certified reference material laver (GWB10023, certified by the Institute of Geophysical and Geochemical Exploration, China) was used as a standard reference material for Cd, Ni, Cu, and Zn determination.

Data Analysis and Availability

Statistical analysis was performed with SPSS (IBM, Armonk, United States) and Office suits (Microsoft, Redmond, United States). Full genome of strain Y8 can be accessed via the accession number CP041203.1 in the NCBI database.

RESULTS

The Morphological and Physiological Features of *Cellulomonas* Strain Y8

Strain Y8 was the only isolate identified in this study that could form colonies on solid LB plate supplied with 16 mM of Cd after a 90-day incubation. Cells of Y8 were seen to be aerobic, rod-shaped and Gram-positive. After 48 h of incubation on solid LB agar plate at 30°C, the colonies produced by this bacterium (0.5–1 mm in diameter) were smooth, opaque, moist, and pale yellow in color.

A BLAST search of Y8's 16S rRNA gene showed a 99.57% similarity to that of *C. pakistanensis* NCCP-11, 99.13% to *C. hominis* JCM 12133, and 98.37% to *C. denverensis* W6929, suggesting that Y8 is a member of *Cellulomonas*.

Basic biochemical characteristics of strain Y8 showed that Y8 had an optimum growth at 28–32°C, and was able to ferment a wide variety of sugars like D-cellobiose, D-glucose, D-maltose, and D-mannose but not D-tagatose (**Supplementary Table 1**). Y8 was resistant (μg/ml) to ampicillin (100), apramycin (50), spectinomycin (50), gentamicin (50), and kanamycin (50), and sensitive (μg/ml) to chloramphenicol (25) and erythromycin (100).

DDH and ANI were used as minimal criteria for the identification of novel species here (Chun et al., 2018). The level of DDH between strain Y8 and *C. pakistanensis*, *C. hominis,* and *C. denverensis* were 52.5, 39.5, and 22.3%, respectively, which were below the 70% cutoff value suggested for species identification. ANI was estimated to be 93.79% between strain Y8 and *C. pakistanensis*, 84.25% between strain Y8 and *C. hominis* and 81.47% between strain Y8 and *C. denverensis*.

Full Genome of Strain Y8

We obtained the high-quality full genome of strain Y8 of 4,475,991 bp in this study. Y8's genome has a G+C content of 75.35%, and contains 4,074 coding sequences (CDSs) with an average length of 982 bp.

A whole-genome based phylogenetic tree was constructed (**Supplementary Figure 1**). *C. hominis*, *C. denverensis,* and Y8 were assigned to orthologous groups (orthogroups) of Y8 using OrthoFinder. A total of 10,077 protein-coding genes (90.8% of the total) were assigned to 3,068 orthogroups, of which 2,224 included representatives from all three genomes and 1,715 were single-copy orthogroups. Y8 shared 2,789 orthologs with *C. hominis* and 2,602 with *C. denverensis*.

Cadmium Resistance of Strain Y8

The MIC of Cd for Y8 was found to be 5 mM (**Figure 1A**). At 4 mM Cd, Y8's cells appear in an irregular rod shape with a smooth surface based on the SEM imaging results (**Figure 1B**),

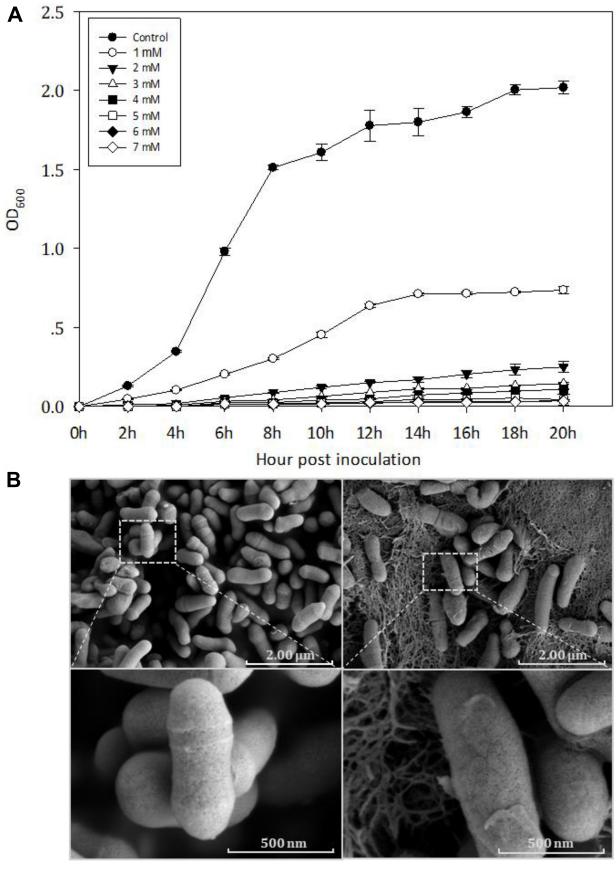

FIGURE 1 | (A) Growth curves of Y8 exposed to Cd of different concentrations; **(B)** scanning electron microscope (SEM) images of Y8's cell morphology without (left) and with Cd (right, 4 mM).

while a thickened cell wall was observed at all Cd treatments. Cd bioaccumulation assay showed that Y8 had an adsorption capacity of 15.80 mg/g Cd when treated with 1 mM $CdCl_2$, and 66.54 mg/g when treated with 4 mM $CdCl_2$.

Cadmium Resistance Genes in Y8's Genome

We identified 54 metal-resistance related genes throughout Y8's genome (**Figure 2** and **Supplementary Table 2**). Four potential Cd transporting genes, namely *zntAY8*, *copAY8*, *HMTY8,* and *czcDY8*, were chosen for functional verification. Flanking genes in the operons and domains of *zntAY8*, *copAY8*, *HMTY8,* and *czcDY8* were analyzed (**Supplementary Figure 2** and **Supplementary Table 3**). Briefly, the *znt* operon carrying *zntAY8* (2,319 bp) comprises three genes including *zntAY8*, a hypothetical gene and an *arsR*-family gene. ZntAY8 shares a sequence similarity of 39.29 and 39.05% with ZntA from *E. coli* K12 and ZntA from *Shigella sonnei* strain Ss046, respectively. The operon carrying *copAY8* is 3,484 bp and comprises four genes including a hypothetical gene, a repressor gene, a Cu chaperone gene *copZ* and *copAY8*. The protein CopAY8 shares a sequence similarity of 47.54 and 40.02% with CopA from *E. coli* K-12 and *B. subtilis* strain 168, respectively. The operon carrying *HMTY8* (3,628 bp) consists of four genes including a thioredoxin reductase gene, *HMTY8*, an *arsR*-family gene and a hypothetical gene. Sequence similarity between HMTY8 and ACR3 from *Corynebacterium glutamicum* strain ATCC 13032 is 33.67%. The operon carrying *czcDY8* (2,728 bp) contains four genes including an *arsR*-family gene, *czcDY8*, *STE14* encoding a putative protein-S-isoprenylcysteine methyltransferase, and *ompR*. CzcDY8 shares a protein similarity of 33.67% with CzcD from *B. subtilis* strain 168 and 39.05% with CzcD from *C. metallidurans* strain ATCC 43123.

A phylogenetic tree (**Figure 3**) was constructed to explore the evolutionary relationships between ZntAY8, CopAY8, HMTY8, CzcDY8, and their homologous proteins.

Time- and Dose-Dependent Expression of Selected Genes in Strain Y8

To determine whether the four candidate genes are Cd-inducible in strain Y8, their *in vivo* expression levels were determined by RT-qPCR (**Figure 4**). After 6 h treatment with 4 mM $CdCl_2$, *zntAY8*, *copAY8,* and *HMTY8* were significantly upregulated, while *czcDY8* was slightly but significantly downregulated (**Figure 4**). In order to gain a more comprehensive understanding of their roles in the response of Y8 to Cd stress, the time-course expression of *zntAY8*, *copAY8,* and *HMTY8* under different Cd concentrations were further quantified.

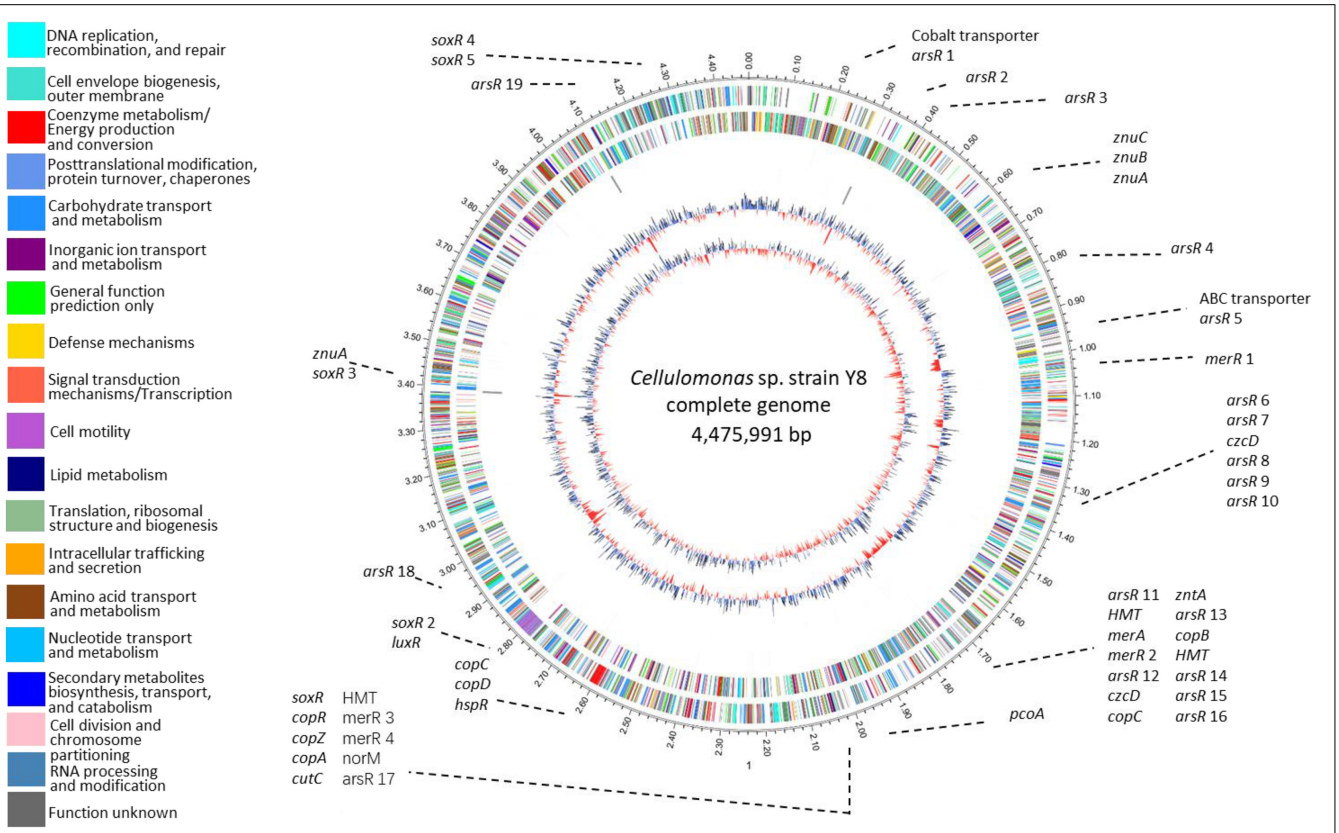

FIGURE 2 | Circular representation of Y8's genome. Circles display from the inside outwards, (1) GC-skew (G-C/G+C ratio) using a 999 bp window; (2) GC-content using a 999 bp window; (3) ncRNA genes on the minus strand; (4) ncRNA genes on the plus strand; (5) COG assignments for predicted CDSs on the minus strand; (6) COG assignments for predicted CDSs on the plus strand; (7) scale in Mb.

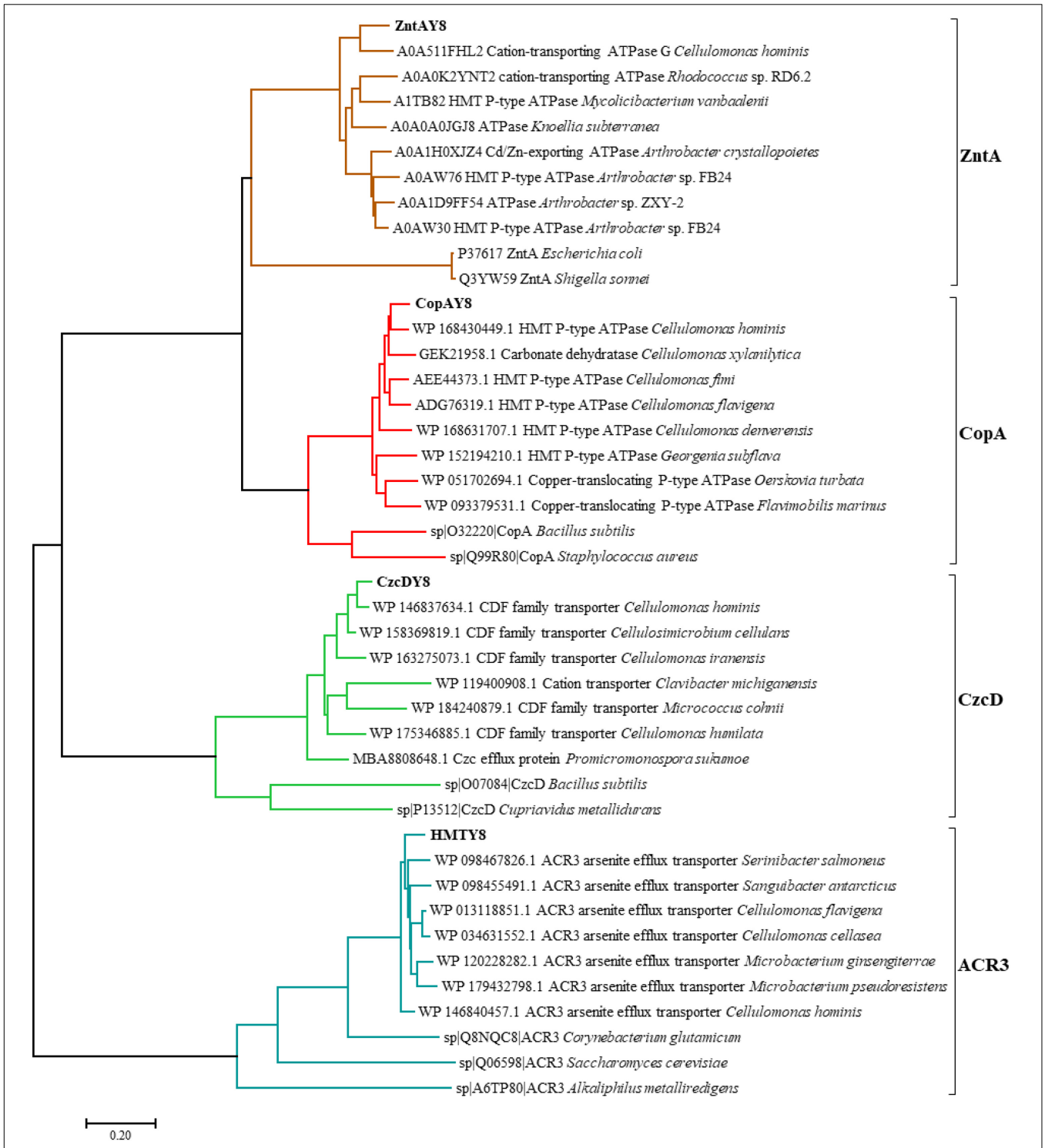

FIGURE 3 | A phylogenetic tree showing the protein sequence similarity of candidate metal resistance genes in strain Y8's genome and homologs. The tree was constructed using the Maximum Likelihood method within MEGA 7.0 (Kumar et al., 2016). Bootstrap values were estimated from 1,000 replicates. Sequence alignment was performed using ClustalX (Larkin et al., 2007).

As shown in **Figure 5**, all the three tested genes were significantly induced at 1 mM Cd at all-time points, while only the gene *zntAY8* responded constantly at higher Cd concentrations. Expression levels of *copAY8* and *HMTY8* decreased over time substantially at higher Cd concentrations (**Figures 5B,C**).

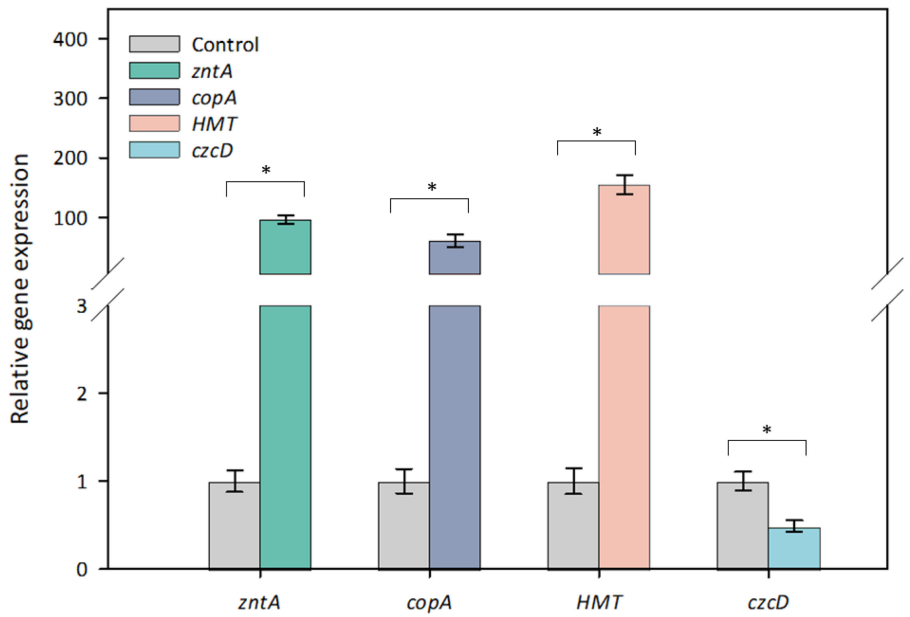

FIGURE 4 | Relative gene expression of the tested genes of strain Y8 in response to 4 mM Cd. Differences between paired values with 3 experiments that are statistically significant as determined by *t*-test are denoted as follows: * $p < 0.01$.

Functional Verification of the Candidate Cadmium Resistant Genes in *Escherichia coli* Strain RW 3110

The four genes, *zntAY8*, *copAY8*, *HMTY8,* and *czcDY8*, were heterologously expressed in Cd-sensitive *E. coli*. Quality of the recombinant plasmids (pTR-*zntAY8*, pTR-*copAY8*, pTR-*HMTY8,* and pTR-*czcDY8*) were checked through double enzyme digestion detection (**Supplementary Figure 3**), and double-checked by Sanger sequencing before being transformed into the hosts.

Growth curves of *E. coli* RW 3110 overexpressed with and without the recombinant plasmids were determined under 0.3 mM Cd stress. The threshold Cd concentration used to test the transformants referred to our previous study (Li et al., 2020). The growth rates of RW 3110 with all the tested genes except for *copAY8* were considerably higher than the control (**Figure 6A**). The transformants *zntAY8*, *HMTY8,* and *czcDY8* reached the exponential phase at 2–3 h.

After 6 h culture, dry biomass of all transformed strains was significantly different from that of the control (**Figure 6B**). The biomass of RW 3110 with *zntAY8*, *HMTY8,* and *czcDY8* was around 10% higher, while RW 3110 with *copAY8* was lower than the control. Cd sorption in RW 3110 with *copAY8* and *HMTY8* increased by 3.22 and 3.68 folds, while that in RW 3110 with *zntAY8* and *czcDY8* decreased by 86 and 53.3% compared with the control, respectively (**Figure 6D**). Uptake of Ni, Cu, and Zn by transformed strains in Cd-containing medium was also determined (**Figure 6C**). Results showed that Zn accumulation in RW 3110 with *copAY8*, *HMTY8,* and *czcDY8* increased by 34–80%, while that of RW 3110 with *zntAY8* decreased by 87.3%. Cu and Ni accumulation in all transformants showed a similar trend to that for Zn.

DISCUSSION

Cadmium is an extremely toxic element, due to its mutagenic effect (Jin et al., 2003) and ability to cause indirect formation of reactive oxygen species (ROS) (Waisberg et al., 2003). Cd tolerance of bacteria varies among species and can be partially reflected in their MIC. The Cd MIC of strain Y8 (5 mM) is much higher than common strains, such as *S. aureus* (<0.16 mM on agar plates) (Rosdahl and Rosendal, 1980), as well as some Cd resistant isolates including *Pseudomonas stutzeri* (0.6 mM on LB plates) (Deb et al., 2013), *Pseudomonas* sp. TeU (0.5 mM on LB plates) (Chien et al., 2011) and *Lactococcus lactis* (1.78 mM on MRS agar plates) (Sheng et al., 2016). While strain Y8 lacks any plasmids for encoding commonly known resistance genetic systems, it is supposed that some chromosome-borne genes are responsible for its Cd resistance.

Bacterial exposure to extreme Cd stress can normally cause a sharp drop in growth rate and a series of morphological changes including cell shrinkage and even the complete loss of cell structure (Hou et al., 2015; Khan et al., 2015; Sheng et al., 2016; Huang et al., 2018). The strain Y8 was significantly inhibited in growth by 4 mM $CdCl_2$ exposure (**Figure 1A**), whereas no obvious change was observed on cell morphology (**Figure 1B**). Meanwhile, Y8 cells produced a large amount of extracellular reticulum structure under Cd stress (**Figure 1B**). These reticulate substances were supposed to be extracellular polymer substances (EPS), which are generally secreted in the form of biofilm (Florentin et al., 2012). Several studies had reported that members

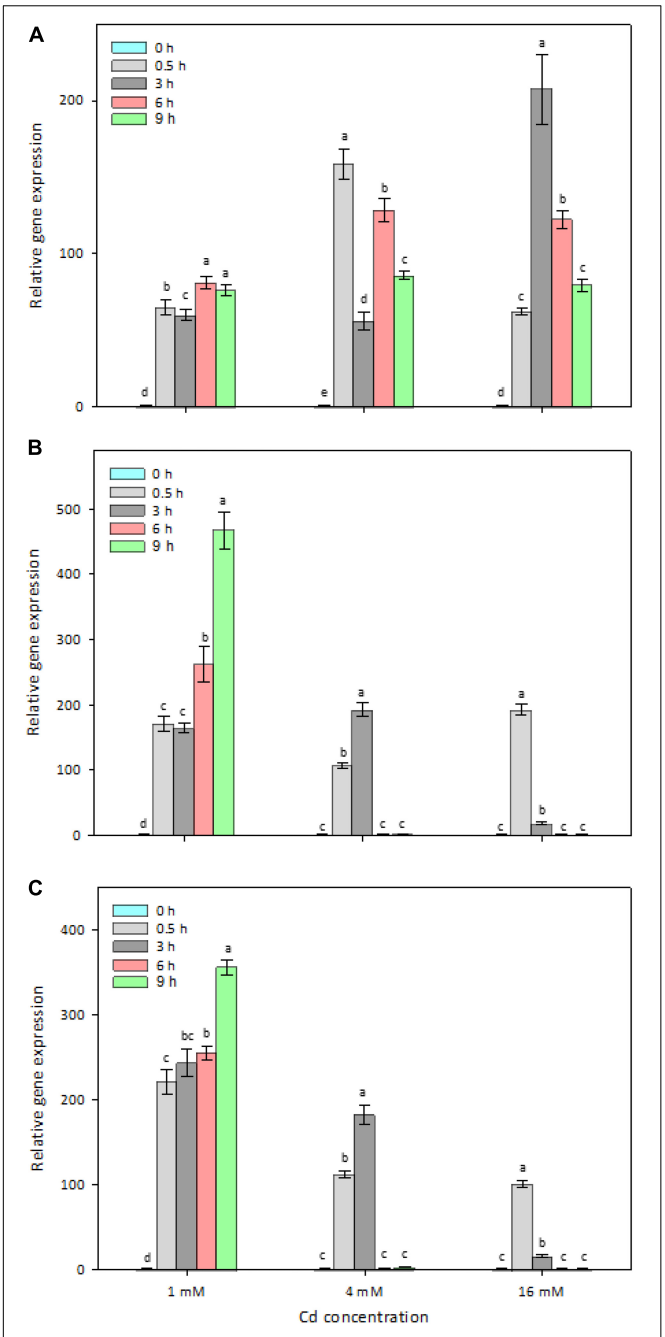

FIGURE 5 | Time-dependent and Cd-level-dependent responses of the Cd-inducible metal resistance genes. **(A)** *zntAY8*; **(B)** *copAY8*; **(C)** *HMTY8*.

of *Cellulomonas* genus such as *C. flavigena*, *C. uda*, and *C. fimi* can form biofilms (McIntosh et al., 2005; Young et al., 2012), which is a curdlan-type matrix. Genome annotation of the strain Y8 here detected multiple copies of biofilm formation related gene such as *wcaA*, *wcaG*, and glycosyltransferases (Zheng et al., 2018; Oehme et al., 2019). Previous studies indicated that EPS can immobilize metals through ionizable groups such as -OH, -NH, and -COOH (Shen et al., 2018; Xie et al., 2020), to reduce the toxicity of heavy metals. We speculated that the observed reticulate substances are EPS and may play a role in Cd resistance of strain Y8, yet further experimental evidences are needed to classify.

An important feature of Y8's genome is its high GC content (**Figure 2**). Strain Y8 has a GC content of more than 75%, which is beyond the currently known range of genomic GC skew (Romiguier and Roux, 2017). Genomic base composition variation is shaped by various evolutionary events, leading to differential biological functions (Wu et al., 2012). It is generally thought that high-GC content is associated with a lower mutation rate under high selective pressure. Our recent study has documented that prokaryotic extremophiles commonly possess high-GC genomes, such as the Cu-resistant *Cupriavidus* strains with an average GC content of 66.2%, the multi-metal resistant *Thiobacillus* strains with an average GC content of 62.6%, the radiation and/or metal tolerant *Deinococcus* strains with an average GC content of 67.3%, and the Zn-resistant *Comamonas* spp. with a GC content of 61.3–61.5% (Chen et al., 2019a,b). A high GC content may help strain Y8 in maintaining its key genetic elements under extreme metal stress which may cause a high rate of DNA damage.

The diversity of genetic elements related to metal stress within Y8's genome is vast. We identified more than 50 genes for dedicated metal stress response (**Figure 2** and **Supplementary Table 2**), accounting for 1.2% of the total genes. This frequency of metal-associated genes is comparable to that of the microbial metagenome from metal mine tailings of extremely abundant heavy metals (Li et al., 2015). Similar to *C. metallidurans* strain CH34, a model bacterium for metal resistance study, a variety of metal efflux systems were detected in Y8's genome, including genes of the P-type ATPase, ABC transporter, and CDF transporter families (Nies). Nevertheless, only two genes, *zntA* and *czcD*, were thought to be dedicated to Cd resistance. Though versatile genes for multi-metal resistance have been reported (Solovieva and Entian, 2004; Steunou et al., 2020), it is unknown whether the remaining metal resistance genes in Y8's genome, like the candidate *copA* and *HMT*, play a potential role in Cd resistance. Surprisingly, all the four genes were Cd-inducible and three of them restored Cd resistance of the Cd sensitive strain heterologously, as discussed below.

It is worth noting that most of Y8's metal resistance genes are organized into operons. Operons are clusters of adjacent genes encoding for proteins with related roles, which provides an efficient mechanism to coordinate the expression of neighboring genes (Sáenz-Lahoya et al., 2019). Roles of the regulator genes in the operons merit further investigation, since more than 20 copies of ArsR-family regulators were identified in Y8's genome. Meanwhile, some unknown coding regions were annotated as structural genes of the detected operons of *znt, cop*, *HMT*, and *czc*, and some of them have overlap regions with main genes (**Supplementary Figure 2**). A study revealed that occurrence of overlapping gene pairs is associated with tight translational coupling (Huber et al., 2019). Basically, organization of these resistance genes in operons may enable strain Y8 a strong ability of rapid transcriptional response to metal stresses.

Modern omics tool has revealed a variety of basic metabolic pathways involved in metal resistance (Sheng et al., 2016;

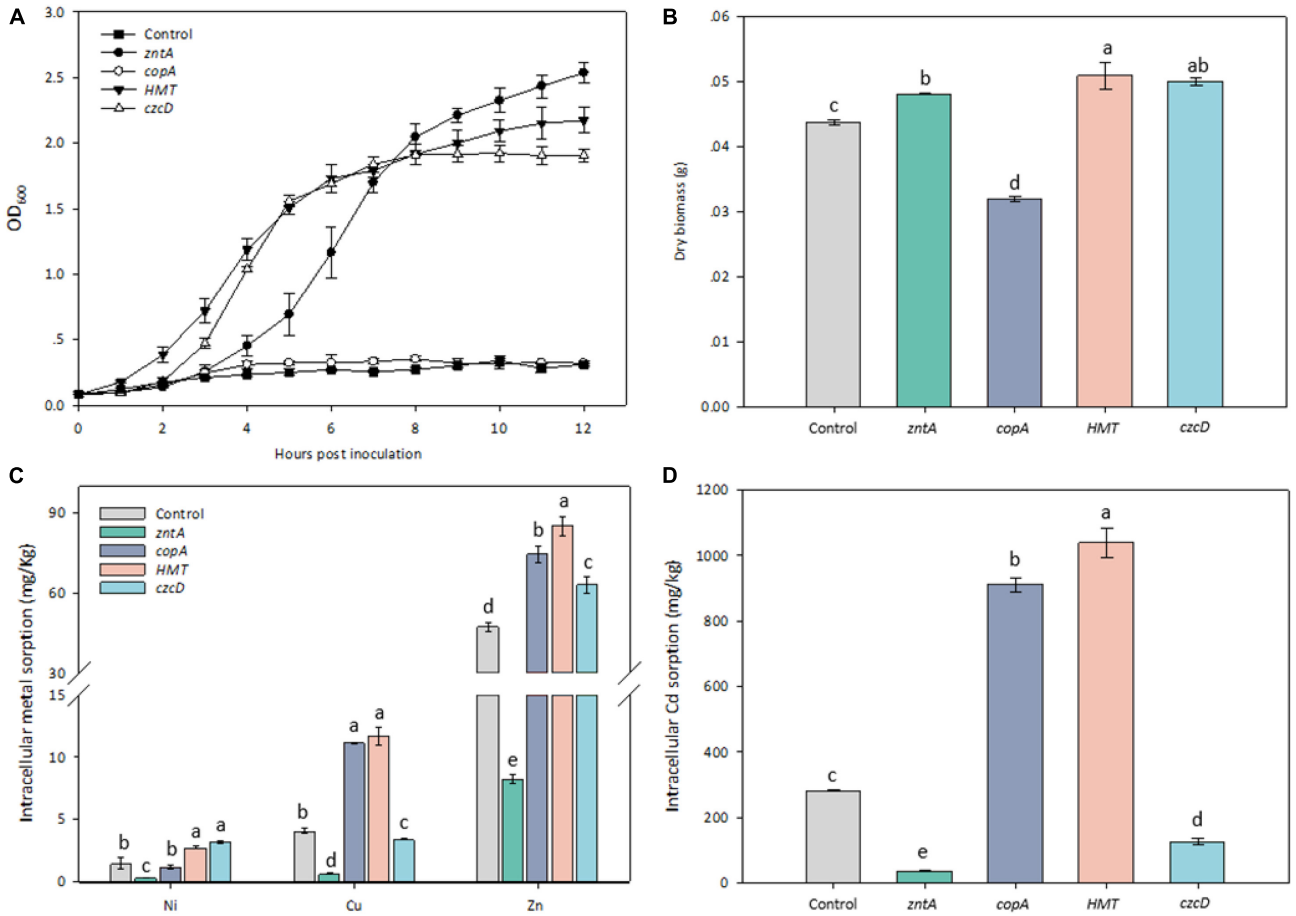

FIGURE 6 | Phenotypic response of Cd-sensitive strain harboring the tested metal resistance genes. **(A)** Growth curves of transformants harboring the tested resistance genes under 0.3 mM Cd; **(B)** dry biomass of transformants harboring the tested resistance genes; **(C)** cellular accumulation of Ni, Cu, and Zn by transformants harboring the tested resistance genes; **(D)** cellular accumulation of Cd by transformants harboring the tested resistance genes.

Isarankura-Na-Ayudhya et al., 2018; Alviz-Gazitua et al., 2019), and for either prokaryotic or eukaryotic cells possession of specific Cd resistance genes/operons is essential for Cd resistance (Intorne et al., 2012; Schwager et al., 2012; Chaoprasid et al., 2015; Zhang et al., 2015). A genome-wide annotation of strain Y8 led to the identification of 54 heavy metal-related genes (**Figure 2**), including potential metal resistance genes homologous to *zntA* of *E. coli*, *czcD* of *C. metallidurans*, *copAB of Legionella pneumophila* (Purohit et al., 2018), *cutC* of *Enterococcus faecalis* (Latorre et al., 2011), *znuA* of *E. coli* (Patzer and Hantke, 1998), etc. It is generally thought that most of metal transporters (Dutta et al., 2007; Smith et al., 2014) as well as regulators (Brocklehurst et al., 2003; Radford et al., 2003) are relatively specific. While it was supposed that these annotated metal resistance genes, particularly *copA*, may be dedicated for a specific metal, our results showed that at least the four tested non-Cd-specific genes responded collectively to Cd stress, which was implied by their Cd-inducible expression and Cd resistance function in *E. coli* (**Figures 4**–**6**).

The involvement of *zntAY8* and *czcDY8* in Y8's Cd stress response (**Figures 4**, **5A**) may be not surprising, considering that *EczntA* is responsible for specific resistance to both Zn and Cd (Rensing et al., 1997), and the *czc* system was a well-known Cd resistance determinant (Hassan et al., 1999). *zntAY8* was shown to be effective in enhancing Cd resistance of *E. coli* RW 3110 heterologously, probably as a potent multi-purpose metal exporter which was implied by the sharp reduction in *E. coli*'s Cd/Ni/Zn/Cu sorption (**Figures 6B,D**). With typical metal binding motifs as well as the ATPase binding site, the *zntAY8* gene is phylogenetically close to P-type ATPase genes, like the typical Cd resistance genes *cadA* and *czcP* that can mediate the extrusion of metals including Cd from cytoplasm by hydrolysis of ATP (Lee et al., 2001; Smith et al., 2014). The *czcDY8* gene was seen to be a cation diffusion facilitator. *czcD* was previously found to be part of the high-level metal resistance system *czc* that mediates the efflux of Co, Zn, and Cd ions (Munkelt et al., 2004). Different from the known czc system, two copies of *czcDY8* were detected in Y8's genome with no *czcCBA* flanked, implying that the *czcDY8* may function independently. The function of *copAY8* and *HMTY8* seems unusual here, which both increased intracellular Cd accumulation (**Figure 6D**). To our knowledge, *copA* is specific for Cu translocating and resistance (Giachino and Waldron, 2020), although two studies

have reported the Cd-inducible *copA* variants (Toes et al., 2008; Steunou et al., 2020). Moreover, the ACR3 gene, the closest homolog to *HMTY8*, has been rarely reported to play a role in Cd resistance (Markowska et al., 2015). Phylogenetic analysis indicated that closest homologs of these four genes are all from the genus of *Cellulomonas* (**Figure 3**), which is consistent with the previous viewpoint that heavy metal transporters are mostly evolving via vertical descent (Li et al., 2015). Considering that none of their homologs from this genus have been reported in terms of a role in Cd resistance, we speculate that *zntAY8*, *copAY8*, *HMTY8,* and *czcDY8* are novel metal resistance genes playing a role in Cd resistance of the genus *Cellulomonas.*

Determination of Cd-induced *in vivo* expression of *zntAY8*, *copAY8,* and *HMTY8* indicated that their response to Cd stress in Y8 was dose- and time-dependent (**Figure 5**). The expression of heavy metal transport systems is normally controlled at the level of transcription in order to minimize the associated metabolic burden to the host (Hynninen, 2010; Alviz-Gazitua et al., 2019). From this perspective, it is unwise for bacteria to express multiple transporters simultaneously, especially under severe Cd stress. Our results imply that *copAY8* and *HMTY8* seems to favor a low Cd stress while *zntAY8* favors a high Cd stress of up to 16 mM (**Figure 5**). In combination with the results of their roles in Cd accumulation (**Figure 6D**), the dose- and time-dependent expression of the three genes may indicate that strain Y8 may recruit a mechanism for Cd sequestration by *copAY8* and *HMTY8* under minor Cd stress which increases intracellular Cd, and trigger a mechanism for Cd exporting by *zntAY8* under sever Cd stress. Such dose-dependent mechanism for metal resistance has been inferred by cellular Cu homeostasis. Recruiting different genetic pathways for coping with high levels of metal stress has also been reported for Cu and Zn in eukaryotic cells. For example, tripeptide glutathione (GSH) is heavily produced for Cu excretion when Cu stress is high, and metallothioneins increased when Zn is absorbed in a large quantity in mammalian cells (Bertinato and L'Abbé, 2004).

Though our current results showed that the four genes that function in Cd resistance can promote either Cd intake or export and also to some extent play a role in Ni, Cu, and Zn trafficking (**Figures 6C,D**), more experimental evidences are needed to describe the process of metal transport as well as their affinity to metals. Their intracellular expression regulation under Cd stress remains unknown, considering that a large number of *arsR/merR* family regulator genes were detected in Y8's genome. Available evidence allows us to conclude that *zntAY8*, *copAY8*, *HMTY8,* and *czcDY8* are novel metal resistance genes of the genus *Cellulomonas*, and they respond to Cd stress collectively in strain Y8. Meanwhile, ZntAY8 seems to be a strong Cd/Ni/Cu/Zn exporter that can substantially improve the host's growth under metal stress.

DATA AVAILABILITY STATEMENT

The datasets presented in this study can be found in online repositories. The names of the repository/repositories and accession number(s) can be found below: https://www.ncbi.nlm.nih.gov/genbank/, CP041203.1.

AUTHOR CONTRIBUTIONS

XL initiated the concept and designed the experiment. JC, WL, and XZ performed the molecular experiments. LW and XL analyzed the genomic data. JC, XL, and LW draft the manuscript. All authors revised the manuscript and approved the submission.

FUNDING

This work was supported by the Hebei Science Fund for Distinguished Young Scholars (No. D2018503005), the National Natural Science Foundation of China (No. 41877414), and the National Key Research and Development Program of China (No. 2018YFD0800306).

SUPPLEMENTARY MATERIAL

The Supplementary Material for this article can be found online at: https://www.frontiersin.org/articles/10.3389/fmicb.2021.784575/full#supplementary-material

REFERENCES

Aleem, A., Isar, J., and Malik, A. (2003). Impact of long-term application of industrial wastewater on the emergence of resistance traits in *Azotobacter chroococcum* isolated from rhizospheric soil. *Bioresour. Technol.* 86, 7–13. doi: 10.1016/S0960-8524(02)00134-7

Alviz-Gazitua, P., Fuentes-Alburquenque, S., Rojas, L. A., Turner, R. J., Guiliani, N., and Seeger, M. (2019). The response of *Cupriavidus metallidurans* CH34 to cadmium involves inhibition of the initiation of biofilm formation, decrease in intracellular c-di-GMP levels, and a novel metal regulated phosphodiesterase. *Front. Microbiol.* 10:1499. doi: 10.3389/fmicb.2019.01499

Andrews, J. M. (2001). Determination of minimum inhibitory concentrations. *J. Antimicrob. Chemother.* 48 Suppl 1, 5–16. doi: 10.1093/jac/48.suppl_1.5

Arguello, J. M. (2003). Identification of ion-selectivity determinants in heavy-metal transport P1B-type ATPases. *J. Membr. Biol.* 195, 93–108. doi: 10.1007/s00232-003-2048-2

Argüello, J. M., Eren, E., and González-Guerrero, M. (2007). The structure and function of heavy metal transport P1B-ATPases. *Biometals* 20, 233–248. doi: 10.1007/s10534-006-9055-6

Baati, H., Siala, M., Azri, C., Ammar, E., Dunlap, C., and Trigui, M. (2020). Resistance of a *Halobacterium salinarum* isolate from a solar saltern to cadmium, lead, nickel, zinc, and copper. *Antonie Van Leeuwenhoek* 113, 1699–1711. doi: 10.1007/s10482-020-01475-6

Bertinato, J., and L'Abbé, M. R. (2004). Maintaining copper homeostasis: regulation of copper-trafficking proteins in response to copper deficiency or overload. *J. Nutr. Biochem.* 15, 316–322. doi: 10.1016/j.jnutbio.2004.02.004

Binet, M. R., and Poole, R. K. (2000). Cd(II), Pb(II) and Zn(II) ions regulate expression of the metal-transporting P-type ATPase ZntA in *Escherichia coli*. *FEBS Lett.* 473, 67–70. doi: 10.1016/S0014-5793(00)01509-X

Brocklehurst, K. R., Megit, S. J., and Morby, A. P. (2003). Characterisation of CadR from *Pseudomonas aeruginosa*: a Cd(II)-responsive MerR homologue. *Biochem. Biophys. Res. Commun.* 308, 234–239. doi: 10.1016/S0006-291X(03)01366-4

Busch, W., and Saier, M. H. Jr. (2002). The transporter classification (TC) system, 2002. *Crit. Rev. Biochem. Mol. Biol.* 37, 287–337.

Chaoprasid, P., Nookabkaew, S., Sukchawalit, R., and Mongkolsuk, S. (2015). Roles of *Agrobacterium tumefaciens* C58 ZntA and ZntB and the transcriptional regulator ZntR in controlling Cd2+/Zn2+/Co2+ resistance and the peroxide stress response. *Microbiology (Reading)* 161, 1730–1740. doi: 10.1080/10409230290771528

Chen, J., Xing, C., Zheng, X., and Li, X. (2019b). Functional genomic identification of cadmium resistance genes from a high gc clone library by coupling the sanger and PacBio sequencing strategies. *Genes (Basel)* 11:7. doi: 10.1128/MRA.01066-19

Chen, J., Xing, C., Zheng, X., and Li, X. (2019a). Complete genome sequence of *Cellulomonas* sp. Strain Y8, a high-GC-content plasmid-free heavy metal-resistant bacterium isolated from farmland soil. *Microbiol. Resour. Announc.* 8:e01066. doi: 10.1099/mic.0.000135

Chien, C. C., Jiang, M. H., Tsai, M. R., and Chien, C. C. (2011). Isolation and characterization of an environmental cadmium- and tellurite-resistant *Pseudomonas* strain. *Environ. Toxicol. Chem.* 30, 2202–2207. doi: 10.3390/genes11010007

Chun, J., Oren, A., Ventosa, A., Christensen, H., Arahal, D. R., da Costa, M. S., et al. (2018). Proposed minimal standards for the use of genome data for the taxonomy of prokaryotes. *Int. J. Syst. Evol. Microbiol.* 68, 461–466. doi: 10.1002/etc.620

Das, S., Dash, H. R., and Chakraborty, J. (2016). Genetic basis and importance of metal resistant genes in bacteria for bioremediation of contaminated environments with toxic metal pollutants. *Appl. Microbiol. Biotechnol.* 100, 2967–2984. doi: 10.1099/ijsem.0.002516

Deb, S., Ahmed, S. F., and Basu, M. (2013). Metal accumulation in cell wall: a possible mechanism of cadmium resistance by *Pseudomonas* stutzeri. *Bull. Environ. Contam. Toxicol.* 90, 323–328. doi: 10.1007/s00253-016-7364-4

Dell'Amico, E., Cavalca, L., and Andreoni, V. (2005). Analysis of rhizobacterial communities in perennial Graminaceae from polluted water meadow soil, and screening of metal-resistant, potentially plant growth-promoting bacteria. *FEMS Microbiol. Ecol.* 52, 153–162. doi: 10.1007/s00128-012-0933-z

Diels, L., Dong, Q., van der Lelie, D., Baeyens, W., and Mergeay, M. (1995). The czc operon of Alcaligenes eutrophus CH34: from resistance mechanism to the removal of heavy metals. *J. Ind. Microbiol.* 14, 142–153. doi: 10.1016/j.femsec.2004.11.005

Dutta, S. J., Liu, J., Stemmler, A. J., and Mitra, B. (2007). Conservative and nonconservative mutations of the transmembrane CPC motif in ZntA: effect on metal selectivity and activity. *Biochemistry* 46, 3692–3703. doi: 10.1007/BF01569896

El-Gebali, S., Mistry, J., Bateman, A., Eddy, S. R., Luciani, A., Potter, S. C., et al. (2019). The Pfam protein families database in 2019. *Nucleic Acids Res.* 47, D427–D432. doi: 10.1021/bi0616394

Emms, D. M., and Kelly, S. (2015). OrthoFinder: solving fundamental biases in whole genome comparisons dramatically improves orthogroup inference accuracy. *Genome Biol.* 16:157. doi: 10.1093/nar/gky995

Florentin, D. F., Angélique, Baccou, J. C., and Schorr-Galindo, S. (2012). Microbial exopolysaccharides: main examples of synthesis, excretion, genetics and extraction. *Carbohydr. Polym.* 87, 951–962. doi: 10.1186/s13059-015-0721-2

Fouché, J. (2018). *"The Effect Of Cadmium On Earthworms (Eisenia andrei) And Their Intestinal Bacteria."* Ph.D. Thesis. Potchefstroom: North-West University. doi: 10.1016/j.carbpol.2011.08.083

Giachino, A., and Waldron, K. J. (2020). Copper tolerance in bacteria requires the activation of multiple accessory pathways. *Mol. Microbiol.* 114, 377–390.

Harris, M. A., Clark, J., Ireland, A., Lomax, J., Ashburner, M., Foulger, R., et al. (2004). The Gene Ontology (GO) database and informatics resource. *Nucleic Acids Res.* 32, D258–D261. doi: 10.1111/mmi.14522

Hassan, M. T., van der Lelie, D., Springael, D., Romling, U., Ahmed, N., and Mergeay, M. (1999). Identification of a gene cluster, czr, involved in cadmium and zinc resistance in *Pseudomonas aeruginosa*. *Gene* 238, 417–425. doi: 10.1093/nar/gkh036

Hou, Y., Cheng, K., Li, Z., Ma, X., Wei, Y., Zhang, L., et al. (2015). Biosorption of cadmium and manganese using free cells of *Klebsiella* sp. isolated from waste water. *PLoS One* 10:e0140962. doi: 10.1016/S0378-1119(99)00349-2

Huang, F., Wang, Z. H., Cai, Y. X., Chen, S. H., Tian, J. H., and Cai, K. Z. (2018). Heavy metal bioaccumulation and cation release by growing *Bacillus cereus* RC-1 under culture conditions. *Ecotoxicol. Environ. Saf.* 157, 216–226. doi: 10.1371/journal.pone.0140962

Huber, M., Faure, G., Laass, S., Kolbe, E., Seitz, K., Wehrheim, C., et al. (2019). Translational coupling via termination-reinitiation in archaea and bacteria. *Nat. Commun.* 10:4006. doi: 10.1016/j.ecoenv.2018.03.077

Hynninen, A. (2010). *Zinc, Cadmium And Lead Resistance Mechanisms In Bacteria And Their Contribution To Biosensing*. Helsinki: Helsingin Yliopisto. doi: 10.1038/s41467-019-11999-9

Intorne, A. C., de Oliveira, M. V., de, M. P. L., and de Souza Filho, G. A. (2012). Essential role of the czc determinant for cadmium, cobalt and zinc resistance in *Gluconacetobacter diazotrophicus* PAl 5. *Int. Microbiol.* 15, 69–78.

Isarankura-Na-Ayudhya, P., Thippakorn, C., Pannengpetch, S., Roytrakul, S., Isarankura-Na-Ayudhya, C., Bunmee, N., et al. (2018). Metal complexation by histidine-rich peptides confers protective roles against cadmium stress in *Escherichia coli* as revealed by proteomics analysis. *PeerJ* 6:e5245.

Jain, C., Rodriguez, R. L., Phillippy, A. M., Konstantinidis, K. T., and Aluru, S. (2018). High throughput ANI analysis of 90K prokaryotic genomes reveals clear species boundaries. *Nat. Commun.* 9:5114. doi: 10.7717/peerj.5245

Jin, Y. H., Clark, A. B., Slebos, R. J., Al-Refai, H., Taylor, J. A., Kunkel, T. A., et al. (2003). Cadmium is a mutagen that acts by inhibiting mismatch repair. *Nat. Genet.* 34, 326–329. doi: 10.1038/s41467-018-07641-9

Kanehisa, M., and Goto, S. (2000). KEGG: kyoto encyclopedia of genes and genomes. *Nucleic Acids Res.* 28, 27–30. doi: 10.1038/ng1172

Khan, Z., Nisar, M. A., Hussain, S. Z., Arshad, M. N., and Rehman, A. (2015). Cadmium resistance mechanism in *Escherichia coli* P4 and its potential use to bioremediate environmental cadmium. *Appl. Microbiol. Biotechnol.* 99, 10745–10757. doi: 10.1093/nar/28.1.27

Kotoky, R., and Pandey, P. (2020). Rhizosphere assisted biodegradation of benzo(a)pyrene by cadmium resistant plant-probiotic *Serratia marcescens* S2I7, and its genomic traits. *Sci. Rep.* 10:5279. doi: 10.1007/s00253-015-6901-x

Krogh, A., Larsson, B., von Heijne, G., and Sonnhammer, E. L. (2001). Predicting transmembrane protein topology with a hidden Markov model: application to complete genomes. *J. Mol. Biol.* 305, 567–580. doi: 10.1038/s41598-020-62285-4

Krzywinski, M., Schein, J., Birol, I., Connors, J., Gascoyne, R., Horsman, D., et al. (2009). Circos: an information aesthetic for comparative genomics. *Genome Res.* 19, 1639–1645. doi: 10.1006/jmbi.2000.4315

Kumar, S., Stecher, G., and Tamura, K. (2016). MEGA7: molecular evolutionary genetics analysis Version 7.0 for bigger datasets. *Mol. Biol. Evol.* 33, 1870–1874. doi: 10.1101/gr.092759.109

Lagesen, K., Hallin, P., Rodland, E. A., Staerfeldt, H. H., Rognes, T., and Ussery, D. W. (2007). RNAmmer: consistent and rapid annotation of ribosomal RNA genes. *Nucleic Acids Res.* 35, 3100–3108. doi: 10.1093/molbev/msw054

Larkin, M. A., Blackshields, G., Brown, N. P., Chenna, R., McGettigan, P. A., McWilliam, H., et al. (2007). Clustal W and Clustal X version 2.0. *Bioinformatics* 23, 2947–2948. doi: 10.1093/nar/gkm160

Latorre, M., Olivares, F., Reyes-Jara, A., López, G., and González, M. (2011). CutC is induced late during copper exposure and can modify intracellular copper content in *Enterococcus faecalis*. *Biochem. Biophys. Res. Commun.* 406, 633–637. doi: 10.1093/bioinformatics/btm404

Lee, S. W., Glickmann, E., and Cooksey, D. A. (2001). Chromosomal locus for cadmium resistance in *Pseudomonas* putida consisting of a cadmium-transporting ATPase and a MerR family response regulator. *Appl. Environ. Microbiol.* 67, 1437–1444. doi: 10.1016/j.bbrc.2011.02.109

Legatzki, A., Grass, G., Anton, A., Rensing, C., and Nies, D. H. (2003). Interplay of the Czc system and two P-type ATPases in conferring metal resistance to *Ralstonia metallidurans*. *J. Bacteriol.* 185, 4354–4361. doi: 10.1128/AEM.67.4.1437-1444.2001

Li, X., Islam, M. M., Chen, L., Wang, L., and Zheng, X. (2020). Metagenomics-guided discovery of potential bacterial metallothionein genes from the soil microbiome that confer Cu and/or Cd resistance. *Appl. Environ. Microbiol.* 86, e2907–e2919. doi: 10.1128/JB.185.15.4354-4361.2003

Li, X., Zhu, Y.-G., Shaban, B., Bruxner, T. J. C., Bond, P. L., and Huang, L. (2015). Assessing the genetic diversity of Cu resistance in mine tailings through high-throughput recovery of full-length copA genes. *Sci. Rep.* 5:13258. doi: 10.1128/AEM.02907-19

Lombard, V., Golaconda Ramulu, H., Drula, E., Coutinho, P. M., and Henrissat, B. (2014). The carbohydrate-active enzymes database (CAZy) in 2013. *Nucleic Acids Res.* 42, D490–D495. doi: 10.1038/srep13258

Lowe, T. M., and Eddy, S. R. (1997). tRNAscan-SE: a program for improved detection of transfer RNA genes in genomic sequence. *Nucleic Acids Res.* 25, 955–964. doi: 10.1093/nar/gkt1178

Markowska, K., Maciaszczyk-Dziubinska, E., Migocka, M., Wawrzycka, D., and Wysocki, R. (2015). Identification of critical residues for transport activity of Acr3p, the *Saccharomyces cerevisiae* As(III)/H+ antiporter. *Mol. Microbiol.* 98, 162–174. doi: 10.1093/nar/25.5.955

McIntosh, M., Stone, B. A., and Stanisich, V. A. (2005). Curdlan and other bacterial (1–>3)-beta-D-glucans. *Appl. Microbiol. Biotechnol.* 68, 163–173. doi: 10.1111/mmi.13113

Meier-Kolthoff, J. P., Auch, A. F., Klenk, H. P., and Goker, M. (2013). Genome sequence-based species delimitation with confidence intervals and improved distance functions. *BMC Bioinformatics* 14:60. doi: 10.1007/s00253-005-1959-5

Methé, B. A., and Lasa, I. (2013). Microbiology in the 'omics era: from the study of single cells to communities and beyond. *Curr. Opin. Microbiol.* 16, 602–604. doi: 10.1186/1471-2105-14-60

Minari, G. D., Saran, L. M., Lima Constancio, M. T., Correia da Silva, R., Rosalen, D. L., José de Melo, W., et al. (2020). Bioremediation potential of new cadmium, chromium, and nickel-resistant bacteria isolated from tropical agricultural soil. *Ecotoxicol. Environ. Saf.* 204:111038. doi: 10.1016/j.mib.2013.10.002

Monchy, S., Benotmane, M. A., Janssen, P., Vallaeys, T., Taghavi, S., van der Lelie, D., et al. (2007). Plasmids pMOL28 and pMOL30 of *Cupriavidus metallidurans* are specialized in the maximal viable response to heavy metals. *J. Bacteriol.* 189, 7417–7425. doi: 10.1016/j.ecoenv.2020.111038

Munkelt, D., Grass, G., and Nies, D. H. (2004). The chromosomally encoded cation diffusion facilitator proteins DmeF and FieF from *Wautersia metallidurans* CH34 are transporters of broad metal specificity. *J. Bacteriol.* 186, 8036–8043. doi: 10.1128/JB.00375-07

Nies, D. H. (2003). Efflux-mediated heavy metal resistance in prokaryotes. *Fems Microbiol. Rev.* 27, 313–339. doi: 10.1128/JB.186.23.8036-8043.2004

Nies, D. H., Nies, A., Chu, L., and Silver, S. (1989). Expression and nucleotide sequence of a plasmid-determined divalent cation efflux system from *Alcaligenes eutrophus*. *Proc. Natl. Acad. Sci. U.S.A.* 86, 7351–7355. doi: 10.1016/S0168-6445(03)00048-2

Nucifora, G., Chu, L., Misra, T. K., and Silver, S. (1989). Cadmium resistance from *Staphylococcus aureus* plasmid pI258 cadA gene results from a cadmium-efflux ATPase. *Proc. Natl. Acad. Sci. U.S.A.* 86, 3544–3548. doi: 10.1073/pnas.86.19.7351

Oehme, D. P., Shafee, T., Downton, M. T., Bacic, A., and Doblin, M. S. (2019). Differences in protein structural regions that impact functional specificity in GT2 family β-glucan synthases. *PLoS One* 14:e0224442. doi: 10.1073/pnas.86.10.3544

Okkeri, J., and Haltia, T. (2006). The metal-binding sites of the zinc-transporting P-type ATPase of *Escherichia coli*. Lys693 and Asp714 in the seventh and eighth transmembrane segments of ZntA contribute to the coupling of metal binding and ATPase activity. *Biochim. Biophys. Acta* 1757, 1485–1495. doi: 10.1371/journal.pone.0224442

Patel, S. J., Lewis, B. E., Long, J. E., Nambi, S., Sassetti, C. M., Stemmler, T. L., et al. (2016). Fine-tuning of substrate affinity leads to alternative roles of *Mycobacterium tuberculosis* Fe2+-ATPases. *J. Biol. Chem.* 291, 11529–11539. doi: 10.1016/j.bbabio.2006.06.008

Patzer, S. I., and Hantke, K. (1998). The ZnuABC high-affinity zinc uptake system and its regulator Zur in *Escherichia coli*. *Mol. Microbiol.* 28, 1199–1210. doi: 10.1074/jbc.M116.718239

Paulsen, I. T., and Saier, M. H. Jr. (1997). A novel family of ubiquitous heavy metal ion transport proteins. *J. Membr. Biol.* 156, 99–103. doi: 10.1046/j.1365-2958.1998.00883.x

Pruitt, K. D., Tatusova, T., and Maglott, D. R. (2005). NCBI reference sequence (RefSeq): a curated non-redundant sequence database of genomes, transcripts and proteins. *Nucleic Acids Res.* 33, D501–D504. doi: 10.1007/s002329900192

Purohit, R., Ross, M. O., Batelu, S., Kusowski, A., Stemmler, T. L., Hoffman, B. M., et al. (2018). Cu(+)-specific CopB transporter: revising P1B-type ATPase classification. *Proc. Natl. Acad. Sci. U.S.A.* 115, 2108–2113. doi: 10.1093/nar/gki025

Qin, W., Zhao, J., Yu, X., Liu, X., Chu, X., Tian, J., et al. (2019). Improving cadmium resistance in *Escherichia coli* through continuous genome evolution. *Front. Microbiol.* 10:278. doi: 10.1073/pnas.1721783115

Radford, D. S., Kihlken, M. A., Borrelly, G. P., Harwood, C. R., Le Brun, N. E., and Cavet, J. S. (2003). CopZ from *Bacillus subtilis* interacts in vivo with a copper exporting CPx-type ATPase CopA. *FEMS Microbiol. Lett.* 220, 105–112. doi: 10.3389/fmicb.2019.00278

Rensing, C., Mitra, B., and Rosen, B. P. (1997). The zntA gene of *Escherichia coli* encodes a Zn(II)-translocating P-type ATPase. *Proc. Natl. Acad. Sci. U.S.A.* 94, 14326–14331. doi: 10.1016/S0378-1097(03)00095-8

Romiguier, J., and Roux, C. (2017). Analytical biases associated with GC-content in molecular evolution. *Front. Genet.* 8:16. doi: 10.1073/pnas.94.26.14326

Rosdahl, V. T., and Rosendal, K. (1980). Resistance to cadmium, arsenate and mercury among Danish strains of *Staphylococcus aureus* isolated from cases of bacteriaemia, 1957-74. *J. Med. Microbiol.* 13, 383–391. doi: 10.3389/fgene.2017.00016

Sáenz-Lahoya, S., Bitarte, N., García, B., Burgui, S., Vergara-Irigaray, M., Valle, J., et al. (2019). Noncontiguous operon is a genetic organization for coordinating bacterial gene expression. *Proc. Natl. Acad. Sci. U.S.A.* 116, 1733–1738. doi: 10.1099/00222615-13-3-383

Saier, M. H. Jr., Tran, C. V., and Barabote, R. D. (2006). TCDB: the transporter classification database for membrane transport protein analyses and information. *Nucleic Acids Res.* 34, D181–D186. doi: 10.1073/pnas.1812746116

Scherer, J., and Nies, D. H. (2009). CzcP is a novel efflux system contributing to transition metal resistance in *Cupriavidus metallidurans* CH34. *Mol. Microbiol.* 73, 601–621. doi: 10.1093/nar/gkj001

Schwager, S., Lumjiaktase, P., Stöckli, M., Weisskopf, L., and Eberl, L. (2012). The genetic basis of cadmium resistance of *Burkholderia cenocepacia*. *Environ. Microbiol. Rep.* 4, 562–568. doi: 10.1111/j.1365-2958.2009.06792.x

Shamim, S., Rehman, A., and Qazi, M. H. (2014). Cadmium-resistance mechanism in the bacteria *Cupriavidus metallidurans* CH34 and *Pseudomonas* putida mt2. *Arch. Environ. Contam. Toxicol.* 67, 149–157. doi: 10.1111/j.1758-2229.2012.00372.x

Sharma, R., Rensing, C., Rosen, B. P., and Mitra, B. (2000). The ATP hydrolytic activity of purified ZntA, a Pb(II)/Cd(II)/Zn(II)-translocating ATPase from *Escherichia coli*. *J. Biol. Chem.* 275, 3873–3878. doi: 10.1007/s00244-014-0009-7

Shen, L., Li, Z., Wang, J., Liu, A., Li, Z., Yu, R., et al. (2018). Characterization of extracellular polysaccharide/protein contents during the adsorption of Cd(II) by Synechocystis sp. PCC6803. *Environ. Sci. Pollut. Res. Int.* 25, 20713–20722. doi: 10.1074/jbc.275.6.3873

Sheng, Y., Wang, Y., Yang, X., Zhang, B., He, X., Xu, W., et al. (2016). Cadmium tolerant characteristic of a newly isolated *Lactococcus lactis* subsp. lactis. *Environ. Toxicol. Pharmacol.* 48, 183–190. doi: 10.1007/s11356-018-2163-3

Shi, Z., Zhang, Z., Yuan, M., Wang, S., Yang, M., Yao, Q., et al. (2020). Characterization of a high cadmium accumulating soil bacterium, *Cupriavidus* sp. WS2. *Chemosphere* 247:125834. doi: 10.1016/j.etap.2016.10.007

Sitsel, O., Gronberg, C., Autzen, H. E., Wang, K., Meloni, G., Nissen, P., et al. (2015). Structure and Function of Cu(I)- and Zn(II)-ATPases. *Biochemistry* 54, 5673–5683. doi: 10.1016/j.chemosphere.2020.125834

Smith, A. T., Barupala, D., Stemmler, T. L., and Rosenzweig, A. C. (2015). A new metal binding domain involved in cadmium, cobalt and zinc transport. *Nat. Chem. Biol.* 11, 678–684. doi: 10.1021/acs.biochem.5b00512

Smith, A. T., Smith, K. P., and Rosenzweig, A. C. (2014). Diversity of the metal-transporting P1B-type ATPases. *J. Biol. Inorg. Chem.* 19, 947–960. doi: 10.1038/nchembio.1863

Solovieva, I. M., and Entian, K. D. (2002). Investigation of the yvgW *Bacillus subtilis* chromosomal gene involved in Cd(2+) ion resistance. *FEMS Microbiol. Lett.* 208, 105–109. doi: 10.1007/s00775-014-1129-2

Solovieva, I. M., and Entian, K. D. (2004). Metalloregulation in *Bacillus subtilis*: the copZ chromosomal gene is involved in cadmium resistance. *FEMS Microbiol. Lett.* 236, 115–122. doi: 10.1111/j.1574-6968.2002.tb11068.x

Solovyev, V. S., and Asaf, S. (2011). "Automatic annotation of microbial genomes and metagenomic sequences," in *Metagenomics And Its Applications In Agriculture, Biomedicine And Environmental Studies*, ed. R. W. Li (Hauppauge, NY: Nova Science Publishers), 61–78. doi: 10.1111/j.1574-6968.2004.tb09636.x

Steunou, A. S., Durand, A., Bourbon, M. L., Babot, M., Tambosi, R., Liotenberg, S., et al. (2020). Cadmium and copper cross-tolerance. Cu(+) Alleviates Cd(2 +)

Toxicity, and both cations target heme and chlorophyll biosynthesis pathway in *Rubrivivax gelatinosus*. *Front. Microbiol.* 11:893.

Stroebel, D., Sendra, V., Cannella, D., Helbig, K., Nies, D. H., and Covès, J. (2007). Oligomeric behavior of the RND transporters CusA and AcrB in micellar solution of detergent. *Biochim. Biophys. Acta* 1768, 1567–1573. doi: 10.3389/fmicb.2020.00893

Sweeney, H. M., and Cohen, S. (1968). Wild-type strain of Staphylococcus aureus containing two genetic linkage groups for penicillinase production. *J. Bacteriol.* 96, 920–924. doi: 10.1016/j.bbamem.2007.03.008

Tal, N., and Schuldiner, S. (2009). A coordinated network of transporters with overlapping specificities provides a robust survival strategy. *Proc. Natl. Acad. Sci. U.S.A.* 106, 9051–9056. doi: 10.1128/jb.96.4.920-924.1968

Tatusov, R. L., Koonin, E. V., and Lipman, D. J. (1997). A genomic perspective on protein families. *Science* 278, 631–637. doi: 10.1073/pnas.0902400106

Terhune, C. (2017). Vitek 2 GP in vitro device. *Biomed. Saf. Stand.* 47:418. doi: 10.1126/science.278.5338.631

Toes, A. M., Daleke, M. H., Kuenen, J. G., and Muyzer, G. (2008). Expression of copA and cusA in Shewanella during copper stress. *Microbiology (Reading)* 154(Pt 9), 2709–2718.

UniProt Consortium. (2019). UniProt: a worldwide hub of protein knowledge. *Nucleic Acids Res.* 47, D506–D515. doi: 10.1099/mic.0.2008/016857-0

Waisberg, M., Joseph, P., Hale, B., and Beyersmann, D. (2003). Molecular and cellular mechanisms of cadmium carcinogenesis. *Toxicology* 192, 95–117. doi: 10.1093/nar/gky1049

Wang, K., Sitsel, O., Meloni, G., Autzen, H. E., Andersson, M., Klymchuk, T., et al. (2014). Structure and mechanism of Zn2+-transporting P-type ATPases. *Nature* 514, 518–522. doi: 10.1016/S0300-483X(03)00305-6

Weisburg, W. G., Barns, S. M., Pelletier, D. A., and Lane, D. J. (1991). 16S ribosomal DNA amplification for phylogenetic study. *J. Bacteriol.* 173, 697–703. doi: 10.1038/nature13618

Wu, H., Zhang, Z., Hu, S. N., and Yu, J. (2012). On the molecular mechanism of GC content variation among eubacterial genomes. *Biol. Direct* 7:2. doi: 10.1128/jb.173.2.697-703.1991

Xie, Q., Liu, N., Lin, D., Qu, R., Zhou, Q., and Ge, F. (2020). The complexation with proteins in extracellular polymeric substances alleviates the toxicity of Cd (II) to Chlorella vulgaris. *Environ. Pollut.* 263(Pt A):114102. doi: 10.1186/1745-6150-7-2

Xing, C., Chen, J., Zheng, X., Chen, L., Chen, M., Wang, L., et al. (2020). Functional metagenomic exploration identifies novel prokaryotic copper resistance genes from the soil microbiome. *Metallomics* 12, 387–395. doi: 10.1016/j.envpol.2020.114102

Yan, X., Zhang, Q., Zou, J., He, C., and Tao, J. (2019). Selection of optimized reference genes for qRT-PCR normalization in *Xanthomonas campestris* pv. campestris cultured in different media. *Curr. Microbiol.* 76, 613–619. doi: 10.1039/c9mt00273a

Young, J. M., Leschine, S. B., and Reguera, G. (2012). Reversible control of biofilm formation by *Cellulomonas* spp. in response to nitrogen availability. *Environ. Microbiol.* 14, 594–604. doi: 10.1007/s00284-019-01667-y

Zhang, H., Zhou, Y., Bao, H., Zhang, L., Wang, R., and Zhou, X. (2015). Plasmid-borne cadmium resistant determinants are associated with the susceptibility of Listeria monocytogenes to bacteriophage. *Microbiol. Res.* 172, 1–6. doi: 10.1111/j.1462-2920.2011.02596.x

Zheng, J. X., Lin, Z. W., Chen, C., Chen, Z., Lin, F. J., Wu, Y., et al. (2018). Biofilm formation in *Klebsiella pneumoniae* bacteremia strains was found to be associated with CC23 and the presence of wcaG. *Front. Cell Infect. Microbiol.* 8:21. doi: 10.1016/j.micres.2015.01.008

Zheng, X. C. L., Chen, M. M., Chen, J. H., and Li, X. F. (2019). Functional metagenomics to mine soil microbiome for novel cadmium resistance genetic determinants. *Pedosphere* 19, 29, 298–310. doi: 10.3389/fcimb.2018.00021

Zielazinski, E. L., Cutsail, G. E. III, Hoffman, B. M., Stemmler, T. L., and Rosenzweig, A. C. (2012). Characterization of a cobalt-specific P(1B)-ATPase. *Biochemistry* 51, 7891–7900. doi: 10.1016/S1002-0160(19)60804-0

Zuo, G., Qi, J., and Hao, B. (2018). Polyphyly in 16S rRNA-based LVTree versus monophyly in whole-genome-based CVTree. *Genomics Proteomics Bioinformatics* 16, 310–319. doi: 10.1021/bi3006708

Conflict of Interest: The authors declare that the research was conducted in the absence of any commercial or financial relationships that could be construed as a potential conflict of interest.

Publisher's Note: All claims expressed in this article are solely those of the authors and do not necessarily represent those of their affiliated organizations, or those of the publisher, the editors and the reviewers. Any product that may be evaluated in this article, or claim that may be made by its manufacturer, is not guaranteed or endorsed by the publisher.

frontiers in Microbiology

ORIGINAL RESEARCH
published: 16 February 2022
doi: 10.3389/fmicb.2022.820048

Strong Antimicrobial Activity of Silver Nanoparticles Obtained by the Green Synthesis in *Viridibacillus sp*. Extracts

Priyanka Singh[1]* *and Ivan Mijakovic*[2]*

[1] The Novo Nordisk Foundation, Center for Biosustainability, Technical University of Denmark, Kongens Lyngby, Denmark, [2] Systems and Synthetic Biology Division, Department of Biology and Biological Engineering, Chalmers University of Technology, Gothenburg, Sweden

Recently, green silver nanoparticles (G-AgNPs) have gained much attention in medical science due to their extraordinary effects against multidrug-resistant microorganisms. The strong antimicrobial nature of G-AgNPs corresponds to their unique physicochemical properties such as size, shape, surface charge, and active surface groups available to interact with the pathogens. The current study demonstrates a simple, environmentally friendly, and economical method to produce G-AgNPs from an environmental isolate of *Viridibacillus* sp. The produced G-AgNPs were characterized by various analytical methods, including UV-Vis spectroscopy, single-particle inductively coupled plasma-mass spectrometry (sp-ICP-MS), scanning electron microscopy (SEM), energy dispersive x-ray spectroscopy (EDX), elemental mapping, transmission electron microscopy (TEM), dynamic light scattering (DLS), Fourier-transform infrared spectroscopy (FTIR), and Thermogravimetric analysis (TGA). The reduction of Ag^{+} to Ag° was observed by UV-Vis spectroscopy, which demonstrated the formation of stable G-AgNPs with a Surface Plasmon Resonance (SPR) band at the maximum of 430 nm. TEM analysis demonstrated that the G-AgNPs were spherical with a 5–30 nm size range. The produced G-AgNPs were stable for more than 1 year in an aqueous solution at 4°C. Importantly, G-AgNPs showed remarkable antimicrobial activity against Gram-negative pathogens- *E. coli* and *P. aeruginosa* with MIC values of 0.1 and 4 μg/mL and MBC values of 1 and 8 μg/mL, respectively. This level of antimicrobial activity is superior to other AgNPs reported in the literature.

Keywords: silver nanoparticles, green synthesis, strong antimicrobial activity, highly stable AgNPs, Gram-negative pathogenic microorganisms, environmental isolate

OPEN ACCESS

Edited by:
Mirian A. F. Hayashi,
Federal University of São Paulo, Brazil

Reviewed by:
Santosh Kumar,
Central Institute of Technology, Kokrajhar, India
Gajanan Ghodake,
Dongguk University Seoul, South Korea

***Correspondence:**
Priyanka Singh
prisin@biosustain.dtu.dk
Ivan Mijakovic
ivan.mijakovic@chalmers.se

Specialty section:
This article was submitted to Antimicrobials, Resistance and Chemotherapy, a section of the journal Frontiers in Microbiology

Received: *22 November 2021*
Accepted: *25 January 2022*
Published: *16 February 2022*

Citation:
Singh P and Mijakovic I (2022) Strong Antimicrobial Activity of Silver Nanoparticles Obtained by the Green Synthesis in Viridibacillus sp. Extracts. Front. Microbiol. 13:820048. doi: 10.3389/fmicb.2022.820048

INTRODUCTION

Silver nanoparticles (AgNPs) are widely known for their industrial applications in the field of medicine, pharmacology, food, agriculture, cosmetics, and textiles due to their unique antimicrobial properties, which further depend on nanoparticles (NPs) structure (Gherasim et al., 2020). The most common methods applied for AgNPs production are physiochemical methods such as laser irradiation, thermal decomposition, electrochemical synthesis, chemical reduction, etc.

(Zhang et al., 2018). However, these methodologies also bring many limitations, for instance, the use of toxic materials and volatiles organic solvents, demand for high energy consumption by using high temperature and pressure, the release of harmful byproducts, and toxic waste, which causes potential environmental damage (Garg et al., 2020). The most important limitation is the absorbance of unwanted toxic materials on the surface of produced nanoparticles, which further provide human and environmental toxicity, thus limiting the clinical use of NPs. These limitations motivate the development of green alternative methodologies, which leads to the formation of uniform and stable NPs with a biocompatible layer (called the corona) around them (Singh et al., 2016a; Heinemann et al., 2021). These green nanoparticles have a range of unlimited pharmaceutical applications, including drugs delivery, gene delivery, as a sensor for pathogens detection, and tissue engineering. Various green approaches to produce nanoparticles by using living entities have been reported, such as plant extracts, fungi, yeast, actinomycetes, algae, bacteria, and viruses (Zhang et al., 2020). One such popular approach is using bacteria as a cell factory to produce the AgNPs extracellularly. In addition, to producing biocompatible NPs, bacteria-mediated synthesis is low-cost, environmentally friendly, safe, and simple (Xu et al., 2020; Ssekatawa et al., 2021).

Developing resistance mechanisms in pathogenic microorganisms against current and developing drugs has become a prime concern in the medical field. Understanding the developing resistance mechanisms in these pathogens is important, and designing novel and strong antimicrobial agents that can overcome or circumvent the resistance is equally important (Liu et al., 2021). Indeed, with exposure to novel antimicrobial agents, there are always opportunities for microbes to become unresponsive or resistant. Pathogenic bacteria exert resistance by four different mechanisms: (a) by modification of target proteins, (b) enzymatic degradation or inactivation of drug, (c) decreased membrane permeability which blocks drugs intake, and (d) increased efflux of the drug (Kumar et al., 2021). In this context, G-AgNPs display a broad spectrum of antimicrobial activities and are therefore likely to escape the common mechanisms of resistance development (Prasher et al., 2018). G-AgNPs have been reported as effective treatments against many drug-resistant microorganisms, individually or with traditional/modern antibiotics (Burdusel et al., 2018; Deshmukh S.P. et al., 2019). AgNPs exert killing against multidrug-resistance bacteria by various mechanisms, including membrane damage/leakage, DNA damage, ROS generation, inactivation of intracellular proteins/enzymes, etc. (**Figure 1**). Recently Ssekatawa et al. (2021) showed the green synthesis of AgNPs from the extract of medicinal plants–*Camellia sinensis* and *Prunus Africana*. The current study deals with the extracellular synthesis of G-AgNPs from an environmental isolate without any additives for the reduction or stabilization process. The extracellular constituents of cells act as reducing and stabilizing agents. In addition to extensive characterization, we explored the synthesized G-AgNPs against *E. coli*, and *P. aeruginosa*, to study their antibacterial property.

MATERIALS AND METHODS

Materials

Silver nitrate ($AgNO_3$), tryptic soya agar (TSA), tryptic soya broth (TSB), and Luria broth (LB) were purchased from Sigma-Aldrich Chemicals, St. Louis, MO, United States.

Identification of Potential Strain

A soil sample was collected in sterile poly bags from the Technical University of Denmark (DTU) field, Lyngby, Denmark. Single colonies were isolated by using the serial dilution technique on TSA plates. All the isolates were tested for primary AgNPs production, and the strongest strain was chosen for further studies. Molecular identification of the isolated potential strain was performed using 16S rDNA amplification and sequencing. Genomic DNA was isolated using the DNeasy Blood and Tissue Kit (Qiagen) and used as a template for PCR with the universal primers 27 F (5′-AGAGTTTGATCMTGGCTCAG-3′) and 1492 R (3′-TACGGYTACCTTGTTACGACTT-5′) (Singh et al., 2017). Eurofins Genomics (Ebensburg, Germany) sequenced the PCR product, and the sequence was analyzed using the NCBI BLAST homepage against the reference sequence database.

Green Synthesis of Green Silver Nanoparticles

The isolated strain was cultured overnight in 100 mL of TSB, at 37°C, 120 rpm. Next, the growth medium was centrifuged to separate the cells at 8,000 rpm for 10 min. The cell-free supernatant was supplemented with 1 mM $AgNO_3$ and incubated in a shake flask incubator at 37°C, 200 rpm, and 24–48 h. The silver salt mix supernatant (reaction medium) was monitored continuously for AgNPs production, by visual inspection, and by recording the UV-Vis spectra of the reaction medium at definite time intervals. Once the G-AgNPs were formed, for purification, the reaction medium was centrifuged at 3,000 for 5 min to remove any big and unwanted components. Then the same medium was centrifuged at 14,000 rpm for 15 min (Singh et al., 2016b). The supernatant was decanted off to collect the pellets then washed several times with distilled water. This residue was suspended again into sterile water and used for all experiments.

Analytical Characterization of Green Silver Nanoparticles

UV-Vis Study

The reduction of silver ions (Ag +) to G-AgNPs was initially monitored *via* visible inspection and then by scanning the reaction medium in UV-Vis spectroscopy at a specific interval. The UV-Vis spectrum was obtained using 6705 UV-Vis spectrophotometer, JENWAY, by scanning 1 mL of the reaction medium in the range of 300–700 nm. The optimization studies for G-AgNPs production were also conducted using visible and UV-Vis spectrum analysis.

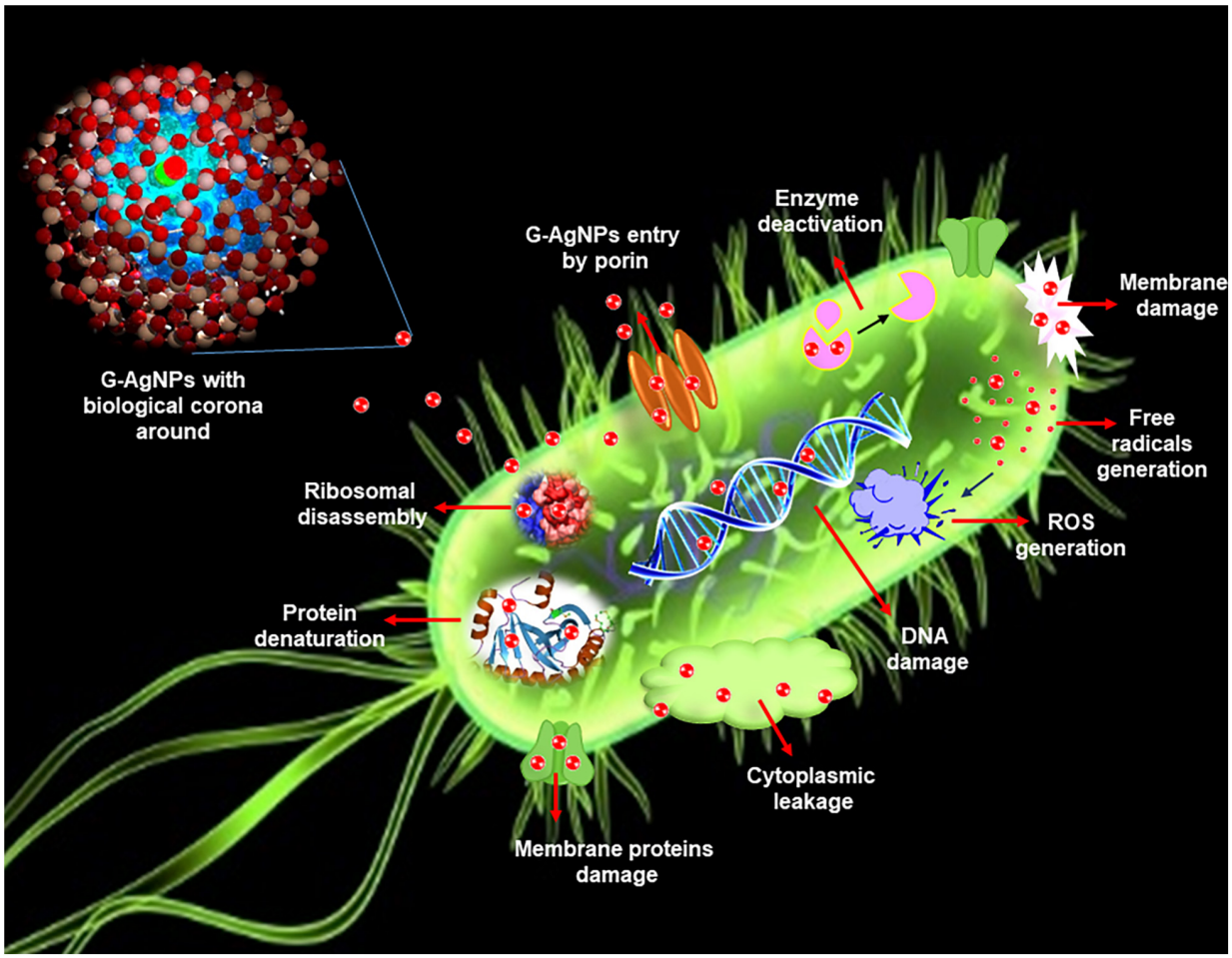

FIGURE 1 | Schematic representation of silver nanoparticles (AgNPs) antimicrobial mechanisms in *Escherichia coli*.

Single-Particle Inductively Coupled Plasma-Mass Spectrometry

To know the concentration of produced G-AgNPs, sp-ICP-MS (NexION 350D; PerkinElmer Inc., Waltham, MA, United States) was performed. The stability of G-AgNPs was examined by using the purified G-AgNPs and keeping them for a different time, temperatures, and indifferent bacteriological media such as TSB and LB. The results were observed by visible inspection of which pictures are taken, UV-Vis, and sp-ICP-MS analysis before and after the defined period (Singh et al., 2021).

Thermogravimetric Analysis Examination

Thermogravimetric analysis (TA Instruments, New Castle, DE, United States) was performed to check the temperature stability G-AgNPs. For analysis, G-AgNPs samples in dried and powdered form were placed in an alumina pan and heated from 20 to 700°C at a ramping time of 10°C/min.

Scanning Electron Microscopy

Scanning electron microscopy examination with energy dispersive X-ray (EDX) and elemental mapping was performed to study the G-AgNPs morphology and elemental composition. EDX analysis setup was coupled with the SEM instrument. Sample preparation was done by dropping 5 μl of pure G-AgNPs (0.1 mg/mL) on carbon tape and air-dried at room temperature (RT) for 15 min. SEM Micrographs were recorded using a Quanta FEG 200 ESEM microscope (Quorum Technologies, Hitachi High-Tech Europe GmbH, Sweden).

Transmission Electron Microscopy

Transmission electron microscopy study using FEI Tecnai T20 G2 was conducted to analyze the internal morphology, composition, and crystallographic information of G-AgNPs. The instrument was operated at an acceleration voltage of 200 kV. A sample of G-AgNPs was prepared by spotting a drop of pure NPs solution suspended in water on a carbon-coated copper grid. The sample-containing grid was completely dried before analysis.

Atomic Force Microscopy

Atomic force microscopy (Park NX20)[1] measurements were carried out in intermittent contact mode using standard probes

[1]www.parkafm.com

of single-crystal highly doped silicon with a radius of curvature of less than 30 nm (SuperSharpSiliconTM Non-contact AFM probes from Nanosensors). The standard uncertainty u(d) of the measured diameters is u(d) < 0.05 day (Singh et al., 2018c).

Dynamic Light Sattering Analysis

Dynamic light sattering measurements were performed to study the size distribution concerning intensity and zeta potential of pure G-AgNPs. Particle size measurement was executed using Zetasizer Nano ZS, Chuo-ku Kobe-shi, Japan. The autocorrelation functions of the samples were analyzed using the Contin algorithm through the Zetasizer 7.12 software. Samples were run in triplicates (Wypij et al., 2021).

Fourier Transform-Infrared Spectroscopy

Green silver nanoparticles were subjected to Fourier transform infrared (FTIR) analysis to determine the presence of biomolecules, functional groups responsible for the reduction and capping/stabilization. The FTIR measurements were carried out using Nicolet iS50 (Thermo Fisher Scientific, Waltham, MA, United States) by scanning the air-dried purified G-AgNPs and freeze-dried cell's supernatant within the range of 500–4,000 cm^{-1}. The recorded spectra recorded were plotted as transmittance (%) vs. wavenumber (cm^{-1}).

Antimicrobial Activity of Green Silver Nanoparticles

Green Silver Nanoparticles Effects on Gram-Negative Pathogens

The antimicrobial activity of G-AgNPs was evaluated against two Gram-negative pathogens: *Escherichia coli* UTI 89, and *Pseudomonas aeruginosa* PAO1. Both the strains were grown overnight in LB medium at 37°C for 24 h. The overnight grown cultures were diluted to approximately $1–2 \times 10^5$ colony-forming units (CFU)/mL using LB medium. Then, the G-AgNPs were added in concentrations ranging from 0.1 to 16 μg/mL. The LB medium containing respective pathogenic bacteria and G-AgNPs were further incubated in a shake flask incubator at 37°C, 150 rpm, for 24 h. After 24 h, the samples were analyzed by measuring the optical density (OD) at 550 nm. The MIC was defined as the lowest concentration of G-AgNPs, which inhibited the bacterial growth, measured as OD_{550}. The MBC value was defined as the lowest concentration of G-AgNPs required to kill the respective bacterial strain. To measure MBC, 100 μL of the LB medium containing respective pathogenic bacteria and G-AgNPs were spread on agar plates and incubated at 37°C overnight, followed by a CFU count.

Live and Dead Staining

To visualize the viable and dead cells, control cells and cells treated with G-AgNPs were stained for 20 min with a mixture of 6.0 μM SYTO 9 and 30 μM KI from Live/Dead BacLight Viability kit L13152 (Invitrogen, Molecular Probes, Inc., Eugene, OR, United States). Fluorescence microscopic imaging of the cells was performed using a LEICA DM 4000 B (Leica Microsystems, Copenhagen, Denmark).

Scanning Electron Microscopy Analysis of Treated Cells

To evaluate the drastic effects of G-AgNPs on individual cells, SEM was carried out. SEM was performed by fixing the control and treated cells with 3% of glutaraldehyde overnight at 4°C. The next day, the samples were dehydrated with graded series of ethanol concentrations (40, 50, 60, 70, 80, and 90%) for 15 min and with absolute ethanol for 20 min. The dehydrated samples were placed on SEM carbon tape and left to dry at RT. The samples were coated with gold before SEM imaging. EDX and elemental mapping of G-AgNPs treated cells was also performed to check that the killing effects are due to the action of G-AgNPs only.

RESULTS

Molecular Characterization of the Isolate

The rRNA sequencing of isolated bacterial strain indicated 99.05% identity with *Viridibacillus arvi* strain LMG 22165. The isolated strain sequence number is submitted to NCBI with GenBank ID: SUB10641455. *Viridibacillus arvi* is reported to be Gram-positive, aerobic, spore-forming, rod-shaped bacteria (Albert et al., 2007). Based on 16rRNA sequence similarity, the isolated strain was referred to as *Viridibacillus* sp.

Green Synthesis of Green Silver Nanoparticles

The supernatant of a culture of *Viridibacillius* sp. grown for 24 h was used as a reaction medium to reduce silver salt and provide capping/stabilizing components to the formed G-AgNPs. The culture supernatant was supplemented with 1 mM $AgNO_3$ and incubated further in a shake flask incubator at 37°C, 200 rpm, for 24–48 h. After the incubation period, the supernatant showed a visible color change from pale yellow to deep brown, which is attributed to the surface plasmon resonance (SPR) property of G-AgNPs (Ronavari et al., 2021). The observation was further confirmed by simultaneously recording the SPR band *via* UV-Vis at a specified time interval. After incubation, the reaction medium was first directly scanned, and then the purified G-AgNPs samples were also scanned to confirm the peaks intensity and overlapping range (**Figures 2A,B**). Purified G-AgNPs showed a strong and sharp SPR peak at 430 nm. The kinetics of G-AgNPs formation was monitored by recording the spectrum of the reaction medium at different temperatures, times, and various salt concentrations. For temperature optimization studies, the highest and clear peak in UV-Vis spectra was observed at 37°C (**Figure 2C**). According to the time-resolved UV-Vis spectra, the SPR absorbance band increased with the reaction time for up to 48 h (**Figure 2D**). For the salt concentration optimization, as the salt concentration increased, the intensity of the SPR band also increased. This trend continued to up to 3.5 mM (**Figures 2E–H**); any further increase in salt concentration led to broadening the peak and accumulation of NPs in the reaction medium. Thus the optimal conditions for G-AgNPs production using cell-free supernatant

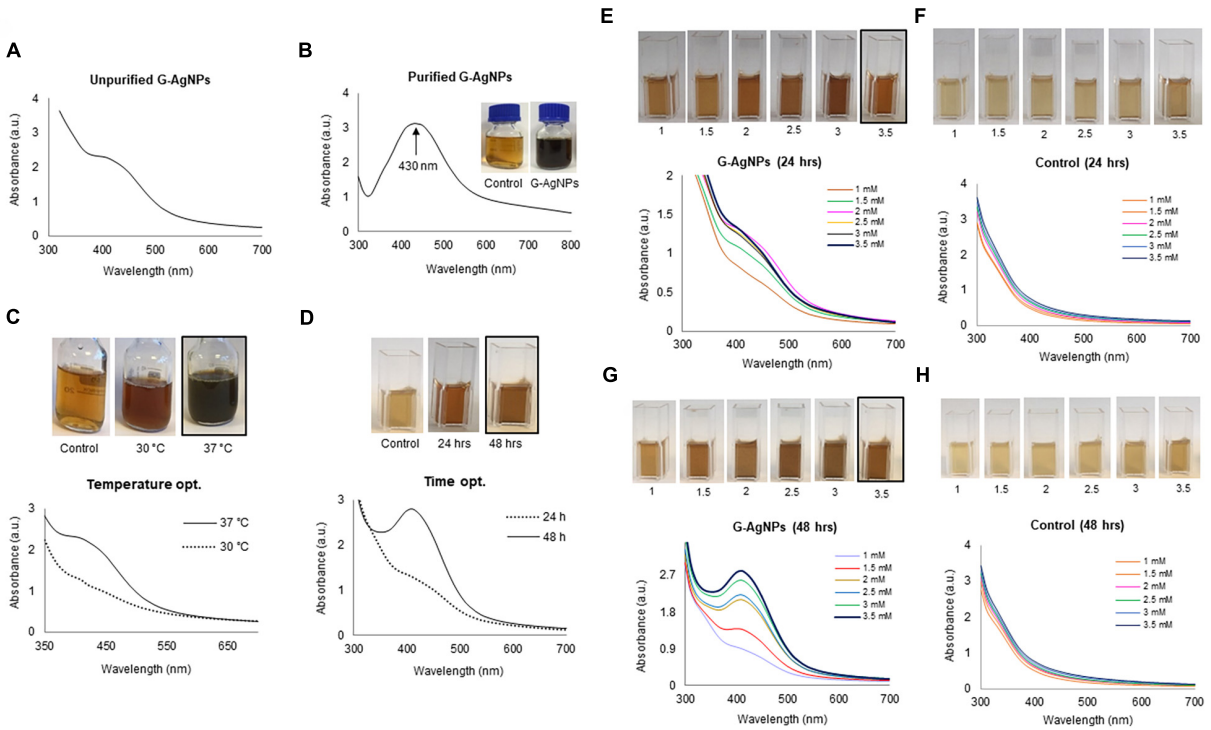

FIGURE 2 | Visible and UV-Vis spectral examination of optimization studies for green silver nanoparticles (G-AgNPs) production. **(A)** UV-Vis peak of unpurified G-AgNPs after 48 h of synthesis, **(B)**, purified G-AgNPs. **(C)** Visible and UV-Vis peaks for temperature optimization, **(D)** time optimization, **(E–H)** salt optimization for G-AgNPs production at 24 and 48 h.

of *Viridibacillus* sp., were $AgNO_3$ concentration of 3.5 mM, the temperature of 37°C, and the incubation period of 48 h. Any deviations from these key parameters resulted in disturbance of the UV-Vis peaks, signifying particle agglomeration.

Characterization of Green Silver Nanoparticles

To check the yield of G-AgNPs, sp-ICP-MS was used. The result showed that the measured total mass concentration of G-AgNPs was 0.078 μg/μl, with a negligible dissolved fraction (<0.1 ppb). We then examined the stability of G-AgNPs over short and long periods. The measurements were made after 24, 48, 86 h, and 1 year (**Figures 3A–D**). Our study found no significant differences in particle size recorded using sp-ICP-MS, resulting in mean diameter of 15–60 nm, thus indicating the long-term stability of produced G-AgNPs. Based on visible observation, no dissolution or agglomeration of G-AgNPs occurred even after 1 year of storage in an aqueous solution. In addition, UV-Vis observations of G-AgNPs showed a sharp and overlapping peak before and after 1 year, thus confirming their aqueous stability (**Figure 3E**). A bacterial growth medium, such as TSB and LB, and water were tested for G-AgNPs stability (**Figure 3F**). The results showed that the G-AgNPs are completely stable in water as well as in the growth media. For thermal stability, the TGA measurement was taken (**Figure 3G**). According to the obtained spectra, there were two stages of weight loss, first at 150°C and second at 400°C. The physical adsorption of water molecules caused the initial loss of weight up to 150°C on the surfaces of the G-AgNPs. At 400°C, most of the weight loss was due to the biomolecules decomposing and evaporating from the surface of the G-AgNPs (Deshmukh A.R. et al., 2019). A further increase in temperature led to the complete degradation of G-AgNPs.

The purity and crystalline nature of G-AgNPs that were produced under optimized conditions were investigated by conducting SEM, EDX, elemental mapping, TEM, and Selected area (electron) diffraction (SAED) studies. SEM image examination showed the spherical structure of G-AgNPs (**Figures 4A,B**). The elemental mapping results demonstrated the selected scanned area of the G-AgNPs sample (**Figures 4C–E**) resembles the silver element (pink color) (Deshmukh A.R. et al., 2019). The elemental composition of G-AgNPs was determined *via* EDX spectroscopy, which reveals the presence of the strong elemental signal from silver at 3 keV (**Figure 4F**; Singh et al., 2018a). The core size and morphology of G-AgNPs were determined *via* TEM, which displayed the G-AgNPs are approximately spherical and uniformly distributed with an average particles size of 5–30 nm (**Figure 4G**). However, few polydispersity were found in hexagonal and truncated triangular form NPs. This morphology of nanoparticles depends on the experimental conditions and the constituents of the cellular supernatant. The SAED pattern of G-AgNPs indicated characteristic rings at 111, 200, 220, and 311 crystallographic planes, which corresponds to the face-centered cubic (fcc) of

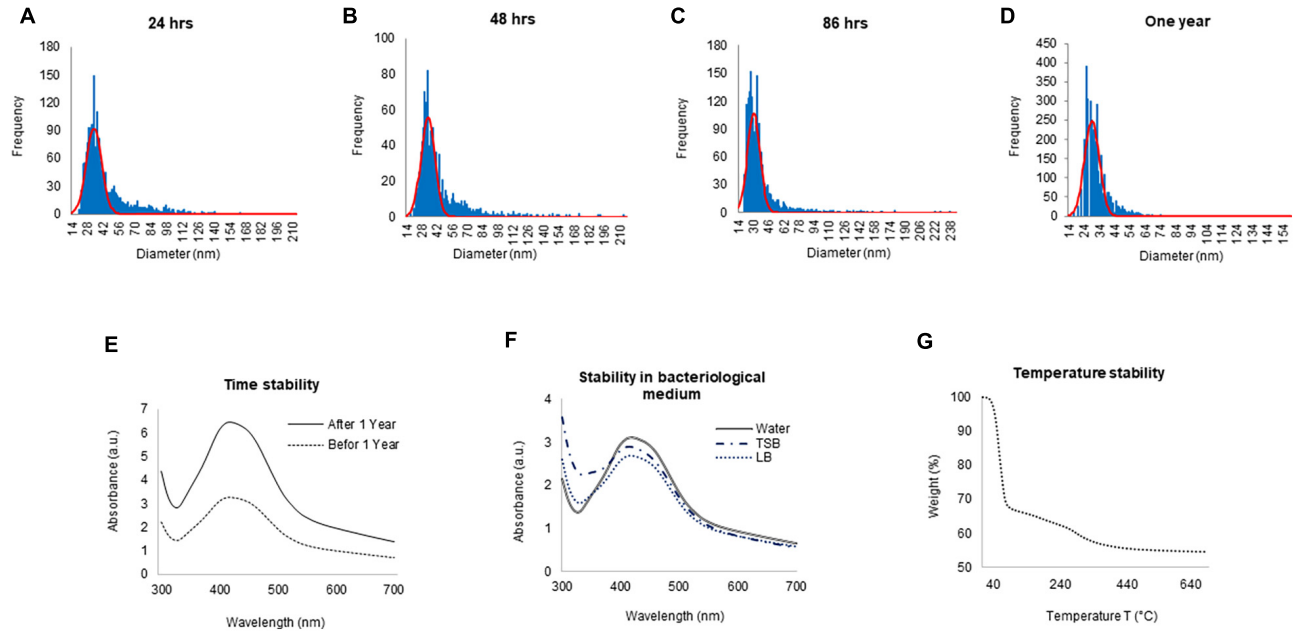

FIGURE 3 | ICPMS and stability analysis of green silver nanoparticles (G-AgNPs). ICPMS histogram of G-AgNPs at different time intervals **(A)** 24 h, **(B)** 48 h, **(C)** 86 h, **(D)** 1 year. UV-Vis spectrum representing the stability analysis of G-AgNPs **(E)** before and after 1 year, **(F)** in a different medium, **(G)** at the temperature range from 20 to 700°C measured by the TGA instrument.

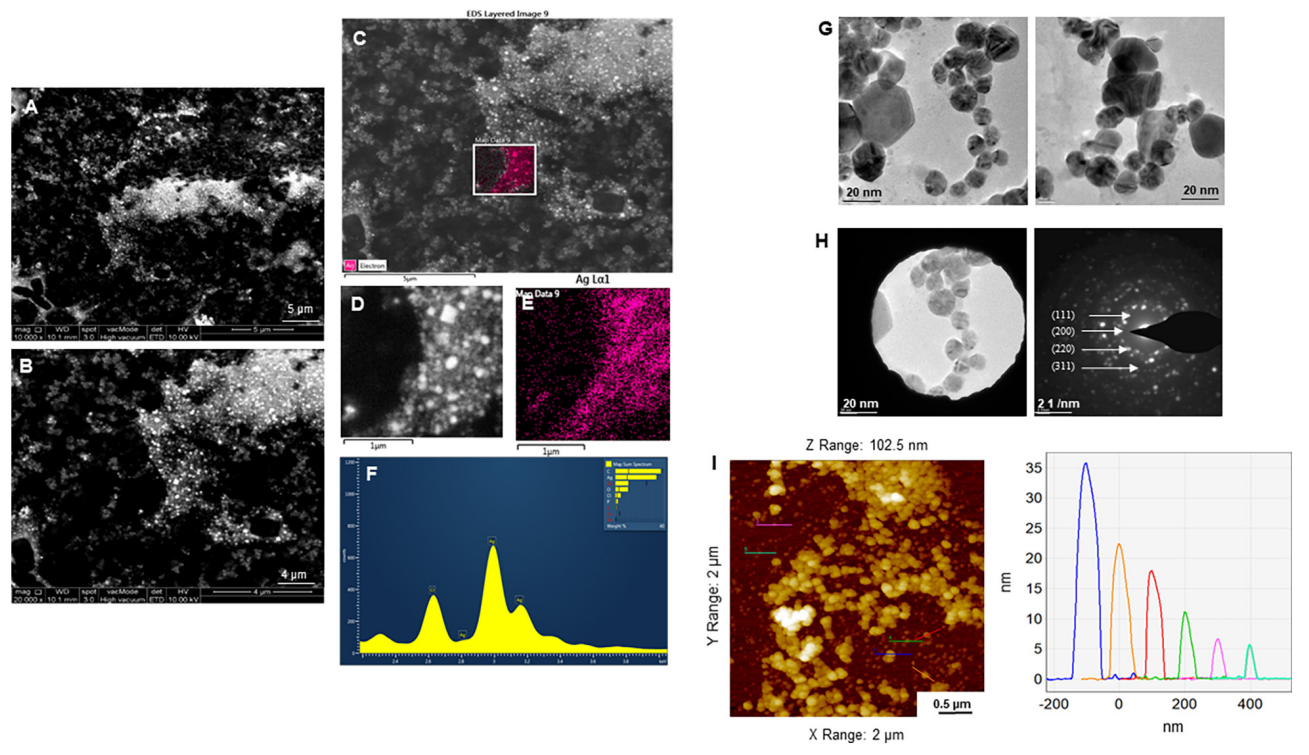

FIGURE 4 | Structural analysis of green silver nanoparticles (G-AgNPs). **(A,B)** Scanning electron microscopy (SEM) images of nanoparticles, **(C–E)** elemental mapping of G-AgNPs showing scanned image of NPs and respective region with the individual silver nanoparticles (pink color), **(F)** energy dispersive x-ray spectroscopy (EDX) spectrum of the elemental mapped region is showing highest peak for silver element. **(G)** Transmission electron microscopy (TEM) image of G-AgNPs showing spherical nanoparticles, **(H)** selected area (electron) diffraction (SAED) pattern of G-AgNPs, and **(I)** AFM size analysis representation of G-AgNPs.

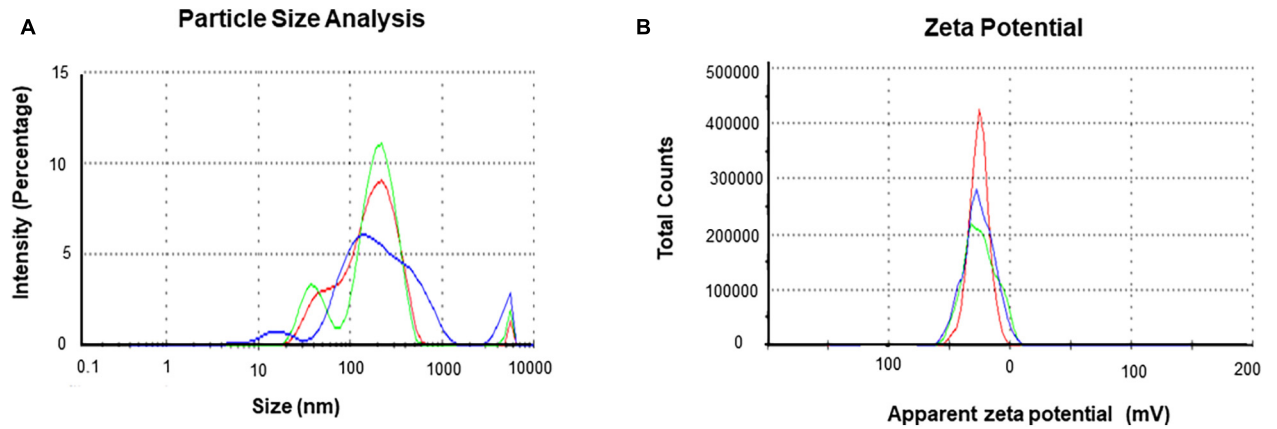

FIGURE 5 | Dynamic light scattering (DLS) analysis of green silver nanoparticles (G-AgNPs) **(A)** nanoparticles distribution concerning size and intensity and **(B)** zeta potential of G-AgNPs representing highly negative surface charge.

AgNPs (**Figure 4H**). These values are in accord with those reported in earlier studies (Sangaonkar and Pawar, 2018); they suggest the crystalline nature of AgNPs. Moreover, the AFM analysis also revealed similar size distribution, from 5 to 35 nm (**Figure 4I**). Hydrodynamic diameter and surface charge of the produced G-AgNPs were determined by DLS. The diameter and PDI were found to be 154.4 nm and 0.378, respectively (**Figure 5A**). The zeta potential value of the aqueous G-AgNPs solution at RT was found to be −25.7 mV (**Figure 5B**), which suggested that the G-AgNPs are negatively charged and quite stable at neutral conditions.

Fourier-transform infrared spectroscopy measurements were conducted to identify the extracellular components released from isolated strain, present in the reaction medium, responsible for reducing, capping, and stabilizing G-AgNPs. The FTIR spectra of freeze-dried cell-free supernatant and purified G-AgNPs are shown in **Figures 6A,B** and **Table 1**. Comparing the FTIR spectrum of cellular supernatant with G-AgNPs, the high broad peaks for G-AgNPs appear at 2884.93 (asymmetric and symmetric C-H stretching, or secondary amines), 1635.21 [carboxyl groups (-C=O), and carbonyl group (-C=O)-stretching vibration of proteins], 1430.79 (C-H bending of COO^{-} or carboxylate groups), 561.08 which are identical to the supernatant spectrum. The FTIR results indicate the presence of carboxyl groups (-C=O), and amine groups (−NH) which represents the presence of proteins, amino acids, and other biomolecules originating from the supernatant on the surface of the produced G-AgNPs, responsible for capping and stabilizing G-AgNPs (Abbai et al., 2016). The FTIR spectrum proved that the reaction medium contains reducing and stabilizing agents such as sugar, proteins, and amino acids responsible for the green synthesis of G-AgNPs.

Strong Antimicrobial Activity of Green Silver Nanoparticles

The most remarkable feature of the G-AgNPs synthesized in this study is their strong bacteriostatic and bactericidal activity against pathogenic *E. coli* and *P. aeruginosa*. The recorded MIC values against *E. coli* and *P. aeruginosa* were 4 and 0.1 μg/mL, respectively, while the respective MBC values were 8 and 1 μg/mL (**Figures 7A,B**). We used the live and dead staining technique to confirm the viability results. This technique allows one to distinguish the live cells (stained green) and dead cells (stained red) under a fluorescence microscope (**Figures 8A–N**). These results confirmed a dramatic onset of killing bacterial cells at G-AgNPs concentrations above 4 μg/mL for *E. coli* (**Figure 8A–H**) and 0.1 μg/mL for *P. aeruginosa* (**Figures 8I–N**). To investigate whether the killing effects involve drastic morphological changes in treated cells, we used SEM. A significant morphological alteration was observed in G-AgNPs treated cells *E. coli* cells (**Figures 9A–F,K–P**) and *P. aeruginosa* cells (**Figures 10A–F,K–P**). The severity of these effects was correlated to the concentration of applied G-AgNPs for both bacterial species. To confirm the damage that G-AgNPs provoked, we performed EDX and elemental mapping of individual cells. The results disclosed that the damaged cells generate a clear peak of the silver element in the EDX spectrum for *E. coli* (**Figures 9G–J,Q–T**) and *P. aeruginosa* cells (**Figures 10G–J,Q–T**). In addition, the mapping results also resemble the silver element in the scanned image of treated cells, indicating that G-AgNPs get internalized.

DISCUSSION

The cell-free supernatant of environmental isolate *Viridibacillus* sp. acted as a reducing and stabilizing agent, which led to the formation of highly stable and monodisperse G-AgNPs. The reduction process does not require any additional reducing or stabilizing agents. Moreover, the synthesis took place in the cell-free medium, which means with the help of extracellularly released biomolecules from the isolated *Viridibacillus* sp. The extracellular components in the reaction medium form a biological corona around the nanoparticles, which helps long-term stabilization. This is an important feature of

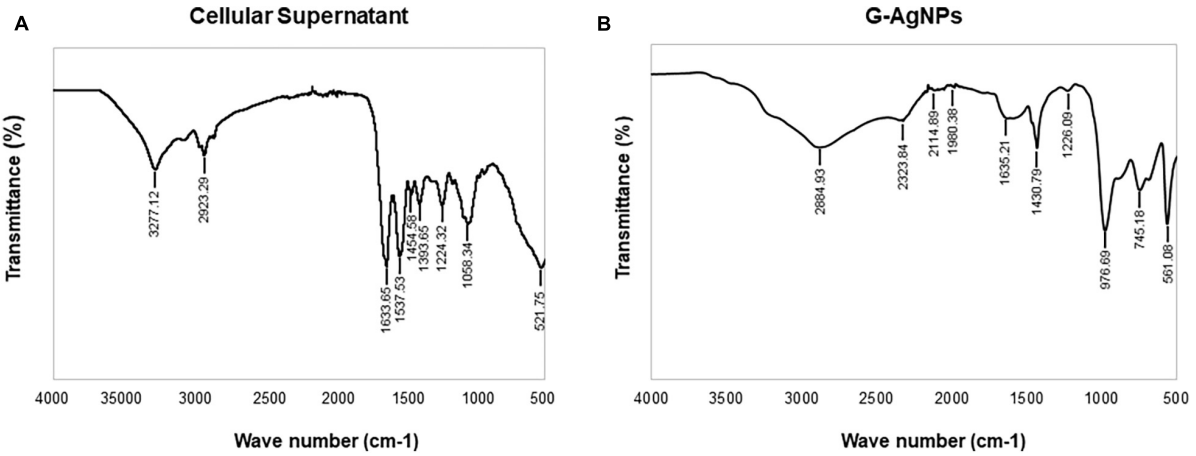

FIGURE 6 | Fourier-transform infrared spectroscopy (FTIR) spectrum of panel **(A)** freeze-dried cellular supernatant and **(B)** green silver nanoparticles (G-AgNPs), which demonstrate the active surface groups for respective samples.

bacteria-mediated extracellular synthesis. Unlike intracellular synthesis, extracellular synthesis provides an opportunity to avoid additional steps in downstream processing, such as cell disruption by membrane lysis or sonication, removal of insoluble components, extraction of complete nanoparticles from intracellular organelles, etc. (Singh et al., 2018b). Thus, the proposed methodology is more economical once an appropriate bacterial strain is identified (Kapoor et al., 2021).

The G-AgNPs formation in our study was supported by visual observation and UV-Vis analysis. Based on kinetics and optimization studies, no significant change in the absorbance was observed beyond the optimized parameters, which suggested that the nucleation and growth process during this period supported the complete reduction of silver salt into G-AgNPs. Moreover, the color, ICPMS, and UV-Vis spectrum of G-AgNPs remained stable for more than 1 year and showed no aggregation (Singh et al., 2021). FTIR was used as a powerful tool to study the functional molecular vibrations. The spectrum of freeze-dried cell-free supernatant of *Viridibacillus* sp. showed that the medium contains proteins, reducing sugars, polysaccharides, various biomolecules, and amino acids, which help reduce and inhibit further agglomeration of produced G-AgNPs. This is the most important advantage of using green nano factories to produce AgNPs. It provides the additional biocompatible layer, which can keep nanoparticles stable for many years without any additives, thus enhancing colloidal stability (Belteky et al., 2019). In contrast, the physically or chemically produced NPs lack the additional biocompatible layer and require a surplus stabilizer. Most of the NPs produced by physical or chemical methods show complete agglomeration with time, even in the presence of stabilizing agents (Deshmukh A.R. et al., 2019).

TABLE 1 | Fourier transform-infrared spectroscopy (FT-IR) spectra of cellular extract and green silver nanoparticles (G-AgNPs).

Type of Bond	Cellular extract Wavenumber (cm^{-1})	G-AgNPs Wavenumber (cm^{-1})
-OH (hydroxyl group) of phenolic compounds and N-H group	3277.12	
asymmetric stretching of a methyl group -CH_3 C-H stretching of alkanes or secondary amine	2923.29	2884.93
Alkyne group		2114.89, 1980.38
-C=O stretching vibration in flavonoids and terpenoids, and carbonyl group (-C=O) stretching vibration of proteins or amide I)	1633.65, 1537.53	1635.21
N-H stretching vibration of proteins	1454.58	1430.79
C-N aromatic amino groups	1393.65	
Overlapping of C-O, C-N, C-O-C and C-O-P stretching modes	1058.34	
C-C deformation	521.75	561.08

Silver nanoparticles effects on pathogenic bacteria are well known (**Figure 1**; Liao et al., 2019; Crisan et al., 2021). The effects of AgNPs on Gram-negative and Gram-positive bacteria are mainly influenced by the thickness and composition of the cell wall, which means that Gram-negative bacteria are more susceptible, and Gram-positive bacteria can show resistance to some extent. Except for the thin cell membrane, the lipopolysaccharides (LPS) in the cell membrane promote the chemical interaction of the membrane with AgNPs (Loo et al., 2018). Although many studies have reported the antimicrobial activity and possible action mechanism of biological AgNPs, strong effects at a very low concentration of AgNPs are rare. The produced G-AgNPs were explored against two Gram-negative strains in the current study. Results showed extremely strong antimicrobial activity, i.e., total killing at 8 μg/mL for *E. coli* and 1 μg/mL for *P. aeruginosa*. The mentioned concentrations for total killing are very low compared to other reported green AgNPs. For instance, recently, Shah et al. (2021) showed that

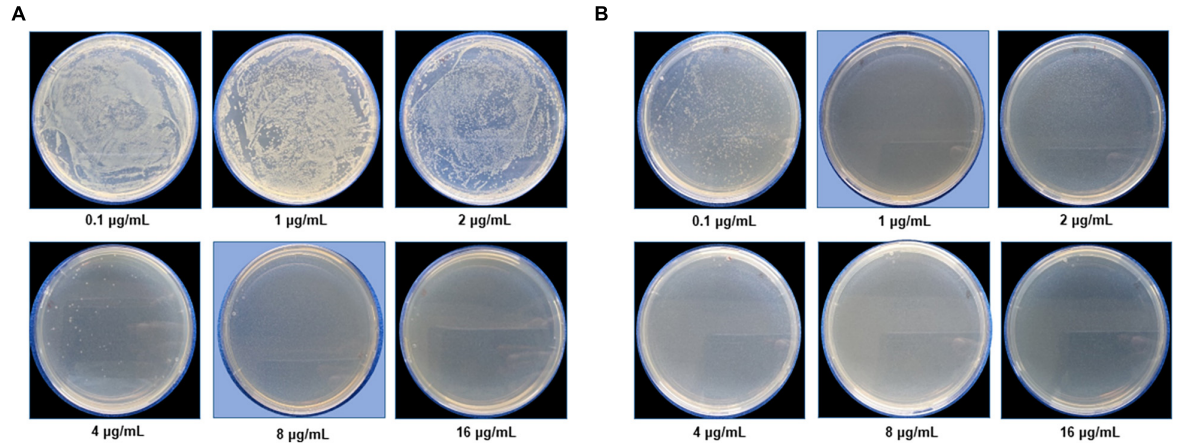

FIGURE 7 | Cell viability test at a different concentration range from 0.1 to 16 µg/mL for **(A)** *Escherichia coli* and **(B)** *Pseudomonas aeruginosa* after green silver nanoparticles (G-AgNPs) treatment. The blue background shows the MBC values of G-AgNPs for respective pathogens.

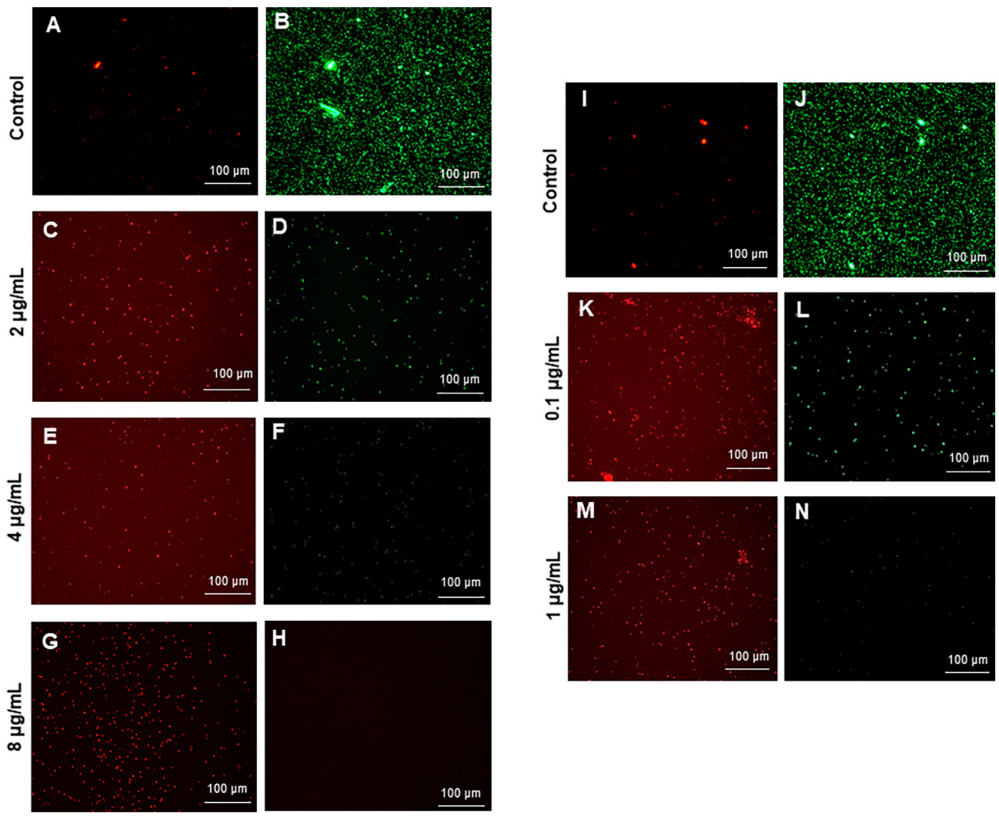

FIGURE 8 | Live and dead staining of **(A–H)** *Escherichia coli*, and (I-N) *Pseudomonas aeruginosa* after treatment with green silver nanoparticles (G-AgNPs) at selected concentrations. *E. coli* cells: **(A,B)** control without G-AgNPs; **(C,D)** 2 µg/mL; **(E,F)** 4 µg/mL; **(G,H)** 8 µg/mL of G-AgNPs. *P. aeruginosa* cells: **(I,J)** control without G-AgNPs; **(K,L)** 0.1 µg/mL; **(M,N)** 1 µg/mL of G-AgNPs.

the LD50 dose (concentration of AgNPs causing 50% inhibition) obtained from *Plantago lanceolate* against *E. coli* was 45.54 mg/L, which is much higher than the G-AgNPs MBC value (kill 100% bacteria) against *E. coli*, i.e., 8 µg/mL, in our study. Similarly, Devanesan and AlSalhi, 2021 demonstrated the antimicrobial activity of AgNPs originated from flower extract of *Abelmoschus esculentus*. The authors showed the MBC value of AgNPs against *E. coli* and *P. aeruginosa* were 110 and 105 µg/mL (Devanesan and AlSalhi, 2021). Loo et al. (2018) described the MBC value of extremely small 4 nm AgNPs produced using pu-erh tea leaves

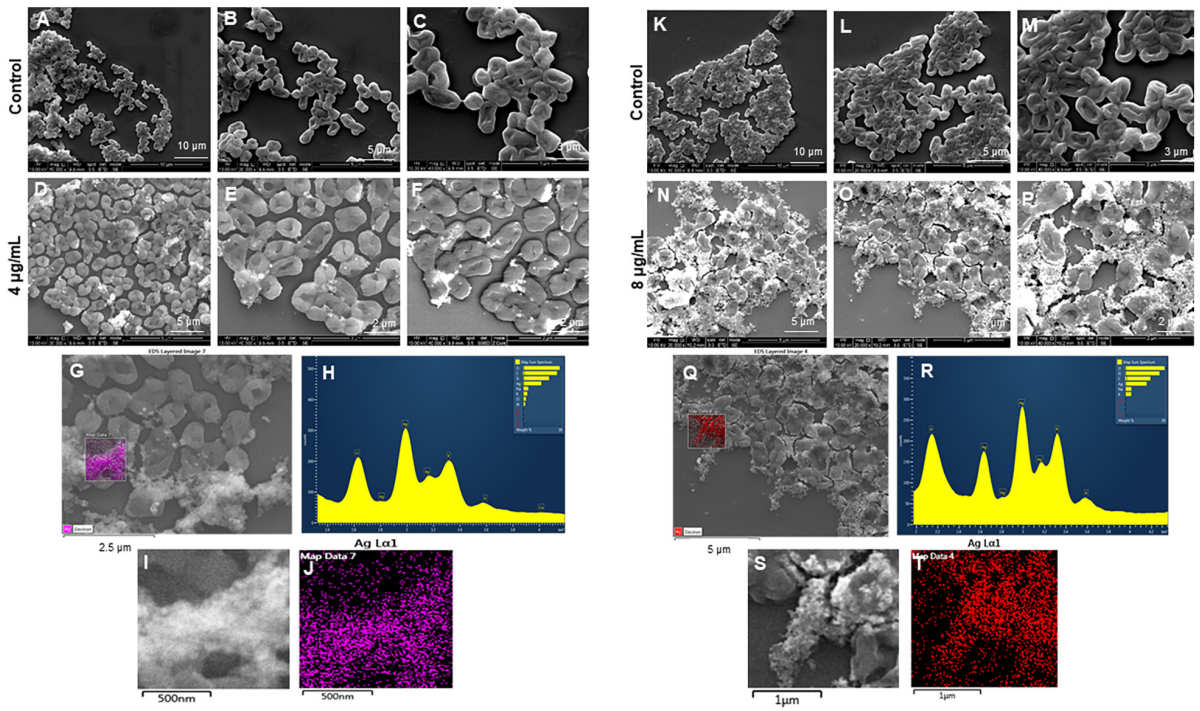

FIGURE 9 | Scanning electron microscopy (SEM) analysis of *Escherichia coli* cells after treatment with green silver nanoparticles (G-AgNPs). **(A–F)** Control *E. coli* cells and G-AgNPs treated 4 µg/mL at different scales. **(G)** Scanned image of treated cells **(H)** energy dispersive x-ray spectroscopy (EDX) spectrum of choose area **(I,J)** elemental mapping of the selected area showing silver element in the treated cells, **(K–P)** control *E. coli* cells and G-AgNPs treated cells with 8 µg/mL at different scales. **(Q)** Scanned image of treated cells **(R)** energy dispersive x-ray spectroscopy (EDX) spectrum of choose area **(S,T)** elemental mapping of the selected area showing silver element in the treated cells.

against *E. coli* as 7.8 µg/mL. Ssekatawa et al. (2021) described the MBC value of two green AgNPs originating from *Prunus africana* and *Camellia sinensis*. The MIC and MBC value of 125 and 250 µg/mL against *E. coli* (Ssekatawa et al., 2021). Thus, our G-AgNPs showed MBC at 8 and 1 µg/mL against *E. coli* and *P. aeruginosa*, superior to all the cited examples. The possible reason for the strong antibacterial ability of G-AgNPs could be the biological corona, which provides a high negative surface charge, spherical shape of NPs, which allow them to interact with pathogens with the maximum surface area available.

We further confirmed the cells' death by SEM. SEM has revealed that after contact with G-AgNPs, the cell membrane of *E. coli* and *P. aeruginosa* cells is completely ruptured. Thus, the G-AgNPs attach onto the negatively charged surface of the cell wall and membrane, which leads to the shrinkage of the cytoplasm and membrane detachment, finally leading to rupture of the cell wall. In addition, the interaction of G-AgNPs with the sulfur-containing proteins present in the cell wall could also affect the membrane permeability and cause cell leakage. It is reported that the porins on Gram-negative bacteria are also responsible for AgNPs uptake. Following penetration, G-AgNPs may interact with cellular components such as proteins, lipids, and DNA, corresponding to the damaging effects (Ullah Khan et al., 2018). AgNPs also cause DNA damage, mutations, inhibition of enzymes and proteins (Singh et al., 2020). It has been found that Ag (+) ions intercalate between the purine and pyrimidine base pairs, disrupt the H-bonds between base pairs of the anti-parallel DNA strands, and thereby disrupt the double-helical structure (Joshi et al., 2020). Another well-known mechanism of AgNPs action is their ability to produce ROS and free radical species and consequent increase in oxidative stress in cells and apoptosis (Loo et al., 2018; Ullah Khan et al., 2018). All these mechanisms were presented in **Figure 1**.

One of the most important physicochemical properties that affect antimicrobial activity is the size and shape of NPs (Karade et al., 2021). Typically, smaller NPs have the larger surface area available to interact and ascend intracellular penetration (Ginjupalli et al., 2018). We hypothesized that the bigger G-AgNPs >10 nm could cause membrane damage. In contrast, the smaller NPs (less than 10 nm) could enter the cells after adhesion and damage the intracellular structures, thus affecting vital cellular functioning. Thus, we believe that the size range of G-AgNPs from 5 to 30 nm offered strong interaction of nanoparticles on the surface (bigger NPs) and internal organelles (smaller NPs). In addition, sphere-shaped or quasi-spherical AgNPs are more susceptible to releasing Ag + ions; thus, G-AgNPs showed high antimicrobial effects. Moreover, as mentioned above, strong negative zeta potential and biological corona also play an important role in providing strong antimicrobial activity and stability in the biological environment so that NPs won't degrade and act with their full potential. Thus, we strongly

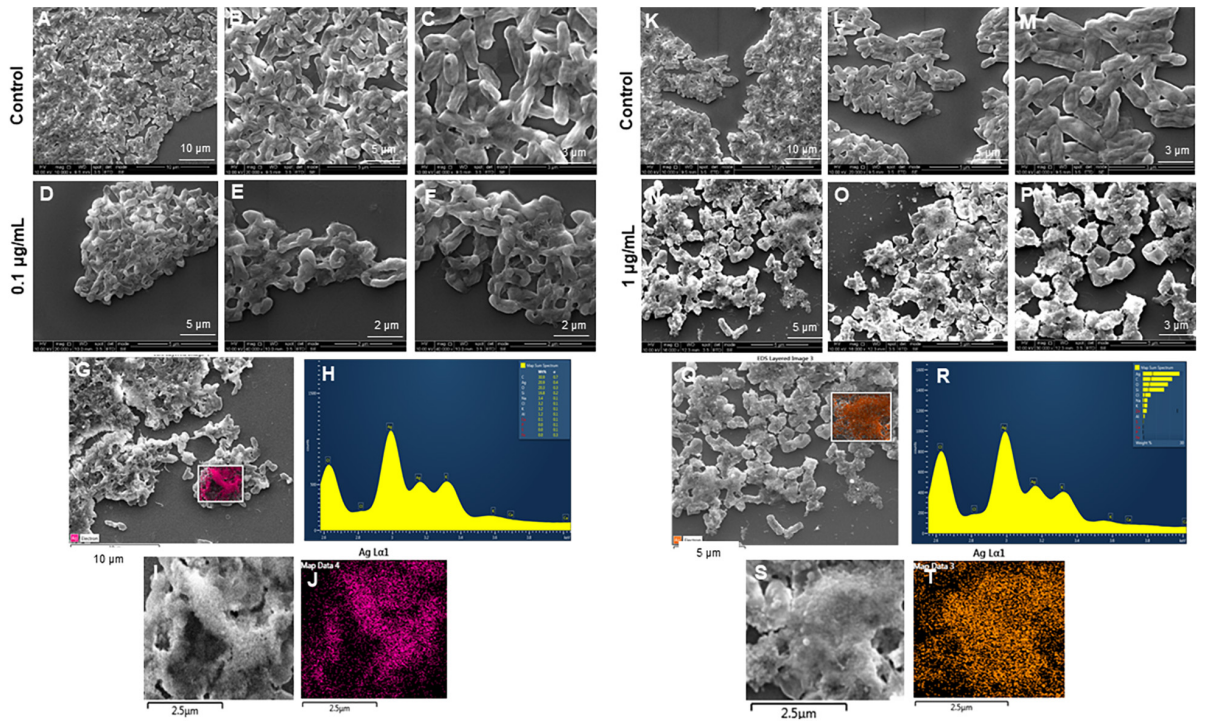

FIGURE 10 | Scanning electron microscopy (SEM) analysis of *Pseudomonas aeruginosa* cells after treatment with green silver nanoparticles (G-AgNPs). **(A–F)** Control *P. aeruginosa* cells and G-AgNPs treated cells with 0.1 μg/mL at different scales. **(G)** Scanned image of treated cells **(H)** energy dispersive x-ray spectroscopy (EDX) spectrum of choose area **(I,J)** elemental mapping of the selected area showing silver element in the treated cells, **(K–P)** control *P. aeruginosa* cells and G-AgNPs treated cells with 1 μg/mL at different scales. **(Q)** Scanned image of treated cells **(R)** energy dispersive x-ray spectroscopy (EDX) spectrum of choose area **(S,T)** elemental mapping of the selected area showing silver element in the treated cells.

believe that the strong antimicrobial activity of produced G-AgNPs is due to the above-discussed mechanism. Exploring these nanoparticles further against more multidrug-resistant pathogens will answer the desire for strong antimicrobial agents in medical fields.

CONCLUSION

Green silver nanoparticles were successfully formed *via* a green synthetic method using cell-free supernatant of *Viridibacillus* sp., which acted as a reducing and capping agent. The G-AgNPs production was confirmed by the appearance of SPR band 430 nm and found to be highly stable, crystalline, and nearly spherical in size. The G-AgNPs showed excellent antimicrobial activity against two Gram-negative strains at very low concentrations. We propose that these nanoparticles constitute a promising opportunity for developing antimicrobial weapons with efficient antimicrobial properties, stability, and recyclability.

DATA AVAILABILITY STATEMENT

The datasets presented in this study can be found in online repositories. The names of the repository/repositories and accession number(s) can be found in the article/supplementary material.

ETHICS STATEMENT

Ethical review and approval was not required for the study on human participants in accordance with the local legislation and institutional requirements. Written informed consent for participation was not required for this study in accordance with the national legislation and the institutional requirements.

AUTHOR CONTRIBUTIONS

PS designed and performed the experiments, analyzed the results, and prepared the manuscript and figures. IM supervised all experimental work and edited the manuscript. Both authors contributed to the article and approved the submitted version.

FUNDING

Lundbeckfonden to PS (R303-2018-3499), Novo Nordisk Foundation (NNF10CC1016517) and the NordForsk (project number 105121) to IM.

ACKNOWLEDGMENTS

ICPMS was performed at DTU Environmental; TEM was performed at Center for electron microscopy; DTU and FTIR were conducted at Department of Chemical Engineering, DTU. Jørgen Garnaes helped with AFM analysis. Funds support AFMs contribution from The Danish Agency for Institutions and Educational Grants.

REFERENCES

Abbai, R., Mathiyalagan, R., Markus, J., Kim, Y. J., Wang, C., Singh, P., et al. (2016). Green synthesis of multifunctional silver and gold nanoparticles from the oriental herbal adaptogen: siberian ginseng. *Int. J. Nanomed.* 11, 3131–3143. doi: 10.2147/IJN.S108549

Albert, R. A., Archambault, J., Lempa, M., Hurst, B., Richardson, C., Gruenloh, S., et al. (2007). Proposal of *Viridibacillus* gen. nov. and reclassification of Bacillus arvi, Bacillus arenosi and Bacillus neidei as *Viridibacillus arvi* gen. nov., comb. nov., *Viridibacillus arenosi* comb. nov. and *Viridibacillus neidei* comb. nov. *Int. J. Syst. Evol. Microbiol.* 57, 2729–2737. doi: 10.1099/ijs.0.65256-0

Belteky, P., Ronavari, A., Igaz, N., Szerencses, B., Toth, I. Y., Pfeiffer, I., et al. (2019). Silver nanoparticles: aggregation behavior in biorelevant conditions and its impact on biological activity. *Int. J. Nanomed.* 14, 667–687. doi: 10.2147/IJN.S185965

Burdusel, A. C., Gherasim, O., Grumezescu, A. M., Mogoanta, L., Ficai, A., and Andronescu, E. (2018). Biomedical applications of silver nanoparticles: an up-to-date overview. *Nanomaterials* 8:681. doi: 10.3390/nano8090681

Crisan, C. M., Mocan, T., Manolea, M., Lasca, L. I., Tăbăran, F.-A., and Mocan, L. (2021). Review on silver nanoparticles as a novel class of antibacterial solutions. *Appl. Sci.* 11:1120. doi: 10.3390/app11031120

Deshmukh, A. R., Gupta, A., and Kim, B. S. (2019). Ultrasound assisted green synthesis of silver and iron oxide nanoparticles using fenugreek seed extract and their enhanced antibacterial and antioxidant activities. *Biomed. Res. Int.* 2019:1714358. doi: 10.1155/2019/1714358

Deshmukh, S. P., Patil, S. M., Mullani, S. B., and Delekar, S. D. (2019). Silver nanoparticles as an effective disinfectant: a review. *Mater Sci. Eng. C Mater. Biol. Appl.* 97, 954–965. doi: 10.1016/j.msec.2018.12.102

Devanesan, S., and AlSalhi, M. S. (2021). Green synthesis of silver nanoparticles using the flower extract of abelmoschus esculentus for cytotoxicity and antimicrobial studies. *Int. J. Nanomed.* 16, 3343–3356. doi: 10.2147/IJN.S307676

Garg, D., Sarkar, A., Chand, P., Bansal, P., Gola, D., Sharma, S., et al. (2020). Synthesis of silver nanoparticles utilizing various biological systems: mechanisms and applications—a review. *Prog. Biomater.* 9, 81–95. doi: 10.1007/s40204-020-00135-2

Gherasim, O., Puiu, R. A., Birca, A. C., Burdusel, A. C., and Grumezescu, A. M. (2020). An updated review on silver nanoparticles in biomedicine. *Nanomaterials* 10:2318. doi: 10.3390/nano10112318

Ginjupalli, K., Shaw, T., Tellapragada, C., Alla, R., Gupta, L., and Perampalli, N. U. (2018). Does the size matter? Evaluation of effect of incorporation of silver nanoparticles of varying particle size on the antimicrobial activity and properties of irreversible hydrocolloid impression material. *Dent Mater* 34:e158–e165. doi: 10.1016/j.dental.2018.03.016

Heinemann, M. G., Rosa, C. H., Rosa, G. R., and Dias, D. (2021). Biogenic synthesis of gold and silver nanoparticles used in environmental applications: a review. *Trends Environ. Anal. Chem.* 30:e00129.

Joshi, A. S., Singh, P., and Mijakovic, I. (2020). Interactions of gold and silver nanoparticles with bacterial biofilms: molecular interactions behind inhibition and resistance. *Int. J. Mol. Sci.* 21:7658. doi: 10.3390/ijms21207658

Kapoor, R. T., Salvadori, M. R., Rafatullah, M., Siddiqui, M. R., Khan, M. A., and Alshareef, S. A. (2021). Exploration of microbial factories for synthesis of nanoparticles - a sustainable approach for bioremediation of environmental contaminants. *Front. Microbiol.* 12:658294. doi: 10.3389/fmicb.2021.658294

Karade, V. C., Patil, R. B., Parit, S. B., Kim, J. H., Chougale, A. D., and Dawkar, V. V. (2021). Insights into shape-based silver nanoparticles: a weapon to cope with pathogenic attacks. *ACS Sustain. Chem. Eng.* 9, 12476–12507. doi: 10.1021/acssuschemeng.1c03797

Kumar, S., Basumatary, I. B., Sudhani, H. P. K., Bajpai, V. K., Chen, L., Shukla, S., et al. (2021). Plant extract mediated silver nanoparticles and their applications as antimicrobials and in sustainable food packaging: a state-of-the-art review. *Trends Food Sci. Technol.* 112, 651–666. doi: 10.1016/j.tifs.2021.04.031

Liao, C., Li, Y., and Tjong, S. C. (2019). Bactericidal and cytotoxic properties of silver nanoparticles. *Int. J. Mol. Sci.* 20:449.

Liu, X., Chen, J.-L., Yang, W.-Y., Qian, Y.-C., Pan, J.-Y., Zhu, C.-N., et al. (2021). Biosynthesis of silver nanoparticles with antimicrobial and anticancer properties using two novel yeasts. *Scie. Rep.* 11:15795. doi: 10.1038/s41598-021-95262-6

Loo, Y. Y., Rukayadi, Y., Nor-Khaizura, M.-A.-R., Kuan, C. H., Chieng, B. W., Nishibuchi, M., et al. (2018). *In Vitro* antimicrobial activity of green synthesized silver nanoparticles against selected gram-negative foodborne pathogens. *Front. Microbiol.* 9:1555. doi: 10.3389/fmicb.2018.01555

Prasher, P., Singh, M., and Mudila, H. (2018). Silver nanoparticles as antimicrobial therapeutics: current perspectives and future challenges. *3 Biotech* 8:411. doi: 10.1007/s13205-018-1436-3

Ronavari, A., Igaz, N., Adamecz, D. I., Szerencses, B., Molnar, C., Konya, Z., et al. (2021). Green silver and gold nanoparticles: biological synthesis approaches and potentials for biomedical applications. *Molecules* 26:844. doi: 10.3390/molecules26040844

Sangaonkar, G. M., and Pawar, K. D. (2018). Garcinia indica mediated biogenic synthesis of silver nanoparticles with antibacterial and antioxidant activities. *Colloids Surf. B Biointerfaces* 164, 210–217. doi: 10.1016/j.colsurfb.2018.01.044

Shah, M. Z., Guan, Z.-H., Din, A. U., Ali, A., Rehman, A. U., Jan, K., et al. (2021). Synthesis of silver nanoparticles using Plantago lanceolata extract and assessing their antibacterial and antioxidant activities. *Sci. Rep.* 11:20754. doi: 10.1038/s41598-021-00296-5

Singh, P., Pandit, S., Garnaes, J., Tunjic, S., Mokkapati, V. R., Sultan, A., et al. (2018c). Green synthesis of gold and silver nanoparticles from *Cannabis sativa* (industrial hemp) and their capacity for biofilm inhibition. *Int. J. Nanomed.* 13, 3571–3591. doi: 10.2147/IJN.S157958

Singh, H., Du, J., Singh, P., and Yi, T. H. (2018a). Ecofriendly synthesis of silver and gold nanoparticles by Euphrasia officinalis leaf extract and its biomedical applications. *Artif Cells Nanomed. Biotechnol.* 46, 1163–1170. doi: 10.1080/21691401.2017.1362417

Singh, H., Du, J., Singh, P., and Yi, T. H. (2018b). Extracellular synthesis of silver nanoparticles by *Pseudomonas* sp. THG-LS1.4 and their antimicrobial application. *J. Pharm. Anal.* 8, 258–264. doi: 10.1016/j.jpha.2018.04.004

Singh, P., Kim, Y. J., Singh, H., Farh, M. E., and Yang, D. C. (2017). *Achromobacter panacis* sp. nov., isolated from rhizosphere of Panax ginseng. *J. Microbiol.* 55, 428–434. doi: 10.1007/s12275-017-6612-3

Singh, P., Kim, Y.-J., Zhang, D., and Yang, D.-C. (2016a). Biological synthesis of nanoparticles from plants and microorganisms. *Trends Biotechnol.* 34, 588–599. doi: 10.1016/j.tibtech.2016.02.006

Singh, P., Singh, H., Kim, Y. J., Mathiyalagan, R., Wang, C., and Yang, D. C. (2016b). Extracellular synthesis of silver and gold nanoparticles by *Sporosarcina koreensis* DC4 and their biological applications. *Enzyme Microb. Technol.* 86, 75–83. doi: 10.1016/j.enzmictec.2016.02.005

Singh, P., Pandit, S., Jers, C., Joshi, A. S., Garnaes, J., and Mijakovic, I. (2021). Silver nanoparticles produced from *Cedecea* sp. exhibit antibiofilm activity and remarkable stability. *Sci. Rep.* 11:12619. doi: 10.1038/s41598-021-92006-4

Singh, P., Pandit, S., Mokkapati, V., Garnaes, J., and Mijakovic, I. (2020). A sustainable approach for the green synthesis of silver nanoparticles from solibacillus isronensis sp. and their application in biofilm inhibition. *Molecules* 25:2783. doi: 10.3390/molecules25122783

Ssekatawa, K., Byarugaba, D. K., Kato, C. D., Wampande, E. M., Ejobi, F., Nakavuma, J. L., et al. (2021). Green strategy–based synthesis of silver nanoparticles for antibacterial applications. *Fron. Nanotechnol.* 3:697303. doi: 10.3389/fnano.2021.697303

Ullah Khan, S., Saleh, T. A., Wahab, A., Khan, M. H. U., Khan, D., Ullah Khan, W., et al. (2018). Nanosilver: new ageless and versatile biomedical therapeutic scaffold. *Int. J. Nanomed.* 13, 733–762. doi: 10.2147/IJN.S153167

Wypij, M., Jędrzejewski, T., Trzcińska-Wencel, J., Ostrowski, M., Rai, M., and Golińska, P. (2021). Green synthesized silver nanoparticles: antibacterial and anticancer activities, biocompatibility, and analyses of surface-attached proteins. *Front. Microbiol.* 12:632505. doi: 10.3389/fmicb.2021.632505

Xu, L., Wang, Y. Y., Huang, J., Chen, C. Y., Wang, Z. X., and Xie, H. (2020). Silver nanoparticles: Synthesis, medical applications and biosafety. *Theranostics* 10, 8996–9031. doi: 10.7150/thno.45413

Zhang, D., Ma, X.-L., Gu, Y., Huang, H., and Zhang, G.-W. (2020). Green synthesis of metallic nanoparticles and their potential applications to treat cancer. *Front. Chem.* 8:799. doi: 10.3389/fchem.2020.00799

Zhang, Z., Shen, W., Xue, J., Liu, Y., Liu, Y., Yan, P., et al. (2018). Recent advances in synthetic methods and applications of silver nanostructures. *Nanosc. Res. Lett.* 13:54. doi: 10.1186/s11671-018-2450-4

Conflict of Interest: The authors declare that the research was conducted in the absence of any commercial or financial relationships that could be construed as a potential conflict of interest.

Publisher's Note: All claims expressed in this article are solely those of the authors and do not necessarily represent those of their affiliated organizations, or those of the publisher, the editors and the reviewers. Any product that may be evaluated in this article, or claim that may be made by its manufacturer, is not guaranteed or endorsed by the publisher.

frontiers in Microbiology

REVIEW
published: 10 March 2022
doi: 10.3389/fmicb.2022.822197

Molecular Mechanisms Underlying Bacterial Uranium Resistance

*Tom Rogiers[1,2], Rob Van Houdt[1], Adam Williamson[3], Natalie Leys[1], Nico Boon[2] and Kristel Mijnendonckx[1]**

[1] Microbiology Unit, Interdisciplinary Biosciences, Belgian Nuclear Research Centre, SCK CEN, Mol, Belgium, [2] Center for Microbial Ecology and Technology, Ghent University, Ghent, Belgium, [3] Centre Etudes Nucléaires de Bordeaux Gradignan (CENBG), Bordeaux, France

Environmental uranium pollution due to industries producing naturally occurring radioactive material or nuclear accidents and releases is a global concern. Uranium is hazardous for ecosystems as well as for humans when accumulated through the food chain, through contaminated groundwater and potable water sources, or through inhalation. In particular, uranium pollution pressures microbial communities, which are essential for healthy ecosystems. In turn, microorganisms can influence the mobility and toxicity of uranium through processes like biosorption, bioreduction, biomineralization, and bioaccumulation. These processes were characterized by studying the interaction of different bacteria with uranium. However, most studies unraveling the underlying molecular mechanisms originate from the last decade. Molecular mechanisms help to understand how bacteria interact with radionuclides in the environment. Furthermore, knowledge on these underlying mechanisms could be exploited to improve bioremediation technologies. Here, we review the current knowledge on bacterial uranium resistance and how this could be used for bioremediation applications.

Keywords: reduction, phosphatases, efflux systems, regulation, bioremediation

OPEN ACCESS

Edited by:
Daniela Ceccarelli, European Commission, Belgium

Reviewed by:
Celin Acharya, Bhabha Atomic Research Centre (BARC), India
Raluca Maria Hlihor, Ion Ionescu de la Brad University of Agricultural Sciences and Veterinary Medicine of Iaşi, Romania
Alexey Vladimirovich Safonov, Frumkin Institute of Physical Chemistry and Electrochemistry RAS, Russia

****Correspondence:***
Kristel Mijnendonckx
kmijnend@sckcen.be

Specialty section:
This article was submitted to Antimicrobials, Resistance and Chemotherapy, a section of the journal Frontiers in Microbiology

Received: *25 November 2021*
Accepted: *27 January 2022*
Published: *10 March 2022*

Citation:
Rogiers T, Van Houdt R, Williamson A, Leys N, Boon N and Mijnendonckx K (2022) Molecular Mechanisms Underlying Bacterial Uranium Resistance. Front. Microbiol. 13:822197. doi: 10.3389/fmicb.2022.822197

INTRODUCTION

Controlled and accidental releases by nuclear industries, nuclear weapon tests and nuclear accidents have globally spread radionuclides in our environment, including synthetic radionuclides like ^{3}H, ^{90}Sr, ^{131}I, ^{137}Cs, and ^{241}Am (UNSCEAR, 1988; Van der Stricht and Janssens, 2010; Taira et al., 2013; Prăvălie, 2014; International Atomic Energy Agency [IAEA], 2018). In addition, human activities can lead to an increased exposure to naturally occurring radioactive material (NORM), which primarily include ^{238}U, ^{232}Th, ^{40}K and their decay products (International Atomic Energy Agency [IAEA], 2003). Examples of NORM industries are oil and gas production, coal mining and combustion, metal and uranium mining and processing, geothermal energy production, groundwater treatment, and phosphate mining for fertilizer production (International Atomic Energy Agency [IAEA], 2003; UNSCEAR, 2008). Environmental accumulation of natural and synthetic radionuclides can be hazardous for ecosystems. Transfer of radionuclides to vegetation mainly occurs through water bodies (Salbu et al., 2013), resulting in cytogenetic damage that decreases the reproductive ability (Geras'kin et al., 2013). Furthermore, contamination of water bodies, such as lakes, results in a substantial transfer of radionuclides to fish, herbivores and carnivores (Whicker, 1983; Salbu et al., 2013; Strømman et al., 2013). Humans can be exposed when radionuclides are accumulated through the food chain, through contaminated potable water sources, such as groundwater, or through inhalation (Tompson et al., 2002; Tykva, 2004; Zachara et al., 2013).

Uranium, atomic number 92, is a silvery-white metal belonging to the actinides that is naturally found in minerals such as pitchblende, uraninite, carnotite, autunite, uranophane, davidite and tobernite, but can also occur in phosphate rock, lignite and monazite sands (Lide, 2003). It is one of the principal contaminants of concern in NORM and nuclear industry (NEA/IAEA, 1999; International Atomic Energy Agency [IAEA], 2003). The most common natural isotopes are ^{238}U (99.27%), ^{235}U (0.72%) and ^{234}U (<0.01%). Both ^{238}U and ^{235}U can be used as nuclear fuel, but ^{235}U is more important as it is able to self-sustain a fission chain reaction. Therefore, ^{238}U with slightly enriched ^{235}U is used for the generation of electricity (Hammond, 2004). ^{238}U, ^{235}U, and ^{234}U decay by emitting an alpha particle and have half-lives of 4.5×10^9 years, 700×10^6 years, and 246×10^3 years, respectively. ^{238}U decays 14 times by alpha or beta emission before reaching stable lead-206 (^{206}Pb).

As uranium accumulation could potentially be harmful for humans and ecosystems, strict control and monitoring is essential, and protection and remediation strategies are deployed. Various physical and chemical methods are available, some more advanced than others, but each with its own limitations and drawbacks such as high cost, high complexity and long time span (Godheja et al., 2016). Consequently, there is a need for more simple and ecofriendly alternatives, including biologically based methods. Microorganisms are often found in uranium-contaminated sites and can influence uranium mobility, toxicity and distribution (Choudhary and Sar, 2015). Processes such as biosorption, bioaccumulation, biomineralization and redox transformations are currently well known (**Figure 1**; Merroun and Selenska-Pobell, 2008). In turn, uranium exerts a permanent pressure on the prevailing microbial population, disrupting microbial communities and processes (Tapia-Rodríguez et al., 2012; Lopez-Fernandez et al., 2017; Sutcliffe et al., 2017). Consequently, fundamental understanding of the interaction between microorganisms and uranium is essential to assess the microbial impact in contaminated environments correctly. Moreover, knowledge on the underlying cellular response can be exploited to improve bioremediation technologies.

The most prevalent oxidation states of uranium in natural environments are U(VI) and U(IV), although it can also exist as U(III) and U(V). Uranium speciation and redox state are important to consider as they influence the mobility of the compound and the toxicity toward biological systems. A large number of factors, such as the aeration state, pH, organic matter, carbonates and phosphates, are able to influence its mobility complicating uranium chemistry (reviewed in Cumberland et al., 2016). In general, the aeration state determines the oxidation state of uranium. Uranyl (UO_2^{2+}) is the main form in oxic systems. Uranyl ions are more mobile and more toxic compared to the reduced uraninite (UO_2), which can be formed in anaerobic conditions and reoxidized with oxygen (Finch and Murakami, 1999; Markich, 2002; Liu et al., 2017). Also pH determines the solubility of U(VI) and U(IV) complexes. In general, the presence of carbonates has a positive effect on the solubility of U(VI) complexes, especially above pH 5.5. On the other hand, U(IV) is expected to be only slightly soluble in most environmental pH conditions, except at extreme low pH (pH < 3), which can be associated with anthropogenic environments such as acid mine drainage. It is also possible that U(IV) could be mobilized in a colloidal phase. Furthermore, the presence of other ions (e.g., PO_4^{3-}, OH^-, SO_4^{2-}) and/or organic material can compete for binding to uranyl ions, thereby influencing the mobility of uranium and its sorption to mineral surfaces (Cumberland et al., 2016). Therefore, it is important to consider these factors when investigating microbial interactions with uranium since the toxicity, mobility and interaction strongly depend on the experimental setup.

Although the interaction of microorganisms with uranium is extensively studied, there is far less information about the cellular response of microorganisms to uranium exposure. Data on bacterial uranium resistance mechanisms is rather exploratory. Therefore, instead of discussing the outcome of bacterial interaction with uranium, this review focusses on the different active cellular mechanisms for uranium processing. Microbial reduction of soluble U(VI) to insoluble U(IV) is one of the best-studied mechanisms and many uranium-reducing bacteria have been identified. As such, different reduction mechanisms are discussed in a first section. In a following section, several types of phosphatases are reviewed as metal-phosphate complexation and metal-phosphate biomineralization are common mechanisms for metal detoxification. Afterward, the involvement of membrane proteins, metal efflux and regulatory systems in uranium resistance is reviewed. Finally, the potential application in bioremediation is discussed.

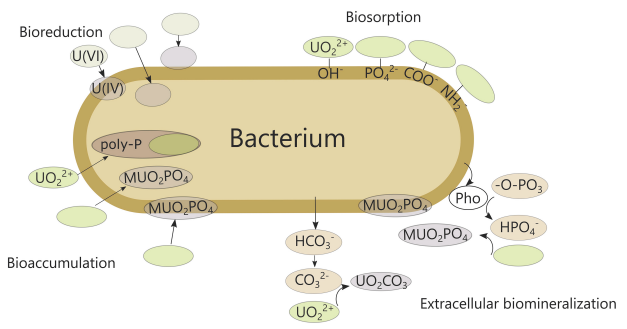

FIGURE 1 | Bacterial interactions with uranium. Uranium minerals are presented as UO_2CO_3 or MUO_2PO_4 with M indicating a metal ion. Pho, phosphatase; poly-P, polyphosphate granules.

URANIUM REDUCTION MECHANISMS

Enzymatic uranium reduction can occur directly or indirectly in the cytoplasm, periplasm, at the outer membrane or extracellularly (**Figure 2** and **Table 1**) (reviewed in You et al., 2021). It has been investigated particularly in *Geobacter* species, which often dominate in anaerobic uranium-reductive bioremediation setups (Yun-Juan et al., 2005; Shelobolina et al., 2008; Chandler et al., 2010). In general, cytochromes are imperative in the reduction process and were found

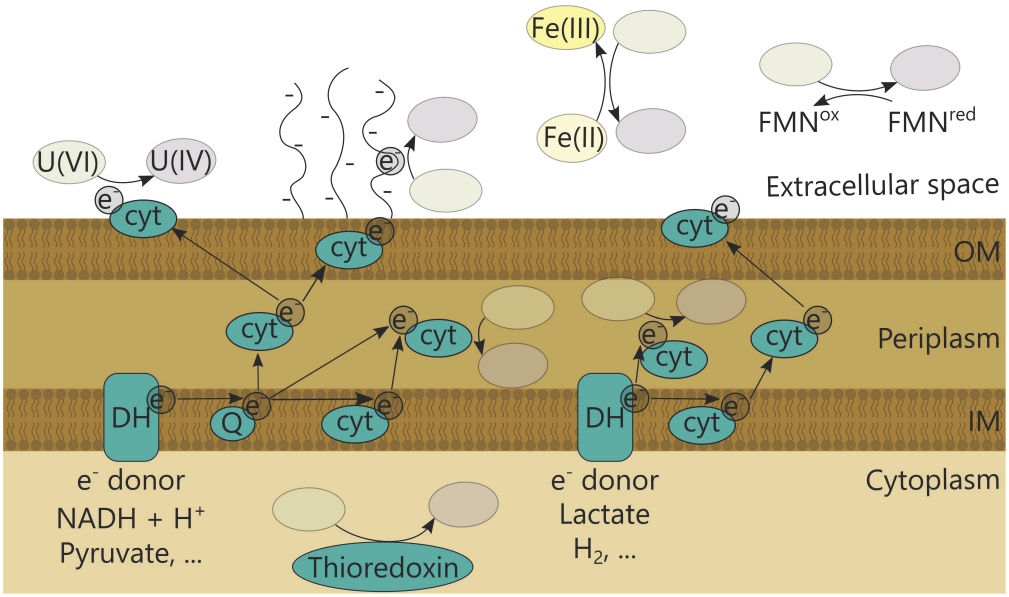

FIGURE 2 | Bacterial uranium reduction mechanisms. DH, Dehydrogenase; Q, quinone; cyt, cytochrome; FMN, flavin mononucleotide.

to be increasingly expressed in *Geobacter uraniireducens* when growing in uranium-contaminated subsurface sediments (Holmes et al., 2009). Moreover, GscA (*Geobacter* subsurface *c*-type cytochrome A) of *Geobacter* sp. M18 was highly abundant during *in situ* uranium bioremediation (Yun et al., 2016). In addition, the diheme c-type cytochrome peroxidase MacA and the outer-surface *c*-type cytochrome OmcZ are essential for uranium reduction, and the periplasmic c_7-type cytochrome PpcA is an important intermediate electron carrier (in the absence of hydrogen) in *Geobacter sulfurreducens* (Lloyd et al., 2003; Shelobolina et al., 2007; Orellana et al., 2013). On the other hand, two outer membrane cytochromes, OmcB and OmcC, showed no or less contribution to U(VI) reduction in *G. sulfurreducens* (Shelobolina et al., 2007). Functional c-type cytochromes were also shown to be essential for uranium reduction in other bacteria. For instance, a cytochrome c maturation deficient mutant of *Shewanella oneidensis* MR-1 was unable to reduce uranium. However, the precise electron transfer pathways involved in uranium reduction are not yet clear. It has been shown that the outer membrane c-type cytochrome MtrC (also known as OmcB), but not OmcA, can function as a terminal uranium reductase. In addition, deletion of both genes decreased the uranium reduction rate and changed the characteristics of the formed uranium nanoparticles (Marshall et al., 2006). A decreased uranium reduction rate was also observed for deletion mutants of *mtrA* (encoding a periplasmic decaheme cytochrome involved in metal reduction), *mtrB* (encoding an outer membrane protein involved in metal reduction) and *menC* (encoding a precursor of menaquinone), which are involved in the electron transfer. In addition, other Mtr-independent pathways can exist (Bencheikh-Latmani et al., 2005). Periplasmic uranium reduction in *Desulfovibrio* occurs mainly via cytochrome c_3. Deletion of *cycA*, encoding cytochrome c_3, in *Desulfovibrio alaskensis* G20 (formerly *Desulfovibrio desulfuricans* G20) reduced the uranium reduction rate in the presence of lactate and pyruvate, and almost completely inhibited it with hydrogen gas as electron donor in sulfate-reducing conditions. This indicates that *cycA* is responsible for uranium reduction with hydrogen gas as electron donor, but can be bypassed in the presence of other electron donors (Payne et al., 2002, 2004).

Uranium can also be reduced abiotically by iron (Du et al., 2011). However, since cytochromes are often involved in iron reduction pathways (Weber et al., 2006), there could be a link between uranium reduction and iron metabolism. Indeed, siderophores have been shown to form stable complexes with metals and some radionuclides (Bouby et al., 1998; Rajkumar et al., 2010; Rashmi et al., 2013). Hydroxamate-type siderophores were shown to chelate uranium better when complexed with carbonate (Mo et al., 2016), and desferrioxamine-B increased dissolution of uraninite under reducing conditions and could therefore increase uranium mobility (Frazier et al., 2005). In addition, uranium stress induced siderophore production in the cyanobacterium *Synechococcus elongatus* BDU 130911 (Rashmi et al., 2013) as well as a large number of proteins related to iron metabolism in the Chernobyl isolate *Microbacterium oleivorans* A9. The latter include components of the siderophore iron uptake system such as ABC-transport type subunits and siderophore modification enzymes (Gallois et al., 2018). Moreover, uranium exposure evokes an iron starvation response, thereby enhancing the synthesis of iron uptake systems. This is in line with observations in *Desulfotomaculum reducens* MI-1, where several ferrous iron uptake and transport proteins, and a transcriptional regulator of the Fur family were upregulated in the presence of U(VI) (Junier et al., 2011). Although the actual link between iron metabolism and uranium resistance is currently unknown, these

TABLE 1 | Overview of uranium interaction mechanisms in bacteria.

BACTERIA	Conditions/medium	[U] (mM)	Speciation	Key genes/proteins	References	Comment
Uranium reduction						
Geobacter sp. M18	*In situ* uranium-contaminated aquifer at ORFRC	NA	NA	GscA?	Yun et al., 2016	Metaproteomic community analysis, no protein with significant similarity to GscA in the genomes of *G. sulfurreducens*, *G. metallireducens*, *G. uraniireducens* or *G. daltonii*
G. uraniireducens strain RF4	Heat-sterilized uranium-contaminated sediments	NA	NA	c-type cytochromes	Holmes et al., 2009	/
G. sulfurreducens	Fumarate and acetate amended basal bicarbonate buffered medium	1	A	Diheme c-type cytochrome peroxidase MacA	Shelobolina et al., 2007	Decreased U(VI) reduction rate by 98%
G. sulfurreducens	Modified freshwater medium	NA	U(VI)	Outer-surface c-type cytochrome OmcZ	Orellana et al., 2013	Approximately 50% less reduction compared to the wild type
G. sulfurreducens	Modified freshwater medium	NA	U(VI)	Periplasmic c_7-type cytochrome PpcA	Lloyd et al., 2003	Depending on the type of electron donor provided, a decrease in reduction is observed
G. sulfurreducens	Fumarate and acetate amended modified freshwater medium	1	A	PilA	Cologgi et al., 2011, 2014	Conductive pili
S. oneidensis MR-1	Lactate and bicarbonate buffer	0.25	A	$CcmC^-$	Marshall et al., 2006	Mutant lacking the ability to covalently incorporate heme into nascent apocytochromes, no U(VI) reduction
S. oneidensis MR-1	Lactate and bicarbonate buffer	0.1, 0.25	A	Outer membrane c-type cytochrome MtrC/OmcB	Bencheikh-Latmani et al., 2005; Marshall et al., 2006	Terminal uranium reductase, reduced U(VI) rate
S. oneidensis MR-1	Lactate and bicarbonate buffer	0.1, 0.25	A	Outer membrane c-type cytochrome OmcA	Bencheikh-Latmani et al., 2005; Marshall et al., 2006	Reduced U(VI) reduction rate
S. oneidensis MR-1	*Shewanella* medium (SM) with lactate and bicarbonate	0.1	A	Periplasmic decaheme cytochrome mtrA, outer membrane protein mtrB, precursor of menaquinone menC	Bencheikh-Latmani et al., 2005	Reduced U(VI) reduction rate
D. alaskensis G20	Lactate-Sulfate medium	1	A	cytochrome c_3 CycA	Payne et al., 2002, 2004	Depending on the electron donor provided, U(VI) reduction rates are reduced or completely inhibited
D. alaskensis G20	Modified Lactate-Sulfate medium	2	A	Thioredoxin (MreD), Thioredoxin reductase (MreE), Oxidoreductase (MreG)	Li and Krumholz, 2009; Li et al., 2014	/

(Continued)

TABLE 1 | (Continued)

Bacteria	Conditions/medium	[U] (mM)	Speciation	Key genes/proteins	References	Comment
Iron-related response						
S. elongatus BDU 130911	ASN III marine synthetic medium	1	A	Siderophores	Rashmi et al., 2013	Uranium stress induced siderophore production, uranium siderophore complexation was confirmed
M. oleivorans A9	0.1 M NaCl	0.01	N	Siderophore iron uptake system	Gallois et al., 2018	Uranium induces an iron starvation response
D. reducens MI-1	Modified widdel low phosphate (WLP) medium	0.1	A	Ferrous iron uptake and transport proteins, and a transcriptional regulator of the Fur family upregulated	Junier et al., 2011	/
U-phosphate precipitation in acid conditions						
Serratia sp. N14	Metal challenge solution; MOPS buffer (purified phosphatase); citrate buffer with G2P	1; ± 0.0125 – 0.3, 1	N	PhoN	Macaskie et al., 1994; Jeong and Macaskie, 1995; Jeong et al., 1997	/
E. coli DH5α expressing PhoN from *S. typhi*	Citrate, MOPS NaOH, G2P test solution	1	N	PhoN	Basnakova et al., 1998	/
E. coli DH5α expressing PhoC from *M. morganii*	Citrate, MOPS NaOH, G2P test solution	1	N	PhoC	Basnakova et al., 1998	/
E. coli DH5α expressing PhoN from a *S.* Typhi isolate	Acetate buffer with G2P	0.8	N	PhoN	Appukuttan et al., 2006	/
D. radiodurans R1 expressing PhoN from a *S.* Typhi isolate	Acetate buffer with G2P	0.8	N	PhoN	Appukuttan et al., 2006	/
M. oleivorans A9	0.1 M NaCl	0.01	N	PhoE	Gallois et al., 2018	Expression coincided with phosphate efflux and showed uranium-phosphate precipitation
Caulobacter OR37	M5G minimal medium with B-vitamins and G2P	0.0005	^{233}U	/	Morrison et al., 2021	/

(Continued)

TABLE 1 | (Continued)

Bacteria	Conditions/medium	[U] (mM)	Speciation	Key genes/proteins	References	Comment
Arthrobacter sp. X34	Simulated groundwater with G3P	0.2	A	/	Beazley et al., 2007; Martinez et al., 2007	/
Bacillus sp. Y9-2	Simulated groundwater with G3P	0.2	A	/	Beazley et al., 2007; Martinez et al., 2007	/
Rahnella sp. Y9602	Simulated groundwater with G3P	0.2	A	/	Beazley et al., 2007; Martinez et al., 2007	/
Rahnella sp. Y9602	Simulated groundwater with G3P with NO_3^-	0.2	A	/	Beazley et al., 2009	/
U-phosphate precipitation in acid and alkaline conditions						
Serratia sp. strain OT II 7	Acetate (pH 5) or MOPS buffer (pH 7 and 9)	1	N, C	/	Chandwadkar et al., 2018	/
Chryseobacterium sp. strain PMSZPI	Acetate (pH 5) or MOPS buffer (pH 7 and 9)	1	N, C	/	Khare et al., 2020	/
U-phosphate precipitation in alkaline conditions						
Sphingomonas sp. BSAR-1	Carbonate-bicarbonate buffer with G2P	0.5 – 5	C	PhoK	Nilgiriwala et al., 2008	/
E. coli BL21 expressing PhoK from *Sphingomonas* sp. BSAR-1	Carbonate-bicarbonate buffer with G2P	0.5 - 5	C	PhoK	Nilgiriwala et al., 2008	/
E. coli DH5α expressing PhoK from *Sphingomonas* sp. BSAR-1	MOPS buffer with/without carbonate (pH 9 and 6.8, respectively) with G2P	1	N, C	PhoK	Kulkarni et al., 2016	/
E. coli DH5α expressing PhoN from *S.* Typhi	MOPS buffer with/without carbonate (pH 9 and 6.8, respectively) with G2P	1	N, C	PhoN	Kulkarni et al., 2016	/
D. radiodurans R1 expressing PhoK from *Sphingomonas* sp. BSAR-1	MOPS buffer with G2P	1 - 10	C	PhoK	Kulkarni et al., 2013	/
D. radiodurans R1 expressing PhoK from *Sphingomonas* sp. BSAR-1	MOPS buffer with/without carbonate (pH 9 and 6.8, respectively) with G2P	1	N, C	PhoK	Kulkarni et al., 2016	/
D. radiodurans R1 expressing PhoN from *S.* Typhi	MOPS buffer with/without carbonate (pH 9 and 6.8, respectively) with G2P	1	N, C	PhoN	Kulkarni et al., 2016	/
C. crescentus NA1000	PIPES buffer (pH 7) with G2P	0.5	N	PhoY	Yung and Jiao, 2014	/

(Continued)

TABLE 1 | (Continued)

Bacteria	Conditions/medium	[U] (mM)	Speciation	Key genes/proteins	References	Comment
P. rhodesiae R1.2 + *P. veronii V1.2* expressing PhoA from *E. coli*	Sterilized soil slurries amended with glycerol 3-phosphate	0.02	A	PhoA	Powers et al., 2002	/
S. bentonitica BII-R7	Tris minimal medium amended with G2P	0.1; 0.25	N	Phosphatases?	Pinel-Cabello et al., 2021	Increased induction of four phosphatases
Phytases						
Microbial communities from ORFRC	Sediment slurries	NA	NA	Acid phytase activity	Salome et al., 2017	/
C. crescentus CB15N	M2G/M5G minimal medium	0.2 - 1	N	Phytase?	Hu et al., 2005; Yung et al., 2014	Putative phytase was the most highly upregulated protein, involved in uranium resistance when phytate is the only phosphate source
Phosphate release from cellular phosphate sources						
P. aeruginosa	MOPS minimal medium	1	N	Polyphosphate kinase	Renninger et al., 2004	Phosphate release from polyphosphate
D. radiodurans	0.1 M NaCl	± 0.336	N	/	Suzuki and Banfield, 2004	Phosphate release during cell lysis
A. torulosa	Nitrogen-supplemented BG-11 medium lacking phosphate	0.1	C	/	Acharya et al., 2017	Alkaline phosphatases liberate Pi from organophosphate substrates
Paenibacillus sp. JG-TB8	0.1 M $NaClO_4$ pH 2 – 6, oxic + anoxic	0.5 (pH 2, 3, 4.5), 0.05 (pH 6)	N	/	Reitz et al., 2014	Organic bound uranium at pH 2 and 3; uranium-phosphate at higher pH and oxic conditions
C. metallidurans NA4	RM medium	0.1	N	/	Rogiers et al., 2021b	PHB-associated uranium-phosphate
Membrane proteins						
C. crescentus NA1000	PYE medium with MES buffer	0.25 – 0.275	N	$rsaF_a$ and $rsaF_b$	Yung et al., 2015	/
B. sphaericus JG-A12	Nutrient broth (8 g/L)	0.9 (pH 4.5)	N	SlfA	Merroun et al., 2005	Cells, native and recrystallized S-layers
B. sphaericus NCTC9602	NA	0.9 (pH 4.5)	NA	SlfB	Raff et al., 2002	native and recrystallized S-layers

(Continued)

TABLE 1 | (Continued)

Bacteria	Conditions/medium	[U] (mM)	Speciation	Key genes/proteins	References	Comment
D. radiodurans	20 mM MOPS buffer	1	N	Hpi-PhoN	Misra et al., 2021	Cell-free protein extract
Microbacterium	0.1 × TSB medium	0.001	N	UipA	Gallois et al., 2021	
S. bentonitica BII-R7	Tris minimal medium amended with glycerol 2-phosphate	0.1, 0.25	N	CreD	Pinel-Cabello et al., 2021	
Metal efflux systems						
C. metallidurans NA4	RM medium	0.1	N	*sil, cop* and *czc* genes	Rogiers et al., 2021b	/
Chryseobacterium sp. strain PMSZPI	Tris buffered medium	0.5	N	CzcA, czcD, cadA	Nongkhlaw and Joshi, 2019	/
S. bentonitica BII-R7	Tris minimal medium amended with glycerol 2-phosphate	0.1, 0.25	N	*czcA/cusA*, *czcD, rcnB, mdtAB*	Pinel-Cabello et al., 2021	/
G. sulfurreducens	Fumarate and acetate amended basal bicarbonate buffered medium (anoxic)	0.1	A	Three membrane fusion proteins and two outer membrane factors	Orellana et al., 2014	/
D. reducens MI-1	Modified widdel low phosphate (WLP) medium	0.1	A	Cadmium- and copper-translocating P-type ATPAse	Junier et al., 2011	/
M. oleivorans A9	0.1 M NaCl	0, 0.01, 0.05	N	/	Theodorakopoulos et al., 2015	Evidence for uranium release
M. oleivorans A9	0.1 M NaCl	0.01	N	Upregulation of several cation transporters	Gallois et al., 2018	/
H. noricense	3 M NaCl	0.01 -0.12	N	/	Bader et al., 2017	Evidence for uranium release
Regulatory systems						
C. crescentus CB15N/NA1000	M2G minimal medium/M5G minimal medium with G2P	0.05 – 1	N	*UrcA*, UzcRS + auxiliary regulators, UrpRS	Hu et al., 2005; Park et al., 2017, 2019; Park and Taffet, 2019	/
M. oleivorans A9	0.1 M NaCl	0.01	N	ArsR	Gallois et al., 2018	/
D. alaskensis G20	Modified Lactate-Sulfate medium	1 - 2	A	cyclic AMP receptor protein (CRP)	Li and Krumholz, 2009	/

NA, Not Available; G2P, glycerol-2-phosphate; G3P, glycerol-3-phosphate; N, uranyl nitrate; A, uranyl acetate; C, uranyl carbonate.

observations indicate that siderophores could protect cells from uranium stress through sequestration.

In *Geobacter* species, evidence has also emerged for U(VI) reduction farther from the cell via extracellular pili. *G. sulfurreducens* expressing pili increased the rate and extent of uranium reduction with carbon ligands outside of the cell, while pili-deficient strains precipitated U(IV) mainly in the periplasm (Cologgi et al., 2011). Furthermore, these conductive pili contributed more to uranium reduction than cytochrome OmcZ (Cologgi et al., 2014). This could indicate that the extracellular pili function as a protective mechanism to avoid excessive precipitation in the periplasm, thereby minimizing cytotoxic effects. Furthermore, the metal-chelating properties of rough lipopolysaccharides could complement the extracellular pili by preventing uranium crossing the outer membrane, thereby creating a barrier to maximize extracellular reduction (Clark et al., 2021). However, detailed knowledge about the mechanism is currently lacking. Another form of extracellular U(VI) reduction is through extracellular electron shuttle compounds. The electron shuttle is able to transfer electrons to an electron acceptor in the extracellular environment, such as U(VI), without the direct interaction of cellular compounds with the electron acceptor. This was shown for *Shewanella* species that secreted a flavin mononucleotide, which is able to mediate and accelerate reduction of U(VI) (Suzuki et al., 2010; Yamasaki et al., 2017).

Most studies demonstrated that reduced U(IV) was predominantly localized in the periplasm and at the outside of the cell. Nevertheless, cytoplasmic U(VI) reduction with thioredoxins as electron donor was also found. Transposon mutagenesis studies in *D. alaskensis* G20 showed that the *mre* operon, coding for a thioredoxin (MreD), thioredoxin reductase (MreE) and an additional oxidoreductase (MreG) was essential for uranium reduction (Li and Krumholz, 2009; Li et al., 2014).

Although much research has been performed to elucidate the precise uranium reduction pathway, there is currently no general model that completely explains the electron transport chain during uranium reduction. Moreover, different mechanisms seem to exist in different strains. More research is necessary to reveal the molecular pathways allowing uranium reduction.

PHOSPHATASES

Metal-phosphate complexation and biomineralization are common mechanisms for limiting metal bioavailability and toxicity (Gudavalli et al., 2018; Zhang et al., 2021), including uranium (**Table 1**; Wufuer et al., 2017). Since phosphorus is an essential element (Smil, 2000) and soluble phosphate can be scarce in some environments like soil and water bodies, many bacteria use phosphatases to liberate phosphate ions from mineral or organic phosphorus. In fact, organic forms of phosphorus often constitute 30–50% of the total phosphorus (Ruttenberg, 2014). The liberated phosphate ions are able to interact with uranyl, facilitating complexation and precipitation of uranium. Phosphatases, which are either secreted outside the cell or membrane-bound, are broadly categorized based on the pH required for their optimum activity as acid or alkaline. Different sources of phosphate have been used to study phosphatase-mediated uranium-phosphate biomineralization, such as glycerol-2-phosphate (Appukuttan et al., 2006), glycerol-3-phosphate (Powers et al., 2002), phytate (Li et al., 2019) and polyphosphate (Renninger et al., 2004). An overview of the current knowledge of each of these mechanisms is discussed in the following subsections.

Acid Phosphatase

Enzymatic uranium phosphate precipitation was first observed in *Serratia* sp. N14 (Macaskie et al., 1992), originally classified as *Citrobacter* sp. N14 (Pattanapipitpaisal et al., 2002). Since then, uranium phosphate biomineralization has been shown in different *Serratia* spp. under diverse conditions, including anaerobic conditions and even in the presence of high doses of gamma irradiation (Newsome et al., 2015; Chandwadkar et al., 2018). The periplasmic acid phosphatase PhoN was responsible for uranium complexation as a phosphatase deficient mutant was unable to remove uranium from the growth medium (Macaskie et al., 1994; Jeong et al., 1997). Fragments of the purified PhoN were homologous to PhoN of *Morganella morganii*, *Providencia stuartii*, and *Salmonella enterica* subsp. *enterica* serovar Typhimurium (Macaskie et al., 1994; Jeong et al., 1997). However, uranium removal in those strains was negligible (Macaskie et al., 1994), indicating that additional strain-specific characteristics were needed, e.g., suitable sites for uranium nucleation (Macaskie et al., 2000). While the inner and outer membrane were initially identified as nucleation sites for biocrystallization, further research also proposed initial exocellular nucleation within the lipopolysaccharides aided by supposedly liposome-entrapped acid phosphatases that released Pi in close juxtaposition (Jeong et al., 1997; Macaskie et al., 2000). Moreover, the presence of phosphate-containing extracellular polymeric material putatively provided a protective function and enabled uranium removal (Jeong et al., 1997; Macaskie et al., 2000). Other studies on PhoN-type acid phosphatases of *Serratia* spp. showed that two isoenzymes exhibited a different pH optimum and glycerol 2-phosphate affinity (Jeong et al., 1998). Both isoenzymes were also sensitive to uranyl causing a reduction in their activity (Jeong and Macaskie, 1995).

To explore the role of phosphatases in uranium biomineralization more in detail, several recombinant strains expressing phosphatases have been studied (Basnakova et al., 1998). Although *E. coli* DH5α expressing either *phoN* from *S.* Typhi or the related *phoC* from *M. morganii* exhibited acid phosphatase activity comparable to *Serratia* sp. N14, different uranium removal capabilities were observed. *E. coli* expressing *phoN* exhibited increased removal compared to *Serratia* sp., and both were superior to *E. coli* expressing *phoC* (Basnakova et al., 1998), suggesting different *in vivo* properties of both phosphatases. Putatively, the tertiary structure of PhoN protects the sensitive sites of the enzyme for uranyl ions to access (Basnakova et al., 1998). In addition, heterologous expression of PhoN from a *S.* Typhi isolate in *Deinococcus radiodurans* R1 and in *E. coli* showed comparable uranium removal although a higher phosphatase activity was observed in *E. coli* (Appukuttan et al., 2006). Also, in *M. oleivorans* A9, the expression of a broad

specificity phosphatase PhoE coincided with phosphate efflux and showed uranium-phosphate precipitation in different stadia (Gallois et al., 2018).

Acid phosphatase activity and its involvement in uranium biomineralization was also observed in multiple isolates from uranium-contaminated environments. In Jaduguda (India), nine out of twelve strains isolated from uranium mine wastes possessed phosphatase activity (Choudhary et al., 2012). Furthermore, four out of eight isolates from uranium mill tailings pore waters in the region of Limousin (France) possessed acid phosphatase activity, while only one, *Microbacterium oxydans* Br5, possessed alkaline and acid phosphatase activity (Sanchez-Castro et al., 2017). *Caulobacter* sp. OR37, *Rahnella* sp. strain Y9602 and *Bacillus* sp. strain Y9-2 isolated from the Oak Ridge Field Research Center (ORFRC) were phosphatase-positive and removed uranium from growth medium supplemented with organic phosphate in different pH conditions (Beazley et al., 2007; Martinez et al., 2007; Morrison et al., 2021). Moreover, *Rahnella* sp. Y9602 was able to induce uranium phosphate complexation in nitrate-reducing conditions at pH 5.5, albeit with some differences in initial precipitation rates. The same uranium mineral was formed in both aerobic and anaerobic conditions and this was similar to uranium precipitated with free orthophosphate, suggesting that the precipitation is purely chemical through the liberation of Pi from organophosphate by phosphatases (Beazley et al., 2009). This further supports the hypothesis that cells govern nucleation sites for uranium phosphate complexation. Indeed, Morrison et al. (2021) indicated that abiotic precipitation does not occur at uranium concentrations below 1 μM with 500 μM Pi and below pH 5. However, introducing *Caulobacter* sp. strain OR37 resulted in uranium precipitation and the formation of intracellular polyphosphate granules. Presumably, the cells concentrated uranium at the membrane by sorption, which lowered the activation energy required for nucleation and mineralization that prevented abiotic uranium-phosphate mineralization. While most studies investigate uranium biomineralization at uranium concentrations higher than 20 μM, where uranium-phosphate precipitates will inevitable form if Pi is released, many contaminated sites have lower uranium concentrations (Morrison et al., 2021). Moreover, limitations for uranium in drinking water are often below 1 μM (Nolan and Weber, 2015). Therefore, studies investigating microbial interactions with low uranium concentrations are essential.

Results discussed above are mainly from acidic or near neutral environments. However, different observations could be made in alkaline conditions. *Serratia* sp. strain OT II 7, isolated from the acidic sub-surface soil of a uranium ore deposit, exhibited much higher phosphatase activity at pH 5 compared to pH 7 and 9 in the absence of uranium. However, this strain removed uranium much faster at pH 9 and pH 7, than at pH 5 (Chandwadkar et al., 2018). Moreover, for *Serratia* sp. strain OT II 7 as well as *Chryseobacterium* PMSPZI uranium precipitates were formed at a different cellular location depending on the pH. At pH 9, uranyl precipitated always extracellular. At pH 7, extracellular and cell-bound uranium precipitates were formed. Whereas, at pH 5, uranyl precipitates were mainly cell surface-associated or intracellular, which also decreased phosphatase activity and negatively impacted cell viability (Chandwadkar et al., 2018; Khare et al., 2020). It is clear that acid phosphatases play a prominent role in the precipitation of uranium and enable bacteria to withstand high uranium concentrations. Furthermore, uranium-contaminated environments are often acidic, also evidenced by mainly acidic phosphatase activity of environmental isolates.

Alkaline Phosphatases

Industrial processes can also lead to alkaline uranium waste (Seidel, 1981), for example by using carbonate-based reagents to recover uranium from historical mine waste (Santos and Ladeira, 2011) via soluble and stable uranium-carbonate complexes (Duff et al., 2004). In those environments, uranium phosphate mineralization is not expected, which indicates the need to study the physicochemical conditions to determine possible uranium-phosphate complexation. Uranium precipitation is possible at pH 9 in the presence of excess carbonate if $\log(HPO_4^{2-}/HCO_3^{-}) > -3$ (Zheng et al., 2006). Indeed, the secreted alkaline phosphatase PhoK from *Sphingomonas* sp. BSAR-1 precipitated the supplemented uranyl-carbonate at pH 9 as uranium-phosphate through glycerol-2-phosphate cleavage. The precipitation was even more rapidly at higher uranium concentrations when PhoK was over-expressed in *Escherichia coli* BL21 (Nilgiriwala et al., 2008). This PhoK has also been used to create the recombinant *Deinococcus radiodurans* Deino-PhoK strain, resulting in efficient extracellular uranium-phosphate precipitation in planktonic and alginate-encapsulated state. Precipitation occurred also during high doses of ionizing radiation and in the presence of cesium and strontium, which are often present in intermediate and low level liquid radioactive waste (Kulkarni et al., 2013). The advantages of using *D. radiodurans* in treating radioactive waste have recently been reviewed in Li et al. (2021). Uranium precipitation with PhoK-expressing recombinant *E. coli* DH5α and *D. radiodurans* was also examined in a carbonate-deficient condition at pH 6.8 (GC 1) versus a carbonate-abundant condition at pH 9 (GC 2). Uranium toxicity was clearly higher in GC 1 coinciding with more uranium adsorption to the biomass. Consequently, uranium precipitation was cell-associated in GC 1 for both *E. coli* and *D. radiodurans*, whereas precipitates were located more distant from cells in GC 2 (Kulkarni et al., 2016). These observations corroborate that uranium speciation and toxicity depend on the environmental conditions.

C. crescentus NA1000 forms uranium-phosphate precipitates extracellularly or on the cell surface by releasing Pi in modified M5G medium. The periplasmic alkaline phosphatase PhoY, related to the secreted PhoK from *Sphingomonas* sp. BSAR-1 (39% amino acid identity and 51% similarity), was identified as essential in this process and consequently also for uranium resistance (Yung and Jiao, 2014). Furthermore, heterologous expression of the *E. coli* alkaline periplasmic phosphatase PhoA in three *Pseudomonas* subsurface isolates released sufficient Pi in sterilized soil slurries to remove uranium from the cell-free supernatant (up to 69% of 20 μM uranyl acetate) for

P. rhodesiae R1.2 and *P. veronii* V1.2, but not *P. fluorescens* F1.2 (Powers et al., 2002). In *Stenotrophomonas bentonitica* BII-R7, isolated from Spanish bentonite clay formations, four phosphatases were upregulated in the presences of uranium and facilitated the formation of extracellular uranium-phosphate precipitates (Pinel-Cabello et al., 2021). Overall, bacterial alkaline phosphatases are present in a wide range of species and could result in the precipitation of uranium. In the studies presented here, organophosphate was often provided as glycerol-2- or glycerol-3-phosphate. However, in natural environments, other forms of organophosphate can be present such as phytate, which requires specialized phosphatases to release inorganic phosphate.

Phytases

Phytate, or inositol hexaphosphate, is a naturally occurring organic phosphate that can be abundant in soils and is the main form of phosphorous storage in plants (Turner, 2006). Depending on the pH, on the amount of phytate present and on the available carbonates, abiotic uranium precipitation is not expected and thus phosphate needs to be released for uranium immobilization (Langmuir, 1978; Oh et al., 2004; Salome et al., 2017; Li et al., 2019). Phytases are a special class of phosphatases that catalyze the sequential hydrolysis of phytate to less phosphorylated *myo*-inositol derivatives and inorganic phosphate (Wyss et al., 1999). Although distinct phytate types exist, histidine acid phytases are mostly identified in microorganisms. Acidic, but not alkaline phytase activity was shown to be present in microbial communities from the uranium contaminated ORFRC. Experiments with sediment slurries at pH 5.5 indicated that uranium enhanced phytase activity but also resulted in the production of intermediate inositol phosphate species, probably due to the inactivation of other phosphatases, with a decrease in uranium solubility (Salome et al., 2017). *C. crescentus* CB15N is able to form calcium-uranium-phosphate precipitates in oligotrophic medium in the presence of inorganic phosphate. Interestingly, a putative phytase was the most highly upregulated protein in response to uranium in these conditions (Hu et al., 2005). The phytase is not essential for uranium resistance in M2G medium nor in rich PYE medium but does seem to enhance survival in the presence of uranium when phytate is provided as sole phosphate source. Furthermore, since the phytase-deficient mutant already showed reduced growth in the absence of uranium, it seems essential for growth but not necessarily for uranium biomineralization (Yung et al., 2014).

Phosphate Release From Cellular Phosphate Sources

Whereas most studies investigated bacterial uranium-phosphate precipitation by supplementing organic or inorganic phosphate, the possibility of phosphate release from innate phosphate sources for uranium biomineralization is also being scrutinized. In *P. aeruginosa*, overexpression of a polyphosphate kinase resulted in 100 times more accumulated polyphosphate. In the presence of uranyl nitrate, it was shown that uranyl adsorbed initially to the cells and was consecutively precipitated as uranyl phosphate mediated by the release of phosphate from polyphosphate (Renninger et al., 2004). In addition, *D. radiodurans* was shown to precipitate uranium in non-growth conditions at pH 4 without any supplemented phosphate source. Therefore, phosphate had to come from cellular material, such as polyphosphate, which was released during cell lysis (Suzuki and Banfield, 2004). Acharya et al. (2017) also hypothesized that in the cyanobacterium *Anabaena torulosa* alkaline phosphatases liberate Pi from organophosphate substrates released during the decomposition or degradation of cells by uranium. For *Paenibacillus* sp. JG-TB8, uranium was bound by organic phosphate at pH 2 and pH 3 independent on aeration conditions (Reitz et al., 2014). However, uranium seemed to precipitate more as meta-autunite-like uranyl phosphate at higher pH and in oxic conditions, while under anaerobic conditions no mineralization was observed due to decreased Pi release. Nonetheless, the only phosphate sources during the experiment were organic substrates from damaged cells (Reitz et al., 2014).

MEMBRANE PROTEINS

The outer surface of many bacteria and archaea is covered by a proteinaceous surface layer (S-layer) that serves multiple functions, including survival in specific niches. Although its precise role in many organisms has not yet been identified (Fagan and Fairweather, 2014), its involvement in uranium biosorption has been shown in multiple bacteria (**Table 1**; Pollmann et al., 2006; Yung et al., 2015). This is mostly considered to be a passive process, but evidence emerged that bacteria might modulate their cell envelope to become more resistant. In *C. crescentus* NA1000, transposon mutagenesis revealed that the $rsaF_a$ and $rsaF_b$ genes encoding outer membrane transporters conferred uranium tolerance. While $RsaF_a$ and $RsaF_b$ are known for exporting the highly abundant S-layer protein RsaA, a role for the S-layer itself and other S-layer transport systems in uranium resistance was excluded. However, RsaF was found to be homologous to TolC and mutation resulted in a decreased resistance to cadmium and tetracycline, suggesting that resistance could be governed by interacting with other translocases/pumps. Furthermore, contrary to deletion of $rsaF_b$ and *rsaA*, deletion of $rsaF_a$ and $rsaF_aF_brsaA$ increased uranium accumulation. However, a role for RsaF in outer membrane integrity, which could have increased uranium accumulation, could not be excluded. Nevertheless, RsaF plays an important role in uranium resistance either via uranium efflux or via protection of the outer membrane integrity (Yung et al., 2015). The SlfB S-layer protein of *B. sphaericus* JG-A12, isolated from a uranium mining waste pile is much more effective in uranium binding than the SlfA S-layer protein of the reference strain *B. sphaericus* NCTC 9602. The different affinity for uranium could be explained by a distinct C-terminal region of both proteins. The C-terminal region of SlfB harbors significantly more serine and threonine residues, which are potential phosphorylation sites. Notably, analysis of the downstream region of *slfA* and *slfB* and comparison with S-layer proteins from other *B. sphaericus* strains indicated the involvement of horizontal gene transfer and genomic rearrangements (Pollmann et al., 2005). Interestingly,

S-layer proteins can also be utilized to increase uranium removal. A protein fusion of the S-layer protein Hpi of *D. radiodurans* with PhoN displayed efficient uranium removal (Misra et al., 2021). Furthermore, a uranyl specific biosensor based on the S-layer proteins of *B. sphaericus* JG-A12 was developed (Conroy et al., 2010).

The involvement of other membrane proteins in uranium binding and resistance has also been shown recently. Comparison of four *Microbacterium* species revealed that protein UipA was only present in uranium-tolerant strains and was the most upregulated protein after uranium induction. Moreover, the C-terminal part of this single-pass transmembrane protein has a high uranyl binding affinity. The crystal structure of UipA displayed a tandem of PepSY domains in a swapped dimer with a negatively charged face, responsible for uranium binding (Gallois et al., 2021). In addition, the production of carboxymethyl cellulose modified iron sulfide complex (CMC-FeS) by sulfate reducing bacteria was shown to have increased U(VI) removal capacity compared to chemically produced CMC-FeS because of the presence of extracellular polymeric substances (EPS) containing tryptophan and tyrosine residues (He et al., 2021). Finally, increased expression of CreD, an inner membrane protein from *S. bentonitica* BII-R7, decreased membrane permeability and prevented uranium from entering the cytoplasm, thereby increasing uranium resistance during the lag phase (Pinel-Cabello et al., 2021).

METAL EFFLUX SYSTEMS

As evidenced in the previous sections, it is clear that bacteria are able to detoxify uranium via different mechanisms. Nevertheless, in some cases the actual process is not directly deducible. For instance, *Arthrobacter* sp. X34, isolated from the ORFRC, did not exhibit phosphatase activity and did not precipitate any uranium, but was equally and even more resistant to uranium than the uranium-biomineralizing *Bacillus* sp. strain Y9-2 and *Rahnella* sp. strain Y9602, respectively (Beazley et al., 2007; Martinez et al., 2007). Another example is the association of uranium-phosphate minerals with polyhydroxybutyrate in *Cupriavidus metallidurans* NA4 (Rogiers et al., 2021b), which is resistant to uranium independent of the presence of *phaC1*, encoding the poly(3-hydroxyalkanoate) polymerase subunit PhaC (Rogiers, 2022). Therefore, other mechanisms could mediate resistance, including metal efflux systems as uranium toxicity is mainly exerted through its chemical metal-related properties.

Metal efflux is a common detoxification strategy employed by bacteria. Although multiple systems exist, three systems are most common (**Figure 3**; **Table 1**; Nies, 2003). First, the resistance-nodulation-cell division (RND) superfamily includes seven protein families involved in several functions such as transport of hydrophobic compounds and nodulation factors, but also heavy metal efflux (HME-RND). The HME-RND protein (A) is usually combined with a membrane fusion protein (MFP, B) and an outer membrane factor (OMF, C) to form a protein efflux complex that can transport substrates from the cytoplasm, cytoplasmic membrane or periplasm to the outside (Nies, 2003). Typical examples are CzcCBA conferring resistance toward Cd^{2+}, Zn^{2+}, and Co^{2+} (Mergeay et al., 1985), and CusCBA and SilCBA providing resistance toward Cu^{+}, Cu^{2+}, and Ag^{+} ions (Munson et al., 2000; Mijnendonckx et al., 2013; Randall et al., 2014). A second export mechanism comprises efflux pumps driven by the proton motive force or potassium gradient known as cation diffusion facilitators (CDF) (Nies, 2003), such as CzcD mediating a small degree of Cd^{2+}, Zn^{2+}, and Co^{2+} resistance (Nies, 1992; Anton et al., 1999). Lastly, P-type ATPases are able

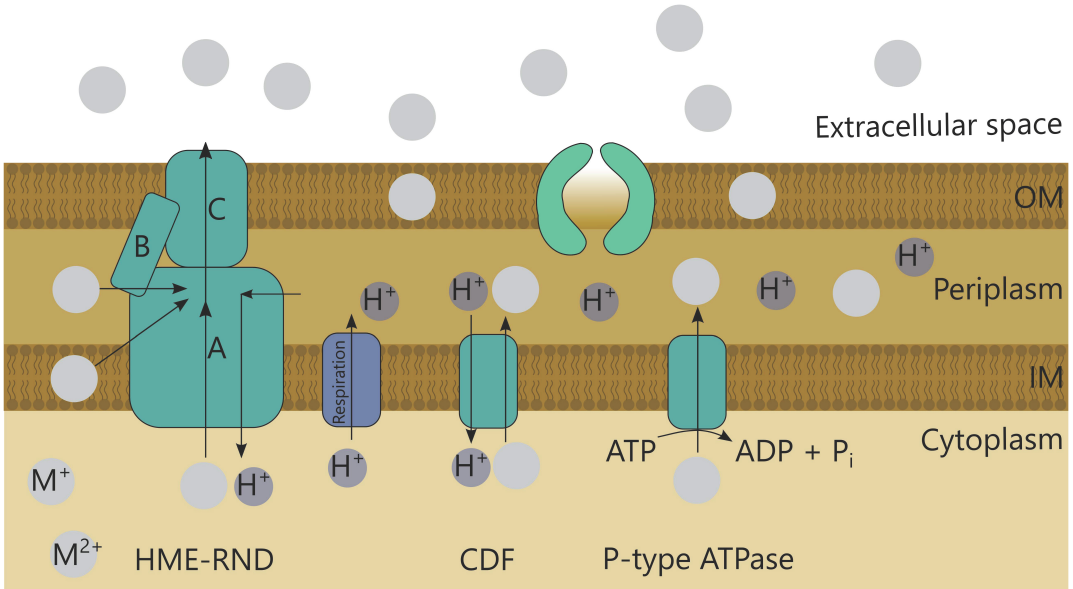

FIGURE 3 | Overview of bacterial efflux systems HME-RND, CDF, and P-type ATPase.

to import and export cations through the hydrolysis of ATP (Nies, 2003). Import is important for essential metals, such as MgtA for Mg^{2+} (Snavely et al., 1989), but ATPases can also detoxify metals through export. Several examples are CadA for Cd^{2+} resistance (Nucifora et al., 1989), ZntA for Zn^{2+} resistance (Beard et al., 1997), and CzcP for Cd^{2+}, Zn^{2+}, and Co^{2+} resistance (Scherer and Nies, 2009).

Although efflux systems are often upregulated after uranium exposure, a designated efflux system for uranium has not yet been identified. For instance, in *C. metallidurans* NA4 almost all genes (from nine different clusters) involved in the response to and detoxification of silver and copper were upregulated after uranium exposure (Rogiers et al., 2021b). In *Chryseobacterium* sp. strain PMSZPI, isolated from a uranium-enriched environment and in *S. bentonitica* BII-R7 *czcA* and *czcA/cusA* genes were upregulated after uranium exposure, respectively (Nongkhlaw and Joshi, 2019; Pinel-Cabello et al., 2021). The expression of one of the two *czc* gene clusters present in *C. metallidurans* NA4 was also induced after exposure to uranium (Rogiers et al., 2021b). Three membrane fusion proteins and two outer membrane factors assisting HME-RND pumps were also upregulated in *G. sulfurreducens* after uranium induction, amongst which CzcC (Orellana et al., 2014). The expression of another *czc* gene, namely of the CDF encoding *czcD*, was found upregulated in both *Chryseobacterium* sp. strain PMSZPI and *S. bentonitica* BII-R7 (Nongkhlaw and Joshi, 2019; Pinel-Cabello et al., 2021). Furthermore, P-type ATPases are also often found upregulated after uranium exposure, such as *cadA* in *Chryseobacterium* sp. strain PMSZPI (Nongkhlaw and Joshi, 2019) and a cadmium- and copper-translocating P-type ATPase in *Desulfotomaculum reducens* MI-1 (Junier et al., 2011). Altogether, these results suggest that uranium efflux, if active, occurs through systems conferring resistance to Cd^{2+}, Zn^{2+}, Co^{2+} or Cu^{2+}, and Ag^{+}. Other efflux-related genes are sometimes upregulated as well, such as the nickel and cobalt efflux regulator *rcnB* and antibiotic resistance efflux genes (*mdtAB*) in *S. bentonitica* BII-R7 (Pinel-Cabello et al., 2021).

In *M. oleivorans* A9, a fast initial biotic removal of uranium was followed by an active release of U(VI), which was accompanied with phosphate efflux for uranium-phosphate biomineralization. However, this release was only seen at a concentration of 10 μM but not at 50 μM uranyl nitrate. It was therefore hypothesized that higher concentrations of U(VI) could inhibit efflux-mediated resistance or that the influx of uranium into the cell would mask the efflux (Theodorakopoulos et al., 2015). In a follow-up proteomic study, the upregulation of several cation transporters (K^{+}, Mn^{2+}, Zn^{2+}, Mg^{2+}, and Co^{2+}) and an ABC-type transport system co-occurred with uranium efflux (Gallois et al., 2018). A similar release of uranium after initial biosorption was observed for *Halobacterium noricense* (Bader et al., 2017). The studies on *M. oleivorans* A9 and *H. noricense* could indicate that uranium efflux is possible, but that uranium resistance is a complex process mediated by a combination of different mechanisms. This could explain why, although efflux systems are often upregulated, proof of essential efflux systems for uranium resistance is still lacking. Uranium efflux could contribute to limit uranium entry, but detoxification seems to be mediated by biomineralization, bioreduction or biosorption.

REGULATORY SYSTEMS

To sense and respond to environmental changes bacteria deploy different regulatory systems, including two-component systems (TCSs) that are often involved in the response to metals (Chang and Stewart, 1998; Mergeay and Van Houdt, 2015). Typically, the sensor histidine kinase (HK) senses the metal ion, uses ATP to autophosphorylate a conserved histidine residue and transfers the phosphate group to a conserved aspartate residue on the corresponding response regulator (RR) (Chang and Stewart, 1998). On its turn, the phosphorylated RR regulates the expression of metal resistance genes, but often also autoregulates the expression of the TCS. In *C. crescentus* NA1000, two uranium-responsive TCSs have been identified by analyzing transcriptomic and proteomic data after exposure to non-toxic uranium concentrations (Hu et al., 2005; Yung et al., 2014; Park et al., 2017; Park and Taffet, 2019). UrpRS (uranium responsive phytase regulator and sensor, respectively, CCNA_01362 + 01363) was found to regulate a phytase gene (CCNA_01353) that confers uranium resistance when phytate is provided as the sole phosphate source (Yung et al., 2014; Park and Taffet, 2019). UzcRS (CCNA_02842 + 02845), also responsive toward zinc and copper, regulates the expression of *urcA* (uranium response in *caulobacter*, CC3302), the highest uranium-specific induced gene encoding a periplasmic protein with unknown function (Hu et al., 2005; Park et al., 2017). The promoter region of *urcA* contains two m_5 motives specific for uranium induction that are nearly identical to the 18-bp UzcR recognition motif (Hillson et al., 2007). This site contains the partially palindromic half sites 5′-CATTAC-N_6-TTAA-3′ found in 44 of 57 UzcR binding regions determined by ChIP-seq (Park et al., 2017). Furthermore, deleting *uzcR* or *uzcS* prevented the Zn-, U- and Cu-dependent induction of the promoter region of *urcA* (P_{urcA}). UzcR is thus presumably the regulator of the m_5 motif and could be involved in the direct recruitment of the RNA polymerase holoenzyme since the m_5 motif is located at a common binding site for transcriptional activators, 43 or 53 bp upstream of the transcription start site (Lee et al., 2012). In general, UzcR binds extensively throughout the genome mainly activating genes encoding proteins with a putative signal secretion signal and/or transmembrane domains (52 of 66 genes) such as metallopeptidases, multidrug-resistant efflux (MDR) pumps, TonB-dependent receptors and many proteins of unknown function (Park et al., 2017). The expression of *uzcRS* is modulated by auxiliary regulators and the TCS is part of a complex signaling network (Park et al., 2019). However, deletion mutants of *uzcRS* disputed an essential role in uranium resistance and the manner of uranium sensing is still unclear since UO_2^{2+}, Zn^{2+}, and Cu^{2+} displayed different coordination preferences (Haas and Franz, 2009; Park et al., 2017). It is hypothesized that expression of *uzcRS* and *urpRS* is induced indirectly by uranium. Nevertheless, the combination of both TCS systems has been used to develop a whole-cell biosensor for uranium that

showed a highly improved selectivity toward uranium compared to the previously designed whole-cell biosensor based on the *urcA* promoter (Hillson et al., 2007; Park et al., 2019; Park and Taffet, 2019).

Upregulation of regulatory systems after uranium induction has also been observed in other bacteria. A negative regulator of stress-induced operons, ArsR (Silver and Phung, 2005), seemed to be less abundant when uranium is internally biomineralized in *M. oleivorans* A9 but more abundant as long as uranium remains extracellularly (Gallois et al., 2018). Interestingly, the TCS UipRS is located upstream the uranium binding protein UipA in multiple *Microbacterium* species, but a role in uranium sensing and resistance has not yet been shown (Gallois et al., 2021). In *D. alaskensis* G20, a cyclic AMP receptor protein (CRP) was found to possibly regulate expression of the *mre* operon for metal reduction, facilitating uranium reduction through thioredoxin (Li and Krumholz, 2009). Finally, ten TCSs are upregulated in *C. metallidurans* after uranium induction of which five are known to be involved in metal resistance (Rogiers et al., 2021b). While extensive work has only been done in *C. crescentus*, there is currently little known on how uranium is sensed and how this results in the transcription of target genes. Further research is therefore necessary, also in other bacteria, to unravel the underlying regulatory mechanisms. An overview of the current knowledge on the different molecular interaction mechanisms is presented in **Table 1**.

GENERAL IMPLICATIONS FOR TECHNOLOGICAL APPLICATIONS

The toxic characteristics of uranium urged researchers to investigate possible remediation strategies. This led to the discovery that bacteria could be used for uranium bioremediation, which is now one of the most promising bio-based approaches for the remediation of uranium-contaminated sites (Newsome et al., 2014). Uranium reduction is one of the most studied processes. Although the extensive research has already elucidated large parts of the uranium reduction pathway, it is not yet completely clarified. Further research on these pathways could be useful to understand the uranium reduction mechanism completely, but it could also enable full exploitation and modulation of the reduction process for bioremediation applications. However, one of the disadvantages of uranium reduction for bioremediation purposes is that it depends highly on environmental factors as it necessitates reducing conditions and often requires removal of soil compounds (e.g., nitrate) before it can be applied. In addition, one of the remaining problems for *in situ* bioremediation is that reduced uranium is more or less prone to reoxidation depending on the minerals formed. Moreover, the addition of cadmium, a known inhibitor of thioredoxin, showed complete inhibition of uranium reduction in some conditions, which is important to take into account for bioremediation purposes as uranium contaminated soils are very often co-contaminated with metals such as cadmium, zinc and copper (Li and Krumholz, 2009; Bigalke et al., 2017; Lu and Liu, 2018). Furthermore, zinc and copper were also found to completely inhibit uranium reduction when concentrations reached 25 and 15 mg/L, respectively, due to their toxic effects on sulfate-reducing bacteria (Yi et al., 2007). A more extensive screening of different metals can be useful to identify key inhibitors of uranium reduction. Besides metal ions, also uranyl speciation and concentration, pH, temperature, electron donors and acceptors can affect uranium reduction rates (recently reviewed by You et al., 2021). Nevertheless, uranium reduction can still be an asset in several conditions. For example, if *in situ* conditions are anaerobic, providing electron donors could quickly immobilize uranyl by forming uraninite. Also, if the recovery of uranium is necessary during *ex situ* remediation, reduction in column or batch setups could be more favorable, since U(IV) is easily remobilized.

To overcome a number of the limitations for long-term processes, the research focus shifted in recent years to other uranium interaction mechanisms, such as uranium phosphate biomineralization. For instance, if long-term immobilization is preferential or if the removal of uranium without recovery is the main goal, uranium-phosphate precipitation could be the best option. Uranium-phosphate minerals, such as autunite or meta-autunite, have generally low aqueous solubility (Lobeck et al., 2020), are stable over a wide temperature and pH range (Dzik et al., 2017; Wufuer et al., 2017; Gudavalli et al., 2018) and are not prone to remobilization through reoxidation (Williamson et al., 2014; Romanchuk et al., 2020). Abiotic remediation with Pi has been tested, but resulted rapidly in phosphate mineral precipitation not linked with uranium and clogged pore spaces that inhibited further diffusion, which was alleviated by using microbial activity to release Pi continuously from polyphosphates or phytate (Wellman et al., 2006). Phytate has been shown to be more recalcitrant to degradation than other organic phosphates, which may facilitate its migration in contaminated soils and can be advantages for bioremediation purposes (Wellman et al., 2006). However, also uranium phosphate biomineralization still depends on the environmental conditions. Partial protonation of inorganic phosphate starting below pH 4 could hamper abiotic uranyl phosphate mineralization (Hinsinger, 2001). Above circumneutral pH and in the presence of high (bi)carbonate concentrations, highly soluble uranium-carbonate complexes are formed, which can prevent uranyl phosphate precipitation or can solubilize autunite minerals (Pablo et al., 1999; Gudavalli et al., 2018). On the other hand, uranyl-hydroxide formation could allow precipitation (Chandwadkar et al., 2018). Furthermore, strong organic acids, such as oxalate and citrate, interact directly with uranyl and could affect uranium-phosphate biomineralization. However, organic ligands could also promote the conversion of colloidal particles $UO_2(OH)_2$ to free UO_2^{2+}, which could facilitate uranyl phosphate biomineralization. Nonetheless, uranium-phosphate biomineralization was completely inhibited when organic ligands compete with biotic PO_4^{3-} (Tu et al., 2019). Moreover, in anaerobic nitrate-reducing conditions, the combined toxicity of uranium and produced nitrite after nitrate reduction suppressed growth (Beazley et al., 2009). Even though uranium was still precipitated, presumably due to the early release of Pi before uranium addition or the continued activity of the phosphatases, nitrite accumulation might have implications on the sustainability of the process. Knowledge on compounds

preventing uranium-phosphate biomineralization is currently limited to metals. Chromium was able to interfere with uranium biomineralization by PhoN-expressing *D. radiodurans* cells. Furthermore, introducing YieF, which is able to convert Cr(VI) to the less toxic Cr(III), alleviated this problem (Xu et al., 2018). Cd^{2+} and Hg^{2+} are known to affect soil acid phosphatase activity and Hg^{2+}, Cu^{2+}, and Cd^{2+} are able to inhibit *E. coli* alkaline phosphatase activity (Alnuaimi et al., 2012; Zheng et al., 2019). In general, since phosphatases are known to play a pivotal role, one can hypothesize that inhibition of phosphatase activity also inhibits uranium-phosphate biomineralization.

Overall, it is clear that the physico-chemical environment imposes restrictions on the applied method, especially for *in situ* processes. Since uranium-contaminated sites or often co-contaminated with toxic metals (Sitte et al., 2015; Boteva et al., 2016; Rogiers et al., 2021a), *in situ* bioremediation necessitates the presence of multiple metal resistance mechanisms, which are often present in the indigenous microbial communities thriving in such contaminated sites (Choudhary and Sar, 2015; Agarwal et al., 2020; Rogiers et al., 2021a).

CONCLUSION

We provided an overview of the state-of-the-art on active bacterial uranium detoxification mechanisms including uranium reduction, phosphatases, membrane proteins, efflux and regulatory systems. Although extensive work has been done, completely unraveling the molecular mechanistic insights behind uranium resistance and its regulation necessitates further research. Such mechanistic insights can augment bioremediation processes as evidenced throughout this review.

AUTHOR CONTRIBUTIONS

TR, KM, and RV contributed to the conceptualization. TR wrote the original draft of the manuscript. KM and RV performed a critical revision of the manuscript. NL, AW, and NB contributed to the manuscript revision, read, and approved the submitted version. All authors contributed to the article and approved the submitted version.

REFERENCES

Acharya, C., Chandwadkar, P., and Nayak, C. (2017). Unusual versatility of the filamentous, diazotrophic cyanobacterium *Anabaena torulosa* revealed for its survival during prolonged uranium exposure. *Appl. Environ. Microbiol.* 83, 1–17. doi: 10.1128/AEM.03356-16

Agarwal, M., Rathore, R. S., Black, A., Xu, X., Seaman, J., Chauhan, A., et al. (2020). Announcing the availability of a culture Collection of Uranium-Resistant Microbial Assemblages (CURMA) obtained from metalliferous soils of the Savannah River Site, USA. *Microbiol. Resour. Announcements* 9, e551–e520. doi: 10.1128/MRA.00551-20

Alnuaimi, M., Saeed, I., and Ashraf, S. (2012). *Effect of Various Heavy Metals on the Enzymatic Activity of E. coli Alkaline Phosphatase*. Asharij: United Arab Emirates University.

Anton, A., Große, C., Reißmann, J., Pribyl, T., and Nies, D. H. (1999). CzcD is a heavy metal ion transporter involved in regulation of heavy metal resistance in *Ralstonia* sp. strain CH34. *J. Bacteriol.* 181, 6876–6881. doi: 10.1128/jb.181.22.6876-6881.1999

Appukuttan, D., Rao, A. S., and Apte, S. K. (2006). Engineering of *Deinococcus radiodurans* R1 for bioprecipitation of uranium from dilute nuclear waste. *Appl. Environ. Microbiol.* 72, 7873–7878. doi: 10.1128/AEM.01362-06

Bader, M., Müller, K., Foerstendorf, H., Drobot, B., Schmidt, M., Musat, N., et al. (2017). Multistage bioassociation of uranium onto an extremely halophilic archaeon revealed by a unique combination of spectroscopic and microscopic techniques. *J. Hazardous Mater.* 327, 225–232. doi: 10.1016/j.jhazmat.2016.12.053

Basnakova, G., Stephens, E. R., Thaller, M. C., Rossolini, G. M., and Macaskie, L. E. (1998). The use of *Escherichia coli* bearing a phoN gene for the removal of uranium and nickel from aqueous flows. *Appl. Microbiol. Biotechnol.* 50, 266–272. doi: 10.1007/s002530051288

Beard, S. J., Hashim, R., Membrillo-Hernández, J., Hughes, M. N., and Poole, R. K. (1997). Zinc(II) tolerance in *Escherichia coli* K-12: evidence that the *zntA* gene (o732) encodes a cation transport ATPase. *Mol. Microbiol.* 25, 883–891. doi: 10.1111/j.1365-2958.1997.mmi518.x

Beazley, M. J., Martinez, R. J., Sobecky, P. A., Webb, S. M., and Taillefert, M. (2007). Uranium biomineralization as a result of bacterial phosphatase activity: insights from bacterial isolates from a contaminated subsurface. *Environ. Sci. Technol.* 41, 5701–5707. doi: 10.1021/es070567g

Beazley, M. J., Martinez, R. J., Sobecky, P. A., Webb, S. M., and Taillefert, M. (2009). Nonreductive biomineralization of uranium(VI) phosphate via microbial phosphatase activity in anaerobic conditions. *Geomicrobiol. J.* 26, 431–441. doi: 10.1080/01490450903060780

Bencheikh-Latmani, R., Williams, S. M., Haucke, L., Criddle, C. S., Wu, L., Zhou, J., et al. (2005). Global transcriptional profiling of *Shewanella oneidensis* MR-1 during Cr(VI) and U(VI) reduction. *Appl. Environ. Microbiol.* 71, 7453–7460. doi: 10.1128/AEM.71.11.7453-7460.2005

Bigalke, M., Ulrich, A., Rehmus, A., and Keller, A. (2017). Accumulation of cadmium and uranium in arable soils in Switzerland. *Environ. Pollut.* 221, 85–93. doi: 10.1016/j.envpol.2016.11.035

Boteva, S., Radeva, G., Traykov, I., and Kenarova, A. (2016). Effects of long-term radionuclide and heavy metal contamination on the activity of microbial communities, inhabiting uranium mining impacted soils. *Environ. Sci. Pollut. Res. Int.* 23, 5644–5653. doi: 10.1007/s11356-015-5788-5

Bouby, M., Billard, I., MacCordick, J., and Rossini, I. (1998). Complexation of Uranium (VI) with the Siderophore Pyoverdine. *Radiochimica Acta* 80, 95–100. doi: 10.1007/s10967-007-0931-5

Chandler, D. P., Kukhtin, A., Mokhiber, R., Knickerbocker, C., Ogles, D., Rudy, G., et al. (2010). Monitoring microbial community structure and dynamics during *in situ* U(VI) bioremediation with a field-portable microarray analysis system. *Environ. Sci. Technol.* 44, 5516–5522. doi: 10.1021/es1006498

Chandwadkar, P., Misra, H. S., and Acharya, C. (2018). Uranium biomineralization induced by a metal tolerant Serratia strain under acid, alkaline and irradiated conditions. *Metallomics* 10, 1078–1088. doi: 10.1039/c8mt00061a

Chang, C., and Stewart, R. C. (1998). The Two-component system. regulation of diverse signaling pathways in prokaryotes and eukaryotes. *Plant Physiol.* 117, 723–731. doi: 10.1104/pp.117.3.723

Choudhary, S., Islam, E., Kazy, S. K., and Sar, P. (2012). Uranium and other heavy metal resistance and accumulation in bacteria isolated from uranium mine wastes. *J. Environ. Sci. Health Part a-Toxic/Hazardous Substances Environ. Eng.* 47, 622–637. doi: 10.1080/10934529.2012.650584

Choudhary, S., and Sar, P. (2015). Interaction of uranium (VI) with bacteria: potential applications in bioremediation of U contaminated oxic environments. *Rev. Environ. Sci. Bio-Technol.* 14, 347–355. doi: 10.1007/s11157-015-9366-6

Clark, M. M., Paxhia, M. D., Young, J. M., Manzella, M. P., and Reguera, G. (2021). Adaptive synthesis of a rough lipopolysaccharide in geobacter sulfurreducens for metal reduction and detoxification. *Appl. Environ. Microbiol.* 87:e0096421. doi: 10.1128/AEM.00964-21

Cologgi, D. L., Lampa-Pastirk, S., Speers, A. M., Kelly, S. D., and Reguera, G. (2011). Extracellular reduction of uranium via *Geobacter* conductive pili as a protective cellular mechanism. *Proc. Natl. Acad. Sci. U.S.A.* 108, 15248–15252. doi: 10.1073/pnas.1108616108

Cologgi, D. L., Speers, A. M., Bullard, B. A., Kelly, S. D., and Reguera, G. (2014). Enhanced uranium immobilization and reduction by *Geobacter sulfurreducens* biofilms. *Appl. Environ. Microbiol.* 80, 6638–6646. doi: 10.1128/AEM.02289-14

Conroy, D. J. R., Millner, P. A., Stewart, D. I., and Pollmann, K. (2010). Biosensing for the environment and defence: aqueous Uranyl detection using bacterial surface layer proteins. *Sensors* 10, 4739–4755. doi: 10.3390/s100504739

Cumberland, S. A., Douglas, G., Grice, K., and Moreau, J. W. (2016). Uranium mobility in organic matter-rich sediments: a review of geological and geochemical processes. *Earth-Sci. Rev.* 159, 160–185. doi: 10.1016/j.earscirev.2016.05.010

Du, X., Boonchayaanant, B., Wu, W.-M., Fendorf, S., Bargar, J., and Criddle, C. S. (2011). Reduction of Uranium(VI) by Soluble Iron(II) conforms with thermodynamic predictions. *Environ. Sci. Technol.* 45, 4718–4725. doi: 10.1021/es2006012

Duff, M. C., Hunter, D. B., Hobbs, D. T., Fink, S. D., Dai, Z., and Bradley, J. P. (2004). Mechanisms of strontium and uranium removal from high-level radioactive waste simulant solutions by the sorbent monosodium titanate. *Environ. Sci. Technol.* 38, 5201–5207. doi: 10.1021/es035415+

Dzik, E. A., Lobeck, H. L., Zhang, L., and Burns, P. C. (2017). Thermodynamic properties of phosphate members of the meta-autunite group: a high-temperature calorimetric study. *J. Chem. Thermodynamics* 114, 165–171. doi: 10.1016/j.jct.2017.07.007

Fagan, R. P., and Fairweather, N. F. (2014). Biogenesis and functions of bacterial S-layers. *Nat. Rev. Microbiol.* 12, 211–222. doi: 10.1038/nrmicro3213

Finch, R., and Murakami, T. (1999). "Systematics and paragenesis of uranium minerals," in *Uranium: Mineralogy, Geochemistry, and the Environment*, eds P. C. Burns and R. J. Finch (Berlin: De Gruyter), 91–179. doi: 10.1515/9781501509193-008

Frazier, S. W., Kretzschmar, R., and Kraemer, S. M. (2005). Bacterial siderophores promote dissolution of UO_2 under reducing conditions. *Environ. Sci. Technol.* 39, 5709–5715. doi: 10.1021/es050270n

Gallois, N., Alpha-Bazin, B., Bremond, N., Ortet, P., Barakat, M., Piette, L., et al. (2021). Discovery and characterization of UipA, a uranium- and iron-binding PepSY protein involved in uranium tolerance by soil bacteria. *ISME J.* doi: 10.1038/s41396-021-01113-7

Gallois, N., Alpha-bazin, B., Ortet, P., Barakat, M., Piette, L., Long, J., et al. (2018). Proteogenomic insights into uranium tolerance of a Chernobyl's *Microbacterium* bacterial isolate. *J. Proteomics* 177, 148–157. doi: 10.1016/j.jprot.2017.11.021

Geras'kin, S., Evseeva, T., and Oudalova, A. (2013). Effects of long-term chronic exposure to radionuclides in plant populations. *J. Environ. Radioact.* 121, 22–32. doi: 10.1016/j.jenvrad.2012.03.007

Godheja, J., Sk, S., Siddiqui, S. A., and Modi, D. R. (2016). Xenobiotic compounds present in soil and water: a review on remediation strategies. *J. Environ. Analytical Toxicol.* 6. doi: 10.4172/2161-0525.1000392

Gudavalli, R., Katsenovich, Y., and Wellman, D. (2018). Quantification of kinetic rate law parameters for the dissolution of natural autunite in the presence of aqueous bicarbonate ions at high concentrations. *J. Environ. Radioact.* 19, 1–9. doi: 10.1016/j.jenvrad.2018.04.007

Haas, K. L., and Franz, K. J. (2009). Application of metal coordination chemistry to explore and manipulate cell biology. *Chem. Rev.* 109, 4921–4960. doi: 10.1021/cr900134a

Hammond, C. R. (2004). *The Elements, Handbook of Chemistry and Physics*, 84th Edn. Boca Raton, FL: CRC Press.

He, S., Hu, W., Liu, Y., Xie, Y., Zhou, H., Wang, X., et al. (2021). Mechanism of efficient remediation of U(VI) using biogenic CMC-FeS complex produced by sulfate-reducing bacteria. *J. Hazardous Mater.* 420:126645. doi: 10.1016/j.jhazmat.2021.126645

Hillson, N. J., Hu, P., Andersen, G. L., and Shapiro, L. (2007). *Caulobacter crescentus* as a whole-cell uranium biosensor. *Appl. Environ. Microbiol.* 73, 7615–7621. doi: 10.1128/AEM.01566-07

Hinsinger, P. (2001). Bioavailability of soil inorganic P in the rhizosphere as affected by root- induced chemical changes: a review. *Plant Soil* 237, 173–195. doi: 10.1023/A

Holmes, D. E., O'Neil, R. A., Chavan, M. A., N'Guessan, L. A., Vrionis, H. A., Perpetua, L. A., et al. (2009). Transcriptome of *Geobacter uraniireducens* growing in uranium- contaminated subsurface sediments. *ISME J.* 3, 216–230. doi: 10.1038/ismej.2008.89

Hu, P., Brodie, E. L., Suzuki, Y., McAdams, H. H., and Andersen, G. L. (2005). Whole-Genome transcriptional analysis of heavy metal stresses in *Caulobacter crescentus*. *J. Bacteriol.* 187, 8437–8449. doi: 10.1128/JB.187.24.8437

International Atomic Energy Agency [IAEA] (2003). *Extent of Environmental Contamination by Naturally Occurring Radioactive Material (NORM) and Technological Options for Mitigation*. IAEA Report 419. Vienna: IAEA

International Atomic Energy Agency [IAEA] (2018). *The Fukushima Daiichi Accident*. Vienna: IAEA.

Jeong, B. C., Hawes, C., Bonthrone, K. M., and Macaskie, L. E. (1997). Localization of enzymically enhanced heavy metal accumulation by *Citrobacter* sp . and metal accumulation in vitro by liposomes containing entrapped enzyme. *Microbiology* 143, 2497–2507. doi: 10.1099/00221287-143-7-2497

Jeong, B. C., and Macaskie, L. E. (1995). PhoN-type acid phosphatases of a heavy metal-accumulating *Citrobacter* sp .: resistance to heavy metals and affinity towards phosphomonoester substrates. *FEMS Microbiol. Lett.* 130, 211–214. doi: 10.1111/j.1574-6968.1995.tb07722.x

Jeong, B. C., Poole, P. S., Willis, A. C., and Macaskie, L. E. (1998). Purification and chacterization of acid-type phosphatases from a heavy-metal-accumulating *Citrobacter* sp. *Arch. Microbiol.* 169, 166–173. doi: 10.1007/s002030050556

Junier, P., Vecchia, E. D., and Bernier-Latmani, R. (2011). The response of *Desulfotomaculum reducens* MI-1 to U(VI) exposure: a transcriptomic study. *Geomicrobiol. J.* 28, 483–496. doi: 10.1080/01490451.2010.512031

Khare, D., Kumar, R., and Acharya, C. (2020). Genomic and functional insights into the adaptation and survival of *Chryseobacterium* sp. strain PMSZPI in uranium enriched environment. *Ecotoxicol. Environ. Saf.* 191:110217. doi: 10.1016/j.ecoenv.2020.110217

Kulkarni, S., Ballal, A., and Apte, S. K. (2013). Bioprecipitation of uranium from alkaline waste solutions using recombinant *Deinococcus radiodurans*. *J. Hazardous Mater.* 262, 853–861. doi: 10.1016/j.jhazmat.2013.09.057

Kulkarni, S., Misra, C. S., Gupta, A., Ballal, A., and Apte, S. K. (2016). Interaction of uranium with bacterial cell surfaces: inferences from phosphatase-mediated uranium precipitation. *Appl. Environ. Microbiol.* 82, 4965–4974. doi: 10.1128/AEM.00728-16

Langmuir, D. (1978). Uranium solution-mineral equilibria at low temperatures with applications to sedimentary ore deposits. *Geochimica Cosmochimica Acta* 42, 547–569. doi: 10.1016/0016-7037(78)90001-7

Lee, D. J., Minchin, S. D., and Busby, S. J. W. (2012). Activating transcription in bacteria. *Annu. Rev. Microbiol.* 66, 125–152. doi: 10.1146/annurev-micro-092611-150012

Li, R., Ibeanusi, V., Hoyle-Gardner, J., Crandall, C., Jagoe, C., Seaman, J., et al. (2019). Bacterial-facilitated uranium transport in the presence of phytate at Savannah River Site. *Chemosphere* 223, 351–357. doi: 10.1016/j.chemosphere.2019.02.064

Li, S., Zhu, Q., Luo, J., Shu, Y., Guo, K., Xie, J., et al. (2021). Application progress of deinococcus radiodurans in biological treatment of radioactive uranium-containing wastewater. *Ind. J. Microbiol.* 61, 417–426. doi: 10.1007/s12088-021-00969-9

Li, X., and Krumholz, L. R. (2009). Thioredoxin is involved in U(VI) and Cr(VI) reduction in *Desulfovibrio desulfuricans* G20. *J. Bacteriol.* 191, 4924–4933. doi: 10.1128/JB.00197-09

Li, X., Zhang, H., Ma, Y., Liu, P., and Krumholz, L. R. (2014). Genes required for alleviation of uranium toxicity in sulfate reducing bacterium *Desulfovibio alaskensis* G20. *Ecotoxicology* 23, 726–733. doi: 10.1007/s10646-014-1201-2

Lide, D. R. (2003). *CRC Handbook of Chemistry and Physics, 2003-2004*. Boca Raton, FL: CRC Press.

Liu, W., Dai, X., Bai, Z., Wang, Y., Yang, Z., Zhang, L., et al. (2017). Highly sensitive and selective uranium detection in natural water systems using a luminescent mesoporous metal-organic framework equipped with abundant lewis basic sites: a combined batch, X-ray absorption spectroscopy, and first principles simulation Inv. *Environ. Sci. Technol.* 51, 3911–3921. doi: 10.1021/acs.est.6b06305

Lloyd, J. R., Leang, C., Hodges Myerson, A. L., Coppi, V. M., Cuifo, S., Methe, B., et al. (2003). Biochemical and genetic characterization of PpcA, a periplasmic c-type cytochrome in *Geobacter sulfurreducens*. *Biochem. J.* 369, 153–161. doi: 10.1042/BJ20020597

Lobeck, H. L., Balboni, E., Parker, C. J., Kohlgruber, T. A., Xu, M., Boukdad, S., et al. (2020). Dissolution of poorly soluble uranyl phosphate phases in the Metaautunite Subgroup under uranyl peroxide cage cluster forming conditions. *Am. Mineralogist* 105, 182–193. doi: 10.2138/am-2020-7106

Lopez-Fernandez, M., Vilchez-Vargas, R., Jroundi, F., Boon, N., Pieper, D., and Merroun, M. L. (2017). Microbial community changes induced by uranyl nitrate

in bentonite clay microcosms. *Appl. Clay Sci.* 160, 206–216. doi: 10.1016/j.clay.2017.12.034

Lu, Z., and Liu, Z. (2018). Pollution characteristics and risk assessment of uranium and heavy metals of agricultural soil around the uranium tailing reservoir in Southern China. *J. Radioanalytical Nuclear Chem.* 318, 923–933. doi: 10.1007/s10967-018-6081-0

Macaskie, L. E., Bonthrone, K. M., and Rouch, D. A. (1994). Phosphatase-mediated heavy metal accumulation by a *Citrobacter* sp. and related enterobacteria. *FEMS Microbiol. Lett.* 121, 141–146. doi: 10.1111/j.1574-6968.1994.tb07090.x

Macaskie, L. E., Bonthrone, K. M., Yong, P., and Goddard, D. T. (2000). Enzymically mediated bioprecipitation of uranium by a *Citrobacter* sp.: a concerted role for exocellular lipopolysaccharide and associated phosphatase in biomineral formation. *Microbiology* 146, 1855–1867. doi: 10.1099/00221287-146-8-1855

Macaskie, L. E., Empson, R. M., Cheetham, A. K., Grey, C. P., and Skarnulis, A. J. (1992). Uranium bioaccumulation by a *Citrobacter* sp. as a result of enzymically mediated growth of polycrystalline HUO_2PO_4. *Science* 257, 782–785. doi: 10.1126/science.1496397

Markich, S. J. (2002). Uranium speciation and bioavailability in aquatic systems: an overview. *ScientificWorldJournal* 2, 707–729. doi: 10.1100/tsw.2002.130

Marshall, M. J., Beliaev, A. S., Dohnalkova, A. C., Kennedy, D. W., Shi, L., Wang, Z., et al. (2006). c-Type cytochrome-dependent formation of U(IV) nanoparticles by *Shewanella oneidensis*. *PLoS Biol.* 4:e268. doi: 10.1371/journal.pbio.0040268

Martinez, R. J., Beazley, M. J., Taillefert, M., Arakaki, A. K., Skolnick, J., and Sobecky, P. A. (2007). Aerobic uranium (VI) bioprecipitation by metal-resistant bacteria isolated from radionuclide- and metal-contaminated subsurface soils. *Environ. Microbiol.* 9, 3122–3133. doi: 10.1111/j.1462-2920.2007.01422.x

Mergeay, M., Nies, D. H., Schlegel, H. G., Gerits, J., Charles, P., and Van Gijsegem, F. (1985). *Alcaligenes eutrophus* CH34 is a facultative chemolithotroph with plasmid-bound resistance to heavy metals. *J. Bacteriol.* 162, 328–334. doi: 10.1128/jb.162.1.328-334.1985

Mergeay, M., and Van Houdt, R. (2015). Metal Response in Cupriavidus Metallidurans. Volume I, From Habitats to Genes and Proteins. Berlin: Springer.

Merroun, M. L., Raff, J., Rossberg, A., Hennig, C., Reich, T., and Selenska-Pobell, S. (2005). Complexation of uranium by cells and S-layer sheets of Bacillus sphaericus JG-A12. *Appl. Environ. Microbiol.* 71, 5532–5543. doi: 10.1128/AEM.71.9.5532-5543.2005

Merroun, M. L., and Selenska-Pobell, S. (2008). Bacterial interactions with uranium: an environmental perspective. *J. Contaminant Hydrol.* 102, 285–295. doi: 10.1016/j.jconhyd.2008.09.019

Mijnendonckx, K., Leys, N., Mahillon, J., Silver, S., and Van Houdt, R. (2013). Antimicrobial silver: uses, toxicity and potential for resistance. *BioMetals* 26, 609–621. doi: 10.1007/s10534-013-9645-z

Misra, C. S., Sounderajan, S., and Apte, S. K. (2021). Metal removal by metallothionein and an acid phosphatase PhoN, surface-displayed on the cells of the extremophile, Deinococcus radiodurans. *J. Hazardous Mater.* 419:126477. doi: 10.1016/j.jhazmat.2021.126477

Mo, K. F., Dai, Z., and Wunschel, D. S. (2016). Production and characterization of desmalonichrome relative binding affinity for Uranyl ions in relation to other siderophores. *J. Nat. Prod.* 79, 1492–1499. doi: 10.1021/acs.jnatprod.5b00933

Morrison, K. D., Zavarin, M., Kersting, A. B., Begg, J. D., Mason, H. E., Balboni, E., et al. (2021). Influence of Uranium concentration and pH on U-Phosphate biomineralization by *Caulobacter* OR37. *Environ. Sci. Technol.* 55, 1626–1636. doi: 10.1021/acs.est.0c05437

Munson, G. P., Lam, D. L., Outten, F. W., and O'Halloran, V. T. (2000). Identification of a copper-responsive two-component system on the chromosome of *Escherichia coli* K-12. *J. Bacteriol.* 182, 5864–5871. doi: 10.1128/JB.182.20.5864-5871.2000

NEA/IAEA (1999). "Environmental activities in uranium mining and milling," in *Nuclear Development*, ed. OECD (Vienna: IAEA).

Newsome, L., Morris, K., and Lloyd, J. R. (2014). The biogeochemistry and bioremediation of uranium and other priority radionuclides. *Chem. Geol.* 363, 164–184. doi: 10.1016/j.chemgeo.2013.10.034

Newsome, L., Morris, K., and Lloyd, J. R. (2015). Uranium biominerals precipitated by an environmental isolate of serratia under anaerobic conditions. *PLoS One* 10:e0132392. doi: 10.1371/journal.pone.0132392

Nies, D. H. (1992). CzcR and CzcD, gene products affecting regulation of resistance to cobalt, zinc, and cadmium (czc system) in *Alcaligenes eutrophus*. *J. Bacteriol.* 174, 8102–8110. doi: 10.1128/jb.174.24.8102-8110.1992

Nies, D. H. (2003). Efflux-mediated heavy metal resistance in prokaryotes. *FEMS Microbiol. Rev.* 27, 313–339. doi: 10.1016/S0168-6445(03)00048-2

Nilgiriwala, K. S., Alahari, A., Rao, A. S., and Apte, S. K. (2008). Cloning and overexpression of alkaline phosphatase PhoK from *Sphingomonas* sp. strain BSAR-1 for bioprecipitation of uranium from alkaline solutions. *Appl. Environ. Microbiol.* 74, 5516–5523. doi: 10.1128/AEM.00107-08

Nolan, J., and Weber, K. A. (2015). Natural Uranium contamination in Major U.S. Aquifers linked to nitrate. *Environ. Sci. Technol. Lett.* 2, 215–220. doi: 10.1021/acs.estlett.5b00174

Nongkhlaw, M., and Joshi, S. R. (2019). Molecular insight into the expression of metal transporter genes in *Chryseobacterium* sp. PMSZPI isolated from uranium deposit. *PLoS One* 14:e0216995. doi: 10.1371/journal.pone.0216995

Nucifora, G., Chu, L., Misra, T. K., and Silver, S. (1989). Cadmium resistance from *Staphylococcus aureus* plasmid pI258 *cadA* gene results from a cadmium-efflux ATPase. *Proc. Natl. Acad. Sci. U.S.A.* 86, 3544–3548. doi: 10.1073/pnas.86.10.3544

Oh, B. C., Choi, W. C., Park, S., Kim, Y. O., and Oh, T. K. (2004). Biochemical properties and substrate specificities of alkaline and histidine acid phytases. *Appl. Microbiol. Biotechnol.* 63, 362–372. doi: 10.1007/s00253-003-1345-0

Orellana, R., Hixson, K. K., Murphy, S., Mester, T., Sharma, M. L., Lipton, M. S., et al. (2014). Proteome of *Geobacter sulfurreducens* in the presence of U(VI). *Microbiology (United Kingdom)* 160, 2607–2617. doi: 10.1099/mic.0.081398-0

Orellana, R., Leavitt, J. J., Comolli, L. R., Csencsits, R., Janot, N., Flanagan, K. A., et al. (2013). U(VI) reduction by diverse outer surface c-type cytochromes of *Geobacter sulfurreducens*. *Appl. Environ. Microbiol.* 79, 6369–6374. doi: 10.1128/AEM.02551-13

Pablo, D. J., Casas, I., Giménez, J., Molera, M., Rovira, M., Duro, L., et al. (1999). The oxidative dissolution mechanism of uranium dioxide. I. The effect of temperature in hydrogen carbonate medium. *Geochimica Cosmochimica Acta* 63, 3097–3103. doi: 10.1016/S0016-7037(99)00237-9

Park, D. M., Overton, K. W., and Jiao, Y. (2019). The UzcRS two-component system in *Caulobacter crescentus* integrates regulatory input from diverse auxiliary regulators. *Mol. Microbiol.* 111, 678–699. doi: 10.1111/mmi.14180

Park, D. M., Overton, K. W., Liou, M. J., and Jiao, Y. (2017). Identification of a U/Zn/Cu responsive global regulatory two-component system in *Caulobacter crescentus*. *Mol. Microbiol.* 104, 46–64. doi: 10.1111/mmi.13615

Park, D. M., and Taffet, M. J. (2019). Combinatorial sensor design in *Caulobacter crescentus* for selective environmental uranium detection. *ACS Synthetic Biol.* 8, 807–817. doi: 10.1021/acssynbio.8b00484

Pattanapipitpaisal, P., Mabbett, A. N., Finlay, J. A., Beswick, A. J., Paterson-Beedle, M., Essa, A., et al. (2002). Reduction of Cr(VI) and bioaccumulation of chromium by gram positive and gram negative microorganisms not previously exposed to Cr-stress. *Environ. Technol.* 23, 731–745. doi: 10.1080/09593332308618367

Payne, R. B., Casalot, L., Rivere, T., Terry, J. H., Larsen, L., Giles, B. J., et al. (2004). Interaction between uranium and the cytochrome c3 of *Desulfovibrio desulfuricans* strain G20. *Arch. Microbiol.* 181, 398–406. doi: 10.1007/s00203-004-0671-7

Payne, R. B., Gentry, D. M., Rapp-Giles, B. J., Casalot, L., and Wall, J. D. (2002). Uranium reduction by *Desulfovibrio desulfuricans* strain G20 and a cytochrome c3 mutant. *Appl. Environ. Microbiol.* 68, 3129–3132. doi: 10.1128/AEM.68.6.3129-3132.2002

Pinel-Cabello, M., Jroundi, F., López-Fernández, M., Geffers, R., Jarek, M., Jauregui, R., et al. (2021). Multisystem combined uranium resistance mechanisms and bioremediation potential of *Stenotrophomonas bentonitica* BII-R7: transcriptomics and microscopic study. *J. Hazardous Mater.* 403:123858. doi: 10.1016/j.jhazmat.2020.123858

Pollmann, K., Raff, J., Merroun, M., Fahmy, K., and Selenska-Pobell, S. (2006). Metal binding by bacteria from uranium mining waste piles and its technological applications. *Biotechnol. Adv.* 24, 58–68. doi: 10.1016/j.biotechadv.2005.06.002

Pollmann, K., Raff, J., Schnorpfeil, M., Radeva, G., and Selenska-Pobell, S. (2005). Novel surface layer protein genes in Bacillus sphaericus associated with unusual insertion elements. *Microbiology* 151, 2961–2973. doi: 10.1099/mic.0.28201-0

Powers, L. G., Mills, H. J., Palumbo, V. A., Zhang, C., Delaney, K., and Sobecky, P. A. (2002). Introduction of a plasmid-encoded *phoA* gene for constitutive overproduction of alkaline phosphatase in three subsurface *Pseudomonas* isolates. *FEMS Microbiol. Ecol.* 41, 115–123. doi: 10.1016/S0168-6496(02)00263-5

Prăvălie, R. (2014). Nuclear weapons tests and environmental consequences: a global perspective. *Ambio* 43, 729–744. doi: 10.1007/s13280-014-0491-1

Raff, J., Merroun, M., Roßberg, A., Hennig, C., and Selenska-Pobell, S. (2002). *EXAFS Study of Uranium (VI) Complexes Formed by Native and Recrystallized S-layers of the Bacillus sphaericus StrainsJG-A12andNCTC9602*, Vol. 36. Annual Report 2002 Institute of Radiochemistry. Warszawa.

Rajkumar, M., Ae, N., Prasad, M. N. V., and Freitas, H. (2010). Potential of siderophore-producing bacteria for improving heavy metal phytoextraction. *Trends Biotechnol.* 28, 142–149. doi: 10.1016/j.tibtech.2009.12.002

Randall, C. P., Gupta, A., Jackson, N., Busse, D., and O'Neill, A. J. (2014). Silver resistance in Gram-negative bacteria: a dissection of endogenous and exogenous mechanisms. *J. Antimicrob. Chemother.* 70, 1037–1046. doi: 10.1093/jac/dku523

Rashmi, V., ShylajaNaciyar, M., Rajalakshmi, R., D'Souza, S. F., Prabaharan, D., and Uma, L. (2013). Siderophore mediated uranium sequestration by marine cyanobacterium *Synechococcus elongatus* BDU 130911. *Bioresour. Technol.* 130, 204–210. doi: 10.1016/j.biortech.2012.12.016

Reitz, T., Rossberg, A., Barkleit, A., Selenska-Pobell, S., and Merroun, M. L. (2014). Decrease of U(VI) immobilization capability of the facultative anaerobic strain *Paenibacillus* sp. JG-TB8 under anoxic conditions due to strongly reduced phosphatase activity. *PLoS One* 9:e102447. doi: 10.1371/journal.pone.0102447

Renninger, N., Knopp, R., Nitsche, H., Clark, D. S., and Keasling, J. D. (2004). Uranyl precipitation by *Pseudomonas aeruginosa* via controlled polyphosphate metabolism. *Appl. Environ. Microbiol.* 70, 7404–7412. doi: 10.1128/AEM.70.12.7404-7412.2004

Rogiers, T. (2022). *Uranium Resistance Mechanisms in Cupriavidus Metallidurans: From Environmental Relevance to Potential Applications*. Ph.D. thesis. Ghent: Ghent University.

Rogiers, T., Claesen, J., Gompel, A. V., Vanhoudt, N., Mysara, M., Williamson, A., et al. (2021a). Soil microbial community structure and functionality changes in response to long-term metal and radionuclide pollution. *Environ. Microbiol.* 23, 1670–1683. doi: 10.1111/1462-2920.15394

Rogiers, T., Merroun, M. L., Williamson, A., Leys, N., Houdt, R. V., Boon, N., et al. (2021b). *Cupriavidus metallidurans* NA4 actively forms polyhydroxybutyrate-associated uranium-phosphate precipitates. *J. Hazard Mater.* 421:126737. doi: 10.1016/j.jhazmat.2021.126737

Romanchuk, A. Y., Vlasova, I. E., and Kalmykov, S. N. (2020). Speciation of uranium and plutonium from nuclear legacy sites to the environment: a mini review. *Front. Chem.* 8:630. doi: 10.3389/fchem.2020.00630

Ruttenberg, K. C. (2014). "10.13 - The global phosphorus cycle," in *Treatise on Geochemistry*, 2nd Edn, eds H. D. Holland and K. K. Turekian (Oxford: Elsevier), 499–558. doi: 10.1016/b978-0-08-095975-7.00813-5

Salbu, B., Burkitbaev, M., Strømman, G., Shishkov, I., Kayukov, P., Uralbekov, B., et al. (2013). Environmental impact assessment of radionuclides and trace elements at the Kurday U mining site, Kazakhstan. *J. Environ. Radioact.* 123, 14–27. doi: 10.1016/j.jenvrad.2012.05.001

Salome, K. R., Beazley, M. J., Webb, S. M., Sobecky, P. A., and Taillefert, M. (2017). Biomineralization of U(VI) phosphate promoted by microbially-mediated phytate hydrolysis in contaminated soils. *Geochimica Cosmochimica Acta* 197, 27–42. doi: 10.1016/j.gca.2016.10.008

Sanchez-Castro, I., Amador-Garcia, A., Moreno-Romero, C., Lopez-Fernandez, M., Phrommavanh, V., Nos, J., et al. (2017). Screening of bacterial strains isolated from uranium mill tailings porewaters for bioremediation purposes. *J. Environ. Radioact.* 166(Pt 1), 130–141. doi: 10.1016/j.jenvrad.2016.03.016

Santos, E. A., and Ladeira, A. C. Q. (2011). Recovery of uranium from mine waste by leaching with carbonate-based reagents. *Environ. Sci. Technol.* 45, 3591–3597. doi: 10.1021/es2002056

Scherer, J., and Nies, D. H. (2009). CzcP is a novel efflux system contributing to transition metal resistance in *Cupriavidus metallidurans* CH34. *Mol. Microbiol.* 73, 601–621. doi: 10.1111/j.1365-2958.2009.06792.x

Seidel, D. C. (1981). Extracting uranium from its ores. *IAEA Bull.* 23, 24–26.

Shelobolina, E. S., Coppi, V. M., Korenevsky, A. A., Didonato, L. N., Sullivan, S. A., Konishi, H., et al. (2007). Importance of c-Type cytochromes for U(VI) reduction by *Geobacter sulfurreducens*. *BMC Microbiol.* 7:16. doi: 10.1186/1471-2180-7-16

Shelobolina, E. S., Vrionis, H. A., Findlay, R. H., and Lovley, D. R. (2008). *Geobacter uraniireducens* sp. nov., isolated from subsurface sediment undergoing uranium bioremediation. *Int. J. Syst. Evol. Microbiol.* 58, 1075–1078. doi: 10.1099/ijs.0.65377-0

Silver, S., and Phung, L. T. (2005). A bacterial view of the periodic table: genes and proteins for toxic inorganic ions. *J. Industrial Microbiol. Biotechnol.* 32, 587–605. doi: 10.1007/s10295-005-0019-6

Sitte, J., Loffler, S., Burkhardt, E. M., Goldfarb, K. C., Buchel, G., Hazen, T. C., et al. (2015). Metals other than uranium affected microbial community composition in a historical uranium-mining site. *Environ. Sci. Pollut. Res. Int.* 22, 19326–19341. doi: 10.1007/s11356-015-4791-1

Smil, V. (2000). Phosphorus in the environment: natural flows and human interferences. *Annu. Rev. Energy Environ.* 25, 53–88. doi: 10.1146/annurev.energy.25.1.53

Snavely, M. D., Florer, J. B., Miller, C. G., and Maguire, M. E. (1989). Magnesium transport in *Salmonella typhimurium*: $^{28}Mg^{2+}$ transport by the CorA, MgtA, and MgtB systems. *J. Bacteriol.* 171, 4761–4766. doi: 10.1128/jb.171.9.4761-4766.1989

Strømman, G., Rosseland, B. O., Skipperud, L., Burkitbaev, L. M., Uralbekov, B., Heier, L. S., et al. (2013). Uranium activity ratio in water and fish from pit lakes in Kurday, Kazakhstan and Taboshar, Tajikistan. *J. Environ. Radioact.* 123, 71–81. doi: 10.1016/j.jenvrad.2012.05.014

Sutcliffe, B., Chariton, A. A., Harford, A. J., Hose, G. C., Greenfield, P., Elbourne, L. D. H., et al. (2017). Effects of uranium concentration on microbial community structure and functional potential. *Environ. Microbiol.* 19, 3323–3341. doi: 10.1111/1462-2920.13839

Suzuki, Y., and Banfield, J. F. (2004). Resistance to, and accumulation of, uranium by bacteria from a uranium-contaminated site. *Geomicrobiol. J.* 21, 113–121. doi: 10.1080/01490450490266361

Suzuki, Y., Kitatsuji, Y., Ohnuki, T., and Tsujimura, S. (2010). Flavin mononucleotide mediated electron pathway for microbial U(VI) reduction. *Phys. Chem. Chem. Phys.* 12, 10081–10087. doi: 10.1039/c0cp00339e

Taira, Y., Hayashida, N., Tsuchiya, R., Yamaguchi, H., Takahashi, J., Kazlovsky, A., et al. (2013). Vertical distribution and estimated doses from artificial radionuclides in soil samples around the chernobyl nuclear power plant and the semipalatinsk nuclear testing site. *PLoS One* 8:e57524. doi: 10.1371/journal.pone.0057524

Tapia-Rodríguez, A., Luna-Velasco, A., Field, J. A., and Sierra-Alvarez, R. (2012). Toxicity of uranium to microbial communities in anaerobic biofilms. *Water Air Soil Pollut.* 223, 3859–3868. doi: 10.1007/s11270-012-1154-0

Theodorakopoulos, N., Chapon, V., Coppin, F., Floriani, M., Vercouter, T., Sergeant, C., et al. (2015). Use of combined microscopic and spectroscopic techniques to reveal interactions between uranium and *Microbacterium* sp. A9, a strain isolated from the Chernobyl exclusion zone. *J. Hazardous Mater.* 285, 285–293. doi: 10.1016/j.jhazmat.2014.12.018

Tompson, A. F. B., Bruton, C. J., Pawloski, G. A., Smith, D. K., Bourcier, W. L., Shumaker, D. E., et al. (2002). On the evaluation of groundwater contamination from underground nuclear tests. *Environ. Geol.* 42, 235–247. doi: 10.1007/s00254-001-0493-8

Tu, H., Yuan, G., Zhao, C., Liu, J., Li, F., Yang, J., et al. (2019). U-phosphate biomineralization induced by *Bacillus* sp. dw-2 in the presence of organic acids. *Nuclear Eng. Technol.* 51, 1322–1332. doi: 10.1016/j.net.2019.03.002

Turner, B. L. (2006). "Inositol phosphates: linking agriculture and the environment," in *Inositol Phosphates in Soil: Amounts, Forms and Significance of the Phosphorylated Inositol Stereoisomers*, eds B. L. Turner, A. E. Richardson, and E. J. Mullaney (Wallingford: CABI), 186–206. doi: 10.1079/9781845931520.0186

Tykva, R. (2004). Sources of environmental radionuclides and recent results in analyses of bioaccumulation. A review. *Nukleonika* 49(Suppl. 1), 3–7.

UNSCEAR (1988). *Report to The General Assembly (Annex D— Exposures from Chernobyl Accident)*. New York, NY: UNSCEAR.

UNSCEAR (2008). *Sources and Effects of Ionizing Radiation Volume I: Sources*. New York, NY: UNSCEAR.

Van der Stricht, S., and Janssens, A. (2010). *Radioactive Effluents from Nuclear Power Stations and Nuclear Fuel Reprocessing Plants in the European Union, 2004-08*. Brussels: European Commission.

Weber, K. A., Achenbach, L. A., and Coates, J. D. (2006). Microorganisms pumping iron: anaerobic microbial iron oxidation and reduction. *Nat. Rev. Microbiol.* 4, 752–764. doi: 10.1038/nrmicro1490

Wellman, D. M., Icenhower, J. P., and Owen, A. T. (2006). Comparative analysis of soluble phosphate amendments for the remediation of heavy metal contaminants: effect on sediment hydraulic conductivity. *Environ. Chem.* 3, 219–224. doi: 10.1071/EN05023

Whicker, F. W. (1983). Radionuclide transport processes in terrestrial ecosystems. *Radiation Res.* 94, 135–150. doi: 10.2307/3575869

Williamson, A. J., Morris, K., Law, G. T. W., Rizoulis, A., Charnock, J. M., and Lloyd, J. R. (2014). Microbial reduction of U(VI) under alkaline conditions: implications for radioactive waste geodisposal. *Environ. Sci. Technol.* 48, 13549–13556. doi: 10.1021/es5017125

Wufuer, R., Wei, Y., Lin, Q., Wang, H., Song, W., Liu, W., et al. (2017). Uranium bioreduction and biomineralization. *Adv. Appl. Microbiol.* 101, 137–168. doi: 10.1016/bs.aambs.2017.01.003

Wyss, M., Brugger, R., Kronenberger, A., Re, R., Fimbel, R., Oesterhelt, G., et al. (1999). Biochemical characterization of fungal phytases (*myo*-Inositol Hexakisphosphate Phosphohydrolases): catalytic properties. *Appl. Environ. Microbiol.* 65, 367–373. doi: 10.1128/AEM.65.2.367-373.1999

Xu, R., Wu, K., Han, H., Ling, Z., Chen, Z., Liu, P., et al. (2018). Co-expression of YieF and PhoN in Deinococcus radiodurans R1 improves uranium bioprecipitation by reducing chromium interference. *Chemosphere* 211, 1156–1165. doi: 10.1016/j.chemosphere.2018.08.061

Yamasaki, S., Tanaka, K., Kozai, N., and Ohnuki, T. (2017). Effect of flavin compounds on uranium(VI) reduction- kinetic study using electrochemical methods with UV-vis spectroscopy. *Appl. Geochem.* 78, 279–286. doi: 10.1016/j.apgeochem.2017.01.014

Yi, Z.-J., Tan, K.-X., Tan, A.-L., Yu, Z.-X., and Wang, S.-Q. (2007). Influence of environmental factors on reductive bioprecipitation of uranium by sulfate reducing bacteria. *Int. Biodeterioration Biodegradation* 60, 258–266. doi: 10.1016/j.ibiod.2007.04.001

You, W., Peng, W., Tian, Z., and Zheng, M. (2021). Uranium bioremediation with U(VI)-reducing bacteria. *Sci. Total Environ.* 798:149107. doi: 10.1016/j.scitotenv.2021.149107

Yun, J., Malvankar, N. S., Ueki, T., and Lovley, D. R. (2016). Functional environmental proteomics: elucidating the role of a *c*-type cytochrome abundant during uranium bioremediation. *ISME Journal* 10, 310–320. doi: 10.1038/ismej.2015.113

Yung, M. C., and Jiao, Y. (2014). Biomineralization of uranium by PhoY phosphatase activity aids cell survival in *Caulobacter crescentus*. *Appl. Environ. Microbiol.* 80, 4795–4804. doi: 10.1128/AEM.01050-14

Yung, M. C., Ma, J., Salemi, M. R., Phinney, B. S., Bowman, G. R., and Jiao, Y. (2014). Shotgun proteomic analysis unveils survival and detoxification strategies by *Caulobacter crescentus* during exposure to uranium, chromium, and cadmium. *J. Proteome Res.* 13, 1833–1847. doi: 10.1021/pr400880s

Yung, M. C., Park, D. M., Overton, K. W., Blow, M. J., Hoover, C. A., Smit, J., et al. (2015). Transposon mutagenesis paired with deep sequencing of *Caulobacter crescentus* under Uranium stress reveals genes essential for detoxification and stress tolerance. *J. Bacteriol.* 197, 3160–3172. doi: 10.1128/jb.00382-15

Yun-Juan, C., Long, P. E., Geyer, R., Peacock, A. D., Resch, C. T., Sublette, K., et al. (2005). Microbial incorporation of 13C-labeled acetate at the field scale: detection of microbes responsible for reduction of U(VI). *Environ. Sci. Technol.* 39, 9039–9048. doi: 10.1021/es051218u

Zachara, J. M., Long, P. E., Bargar, J., Davis, J. A., Fox, P., Fredrickson, J. K., et al. (2013). Persistence of uranium groundwater plumes: contrasting mechanisms at two DOE sites in the groundwater-river interaction zone. *J. Contaminant Hydrol.* 147, 45–72. doi: 10.1016/j.jconhyd.2013.02.001

Zhang, K., Zhang, D., Wu, X., and Xue, Y. (2021). Continuous and efficient immobilization of heavy metals by phosphate-mineralized bacterial consortium. *J. Hazardous Mater.* 416:125800. doi: 10.1016/j.jhazmat.2021.125800

Zheng, L., Li, Y., Shang, W., Dong, X., Tang, Q., and Cheng, H. (2019). The inhibitory effect of cadmium and/or mercury on soil enzyme activity, basal respiration, and microbial community structure in coal mine–affected agricultural soil. *Ann. Microbiol.* 69, 849–859. doi: 10.1007/s13213-019-01478-3

Zheng, Z., Wan, J., Song, X., and Tokunaga, T. K. (2006). Sodium meta-autunite colloids: synthesis, characterization, and stability. *Colloids Surfaces A: Physicochem. Eng. Aspects* 274, 48–55. doi: 10.1016/j.colsurfa.2005.08.032

Conflict of Interest: The authors declare that the research was conducted in the absence of any commercial or financial relationships that could be construed as a potential conflict of interest.

Publisher's Note: All claims expressed in this article are solely those of the authors and do not necessarily represent those of their affiliated organizations, or those of the publisher, the editors and the reviewers. Any product that may be evaluated in this article, or claim that may be made by its manufacturer, is not guaranteed or endorsed by the publisher.

frontiers in Microbiology

ORIGINAL RESEARCH
published: 15 March 2022
doi: 10.3389/fmicb.2022.822541

Effect of Endosymbiotic Bacteria on Fungal Resistance Toward Heavy Metals

*Simone Lupini[1,2], Janire Peña-Bahamonde[1], Gregory Bonito[3] and Debora F. Rodrigues[1,2]**

[1] Department of Civil and Environmental Engineering, University of Houston, Houston, TX, United States, [2] Department of Biology and Biochemistry, University of Houston, Houston, TX, United States, [3] Department of Plant, Soil, and Microbial Sciences, College of Agriculture and Natural Resources, Michigan State University, East Lansing, MI, United States

Most studies on metal removal or tolerance by fungi or bacteria focus on single isolates, without taking into consideration that some fungi in nature may be colonized by endobacteria. To address this knowledge gap, we investigated the tolerance and removal of diverse metals with two fungal species: *Linnemannia elongata* containing Burkholderia-related endobacteria and *Benniella erionia* containing Mollicute-related endobacteria. Isogenic lines of both species were generated with antibiotic treatments to remove their respective endobacteria. Experiments involved comparing the isogenic lines and wild type fungi in relation to the minimum inhibitory concentration for the metals, the fungal ability to remove these different metals *via* atomic adsorption spectroscopy, and the interaction of the metals with specific functional groups of the fungi and fungi-bacteria to determine the role of the bacteria *via* attenuated total reflection fourier transformed infrared (ATR-FTIR). Finally, we determined the influence of different metal concentrations, associated with moderate and high fungal growth inhibition, on the presence of the endobacteria inside the fungal mycelium *via* quantitative real-time PCR. Results showed that the presence of the endosymbiont increased *B. erionia* resistance to Mn^{2+} and increased the removal of Fe^{2+} compared to isogenic lines. The absence of the endosymbiont in *L. elongata* increased the fungal resistance toward Fe^{2+} and improved the removal of Fe^{2+}. Furthermore, when the bacterial endosymbiont was present in *L. elongata*, a decrease in the fungal resistance to Ca^{2+}, Fe^{2+}, and $Cr^{6+}$was noticeable. In the ATR-FTIR analysis, we determined that C-H and C = O were the major functional groups affected by the presence of Cu^{2+}, Mn^{2+}, and Fe^{2+} for *L. elongata* and in the presence of Cu^{2+} and Ca^{2+} for *B. eronia*. It is noteworthy that the highest concentration of Pb^{2+} led to the loss of endobacteria in both *L. elongata* and *B. eronia*, while the other metals generally increased the concentration of endosymbionts inside the fungal mycelium. From these results, we concluded that bacterial endosymbionts of fungi can play a fundamental role in fungal resistance to metals. This study provides the first step toward a greater understanding of symbiotic interactions between bacteria and fungi in relation to metal tolerance and remediation.

Keywords: endobacteria, heavy metals, fungi, metal removal, adsorption, host resistance

OPEN ACCESS

Edited by:
Jean-Yves Matroule, University of Namur, Belgium

Reviewed by:
Ravindra Soni, Indira Gandhi Krishi Vishva Vidyalaya, India
Peter Pristas, Pavol Jozef Šafárik University in Košice, Slovakia

***Correspondence:**
Debora F. Rodrigues
dfrigirodrigues@uh.edu

Specialty section:
This article was submitted to Antimicrobials, Resistance and Chemotherapy, a section of the journal Frontiers in Microbiology

Received: *25 November 2021*
Accepted: *26 January 2022*
Published: *15 March 2022*

Citation:
Lupini S, Peña-Bahamonde J, Bonito G and Rodrigues DF (2022) Effect of Endosymbiotic Bacteria on Fungal Resistance Toward Heavy Metals. Front. Microbiol. 13:822541. doi: 10.3389/fmicb.2022.822541

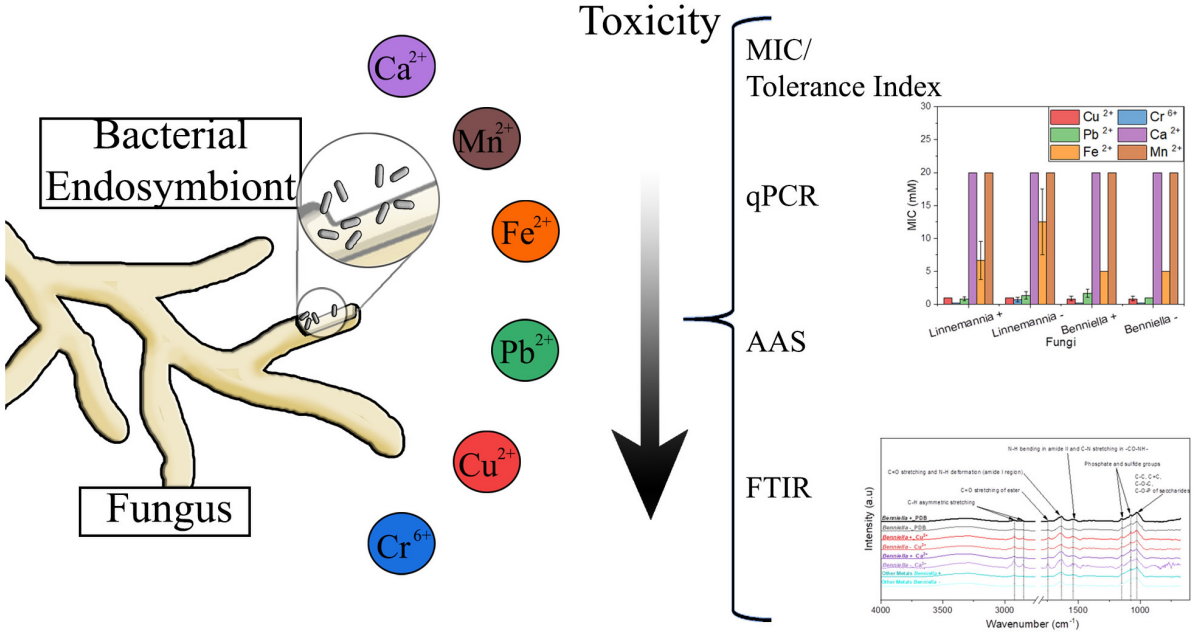

GRAPHICAL ABSTRACT |

INTRODUCTION

Fungi and bacteria are known for their resistance toward metals (Zafar et al., 2007; Aguirre and Culotta, 2012; Lisher and Giedroc, 2013; Kumar and Dwivedi, 2021). However, most studies regarding the ability of fungi and bacteria to resist and remove metals from the environment are still focused on pure cultures and do not take into consideration the impacts of symbionts. In the environment, fungi and bacteria take part in a wide range of biogeochemical cycles, with consequent formation of intimate relationships. In fact, in recent years fungi have also been characterized for their capacity to harbor bacteria in their microbiome, both inside and outside (Robinson et al., 2021). However, little is known about the functionalities of these relationships, or how the external environment impacts these interactions.

Metals are important elements in the environment that can directly impact the survival of diverse organisms. Metals can be classified as non-essential or essential based on their positive or negative interactions with living organisms (Gadd, 1994) and their long-term effects on biological systems (Rainbow, 1995; Appenroth, 2010). Essential and non-essential metals at different concentrations can be found depending on the location, e.g., proximity to mining (Navarro et al., 2008), agriculture (Vaalgamaa and Conley, 2008), or other industries (Cortes et al., 2003). Furthermore, metals do not biodegrade; they can only be extracted or transformed (ul Hassan et al., 2017).

Non-essential metals, commonly called heavy metals, are among the environmental contaminants most affecting the balance of ecosystems (Smejkalova et al., 2003). Unlike essential metals (including Ca^{2+}, Mn^{2+}, and Fe^{2+}), which take part in various biological processes as micronutrients and co-factors of enzymes (Tebo et al., 2005), heavy metals (including Cu^{2+}, Cr^{6+}, and Pb^{2+}) are characterized by a broad range of cytotoxicity. In general, all metals, essential or not, can be toxic to microorganisms depending on their concentration. For this reason, different biological systems have evolved different mechanisms to mitigate their toxicity (Temple and Le Roux, 1964; Bitton and Freihofer, 1977; Cervantes and Gutierrez-Corona, 1994). Fungi tend to be the most resistant to metals compared to bacteria and other microorganisms (Mejias Carpio et al., 2018). The innate ability of fungi to resist heavy metals has been studied and is considered a sustainable approach for remediation processes (Johnson and Choudhary, 2016; Cecchi et al., 2019; Qin et al., 2020; Gunjal, 2021; Kumar and Dwivedi, 2021; Neogi et al., 2021; Tomer et al., 2021). However, the possibility that fungal resistance to metals may be influenced by the presence of endobacteria has not been considered previously.

This study aimed to determine whether the presence of intracellular bacterial symbionts of fungi influence the response of their host to different types and concentrations of metals. For this purpose, two fungi, *Linnemannia elongata* (NVP64) and *Benniella erionia* (GBAus27b), previously determined to harbor endobacteria, were selected as candidates in this present study (Uehling et al., 2017; Desirò et al., 2018). Isogenic lines of both species were generated with antibiotic treatments to remove their respective endobacteria and serve as control treatments. We tested the innate metal tolerance and capacity to remove the metals by these two fungal species with and without endosymbionts through Minimum Inhibitory Concentration, Tolerance Index, Atomic Absorption Spectroscopy (AAS), and Fourier Infrared Spectroscopy. This study offers a broader view

of the impact of impending metal contamination on the tolerance and survival of fungi, the role of bacterial endosymbionts in fungi on the metal resistance, and the part that diverse types of metals may exert, as environmental stressors, to fungal microbiomes.

MATERIALS AND METHODS

Media and Solution Preparations

Separate metal stock solutions containing 0.1 M of Cu^{2+}, Cr^{6+}, Ca^{2+}, Pb^{2+}, Mn^{2+}, and Fe^{2+} were prepared by dissolving the following salts in distilled water (DIW) followed by filter sterilization [0.2 μm Polyethersulfone membrane filter (Thermo Fisher Scientific)], e.g., copper sulfate ($CuSO_4$), chromium oxide (CrO_3), lead nitrate [Pb $(NO_3)_2$], calcium chloride ($CaCl_2$), manganese sulfate ($MnSO_4$), and iron sulfate ($FeSO_4$). The media used to grow the fungi were Potato Dextrose Broth (PDB) and Potato Dextrose Agar (PDA); both were purchased from Sigma-Aldrich. The pH of the media was adjusted to pH ≈5.6 with either 1 M NaOH or 1 M HCl (Hitchins et al., 1998), and autoclaved at 121°C for 15 min. The sterilized media was then supplemented with the sterile metal stock solution to obtain the appropriate final concentration of the metal (Zhang et al., 2020). All the reagents were purchased from Sigma Aldrich and were used as received.

Fungal Isolates and Growing Conditions

The fungal cultures used in this study were *Linnemannia elongata* (NVP64), previously characterized for the presence of *Burkholderia*-related endosymbiont (BRE) (Uehling et al., 2017), and *Benniella erionia* (GBAus27b), characterized for Mollicute-related endosymbiont (MRE) (Desirò et al., 2018). Both species were investigated with cultures containing their respective endobacteria, denoted as wild-type, and isogenic lines that were "cured" from their endobacteria through antibiotic treatments (Uehling et al., 2017).

The successful removal of MRE and BRE with antibiotics to generate endobacterial-free isogenic fungal lines was confirmed by TEM and qPCR in previous publications (Uehling et al., 2017; Desirò et al., 2018). We used these same isogenic lines. All isolates are maintained on antibiotic-free media, and have been for years, and experiments were carried out in antibiotic-free media. Thus, it is unlikely that antibiotic treatments impacted the presented data. For simplification, in the present study, we will refer to *L. elongata* NVP64 as *Linnemannia* and *B. erionia* GBAus27b as *Benniella*. Also, the wild-type (WT) strains will be named as either *Linnemannia*+ or *Benniella* +, and control isogenic fungi lacking endobacteria will be abbreviated as *Linnemannia* – or *Benniella* –. The isogenic lines were also tested for the presence/absence of the bacteria signal prior to the start of the experiments in the present study (data not shown).

Minimum Inhibitory Concentration and Tolerance Index

The tolerance of chosen fungal isolates toward heavy metals was tested by assessing the minimum inhibitory concentration (MIC) (Zafar et al., 2007). Different amounts of each metal stock (Cu^{2+}, Cr^{6+}, Ca^{2+}, Pb^{2+}, Mn^{2+}, and Fe^{2+}) were added to the PDA culture media, to obtain the desired final concentrations in the range of 0.1–20 mM. Each plate was prepared in triplicate and subsequently divided into four sections of equal size. For each of the four isolates, an 8-mm agar plug with mycelium was taken from a 7-day-old pre-grown PDA plate and placed in the center of test plates under sterile conditions. The plates were incubated at 25°C between 2 and 5 days, based on the fungal growth. Three different plates were used for each concentration of the different metals. The diameter of each fungus was monitored for 5 days. The MIC value for each metal was defined as the minimum metal concentration at which no fungal growth was observed on all the replicates (Zafar et al., 2007). As a control, the growth of the fungi was also monitored in the presence of PDA media, not supplemented with metals.

Once determined the MIC value for each metal, the fungi were grown in PDA plates amended with the metal at a final concentration corresponding to a visible inhibition (slightly lower than the MIC value) (0.5 mM Cu^{2+}, 0.1 mM Cr^{6+}, 20 mM Ca^{2+}, 0.5 mM Pb^{2+}, 20 mM Mn^{2+}, and 2 mM Fe^{2+}) and incubated at 25°C. After 3 days of growth, the diameter of the fungal mycelium was measured to determine the tolerance index (TI). The TI can be defined as the ratio between the diameter of the fungus in the presence of metals and its control without any metals (Joo and Hussein, 2012).

Endobacteria Quantification: DNA Extraction and Quantitative Polymerase Chain Reaction

The quantification of endobacteria was determined *via* quantitative polymerase chain reaction (qPCR) after the exposure to two different metal concentrations, e.g., visible inhibition and non-visible inhibition (Uehling et al., 2017; Desirò et al., 2018). In the present study, visible inhibition was defined as the concentration, below the MIC value, at which the growth of the fungus was still possible. Non-visible inhibition was defined as an intermediate concentration of metals between MIC and the absence of metal, characterized by a negligible inhibition of the fungal growth compared to the control. These conditions have been chosen to determine if, at different degrees of fungal growth inhibition by the metals, there were changes in the endobacteria concentration. To investigate that, 8-mm agar plugs containing 7-day-old fungal mycelium were added to flasks containing 100 ml of PDB media supplemented or not with metals (Cu^{2+}: 0.5 and 0.01 mM; Cr^{6+}:0.1 and 0.05 mM; Ca^{2+}: 20 and 10 mM; Pb^{2+}:0.5 and 0.01 mM; Fe^{2+}: 2 and 1 mM; and Mn^{2+}: 20 and 10 mM). The flasks were kept for 5 days at 25°C at constant shaking. Then, the biomass was separated from the supernatant and weighted, and 100 mg of grown biomass was added in a tube. The extraction was carried using the Zymo extraction kit (Zymo Quick-DNA Fungal/Bacterial Kit, D6005). The extracted DNA was checked for quality control with a microplate reader (Take3, BioTek Instruments, Winooski, VT,

United States) to evaluate the DNA concentration and degree of purity (260/280 nm ratio).

The PCR mix was prepared following the protocol for the PowerUp SYBR Green Master Mix (Applied Biosystems) (Mix, 2011). The primers used for this study were E8-F and E533-R (Nguyen et al., 2017). The quantification of the bacteria in the fungal isolates was performed on a StepOnePlus (Applied Biosystems) qPCR machine using the following protocol: enzyme activation at 95°C for 10 min, followed by 40 cycles of denaturing at 95°C for 15 s, and annealing at 60°C for 1 min. The melting curve was also monitored to determine non-specific amplification. The endobacterial quantification was estimated by comparing the C_t value with the standard curve obtained from serial dilutions of *E. coli* K12 genomic DNA (R^2 = 0.9948, Supporting information **Supplementary Figures 1, 2**) as previously described (Lee et al., 2008). The gene copy was normalized by nanograms of DNA and grams of biomass.

Quantification of Metal Removal *via* Flame Atomic Adsorption Spectroscopy

To investigate the metal removal, 8-mm agar plugs containing the fungal mycelium were transferred to flasks containing 100 ml of PDB media supplemented with the metals, e.g., 0.5 mM Cu^{2+}, 0.1 mM Cr^{6+}, 20 mM Ca^{2+}, 0.5 mM Pb^{2+}, 20 mM Mn^{2+}, and 2 mM Fe^{2+}. Positive and negative controls for this experiment were also evaluated and included sterile metal-free medium, sterile metal-added medium, and fungus grown in absence of metal. The flasks were kept for 5 days at 25°C at constant shaking at 125 rpm. The supernatant and biomass were separated by filtration using a 0.45 μm PES (Polyethersulfone) membrane filter (Thermo Scientific), and then the supernatant was transferred to a clean sterile tube for further analysis. The quantification of metal biosorption by the different fungi was evaluated using flame atomic absorption spectroscopy (AAS) (AAnalyst 200, Perkin Elmer) with Cu^{2+}, Cr^{6+}, Ca^{2+}, Pb^{2+}, Mn^{2+}, and Fe^{2+} lamps from Perkin Elmer. To determine if the removal was due to metabolic processes, the adsorption of the metals to the mycelium was also performed using dead fungal biomass. For the dead fungal biomass assay, the fungi were grown for 5 days in liquid culture and subsequently autoclaved for 30 min at 121°C and 103 kPa. The same weight of mycelium obtained in the previous experiment was introduced as dead biomass to reduce the variability between the two experiments. Then, the culture obtained was incubated for 1 day at 25°C in the presence and absence of metals (0.5 mM Cu^{2+}, 0.1 mM Cr^{6+}, 20 mM Ca^{2+}, 0.5 mM Pb^{2+}, 20 mM Mn^{2+}, and 2 mM Fe^{2+}). After that, the supernatant obtained from the liquid culture was filtered using 0.2 μm PES (Polyethersulfone) syringe filters (Thermo Scientific), diluted based on the range of optimal concentrations for the lamps (0.03–2 ppm for Cu^{2+}, 0.1–5 ppm for Cr^{6+}, 0.1–5 ppm for Ca^{2+}, 0.2–10 ppm for Pb^{2+}, 0.2–7 ppm for Mn^{2+}, and 0.01–3 ppm for Fe^{2+}). The solutions relative to each experiment were amended with HNO_3 to obtain a 2% final concentration of the acid before being analyzed. A seven-point standard curve was prepared for each of the elements analyzed. For Cu^{2+}, we used seven different concentrations in the range 0.5–15 ppm, for Cr^{6+} from 0.5 to 10 ppm, for Pb^{2+} from 0.02 to 30 ppm, for Ca^{2+} from 0.5 to 10 ppm, for Fe^{2+} from 0.5 to 20 ppm, and for Mn^{2+} from 0.5 to 20 ppm. Then, the absorbance of each of the different metals was interpolated in the calibration curve to determine the residual metal concentrations in the solution.

Each experiment was conducted in triplicates, and the obtained mean for each condition was compared to the respective control metal-containing media to determine the percentage of removal. A Student's *t*-test was also performed to determine if the means of the values were statistically significant.

Morphological Analysis of the Functional Groups With Fourier Transformed Infrared Spectroscopy

The effect of the biosorption of the different metals toward the physiochemical properties of the fungi was evaluated *via* Fourier Infrared Spectroscopy (FTIR) Digilab FTS 7000 equipped with an HgCdTe detector analysis and combined with Attenuated Total Reflection (ATR). For the analysis, the biomass obtained after the incubation (5 days at 25°C at constant shaking) of flasks containing 100 ml of PDB media supplemented with metals (0.5 mM Cu^{2+}, 0.1 mM Cr^{6+}, 20 mM Ca^{2+}, 0.5 mM Pb^{2+}, 20 mM Mn^{2+}, and 2 mM Fe^{2+}) with 8-mm agar plugs of the fungal mycelium grown for 7 days on a plate was separated by filtration using a 0.45-μm PES (Polyethersulfone) membrane filter (Thermo Fisher Scientific) from the supernatant. A control was also prepared by inoculating the media without any metals. Approximately, 0.5 g of biomass obtained from the liquid culture was collected, transferred to a petri dish, and dried at room temperature under the biohood until completely dry. The dry mycelium was transferred using tweezers with the mycelium facing down and scanned in the medium range (4,000–670 cm^{-1}) with a 4 cm^{-1} resolution. The data from the ATR-FTIR was processed using the R package Chemospec (Lucas, 2006; Hanson, 2014).

Statistical and Data Analysis

All the experiments reported were carried out in triplicate. The averages and standard deviations of triplicate measurements were reported for all the experiments. Statistical analysis was carried out using Excel (Microsoft Corporation, Redmond, WA, United States), R studio, and Origin (OriginLab Corporation, Northampton, MA, United States).

The ATR-FTIR spectra were normalized based on the most intense peak (1,030 cm^{-1}) and loaded in R-Studio. Using the R-package ChemoSpec (Hanson, 2014), the region with no peaks was removed (1,900–2,600 cm^{-1}) using the command "removeFreq" to reduce the noise. After the removal of the regions with no interest, the hcaSpectra command was used to obtain the Euclidean distance between the samples and plot the Principal Component Analysis (PCA) and Hierarchical Cluster Analysis (HCA) results (Varmuza and Filzmoser, 2016).

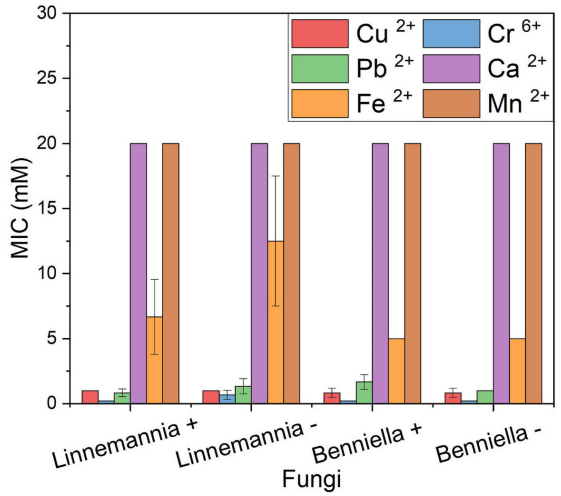

FIGURE 1 | MIC of heavy metals of the WT strains (+) and cured (–) fungi *Benniella* - and *Linnemannia* -. The fungi were grown in PDA plates supplemented with different metal concentrations (range, 0.1–20 mM). The growth at 25°C was monitored for up to 5 days to determine the minimum concentration of the metal that completely inhibited the fungal growth. Statistically significant differences between WT strains (+) and cured (–) were evaluated using the Student's *t*-test. No statistically significant difference was found between the different isogenic fungi.

RESULTS

Determination of Minimum Inhibitory Concentration

The resistance against six different metal ions of the two fungi, *L. elongata* (*Linnemannia*) and *B. erionia* (*Benniella*) is reported as MICs in **Figure 1**. In the presence of concentrations as high as 5 mM for Cu^{2+}, Cr^{6+}, and Pb^{2+}, both fungi displayed a complete inhibition, while for Fe^{2+}, the maximum MIC concentration was 10 mM. The presence of Ca^{2+} and Mn^{2+} in the media did not inhibit the fungal growth, even at concentrations as high as 20 mM. From the comparison of the MIC between cured and the wild type, the absence of the endobacteria seemed to have promoted the resistance of *L. elongata* toward Pb^{2+}, Cr^{6+}, and Fe^{2+} while an inverted trend was observed for the fungus *B. erionia*. Clearly, the presence of endobacteria had different effects on different fungi.

Tolerance Index

The tolerance index, calculated as the ratio between the radial growth of the treated fungus to their respective control, was determined based on the concentrations obtained through the MIC assays, as shown in **Figure 2**. The percentage reduction of the tolerance index was calculated based on the control without metal. In the presence of Cu^{2+}, the fungus *Benniella* exhibited a decrease in tolerance of approximately 40% with no statistically significant difference between *Benniella*+ and *Benniella* –. The occurrence of the endobacteria for the fungus *L. elongata* was beneficial regarding the presence of Cu^{2+} in the media. Compared to the control, *L. elongata* – had a reduction in the tolerance index of 45%, while *Linnemannia*+ had 35%. When exposed to Cr^{6+} the fungus *Benniella* showed a reduction of the tolerance index of approximately 25%, for both *Benniella* – and *Benniella*+, with no statistical significance between the fungi with or without endobacteria. For the *Linnemannia* fungus, in the presence of Cr^{6+}, a reduction of approximately 15% with no statistically significant difference was observed for both *Linnemannia* + and *Linnemannia* -. The presence of Pb^{2+} displayed a greater inhibitory effect in the *Benniella* fungi with a reduction of the tolerance index of 15–37% for *Benniella* + and *Benniella* -, respectively. Opposite results were noticed for the fungus *Linnemannia* in the presence of lead, where the tolerance index of *Linnemannia*+ decreased by 42% while *Linnemannia* – 17%. In the presence of Ca^{2+}, both *Benniella* and *Linnemannia* performed better than their control media without this metal supplement, with an average increase tolerance index of 12%. Fe^{2+} led to a tolerance index reduction of about 60% for both *Benniella* – and *Benniella*+, with no statistical significance between the two. For *Linnemannia,* the presence of Fe^{2+} in the media reduced the tolerance index by 54% for *Linnemannia*+ and by 29% for *Linnemannia* –. Furthermore, both *Benniella* - and *Benniella*+ were affected by the presence of Mn^{2+}, with a respective tolerance reduction of 11 and 34%, while the growth of *Linnemannia* was improved by about 35%. The comparison between *Benniella*+ and *Benniella* – showed that the presence of the endobacteria improved the tolerance of the fungus toward the metals and, particularly, toward Pb^{2+} and Mn^{2+}. For *Linnemannia*+ and *Linnemannia* –, the presence of the endobacteria enhanced the fungal resistance only in the presence of Cu^{2+}, but not for the other metals.

Metal Removal Quantification by Flame Atomic Absorption Spectroscopy

The metal removal by the fungal biomass was investigated as shown in **Figures 3**, **4**. The figures represent the residual metal concentrations in the solution for each metal evaluated. In relation to the toxic metals, we observed different removal patterns for the different fungi. In the presence of Cu^{2+}, the *Benniella* – exhibited almost three times more metal removal than *Benniella*+ (3.6% for *Benniella* – and 10% for *Benniella*+), while the dead fungi were able to adsorb 9 and 13% of Cu^{2+}, respectively. *Linnemannia* also exhibited the ability to remove Cu^{2+}, approximately 20% for both *Linnemannia*+ and *Linnemannia* –, while the dead mycelium removed roughly 9% with no statistical significance between cured and non-cured strains. The fungus *Benniella* displayed no removal for Cr^{6+}, while the dead mycelium, for both *Benniella*+ and *Benniella* –, removed less than 10%. A similar trend was also observed for the fungus *Linnemannia* in the presence of Cr^{6+}.

Regarding essential metals, we also observed different behaviors in relation to metal removal for the different fungi investigated. When the fungi were inoculated with Ca^{2+}, the results showed that *Benniella* - removed approximately two times more compared to *Benniella*+ (4% for *Benniella*+, 8% for *Benniella* –, 3% for dead *Benniella*+, 9% dead *Benniella* –). The highest removal for the fungus *Linnemannia* coincided with

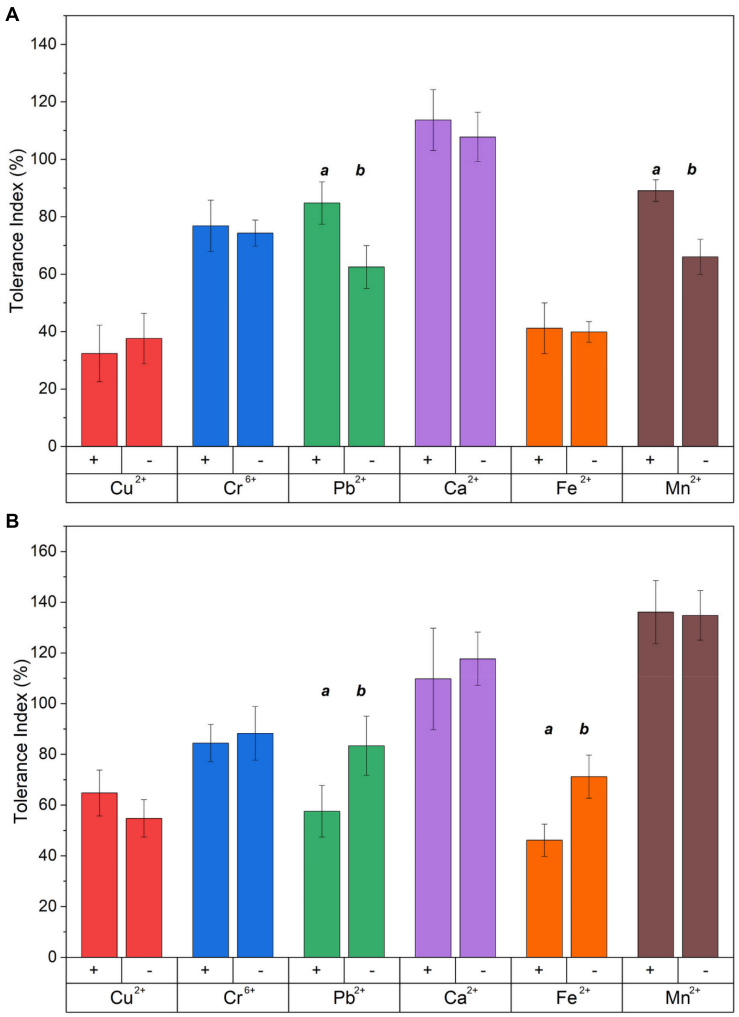

FIGURE 2 | Tolerance index of **(A)** *Benniella* and **(B)** *Linnemannia* in the presence of different metals. The fungi were grown in PDA plates supplemented with different metals (0.5 mM Cu^{2+}, 1 mM Cr^{6+}, 20 mM Ca^{2+}, 0.5 mM Pb^{2+}, 20 mM Mn^{2+}, and 2 mM Fe^{2+}). The diameter of the fungal mycelium after 3 days was compared to the control (PDA) without metal. Statistically significant differences between WT strains (+) and cured (–) fungi were evaluated using the Student's *t*-test. The significance among the samples was assessed using the Student's *t*-test and reported as alphabet letters. Same letters were attributed for *p*-values > 0.05, while different letters were attributed to *p*-values < 0.05. The lack of letters means that the results were not statistically significant.

the dead mycelium, with a percentage removal of over 11%. Furthermore, the living *Linnemannia* + removed only 7% of the Ca^{2+}, while *Linnemannia* - had no difference compared to the control. In the presence of Fe^{2+}, no removal was observed for *Benniella* –. On the other hand, for *Benniella* +, this fungus adsorbed 6% when dead, while the removal for both *Benniella* – and *Benniella* + was over 15%. *Linnemannia in* the presence of Fe^{2+}, showed an inverted trend, compared to *Benniella*. Around 5% more removal was observed when *Linnemannia* - was used, compared to *Linnemannia*+. In the presence of Mn^{2+}, the supernatant of both *Linnemannia* and *Benniella*, dead and alive, was characterized by having a higher concentration compared to the control, probably due to the release of the manganese from the biomass to the supernatant.

From the comparison between *Benniella*+ and *Benniella* –, the absence of the endobacteria did not appear to affect the overall capacity of the fungus to remove the metals, apart from Fe^{2+}, where the presence of the endobacteria enhanced the removal of the metals. A different trend was seen from the comparison of *Linnemannia*+ and *Linnemannia* –, where the presence of the endobacteria did not improve the removal of the metals, except for Ca^{2+}. The effect of the inactivation of the fungi was associated with an overall improved metal removal, especially evident in the presence of Pb^{2+} for both *Benniella* and *Linnemannia*.

Effect on the Abundance of Bacterial Endosymbionts Presence on the Fungal Host Exposure to Metals

The effect of different concentrations of metals on the endobacteria presence in the mycelium was evaluated by comparing the relative quantity of the bacterial 16S rRNA gene

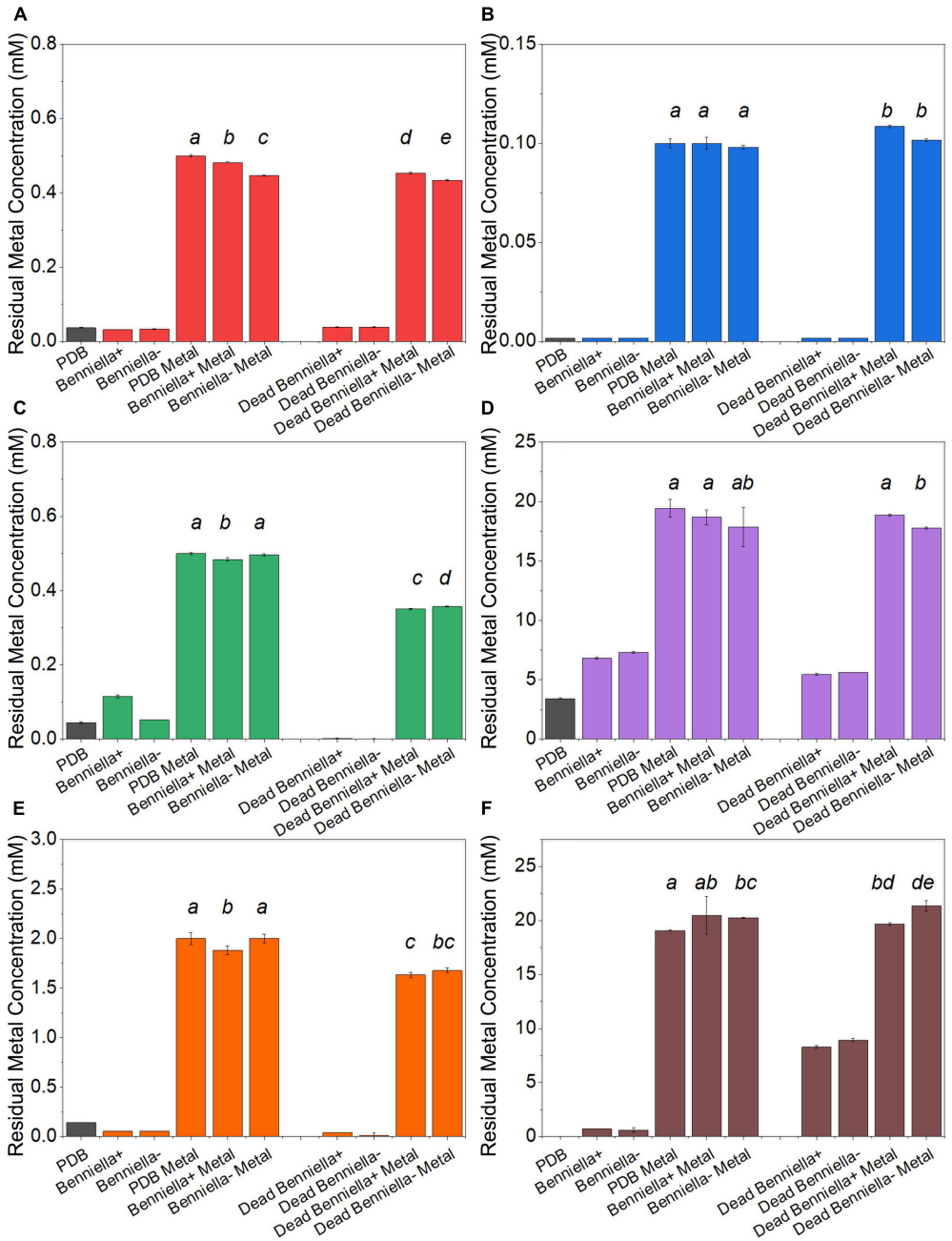

FIGURE 3 | Residual metal concentration by dead and live *Benniella* + and *Benniella* - in the presence of different metals: **(A)** Cu^{2+}, **(B)** Cr^{6+}, **(C)** Pb^{2+}, **(D)** Ca^{2+}, **(E)** Fe^{2+}, and **(F)** Mn^{2+}. The living fungi were grown on PDB supplemented with different metal concentrations (0.5 mM Cu^{2+}, 1 mM Cr^{6+}, 20 mM Ca^{2+}, 0.5 mM Pb^{2+}, 20 mM Mn^{2+}, and 2 mM Fe^{2+}) and incubated for 5 days at 25°C under constant shaking. The dead fungus was added after sterilization and incubated for 1 day at 25°C under constant shaking. Controls for this experiment included metal-free medium, metal-added medium, and fungus grown in the absence of metal. The significance among the samples was assessed using the Student's *t*-test and reported as alphabet letters. Same letters were attributed for *p*-values > 0.05, while different letters were attributed to *p*-values < 0.05. No letters mean that they were not statistically significant at all. Following the qPCR analysis, it emerged that in presence of Pb^{2+} at 0.5 mM, the presence of the endobacterium was no longer detectable inside the host at the end of the experiment.

at the visible inhibition in the MIC, non-visible inhibition, and the media without the metal, as control (**Figure 5**). For *Benniella*, the presence of essential metals, *i.e.*, Ca^{2+}, Fe^{2+}, and Mn^{2+}, led to a higher relative abundance of the 16S rRNA gene compared to the control at both visible and non-visible inhibitions. The only exception was for Fe^{2+}, in which the highest relative abundance of the 16S rRNA gene coincided (**Figure 5A**) with the highest metal concentration. Different endobacterial abundance

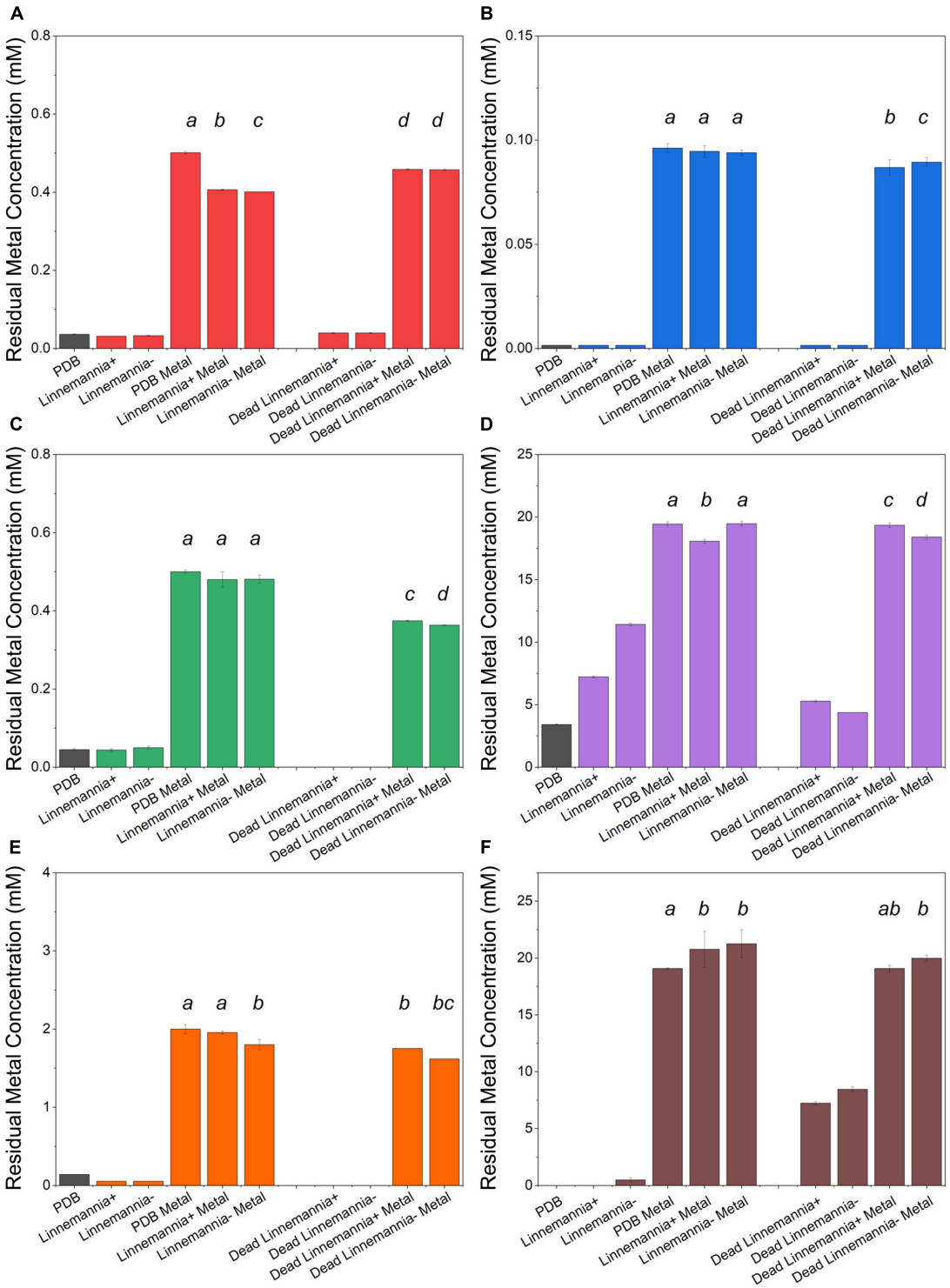

FIGURE 4 | Residual metal concentration by dead and live *Linnemannia* + and *Linnemannia* - in the presence of different metals: **(A)** Cu^{2+}, **(B)** Cr^{6+}, **(C)** Pb^{2+}, **(D)** Ca^{2+}, **(E)** Fe^{2+}, and **(F)** Mn^{2+}. The living fungi were grown on PDB supplemented with different metal concentrations (0.5 mM Cu^{2+}, 1 mM Cr^{6+}, 20 mM Ca^{2+}, 0.5 mM Pb^{2+}, 20 mM Mn^{2+}, and 2 mM Fe^{2+}) and incubated for 5 days at 25°C under constant shaking. The dead fungus was added after sterilization and incubated in the same conditions as the samples. Controls for this experiment included metal-free medium, metal-added medium, and fungus grown in the absence of metal. The significance among the samples was assessed using the Student's *t*-test and reported as alphabet letters. Same letters were attributed for *p*-values > 0.05, while different letters were attributed to *p*-values < 0.05. No letters mean that they were not statistically significant at all. Following the qPCR analysis, it emerged that in presence of Pb^{2+} at 0.5 mM, the presence of the endobacterium was no longer detectable inside the host.

was observed for *Linnemannia* (**Figure 5B**), where only in the presence of Cu^{2+}, Cr^{6+}, and Mn^{2+}, the bacterial load was higher compared to the control at both visible and non-visible inhibitions. We also noticed that the presence of Cu^{2+}, Cr^{6+}, and Pb^{2+} at a lower metal concentration in the media coincided with a higher relative abundance of endobacteria. Interestingly, for both *Benniella* and *Linnemannia*, we did not detect any bacterial amplification at the highest concentration of Pb^{2+}(0.5 mM).

Interactions of the Metals With the Surface Functional Groups (Attenuated Total Reflection-Fourier Transformed Infrared) of the Fungi

The characterization of the interactions of different metals with the functional groups present on the fungal mycelium was conducted *via* ATR-FTIR analysis. The comparisons of the spectra for *Benniella* and *Linnemannia* are presented in **Figures 6**, **7**, respectively (complete ATR-FTIR spectra of *Benniella* and *Linnemannia*, **Supplementary Figures 3, 4**, Relative peak intensities, **Supplementary Table 1**). Both fungi, *Benniella* and *Linnemannia*, showed spectra containing the main functional groups related to proteins and lipids. The spectra showed a broad band in the range 3,000–3,550 cm^{-1}, which correspond to the hydroxyl and amino groups (Rao, 1963) present in proteins (Park et al., 2005; Bombalska et al., 2011), followed by two distinct peaks at 2,924 and 2,853 cm^{-1} relative to the asymmetric and symmetric stretching vibration of the -CH present in the lipids (Solomons, 2016). Furthermore, the spectra showed the presence of peaks related to the protein at 1,743, 1,643.6, and 1,546 cm^{-1}, associated with the *C* = O stretching, protein amide I, and protein amide II (Kaushik et al., 2010).

The changes observed in the ATR-FTIR for the different fungi were attributed depending on whether they were cured from the bacteria or were exposed to different metals. The ATR-FTIR spectra of the fungus *Benniella* + in the presence of Cu^{2+}, Cr^{6+}, and Ca^{2+} showed an increased intensity in the C-H stretching from the lipids (2,924 and 2,853 cm^{-1}), and the amide from the protein (1,742 cm^{-1}). For *Benniella* + in the presence of Pb^{2+} and Fe^{2+}, we observed a noticeably decrease in intensity of the peaks associated with the amide group of the protein (1,742, 1,637, and 1,544 cm^{-1}) and the C-H of the lipid (2,924 and 2,853 cm^{-1}). When the same fungus was grown in the presence of Mn^{2+}, a slight decrease in the symmetrical and asymmetrical stretching of PO^{2-} and P $(OH)_2$ at 1,150, 1,077, and 1,026 cm^{-1} was observed (Amann et al., 1990; Bombalska et al., 2011) compared to the control without the metal.

In the case of *Benniella* –, when it was in contact with Cu^{2+}, Cr^{6+}, and Ca^{2+}, an increase in the intensity of the C-H stretching from the lipids (2,924 and 2,853 cm^{-1}) and the amide from proteins (1,742 cm^{-1}) were observed. Especially, the increase in intensity was more notable in the presence of Ca^{2+}. However, from **Supplementary Table 1**, we can see that in the presence of Pb^{2+}, Mn^{2+}, and Fe^{2+}, there was a decrease in intensity of the C-H stretching from the lipids (2,924 and 2,853 cm^{-1}), and the amide from the protein (1,742 cm^{-1}). The comparison between

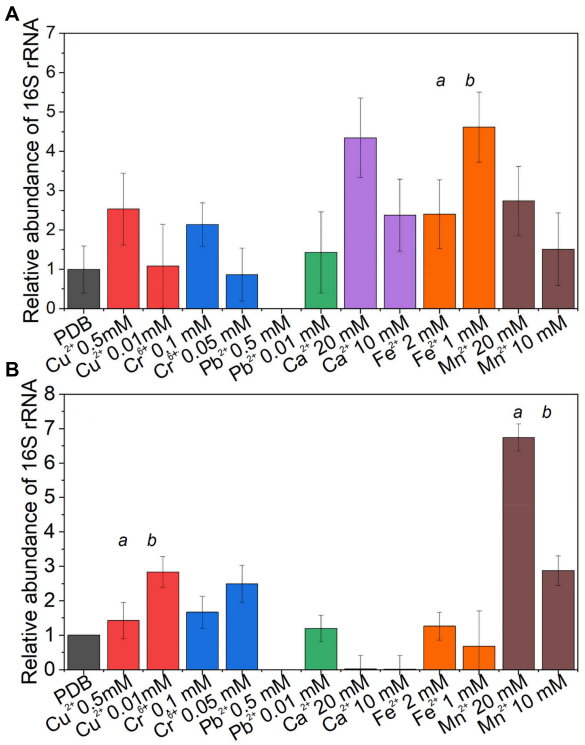

FIGURE 5 | Relative abundance of the bacterial 16S rRNA gene in the fungus **(A)** *Benniella* and **(B)** *Linnemannia* in response to metal presence. The fungi WT were grown in PDB supplemented with two metal concentrations, where visible and non-visible inhibition growth was observed. The fungi were incubated for 5 days at 25°C under constant shaking. An equal amount of mycelium was processed for DNA extraction and qPCR amplification. The significance among the samples was assessed using the Student's *t*-test and reported as alphabet letters. Same letters were attributed for *p*-values > 0.05, while different letters were attributed to *p*-values < 0.05. No letters mean that they were not statistically significant at all.

Benniella+ and *Benniella* – showed that the previously discussed peaks, *i.e.*, lipidic, protein, and phosphate functional groups are enhanced in the presence of endobacteria, indicating that the presence of endobacteria is playing an important role in the presence of those functional groups when the metals are present.

In the case of the fungus *Linnemannia*, the spectra of *Linnemannia*+ in the presence of Cr^{6+} showed a decreased intensity of the amide functional group of the protein (1,742 and 1,544 cm^{-1}) compared to the *Linnemannia* without the metal. In the presence of Ca^{2+}, an increase of the C-H stretching from the lipids was noticeable when compared to the control with no metal (2,924 and 2,853 cm^{-1}) followed by the amide peak of the protein (1,742 cm^{-1}). Furthermore, the amide group of the protein was slightly shifted from 1,747 to 1,743 cm^{-1} when *Linnemannia* + was incubated with Ca^{2+}. Moreover, in the presence of $Fe^{2+}$and Mn^{2+}, the lipidic peak also shifted to higher wavenumbers, from 2,924 to 2,980 cm^{-1}.

For *Linnemannia* –, a sharp increase in peaks associated with the C-H stretching from the lipids (2,924 and 2,853 cm^{-1}) and amide functional group from the proteins (1,742 cm^{-1}) was

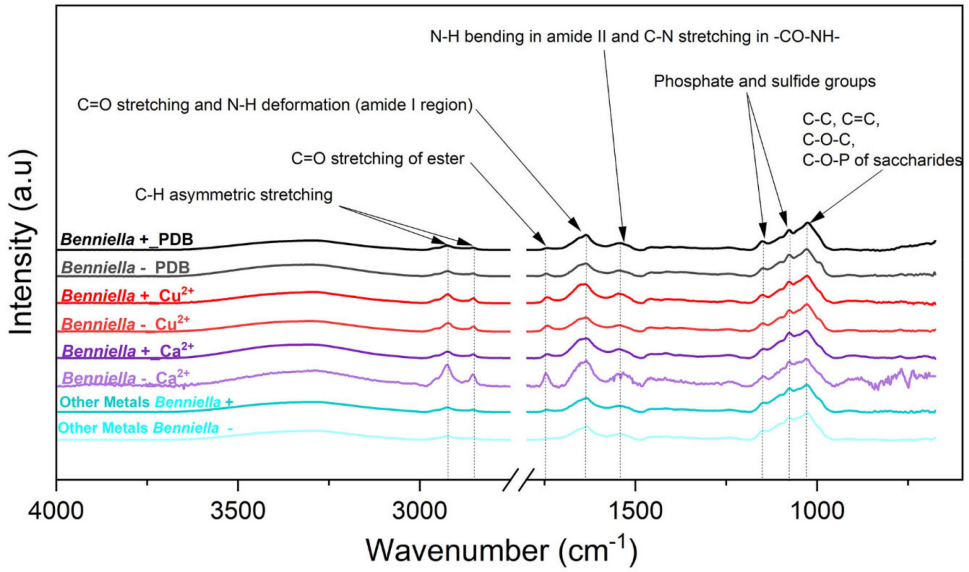

FIGURE 6 | ATR-FTIR spectra of *Benniella* + and *Benniella* - for Ca^{2+}, Cu^{2+}, and PDB media (control). The spectra of metals Cr^{6+}, Pb^{2+}, Fe^{2+}, and Mn^{2+} had identical peaks; hence, they were merged into "Other metals." The fungi were grown in PDB added with different metals (0.5 mM Cu^{2+}, 1 mM Cr^{6+}, 20 mM Ca^{2+}, 0.5 mM Pb^{2+}, 20 mM Mn^{2+}, and 2 mM Fe^{2+}) for 5 days at 25°C under constant shaking.

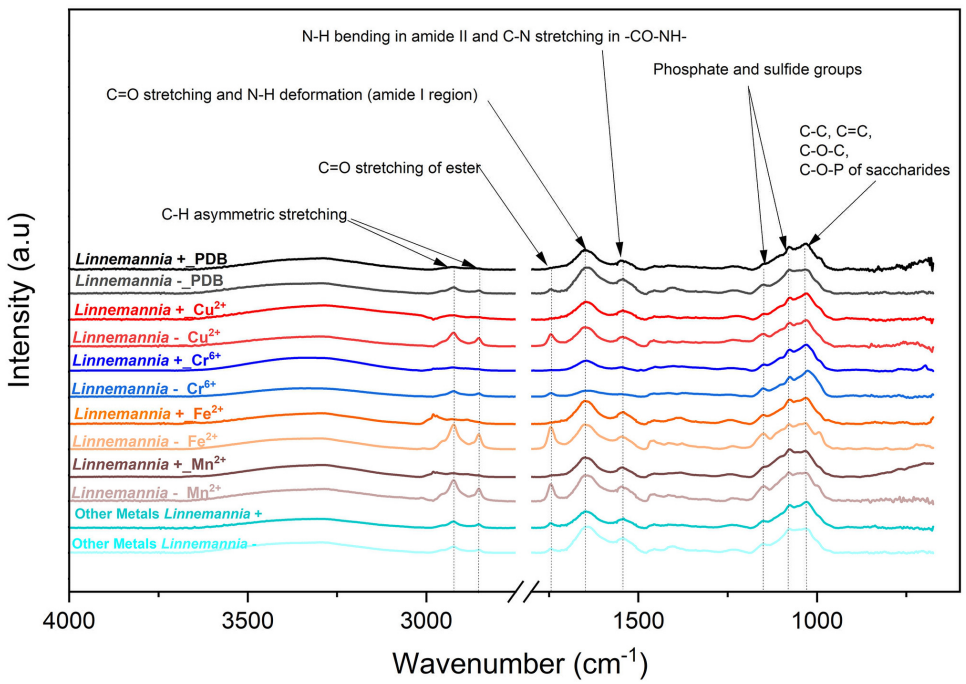

FIGURE 7 | ATR-FTIR spectra of *Linnemannia* + and *Linnemannia* - with PDB, Cu^{2+}, Cr^{6+}, Fe^{2+}, and Mn^{2+}. The spectra of metals $Pb^{2+}$and Ca^{2+}were identical; hence, they were merged into "Other Metals." The fungi were grown in PDB added with different metals (0.5 mM Cu^{2+}, 1 mM Cr^{6+}, 20 mM Ca^{2+}, 0.5 mM Pb^{2+}, 20 mM Mn^{2+}, and 2 mM Fe^{2+}) for 5 days at 25°C under constant shaking.

noticeable when the fungus was in the presence of Cu^{2+}, Fe^{2+}, and Mn^{2+}. However, in the presence of Cr^{6+}, a significant reduction in the functional groups was observed. Furthermore, in the presence of Ca^{2+}, the intensity of the peaks associated with the amide functional group of the protein (1,637 and 1,544 cm^{-1}) was reduced. Overall, the comparison between *Linnemannia* + and *Linnemannia* - showed that the presence of endobacteria led to stronger intensity and interactions of the

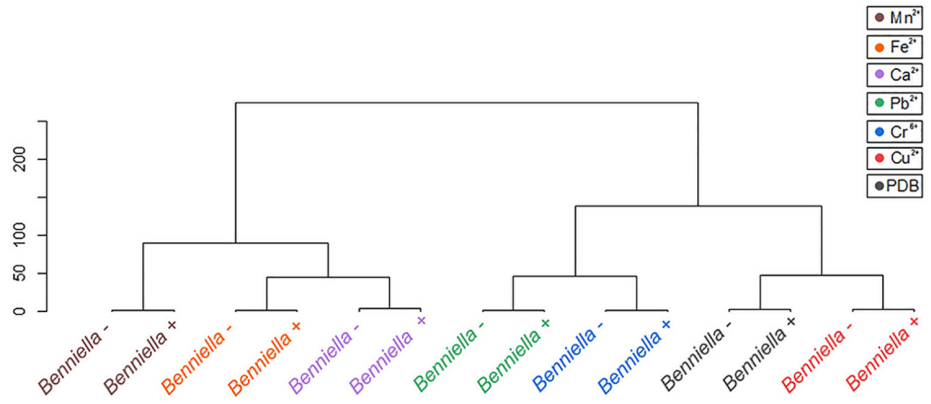

FIGURE 8 | Hierarchical cluster analysis of the ATR-FTIR spectra of the *Benniella* + and *Benniella* –. The Euclidean method was used to determine the distance between the different samples.

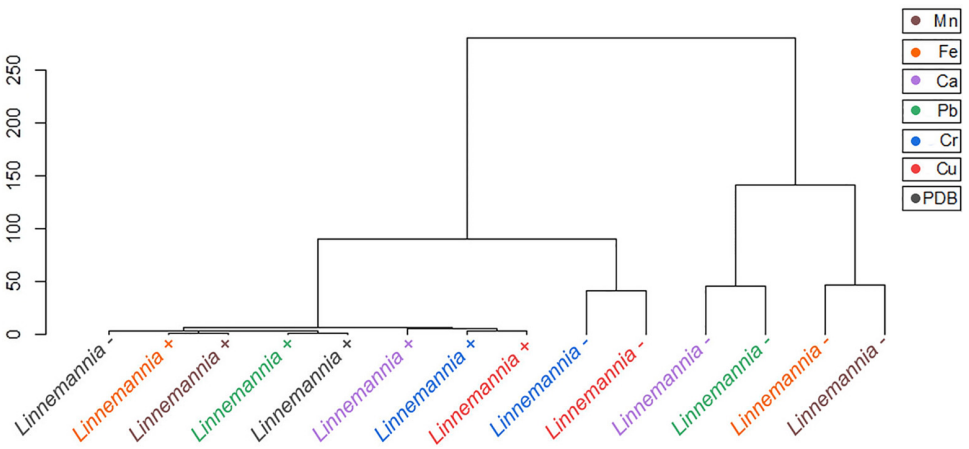

FIGURE 9 | Hierarchical cluster analysis of the ATR-FTIR spectra of the *Linnemannia* + and *Linnemannia* –. The Euclidean method was used to determine the distance between the different samples.

functional groups associated with the lipids and proteins with the metals, indicating again that the presence of endobacteria is playing an important role in the presence of lipids and proteins when the metals were present.

Statistical tools, such as HCA and PCA as shown in **Figures 8**, **9** and **Supplementary Figures 5, 6**, were used to assess the interaction between the different functional groups of the fungi and the metals evaluated. The analysis of the *Benniella*+ and *Benniella* – fungi in combination with all the metals evaluated i.e., Mn^{2+}, Fe^{2+}, Ca^{2+}, Cu^{2+}, Pb^{2+}, and Cr^{6+}, showed two different clusters (**Figure 8**). Those clusters, i.e., Mn^{2+}, Fe^{2+}, and Ca^{2+} (essential metals), and Cu^{2+}, Pb^{2+}, and Cr^{6+} (non-essential metals) indicated that the differences observed in the spectra are not related to the presence or absence of endobacteria, but to the type of metal. The type of metals seems to play an important role in the interaction strength between the functional groups and the metals. However, the HCA analysis for *Linnemannia* – and *Linnemannia*+ (shown in **Figure 9**) indicated that the presence or absence of endobacteria plays a major role in the interaction between the microorganism and the metals. The clusters are clearly based on the presence of endobacteria rather than on the type of metal.

DISCUSSION

The metals in diverse environments can be classified as essential (e.g., Ca^{2+}, Fe^{2+}, and Mn^{2+}) or non-essential (e.g., Cr^{6+}, Cu^{2+}, and Pb^{2+}) based on their interaction with living organisms (Gadd, 1994). Fungi and bacteria are both important in the biological cycles of metals; however, the effect that the fungal endobacteria can have on resistance and uptake of essential and non-essential metals by the fungal host has not yet been demonstrated.

This study was focused on determining the effects of endohyphal bacteria on the response of fungal hosts to essential and non-essential metals. The fungi *L. elongata* (NVP64) and *B. erionia* (GBAus27b) were selected as candidates

for this study for their capacity to harbor BRE and MRE endobacteria, respectively, and for their ability to be cured of their endosymbionts.

The results showed that the two fungal species have different susceptibilities toward certain metals, with Cr^{6+} presenting the highest toxicity toward both fungi, with MIC 0.2 mM for *Benniella* and 0.5 mM for *Linnemannia* – and 0.2 mM *Linnemannia*+, followed by Cu^{2+}, 1 mM for both *Benniella* and *Linnemannia*, and Pb^{2+}, 2 mM for *Benniella*+, 1 mM for *Benniella* –, 0.5 mM for *Linnemannia*+, and 1 mM for *Linnemannia* –. Regarding the susceptibility of both fungi, independently from the endobacterial presence, non-essential metals such as Cu^{2+}, Cr^{6+}, and Pb^{2+} had a greater inhibitory effect compared to the other three metals, Ca^{2+}, Fe^{2+}, and Mn^{2+}. For these non-essential metals, the level of inhibition followed this order: $Cr^{6+} > Cu^{2+} > Pb^{2+}$. This result validates the non-essentiality characteristics of Cr^{6+} and Pb^{2+} since these metals are known for their antimicrobial activities, and Cu^{2+}, which, although essential, is toxic at high concentrations (Lemire et al., 2013; Mejias Carpio et al., 2018).

Regarding the general performance toward different metals, we observed that the fungus *Linnemannia*, both cured and WT, had an overall higher metal removal capacity than *Benniella*. In fact, although the two fungi are closely related, the associated endosymbionts are phylogenetically distant. Both endosymbionts have a major effect on the metabolism and growth of the fungal host (Li et al., 2017; Uehling et al., 2017), especially in the presence of metals. This was particularly evident for Cu^{2+}, Fe^{2+}, and Mn^{2+}. This result is aligned with the results of the tolerance test, where the *Linnemannia* had a higher tolerance to these metals than *Benniella* (**Figure 2**). The relationship between the tolerance and the metal removal was further confirmed by linear correlation analysis (Pearson's R = 0.72) for the fungus *Linnemannia* (**Figure 10**).

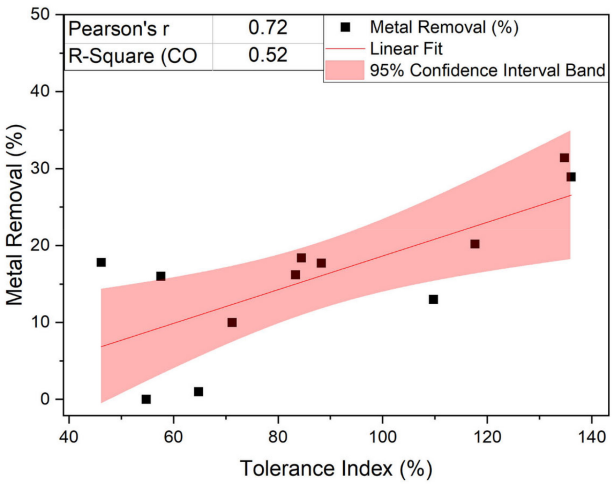

FIGURE 10 | Linear fit of the percentage of removal and metal tolerance of the fungus *Linnemannia*.

Endosymbionts Can Affect Differently Fungal Metal Resistance

In the present study, the fungal candidates have been chosen to gain a better understanding of the functionality of the fungal microbiomes in relation to metal tolerance and removal and also to determine the importance of inter-Kingdom cooperation in metal-stressed environments. This work also evaluates the role that endobacteria have on the innate resistance of the fungus for metals known for their toxicity (Cr^{6+}, Cu^{2+}, and Pb^{2+}) and metals, such as Ca^{2+}, Fe^{2+}, and Mn^{2+} which, although considered essential, can be potentially toxic at high concentrations.

To further gain an understanding of the increase in metal resistance due to the presence of endobacteria, we analyzed the data obtained from the MIC and tolerance index of the two fungi and compared it to the performance of the WT and the fungi cured from the bacteria. Our results show that the metal resistance is influenced by the type of endosymbiont, BRE *vs.* MRE, as well as the type of metals. In the case of the type of endosymbiont, for instance, the presence of the endobacteria in the fungus *Benniella* was clearly beneficial for the fungus with respect to metal tolerance, whether the metal was essential or not. The fungus *Linnemannia*, when cured from its endosymbiont, was more resistant to Fe^{2+}, while for the other metals no statistically significant difference was found. This result is surprising since *Burkholderia* species have been described to be resistant to different metals (Caballero-Mellado et al., 2007; Jiang et al., 2008; Schwager et al., 2012; Mullins et al., 2019). In fact, for *Linnemannia*, the presence of this group of bacteria does not appear to be beneficial to the fungi to improve the MIC or the tolerance index toward the presence of metals. This result could be linked to the fact that the maintenance of the endosymbiont leads to a metabolic cost to the host, previously reported to be around 30% (Uehling et al., 2017). Therefore, in the case of *Linnemannia*, the presence of the endobacteria and toxic concentrations of metals might have exacerbated the metabolic cost incurred to the fungus by the endosymbiont. Hence, we conclude that the type of endosymbiont in the fungus can have a direct effect on the tolerance of the fungi to metals.

In the case of the effects of types of metals, for non-essential metals (such as Cr^{6+}, Cu^{2+}, and Pb^{2+}), compared to essential metals (Ca^{2+}, Fe^{2+}, and Mn^{2+}), the former was responsible for greater fungal inhibition. The inhibitory effect of these metals was particularly evident when we considered Cu^{2+} and Cr^{6+}. For both *Linnemannia* and *Benniella* with or without endobacteria, for the concentrations tested, the presence of Cu^{2+} (0.5 mM) and Cr^{6+} (1 mM) did not affect the metal tolerance index. This demonstrates that the endosymbionts will not always benefit the host for all types of toxic metals. Hence the toxicity can be related to the type of metal, not necessarily to the presence or absence of the endosymbiont. On the other hand, when the metal is less toxic or beneficial (essential metal) for the microorganisms, the effect due to the presence of the bacteria will be more visible, increasing, in the case of *Benniella*, or lowering, in the case of *Linnemannia*, the tolerance toward the metals. For instance, for both *Linnemannia* and *Benniella* with

or without endobacteria, in the presence of Ca^{2+}, the growth increased compared to the control, *i.e.*, the fungi without the metal. This result might be explained by the fact that an increased concentration of calcium in the cytosol was associated with fungal growth through hyphal elongation (Juvvadi et al., 2011; Hu et al., 2014) and cell cycle progression (Nanthakumar et al., 1996; Miyakawa and Mizunuma, 2007). A similar result was also noticed for *Linnemannia* in the presence of Mn^{2+}, where both *Linnemannia* + and *Linnemannia* -, with no statistically significant difference between the two, had a noticeable increase in growth compared to the control without the metal. This can be explained by the fact that Mn^{2+} can be a limiting factor for the fungal metabolism (Manikan et al., 2014), and an increased concentration available for the fungus could have increased fungal growth.

Our results show that in the case of highly toxic metals, such as Cu^{2+} and Cr^{6+}, the influence on MIC and tolerance index due to the presence of the endobacterium was negligible. On the other hand, when the toxicity of the metal decreased, the contribution of the endobacterium toward the fungus resistance became more evident and therefore dependent on the type of interaction existing between the host and the symbiont.

The Effect of Endosymbiont on the Fungal Metal Biosorption Properties

Fungi and bacteria, in recent years, have been considered for their ability to remove metals as a sustainable alternative for metal remediation (Fan et al., 2014; Mejias Carpio et al., 2018). To verify whether the metal removal was attributable to adsorption or active metabolic processes, experiments were carried out on dead and live fungi. Fungi are in fact capable of uptake metal ions through transport channels (Ohsumi and Anraku, 1981; White and Gadd, 1987; Cohen et al., 2000), low-affinity permeases of divalent metal ions (Nelissen et al., 1997; Kosman, 2003), or non-specific metalloreductase (Kosman, 2020) and also of carrying out metabolic activities aimed at reducing the toxicity of the metals present, e.g., chelation or translocation of the metal (Ahmad et al., 2005). Unlike living mycelium, the dead biomass can only carry out adsorption on the surface of the mycelium.

In general, we have noticed that the presence of endobacteria, both for *Benniella* and *Linnemannia*, was not linked to greater removal of metals. Both dead *Benniella*+ and dead *Benniella* – removed high concentrations of Cu^{2+}, Cr^{6+}, Pb^{2+}, and Fe^{2+} compared to living mycelium, which suggests that adsorption can be happening. In the case of dead *Linnemannia* + and dead *Linnemannia* -, a greater removal of Cr^{6+}, Pb^{2+}, Ca^{2+}, and Fe^{2+} was observed compared to live biomass. These results demonstrate that the removal of non-essential metals (e.g., Cr^{6+}, Pb^{2+}) and essential metals (e.g., Ca^{2+}, and Fe^{2+}), for both *Linnemannia* and *Benniella*, can be largely attributed to adsorption (Lilly et al., 1992; Butter et al., 1998) and that the live fungi are actively putting in place mechanisms aimed at reducing the uptake of the metal. Furthermore, we also observed that the metal removal performed by the dead fungus was less affected by the presence or absence of bacteria when compared to the respective live fungus. This result might indicate that the bacteria, when present in the fungus, could also influence the metal uptake activity once the metal ions have entered the fungus.

In addition to the comparison between the metal removal performed by dead and live biomass, we determined whether the presence of endobacteria could affect metal removal in the live biomass. In general, we observed that the presence of endobacteria, both BRE and MRE, was not linked to higher removal of metals except for Fe^{2+} for the fungus *Benniella*+ and Ca^{2+} for the fungus *Linnemannia*+. These results could be because the endosymbionts, localized in the vicinity of lipid bodies, were responsible for a reduction in the number of these lipid-rich organelles compared to the cured fungus (Uehling et al., 2017; Desirò et al., 2018). A reduction in lipid bodies, which can be used as storage for potentially toxic compounds, such as heavy metals (Clark and Zeto, 2000; Fayeulle et al., 2014), could explain how the cured fungi led to a generally greater removal of metals.

Therefore, these results demonstrate that for non-metal resistant fungi, such as those selected in this study, the main method of metal removal is due to adsorption by the hypha. Additionally, the presence of endobacteria, which affect the composition of the lipid bodies associated with the fungus, may have reduced the metal uptake by the host.

Effect of Different Metals on the Abundance of Endosymbionts

Bacteria are known for their ability to resist and accumulate metals present in the external environment. Currently, there is still a vast knowledge gap regarding how this ability is maintained when the bacterium has established a symbiotic interaction within the fungal hypha. To shed light on this knowledge gap, different concentrations of essential and non-essential metals were tested in this study to determine their influence on the presence of endobacteria.

Our results show that, although not statistically significant, the abundance of BRE and MRE are characterized by two different trends. In the case of *Benniella*+, the relative abundance of the bacterium increased when the fungus was exposed to a higher concentration of the metal (Cu^{2+}, Cr^{6+}, Ca^{2+}, Mn^{2+}), while for *Linnemannia*+, an increase in the concentration of the metal coincided with a reduction in the abundance of the endobacteria (Cu^{2+}, Cr^{6+}, Pb^{2+}, Fe^{2+}, Mn^{2+}). This result could be linked to the fact that, as noticed by the tolerance index, in the case of *Benniella* +, the endobacteria contributes to facilitating the resistance of the host to different metals. Also, in the case of this fungus, for metals in which the presence of the endobacteria increased the tolerance index (Cr^{6+}, Ca^{2+}, and Mn^{2+}), we found a linear correlation between the metal removal ratio between *Benniella*+ and *Benniella* –, and the relative abundance of 16S rRNA gene (**Supplementary Figure 7**).

As for the fungus *Linnemannia*+, as observed from the MIC and tolerance index results, increasing concentration of the endobacteria did not coincide with an increase in the metal removal ratio in *Linnemannia*+ compared to *Linnemannia* –. This result could be explained by the fact that, because of the

stress ratio to which the fungus is subjected, this has led to exacerbating the energy deficit sustained for the maintenance of the bacterium (Wernegreen, 2012; Bastías et al., 2020). It is in fact suspected that in symbiotic relationships, there may be a modulation of the flow of nutrients from the host to the symbiont to consequently control the growth rate of the latter (González-Guerrero et al., 2016). Interestingly, for both fungi, we determined that the relative abundance of the bacteria in the presence of the metal was in general higher compared to the control. This result could be explained by the fact that the endobacteria is subjected only to a portion of metals that cross the fungal cell wall, leading to a change in the growth ratio between the host and symbiont.

The results show that depending on the type of host-symbiont system, the fungus can perform a potential modulation of the endobacteria and, in the case of *Benniella*+, there is a dependency between the abundance of the symbiont and metal removal.

Interactions of the Fungal and Bacterial-Fungal Functional Groups With Different Metals

The uptake of heavy metals by fungi may impact complex metabolic processes, which can cause various morphological modifications, including the reduction of growth, alteration of the structure of the mycelium (Baldrian, 2003), and the modification of the composition of the membrane (Howlett and Avery, 1997). These effects are caused by the powerful inhibitory action of heavy metals against enzymes, cell membranes, and organelles (Vallee and Ulmer, 1972), which can lead to oxidative stress (Stohs and Bagchi, 1995). Fungi are able, through the use of different methods (e.g., valence transformation, intra- and extracellular precipitation, uptake and translocation into lipid bodies, complexation with chelators, and low molecular weight peptides), to reduce the metal toxicity and improve tolerance (Tomsett, 1993; Clark and Zeto, 2000; Zafar et al., 2007; Fayeulle et al., 2014).

The variation in the functional groups associated with essential and non-essential metal treatments in the presence or not of endobacteria was determined by ATR-FTIR analysis. This analysis has allowed us to determine the possible structural modification that could be occurring in the two fungi studied, which can be associated to the presence of metals or the endobacteria. HCA was used as a tool to determine the distances between the samples spectra and determine possible clusters attributable to the presence/absence of endobacteria and the type of metal. In order to determine which single or multiple functional groups may have been influenced by the presence of the metal treatment and presence/absence of endobacteria, the different peaks were analyzed individually (**Figures 6**, **7** and **Supplementary Table 1**).

Based on the comparison of the spectra obtained from the controls and the metal-exposed fungi, we noticed that the difference between the individual functional groups of *Benniella*+ and *Benniella* – was mainly attributable to the type of metal. The results were also confirmed by HCA (**Figure 8**) where we could observe that the distance calculated between the samples shows how the different isogenic lines, *Benniella*+ and *Benniella* –, are strongly similar to each other while they differ based on the type of metal exposure. We also noticed that there were two separate clusters for *Benniella* splitting essential metals (Fe^{2+}, Ca^{2+}, and Mn^{2+}) from non-essential metals (Cu^{2+}, Cr^{6+}, Pb^{2+}). Demonstrating that the types of metals can play a more important role in the functional groups expressed in the fungi.

Regarding the effect induced by the treatment with metals, we can see that *Benniella* –, when compared to *Benniella*+ in the presence of Ca^{2+} and Cu^{2+}, triggered an increase in the intensity of the peaks related to the C-H asymmetric stretching (2,924 and 2,853 cm^{-1}) and carbonyl group (1,745 cm^{-1}) (**Figure 6**). Previous study has shown that the curation of the fungus from its endosymbiont could lead to an increase in the number of lipidic bodies compared to the WT fungus (Uehling et al., 2017). The increase of these functional groups could also be caused by oxidative stress on the cell membrane wall, as evidenced by the peak at 1,742 cm^{-1} related to the carbonyl group from the ester. This particular peak is typically generated after the peroxidation of fatty acids (Fuchs et al., 2011; Oleszko et al., 2015). The oxidation of lipids is known to increase in the presence of transition metals (Cu^{2+}, Cr^{6+}, Fe^{2+}, and Mn^{2+}) (Zschornig et al., 2004) and post-transitional metal (Adonaylo and Oteiza, 1999). Moreover in the presence of reactive oxygen species (ROS), it is hypothesized that these metals can also act as catalysts in the decomposition process of hydrogen peroxide (Fenton reaction) (Oteiza et al., 2004; Repetto et al., 2010). Additionally, in the presence of Fe^{2+} and Mn^{2+}, the *Benniella*+ fungus appears to have a reduction in the intensity of the same peaks, suggesting a lower susceptibility to these metals. This hypothesis is also sustained by the tolerance index (**Figure 2**) where, except for Fe^{2+}, it is evident that the *Benniella* + is less inhibited by the presence of these metals.

Linnemannia elongata, on the other hand, from the HCA (**Figure 9**) results, shows the importance of the presence of endobacteria rather than the type of metal, since two clusters were formed. One of the clusters contained the fungi with the presence of endobacteria and the other one was the cured fungi. The presence of endobacteria caused clear changes in the functional groups present on the surface of the fungus. From the ATR-FTIR data, it emerged that in the presence or not of the different metals, the fungus *Linnemannia* –, when compared to *Linnemannia*+, presented a marked increase in the peaks related to lipidic (2,924 and 2,853 cm^{-1}) and protein (1,742 and 1,544 cm^{-1}) regions. As previously described, the endobacteria elimination from the fungal host led to an increased number of lipidic bodies compared to the WT fungus (Uehling et al., 2017). These lipid bodies are used for the compartmentalization of pollutants as a form of defense mechanism (Lenoir et al., 2016). In addition to the increase in lipidic and protein-related peaks, in the presence of Cu^{2+}, Fe^{2+}, and Mn^{2+} for *Linnemannia* –, it was also observed that there was an increase in the intensity of the peaks at 1,150 and 1,077 cm^{-1} corresponding to phosphate and sulfide groups. These negatively charged functional groups are known to take part in the physicochemical process of cell adsorption (Dhankhar and Hooda, 2011; Pugazhendhi et al., 2018; Chen et al., 2019). These results appear to agree with the data related to the tolerance

index (**Figure 2**), MIC (**Figure 1**), and metal removal (**Figure 4**), where we were able to notice not only an overall higher tolerance of *Linnemannia* – compared to *Linnemannia*+, especially toward Fe^{2+} and Mn^{2+}, but also an increase in metal removal.

In general, the functional groups that exhibited intensity changes could potentially be involved in the adsorption process of the metals by these fungi. In this study, the major functional group changes were the C-H stretching from the lipids (2,924 and 2,853 cm^{-1}), amide functional group from the proteins (1,742 cm^{-1}), and to a lesser extent the symmetrical and asymmetrical stretching of PO_2^- and P $(OH)_2$ at 1,150, 1,077, and 1,026 cm^{-1}.

In conclusion, through this research, we have characterized the impact of endosymbiotic bacteria on the response and uptake of essential and non-essential metals by non-metal-resistance in early diverging fungi in Mortierellaceae. The results showed that the response toward essential and non-essential metals is mainly driven by the type of endobacteria colonizing the fungal mycelium. For *L. elongata* (*Linnemannia*), the presence of *Burkholderia*-related endobacterial symbiont was detrimental; in fact, curation of the fungi from the endobacteria led to increasing fungal tolerance to different metals. Curing *L. elongata* also influenced the physicochemical composition of the functional groups present on the mycelium to allow the fungus to tolerate different metals (Cr^{6+}, Pb^{2+}, Ca^{2+}, and Fe^{2+}). Furthermore, the presence of the endosymbiont did not lead to an appreciable increase in uptake of the metals.

On the other hand, *B. eronia* (*Benniella*) benefited from the presence of the endobacteria by increasing the fungal tolerance to Cr^{6+}, Pb^{2+}, Ca^{2+}, and Mn^{2+}, which was demonstrated by a positive correlation between endobacterium abundance and relative metal removal. This study provides a broad view on how the response toward different metals, whether essential or non-essential, is influenced by the type of fungus-bacterium association and, more specifically, by the fact that the maintenance of the endobacteria can have a metabolic cost for the host in certain cases. It is also possible that lipids play an important role in the fungal defense against metal pollutants and that the endobacteria in the fungal microbiome can potentially affect their composition and consequently affect the host resistance to metals. This study, therefore, informs future studies on fungal endobacteria and underlying mechanisms in the resistance and uptake of different metals from the environment.

To answer this question, various metals were selected based on their known cell toxicity (Cu^{2+}, Cr^{6+}, and Pb^{2+}) and essentiality for biological processes (Ca^{2+}, Mn^{2+}, and Fe^{2+}). This question was addressed using an interdisciplinary approach, to evaluate the biological and physicochemical aspects associated with the presence of the endobacterium within the fungus.

The results show that the type of host–symbiont association can alter the resistance of the fungal host and modulate the functional groups expressed and exposed on the hyphae in the presence of metals. This study is, therefore, an initial step in evaluating the potential functionalities of endobacteria associated with fungi.

DATA AVAILABILITY STATEMENT

The original contributions presented in the study are included in the article/**Supplementary Material**, further inquiries can be directed to the corresponding author/s.

AUTHOR CONTRIBUTIONS

DR, GB, and SL contributed to the conception and design of the study. GB provided the cured and wild-type strains for the study. DR contributed to data validation and interpretation, overall manuscript writing and editing, resources for the execution of the project, supervision, administration of the overall project, and funding acquisition. SL and JP-B performed the experiments, data collection, data analysis, and data visualization. SL wrote most parts of the manuscript. JP-B wrote the ATR-FTIR section of the manuscript and assisted in the overall manuscript editing. All authors contributed to manuscript revision and approved the submitted version.

FUNDING

This study was partially funded by the US Department of Energy, Office of Science, Biological and the Environmental Research Division, under the award number LANLF59T, the Welch Foundation award number (E-2011-20190330), and the NSF awards #2125480/2125104/2125298.

ACKNOWLEDGMENTS

We thank Charisma Lattao for her help and support, which allowed the realization of this study.

SUPPLEMENTARY MATERIAL

The Supplementary Material for this article can be found online at: https://www.frontiersin.org/articles/10.3389/fmicb.2022.822541/full#supplementary-material

REFERENCES

Adonaylo, V., and Oteiza, P. I. (1999). Pb2+ promotes lipid oxidation and alterations in membrane physical properties. *Toxicology* 132, 19–32. doi: 10.1016/s0300-483x(98)00134-6

Aguirre, J. D., and Culotta, V. C. (2012). Battles with iron: manganese in oxidative stress protection. *J. Biol. Chem.* 287, 13541–13548. doi: 10.1074/jbc.R111.312181

Ahmad, I., Zafar, S., and Ahmad, F. (2005). Heavy metal biosorption potential of *Aspergillus* and *Rhizopus* sp. isolated from wastewater treated soil. *J. Appl. Sci. Environ.* 9, 123–126.

Amann, R. I., Binder, B. J., Olson, R. J., Chisholm, S. W., Devereux, R., and Stahl, D. A. (1990). Combination of 16S rRNA-targeted oligonucleotide probes with flow cytometry for analyzing mixed microbial populations. *Appl. Environ. Microbiol.* 56, 1919–1925. doi: 10.1128/aem.56.6.1919-1925.1990

Appenroth, K.-J. (2010). Definition of "heavy metals" and their role in biological systems. *Soil Heavy Metals* 19, 19–29. doi: 10.1007/978-3-642-02436-8_2

Baldrian, P. (2003). Interactions of heavy metals with white-rot fungi. *Enzyme Microb. Technol.* 32, 78–91. doi: 10.1016/j.biortech.2011.05.092

Bastías, D. A., Johnson, L. J., and Card, S. D. (2020). Symbiotic bacteria of plant-associated fungi: friends or foes? *Curr. Opin. Plant Biol.* 56, 1–8. doi: 10.1016/j.pbi.2019.10.010

Bitton, G., and Freihofer, V. (1977). Influence of extracellular polysaccharides on the toxicity of copper and cadmium toward *Klebsiella aerogenes*. *Microb. Ecol.* 4, 119–125. doi: 10.1007/BF02014282

Bombalska, A., Mularczyk-Oliwa, M., Kwaśny, M., Włodarski, M., Kaliszewski, M., Kopczyński, K., et al. (2011). Classification of the biological material with use of FTIR spectroscopy and statistical analysis. *Spectrochim. Acta A Mol. Biomol. Spectrosc.* 78, 1221–1226. doi: 10.1016/j.saa.2010.10.025

Butter, T., Evison, L., Hancock, I., Holland, F., Matis, K., Philipson, A., et al. (1998). The removal and recovery of cadmium from dilute aqueous solutions by biosorption and electrolysis at laboratory scale. *Water Res.* 32, 400–406. doi: 10.1016/s0043-1354(97)00273-x

Caballero-Mellado, J., Onofre-Lemus, J., Estrada-De Los Santos, P., and Martínez-Aguilar, L. (2007). The tomato rhizosphere, an environment rich in nitrogen-fixing Burkholderia species with capabilities of interest for agriculture and bioremediation. *Appl. Environ. Microbiol.* 73, 5308–5319. doi: 10.1128/AEM.00324-07

Cecchi, G., Vagge, G., Cutroneo, L., Greco, G., Di Piazza, S., Faga, M., et al. (2019). Fungi as potential tool for polluted port sediment remediation. *Environ. Sci. Pollut. Res.* 26, 35602–35609. doi: 10.1007/s11356-019-04844-5

Cervantes, C., and Gutierrez-Corona, F. (1994). Copper resistance mechanisms in bacteria and fungi. *FEMS Microbiol. Rev.* 14, 121–137. doi: 10.1111/j.1574-6976.1994.tb00083.x

Chen, S. H., Cheow, Y. L., Ng, S. L., and Ting, A. S. Y. (2019). Mechanisms for metal removal established via electron microscopy and spectroscopy: a case study on metal tolerant fungi *Penicillium simplicissimum*. *J. Hazardous Mater.* 362, 394–402. doi: 10.1016/j.jhazmat.2018.08.077

Clark, R. Á, and Zeto, S. (2000). Mineral acquisition by arbuscular mycorrhizal plants. *J. Plant Nutr.* 23, 867–902. doi: 10.1080/01904160009382068

Cohen, A., Nelson, H., and Nelson, N. (2000). The family of SMF metal ion transporters in yeast cells. *J. Biol. Chem.* 275, 33388–33394. doi: 10.1074/jbc.M004611200

Cortes, O., Barbosa, L., and Kiperstok, A. (2003). Biological treatment of industrial liquid effluent in copper production industry. *Tecbahia Rev. Baiana Tecnol.* 18, 89–99.

Desirò, A., Hao, Z., Liber, J. A., Benucci, G. M. N., Lowry, D., Roberson, R., et al. (2018). Mycoplasma-related endobacteria within *Mortierellomycotina fungi*: diversity, distribution and functional insights into their lifestyle. *ISME J.* 12, 1743–1757. doi: 10.1038/s41396-018-0053-9

Dhankhar, R., and Hooda, A. (2011). Fungal biosorption–an alternative to meet the challenges of heavy metal pollution in aqueous solutions. *Environ. Technol.* 32, 467–491. doi: 10.1080/09593330.2011.572922

Fan, J., Okyay, T. O., and Rodrigues, D. F. (2014). The synergism of temperature, pH and growth phases on heavy metal biosorption by two environmental isolates. *J. Hazardous Mater.* 279, 236–243. doi: 10.1016/j.jhazmat.2014.07.016

Fayeulle, A., Veignie, E., Slomianny, C., Dewailly, E., Munch, J.-C., and Rafin, C. (2014). Energy-dependent uptake of benzo [a] pyrene and its cytoskeleton-dependent intracellular transport by the telluric fungus *Fusarium solani*. *Environ. Sci. Pollut. Res.* 21, 3515–3523. doi: 10.1007/s11356-013-2324-3

Fuchs, B., Bresler, K., and Schiller, J. (2011). Oxidative changes of lipids monitored by MALDI MS. *Chem. Phys. Lipids* 164, 782–795. doi: 10.1016/j.chemphyslip.2011.09.006

Gadd, G. M. (1994). "Interactions of fungi with toxic metals," in *The Genus Aspergillus. Federation of European Microbiological Societies Symposium Series*, eds K. A. Powell, A. Renwick, and J. F. Peberdy (Boston, MA: Springer), 361–374. doi: 10.1007/978-1-4899-0981-7_28

González-Guerrero, M., Escudero, V., Saéz, Á, and Tejada-Jiménez, M. (2016). Transition metal transport in plants and associated endosymbionts: arbuscular mycorrhizal fungi and rhizobia. *Front. Plant Sci.* 7:1088. doi: 10.3389/fpls.2016.01088

Gunjal, A. (2021). Study of Langmuir kinetics for removal of heavy metals by the fungal biomass. *Proc. Indian Natl. Sci. Acad.* 87, 107–109. doi: /10.1007/s43538-021-00011-y

Hanson, B. A. (2014). *ChemoSpec: An R Package for the Chemometric Analysis of Spectroscopic Data. Package Version, 2.0-2.*

Hitchins, A. D., Feng, P., Watkins, W., Rippey, S., and Chandler, L. (1998). *Bacteriological Analytical Manual*. Washington, DC: Food Drug Administration.

Howlett, N. G., and Avery, S. V. (1997). Induction of lipid peroxidation during heavy metal stress in *Saccharomyces cerevisiae* and influence of plasma membrane fatty acid unsaturation. *Appl. Environ. Microbiol.* 63, 2971–2976. doi: 10.1128/aem.63.8.2971-2976.1997

Hu, Y., Wang, J., Ying, S.-H., and Feng, M.-G. (2014). Five vacuolar Ca2+ exchangers play different roles in calcineurin-dependent Ca2+/Mn2+ tolerance, multistress responses and virulence of a filamentous entomopathogen. *Fungal Genet. Biol.* 73, 12–19. doi: 10.1016/j.fgb.2014.09.005

Jiang, C.-Y., Sheng, X.-F., Qian, M., and Wang, Q.-Y. (2008). Isolation and characterization of a heavy metal-resistant *Burkholderia* sp. from heavy metal-contaminated paddy field soil and its potential in promoting plant growth and heavy metal accumulation in metal-polluted soil. *Chemosphere* 72, 157–164. doi: 10.1016/j.chemosphere.2008.02.006

Johnson, H., and Choudhary, M. (2016). "Heavy metal pollution and use of microorganisms for bioremediation," in *Proceedings of the 2016 ATINER Conference on Environemnt*, Athence.

Joo, J.-H., and Hussein, K. A. (2012). Heavy metal tolerance of fungi isolated from contaminated soil. *Korean J. Soil Sci.* 45, 565–571. doi: 10.7745/KJSSF.2012.45.4.565

Juvvadi, P. R., Fortwendel, J. R., Rogg, L. E., Burns, K. A., Randell, S. H., and Steinbach, W. J. (2011). Localization and activity of the calcineurin catalytic and regulatory subunit complex at the septum is essential for hyphal elongation and proper septation in *Aspergillus fumigatus*. *Mol. Microbiol.* 82, 1235–1259. doi: 10.1111/j.1365-2958.2011.07886.x

Kaushik, A., Sharma, H., Jain, S., Dawra, J., and Kaushik, C. (2010). Pesticide pollution of river Ghaggar in Haryana, India. *Environ. Monit. Assess.* 160, 61–69. doi: 10.1007/s10661-008-0657-z

Kosman, D. J. (2003). Molecular mechanisms of iron uptake in fungi. *Mol. Microbiol.* 47, 1185–1197. doi: 10.1046/j.1365-2958.2003.03368.x

Kosman, D. J. (2020). "Transition metal ion uptake in yeasts and filamentous fungi," in *Metal Ions in Fungi*, ed. G. Winkelmann (Boca Raton, FL: CRC Press), 1–38. doi: 10.1201/9781003067221-1

Kumar, V., and Dwivedi, S. (2021). Mycoremediation of heavy metals: processes, mechanisms, and affecting factors. *Environ. Sci. Pollut. Res.* 28, 10375–10412. doi: 10.1007/s11356-020-11491-8

Lee, C., Lee, S., Shin, S. G., and Hwang, S. (2008). Real-time PCR determination of rRNA gene copy number: absolute and relative quantification assays with *Escherichia coli*. *Appl. Microbiol. Biotechnol.* 78, 371–376. doi: 10.1007/s00253-007-1300-6

Lemire, J. A., Harrison, J. J., and Turner, R. J. (2013). Antimicrobial activity of metals: mechanisms, molecular targets and applications. *Nat. Rev. Microbiol.* 11, 371–384. doi: 10.1038/nrmicro3028

Lenoir, I., Fontaine, J., and Sahraoui, A. L.-H. (2016). Arbuscular mycorrhizal fungal responses to abiotic stresses: a review. *Phytochemistry* 123, 4–15. doi: 10.1016/j.phytochem.2016.01.002

Li, Z., Yao, Q., Dearth, S. P., Entler, M. R., Castro Gonzalez, H. F., Uehling, J. K., et al. (2017). Integrated proteomics and metabolomics suggests symbiotic metabolism and multimodal regulation in a fungal-endobacterial system. *Environ. Microbiol.* 19, 1041–1053. doi: 10.1111/1462-2920.13605

Lilly, W., Wallweber, G., and Lukefahr, T. (1992). Cadmium absorption and its effects on growth and mycelial morphology of the basidiomycete fungus, *Schizophyllum commune*. *Microbios* 72, 227–237.

Lisher, J. P., and Giedroc, D. P. (2013). Manganese acquisition and homeostasis at the host-pathogen interface. *Front. Cell. Infect. Microbiol.* 3:91. doi: 10.3389/fcimb.2013.00091

Lucas, A. (2006). *Another Multidimensional Analysis Package Version 0.8-18*.

Manikan, V., Kalil, M. S., Omar, O., Kader, A. J. A., and Hamid, A. A. (2014). Effects of Mg2+, Fe3+, Mn2+ and Cu2+ ions on lipid accumulation by *Cunninghamella bainieri* 2A1. *Sains Malaysiana* 43, 443–449.

Mejias Carpio, I. E., Ansari, A., and Rodrigues, D. F. (2018). Relationship of biodiversity with heavy metal tolerance and sorption capacity: a meta-analysis approach. *Environ. Sci. Technol.* 52, 184–194. doi: 10.1021/acs.est.7b04131

Mix, P. (2011). *Power SYBR Green RT-PCR Reagents Kit User Guide*. Carlsbad, CA: Life Technologies.

Miyakawa, T., and Mizunuma, M. (2007). Physiological roles of calcineurin in Saccharomyces cerevisiae with special emphasis on its roles in G2/M cell-cycle regulation. *Biosci. Biotechnol. Biochem.* 71, 633–645. doi: 10.1271/bbb.60495

Mullins, A. J., Murray, J. A., Bull, M. J., Jenner, M., Jones, C., Webster, G., et al. (2019). Genome mining identifies cepacin as a plant-protective metabolite of the biopesticidal bacterium *Burkholderia ambifaria*. *Nat. Microbiol.* 4, 996–1005. doi: 10.1038/s41564-019-0383-z

Nanthakumar, N. N., Dayton, J. S., and Means, A. R. (1996). Role of Ca++/calmodulin binding proteins in Aspergillus nidulans cell cycle regulation. *Prog. Cell Cycle Res.* 2, 217–228. doi: 10.1007/978-1-4615-5873-6_21

Navarro, M., Pérez-Sirvent, C., Martínez-Sánchez, M., Vidal, J., Tovar, P., and Bech, J. (2008). Abandoned mine sites as a source of contamination by heavy metals: a case study in a semi-arid zone. *J. Geochem. Explorat.* 96, 183–193. doi: 10.1016/j.gexplo.2007.04.011

Nelissen, B., De Wachter, R., and Goffeau, A. (1997). Classification of all putative permeases and other membrane plurispanners of the major facilitator superfamily encoded by the complete genome of *Saccharomyces cerevisiae*. *FEMS Microbiol. Rev.* 21, 113–134. doi: 10.1111/j.1574-6976.1997.tb00347.x

Neogi, S., Sharma, V., Khan, N., Chaurasia, D., Ahmad, A., Chauhan, S., et al. (2021). Sustainable biochar: a facile strategy for soil and environmental restoration, energygeneration, mitigation of global climate change and circular bioeconomy. *Chemosphere* 293:133474. doi: 10.1016/j.chemosphere.2021.133474

Nguyen, H. N., Castro-Wallace, S. L., and Rodrigues, D. F. (2017). Acute toxicity of graphene nanoplatelets on biological wastewater treatment process. *Environ. Sci. Nano* 4, 160–169. doi: 10.1039/C6EN00442C

Ohsumi, Y., and Anraku, Y. (1981). Active transport of basic amino acids driven by a proton motive force in vacuolar membrane vesicles of *Saccharomyces cerevisiae*. *J. Biol. Chem.* 256, 2079–2082. . doi: S0021-9258(19)69736-X

Oleszko, A., Olsztyńska-Janus, S., Walski, T., Grzeszczuk-Kuæ, K., Bujok, J., Gałecka, K., et al. (2015). Application of FTIR-ATR spectroscopy to determine the extent of lipid peroxidation in plasma during haemodialysis. *BioMed Res. Int.* 2015:245607. doi: 10.1155/2015/245607

Oteiza, P. I., Mackenzie, G. G., and Verstraeten, S. V. (2004). Metals in neurodegeneration: involvement of oxidants and oxidant-sensitive transcription factors. *Mol. Aspects Med.* 25, 103–115. doi: 10.1016/j.mam.2004.02.012

Park, D., Yun, Y.-S., and Park, J. M. (2005). Studies on hexavalent chromium biosorption by chemically-treated biomass of *Ecklonia* sp. *Chemosphere* 60, 1356–1364. doi: 10.1016/j.chemosphere.2005.02.020

Pugazhendhi, A., Boovaragamoorthy, G. M., Ranganathan, K., Naushad, M., and Kaliannan, T. (2018). New insight into effective biosorption of lead from aqueous solution using *Ralstonia solanacearum*: characterization and mechanism studies. *J. Clean. Product.* 174, 1234–1239. doi: 10.1016/j.jclepro.2017.11.061

Qin, H., Hu, T., Zhai, Y., Lu, N., and Aliyeva, J. (2020). The improved methods of heavy metals removal by biosorbents: a review. *Environ. Pollut.* 258:113777. doi: 10.1016/j.envpol.2019.113777

Rainbow, P. S. (1995). Biomonitoring of heavy metal availability in the marine environment. *Mar. Pollut. Bull.* 31, 183–192. doi: 10.1016/0025-326X(95)00116-5

Rao, C. N. R. (1963). *Chemical Applications of Infrared Spectroscopy*. New York, NY: Academic Press, 681–681.

Repetto, M. G., Ferrarotti, N. F., and Boveris, A. (2010). The involvement of transition metal ions on iron-dependent lipid peroxidation. *Arch. Toxicol.* 84, 255–262. doi: 10.1007/s00204-009-0487-y

Robinson, A. J., House, G. L., Morales, D. P., Kelliher, J. M., Gallegos-Graves, L. V., LeBrun, E. S., et al. (2021). Widespread bacterial diversity within the bacteriome of fungi. *Commun. Biol.* 4, 1–13. doi: 10.1038/s42003-021-02693-y

Schwager, S., Lumjiaktase, P., Stöckli, M., Weisskopf, L., and Eberl, L. (2012). The genetic basis of cadmium resistance of B urkholderia cenocepacia. *Environ. Microbiol. Rep.* 4, 562–568. doi: 10.1111/j.1758-2229.2012.00372.x

Smejkalova, M., Mikanova, O., and Boruvka, L. (2003). Effects of heavy metal concentrations on biological activity of soil micro-organisms. *Plant Soil Environ. Microbiol.* 49, 321–326. doi: 10.17221/4131-PSE

Solomons, T. W. G. (2016). *Organic Chemistry*. Hoboken, NJ: Wiley.

Stohs, S. J., and Bagchi, D. (1995). Oxidative mechanisms in the toxicity of metal ions. *Free Radic. Biol. Med.* 18, 321–336. doi: 10.1016/0891-5849(94)00159-h

Tebo, B. M., Johnson, H. A., McCarthy, J. K., and Templeton, A. S. (2005). Geomicrobiology of manganese (II) oxidation. *Trends Microbiol.* 13, 421–428. doi: 10.1016/j.tim.2005.07.009

Temple, K. L., and Le Roux, N. (1964). Syngenesis of sulfide ores; sulfate-reducing bacteria and copper toxicity. *Econ. Geol.* 59, 271–278. doi: 10.2113/gsecongeo.59.2.271

Tomer, A., Singh, R., Singh, S. K., Dwivedi, S., Reddy, C. U., Keloth, M. R. A., et al. (2021). "Role of fungi in bioremediation and environmental sustainability," in *Mycoremediation and Environmental Sustainability. Fungal Biology*, eds R. Prasad, S. C. Nayak, R. N. Kharwar, and N. K. Dubey (Cham: Springer), 187–200. doi: 10.1007/978-3-030-54422-5_8

Tomsett, A. (1993). "Genetic and molecular biology of metal tolerance in fungi," in *Stress Tolerance of Fungi*, ed. D. H. Jennings (New York, NY: Marcel Dekker), 69–95.

Uehling, J., Gryganskyi, A., Hameed, K., Tschaplinski, T., Misztal, P., Wu, S., et al. (2017). Comparative genomics of *Mortierella elongata* and its bacterial endosymbiont *Mycoavidus cysteinexigens*. *Environ. Microbiol.* 19, 2964–2983. doi: 10.1111/1462-2920.13669

ul Hassan, Z., Ali, S., Rizwan, M., Ibrahim, M., Nafees, M., and Waseem, M. (2017). "Role of bioremediation agents (bacteria, fungi, and algae) in alleviating heavy metal toxicity," in *Probiotics in Agroecosystem*, eds V. Kumar, M. Kumar, S. Sharma, and R. Prasad (Cham: Springer), 517–537. doi: 10.1007/978-981-10-4059-7_27

Vaalgamaa, S., and Conley, D. (2008). Detecting environmental change in estuaries: nutrient and heavy metal distributions in sediment cores in estuaries from the Gulf of Finland, Baltic Sea. *Estuarine Coast. Shelf Sci.* 76, 45–56. doi: 10.1016/j.ecss.2007.06.007

Vallee, B. L., and Ulmer, D. D. (1972). Biochemical effects of mercury, cadmium, and lead. *Annu. Rev. Biochem.* 41, 91–128. doi: 10.1146/annurev.bi.41.070172.000515

Varmuza, K., and Filzmoser, P. (2016). *Introduction to Multivariate Statistical Analysis in Chemometrics*. Boca Raton, FL: CRC press. doi: 10.1201/9781420059496

Wernegreen, J. J. (2012). Endosymbiosis. *Curr. Biol.* 22, R555–R561. doi: 10.1016/j.cub.2012.06.010

White, C., and Gadd, G. M. (1987). The uptake and cellular distribution of zinc in *Saccharomyces cerevisiae*. *Microbiology* 133, 727–737. doi: 10.1099/00221287-133-3-727

Zafar, S., Aqil, F., and Ahmad, I. (2007). Metal tolerance and biosorption potential of filamentous fungi isolated from metal contaminated agricultural soil. *Bioresour. Technol.* 98, 2557–2561. doi: 10.1016/j.biortech.2006.09.051

Zhang, D., Yin, C., Abbas, N., Mao, Z., and Zhang, Y. (2020). Multiple heavy metal tolerance and removal by an earthworm gut fungus *Trichoderma brevicompactum* QYCD-6. *Sci. Rep.* 10, 1–9. doi: 10.1038/s41598-020-63813-y

Zschornig, O., Bergmeier, C., Sub, R., Arnold, K., and Schiller, J. (2004). Human low-density lipoprotein oxidation: hypochlorous acid leads to the generation of lysophosphatidylcholines under acidic conditions. *Lett. Organ. Chem.* 1, 381–390. doi: 10.2174/1570178043400668

Conflict of Interest: The authors declare that the research was conducted in the absence of any commercial or financial relationships that could be construed as a potential conflict of interest.

Publisher's Note: All claims expressed in this article are solely those of the authors and do not necessarily represent those of their affiliated organizations, or those of the publisher, the editors and the reviewers. Any product that may be evaluated in this article, or claim that may be made by its manufacturer, is not guaranteed or endorsed by the publisher.

frontiers in Microbiology

ORIGINAL RESEARCH
published: 16 March 2022
doi: 10.3389/fmicb.2022.823176

Evolution of Copper Homeostasis and Virulence in *Salmonella*

Andrea A. E. Méndez, Julián I. Mendoza, María Laura Echarren, Ignacio Terán, Susana K. Checa and Fernando C. Soncini**

Instituto de Biología Molecular y Celular de Rosario, Facultad de Ciencias Bioquímicas y Farmacéuticas, Universidad Nacional de Rosario, Consejo Nacional de Investigaciones Científicas y Técnicas, Rosario, Argentina

Salmonella enterica sv. Typhimurium modulates the expression of factors essential for virulence, contributing to its survival against the surge of copper (Cu) in the *Salmonella*-containing vacuole. This bactericidal host innate immune component primarily targets the bacterial envelope, where most cuproproteins are localized. While in most enteric species periplasmic Cu homeostasis is maintained by the CusR/CusS-controlled CusCFBA efflux system encoded in the *cus* locus, we noticed that these genes were lost from the *Salmonella*-core genome. At the same time, *Salmonella* acquired *cueP*, coding for a periplasmic Cu chaperone. As *cus*, *cueP* was shown to be essential for bacterial survival in a copper-rich environment under anaerobiosis, suggesting that it can functionally substitute the CusCFBA system. In the present study, the whole *Escherichia coli cus* locus was reintroduced to the chromosome of the *Salmonella* wild-type or the Δ*cueP* strain. While the integrated *cus* locus did not affect Cu resistance under aerobic conditions, it increases Cu tolerance under anaerobiosis, irrespective of the presence or absence of *cueP*. In contrast to the Cus system, CueP expression is higher at high copper concentrations and persisted over time, suggesting separate functions. Finally, we observed that, regardless of the presence or absence of *cus*, a mutant deleted of *cueP* shows a deficiency in replication inside macrophages compared to the wild-type strain. Our results demonstrate that CueP and CusCFBA exert redundant functions for metal resistance, but not for intracellular survival, and therefore for the virulence of this pathogen.

Keywords: copper, bacterial envelope, CueP, CusCFBA, host-pathogen interaction

OPEN ACCESS

Edited by:
Jon L. Hobman, University of Nottingham, United Kingdom

Reviewed by:
Nam-chul Ha, Seoul National University, South Korea
Christopher Rensing, Fujian Agriculture and Forestry University, China

****Correspondence:***
Susana K. Checa
checa@ibr-conicet.gov.ar
Fernando C. Soncini
soncini@ibr-conicet.gov.ar

Specialty section:
This article was submitted to Antimicrobials, Resistance and Chemotherapy, a section of the journal Frontiers in Microbiology

Received: *26 November 2021*
Accepted: *14 January 2022*
Published: *16 March 2022*

Citation:
Méndez AAE, Mendoza JI, Echarren ML, Terán I, Checa SK and Soncini FC (2022) Evolution of Copper Homeostasis and Virulence in Salmonella. Front. Microbiol. 13:823176. doi: 10.3389/fmicb.2022.823176

INTRODUCTION

Salmonella enterica encompasses a zoonotic group of pathogens divided into seven subspecies and more than 2,600 serotypes (Alikhan et al., 2018). It is the causative agent of a variety of clinical ailments (from gastroenteritis to more serious systemic diseases) in both humans and animals, including those of economic relevance (Eng et al., 2015). The pathogen is acquired by ingestion of contaminated water or food and more rarely by direct contact with infected individuals (Branchu et al., 2018). Annually, almost 94 million cases of enteric salmonellosis and more than 150,000

deaths are reported worldwide. Most of the cases are self-limited and respond well to antimicrobial therapy. However, in young children, older adults, or immune-compromised patients, non-typhoid *Salmonella* can cause severe infections and sepsis (Eng et al., 2015; Branchu et al., 2018). This pathogen has a remarkable ability to adapt and survive to different harsh conditions, including the host environment. This is reflected by the versatility of its genetic repertoire (Alikhan et al., 2018; Branchu et al., 2018). Recent reports indicate that *Salmonella* detects the surge of copper (Cu) inside the *Salmonella*-containing vacuole (SCV) in infected macrophages, and mutants affected in terms of Cu resistance have a reduced intracellular survival compared to the wild-type strain (Achard et al., 2012; Osman et al., 2013; Fenlon and Slauch, 2017; Ladomersky et al., 2017).

Cu is not only an essential micronutrient but also a potent microbicidal agent (Borkow and Gabbay, 2005; Grass et al., 2011; Djoko and McEwan, 2013; Tan et al., 2017). Because of its ability to donate or accept one electron during Cu(I)/Cu(II) interconversion at a life-compatible redox potential, it was incorporated as a prosthetic group of many redox enzymes, being essential for aerobic growth, such as in cytochrome oxidases or superoxide dismutases (Rubino and Franz, 2012; Stewart et al., 2019). At the same time, the redox activity of the Cu(I)/Cu(II) pair contributes to its toxicity by catalyzing the generation of reactive oxygen species. Also, Cu ions bind with high affinity to S and N groups, affecting the structure and function of macromolecules as well as displacing other transition metals, such as Fe, from their binding sites, which exacerbates the redox stress (Macomber and Imlay, 2009; Djoko and McEwan, 2013; Le Brun, 2014; Tan et al., 2017). The toxicity of Cu has been exploited by eukaryotic cells to limit the growth of invading microorganisms, such as *Salmonella* (Besold et al., 2016). As part of their innate immunity, bacteria-infected macrophages increase the expression of membrane Cu transporters and their coupled chaperones to drive Cu trafficking and influx into the pathogen-containing phagosomes (Achard et al., 2012; Ladomersky et al., 2017). The ability to resist high Cu concentrations is crucial for virulence and involves factors localized to the cell envelope, the primary target of Cu toxicity. Various studies have shown that mutation of the two *Salmonella* Cu(I)-ATPases, CopA, and GolT, decreases survival inside RAW264.7 macrophages as well as in isolated peritoneal myeloid cells from C57BL/6J mice (Osman et al., 2010; Ladomersky et al., 2017). Interestingly, deletion of the gene coding for the *Salmonella*-specific periplasmic Cu chaperone, *cueP*, in *Salmonella enterica* sv. Typhimurium (*S.* Typhimurium hereafter) SL1344 strain also decreases its intracellular survival in macrophages (Yoon et al., 2014). The attenuated phenotype exhibited by these mutants depends on the functionality of the host Cu(I) ATPase ATP7A that delivers cytoplasmic Cu into the *Salmonella*-containing phagolysosomes (Ladomersky et al., 2017). Besides Cu-dependent redox imbalance, the ability of *Salmonella* to overcome the phagosomal oxidative burst also affects virulence (Negrea et al., 2009; Achard et al., 2010; Fenlon and Slauch, 2017; Yucel et al., 2020). This likely involves the redox activity of envelope cuproenzymes such as SodCI, SodCII, and CueO and the ScsABCD system of thioredoxins. Cells lacking SodCI or SodCII are less virulent (Fang et al., 1999), and virulence attenuation was also noticed for the Δ*cueO* or the Δ*scsC* strains (Achard et al., 2010; Yucel et al., 2020).

Most known bacterial cuproproteins localize to the cell envelope, making this compartment the main target of Cu toxicity (Rubino and Franz, 2012; Pontel et al., 2015; Giachino and Waldron, 2020; Checa et al., 2021). While most enteric species rely on CueO, the multicopper oxidase controlled by the cytoplasmic sensor/regulator CueR, to maintain periplasmic Cu homeostasis under aerobic conditions and on the CusR/CusS-controlled CusCFBA efflux system under anaerobic conditions, the *cus* locus is absent in the *Salmonella* genome (Checa et al., 2021). An *in silico* analysis revealed the presence of variable remnants of the outmost *cus* genes in most *Salmonella* strains, suggesting different deletion events during this species evolution (Checa et al., 2021). At the same time or probably before *cus* deletion, *Salmonella* acquired *cueP* (Pontel and Soncini, 2009). Interestingly, *cueP* transcription depends on the coordinated action of CueR, the ancestral Cu-responsive CueR regulator that also controls the expression of *copA* and *cueO* and of CpxR/CpxA, a main two-component system responding to multiple envelope stresses, including Cu and redox oxidative species (Pezza et al., 2016). Thus, CueP-induced expression occurs only under conditions of Cu stress that affect envelope homeostasis. Previously, we showed that, expressed from a multicopy plasmid, CueP can partially complement a Δ*cus Escherichia coli* strain for Cu resistance under anaerobic conditions (Pontel and Soncini, 2009), although these Cu resistance determinants are not structurally or functionally related. CusCFBA is a Cu^{+}-specific envelope detoxification pump (Franke et al., 2003), while CueP is the major periplasmic cuproprotein, with a putative Cu^{2+} reductase activity (Osman et al., 2010, 2013; Yoon et al., 2013, 2014; Abriata et al., 2014). The phenotype analyses of a *S.* Typhimurium Δ*cueP* strain also mimics the *E. coli cus* deletion mutant in (i) its requirement for Cu resistance under anaerobic condition, (ii) the absence of an appreciable phenotype in aerobiosis, (iii) their delayed expression compared to the canonical CueR-regulated *copA* gene, and (iv) their coordinated transcriptional control to specifically respond to a cell-envelope-toxic Cu surge (Outten et al., 2001; Pontel and Soncini, 2009; Pontel et al., 2010; Fung et al., 2013; Pezza et al., 2016). Considering these observations and the proposed functional redundancy between CueP and the CusCFBA system, here we tested the hypothesis that the *cus* locus was selectively lost from *Salmonella* because either it is not required for intracellular survival or it interferes with virulence.

In this study, we reintroduced the *E. coli cus* locus in the identified *cus* scar present in the *S.* Typhimurium genome and evaluated its transcriptional profile and its role in Cu resistance and in virulence, both in the presence and absence of *cueP*. Although the Cus system is expressed in response to Cu in *Salmonella* and conferred high levels of Cu tolerance particularly under anaerobic conditions, we found that, in contrast to CueP, it did not contribute to intracellular survival in macrophages. These results indicate that, although CueP and CusCFBA exert redundant functions for Cu resistance, they are not exchangeable for macrophage survival and therefore for *Salmonella* virulence.

MATERIALS AND METHODS

Bacterial Strains and Growth Conditions

The *E. coli* and *S.* Typhimurium strains and plasmids are listed in **Supplementary Table 1**. The cells were grown overnight at 37°C in Luria–Bertani broth (LB) with shaking or in LB agar plates. Kanamycin (Km) was used at 25 μg ml^{-1}, chloramphenicol (Cm) at 10 μg ml^{-1}, spectinomycin (Sp) at 50 μg ml^{-1}, and ampicillin (Amp) at 100 μg ml^{-1}. Bacterial stocks were stored at −80°C with 15% glycerol. A final concentration of 0.1 mM isopropyl β-D-1-thiogalactopyranoside was added when indicated to express CueP from a plasmid. The culture media was from Difco, whereas the rest of the reagents and chemicals were from Merck and affiliates. The copper salt used was of ACS analytical grade at ≥98.0% purity. The oligonucleotides were provided by Life Technology and are listed in **Supplementary Table 2**.

Genetic and Molecular Biology Techniques

Insertion of the *cus* locus into the *S.* Typhimurium chromosome was carried out after two sequential steps of Red-mediated recombination protocol (Karlinsey, 2007). Briefly, a ∼4,900-bp fragment containing a Cm^R–*cusRS*–*cusCF* region (product I) was amplified from the chromosome of the recombinant *E. coli* strain PB1179 (**Supplementary Table 1**) using the Q5® High-Fidelity DNA polymerase (New England Biolabs) and the oligonucleotides Cus SF P1 Fw and Cus SF P2 Rv (**Supplementary Table 2**). The purified final product was introduced by electroporation into *S.* Typhimurium 14028s carrying the pKD46 plasmid (**Supplementary Table 1**). After selection of chloramphenicol-resistant colonies, proper insertion of product I was verified by colony PCR using the oligonucleotides detailed in **Supplementary Table 2** in order to select strain PB13957 (**Supplementary Table 1**). In parallel, a second ∼6,100-bp fragment containing the final portion of cusF and the *cusBA*:3xFLAG-Km^R region (product II) was PCR-amplified from *E. coli* PB1179 (**Supplementary Table 1**) using the oligonucleotides P1 Fwd CusA Flag Km and Cus FA P2 Rv (**Supplementary Table 2**). After purification, product II was used to transform the PB13957 strain carrying pKD46. Kanamycin- and chloramphenicol-resistant colonies were selected to verify proper product II insertion following product I through colony PCR using the oligonucleotides detailed in **Supplementary Table 2**. After selecting one clone, the presence of the whole *E. coli cusRS–cusCFBA* locus into the *Salmonella* chromosome was verified by DNA sequencing at Macrogen Inc. P22-mediated transduction (Checa et al., 2007) was used to move the whole *cus* locus into the chromosome of the wild-type 14028s to obtain the PB14006 strain or to the chromosome of strains carrying the *cueP*:3xFLAG gene or the Δ*cueP*, Δ*cueO*, Δ*cueO*Δ*cueP*, or Δ*golT* Δ*copA* mutant strains (**Supplementary Table 1**).

Reporter plasmids p*cueP-gfp* and p*cusCFBA-gfp* (**Supplementary Table 1**) were constructed as follows: The *cueP* or the *cusABFC* promoter region was amplified by PCR from the chromosome of the PB14006 strain using the oligonucleotides listed in **Supplementary Table 2**. The product containing the *cueP* promoter was *Sma*I-digested and cloned into pPROBE-OT′ (**Supplementary Table 1**) digested with this enzyme. Similarly, the *cusCFBA* Inc., Hercules, CA, United States promoter was digested with *Hin*dIII/*Eco*RI enzymes and cloned into *Hin*dIII/*Eco*RI-digested pPROBE-OT′.

Fluorescence Determination

A 100-μl aliquot of 1/100 overnight culture of the indicated strains grown in 96-well microplates in LB supplemented without or with 1, 2, 3, or 4 mM $CuSO_4$ was incubated overnight at 37°C with regular shaking. Fluorescence (485-nm excitation/508-nm emission) and optical density ($OD_{600\,nm}$) were determined from p*cueP-gfp* or p*cusCFBA-gfp* harboring *Salmonella* strains using a BioTek™ Sinergy™ HT Microplate reader every 1 h for a period of 16 h and used to calculate the normalized fluorescence expressed as arbitrary units. To prevent dehydration, the perimeter wells were filled with sterile water. Wells containing only culture media with/without $CuSO_4$ were included as controls of background fluorescence.

Western Blot Analysis

Western blot analysis of 3xFLAG-tagged proteins, IgaA or GroEL, were carried out as described previously (Pontel and Soncini, 2009; Pérez Audero et al., 2010). Briefly, cells were grown in the presence of 2 mM $CuSO_4$ until $OD_{600\,nm}$ of 0.5, harvested by centrifugation at 3,500 *g* for 10 min, washed, and resuspended in 1 ml of Tris-EDTA buffer solution (pH 8) supplemented with 1 mM phenylmethylsulfonyl fluoride. The cell suspensions were sonicated (30% amplitude) on ice for 2 min, with on/off intervals of 2 s. The mixtures were then centrifuged at 12,000 *g* for 30 min at 4°C to separate soluble and insoluble (membrane) fractions and determine the protein concentration. Aliquots of the soluble or insoluble fraction containing 20 or 10 μg of total proteins were analyzed in 15% (w/v) and 10% (w/v) sodium dodecyl sulfate polyacrylamide gels, respectively, and transferred to nitrocellulose membranes. Both the soluble CueP-3xFLAG and the membrane-bound CusA-3xFLAG proteins were detected using mouse anti-FLAG monoclonal antibodies (Sigma-Aldrich) and mouse secondary antibody conjugated with horseradish peroxidase (HRP). In parallel, rabbit polyclonal anti-GroEL or anti-IgaA antibodies and the specific secondary antibody conjugated with HRP were employed to detect the loading controls in the soluble and insoluble cell fractions, respectively. Immunoreactive bands were revealed using SuperSignal® West Femto Maximum Sensitivity Western Blotting Substrate (Thermo Fisher Scientific Inc., Waltham, MA, United States) and registered in ChemiDoc™ XRS Imaging System (Bio-Rad Laboratories Inc., Hercules, CA, United States). A densitometric analysis of each band was done using the Gel-Pro software and used to estimate the amount of CueP-3xFLAG or CusA3xFLAG in the samples after normalization against the soluble and insoluble loading controls, GroEL or IgaA, respectively.

Copper Resistance Assays

Minimum inhibitory concentrations (MICs) were determined in LB agar plates supplemented with $CuSO_4$ at the indicated

concentrations as previously described (Pontel and Soncini, 2009). Plates were incubated for 24 h at 37°C under aerobic condition or for 72 h at 37°C under anaerobiosis inside a jar containing Oxoid^{TM} AnaeroGen^{TM} System and Oxoid^{TM} Anaerobic Indicator (Thermo Scientific). After incubation, the plates were photographically recorded, and the MIC values were registered.

Intramacrophage Proliferation Assays

Salmonella proliferation in RAW 264.7 macrophages was tested as described (Echarren et al., 2021). Briefly, macrophages were cultured in 24-well plates containing Dulbecco's modified Eagle's medium (DMEM) supplemented with 10% fetal calf serum. Each *S.* Typhimurium strain tested was grown overnight, harvested, and washed with 1× phosphate-buffered saline (PBS). These bacterial pellets were resuspended in DMEM media and used for cell infection assay at a multiplicity of infection of 10 bacteria per cell at 37°C for 30 min. Afterward, fresh DMEM and 10% FBS medium supplemented with gentamicin (100 μg/ml) was added. After 1 h at 37°C, the infected cells were incubated with a medium containing gentamicin at a concentration of 30 μg/ml for a total of 18 h. At the indicated time points, the cells were washed and lysed with 0.1% Triton X-100 in PBS. Lysates were recovered, serially diluted, and spread on LB agar plates. After overnight incubation at 37°C, colony-forming units were counted and used to calculate the intracellular proliferation relative to the wild-type strain.

RESULTS

The *Escherichia coli cus* Locus Is Transcriptionally Induced by Copper in *Salmonella* Typhimurium

Early in evolution, *S. enterica* acquired *cueP*. This probably accompanied or presided by different *cus* locus deletion events, resulting in variable remnants of the outmost *cus* genes among different *S. enterica* serovars (Checa et al., 2021). As an example, the *S.* Typhimurium 14028s genome harbors a 619-bp DNA fragment, including sequences coding for the last 137 amino acids of CusS (with 65% identity) and the last 83 residues of CusA (with 83% identity) between nucleotides 619898 and 619287 (**Figure 1**), that is, only the C-terminal portion of both gene products, encoded in opposite directions in the ancient *E. coli cus* locus, remains in the *S.* Typhimurium genome. Interestingly, the residual fragments of *cusS* and *cusA* overlap (**Figure 1**), suggesting a site-specific recombination event.

To analyze whether the *E. coli* CusCBA efflux pump and its associated CusF Cu chaperone can substitute CueP for Cu resistance and virulence in the *Salmonella* envelope, the *E. coli cus* locus was inserted into the *S.* Typhimurium 14028s *cus* scar (**Supplementary Figure 1**). We included a 3xFLAG-tag coding sequence at the *cusA* 3′ end to determine its CusR/CusS-dependent expression in response to Cu ions and, in parallel, to verify if the fusion protein is directed into the *S.* Typhimurium inner membrane. As expected, CusA-3xFLAG was detected in the insoluble cell fraction of the *cus*+ strain and only after $CuSO_4$ addition to the culture medium, as occurs in *E. coli*, included as a control (**Figure 2**). No immunoreactive bands were detected in cell extracts from the wild-type *S.* Typhimurium strain.

Copper-Dependent Transcriptional Induction of *cueP* and the *cusCFBA* Operon Occurs at Different Stages of Growth

To compare *cueP* and *cusCFBA* transcription in *S.* Typhimurium, the wild-type, its Δ*cueP* derivative, or the transgenic *cus*+ or *cus*+ Δ*cueP* strains were transformed with p*cueP-gfp* or p*cusC-gfp*, and fluorescence was recorded every hour during 16 h after the addition of different concentrations of Cu to the culture. After a lag period of ∼1 h, fluorescence increased in cultures from the wild-type strain harboring the p*cueP-gfp* reporter plasmid supplemented with $CuSO_4$ (**Figure 3A**). At low or intermediate Cu concentrations (1–2 mM $CuSO_4$), P*cueP*-dependent GFP expression increased for about 4 h, reaching a plateau that persisted for another hour. After that, a new increase in fluorescence was observed, which continued at least during the 16 h that the experiment was recorded (**Figure 3A**). The plateau was less evident at 3 mM $CuSO_4$ and disappeared at 4 mM $CuSO_4$, the higher concentration tested. This expression profile could reflect the need for CueP in conditions of persistent Cu stress and/or at the stationary phase when other toxic species are expected to accumulate. At 1 or 2 mM $CuSO_4$, no significant differences in emitted fluorescence were perceived between cells harboring *cueP* or the transgenic *cus* locus or not, although a lower P*cueP-gfp* promoter expression was evident from *cus*+ cells exposed to 3–4 mM $CuSO_4$ (**Figure 3A**).

In contrast to the abovementioned observations, the CusR/CusS-dependent GFP expression from the *cusC* promoter was evident in the *cus*+ strain during exponential growth and particularly at low or intermediate $CuSO_4$ concentrations, but it decreased at the stationary phase (**Figure 3A**). Interestingly, less induction from P*cusC* was observed at higher Cu concentrations, while this was the condition for maximal fluorescence from the P*cueP-gfp*-expressing strain. As with P*cueP-gfp*, we did observe any significant differences in P*cusC-gfp* expression between the strains bearing *cueP* and those not (**Figure 3A**). As expected, no fluorescence was detected from the wild-type strain or its Δ*cueP* derivative carrying the p*cusC-gfp* reporter but lacking the whole *cus* locus in their chromosomes, indicating that Cu-dependent induction of the *cusCFBA* promoter requires CusR/CusS (**Supplementary Figure 2**). On the other hand and irrespective of the presence or absence of a functional *cueP* and/or *cus*, no differences in growth were detected in these strains even at 4 mM $CuSO_4$ (**Supplementary Figure 3**), suggesting that the stress caused by the metal ion is managed by the innate aerobic Cu resistance apparatus primarily composed of the CueR- and GolS-dependent CopA, GolT, and CueO factors (Espariz et al., 2007; Pontel and Soncini, 2009; Pontel et al., 2010, 2014).

In view of these results, we decided to analyze the accumulation of CueP-3xFLAG and CusA-3xFLAG in the

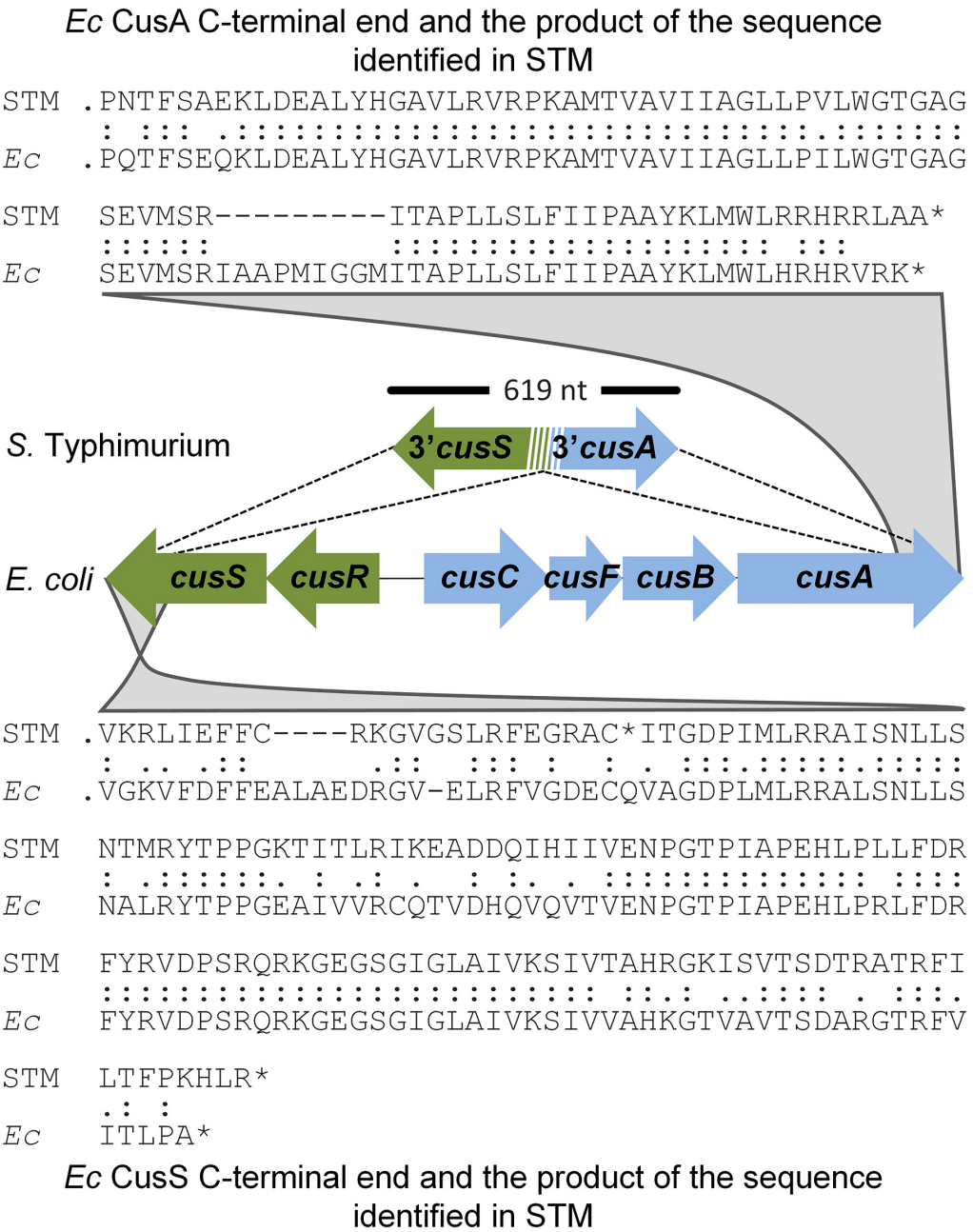

FIGURE 1 | *Cus* remnants in the *Salmonella* Typhimurium chromosome. The figure shows the 619-bp region harboring remnants of the outermost ends of the *cus* locus identified in the *S.* Typhimurium (STM) genome and the homology with the *Escherichia coli (Ec)* CusA and CusS C-termini.

cus+ strain at different time points after Cu exposure to evaluate the effect of the simultaneous presence of both Cu resistance determinants on their reciprocal expression (**Figure 3B** and **Supplementary Figure 4**). Both the wild-type and the *cus*+ Δ*cueP* strain were included as controls. An increased accumulation of CueP-3xFLAG was detected in the otherwise wild-type strain for the first 3–4 h in cells exposed to 2 mM $CuSO_4$ (**Figure 3B**). The maximal concentration reached during that period persisted at least up to 18 h. Interestingly, the tagged protein accumulated to similar levels in cells harboring the *cus* locus during the first 3 h, but a significant reduction was observed at longer times (**Figure 3B**). By contrast, CusA-3xFLAG increased its concentration in the membrane fraction of the recombinant *cus*+ Δ*cueP* strain and reached a maximal level at 3 h. This was followed by a decrease of the immunoreactive band, probably due to degradation of the membrane protein (**Figure 3B** and **Supplementary Figure 4**). Similar to CueP-3xFLAG, a consistent reduction of CusA-3xFLAG was visualized

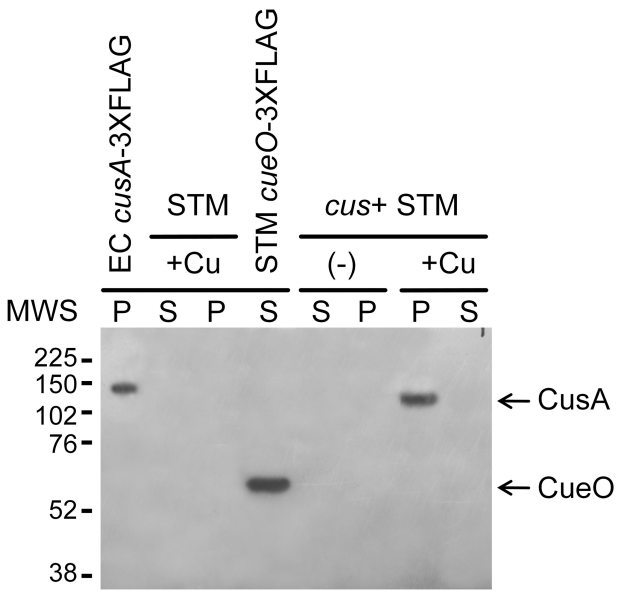

FIGURE 2 | The *cus*+ *Salmonella* Typhimurium strain expresses CusA-3xFLAG in the presence of copper. Western blot analysis of soluble (S) and pellet cell fractions (P) of the transgenic *cus*+ *S*. Typhimurium strain grown overnight in the presence (+Cu) and absence (–) of 2 mM $CuSO_4$. The pellet fraction of the W3110 *cusS*-Cm^R *cusA*:3xFLAG-Km^R *Escherichia coli* strain and the soluble fraction of the *cueO*:3xFLAG *S*. Typhimurium strain were used as positive controls, while the parental *S*. Typhimurium 14028s soluble and insoluble cell fractions were included as negative control. Anti-mouse FLAG monoclonal antibodies were used for the 3xFLAG immunodetection.

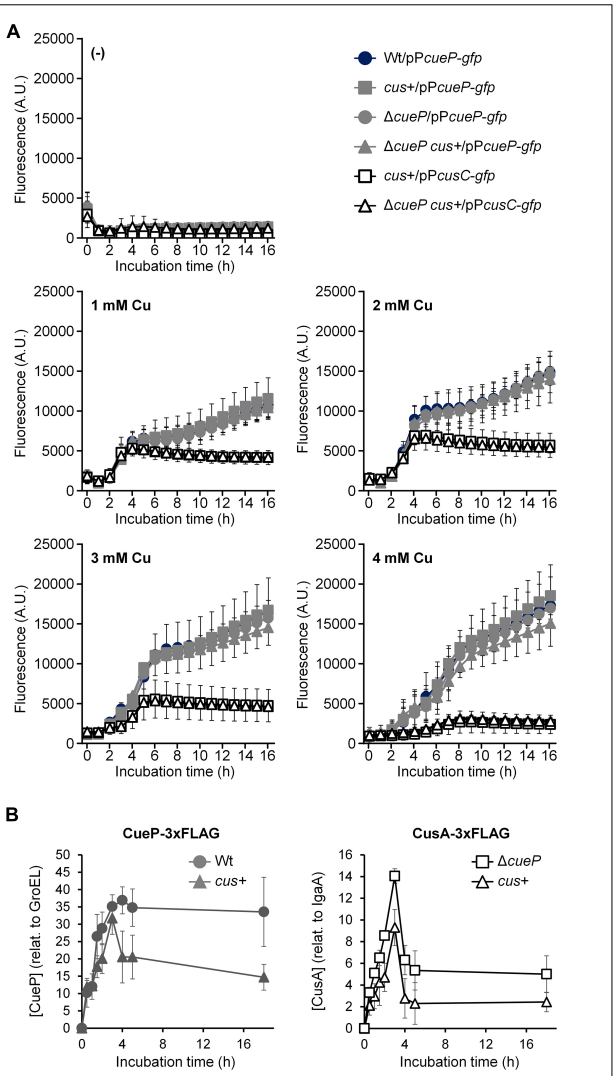

FIGURE 3 | Comparative analysis of the Cu-induced expression of the *cus* locus and *cueP*. **(A)** Kinetic analysis of the Cu-induced fluorescence from the wild type, the *cus*+, the Δ*cueP*, or the Δ*cueP cus*+, harboring *gfp* transcriptional fusions to either P*cueP* or the P*cusC* promoter, as indicated. Either 0, 1, 2, 3, or 4 mM $CuSO_4$ was added to cells exponentially grown in Luria–Bertani broth (LB), and both fluorescence and OD_{600nm} (see **Supplementary Figure 3**) were recorded for 16 h and used to calculate the normalized fluorescence expressed as arbitrary units. The data correspond to mean values of at least three independent experiments performed in duplicate. Error bars represent SD. **(B)** Kinetic analysis of the Cu-induced CueP-3xFLAG or CusA-3xFLAG expression from the *cueP*-3xFLAG (Wt), the *cus*+ *cueP*-3xFLAG *cusA*-3xFLAG (*cus*+), or the *cus*+ *cusA*-3xFLAG Δ*cueP* (Δ*cueP*) strains. Soluble or insoluble extracts from cells grown in LB with the addition of 2 mM $CuSO_4$ were analyzed by SDS/PAGE, followed by transfer to nitrocellulose, and developed using monoclonal anti-FLAG antibodies as described in the Materials and Methods Section. CueP or CusA relative levels were normalized to GroEL or IgaA, respectively. The data correspond to mean values of three independent experiments. Error bars represent SD. A representative western blot is shown in **Supplementary Figure 4**.

in cells also expressing CueP-3xFLAG. This clearly indicates that, at least at the protein level, the simultaneous presence of both components favors a reduction in the quantity of each individual system. In other words, these results are consistent with a functional redundance between the Cus system and the innate *Salmonella* CueP chaperone.

The CusCFBA System Confers Higher Copper Resistance Levels Than CueP in Anaerobiosis

As reported in *E. coli* (Outten et al., 2001), the presence of the *cus* locus in *Salmonella* did not affect Cu resistance under aerobic conditions, even in cells lacking *cueP* (**Supplementary Figure 5** and **Supplementary Table 3**). Because CueO is the main Cu(I) cell envelope detoxification factor when O_2 is available (Espariz et al., 2007), the effect of *cusRS-CFBA* acquisition in *Salmonella* was tested in the Δ*cueO* background, both in the presence and absence of *cueP*. As previously reported for this genetic background (Pontel and Soncini, 2009; Pontel et al., 2010), CueP had only a minimal contribution to Cu tolerance under these conditions (**Supplementary Figure 5**). Surprisingly, the Δ*cueO cus*+ transgenic strain showed an increased resistance to the metal compared to the Δ*cueO* strain (**Supplementary Table 3**). A similar resistance phenotype with the Δ*cueO cus*+ strain was observed for the Δ*cueP*Δ*cueO cus*+ strain (**Supplementary Figure 5**), indicating that CueP has no impact on Cu resistance under these conditions. On the other hand, the presence of *cus* did not increase the Cu tolerance of a *Salmonella* strain deleted of both inner membrane-associated

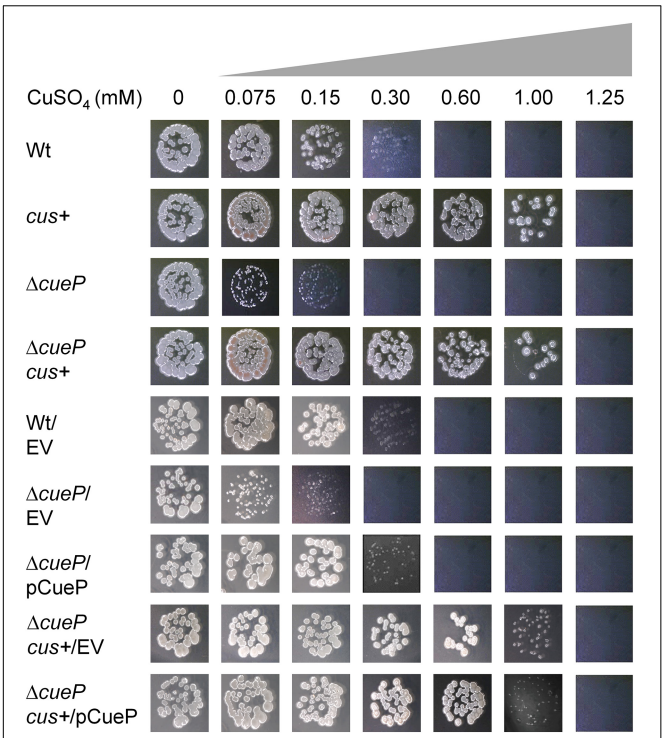

FIGURE 4 | The *Escherichia coli cus* locus increases *Salmonella* tolerance to Cu under anaerobic conditions. Comparative Cu MIC values of wild type (Wt), transgenic *cus*+, Δ*cueP*, or Δ*cueP cus*+ *Salmonella* strains on Luria–Bertani broth plates containing increasing amounts of $CuSO_4$ in anaerobic conditions. The figure also shows the same strains harboring the vector plasmid pUH21-2*lacI*^{q} (EV) or pUH21-2 *lacI*^{q}-based pCueP plasmid (pCueP). After incubation at 37°C for 24 h, the plates were photographed. The data correspond to representative images of at least three independent experiments done in duplicate.

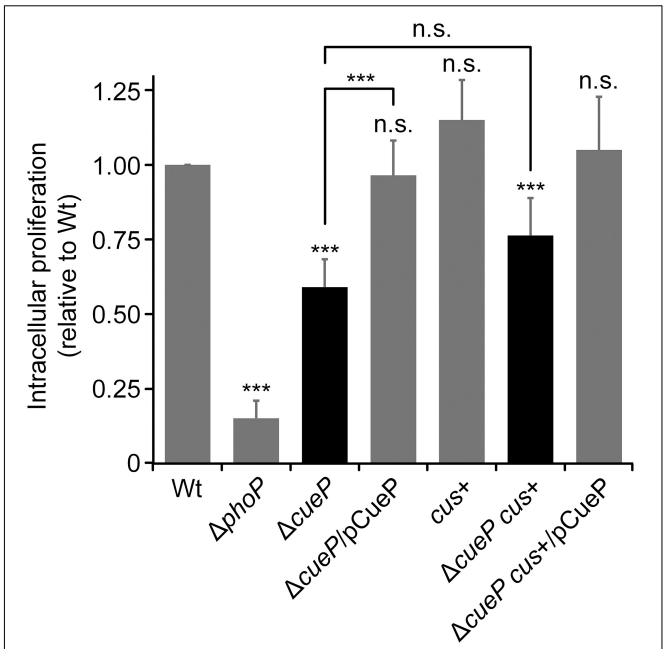

FIGURE 5 | *Cus* cannot substitute *cueP* for intramacrophage proliferation. Replication of wild type (WT), Δ*cueP*, *cus*+, or Δ*cueP cus*+ *Salmonella* Typhimurium strains in RAW 264.7 macrophages at 18 h after infection. The virulence-defective Δ*phoP* strain was included as control. Complementation of Δ*cueP* or Δ*cueP cus*+ strains with pCueP is also shown. The values correspond to the average of at least three independent experiments carried out in duplicate, and the error bars represent SD. The asterisks denote statistical significance between means or with respect to WT. n.s., not significant; ***$P < 0.001$.

Cu(I) transporters *copA* and *golT*-coding genes (**Supplementary Figure 5** and **Supplementary Table 3**), indicating that CusCFBA cannot alleviate the cytoplasmic toxic effect of Cu (Espariz et al., 2007). These results suggest that, despite its low expression under aerobiosis (**Figure 3**), CusCFBA can alleviate the toxic effects of Cu from the cell envelope in cells lacking the main Cu resistance determinant, CueO.

As both CueP and CusCFBA were reported to contribute to Cu resistance under anaerobic conditions (Outten et al., 2001; Pontel and Soncini, 2009), we compared the tolerance to Cu of the transgenic *S.* Typhimurium *cus*+ strain, both in the presence and absence of *cueP* (**Figure 4** and **Supplementary Table 3**). The presence of a functional CusCFBA system increased the Cu tolerance in these conditions up to 1 mM $CuSO_4$, even in the Δ*cueP* strain. These strains were at least three times or six times more resistant than the wild-type strain or the Δ*cueP* mutant (**Figure 4**).

Not only is the CusCFBA system more efficient than CueP to eliminate toxic Cu ions, but also, in its presence, CueP turns non-essential even when it is overexpressed in the cells (**Figure 4**). Thus, why has *Salmonella* lost the beneficial *cus* locus while preserving *cueP*? We can speculate that niches normally encountered by this species would not simultaneously contain such a high Cu concentration and the absence of O_2. Otherwise, the pathogen would retain the ancestral Cu–envelope homeostasis system. The acquired *cueP* gene product could fulfill the necessary metal resistance encountered by *Salmonella* in those particular niches. In this sense, the required co-regulation of *cueP* transcription, recruiting simultaneously the cytoplasmic Cu sensor CueR and the non-specific CpxR/CpxA envelope stress system, integrates different envelope stress signals, such as Cu and redox stress (Pezza et al., 2016; Cerminati et al., 2017; Grabowicz and Silhavy, 2017; Lopez et al., 2018; Subramaniam et al., 2019), that could also be beneficial in these niches.

The Ancestral *Cus* System Does Not Contribute to *Salmonella* Intracellular Macrophage Proliferation

The SCV is known to be enriched in Cu ions and other toxic compounds, such as reactive oxygen/nitrogen species, that are actively delivered or produced by the host cell to eliminate invading pathogen (Negrea et al., 2009; Achard et al., 2010, 2012; Fenlon and Slauch, 2017; Ladomersky et al., 2017; Yucel et al., 2020). Knowing that a mutant deleted in *cueP* has a defect in macrophage proliferation (Yoon et al., 2014) and

in view of the increased tolerance to Cu of the transgenic *S.* Typhimurium *cus*+ strain, we compared the intracellular proliferation of the latter strain with its Δ*cueP* derivative inside RAW 264.7 macrophages (**Figure 5**). As expected, the Δ*cueP* strain exhibited an attenuated phenotype compared to the wild type inside these professional phagocytes, while wild-type proliferation was reestablished by providing *cueP in trans*. The *S.* Typhimurium *cus*+ strain show wild-type levels of macrophage proliferation, indicating that its presence does not provide any advantage for survival in this environment (**Figure 5**) (It is worth noting that this strain harbors its wild-type chromosomal copy of *cueP*).

Surprisingly, the *cus*+ Δ*cueP* strain was as defective as the Δ*cueP* strain to proliferate inside this cell line, indicating that the Cus system cannot substitute CueP for *Salmonella* proliferation inside macrophages (**Figure 5**).

These results altogether indicate that the acquisition of *cueP* by *Salmonella* provides this pathogen with the ability to better replicate inside macrophages, and at the same time, it allows this species to tolerate moderate levels of Cu when facing oxygen limitation and other toxic species, whereas the Cus system cannot. These results indicate that CueP and CusCFBA exert redundant functions for metal resistance, but not for macrophage survival, and therefore for *Salmonella* virulence.

DISCUSSION

It is increasingly evident that, in Gram-negative species, the cell envelope is the primary target for Cu toxicity (Giachino and Waldron, 2020; Checa et al., 2021). It is in this compartment where all known Cu-requiring enzymes, such as multi-copper oxidases, amine oxidases, Cu-dependent superoxide dismutases, and terminal respiratory oxidases, are localized and where Cu-dependent metabolism occurs (Rubino and Franz, 2012; Stewart et al., 2019). Most enteric species rely on the periplasmic multicopper oxidase CueO, controlled by the cytoplasmic sensor/regulator CueR, to maintain the envelope–Cu homeostasis under aerobiosis and on the CusR/CusS-controlled CusCFBA efflux system to get rid of the Cu excess from this compartment when oxygen is absent, a condition in which the oxidase is not active (Outten et al., 2001; Quintana et al., 2017; Checa et al., 2021). We showed that *Salmonella* CueP fulfils similar roles than the *E. coli* CusCFBA system in alleviating Cu stress under anaerobic conditions in their innate bacterial hosts (Pontel and Soncini, 2009; Pontel et al., 2010; Pezza et al., 2016). When overexpressed in *E. coli*, CueP partially complements a Δ*cus* mutant (Pontel and Soncini, 2009), although this periplasmic Cu chaperone with a putative Cu^{2+} reductase activity seems not to be a structural homolog of the CusCFBA system. The transcriptional activation of these Cu resistance determinants also differs but has some common features. The expression of CusCFBA occurs after the detection of surplus Cu by the metal-specific periplasmic sensor, CusS, which, in turn, phosphorylates its coupled cytoplasmic regulator CusR, both encoded within the *cus* locus (Affandi and McEvoy, 2019). *cueP* transcription depends on the simultaneous activation of the cytoplasmic Cu sensor CueR and the envelope stress sensory system CpxR/CpxA that perceives the stress caused by Cu at the bacterial cell envelope (Pezza et al., 2016), mimicking the *E. coli* CusR/CusS-controlled *cusCFBA* induction. We recently showed that *Salmonella* lost the *cus* locus and, at the same time or probably before of that, it gained *cueP* (Checa et al., 2021). However, the reasons that lead to this genetic rearrangement remains unknown.

In this work, we re-introduced the *E. coli cus* locus into the genomic place where ancestral *Salmonella cus* remnants were detected and demonstrated that the *cusCFBA* operon is expressed in response to Cu and provides resistance to this metal to the recombinant strain (**Figures 1–4**). The expression of this operon requires the presence of the CusR/CusS two-component system because no Cu-driven transcriptional induction was detected using the p*PcusC-gfp* plasmid carrying the *gfp* reporter gene under the control of the *cusC* promoter (**Supplementary Figure 2**). Both the indigenous *cueP* gene and the transgenic CusR/CusS-controlled *cusCFBA* operon were transcriptionally induced in response to Cu (**Figures 2**, **3**). However, transcription from the *cueP* promoter remained active over time, even when the bacteria were well into the stationary phase, while the P*cusC* promoter was only transiently induced during the exponential phase (**Figure 3**). In fact, a reduction in expression of both the GFP reporter from the P*cusC-gfp* promoter or CusA-3xFLAG from the chromosomal *cusA*-3xFLAG fusion gene was evident when the bacteria reached the stationary phase. Furthermore, its Cu activation is reduced as the concentration of the metal ion increases in the culture medium. These differences could be attributed by the outcome of the metal ion, although much work is necessary to understand the role of CueP in *Salmonella*. Importantly, the simultaneous presence of both systems influenced the expression of each other (**Figure 3B**), demonstrating that both contribute to alleviate the toxicity caused by the metal ion in the cell envelope when bacteria grow under standard laboratory conditions.

The *cus*+ *Salmonella* transgenic strain shows wild-type resistance to Cu under aerobic conditions and an increased resistance to Cu under anaerobic conditions (**Supplementary Table 3**), where the multicopper oxidase CueO is inactive (Espariz et al., 2007; Pontel et al., 2010). A similar phenotype was observed in Δ*cueO* cells grown aerobically (**Supplementary Figure 5**) that are highly sensitive to Cu, with an exacerbated envelope stress under these conditions (Pontel et al., 2010). This is in agreement with recent *Salmonella* isolates from Cu rich environments that harbor accessory Cu resistance determinants such as Cus-like efflux pumps as well as P-type ATPases and/or periplasmic copper binding proteins encoded in plasmids as well as in other mobile genetic platforms (Mourão et al., 2016; Mastrorilli et al., 2018; Murase et al., 2018; Zhao et al., 2018; Arai et al., 2019; Branchu et al., 2019). Among them, an extrachromosomally encoded *cus* locus was present in clinic isolates (Wiesner et al., 2016). The plasmid harboring this locus also contains genes for tolerance/resistance to mercury, arsenic, and other metals and antimicrobials, indicating a link between metal and antibiotic resistance as well. The importance of these

accessory Cu resistance determinants to ameliorate *Salmonella* fitness in animals that are exposed to large amounts of copper as feed supplement is clear (Mourão et al., 2015, 2016; Branchu et al., 2019). However, their relevance for virulence and, in particular, for intracellular replication of the pathogen is elusive and a matter of current investigation in different laboratories.

In contrast to the conserved arrangement of inner membrane P-type transporters and cytoplasmic Cu chaperones present in all proteobacteria to cope with Cu toxicity in the cytoplasm, different species/strains evolved specific traits to control envelope–Cu homeostasis (Giachino and Waldron, 2020). Particularly for *Salmonella*, this compartment is the main receptor for all the recent horizontally acquired genetic elements encoding Cu resistance factors (Checa et al., 2021). In this work, we showed that, at least for macrophage survival, *cueP* acquisition into the *Salmonella* genome cannot be substituted by the ancestral *cus* locus (**Figure 5**). Although the contribution of the efflux pump to Cu resistance in abiotic environments is clear, particularly under anaerobic conditions (**Figure 4**), it does not favor fitness in the Cu-rich, oxidative intracellular niche (**Figure 5**). Based on these, it can be speculated that the loss of *cus* from this pathogen occurred because there was no selection pressure to keep it, as *Salmonella* would rarely encounter high levels of Cu in an anoxygenic environment. Alternatively, the presence of an efflux pump in the confined space of the SCV is disfavored because the expelled toxic Cu ions rapidly re-enter the bacterial cell, resulting in a futile cycle. Therefore, in this intracellular niche, CueP Cu^{2+} binding (Osman et al., 2010) or its proposed Cu^{2+} reductase activity (Yoon et al., 2014) limits the availability of free Cu ions to exacerbate redox stress in the periplasm (Checa et al., 2021). In this context, the role of CueP as a Cu chaperone providing the metal ion to other ROS-detoxifying enzymes like SodCI and SodCII (Ladomersky et al., 2017) would be also important. In either case, it is clear that the *cueP* gene product was preserved during the evolution of *Salmonella*. Therefore, it emerges as a putative target for anti-virulence therapies to control animal and human salmonellosis.

DATA AVAILABILITY STATEMENT

The original contributions presented in the study are included in the article/**Supplementary Material**, further inquiries can be directed to the corresponding authors.

AUTHOR CONTRIBUTIONS

SC and FS contributed to the conception and design of the study. AM, JM, ME, and IT performed the experiments and analyzed the results. AM, JM, SC, and FS wrote the first draft of the manuscript, contributed to manuscript revision, and read the submitted version. All authors contributed to the article and approved the submitted version.

FUNDING

This work was supported by the Agencia Nacional de Promoción Científica y Tecnológica (under grant PICT-2018-02122) and by the National Institutes of Health (under grant R01GM114949). SC and FS were career investigators of CONICET and FS was also a career investigator of the Rosario National University Research Council.

ACKNOWLEDGMENTS

We thank Ursula Astrid Fels for the technical assistance during the initial steps of this work.

SUPPLEMENTARY MATERIAL

The Supplementary Material for this article can be found online at: https://www.frontiersin.org/articles/10.3389/fmicb.2022.823176/full#supplementary-material

REFERENCES

Abriata, L. A., Pontel, L. B., Vila, A. J., Dal Peraro, M., and Soncini, F. C. (2014). A dimerization interface mediated by functionally critical residues creates interfacial disulfide bonds and copper sites in CueP. *J. Inorg. Biochem.* 140, 199–201. doi: 10.1016/j.jinorgbio.2014.07.022

Achard, M. E., Stafford, S. L., Bokil, N. J., Chartres, J., Bernhardt, P. V., Schembri, M. A., et al. (2012). Copper redistribution in murine macrophages in response to *Salmonella* infection. *Biochem. J.* 444, 51–57. doi: 10.1042/BJ20112180

Achard, M. E., Tree, J. J., Holden, J. A., Simpfendorfer, K. R., Wijburg, O. L., Strugnell, R. A., et al. (2010). The multi-copper-ion oxidase CueO of *Salmonella enterica* serovar Typhimurium is required for systemic virulence. *Infect. Immun.* 78, 2312–2319. doi: 10.1128/IAI.01208-09

Affandi, T., and McEvoy, M. M. (2019). Mechanism of metal ion-induced activation of a two-component sensor kinase. *Biochem. J.* 476, 115–135. doi: 10.1042/BCJ20180577

Alikhan, N.-F., Zhou, Z., Sergeant, M. J., and Achtman, M. (2018). A genomic overview of the population structure of *Salmonella*. *PLoS Genet.* 14:e1007261. doi: 10.1371/journal.pgen.1007261

Arai, N., Sekizuka, T., Tamamura, Y., Kusumoto, M., Hinenoya, A., Yamasaki, S., et al. (2019). *Salmonella* genomic island 3 is an integrative and conjugative element and contributes to copper and arsenic tolerance of *Salmonella enterica*. *Antimicrob. Agents Chemother.* 63:e00429-19. doi: 10.1128/AAC.00429-19

Besold, A. N., Culbertson, E. M., and Culotta, V. C. (2016). The Yin and Yang of copper during infection. *J. Biol. Inorg. Chem.* 21, 137–144. doi: 10.1007/s00775-016-1335-1

Borkow, G., and Gabbay, J. (2005). Copper as a biocidal tool. *Curr. Med. Chem.* 12, 2163–2175. doi: 10.2174/0929867054637617

Branchu, P., Bawn, M., Kingsley, R. A., and Andrews-Polymenis, H. L. (2018). Genome variation and molecular epidemiology of *Salmonella enterica* serovar Typhimurium pathovariants. *Infect. Immun.* 86:e00079-18. doi: 10.1128/IAI.00079-18

Branchu, P., Charity, O. J., Bawn, M., Thilliez, G., Dallman, T. J., Petrovska, L., et al. (2019). SGI-4 in monophasic *Salmonella* Typhimurium ST34 is a novel ICE that enhances resistance to copper. *Front. Microbiol.* 10:1118. doi: 10.3389/fmicb.2019.01118

Cerminati, S., Giri, G. F., Mendoza, J. I., Soncini, F. C., and Checa, S. K. (2017). The CpxR/CpxA system contributes to *Salmonella* gold-resistance by controlling

the GolS-dependent gesABC transcription. *Environ. Microbiol.* 19, 4035–4044. doi: 10.1111/1462-2920.13837

Checa, S. K., Espariz, M., Audero, M. E., Botta, P. E., Spinelli, S. V., and Soncini, F. C. (2007). Bacterial sensing of and resistance to gold salts. *Mol. Microbiol.* 63, 1307–1318. doi: 10.1111/j.1365-2958.2007.05590.x

Checa, S. K., Giri, G. F., Espariz, M., Argüello, J. M., and Soncini, F. C. (2021). Copper handling in the *Salmonella* cell envelope and its impact on virulence. *Trends Microbiol.* 29, 384–387.

Djoko, K. Y., and McEwan, A. G. (2013). Antimicrobial action of copper is amplified via inhibition of heme biosynthesis. *ACS Chem. Biol.* 8, 2217–2223. doi: 10.1021/cb4002443

Echarren, M. L., Figueroa, N. R., Vitor-Horen, L., Pucciarelli, M. G., García-Del Portillo, F., and Soncini, F. C. (2021). Balance between bacterial extracellular matrix production and intramacrophage proliferation by a *Salmonella*-specific SPI-2-encoded transcription factor. *Mol. Microbiol.* 116, 1022–1032. doi: 10.1111/mmi.14789

Eng, S.-K., Pusparajah, P., Ab Mutalib, N.-S., Ser, H.-L., Chan, K.-G., and Lee, L.-H. (2015). *Salmonella*: a review on pathogenesis, epidemiology and antibiotic resistance. *Front. Life Sci.* 8, 284–293. doi: 10.1080/21553769.2015.1051243

Espariz, M., Checa, S. K., Audero, M. E., Pontel, L. B., and Soncini, F. C. (2007). Dissecting the *Salmonella* response to copper. *Microbiology* 153, 2989–2997.

Fang, F. C., Degroote, M. A., Foster, J. W., Baumler, A. J., Ochsner, U., Testerman, T., et al. (1999). Virulent *Salmonella typhimurium* has two periplasmic Cu, Zn-superoxide dismutases. *Proc. Natl. Acad. Sci. U.S.A.* 96, 7502–7507. doi: 10.1073/pnas.96.13.7502

Fenlon, L. A., and Slauch, J. M. (2017). Cytoplasmic copper detoxification in *Salmonella* can contribute to SodC metalation but is dispensable during systemic infection. *J. Bacteriol.* 199:e00437-17. doi: 10.1128/JB.00437-17

Franke, S., Grass, G., Rensing, C., and Nies, D. H. (2003). Molecular analysis of the copper-transporting efflux system CusCFBA of *Escherichia coli*. *J. Bacteriol.* 185, 3804–3812. doi: 10.1128/JB.185.13.3804-3812.2003

Fung, D. K., Lau, W. Y., Chan, W. T., and Yan, A. (2013). Copper efflux is induced during anaerobic amino acid limitation in *Escherichia coli* to protect iron-sulfur cluster enzymes and biogenesis. *J. Bacteriol.* 195, 4556–4568. doi: 10.1128/JB.00543-13

Giachino, A., and Waldron, K. J. (2020). Copper tolerance in bacteria requires the activation of multiple accessory pathways. *Mol. Microbiol.* 114, 377–390. doi: 10.1111/mmi.14522

Grabowicz, M., and Silhavy, T. J. (2017). Envelope stress responses: an interconnected safety net. *Trends Biochem. Sci.* 42, 232–242. doi: 10.1016/j.tibs.2016.10.002

Grass, G., Rensing, C., and Solioz, M. (2011). Metallic copper as an antimicrobial surface. *Appl. Environ. Microbiol.* 77, 1541–1547. doi: 10.1128/AEM.02766-10

Karlinsey, J. E. (2007). λ—Red genetic engineering in *Salmonella enterica* serovar Typhimurium. *Methods Enzymol.* 421, 199–209.

Ladomersky, E., Khan, A., Shanbhag, V., Cavet, J. S., Chan, J., Weisman, G. A., et al. (2017). Host and pathogen copper-transporting P-type ATPases function antagonistically during *Salmonella* infection. *Infect. Immun.* 85:e00351-17. doi: 10.1128/IAI.00351-17

Le Brun, N. E. (2014). "Copper in prokaryotes," in *Binding, Transport and Storage of Metal Ions in Biological Cells. RSC Metallobiology Series No. 2*, eds W. Maret and A. Wedd (Cambridge: RSC Publishing), 461–499.

Lopez, C., Checa, S. K., and Soncini, F. C. (2018). CpxR/CpxA controls *scsABCD* transcription to counteract copper and oxidative stress in *Salmonella enterica* serovar Typhimurium. *J. Bacteriol.* 200:e00126-18. doi: 10.1128/JB.00126-18

Macomber, L., and Imlay, J. A. (2009). The iron-sulfur clusters of dehydratases are primary intracellular targets of copper toxicity. *Proc. Natl. Acad. Sci. U.S.A.* 106, 8344–8349. doi: 10.1073/pnas.0812808106

Mastrorilli, E., Pietrucci, D., Barco, L., Ammendola, S., Petrin, S., Longo, A., et al. (2018). A comparative genomic analysis provides novel insights into the ecological success of the monophasic *Salmonella* serovar 4,[5],12:i. *Front. Microbiol.* 9:715. doi: 10.3389/fmicb.2018.00715

Mourão, J., Marçal, S., Ramos, P., Campos, J., Machado, J., Peixe, L., et al. (2016). Tolerance to multiple metal stressors in emerging non-typhoidal MDR *Salmonella* serotypes: a relevant role for copper in anaerobic conditions. *J. Antimicrob. Chemother.* 71, 2147–2157. doi: 10.1093/jac/dkw120

Mourão, J., Novais, C., Machado, J., Peixe, L., and Antunes, P. (2015). Metal tolerance in emerging clinically relevant multidrug-resistant *Salmonella enterica* serotype 4,[5],12:i:– clones circulating in Europe. *Int. J. Antimicrob. Agents* 45, 610–616.

Murase, T., Ozaki, H., Phuektes, P., and Angkititrakul, S. (2018). Genotypic and phenotypic characterization of *Salmonella enterica* subsp. *enterica* serovar Typhimurium monophasic variants isolated in Thailand and Japan. *J. Vet. Med. Sci.* 80, 1839–1846. doi: 10.1292/jvms.18-0510

Negrea, A., Bjur, E., Puiac, S., Ygberg, S. E., Åslund, F., and Rhen, M. (2009). Thioredoxin 1 participates in the activity of the *Salmonella enterica* serovar Typhimurium pathogenicity island 2 type III secretion system. *J. Bacteriol.* 191, 6918–6927.

Osman, D., Patterson, C. J., Bailey, K., Fisher, K., Robinson, N. J., Rigby, S. E., et al. (2013). The copper supply pathway to a *Salmonella* Cu,Zn-superoxide dismutase (SodCII) involves P(1B)-type ATPase copper efflux and periplasmic CueP. *Mol. Microbiol.* 87, 466–477. doi: 10.1111/mmi.12107

Osman, D., Waldron, K. J., Denton, H., Taylor, C. M., Grant, A. J., Mastroeni, P., et al. (2010). Copper homeostasis in *Salmonella* is atypical and copper-CueP is a major periplasmic metal complex. *J. Biol. Chem.* 285, 25259–25268. doi: 10.1074/jbc.M110.145953

Outten, F. W., Huffman, D. L., Hale, J. A., and O'halloran, T. V. (2001). The independent *cue* and *cus* systems confer copper tolerance during aerobic and anaerobic growth in *Escherichia coli*. *J. Biol. Chem.* 276, 30670–30677. doi: 10.1074/jbc.M104122200

Pérez Audero, M. E., Podoroska, B. M., Ibáñez, M. M., Cauerhff, A., Checa, S. K., and Soncini, F. C. (2010). Target transcription binding sites differentiate two groups of MerR-monovalent metal ion sensors. *Mol. Microbiol.* 78, 853–865. doi: 10.1111/j.1365-2958.2010.07370.x

Pezza, A., Pontel, L. B., Lopez, C., and Soncini, F. C. (2016). Compartment and signal-specific codependence in the transcriptional control of *Salmonella* periplasmic copper homeostasis. *Proc. Natl. Acad. Sci. U.S.A.* 113, 11573–11578. doi: 10.1073/pnas.1603192113

Pontel, L. B., Checa, S. K., and Soncini, F. C. (2015). "Bacterial copper resistance and virulence," in *Bacteria-Metal Interactions*, ed. D. Saffarini (Basel: Springer International Publishing), 1–19. doi: 10.1007/978-3-319-18570-5_1

Pontel, L. B., Pezza, A., and Soncini, F. C. (2010). Copper stress targets the rcs system to induce multiaggregative behavior in a copper-sensitive *Salmonella* strain. *J. Bacteriol.* 192, 6287–6290. doi: 10.1128/JB.00781-10

Pontel, L. B., Scampoli, N. L., Porwollik, S., Checa, S. K., Mcclelland, M., and Soncini, F. C. (2014). Identification of a *Salmonella* ancillary copper detoxification mechanism by a comparative analysis of the genome-wide transcriptional response to copper and zinc excess. *Microbiology* 160, 1659–1669. doi: 10.1099/mic.0.080473-0

Pontel, L. B., and Soncini, F. C. (2009). Alternative periplasmic copper-resistance mechanisms in Gram negative bacteria. *Mol. Microbiol.* 73, 212–225. doi: 10.1111/j.1365-2958.2009.06763.x

Quintana, J., Novoa-Aponte, L., and Arguello, J. M. (2017). Copper homeostasis networks in the bacterium *Pseudomonas aeruginosa*. *J. Biol. Chem.* 292, 15691–15704. doi: 10.1074/jbc.M117.804492

Rubino, J. T., and Franz, K. J. (2012). Coordination chemistry of copper proteins: how nature handles a toxic cargo for essential function. *J. Inorg. Biochem.* 107, 129–143. doi: 10.1016/j.jinorgbio.2011.11.024

Stewart, L. J., Thaqi, D., Kobe, B., Mcewan, A. G., Waldron, K. J., and Djoko, K. Y. (2019). Handling of nutrient copper in the bacterial envelope. *Metallomics* 11, 50–63. doi: 10.1039/c8mt00218e

Subramaniam, S., Muller, V. S., Hering, N. A., Mollenkopf, H., Becker, D., Heroven, A. K., et al. (2019). Contribution of the Cpx envelope stress system to metabolism and virulence regulation in *Salmonella enterica* serovar Typhimurium. *PLoS One* 14:e0211584. doi: 10.1371/journal.pone.0211584

Tan, G., Yang, J., Li, T., Zhao, J., Sun, S., Li, X., et al. (2017). Anaerobic copper toxicity and iron-sulfur cluster biogenesis in *Escherichia coli*. *Appl. Environ. Microbiol.* 83:e00867-17. doi: 10.1128/AEM.00867-17

Wiesner, M., Calva, J. J., Bustamante, V. H., Perez-Morales, D., Fernandez-Mora, M., Calva, E., et al. (2016). A multi-drug resistant *Salmonella* Typhimurium ST213 human-invasive strain (33676) containing the bla CMY-2 gene on an

IncF plasmid is attenuated for virulence in BALB/c mice. *BMC Microbiol.* 16:18. doi: 10.1186/s12866-016-0633-7

Yoon, B.-Y., Kim, Y.-H., Kim, N., Yun, B.-Y., Kim, J.-S., Lee, J.-H., et al. (2013). Structure of the periplasmic copper-binding protein CueP from *Salmonella enterica* serovar Typhimurium. *Acta Crystallogr. Sect. D Struct. Rep. Online* 69, 1867–1875. doi: 10.1107/S090744491301531X

Yoon, B. Y., Yeom, J. H., Kim, J. S., Um, S. H., Jo, I., Lee, K., et al. (2014). Direct ROS scavenging activity of CueP from *Salmonella enterica* serovar Typhimurium. *Mol. Cells* 37, 100–108. doi: 10.14348/molcells.2014.2238

Yucel, B., Robinson, G. K., and Shepherd, M. (2020). The copper-responsive ScsC protein of *Salmonella* promotes intramacrophage survival and interacts with the arginine sensor ArtI. *FEBS J.* 287, 3827–3840. doi: 10.1111/febs.15285

Zhao, H., Chen, W., Xu, X., Zhou, X., and Shi, C. (2018). Transmissible ST3-IncHI2 plasmids are predominant carriers of diverse complex IS26-class 1 integron arrangements in multidrug-resistant *Salmonella*. *Front. Microbiol.* 9:2492. doi: 10.3389/fmicb.2018.02492

Conflict of Interest: The authors declare that the research was conducted in the absence of any commercial or financial relationships that could be construed as a potential conflict of interest.

Publisher's Note: All claims expressed in this article are solely those of the authors and do not necessarily represent those of their affiliated organizations, or those of the publisher, the editors and the reviewers. Any product that may be evaluated in this article, or claim that may be made by its manufacturer, is not guaranteed or endorsed by the publisher.

Advantages of publishing in Frontiers

OPEN ACCESS
Articles are free to read for greatest visibility and readership

FAST PUBLICATION
Around 90 days from submission to decision

HIGH QUALITY PEER-REVIEW
Rigorous, collaborative, and constructive peer-review

TRANSPARENT PEER-REVIEW
Editors and reviewers acknowledged by name on published articles

Frontiers
Avenue du Tribunal-Fédéral 34
1005 Lausanne | Switzerland

Visit us: www.frontiersin.org
Contact us: frontiersin.org/about/contact

REPRODUCIBILITY OF RESEARCH
Support open data and methods to enhance research reproducibility

DIGITAL PUBLISHING
Articles designed for optimal readership across devices

FOLLOW US
@frontiersin

IMPACT METRICS
Advanced article metrics track visibility across digital media

EXTENSIVE PROMOTION
Marketing and promotion of impactful research

LOOP RESEARCH NETWORK
Our network increases your article's readership